University of Antwerp
Particle Physics Group

Search for sterile neutrinos in the eV and MeV mass range with the SoLid detector

Author:
MAJA VERSTRAETEN

Promotor:
PROF. DR. NICK VAN REMORTEL

Thesis submitted in order to obtain the degree of
Doctor in Sciences: Physics

Antwerp, 4 October 2021

Acknowledgements

I wish to express my gratitude to professor Nick Van Remortel for opening the gates to the marvelous world of neutrino physics. Thank you for granting me the opportunity to perform curiosity driven research with the SoLid collaboration. You have been an outstanding coach. You've encouraged me to get out there and challenge myself. In particular when you allowed me to give a preconference lecture at the university of Havana. It was an incredible experience and learning opportunity. Thank you for proofreading and cross checking my thesis, for which I also want to thank Roland Van der Elst.

It was a pleasure and a privilege to work with my wonderful colleagues in our SoLid office. Yamiel, you were not only my mentor but a great friend. You know you have been my rock when times were tough. You are the kindest. Simon and I agree that "everyone should be more like Yamiel, then the world would be a happier place". Simon, I loved doing research with you. I feel like we understand each other and we can discuss and progress together. Let us continue having some 'rum after work' with our high energy physics group.

Thank you to all members of the SoLid collaboration for working as a team on this challenging endeavour, especially to Benoit, David, Valentin, Noé, Daniel, Nick, Giel, Ibrahin, and Ianthe, with whom I worked intensively. I keep fond memories of the fun we had along the way.

I was able to push my limits because I knew I could always fall back on my loving family. Mama, papa, Jonas, Marie, Emma. When returning from some conference or meeting, for which I had gone above and beyond again, it was the best to be welcomed home by all of you and have some frietjes together. Even though you did not always understand everything, you wanted to know what I was doing, you supported me and you were proud of me. You instilled a scientific curiosity and creativity in me ever since I was a little girl.

Sometimes you need a break from all the sciencing. Luckily my friends (especially from the sea-scouts) are always in for a good time, having a laugh, talking nonsense. I have to thank you for keeping me sane. And also for being there for me through whatever life throws on my way, especially to Bente, Gideon, Jonas, Anke, Joris, Jente and also Julie, Sara and Sophia.
Thank you Sibylle, Wout, Jesse and Jonathan for making our student time so much more manageable, interesting and fun. If I could, I would do it all again.

I don't think about it that often anymore, but my deepest gratitude goes to Dr Jacqueline Conings and Dr Veronique Block. I owe you my life. It looked like nothing of this was ever going to happen, but now I'm here, living my dream.

Saving the best for last, I am grateful to have found my partner in crime, my safe haven, the one that makes me smile, Domien. Even during lockdown we were living in our little personal paradise. I love how books and notes with formulas are scattered around our place and science is everywhere. That's the dream.

Enjoy the read,
Maja

Abstract

University of Antwerp

Department of High Energy Physics

Maja Verstraeten

The discovery of neutrino oscillations exposed the need for physics beyond the Standard Model. The neutrinos' behaviour could be explained with additional neutrino states. Different anomalies in a range of neutrino experiments gave rise to the hypothesis of a new sterile neutrino mass state with $\Delta m^2 \sim 1\text{eV}^2$. The SoLid experiment will investigate flavor oscillations into the new state by measuring the dependence of the $\overline{\nu}_e$ flux to a distance -and energy range, with a 1.6 ton, highly segmented detector at very short baseline of 6-9 m from the compact core of the 60 MW BR2 reactor of the Belgian Nuclear Research Center SCK-CEN. In addition, we will investigate the sensitivity of the SoLid detector to probe heavier sterile neutrinos (HNL) in the mass range of 1-10 MeV, by detecting their decay products. This search will be a complementary new physics analysis, in addition to the search for eV-scale oscillations, that extends the BSM program of SoLid without detector modifications. To accomplish the challenging measurement in the high radiation environment - close to the nuclear reactor core and at the earth's surface - an innovative, hybrid scintillator technology was developed, combining Poly-Vinyl Toluene and ^{6}LiF:ZnS(Ag) scintillators into a unit cell of $5\times5\times5$ cm^3, in order to reach the necessary particle identification and energy reconstruction. More than ten thousand of these unit cells make up the detector, which is read out by a network of wavelength shifting fibers and MPPCs. In order to validate the detector operation and to understand and predict the signal of the reactor neutrinos and of the various background sources, a full simulation framework was established. The present thesis describes how the simulation of the detector readout is developed and fine-tuned. The simulation models the energy response of the detector, converting the energy deposits of passing particles to data-like output signals. This covers the photon generation and transport, the sensor response, the construction of digital waveform signals, the trigger operation and the signal readout with zero suppression. The implemented models are based on calibration measurements, detector data taken during reactor on and off periods, dedicated testbenches and specifications from manufacturers. The simulated neutrino and background events are used by the collaboration to construct selection requirements and train the Machine Learning model. For the oscillation analysis, currently a signal excess of 90 ± 22.8 IBD events per day can be reached, with a rather low signal-to-background ratio of 1:5. The full oscillation analysis is expected this year. For the HNL analysis, the sensitivity study indicates that we have the potential to put more stringent exclusion limits on the HNL parameter space in the low mass range than the previous laboratory experiments, namely Bugey and Triumf.

Nederlandse samenvatting

Zoektocht naar steriele neutrino's in het eV en MeV massa bereik met de SoLid detector

Met het Standaardmodel (SM) van de deeltjesfysica kan men ongelooflijk nauwkeurige en accurate voorspellingen doen over de waarnemingen in onze experimenten. Omdat alleen linkshandige neutrino's worden waargenomen door de zwakke interacties, werd deze geformuleerd als een chirale ijktheorie in het Standaardmodel. Door de afwezigheid van rechtshandige neutrino's werden in het Standaardmodel de neutrino's gepostuleerd als massaloze deeltjes. Toen men rond 1970 in staat was de flux van neutrino's uit de zon en de atmosfeer te meten, ontdekte men dat neutrino's van flavour kunnen veranderen. Deze neutrino-oscillatie wordt aangedreven door een massaverschil tussen de neutrino-eigentoestanden, wat impliceert dat de neutrino's toch een massa hebben die niet nul is. Om de massaterm te genereren, kunnen neutrino's met een rechtshandige chiraliteit worden toegoevoegd aan het SM. De rechtshandige neutrino's, als ze bestaan, hebben geen interactie via de natuurkrachten die ons bekend zijn en worden daardoor steriel genoemd.

Hoeveel verschillende steriele neutrino-eigentoestanden in ons universum bestaan en welke massa's zij hebben, is niet geweten. De steriele neutrino's kunnen eigenschappen hebben, die de open vragen in de fysica beantwoorden, zoals waarom ons universum vooral materie bevat, en wat de werkelijke aard is van donkere materie die lijkt bij te dragen aan de massa-inhoud van het universum. Ook de massa van de neutrino's en waarom deze veel kleiner is dan die van de geladen leptonen, kan verklaard worden met de steriele neutrino's in de zogenaamde Seesawmodellen.

Afwijkingen in een reeks neutrino-experimenten leidden tot de hypothese van een steriele neutrino massa-eigentoestand met $\Delta m^2 \sim 1$ eV^2. In dit proefschrift onderzoeken we mogelijke flavour oscillaties naar deze nieuwe eigentoestand met het SoLid experiment. SoLid staat voor "Search for Oscillations with a Lithium-6 detector" en is een neutrino-experiment op zeer korte afstand (6-9 m) van de kern van de Belgische BR2 reactor van het Studiecentrum voor Kernenergie SCK-CEN. We gebruiken een innovatieve, hybride scintillatortechnologie, waarbij de eenheidscel van de detector een polyvinyltolueen scintillator bevat in combinatie met een ^{6}LiF:ZnS(Ag) scherm in een volume van $5 \times 5 \times 5$ cm^3. Meer dan tienduizend van deze eenheidscellen vormen de detector, die wordt uitgelezen door een netwerk van fibers en sensoren die gevoelig zijn aan afzonderlijke fotonen. De hoge segmentatie van het detectievolume van 1.6 ton, samen met een hoge positie en energieresolutie, maakt het mogelijk om de verdwijningskans van reactorantineutrino's te onderzoeken aan de hand van hun IBD interactie in de detector over een bereik van afstand (L) en energie (E). De waarschijnlijkheid tot oscillatie van een actief naar een steriel neutrino wordt bepaald door de eigenschappen van het neutrino en is zichtbaar over L/E.

Daarnaast wordt in dit proefschrift de gevoeligheid van de SoLid detector onderzocht voor zwaardere steriele neutrino's (heavy neutral leptons, HNL) door hun vervalproducten te detecteren. Kosmologische waarnemingen met betrekking tot HNL met massa's van minder dan 100 MeV en experimenten gericht op HNL in het GeV massabereik, hebben geen signaal gevonden en delen van de parameterruimte van de HNL reeds uitgesloten. Met SoLid onderzoeken we HNL met massa's tussen 1-10 MeV

bij een kernreactor, wat voor het laatst werd gedaan in 1995 bij de Franse Bugey reactor. Het Borexino experiment stelde ook grenzen aan dit massabereik op basis van metingen van zonneneutrino's.

De metingen gebeuren in een omgeving met veel straling, dicht bij de kernreactor en aan het aardoppervlak, wat veel achtergrond geeft tegenover het signaal van de neutrino's. Het SoLid experiment vereist fundamenteel inzicht in de productie, interactie en detectie van de reactorneutrino's en van de verschillende achtergrondbronnen. Bovendien moet de werking van de detector worden gevalideerd. Hiervoor werd een reeks van simulaties ontwikkeld. Eerst wordt op basis van de samenstelling en verdeling van de splijtstof in de reactor, de flux en het spectrum van de antineutrino's gesimuleerd voor elke reactorcyclus. Vervolgens worden de deeltjes voor de signaal- en achtergrondbronnen gegenereerd en gepropageerd door de experimentele site. De energie-afzettingen van de deeltjes in gevoelige detectorcomponenten worden ingevoerd in de zogenaamde readout simulatie.

Dit proefschrift is in het bijzonder gewijd aan hoe ik de simulatie van het readoutsysteem heb ontwikkeld en verfijnd. De simulatie modelleert de energierespons van de detector, waarbij de energieafzettingen van passerende deeltjes worden omgezet in signalen zoals deze van de eigenlijke detector. Dit omvat de generatie en het transport van scintillatiefotonen, de respons en interne werking van de sensoren, de constructie van digitale signalen, de werking van het triggersysteem en het uitlezen van het signaal waarbij verwaarloosbare samples worden onderdrukt met een variabele drempelwaarde voor de amplitude. Het gesimuleerde signaal heeft hetzelfde formaat als de gegevens, waardoor het met dezelfde software kan worden geanalyseerd. De verschillende modellen die werden gebruikt in de simulatie zijn opgesteld aan de hand van kalibratiemetingen, metingen met proefopstellingen, specificaties aangeleverd door de producenten van de detectorcomponenten en data die is gemeten gedurende periodes waarin de reactor uit was en die geselecteerd is op basis van de random trigger waardoor deze enkel ruis bevat.

Vergelijkingen tussen de echte data en de gesimuleerde data toonde aan dat de kalibratiemetingen en de resultaten van de verschillende achtergrondanalyses goed worden gereproduceerd door de simulatie. Dit geeft ons vertrouwen dat de gesimuleerde neutrino events een goede voorspelling zijn van het detectorsignaal. De gesimuleerde neutrino- en achtergrond events worden gebruikt om de neutrinoselectie op te stellen en de Machine Learning-modellen te trainen. Er blijft enige discrepantie bestaan in de gereconstrueerde energie van snelle neutronen met kosmische oorsprong, wat waarschijnlijk te wijten is aan het wegvallen van detectorkanalen tijdens de metingen, wat niet werd geimplementeerd in de simulatie.

Voor de analyse van oscillaties naar steriele neutrino's met een massa van $\mathcal{O}$(eV), beschouwt men de overschot van neutrino-achtige (IBD) gebeurtenissen, wanneer men het geslecteerde signaal vergelijkt tussen periodes waarin de reactor aan en uit staat. Momenteel kan een overschot van 90 ± 22.8 IBD gebeurtenissen per dag bereikt worden, met een vrij lage verhouding van signaal ten opzichte van achtergrond van 1:5. Het resultaat van een volledige oscillatie-analyse wordt dit jaar verwacht.
Voor iedere reactorcyclus kan het overschot aan IBD signaal worden vergeleken met de voorspelling van de overeenkomstige simulatie, waarbij oscillatie naar steriele neutrino's kan worden toegepast met verschillende oscillatieparameters. Deze analyse maakt het mogelijk om te beoordelen of de steriele neutrinohypothese een geschikt model biedt voor de geregistreerde resultaten.

Voor de analyse van het HNL verval werd een voorlopige selectie opgesteld. Voor een koppelingsparameter tussen het reactorantineutrino en de HNL van 10^{-4}, wat iets zwakker is dan de sterkste limieten aangeven, wordt een HNL signaal van $\mathcal{O}$(mHz) voorspeld door de simulatie. Op basis van de verwachte gevoeligheid met 90 % zekerheid in de HNL parameterruimt, kan de limiet van het Bugey-experiment worden bereikt en worden overschreden voor een HNL massa onder 4 MeV. Wat betreft laboratoriumexperimenten hebben we het potentieel om strengere limieten op te leggen aan de HNL parameterruimte in het lage massabereik.

Smooth seas never made a skilled sailor

CONTENTS

INTRODUCTION

Physicists have established a firm understanding of the Universe, which culminated in the Standard Model of Particle Physics - the rigorous theory of charges and interactions that is incredibly precise and accurate in its predictions. But are we there yet? Or is there more to life? Are there hidden sectors in the cosmos that we do not know about yet? After all, even our Standard Model can describe merely 5 % of what the Universe is made of.

One thing that the particles of the Standard Model have in common is that they all communicate with one another. More precisely, they communicate with the particles that we are made of and they generate signals in our measuring instruments. However, it is possible, even probable, that we are surrounded and permeated by a whole realm of additional particles. Particles that are completely unbothered by our presence and pass right through us. Although these covert particles might not communicate with the traditional particles of the Standard Model, they could interact among themselves, forming larger structures of their own.

It gets even more exciting in case these mysterious particles do have an ever so small influence on the Standard Model particles. Then they could leave a tiny imprint on the quantities that are accessible in our experiments. And they might answer open questions in physics such as the nature of dark matter or the baryon asymmetry of the Universe. Whenever physicists find a discrepancy between theoretical predictions and experimental observations, attention rises. It might lead the way to physics Beyond the Standard Model. The neutrino sector is rich in anomalies and little understood phenomena. Gaining knowledge about the properties of neutrinos could open the portal to undiscovered particles, forces and laws of nature.

The discovery of neutrino oscillations indicated that neutrinos have non-zero masses, which was the first evidence of physics beyond the Standard Model that postulated neutrinos as massless particles. The neutrinos are known to be orders of magnitude lighter than the charged leptons, which might be related to new physics, as proposed by the see-saw models [1]. To introduce the relevant mass term in the Lagrangian, new interactions or new particle states are required. This could be in the form of light sterile neutrinos or heavier neutral leptons. These possibilities have triggered a vibrant experimental program world-wide that has made rapid progress in the last years. Whereas the search for heavy neutral leptons was motivated by theoretical considerations, the quest for light sterile neutrinos was rather experimentally motivated because of several observed anomalies.

In the present thesis, we will investigate the possible signature of $\mathcal{O}$(eV) sterile neutrinos and $\mathcal{O}$(MeV) heavy neutral leptons in the Phase I data of the SoLid detector. SoLid is a very short-baseline neutrino experiment at the Belgian BR2 reactor of the nuclear research center SCK-CEN. Our main objective is to resolve the so-called reactor antineutrino anomaly and to investigate the existence of sterile neutrinos in light of the anomaly. The detector design and the experimental site will be described in chapters 5 and 6.

Within the collaboration, I was the sole responsible for the simulation of the detector readout. The readout simulation is specific to SoLid and reproduces the detector response, in terms of the photon production and collection, and by modelling the signal as produced by the sensors and readout electronics. The trigger system and readout logic from the data acquisition is emulated in detail as well. The implementation of the readout simulation is described in chapter 13. I obtained the relevant models and parameters from reactor off data, results from test benches and calibration data, which are described in chapters 6 and 9.

The readout simulation is a central component in the chain of simulation codes. The expected interactions in the SoLid detector are simulated with the GEANT4 toolkit [2], as described in chapter 12. The relevant features of the simulated energy deposits are fed into the readout simulation that translates them to data-like output waveforms. The simulated signal has the same format as the actual detector data and can be analysed with SoLid's analysis software, which is described in chapter 8.

In order to approach the visible detector signal accurately, I tuned the different algorithms of the readout simulation. In order to reproduce the signal inhomogeneities from the highly segmented detector, I got involved with the calibration effort, where I pinpointed the variations between the numerous detector cells and channels, as described in section 9.3. To resolve the many issues and discrepancies that arose during implementation and tuning of the readout simulation, I required insight in the various aspects that contribute to the observed signal. My urge for information and the fact that I had to collaborate with various working groups of our collaboration, is reflected by the size of this thesis. I wrote this text over the course of my research. This gave me a clear overview of what I had, what was still needed and what had to be done next. Throughout, I provided updates of the text to the collaboration, to give them insight in the contents and working of the readout simulation and to provoke feedback.

The performance of the readout simulation is demonstrated by the data versus Monte-Carlo comparisons for the calibration measurements at the end of chapter 14 and for the background analysis in chapter 15. This makes us confident that the simulated neutrino events properly predict our signal and can be used to construct the neutrino selection cuts and train the Machine Learning models, as described in chapter 16.

After completion of the simulation effort, I teamed up with some colleagues to perform a sensitivity study for the decay of heavy neutral leptons (HNL) in the MeV mass range within the SoLid detector, which will be described in chapter 18. Since the main background components were known and properly simulated and the data are readily available, this seemed a straight forward study. However, the gamma ray background is not dominant for the sterile neutrino analysis, but problematic for the HNL analysis. I produced new gamma ray simulations and made a background model for the reactor off data in the HNL selection region. Additional work is needed to model the reactor on data. The expected sensitivity to investigate HNL decay in the SoLid detector is determined for the preliminary cut analysis.

Before we proceed to the SoLid experiment, we dive into neutrino physics. After a historical introduction, the neutrino's appearance in the Standard Model is described in chapter 1. The discovery of neutrino oscillations takes us in chapter 2 beyond the Standard Model. In chapter 4 several unresolved

neutrino anomalies emerge, that point towards the existence of an additional, sterile neutrino state.

During my Phd, I did not want to just develop a simulation for the SoLid experiment. I wanted to be part of the neutrino physics community and learn all about the fascinating neutrino sector. I gave talks for conferences and outreach events regarding neutrinos, the SoLid experiment and elementary particle physics. I covered for example the history of the neutrino discovery, the interplay of neutrino research and the development of the atomic bomb and the structure of matter. It was difficult to contain my enthusiasm in the following chapter.

So, down the rabbit hole we go.

1

NEUTRINOS IN THE STANDARD MODEL

Neutrinos are as mysterious as they are abundant; every second, billions of them are passing harmlessly through every inch of the earth's surface. However, neutrinos pass through most matter unnoticed, travelling through our globe without a single collision. Neutrinos interact only via the weak force, which leaves them hard to detect experimentally and makes them the least understood particles of the Standard Model of Particle Physics. Despite enormous experimental progress, the nature and the fundamental properties of neutrinos remain largely unknown: What are the actual values of neutrino masses (absolute mass scale and mass hierarchy)? Why are neutrino masses many orders of magnitude smaller than any other fermion mass in the Standard Model? Are neutrinos their own antiparticles? Is the CP symmetry violated in lepton mixing? What are the precise values of the mixing angles and why is lepton mixing so much different than quark mixing? Are there observable deviations from the standard three-neutrino picture?

However, this cosmic passer-by can provide us information from otherwise unaccessible regions in space like the interior of stars or supernovas. The elusive neutrino could help us unravel some of the universe's most fascinating mysteries, like the excess of matter over anti-matter after the big bang. It is important to understand the neutrinos properly. But each time we think we have a conclusive model to describe the neutrinos, they act in unexpected ways. Neutrinos have puzzled scientists for years and they keep on puzzling us today.

1.1 THE DISCOVERY OF THE NEUTRINO

The neutrino enters the stage in 1914 as a tremendous problem regarding nuclear beta decay. A radioactive nucleus can emit an electron (a beta ray) and decrease its positive charge by one unit to become the nucleus of another element. The electrons were expected to have the same energy, as the atom moves a place on the periodic table of elements, resulting in a well defined energy shift. However, the measurements from James Chadwick [3] showed that the emitted electrons are distributed over a continuous spectrum of energies, as shown on the left panel in figure 1.1.1. Some of the energy released in the decay process was lost, putting the esteemed law of energy conservation into question.

Only in 1930, Pauli came up with a desperate way out [4]. He suggested a yet-to-be-discovered particle was emitted along with the electron, that carried away the missing energy. The new particle caused more questions than it gave answers. If it came out of the atom, it must have been in there. The approximate mass of the atom and of its constituents were known and in agreement, so Pauli suggested the new particle has virtually no mass. Since the particle was never measured, Pauli proposed it is neutral. The hypothetical particle was later dubbed neutrino by Enrico Fermi; Italian for little neutral one. Later in life, Pauli felt guilty about postulating a particle that could not be measured.

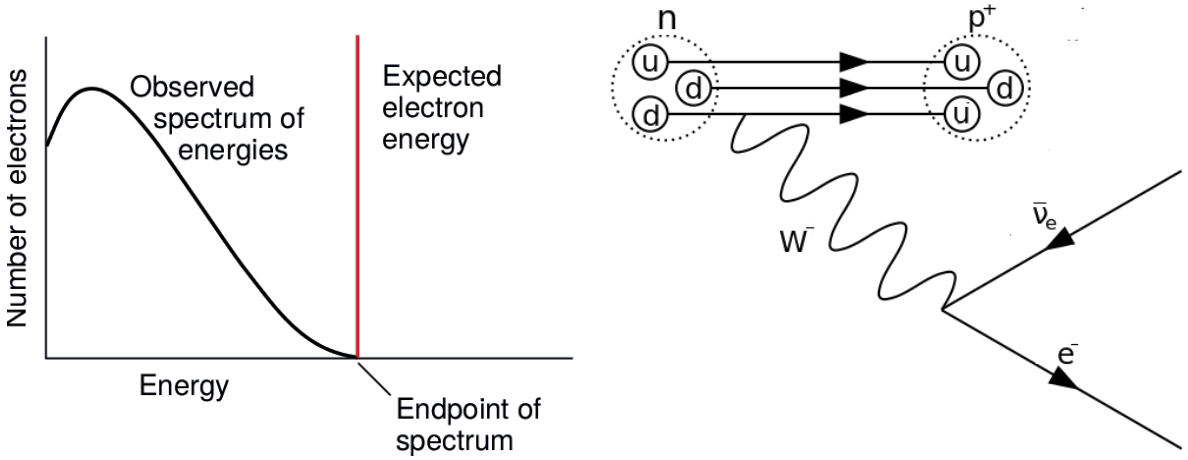

Figure 1.1.1: Left: Expected and observed energy spectrum of electrons emitted in beta decay. Right: β^- decay of a proton, including the new particle $\overline{\nu}_e$.

Finally, in 1933 Enrico Fermi incorporated the neutrino in his theory [5], that would become the precursor of the electroweak theory from Glashow [6], Weinberg [7] and Salam [8] in the 1970s. Fermi linked the neutrino riddle with other open questions of the time. In the 20 years since his measurement of the β spectrum, Chadwick had discovered the neutron. The atomic nucleus is made up of protons and neutrons and scientists wondered whether they had a deeper connection. Fermi proposed a neutron can change into a proton, upon emission of an electron and an anti-electron-neutrino. Conversely, a proton conversion into a neutron, is accompanied by an emitted positron and electron neutrino. Fermi's theory explained β decay by a four-fermion interaction, involving a contact force with no range. Later the theory was updated, as shown on the right panel of figure 1.1.1, with finite range force carriers, the $W^{\pm}$ and Z bosons. The neutrino had found a logical and necessary place in the theories of physics.
Fermi's theory was revolutionary, because the electron and neutrino pop into existence out of thin air. They were not initially inside the nucleus. Elementary particles were no longer merely hard spheres that can collide, but they can interact, disappear and appear. When Fermi submitted his theory to the journal Nature, they did not want to publish it because it contained speculations that were too remote from physical reality to be of any interest to the reader [9].

The neutrino had to be experimentally detected to confirm the theory. The neutrino being massless, chargeless, and weakly interacting, made it nearly impossible to detect. In 1951 Cowan and Reines took on this challenge and started project Poltergeist [10]. Looking at all possible interactions the weak theory predicted (which will be discussed in chapter 1.5), they decided to exploit the inverse beta decay, which is shown in the left panel of figure 1.1.2. The interaction's cross section was estimated by Bethe and Peierls around 10^{-44} cm^2 [11]. The interaction is so unlikely that the detection requires an intense neutrino source and a large detector target. Since Cowan and Reines worked at the Manhattan Project [12], their initial idea was to use the neutrino flux from an atomic weapon's test detonation [10]. However, they would only have one chance to measure a neutrino and an atomic bomb was not detonated every day. During the Manhattan Project, Fermi and Szilard managed to control the nuclear fission reaction and built the first nuclear reactor [13].

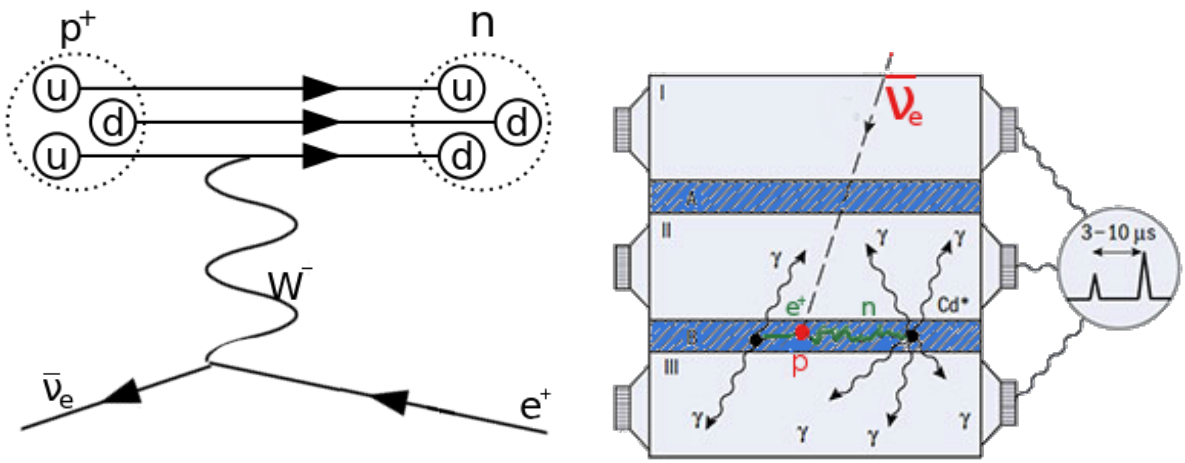

Figure 1.1.2: Left: Inverse beta decay, where a W^- boson exchanges a negative weak charge between weak currents, converting the upquark into a downquark and the $\bar{\nu}_e$ into a positron. Right: Diagram of the experiment carried out by Cowan and Reines at the Savannah River reactor. The blue layers A and B represent the water acting as target and moderator. I, II and III are the liquid scintillator volumes, read by photon multiplier tubes. The expected signal consists of a prompt and delayed peak. [10]

Cowan and Reines built a detector at the Savannah River Nuclear Reactor [10], that gave a stable neutrino flux of 5×10^{13} s^{-1} cm^{-2}. The detector consisted of water tanks interlaced with liquid scintillator, as shown in the right panel of figure 1.1.2. A neutrino can undergo inverse beta decay (IBD) interaction with a proton in the water. This yields a positron that will annihilate into gammas, and a neutron that will be captured by Cd, dissolved in the water, which also emit gammas. The respective gamma rays scintillate with a characteristic time difference, which results in a distinct IBD signal with a signal to background ratio of 3/1. In 1956, Cowan and Reines succeeded in establishing the neutrino experimentally [14]. This was the long awaited unambiguous proof of the existence of the neutrino and the confirmation of Fermi's weak theory. Sadly, Fermi had passed away two years earlier at the age of 53. Cowan and Reines were able to share this discovery with Pauli. When Pauli received the news, he answered by telegram [15]:

Thanks for message. Everything comes to him who knows how to wait. Pauli

1.2 THE STANDARD MODEL OF PARTICLE PHYSICS

The Standard Model of particle physics [16] is the deepest and most comprehensive physical description of our universe to date. It describes three of the four fundamental interactions (gravity not included) between elementary particles, encoded in the compact description of the Lagrangian. About 50 years ago, between 1961 and 1973, the theoretical foundation was developed as a quantum field theory, based on only three symmetries and a symmetry breaking. This is supplemented by experimental knowledge, which cannot be determined a priori by theory. For example, which and how many building blocks of matter (fermions with half-integer spin) exist, is not part of the theoretical structure, but an experimental finding that was included in the Standard Model.

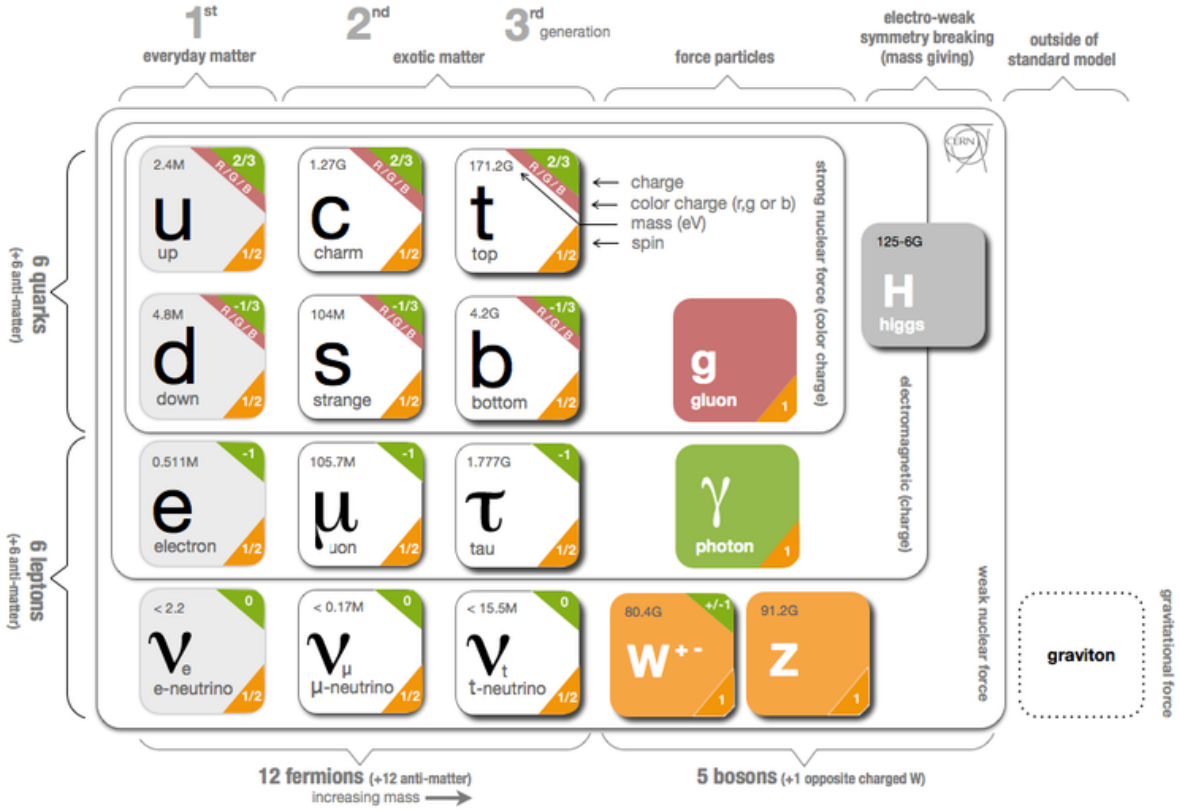

Figure 1.2.1: Diagram of the Standard Model particles, showcasing many of the relevant parameters and characteristics of the particles and their interactions.

This elegant theory sorts elementary particles according to their respective charges, describes how they interact based on symmetry principles, and predicts which messenger particles (bosons with integer spin) convey these interactions [17]. Particles with an electric charge are influenced by the electromagnetic interaction, that is mediated by the photon (γ), which is described by quantum electrodynamics (QED). Particles with a weak charge are influenced by the weak interaction[1], that is mediated by the weak boson (W^+, W^-, Z^0), which is described together with QED in the overarching electroweak theory (EW). Particles with a colour charge are influenced by the strong interaction, mediated by the gluons (g), as described by quantum chromodynamics (QCD). An elementary particle can be influenced by more than one fundamental interaction if it has several types of charges.

QED is responsible for most types of chemistry, and electrodynamic phenomena. In addition, EW is responsible for particle decays and QCD is what binds quarks together into protons and neutrons and what holds the latter together in atomic nuclei. Contrary to the fields associated with the fundamental interactions, the Higgs field is a scalar field. It induces spontaneous symmetry-breaking, which gives mass to all particles it interacts with.

1 To be more exact, the weak interaction influences particles via their weak isospin, T. The third component of the weak isospin, T_3 , is conserved by all SM interactions. In the framework of the electroweak theory, the weak isospin and electromagnetic charge are combined in a property called weak hypercharge, $Y_W = 2(Q - T_3)$ [16].

Within the Standard Model, a neutrino (ν) is a fermion that has no electric charge and no colour charge. The neutrino interacts only via the weak force, which has a very short range (and via gravity, which is extremely weak at particle scale). Therefore, neutrinos typically pass through normal matter unimpeded and undetected. In the 60's, when the Standard Model was proposed, neutrinos were believed to be massless. Therefore, the Standard Model was formulated as a gauge chiral theory in which the neutrino fields have only the left-handed component $\nu_{\alpha L}$. In this way neutrinos are massless, because Dirac mass terms in the Lagrangian require the existence of the right-handed components,

$$\mathscr{L}_D = -m_D(\overline{\psi}_R\psi_L + \overline{\psi}_L\psi_R).$$

The Standard Model of particle physics has a large predictive power and passed numerous precise tests. The biggest success was the verification of the Brout-Englert-Higgs field by ATLAS and CMS at CERN's Large Hadron Collider in 2012 [18, 19]. However, the Standard Model is far from being a complete description of the universe. It describes only 5% of the universe, namely visible matter, while it can not explain dark matter, which accounts for approximately 25% of the universe, or dark energy, which supposedly adds the remaining 70% of the universe. Their description can only be achieved by theories which go beyond the Standard Model of particle physics (BSM).
Moreover, the Standard Model itself is far from being completely understood. The absence of a quantum description for gravity leaves open the quest for a single Theory of Everything [20]. And why are many Standard Model parameters theoretically unexplained? Why are there three replicated generations of elementary particles? Why do some particles have masses while others do not and how do these masses arise? Why is there an excess of matter over anti-matter?

Any signs of irregularities between the predictions of the Standard Model and experimental results spark tremendous excitement. Such as the recent sign of lepton universality breaking in decays of B quarks at LHC-b [21] or the latest measurement of the anomalous magnetic dipole moment of a muon, referred to as the $g-2$ value, at Fermilab [22]. This would enable the physics community to update and modify the current description of nature. The neutrino sector is rich of such irregularities.

1.3 NEUTRINO FLAVORS

Neutrinos participate in weak interactions in one of three leptonic flavors, namely electron neutrinos (ν_e), muon neutrinos (ν_μ), or tau neutrinos (ν_τ). The neutrinos interact in association with the corresponding charged lepton. The latter allows identification of the neutrino flavor, as the neutrino is never observed directly. Each neutrino flavor is considered an elementary particle.

Although Cowan and Reines didn't know at the time, they had actually discovered the electron antineutrino, associated with the electron. In 1962, the muon neutrino was discovered at the Brookhaven National Laboratory [23]. With their AGS accelerator, that was the most powerful in the world at the time, they produced pion showers that decayed into muons and ν_μ. The former were stopped by a steel wall, while the ν_μ interacted with aluminium plates. This neutrino interaction produced only muons, which proved the ν_μ as distinct particles.
The tau neutrino was discovered last of the leptons, only in 2000 at Fermilab [24]. With their Tevatron accelerator, they produced charmed mesons, that decay into tauons and ν_τ. In very rare cases one of

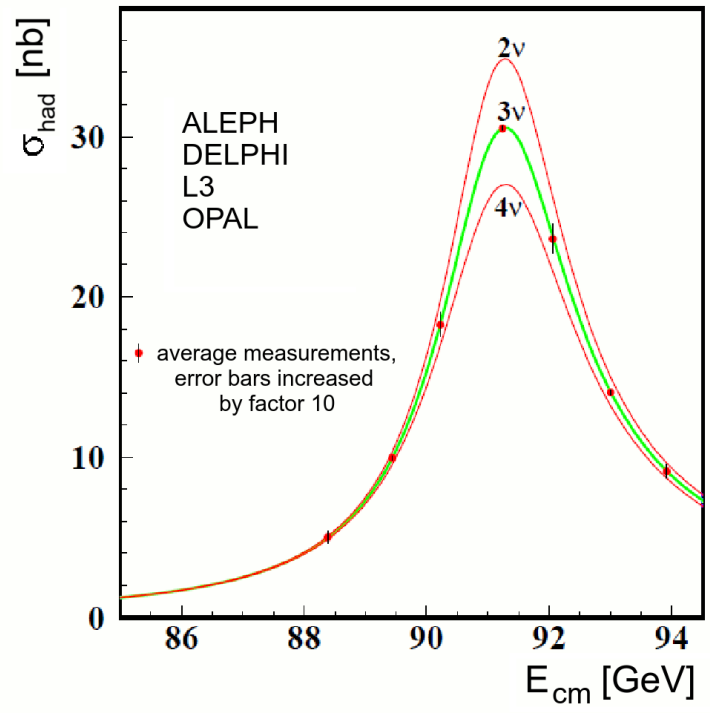

Figure 1.3.1: Expected Z width for different numbers of neutrino types. The measurements indicate the Z boson couples to 3 types of neutrino flavors.[25]

the neutrinos would interact in the DONUT detector, producing electrically charged particles which left visible tracks in emulsion sheets. Discovery of the ν_τ was claimed by observing only four events, but was generally accepted because a lepton doublet for the τ particle was expected.

Already in 1989, it was demonstrated that exactly three types of light, weakly interacting neutrinos are expected. This was determined by the Large Electron-Positron (LEP) collider through the measurement of the width of the mass spectrum of the Z boson [25]. The number of available decay channels influences the lifetime and therefore the width of the Z-resonance. Figure 1.3.1 shows that the curve corresponding to 3 neutrino flavors matches the data best.

1.4 NEUTRINO SOURCES

There are many neutrino sources in the universe, either astrophysical or terrestrial, where the latter are either natural or man made. Neutrinos are produced in nuclear fusion and fission processes and in radioactive decays. The spectrum of neutrinos (and antineutrinos) that are incident on earth spans over 28 orders of magnitude in energy [26], and is shown in figure 1.4.1. Here, the sources relevant for this thesis are described in more detail.
The solar neutrinos, shown in yellow, originate in the nuclear fusion processes in the sun. All solar neutrinos are ν_e and can provide direct insight about the core of our sun. Whereas photons take on average 4000 years to travel from the core to the sun's surface [27], neutrinos are able to escape right away. Observation of solar neutrinos caused the solar neutrino problem (see section 2.1).

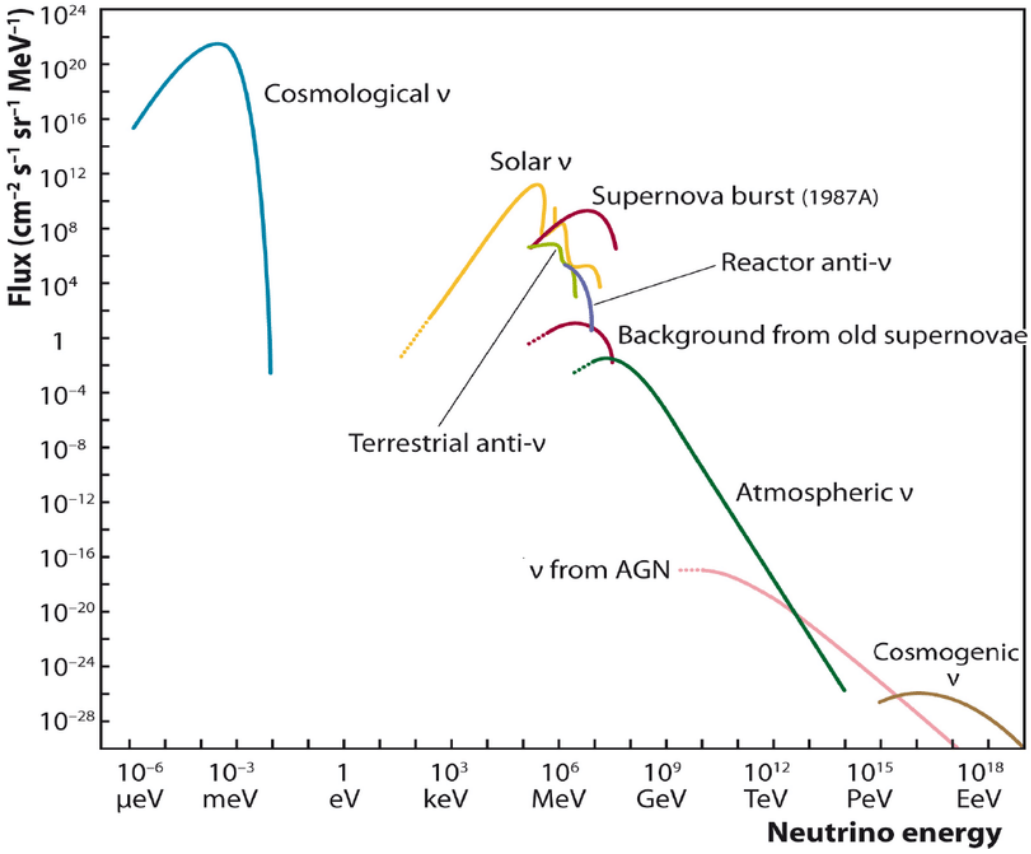

Figure 1.4.1: Fluxes of different terrestrial and cosmic neutrino sources, covering a large range of neutrino energies. [26]

The atmospheric neutrinos, shown in dark green, are typically produced around 15 kilometers above earth's surface, when a cosmic ray interacts with nuclei in our atmosphere. This creates short-lived pions that decay into ν_μ and muons, which decay in turn into an electron, another ν_μ and a $\overline{\nu}_e$ (or the anti matter equivalent),

$$\pi^+ \longrightarrow \mu^+ + \nu_\mu \longrightarrow (e^+ + \overline{\nu}_\mu + \nu_e) + \nu_\mu.$$

Measurements of the atmospheric neutrinos lead, among others, to the discovery of neutrino oscillations (see section 2.2).

Reactor anti neutrinos, shown in purple, are of special interest to us. The fission processes in the reactor fuel result in $\overline{\nu}_e$. Their energy is limited to $\mathcal{O}(10)$ MeV because they are produced by nuclear decays. Reactors are useful for oscillation studies, as they emit a large flux of a single neutrino flavor and the detector can be positioned at a range of distances from the source, called short-, middle-, or long-baseline experiments. Different oscillation parameters have been measured at nuclear reactors most notably the θ_{13} mixing angle between mass states 1 and 3 (see section 2.5.1).

Another man made neutrino source are particle accelerators. Accelerated protons are smashed into a target, such as beryllium, creating pions, $\pi^\pm$. The polarity of a focusing horn allows to select positive or negative pions, which will decay respectively in neutrinos and antineutrinos. Accelerators provide

intense neutrino beams, typically of muon flavor, and the detectors can be positioned again over a wide range. Accelerators were used for the discovery of ν_μ [23] and ν_τ [24] and still provide a powerful tool in neutrino research.

Neutrinos coming from other sources are also studied by physicists with a large variety of neutrino detectors. The neutrinos hardly interact, which makes them outstanding messengers. Cosmological relic neutrinos [28] could give us a glimpse at the state of the universe seconds after the Big Bang. Terrestrial neutrinos [29] from the earth's interior can give us insight in the formation and composition of our planet. Neutrinos from supernovas and other cosmic sources can carry information from the most violent places in the universe directly to us. Sometimes, the cosmic neutrinos can be traced back to their source [30] [31] [32]. Moreover, since neutrinos escape more quickly than light, neutrino observatories will be the first to detect exceptional phenomena. Many neutrino detectors are connected through the Supernova Early Warning System (SNEWS) [33], which will alert experiments to record additional signals such as cosmic rays, gravitational waves, and electromagnetic radiation, to study cosmic phenomena with multi-messenger astronomy.

1.5 NEUTRINO INTERACTIONS

Neutrino interactions are described in the framework of the electroweak theory. The Standard Model description of electroweak interactions [34] is a quantum field theory based on the invariance under the group $SU(2)_L \times U(1)_Y$ of local gauge symmetry transformations. The subscript L indicates that the *SU(2)* transformations operate on the left-handed chiral components of the fields [2]. The electroweak theory was described as a chiral theory because all neutrinos were observed as left handed in the experiment from Goldhaber et al. [35].
Every four-component fermion field Ψ can be split into its left and right chiral components, $\Psi_L + \Psi_R$, with $\Psi_L \equiv (1-\gamma_5)\Psi/2$ and $\Psi_R \equiv (1+\gamma_5)\Psi/2$, with the 4×4 matrix γ_5 defined in terms of the four Dirac γ matrices ($\gamma_5 \equiv i\gamma_0\gamma_1\gamma_2\gamma_3$), such that $\gamma_5^2 = 1$. A chiral gauge theory as the Standard Model of electroweak interactions is formulated in terms of the separate left and right chiral components of the fermion fields.

The neutrino interactions can be mediated by one of the charged $W^\pm$ bosons or by the neutral Z^0 boson, corresponding respectively to the charged (CC) and neutral (NC) current interactions. The weak interactions are observed to conserve lepton number and lepton flavor, which allows to distinguish the neutrino flavor by detecting the corresponding charged lepton. In addition, the weak interactions have to conserve charge and weak isospin.

Charged Current interactions are transferred by weak bosons [16] that have an electric charge, indicated by their exponent, and a weak isospin of $T_{3,W^+} = +1$, $T_{3,W^-} = -1$ and $T_{3,Z} = 0$. This means that in CC interactions, one unit of electrical charge and one unit of weak isospin is exchanged apart from energy and momentum.

2 The subscript Y denotes the weak hypercharge. Only after the Higgs field spontaneously breaks the symmetry, the third generator of $SU(2)_L$ (the weak isospin) and the weak hypercharge result in the description of the electromagnetic interactions by the group $U(1)_{em}$ [34].

Left handed (LH) fermions have a weak isospin of $\pm\frac{1}{2}$. By convention, electrically charged fermions are assigned a T_3 with the same sign as the electric charge. Up-type quarks (u, c, t) have $T_3 = +\frac{1}{2}$ while down-type quarks (d, s, b) have $T_3 = -\frac{1}{2}$. Similarly, charged leptons (e^-, μ^-, τ^-) have $T_3 = -\frac{1}{2}$ and neutrinos (ν_e, ν_μ, ν_τ) have $T_3 = +\frac{1}{2}$. Right handed (RH) fermions (and left handed anti-fermions) have $T_3 = 0$. For antiparticles, the reasoning is always reversed.

Considering the conservation laws of the weak interaction and the particles' charges, in the quark sector, the up-type quarks are always transformed into down-type quarks and vice versa by weak CC interactions. The probability of flavor conversion between the quarks is contained in the Cabibbo-Kobayashi-Maskawa (CKM) matrix [36, 37].

In the lepton sector, the LH leptons exist as doublets under the weak interaction, containing a charged lepton and its respective neutrino.

$$\begin{pmatrix}\nu_e\\ e^-\end{pmatrix}_L \qquad \begin{pmatrix}\nu_\mu\\ \mu^-\end{pmatrix}_L \qquad \begin{pmatrix}\nu_\tau\\ \tau^-\end{pmatrix}_L \tag{1.1}$$

The RH fermions form charged lepton singlets, $l_{\alpha,R}$ with $\alpha \in \{e, \mu, \tau\}$, under the weak interaction and do not undergo CC interactions.

Neutral Current interactions that are mediated by the Z boson can cause any two fermions in the standard model to deflect, although the strength of the interaction differs. The NC interactions couple to both chiralities of charged leptons (LH and RH), but stronger to the LH than the RH ones. The neutrino coupling to the Z boson involves only left handed chiralities.

The CC and NC interactions can be elastic, inelastic, or quasi elastic. If the kinetic energy is conserved in the center-of-mass frame, the interaction is elastic. Otherwise, the reaction is called inelastic. This happens for example when the target breaks apart or goes into an excited state. When a CC interaction causes the particles to change flavor, but does not otherwise change their energy inelastically, this is called quasi-elastic scattering.

The fact that only the left-handed components of particles (and right-handed components of antiparticles) participate in weak CC interactions in the Standard Model, implies that there is no symmetry under the parity transformation. The parity transformation transforms a physical phenomenon into its mirror image (all LH particles are replaced by RH particles and vice versa). Although parity is conserved in electromagnetism, strong interactions and gravity, it is violated in weak interactions. The Standard Model incorporates parity violation by expressing the weak interaction as a chiral gauge interaction. Parity violation was experimentally observed in the β decay of ^{60}Co by Chien-Shiung Wu, as proposed by her theoretical colleagues Lee and Yang [38]. A year later, Goldhaber demonstrated that neutrinos violate parity maximally [35]. He demonstrated that only left handed neutrinos occur, by observing the helicity of the decay products of ^{152}Eu.

1.6 NEUTRINO INTERACTION CROSS SECTIONS

The total neutrino cross section is dominated by different interactions for different energy ranges [39]. Figure 1.6.1 illustrates this for lower and higher energy ranges. Already with very low energy, the

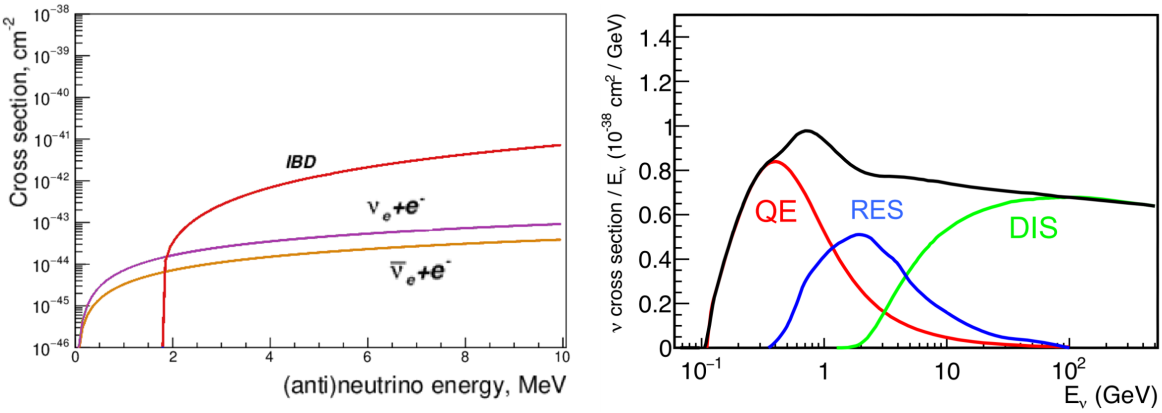

Figure 1.6.1: Neutrino cross sections for different interactions over a broad energy range.[41, 39]

neutrinos can diffract on leptons through a NC interaction. This process has no interaction threshold. Note that for ν_e, the CC interaction contributes as well to this process, which increases the overall cross section. At high energy (> 100 MeV), this reaction is used by Cherenkov detectors. Likewise, the neutrinos can diffract on nuclei, which will cause a small core recoil. This reaction, initially proposed in 1977, was observed for the first time in 2017 by the COHERENT collaboration [40].

The energy range of about 2 MeV to 1 GeV, is dominated by quasi-elastic scattering (QE), where the involved nucleus changes but does not break up. The inverse beta decay process is an example of such a scattering. It has a threshold of 1.806 MeV, due to the mass difference between the reactants (ν_e and p) and the products (e^+ and n). This process was observed by Reines and Cowan as they first detected a neutrino signal (see section 1.1). The SoLid experiment probes this specific channel (see section 6.1). QE scatterings with higher generation flavors require a higher energy threshold for the creation of the corresponding lepton. These CC reactions are very interesting experimentally since they allow to reconstruct the flavor of the incoming neutrino from the flavor of the outgoing lepton.

Around 1 GeV, the total cross section has contributions from multiple processes. The neutrino can excite the nucleon to a baryonic resonance (RES), leading to a single pion production. This is an important regime, as many experiments operate at this range (MINIBOONE [42], MINOS [43] and MINERVA [44]). For neutrino energies above 5 GeV, the deep inelastic scattering (DIS) regime opens up. The energetic neutrino will break the nucleon into fragments, causing hadronic showers.

All the processes listed in this part are predicted by the Standard Model, and the measured cross sections are systematically in agreement with the theory. The neutrino cross sections are small over a wide energy range. The knowledge of the σ_ν is critical to determine the expected interaction rate in the detector.

2

NEUTRINOS GO BEYOND THE STANDARD MODEL

Despite its success, the standard Model appears in need of extension and generalisation. In the Standard Model the neutrinos were postulated massless because in experiments only left handed neutrinos were observed, whereas a right handed neutrino field is needed in order to acquire a Dirac mass by the Higgs mechanism. And yet, it seems like neutrinos do have a small but non-zero mass. Measurements of solar neutrinos and atmospheric neutrinos showed a deficit in comparison to predictions, as described respectively in sections 2.1 and 2.2. This deficit can be explained in terms of neutrino oscillations that are driven by a squared-mass difference between the neutrino mass eigenstates, as described in section 2.3. The experimental confirmation is described in section 2.4. Ever since, the neutrino sector has entered an era of precision measurements of the oscillation parameters that are discussed in section 2.5.

2.1 THE SOLAR NEUTRINO DEFICIT

The sun is an intense neutrino source, with about 100 billion solar neutrinos passing every second through every square centimeter of earth's surface (see section 1.4). The different fusion chain reactions of the sun produce ν_e with different energy spectra, as shown in the top panel of figure 2.1.1. The ν_e travel from the sun's core to the earth without any significant absorption by the sun's outer layers. As neutrino detectors became sensitive enough to measure the solar neutrino flux, it became clear that the number detected was lower than that predicted by models of the solar interior, as indicated in the bottom panel of figure 2.1.1.

Deep underground, in the caverns of the Homestake Gold Mine in South Dakota, the Homestake solar neutrino detector [49] was built, well shielded from cosmic backgrounds. The Homestake experiment (1969-1998), led by Ray Davis, consisted of a tank with 615 ton C_2Cl_4 (perchloroethylene). Solar neutrinos engaged in a quasi-elastic CC interaction, changing the Chlorine into Argon by neutron conversion,

$$\nu_e + {}^{37}Cl \longrightarrow {}^{37}Ar + e^- \qquad E_\nu > 0.8 \text{ MeV}.$$

Periodically, helium was bubbled through the tank to collect the Argon in order to count the number of events. John Bahcall had predicted how many incoming solar neutrinos would interact in the tank [45], based on the Standard Solar Model (SSM) and the neutrino cross section. His updated prediction is shown with the left bar in figure 2.1.1. However, only one third of the neutrinos seemed to arrive (see section 2.5.1 for the explanation of this phenomenon). This *solar neutrino problem* made researchers question Davis' experiment, Bahcall's calculations, and their model of the sun.

However, Davis' observations were confirmed by gallium experiments that are also sensitive to ν_e from the pp reaction, whereas the Homestake detection method was only sensitive to neutrinos

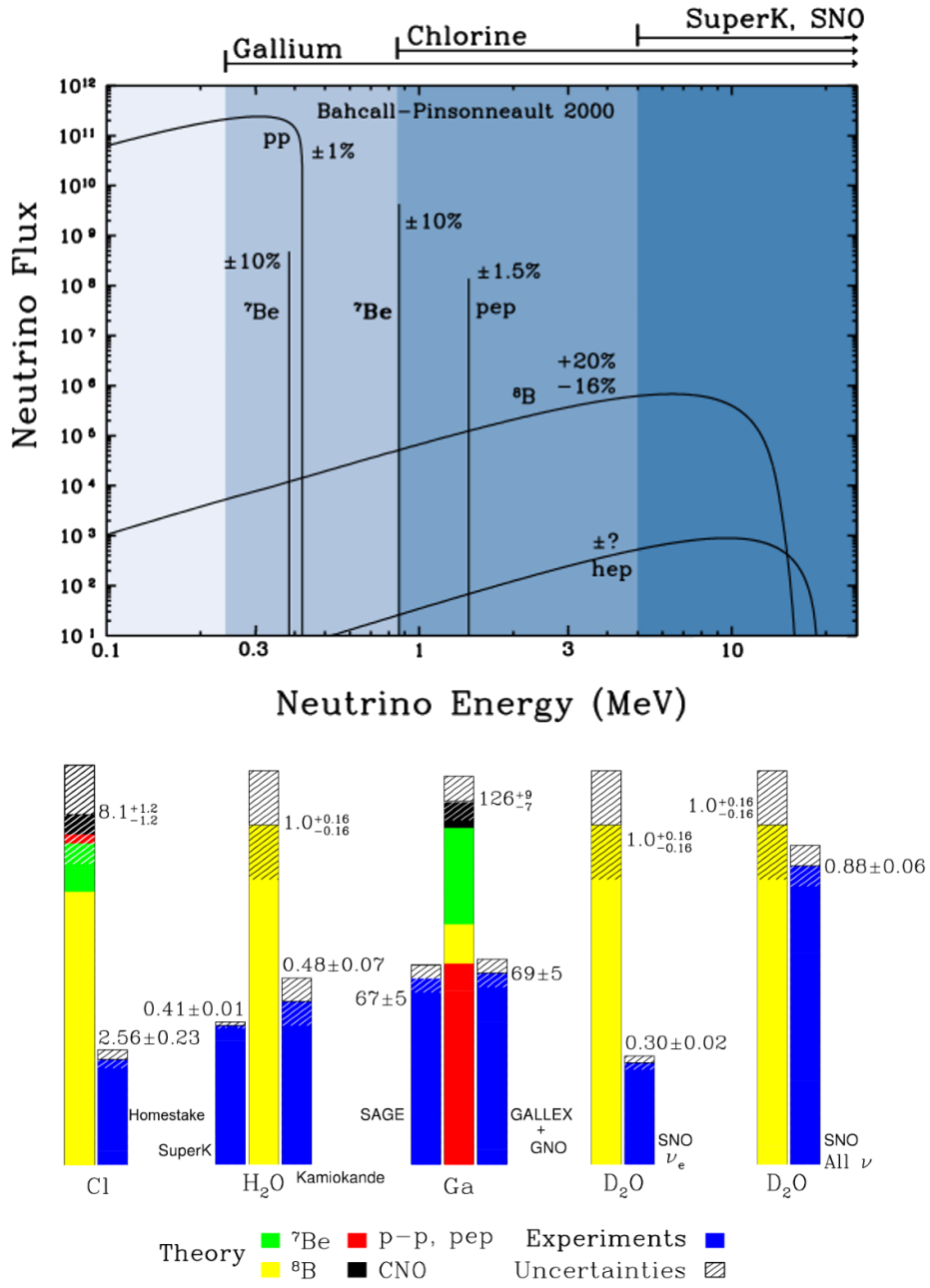

Figure 2.1.1: Top: The Standard Solar Model (SSM) prediction of the solar neutrino fluxes [45], with on top the energy ranges accessible by solar neutrino experiments. Bottom: predicted and measured solar fluxes for experiments using Chlorine, water, Gallium and deuterium. The colored bars show the theoretical SSM prediction, updated by Bahcall et al in 2005 [46]. The colors indicate the solar chain reaction that produced the ν_e. The experimental data, shown in blue, include results reported up to April 2005 [47] [48]. The values are expressed in the solar neutrino unit (SNU). The three left groups show the solar neutrino problem. The two right groups show the confirmation of neutrino oscillations by SNO.

produced by the Boron-8 reaction. The gallium experiments SAGE (1989) [50], shielded by the Kaukasus mountain range, and GALLEX/GNO (1991-2003) [51], situated under the Gran Sasso mountains, used detector tanks with liquid Gallium that can be converted by incoming ν_e with a low energy threshold,

$$\nu_e + {}^{71}Ga \longrightarrow {}^{71}Ge + e^- \qquad E_\nu > 0.23 \text{ MeV}.$$

The gallium experiments measured a clear deficit, as shown in figure 2.1.1, of about 40%. This showed that the deficit is energy dependent.

2.2 THE ATMOSPHERIC NEUTRINO DEFICIT

Neutrinos are also produced isotropically in our atmosphere, albeit with a smaller flux than solar neutrinos (see figure 1.4.1). The discussion in section 1.4 indicates that the expected ratio of neutrino flavors is

$$\frac{\Phi(\nu_\mu + \overline{\nu}_\mu)}{\Phi(\nu_e + \overline{\nu}_e)} \sim 2.$$

The ratio was expected to be the same in all directions. The Super Kamiokande collaboration in Japan detected the high energetic atmospheric neutrinos ($E_\nu \sim$ 100 MeV - 10 GeV), with a detector tank of 50 000 ton ultrapure water, 1 km under Mount Ikeno [52]. The medium is sensitive to both ν_e and ν_μ through quasi-elastic CC interactions,

$$\begin{aligned} \nu_e + n &\longrightarrow p + e^- \qquad & \bar{\nu}_e + p &\longrightarrow n + e^+ \\ \nu_\mu + n &\longrightarrow p + \mu^- \qquad & \overline{\nu}_\mu + p &\longrightarrow n + \mu^+. \end{aligned}$$

The $e^\pm$ and $\mu^\pm$ travel faster than light in water, producing a Cerenkov cone, with an energy threshold of $\sim$ 100 MeV. The Cherenkov light is detected by 13 000 photomultiplier tubes that cover the inside of the enormous vessel. The $e^\pm$ signal can be discriminated from the $\mu^\pm$ as it creates a shower of secondary $e^\pm$ that make the Cherenkov cone fuzzier, as visible in figure 2.2.1. In addition the angle of incidence of the neutrino can be determined from the shape, which allows the estimation of its travelled distance from its creation point in the atmosphere,

Neutrinos coming straight down have an angle $\theta = 0$ and therefore $\cos(\theta) = 1$. They have a flight distance of about 15 km. The axis value 0 indicates horizontally incoming neutrinos and -1 are neutrinos that are coming straight up and traveled 12800 km through the earth. The expected number of neutrinos is indicated on the graphs with a solid line. For multi GeV ν_μ, the measurements deviate from the expectation. Only half the expected upward going neutrinos were observed, echoing the solar neutrino problem. The discrepancy depends on the distance the neutrino travelled and on the neutrino energy. This was another observation that led to the idea of neutrino oscillation.

2.3 NEUTRINO OSCILLATIONS

A possible solution to the solar and atmospheric neutrino problems came from Bruno Pontecorvo [55]. Already in 1957, he suggested that the neutrinos do not conserve lepton number, but oscillate

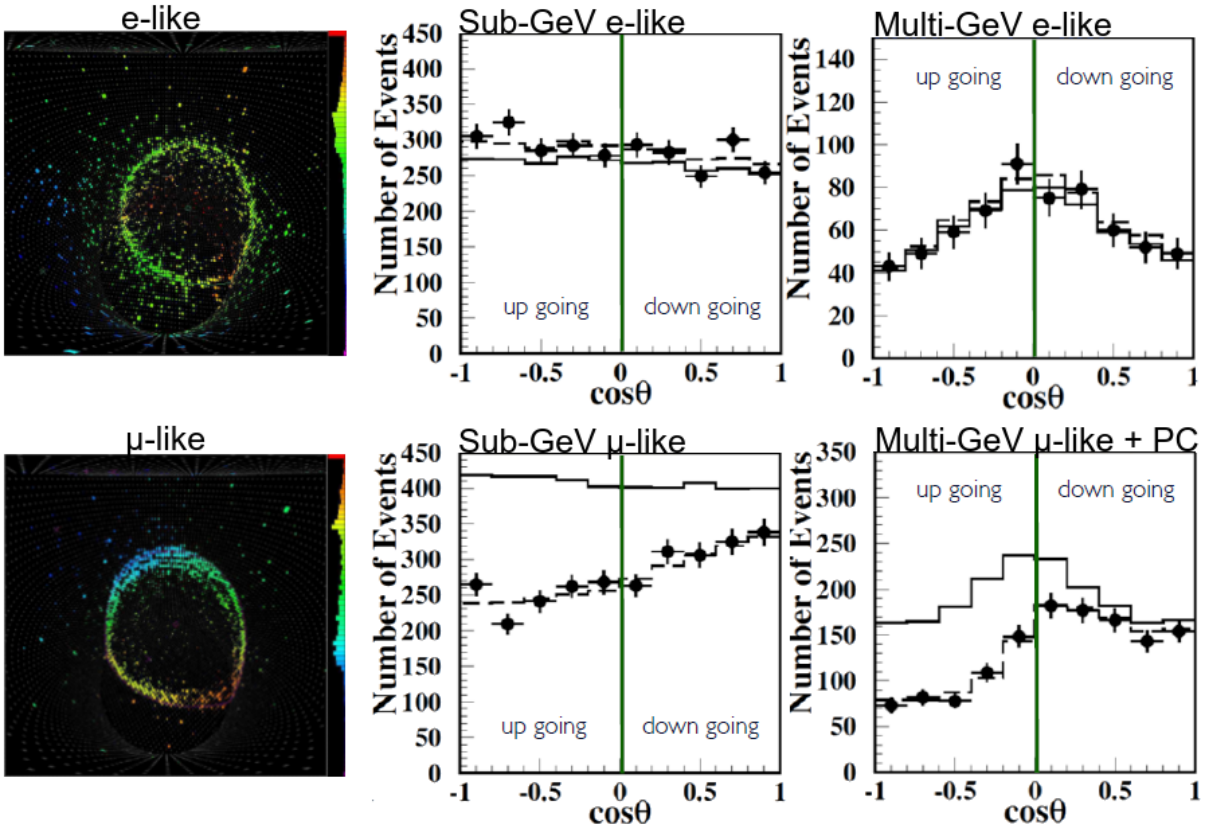

Figure 2.2.1: For atmospheric neutrino like events detected by Super-Kamiokande of flavor ν_e (top) and ν_μ (bottom), the left column shows an example of the measurement of the Cerenkov light cone [53]. The right columns show the Zenith angle distributions of measured neutrino flux for two energy ranges [54]. The full, black line shows the Monte-Carlo prediction (under the assumption of no neutrino oscillation) from standard cosmic ray models. The data points show what Super-Kamiokande measured.

into different states along their journey through space. At that time only one neutrino type was known and the only possible oscillation would be between neutrinos and antineutrinos. Later this idea was adapted to oscillations between the known neutrino flavours. These neutrino oscillations could explain the anomalously low neutrino detection rates but it would also require neutrinos to have a non-zero mass. For example, in case of the atmospheric neutrino problem, the deficit in ν_μ would be explained by their oscillation into ν_τ. They could not have oscillated into ν_e since there was no evidence of a changing ν_e flux.

2.3.1 NEUTRINO EIGENSTATES

As it turns out, neutrino flavors are only one possible representation of the neutrino states. The neutrino flavors are independent eigenstates that are related to specific lepton flavors by the weak coupling. As such, neutrino ν_α couples weakly to the lepton α, where $l_\alpha \in \{e, \mu, \tau\}$. Because the weak interactions occur via the leptonic flavors, the experimental detections showed neutrinos in flavor

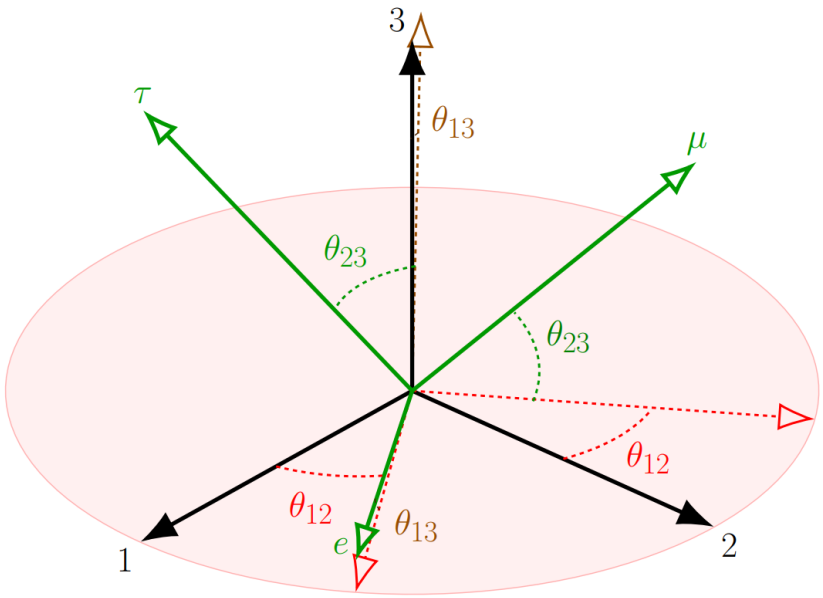

Figure 2.3.1: Representation of the neutrino mass base (black) and the flavor base (green). The neutrino mass eigenstates are used as reference basis. The three lepton mixing angles θ_{ij} show how to transform between bases. [56]

states.

The neutrinos can be represented in another basis of eigenstates. The eigenstates of the free Hamiltonian give rise to the mass basis. The neutrino's mass eigenstates are represented by ν_i with $i \in \{1,2,3\}$. Whereas the neutrino interaction occurs via the flavor eigenstates, the neutrino propagation happens in the mass eigenstates. The flavor basis and the mass basis are related through a unitary transformation

$$|\nu_\alpha\rangle = \sum_i U^*_{\alpha i} |\nu_i\rangle ,$$
$$|\nu_i\rangle = \sum_\alpha U_{\alpha i} |\nu_\alpha\rangle .$$

Here, $U_{\alpha i}$ represents the 3× 3 Pontecorvo-Maki-Nakagawa-Sakata (PMNS) matrix. It is a unitary transformation, that satisfies the relation

$$U^\dagger U = U U^\dagger = I,$$

with I the identity matrix and † the Hermitian conjugate. Unitary transformations can be thought of as the complex analogues of the real orthogonal transformation (which acts as rotation or reflection). Figure 2.3.1 provides a visual representation of the neutrino eigenstates and the transformation between them, by means of the real analogue of rotations.

If the unitary transformation were the identity matrix, then the flavor eigenstates would coincide with the mass eigenstates and there would be no neutrino flavor oscillation. Experiment shows that this is not the case. If only two neutrinos are considered, a 2×2 unitary matrix is used. When adding one or more sterile neutrinos (see section 4.2), the matrix becomes 4×4 or larger. In the 3×3 form for the usual three generations of neutrinos, the generally used parametrisation [57] is the following,

$$\begin{pmatrix}\nu_e\\ \nu_\mu\\ \nu_\tau\end{pmatrix} = \begin{pmatrix} U_{e1} & U_{e2} & U_{e3}\\ U_{\mu 1} & U_{\mu 2} & U_{\mu 3}\\ U_{\tau 1} & U_{\tau 2} & U_{\tau 3}\end{pmatrix}\begin{pmatrix}\nu_1\\ \nu_2\\ \nu_3\end{pmatrix} \tag{2.1}$$

$$= \begin{pmatrix}1 & 0 & 0\\ 0 & c_{23} & s_{23}\\ 0 & -s_{23} & c_{23}\end{pmatrix}\begin{pmatrix} c_{13} & 0 & s_{13}e^{-i\delta}\\ 0 & 1 & 0\\ -s_{13}e^{i\delta} & 0 & c_{13}\end{pmatrix}\begin{pmatrix} c_{12} & s_{12} & 0\\ -s_{12} & c_{12} & 0\\ 0 & 0 & 1\end{pmatrix}\begin{pmatrix} e^{i\alpha_1/2} & 0 & 0\\ 0 & e^{i\alpha_2/2} & 0\\ 0 & 0 & 1\end{pmatrix}\begin{pmatrix}\nu_1\\ \nu_2\\ \nu_3\end{pmatrix}. \tag{2.2}$$

Here, $c_{23} = \cos(\theta_{23})$ and $s_{13} = \sin(\theta_{13})$ etc. The angles θ_{ij} are fixed parameters of the lepton mixing matrix. Note that the real part of the first three matrices represents rotations over Euler's angles, as shown in figure 2.3.1. The mixing angles define how different the flavour states are from the mass states. In addition, there are several complex phase factors. The Dirac CP-violating phase, δ, and two Majorana CP-violating phases, α_1 and α_2. The latter are only meaningful if neutrinos are Majorana particles [58] and do not enter into oscillation phenomena. CP violation means that the combination of Charge-symmetry and Parity-symmetry is broken, i.e. the laws of physics are not the same after the simultaneous application of charge inversion (C) and spatial reflection (P). [1]

2.3.2 NEUTRINO PROPAGATION

The neutrino propagates through vacuum in its mass eigenstates. The time evolution of the mass eigenstates is given by the propagation Hamiltonian. Each mass state will propagate as a plane wave, that is, after time t, the initial state gets a propagation phase factor,

$$\begin{aligned}|\nu_i(t)\rangle &= e^{-ip_i^\mu x_\mu}|\nu_i(0)\rangle\,,\\ &= e^{-i(E_i t - \vec{p}_i\cdot\vec{x})}|\nu_i(0)\rangle\,,\end{aligned}$$

where $p = (E, \vec{p})$ is the four momentum and $x = (t, \vec{x})$ the four position. Natural units $c = \hbar = 1$ are used. E_i is the energy of mass eigenstate i, $\vec{p}_i$ the three dimensional momentum, and $\vec{x}$ the current neutrino position. In natural units, t can be substituted by the traveled distance L. The coordinate system can be oriented along the direction of the neutrino. This leads to

$$|\nu_i(t)\rangle = e^{-i(E_i - |\vec{p}_i|)L}|\nu_i(0)\rangle\,. \tag{2.3}$$

1 While the CP symmetry seems to be conserved in strong and electromagnetic interactions, it is known to be violated in weak decays in the quark sector, namely in decays of kaons [59], B mesons [60] and D mesons [61]. Whether or not weak decays in the lepton sector violate CP symmetry as well, is a hot topic in neutrino research. In 2020, the T2K Collaboration reported some indications of leptonic CP violation for the first time [62], but their results are in tension [63] with similar measurements done by NoVA [64]. Both experiments compared the appearance probabilities $P(\nu_\mu \to \nu_e)$ and $P(\overline{\nu}_\mu \to \overline{\nu}_e)$ from accelerator neutrino beams.

Since the neutrino travels close to the speed of light, the ultrarelativistics limit $\left|\overrightarrow{p}_i\right| \gg m_i$ allows to use the binomial approximation ($(1+x)^a \approx 1+ax$) in the energy momentum relation

$$\begin{aligned} E_i &= \sqrt{\left|\vec{p}_i\right|^2 + m_i^2} \\ &= \left|\vec{p}_i\right| \sqrt{\left(1 + \frac{m_i^2}{\left|\vec{p}_i\right|^2}\right)} \\ &\approx \left|\vec{p}_i\right| + \frac{m_i^2}{2\left|\vec{p}_i\right|}. \end{aligned}$$

Applying this approximation to the neutrino propagation, leads to

$$|\nu_i(t)\rangle = e^{-i\frac{m_i^2 L}{2E_i}} |\nu_i(0)\rangle , \tag{2.4}$$

where $E_i \approx \left|\vec{p}_i\right|$ was used because the energy of the ultrarelativistic neutrino is almost completely due to its momentum. Equation 2.4 shows that eigenstates with different masses have a propagation phase factor with different frequencies. This difference will lead to oscillations between neutrino flavor eigenstates.

2.3.3 NEUTRINO OBSERVATION

When a neutrino is produced through a weak interaction, it appears in a specific flavor eigenstate,

$$|\Psi(0)\rangle = 1\,|\nu_\alpha\rangle .$$

However, the neutrino will propagate through space in its mass eigenstates. Therefore, the neutrino flavor eigenstate has to be expressed in the mass basis,

$$|\Psi(0,E)\rangle = \sum_i U_{\alpha i}^* |\nu_i(0)\rangle .$$

When the neutrino propagates some distance L through vacuum, the mass eigenstates evolve as

$$|\Psi(L,E)\rangle = \sum_i U_{\alpha i}^* e^{-i\frac{m_i^2 L}{2E_i}} |\nu_i(0)\rangle .$$

The neutrino is usually observed through a weak CC interaction in the flavor basis,

$$|\Psi(L,E)\rangle = \sum_i U_{\alpha i}^* e^{-i\frac{m_i^2 L}{2E_i}} \sum_\beta U_{\beta i} \left|\nu_\beta\right\rangle .$$

Here the wavefunction $|\Psi(t)\rangle$ contains the probability of observing the neutrino in any flavor $\beta \in \{e,\mu,\tau\}$, which can be different from the one that was initially created, α. Constructive interference between the mass eigenstate's phase factors makes it possible to observe a neutrino created with

a given flavor to change its flavor during propagation. The probability that a neutrino originally of flavor α will later be observed as having flavor β is

$$P_{\alpha\to\beta}(L,E) = \left|\left\langle \nu_\beta \mid \nu_\alpha(L)\right\rangle\right|^2 = \left|\sum_i U^*_{\alpha i} U_{\beta i} e^{-i\frac{m_i^2 L}{2E}}\right|^2.$$

Using some relations of complex numbers, this probability is written in general [57] as

$$P_{\alpha\to\beta}(L,E) = \delta_{\alpha\beta} - 4\sum_{i>j}\mathrm{Re}\left(U^*_{\alpha i}U_{\beta i}U_{\alpha j}U^*_{\beta j}\right)\sin^2\left(\frac{\Delta m^2_{\mathrm{ij}}L}{4E}\right) + 2\sum_{i>j}\mathrm{Im}\left(U^*_{\alpha i}U_{\beta i}U_{\alpha j}U^*_{\beta j}\right)\sin\left(\frac{\Delta m^2_{\mathrm{ij}}L}{4E}\right).$$

Here, the imaginary part is only non-zero if there is CP violation. $\Delta m^2_{\mathrm{ij}} \equiv m^2_i - m^2_j$.This formulation highlights the fact that the flavor oscillation is driven by the squared-mass differences between the eigenstates. For neutrino oscillations to occur, at least one of the mass states must be non-zero. This has huge implications, and is the first evidence of physics beyond the Standard Model. The oscillation manifests itself over distance and energy. In experiments, these parameters can be controlled.

The probability that a neutrino is observed in the same flavor α as it was created after propagating a distance L through vacuum is given by

$$P_{\alpha\to\alpha}(L,E) = 1 - 4\sum_{i>j}|U_{\alpha i}|^2\left|U_{\alpha j}\right|^2\sin^2\left(\frac{\Delta m^2_{\mathrm{ij}}L}{4E}\right),$$

2.4 CONFIRMATION OF NEUTRINO OSCILLATIONS

The observation that confirmed the oscillation theory and solved the solar and atmospheric neutrino problems came from the Sudbury Neutrino Observation, (SNO) [65]. The former experiments detected solar ν_e through a charged current. They were not able to detect higher generation neutrinos in this way, since the energy threshold to produce their corresponding lepton is higher than the solar neutrino energies provide. The SNO experiment managed to measure the total neutrino flux, regardless of flavour, $\Phi_{\nu_e+\nu_\mu+\nu_\tau}$, by using a detector tank with 1000 ton deuterium, read by 9600 PMTs. As the deuterium nucleus is fragile, a neutrino can break it apart through a Neutral Current (NC) interaction, with a threshold of about 2 MeV. Any neutrino flavor can participate in this interaction and the Z coupling is the same for all flavors.

In addition SNO measured the elastic scattering of ν on e^-, which has a larger cross section for ν_e as both NC and CC feed into this channel. Finally, the CC IBD interactions provided an isolated measurement of Φ_{ν_e}, which SNO used to cross check the ν_e rate with previous experiments. With the measurement of the three independent reaction channels, SNO was able to disentangle the neutrino fluxes. The combined analysis of all three phases of solar neutrino data from SNO [66, 67] resulted in

$$\begin{aligned}\Phi_{CC} = \Phi(\nu_e) &= 1.67^{+0.05+0.07}_{-0.04-0.08}\cdot 10^6\mathrm{cm}^{-2}s^{-1}\\ \Phi_{ES} = \Phi(\nu_e) + 0.15\left(\Phi(\nu_\mu)+\Phi(\nu_\tau)\right) &= 1.77^{+0.24+0.09}_{-0.21-0.10}\cdot 10^6\mathrm{cm}^{-2}s^{-1}\\ \Phi_{NC} = \Phi(\nu_e)+\Phi(\nu_\mu)+\Phi(\nu_\tau) &= 5.25^{+0.16+0.11}_{-0.16-0.13}\cdot 10^6\mathrm{cm}^{-2}s^{-1},\end{aligned}$$

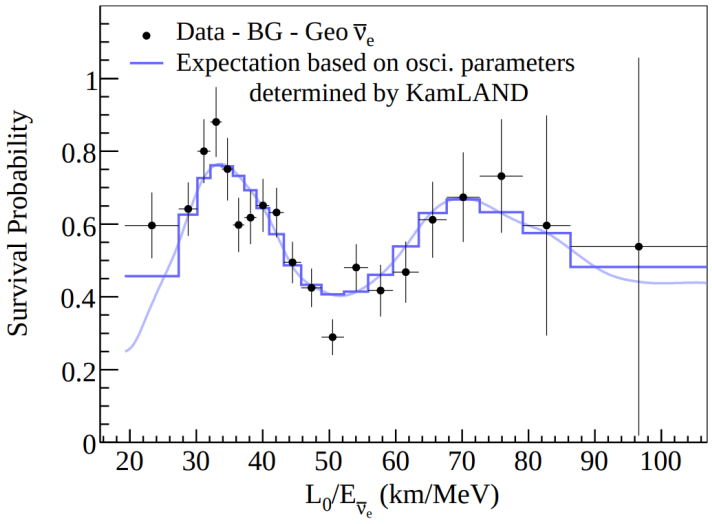

Figure 2.4.1: Ratio of the measured anti-neutrino spectrum to the expectation for no-oscillation as a funcion of L/E[70]. L_0 is the effective baseline taken as a flux-weighted average (L_0 = 180 km).The histogram and curve show the expectation accounting for the distances to the individual reactors, time-dependent flux variations and efficiencies. The figure shows the behavior expected from neutrino oscillation.

with statistical and systematic errors indicated. The measurement shows that the flux of ν_μ and ν_τ is roughly 3 times larger than the flux of ν_e. This result was consistent with but more precise than solar model predictios [68], namely $(5.88 \pm 0.65) \times 10^6 cm^{-2} s^{-1}$ from BPS09(GS), and $(4.85 \pm 0.58) \times 10^6 cm^{-2} s^{-1}$ from BPS09(AGSS09). The SNO Collaboration showed clear evidence for conversion of solar electron-neutrinos into muon or tau neutrinos. Return to figure 2.1.1 that shows how the measured neutrino rate agrees with the predicted rate within error bars. Some ambiguities remain. These could be due to matter effects from the very dense interior of the sun [69] (see section 2.5.1).

However, even the SNO result showed only a distribution of neutrino flavors at a single distance from the source, that could be explained by neutrino oscillations. One of the first lines of evidence of an actual oscillation pattern over multiple L/E values came from the KamLAND experiment [70]. This liquid scintillator detector is situated next to Super-Kamiokande in Japan. It measures the pure $\overline{\nu}_e$ flux of at least 50 nuclear power stations near Kamioka. Figure 2.4.1 shows the ratio of the observed to expected antineutrino events for an L/E, with average distance of L = 180 km. This figure is the first actual proof that oscillations are happening - it is the first picture of an oscillation.

2.5 DETERMINATION OF THE OSCILLATION PARAMETERS

The parameters that govern the flavor oscillations are the three mixing angles θ_{ij}, the squared-mass splittings Δm^2_{ij} and the phase δ_{CP}. Note that the possible Majorana phases do not enter the oscillation formulas. The parameters can be determined by a variety of oscillation experiments. In addition, these experiments allow to verify if the oscillation formalism is in fact true. Although the formalism

works very well, there are not enough measurements yet, to know if what we are doing is indeed correct. An oscillation will be maximal whenever

$$\frac{\Delta m^2_{\text{ij}} L}{4E} = 2n\pi$$
$$\Leftrightarrow L/E = \frac{2\pi}{\Delta m^2_{\text{ij}}}.$$

This dictates the optimal baseline to install a detector with respect to a neutrino source of a certain energy. And this is different for the individual Δm^2_{ij}. In case the squared-mass difference is very small, the oscillation will manifest over large distances.

The atmospheric oscillation only saw a disappearance of ν_μ, while the ν_e flux was as expected. This suggests [71] an oscillation from ν_μ to ν_τ. Based on the knowledge of the neutrino energy spectrum and the distance dependence of the discrepancy, the data indicated a Δm^2_{23} of about 10^{-3} eV^2, and that $\sin^2\theta_{23}$ is about a half which implies maximal mixing between the neutrino flavors. The solar oscillation of ν_e into a linear combination of ν_τ and ν_μ over a long distance could be interpreted by a Δm^2_{12} that is much smaller than Δm^2_{23} and a $\sin^2(\theta_{12})$ of about a third. Both phenomena indicate that θ_{13} is very small, which implies the solar and atmospheric oscillations can be approximated as two-state oscillations and

$$\Delta m^2_{\text{sol}} = \Delta m^2_{12},$$
$$\Delta m^2_{\text{atm}} = \Delta m^2_{13} \approx \Delta m^2_{23}.$$

The oscillation experiments only provide information about the squared-mass difference, not about the individual masses [72]. Therefore, the above observations leave us with the two mass orderings shown in figure 2.5.1. From the small mass splitting, scientists defined by convention the lightest one to be ν_1, and the heavier to be ν_2. Based on the large mass splitting, ν_3 can be much larger than the other, called the Normal Hierarchy (NH), or much smaller, called the Inverted Hierarchy (IH). Both hypotheses are still allowed by data.

Figure 2.5.1 also shows an interpretation of the entries of the mixing matrix. The colors in each bar indicate the probability that the mass eigenstate will appear as any flavor. A neutrino ν_1 has the probability to appear as a ν_e that equals U^2_{e1}, which is indicated in red. Note that ν_e and ν_μ always appear in similar proportions, that ν_2 has almost the same probability to be any flavor and that ν_1 will appear most probably as a ν_e whereas ν_3 will not.

2.5.1 PRECISION MEASUREMENTS OF THE OSCILLATION PARAMETERS

Various oscillation experiments have been conducted in the last 20 years to precisely determine the values of the different mixing angles and squared-mass differences for the three SM neutrinos. There are two types of neutrino oscillation experiments. In disappearance experiments, the survival probability of a neutrino flux with a specific flavor is investigated, by observing the neutrino in a detector near the source and in a far detector. The ratio of the neutrino energy spectra will show the oscillation pattern. In appearance experiments, a neutrino flux of pure flavor is generated and the detector measures how many neutrinos have changed into a different flavor. The position of maximal

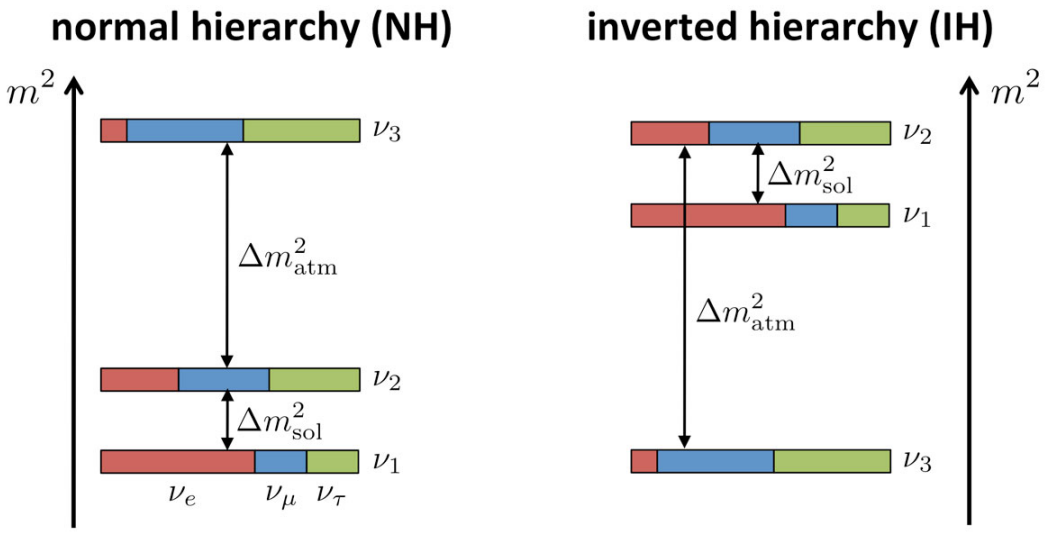

Figure 2.5.1: Two potential mass orderings of neutrinos are the normal ordering (normal hierarchy) and the inverted ordering (inverted hierarchy). A visual representation of the two possible neutrino mass orderings. Left: the normal ordering, where $m_1 < m_2 < m_3$, and the atmospheric mass-squared splitting is positive. On the right side, the inverted ordering, where $m_3 < m_1 < m_2$ and the atmospheric mass-squared splitting is negative. The relative proportion of red (ν_e), blue (ν_μ), and green (ν_τ) in the box corresponding to the mass eigenstates quantifies the relative probability of finding the α flavour eigenstate in the corresponding mass eigenstate. [72]

oscillation gives information about Δm^2, while the amplitude of the oscillation provides information on the mixing angle.

$\Delta m^2_{23} \sim \Delta m^2_{13}$ and θ_{23} that were first estimated with atmospheric neutrinos can be further probed with accelerator neutrinos. Accelerator neutrinos have energies of order $\mathcal{O}(1\text{ GeV})$. Because $\Delta m^2_{23} \sim 10^{-3}\text{ eV}^2$, this corresponds to an optimal baseline of about 400 km. This is experimentally achievable by directing the neutrino beam through earth's mantle towards a large, far detector. A near detector is usually built near the beam production point to measure the neutrino beam before oscillation.

That the atmospheric oscillations are mostly $\nu_\mu \to \nu_\tau$ was validated by the accelerator based experiment OPERA [73], which was running in the CERN-to-Gran-Sasso (CNGS) ~ 17 GeV ν_μ beam at 732 km from CERN. OPERA was a tracking experiment using photographic emulsion, that measures ν_τ appearance by charged-current interactions of a ν_τ generating a short τ track which typically decays hadronically. The oscillation analysis is consistent with other oscillation experiments and confirms the atmospheric oscillation mode is mostly $\nu_\mu \to \nu_\tau$.
Accelerator based experiments make precision measurements of the mixing angle and the mass difference for the 23 sector as shown in figure 2.5.2 [74]. Most notably, the T2K experiment directs a 99.5% pure beam of ν_μ neutrinos from the J-PARC facility at the East coast of Japan in Tokai to Kamioka (T2K), at the West coast of Japan, where it is measured by the Super-Kamiokande water Cerenkov detector. In the United States, the NOνA experiment [75] is situated 810 km from the ν_μ beam source at Fermilab. The detector consists of 500000 liquid scintillator cells, each 4 cm × 6 cm × 16 m, and

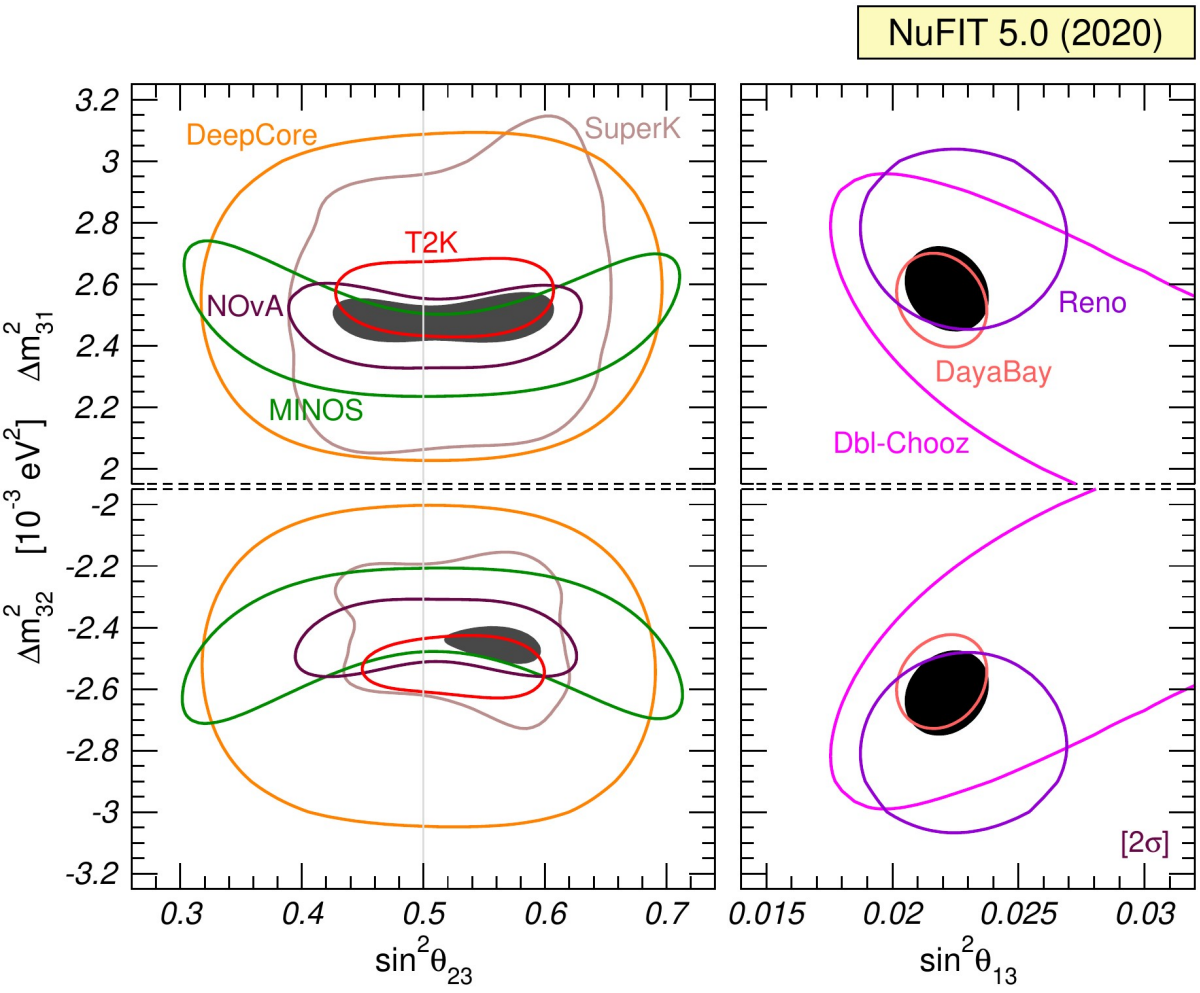

Figure 2.5.2: Left: Determination of Δm^2_{3l} at the 2σ confidence level, where $l = 1$ for NH (upper panels) and $l = 2$ for IH (lower panels). The left panels show regions in the $(\sin^2\theta_{23}, \Delta m^2_{3l})$ plane using both appearance and disappearance data from T2K [62] (red), NOνA [75] (dark red) and MINOS [76] (green), as well as atmospheric data from Super Kamiokande [77](light brown) and DeepCore [78] (orange), and a combination of all of the above (grey region). Here a prior on θ_{13} is included to account for reactor bounds. Right: Regions in the $(\sin^2\theta_{13}, \Delta m^2_{3l})$ plane using data from DayaBay [79] (pink), DoubleChooz [80] (magenta), RENO [81] (violet), and their combination (black regions). In all panels solar and KamLAND [82] data are included to constrain Δm^2_{21} and θ_{12}. Contours are defined with respect to the global minimum of the two orderings.[74]

measures the ν_μ disappearance.

Δm^2_{12} and θ_{12} can be measured with solar neutrinos and reactor neutrinos. The disappearance of electron neutrinos emitted by the sun, is in reality different from the formalisms stated previously. Because the oscillation does not take place in vacuum but in dense matter, a potential term has to be added to the energy in the formula of neutrino propagation (equation 2.3). In the dense solar interior, the potential is different for individual neutrino flavours, since ν_e interact via CC and NC while ν_μ only interact via NC. This introduces a phase difference that drives the neutrino oscillation through matter effects. This phenomenon is called the Mikheyev-Smirnov-Wolfenstein effect (MSW) [69].

Interestingly, the matter effects provide the only means to estimate the sign of the difference between the squared masses. In the matter potential, the amplitude of the oscillation probability becomes

$$\sin(2\theta_m) = \frac{\sin(2\theta)}{\sqrt{(\Delta V/\Delta m^2 - \cos(2\theta))^2 + \sin^2(2\theta)}}$$

In the denominator, $(\Delta V/\Delta m^2 - \cos(2\theta))$ will have different value if $\Delta m^2 \rightarrow -\Delta m^2$, and the effective mixing angle will be different. This cannot be done with vacuum oscillations.
The solar oscillation analysis can not be validated with accelerator experiments. Because $\Delta m^2 \sim 10^{-5}$ eV^2, the 1 GeV accelerator neutrinos imply an optimal baseline of more than 100000 km, which is about 10 times the diameter of the earth. Instead, reactor based experiments with a long baseline are sensitive to the parameters of the 12 sector. Reactors produce $\overline{\nu}_e$ with energies around 5 MeV. The KamLAND experiment was introduced in section 2.4 and measures the reactor $\overline{\nu}_e$ disappearance. Since the amount of matter between the detector and the reactors is too small to support any type of MSW effect, KamLAND should measure the true solar vacuum oscillation parameters.
Figure 2.5.3 shows the allowed regions for solar oscillation parameters in the $(\sin^2\theta_{12}, \Delta m^2_{12})$ plane as measured by KamLAND and by a compilation of solar neutrino experiments [74]. Note that the two are very complementary, with KamLAND having a high energy resolution resulting in a horizontal ellipse, and the solar experiments having a large statistical power, but poor energy resolution, leading to the vertical ellipse. The two constrain the allowed region to the red region where both experiments are consistent. There remains tension with this region and the best fit points.

$\boldsymbol{\theta_{13}}$ can be measured with reactor neutrinos and accelerator neutrinos. The angle θ_{13} is the smallest of the three known mixing angles. Since the measurements of the other mixing angles still have large errors, a process should be regarded that only depends on θ_{13}. For neutrinos of a few MeV, λ_{sol} is $\sim$ 60 km and λ_{atm} is $\sim$ 1 km. Close to the source, the measurement should only be sensitive to the atmospheric-scale oscillation term, while terms with θ_{12} and θ_{23} can be neglected. There are no suitable terrestrial ν_e sources, but CPT invariance allows to use reactor $\overline{\nu}_e$ sources instead, to conduct disappearance experiments at short baseline. This is done by three reactor experiments, Daya-Bay in China [79], DoubleCHOOZ in France [80] and RENO in South Korea [81]. Their results are shown in the left panel of figure 2.5.2. The experiments use liquid scintillator as neutrino target and probe the IBD interaction channel by neutron capture on Gadolinium.
Accelerator based experiments, like T2K and NOνA, were mentioned earlier for their measurements of the 23 parameters. In the future, they will also measure θ_{13}, by looking at ν_e appearance in a ν_μ beam.

The current best fit values for the three-flavor oscillation parameters from global data as of July 2020 are reported in figure 2.5.4. The numbers in the first and second column are obtained assuming respectively Normal Hierarchy and Inverted Hierarchy. Most mixing parameters are measured very well, at the few perfect level. Only δ_{CP} is virtually not measured at all. In about 20 years, we went from the discovery of the phenomenon to precision measurements of the relevant parameters. There has been a lot of progress in a short amount of time for particle physical standards. A major drawback is that even though everything is measured precisely, each bit of information comes from a different experiment and there is very little overlap between them.

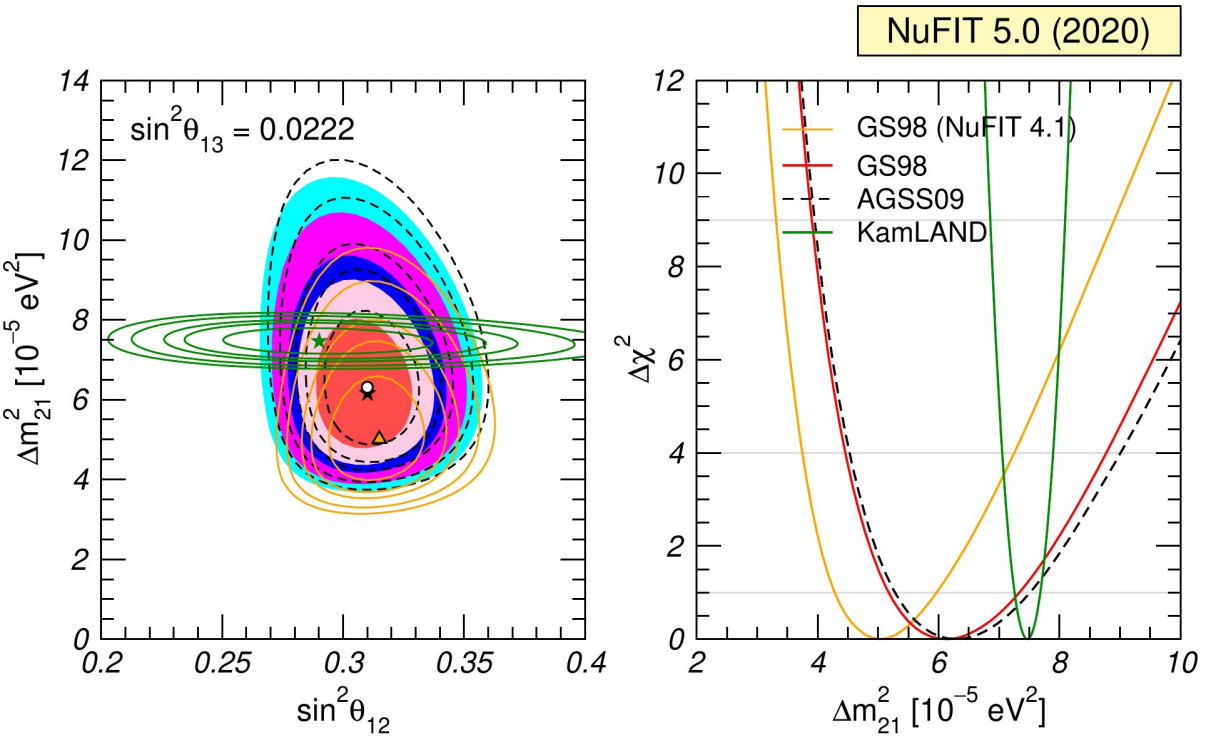

Figure 2.5.3: Left: Allowed parameter regions (at 1σ, 90%, 2σ 99%, 3σ CL for 2 dof) for fixed $\theta_{13} = 8.6°$ from the analysis of KamLAND data [82] (solid green contours) with best fit marked by a green star) and from the combined analysis of solar data for the GS98 model (full regions with best fit marked by black star) and the AGSS09 model (dashed void contours with best fit marked with a white dot). Orange contours show the results of a global analysis for the GS98 model using the previous SK4 neutrino data. Right: $\Delta\chi^2$ dependence on Δm^2_{21} for the same four analyses after marginalizing over θ_{12}.[74]

Recall that the mixing angles resulted from a possible parametrisation of the three-flavour leptonic mixing matrix (see section 2.3). Under the assumption that the matrix is unitary, it can be defined by the following four parameters

$$\tan^2\theta_{12} \equiv \frac{|U_{e2}|^2}{|U_{e1}|^2} \qquad \tan^2\theta_{23} \equiv \frac{|U_{\mu 3}|^2}{|U_{\tau 3}|^2} \qquad U_{e3} \equiv \sin\theta_{13} e^{-i\delta}$$

This leads to the following ranges for the entries of the PMNS matrix [74], with a confidence level of 3σ,

$$|U|_{3\sigma} = \begin{pmatrix} [0.801, 0.845] & [0.513, 0.579] & [0.143, 0.156] \\ [0.233, 0.507] & [0.461, 0.694] & [0.631, 0.778] \\ [0.261, 0.526] & [0.471, 0.701] & [0.611, 0.761] \end{pmatrix}$$

The measurements discussed in the previous section probe at most products of unitary entries and restrict a combination of several entries of the matrix. Therefore, the ranges in the different entries of the matrix are correlated. No direct measurements have been made for $U_{\mu i}$ and $U_{\tau i}$ with $i \in \{1, 2\}$.

NuFIT 5.0 (2020)

	Normal Ordering (best fit)		Inverted Ordering ($\Delta\chi^2 = 2.7$)	
	bfp $\pm 1\sigma$	3σ range	bfp $\pm 1\sigma$	3σ range
$\sin^2\theta_{12}$	$0.304^{+0.013}_{-0.012}$	$0.269 \to 0.343$	$0.304^{+0.013}_{-0.012}$	$0.269 \to 0.343$
$\theta_{12}/^\circ$	$33.44^{+0.78}_{-0.75}$	$31.27 \to 35.86$	$33.45^{+0.78}_{-0.75}$	$31.27 \to 35.87$
$\sin^2\theta_{23}$	$0.570^{+0.018}_{-0.024}$	$0.407 \to 0.618$	$0.575^{+0.017}_{-0.021}$	$0.411 \to 0.621$
$\theta_{23}/^\circ$	$49.0^{+1.1}_{-1.4}$	$39.6 \to 51.8$	$49.3^{+1.0}_{-1.2}$	$39.9 \to 52.0$
$\sin^2\theta_{13}$	$0.02221^{+0.00068}_{-0.00062}$	$0.02034 \to 0.02430$	$0.02240^{+0.00062}_{-0.00062}$	$0.02053 \to 0.02436$
$\theta_{13}/^\circ$	$8.57^{+0.13}_{-0.12}$	$8.20 \to 8.97$	$8.61^{+0.12}_{-0.12}$	$8.24 \to 8.98$
$\delta_{\rm CP}/^\circ$	195^{+51}_{-25}	$107 \to 403$	286^{+27}_{-32}	$192 \to 360$
$\frac{\Delta m^2_{21}}{10^{-5}\ \text{eV}^2}$	$7.42^{+0.21}_{-0.20}$	$6.82 \to 8.04$	$7.42^{+0.21}_{-0.20}$	$6.82 \to 8.04$
$\frac{\Delta m^2_{3\ell}}{10^{-3}\ \text{eV}^2}$	$+2.514^{+0.028}_{-0.027}$	$+2.431 \to +2.598$	$-2.497^{+0.028}_{-0.028}$	$-2.583 \to -2.412$

Figure 2.5.4: Three-flavor oscillation parameters from a fit to global data [74]. The numbers in the 1st (2nd) column are obtained assuming NH (IH). Note that $\Delta m^2_{3l} \equiv \Delta m^2_{31} > 0$ for NH and $\Delta m^2_{3l} \equiv \Delta m^2_{32} < 0$ for IH.

3

CONSEQUENCES OF THE OSCILLATION PARADIGM

The Standard Model of particle physics only contains left handed neutrinos and right handed antineutrinos. These are the only neutrino states that are observed via weak interactions. In addition, by virtue of CPT symmetry, which is assumed to be valid, the existence of ν_L implies the existence of the CPT mirror image, $\overline{\nu}_R$. Right handed components of the neutrino field are absent and no mass term can be generated in the Lagrangian of the Standard Model, leaving the neutrinos massless.

The discovery of neutrino oscillations provided strong evidence that neutrinos do have a small but non-zero mass. We need to understand how the neutrino mass is generated and why it is so small compared to other particles' masses. The latest direct neutrino mass measurement obtained by KATRIN indicates that the neutrino mass is at least 5 orders of magnitude smaller than the electron's mass [83]. One may speculate that there must be a fundamental reason why the neutrino mass has a different scale. The neutrinos can acquire a mass by expanding the Standard Model Lagrangian with a Dirac mass term, a Majorana mass term or a combination of both [84].

For a Dirac neutrino, a mass could be generated via the Higgs mechanism. Particles in vacuum acquire mass as they couple to the Higgs field. The interaction with the Higgs boson changes the particle's chirality; left handed particles become right handed and vice versa. Once ν_R are introduced to the Standard Model, that are singlets under the $SU(2)_L \times U(1)_Y$ gauge transformations, the Lagrangian may contain the Yukawa interaction

$$\mathscr{L}_Y = -yH_0\overline{\nu}_R\nu_L + h.c.$$

where H_0 is the Higgs boson field, and y is a real Yukawa coupling constant. After spontaneous symmetry breaking, H_0 obtains the vacuum expectation value $v \equiv 246.22$ GeV, and the gauge invariant interaction term of the neutrino field becomes

$$\mathscr{L}_D = -m_D(\overline{\nu}_R\nu_L + \overline{\nu}_L\nu_R) = -m_D\overline{\nu}_D\nu_D$$

where $m_D = yv$ is the Dirac neutrino mass and $\nu_D = \nu_L + \nu_R$ is the Dirac neutrino field. When a Dirac mass term in the Lagrangian acts on an incoming ν, it leaves this particle a ν, and the same is true for a $\overline{\nu}$, such that the Lepton number is conserved. To generate sub-eV left handed neutrino masses as required by the neutrino oscillation data, the coupling constant is only $y = mD/v \lesssim 10^{-12}$. Such a small coupling constant leaves doubt if the Dirac mass terms are the sole source of neutrino masses.

The (Dirac) mass term is the only place where the right-handed neutrino interacts with the rest of the Standard Model. Because the neutrinos are neutral with respect to all conserved charges, it is possible to introduce Majorana mass terms for the right-handed neutrino without breaking any symmetry. In that case, the neutrino is a Majorana particle, where the neutrino is identical to its antiparticle.

The Majorana mass term also couples two neutrino fields of opposite chirality to each other. Because charge conjugating a field of definite chirality reverses its chirality, $(\nu_R)^c = \nu_L^c$, one of the two coupled neutrino fields is the charge conjugate of the other. The quarks and charged leptons cannot have Majorana masses because the charge conjugation also inverts the electric charge, which would violate electric charge conservation. Because the charge conjugation turns the particle into its antiparticle, the Majorana mass term is only possible if there is no conservation of lepton number. Majorana mass terms can have several different forms. The right-handed Majorana mass term reads

$$\mathscr{L}_{R,M} = -\frac{m_R}{2}\left(\overline{(\nu_R)^c}\nu_R + \overline{\nu}_R(\nu_R)^c\right) = -\frac{m_R}{2}\overline{\nu}_{R,M}\nu_{R,M}$$

where m_R is a positive, real constant and the superscript c denotes charge conjugation. $\nu_{R,M} = \nu_R + (\nu_R)^c$ is the RH neutrino field that satisfies the Majorana constraint of self-conjugation, $\nu_{R,M} = \nu_{R,M}^c$. This equation does not violate any known conservation law, because a right handed neutrino does not carry any known, non-zero quantum number that is conserved in the Standard Model.

A similar Majorana mass term is possible for LH neutrinos as well

$$\mathscr{L}_{L,M} = -\frac{m_L}{2}\left(\overline{(\nu_L)^c}\nu_L + \overline{\nu}_L(\nu_L)^c\right) = -\frac{m_L}{2}\overline{\nu}_{L,M}\nu_{L,M}$$

where m_L is a positive, real constant. $\nu L, M = \nu_L + (\nu_L)^c$ is the self-conjugate, LH, Majorana neutrino field. m_L can be generated by some heavy new physics, such as the exchange of a very heavy Majorana sterile neutrino (the type I seesaw [1]), a heavy scalar triplet (the type II seesaw [85]), a fermion triplet (the type III seesaw [86]).

In summary, because the neutrinos are massive, either new particles have to be added to the Standard Model in case the neutrinos are Dirac particles (the ν_R and $\overline{\nu}_L$), or, a new particle type has to be added to the Standard Model such that the neutrinos can be promoted to be Majorana particles. Whether or not one of those scenarios is true, is subject to intense investigation. For example, if neutrinos are their own anti-particles, then the neutrinos emitted in simultaneous beta decay could annihilate one another, opening the search for neutrinoless double beta decay [87].

The Dirac and Majorana mass terms can be combined and the resulting neutrino mass part of the Lagrangian can be rewritten as

$$\mathscr{L}_m = -\frac{1}{2}\left[\overline{(\nu_L)^c}, \nu_R\right]\begin{bmatrix} m_L & m_D \\ m_D & m_R \end{bmatrix}\begin{bmatrix} \nu_L \\ (\nu_R)^c \end{bmatrix} + h.c. \tag{3.1}$$

The mass matrix can be diagonalized and the mass-eigenstates can be determined. Several important results can be obtained for some special cases and limits [88]:

- The pure Majorana case: If $m_D = 0$ the neutrinos are purely Majorana and there is no mixing between the active and sterile states, which is not interesting in the context of this thesis.
- The pure Dirac case: If $m_L = m_R = 0$, the neutrinos are purely Dirac and the Lepton number is conserved.
- The active-sterile mixed case: If m_D is comparable to m_R and m_L, the mass eigenstates contain significant contributions of active and sterile states and the latter become mixed.

- The seesaw limit: If $m_R \gg m_D$ and m_L one obtains the seesaw limit, which provides the leading candidate for an explanation of the small neutrino masses.

The most straightforward type I seesaw takes $m_L = 0$. The mass matrix can be diagonalised and becomes

$$\begin{bmatrix} m_D^2/m_R & 0 \\ 0 & m_R \end{bmatrix}$$

where the entries are real and positive by an appropriate phase choice. Once the mass eigenstates of this matrix are identified as ν and N, the neutrino mass Lagrangian takes the form

$$\mathscr{L}_m = -\frac{1}{2}\frac{m_D^2}{m_R}\overline{\nu}\nu - \frac{1}{2}m_R\overline{N}N = -\frac{1}{2}m_\nu\overline{\nu}\nu - \frac{1}{2}m_N\overline{N}N.$$

If m_R is large, then the mass term m_D^2/m_R is small. That is, the heavier N is, the lighter ν will be. This is the famous seesaw mechanism. The mass parameter m_R introduces a completely new scale in the theory, unrelated to the electroweak scale and the Higgs mechanism, unlike all other elementary fermion masses in the SM. The value of this new mass scale m_R can take any possible value and remains an open question for experimental observations to address. In addition, the number of different HNL is not limited, as they are SM gauge singlets. In a general theory n_s right-handed fields, ν_{sR} with $s = 1,...,n_s$, have to be considered. The mass eigenstates ν_{kL}, with $k = 1,...,3+n_s$ are related to the flavor basis of the active and sterile neutrino fields through the unitary transformation

$$\nu_{\alpha L} = \Sigma_{k=1}^{N} U_{\alpha k}\nu_{kL} \qquad (\alpha = e,\mu,\tau), \tag{3.2}$$

$$\nu_{sR}^{C} = \Sigma_{k=1}^{N} U_{(3+s)k}\nu_{kL} \qquad (s = 1,...,n_s) \tag{3.3}$$

where $N = 3+n_s$ and U is a unitary $N \times N$ matrix, an extended version of the PMNS matrix that was introduced in section 2.3.1. The physical mixing is determined by the first three rows of the matrix U, described by the first equation 3.2. The mixing of the sterile neutrino fields in the second equation 3.3, which is determined by the complementary rectangular submatrix, is not observable. For current experiments, it is sufficient to consider only the 3 × N rectangular mixing matrix.

With theory offering little guidance as to what masses those different sterile neutrinos might have, experiments are searching everywhere their techniques permit. At the same time, various new sterile neutrinos could be used to explain a variety of open questions in physics. Sterile neutrinos can be postulated as the only new Beyond the Standard Model (BSM) particles up to a very high energy scale, providing explanations of major observational BSM phenomena [89]. Sterile neutrinos with masses ranging from $\mathcal{O}$(MeV) to $\mathcal{O}(10^{12})$ GeV can provide mechanisms to generate the baryon asymmetry of the Universe, i.e. the observation of a universal excess of matter over antimatter. While sterile neutrinos in the keV mass range may be a viable dark matter candidate [90]. And some neutrino oscillation anomalies hint at sterile neutrinos in the eV mass range, as will be explained later.

3.1 SoLid search program

The SoLid experiment was designed to search for sterile neutrinos with a mass of $\mathcal{O}(1)$ eV. This search is part of a global neutrino program and was primarily motivated based on phenomenology. Several

anomalies pointed to oscillations of active neutrinos into sterile states with $\Delta m_{SBL} \sim 1$ eV^2, as will be discussed in chapter 4. For sterile neutrinos to be relevant for neutrino oscillations, there has to be non-negligible mixing between active and sterile states of the same chirality. That does not occur in the pure Majorana or pure Dirac case but only for the active-sterile cases (and for a pseudo-Dirac case).

In the present thesis, we will also investigate the sensitivity of the SoLid detector to sterile neutrinos with larger masses, that are usually called Heavy Neutral Leptons (HNL). This will be done in chapter 18. Although there are only three active neutrino flavors, all the neutrino mass eigenstates take part in charged-current weak interactions, if their masses are kinematically allowed, through the unitary relation. From an experimental point of view, only the scenarios with $m_N < \mathcal{O}(\text{TeV})$ offer the possibility of being tested in foreseeable future. A lot of interest was given to the GeV scale seesaw models, that can be efficiently searched for with the existing experimental technologies. Due to the absence of a signal, various search experiments have set upper bounds on the mixing parameter $U_{\alpha I}$ in function of the HNL mass for a given flavor α. With the SoLid experiment, we aim to search for HNL that have masses around 1-10 MeV. Due to the presence of mixing these HNL are unstable, and their subsequent decay products could be observed in our detector. The search for HNL is a complementary new physics analysis to the search for eV scale oscillations.

4

THE LIGHT STERILE NEUTRINO HYPOTHESIS

To date, a coherent theory of 3-flavour neutrino oscillations was constructed that seems to be supported by the available data and is therefore widely accepted. However, some short-baseline neutrino experiments are in tension with this theory. This is described in section 4.1 with special emphasis on the reactor antineutrino anomaly (RAA). The anomalous results require the existence of a new Δm^2, pointing to extended frameworks that most likely contain sterile neutrinos, as was introduced in chapter 3. Section 4.2 will investigate the light sterile neutrino in terms of neutrino oscillations in more detail. The global fits in the parameter space of the light sterile neutrino, obtained from oscillation measurements, will be discussed in section 4.3. In addition, section 4.4 describes the recently improved predictions of the reactor neutrino flux, which could (partly) remove the RAA.

4.1 NEUTRINO ANOMALIES

4.1.1 ACCELERATOR ANOMALY

The neutrino oscillation anomalies are as old as the oscillation formalism itself. Around the same period as the Super-Kamiokande collaboration found strong evidence for neutrino oscillations, the LSND experiment was conducted at the accelerator facility of Los Alamos from 1993 to 1998 [91]. The LSND experiment was designed to search $\overline{\nu}_\mu$ to $\overline{\nu}_e$ oscillations through $\overline{\nu}_e$ appearance in a single near detector located 30 m from the accelerator-based neutrino source, making it sensitive to a $\Delta m^2 \sim 1.0$ eV^2. The experiment used a tank filled with 167 tons of mineral oil (CH_2) and liquid scintillator, to detect the $\overline{\nu}_e$ through the IBD interaction, where the prompt e^+ and delayed neutron signal were viewed by 1220 photo multiplier tubes.

Covering the energy range from 20 to 50 MeV, the LSND experiment showed a significant excess of $\overline{\nu}_e$-like events over the background, at the level of 3.8σ [92]. These oscillations can be explained with a $\Delta m^2_{SBL} \gtrsim 0.1$ eV^2, which is far larger than the values obtained from solar and atmospheric neutrino oscillations. The LSND results conflict with the Standard Model expectation of only three neutrino flavors and suggest the possible existence of sterile neutrinos (which will be elaborated in section 4.2). A competing experiment, KARMEN, performed a similar measurement at a shorter baseline of 17.7 m and did not find an excess [93]. This contradicted the LSND results and their anomaly stayed unconfirmed for some time.

The LSND anomaly was explored further by the MiniBooNE experiment that has been operating at Fermilab since 2002 [94]. The detector consists of a tank filled with 818 tons of pure mineral oil (CH2) viewed by 1520 phototubes, and operates at a baseline of 541 m from the Fermilab Booster beam. Since the neutrino energy ranges from 200 MeV to 3 GeV, MiniBooNe has an L/E range from 0.18 to 2.7 m/MeV, which covers the LSND range from 0.5 to 1.5 m/MeV. MiniBooNE is sensitive to

the same mass difference as LSND, but with different systematic effects and in a different, and better understood, neutrino energy regime.
The MiniBooNE experiment operated both in ν_μ and $\overline{\nu}_\mu$ mode. When investigating ν_e appearance, respectively $\overline{\nu}_e$ appearance, in 2007 with an energy threshold of 475 MeV for background reduction, no excess over background was observed, leading to a 98% exclusion of neutrino oscillation as the explanation of the LSND anomaly [94]. However below the energy that was previously used as threshold, an excess of ν_e-like events was observed in 2009 [95]. At lower energies, such an excess is more likely the result of some unknown background. Yet another year later, the MiniBooNE experiment unexpectedly did see an excess, consistent with the LSND result, over the entire energy range in both neutrino and antineutrino mode [96]. The combined significance of the LSND and MiniBooNE observations leads to an excess of 6σ [97], and is known as the accelerator anomaly.
However significant, the true origin of the excess is ambiguous. Different photon backgrounds, for example related to π^0 decay can mimic electron like ν_e signatures. This anomaly is going to be investigated in the MicroBooNE experiment at Fermilab, with a large Liquid Argon Time Projection Chamber (LArTPC) in which electrons and photons can be distinguished [98]. It should bring a new constraint on the accelerator anomalies in the years to come.

4.1.2 GALLIUM NEUTRINO ANOMALY

The Gallium anomaly was discovered in 2005-2006 during calibration of the GALLEX [99] and SAGE [100] solar neutrino detectors, that were introduced in chapter 2.1. The detectors were calibrated with intense radioactive sources, ^{51}Cr and ^{37}Ar. They produce ν_e in the solar energy range below 1 MeV, through the electron capture processes

$$^{51}Cr \longrightarrow ^{51}V + \nu_e \qquad (Q = 752keV)$$
$$^{37}Ar \longrightarrow ^{37}Cl + \nu_e \qquad (Q = 814keV).$$

The sources were placed near the center of each detector and the ν_e were detected in the same way as solar neutrinos. The expected number of neutrinos was calculated from the known source activity. The ratio of the number of measured (N_{exp}) and calculated (N_{cal}) ν_e like events in the two ^{51}Cr GALLEX experiments and in the ^{51}Cr and ^{37}Ar SAGE experiments is shown in figure 4.1.1. The average ratio is R = 0.84 ± 0.05. The significance of the Gallium anomaly was determined as 3σ [101], but was reduced in 2019 to 2.3σ based on new cross-section calculations [102].

Since the average distance that the neutrinos travel in the GALLEX and SAGE experiments are respectively 1.9 m and 0.6 m, and the neutrino energy is about 0.8 MeV, the Gallium neutrino anomaly could be explained by neutrino oscillations generated by a $\Delta m^2_{SBL} \gtrsim 1$ eV^2 [103].

4.1.3 REACTOR ANTINEUTRINO ANOMALY

Measurements of reactor antineutrino spectra have shown evidence of the reactor antineutrino anomaly, that is a global deficit, observed by short baseline reactor experiments with respect to the predicted antineutrino flux. The reactor anomaly arose after the introduction of new and very detailed predictions of the $\overline{\nu}_e$ flux from reactors in 2011 [104]. Up to that point the measured $\overline{\nu}_e$ event rates in short baseline reactor experiments agreed reasonably well with predictions. However, the new

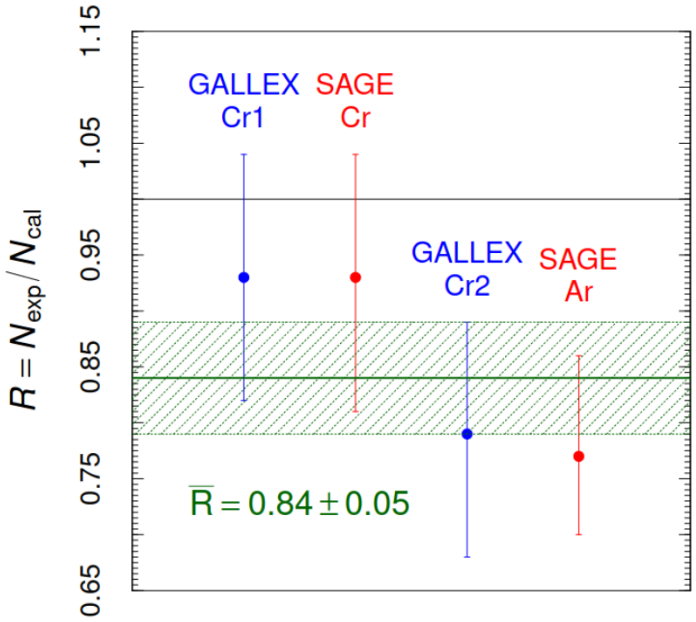

Figure 4.1.1: The Gallium neutrino anomalies from source calibrations of the neutrino experiments GALLEX and SAGE. The data error bars represent the uncorrelated experimental uncertainties. The horizontal solid green line and the band show the average ratio R and its uncertainty.[103]

flux was approximately 3% larger than earlier calculations, which led to the reactor data displaying a disappearance of $\overline{\nu}_e$ by the same 3% . This missing flux could be attributed to neutrino oscillations to some sterile state with $\Delta m^2 \gtrsim 1$ eV^2.

Calculating the reactor flux in detail is a very complex problem. A nuclear reactor emits in the order of 10^7 $\overline{\nu}_e$ per megawatt of thermal power with energies up to about 10 MeV. Per fission there are about six β decays, and hence neutrinos that stem from the beta-decay of the fission products. The reactor antineutrino spectrum is the sum over all beta decays. Fortunately, there are only four isotopes whose fissions make up more than 99% of all reactor neutrinos with an energy above the inverse β decay threshold: ^{235}U, ^{239}Pu, ^{241}Pu, and ^{238}U.

The dominant contributions to the spectrum stem from the thermal neutron induced fission of ^{235}U and ^{239}Pu. Contributions from the fission of ^{238}U and ^{241}Pu are below 10% of the total fission rate. The spectral shapes of these various components are very different. In addition there is a time dependence in the composition of the β spectrum, as ^{239}Pu is bred from ^{238}U and also the ^{241}Pu component varies strongly as a consequence of breeding. The total spectrum alters with the time evolution of the reactor core. The resulting neutrino flux of a nuclear reactor is a superposition of thousands of β-decay branches of the fission fragments of those four isotopes and thus a first-principles calculation is challenging, even with modern nuclear structure data.

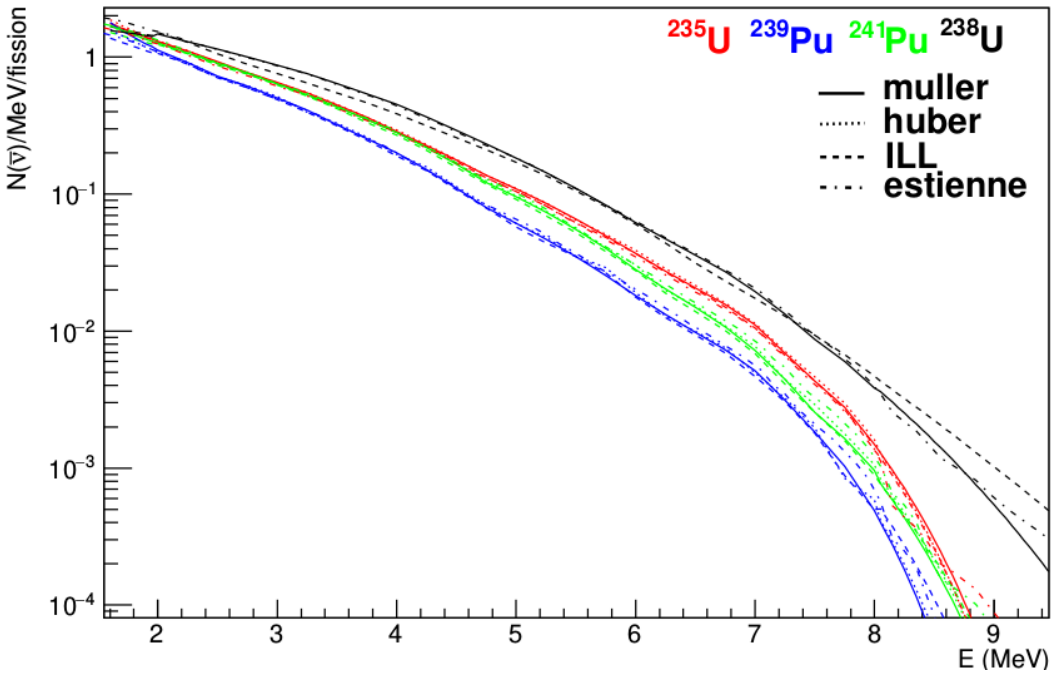

Figure 4.1.2: Reactor antineutrino spectra for the main fissile isotopes, ^{235,238}U, ^{239,241}Pu, obtained by Schreckenbach (ILL) [107], Mueller [108] and Huber [109] via the conversion method and by Estienne[110] via the summation method. These spectra will be used to model the neutrino flux in the SoLid experiment.

CONVERSION METHOD TO PREDICT THE REACTOR $\overline{\nu}_e$ SPECTRUM

The total $\overline{\nu}_e$ spectrum of a nuclear reactor, that can not be directly detected, can be derived from a measurement of the accumulated beta spectra of fission products via a conversion procedure. The $\overline{\nu}_e$ spectrum is correlated with the beta spectrum (electron spectrum) by the energy conservation law for individual beta decay branches $E_\nu + E_\beta = E_0$, where E_0 denotes the end point energy of the branch.

In the 1980s, the total β spectrum from the thermal fission of ^{235}U, ^{239}Pu, and ^{241}Pu were obtained at the Institut Laue-Langevin (ILL) [105]. The β-spectra were acquired from fissions, induced by the irradiation of isotope target foils with reactor neutrons for a few hours up to 2 days. The β-spectrum of ^{238}U was measured much later at the FRM II neutron source in Garching, Germany [106]. The measurements gave access only to the sum of the contributions of all fission products. In the energy range from 1.5 to 8.0 MeV the spectrum was determined per fission with an accuracy of 5%. There are, currently, no corresponding total β spectra for ^{238}U since this isotope is fissioned only by fast neutrons and one still has to rely on theoretical predictions.

Schreckenbach et al. converted the ILL spectrum to a neutrino spectrum [107], taking into account the Z distribution of the fission products. The experimental β spectrum was approximated by a set of hypothetical beta-branches, $\left(a_i, E_0^{(i)}, \overline{Z}(E_0^{(i)})\right)$, with amplitude a_i, end-point energy $E_0^{(i)}$ and $\overline{Z}_i$ the empirical mean proton number of the fission products with beta branches of endpoint energy E_0^i. The conversion procedure consists in dividing the electron spectrum, $S_\beta(E)$, into 30 slices. Starting with the highest energy slice, the data points in this slice were used to fit the endpoint and branching

ratio of the first virtual branch. After subtracting the full contribution of this virtual branch from the experimental spectrum, the procedure is repeated for the next, lower energy, slice. The decomposition,

$$S_\beta(E) = \sum_i S^i_\beta\left(E, E^i_0, \overline{Z}(E^i_0)\right).$$

reproduced, the original spectrum $S_\beta(E)$ to better than 1 %. E^i_0 is the end-point energy of a partial spectrum. The corresponding antineutrino spectrum is then obtained as the sum of all fitted virtual branches, converted to antineutrino branches by replacing E_e by the corresponding $E_{\bar{\nu}}$ and applying the correct radiative corrections,

$$S_{\bar{\nu}}(E) = \sum_i S^i_\beta\left(E^i_0 - E, E^i_0, \overline{Z}(E^i_0)\right).$$

The obtained spectra are shown in figure 4.1.2. This distribution includes the over simplified assumption of exclusive groundstate to groundstate beta decays. In a more realistic model the beta endpoint energies of individual beta branches, including those to excited states in the daughter nucleus, have to be taken into account. With this data the major part of the antineutrino spectrum of a reactor could be constructed, where in general the fission rates for the individual isotopes are well known parameters.

The conversion procedure was revisited in 2011 independently by Huber [109] and by Mueller et al [108]. Leading to new reference antineutrino spectra for ^{235}U, ^{239}Pu, and ^{241}Pu isotopes in the 2-8 MeV range that are shown in figure 4.1.2. While the shapes of the spectra and their uncertainties are comparable to that of the previous analysis, the normalisation is shifted up by about +3% on average.

Mueller developed a more accurate approach for the dominant isotopes ^{235}U, ^{239}Pu, using ab-initio information from nuclear databases. Effective electron and antineutrino spectra were generated as the sum of the spectra of all fission products in the database, weighted by the activity of the fission isotopes. Only for missing contributions coming from unknown nuclei and remaining systematic effects of nuclear databases, some β branches from the ILL reference β spectra were used.

Huber avoided the nuclear databases and their shortcomings. The only place at which information from nuclear databases enters directly is in the form of the effective nuclear charge $\overline{Z}$. Huber treated the theoretical β-spectrum shape to a higher level of accuracy by including several subleading corrections at a branch-by-branch level. Such as corrections based on the finite size of the nucleus and on the screening of the nuclear charge by its bound electrons. And radiative corrections due to the emission of virtual and real photons by the charged particles present in β decay. The results averaged over all energies are in very good agreement with the results found by Mueller and confirmed the overall (2-3)% upward shift relative to the original inversion by Schreckenbach. To a good approximation, this reevaluation applies to all reactor neutrino experiments.

REACTOR ANTINEUTRINO ANOMALY

In a fission reactor, the emitted antineutrino spectrum, mainly coming from beta decays of the fission products of ^{235}U, ^{239}Pu, ^{241}Pu, and ^{238}U, is then given by

$$S_{\text{tot}}(E_\nu) = \sum_k f_k S_k(E_\nu)$$

#	result	Det. type	τ_n (s)	^{235}U	^{239}Pu	^{238}U	^{241}Pu	old	new	err(%)	corr(%)	L(m)
1	Bugey-4	^{3}He+H_2O	888.7	0.538	0.328	0.078	0.056	0.987	0.942	3.0	3.0	15
2	ROVNO91	^{3}He+H_2O	888.6	0.614	0.274	0.074	0.038	0.985	0.940	3.9	3.0	18
3	Bugey-3-I	^{6}Li-LS	889	0.538	0.328	0.078	0.056	0.988	0.946	4.8	4.8	15
4	Bugey-3-II	^{6}Li-LS	889	0.538	0.328	0.078	0.056	0.994	0.952	4.9	4.8	40
5	Bugey-3-III	^{6}Li-LS	889	0.538	0.328	0.078	0.056	0.915	0.876	14.1	4.8	95
6	Goesgen-I	^{3}He+LS	897	0.620	0.274	0.074	0.042	1.018	0.966	6.5	6.0	38
7	Goesgen-II	^{3}He+LS	897	0.584	0.298	0.068	0.050	1.045	0.992	6.5	6.0	45
8	Goesgen-II	^{3}He+LS	897	0.543	0.329	0.070	0.058	0.975	0.925	7.6	6.0	65
9	ILL	^{3}He+LS	889	$\simeq 1$	—	—	—	0.832	0.802	9.5	6.0	9
10	Krasn. I	^{3}He+PE	899	$\simeq 1$	—	—	—	1.013	0.936	5.8	4.9	33
11	Krasn. II	^{3}He+PE	899	$\simeq 1$	—	—	—	1.031	0.953	20.3	4.9	92
12	Krasn. III	^{3}He+PE	899	$\simeq 1$	—	—	—	0.989	0.947	4.9	4.9	57
13	SRP I	Gd-LS	887	$\simeq 1$	—	—	—	0.987	0.952	3.7	3.7	18
14	SRP II	Gd-LS	887	$\simeq 1$	—	—	—	1.055	1.018	3.8	3.7	24
15	ROVNO88-1I	^{3}He+PE	898.8	0.607	0.277	0.074	0.042	0.969	0.917	6.9	6.9	18
16	ROVNO88-2I	^{3}He+PE	898.8	0.603	0.276	0.076	0.045	1.001	0.948	6.9	6.9	18
17	ROVNO88-1S	Gd-LS	898.8	0.606	0.277	0.074	0.043	1.026	0.972	7.8	7.2	18
18	ROVNO88-2S	Gd-LS	898.8	0.557	0.313	0.076	0.054	1.013	0.959	7.8	7.2	25
19	ROVNO88-3S	Gd-LS	898.8	0.606	0.274	0.074	0.046	0.990	0.938	7.2	7.2	18

Figure 4.1.3: N_{obs}/N_{pred} ratios based on old and new spectra. Off-equilibrium corrections have been applied when justified. The err column is the total error published by the collaborations including the error on S_{tot}, the corr column is the part of the error correlated among multiple-baseline experiments, or experiments using the same detector.[104]

where f_k refers to the contribution of the main fissile nuclei to the total number of fissions of the k^{th} branch, and S_k to their corresponding neutrino spectrum per fission. For a certain reactor, the distribution and occurrence of the main fissions has to be determined. Together with the choice of neutrino spectra, like the ones that were discussed in the previous section, the reactor neutrino spectrum can be determined.

After the Huber-Mueller prediction increased the expected mean flux by about 3 percent, for several neutrino experiments at nuclear reactors, the predicted neutrino rates were reevaluated separately, while the observed event rates and their associated errors were unchanged. Experiments that were available at the time were performed at a few tens of meters from nuclear reactor cores at ILL [111], Goesgen [112], Rovno [113], Krasnoyarsk [114], Bugey-3[115], Bugey-4 [116] and Savannah River [117]. Middle- and long-baseline experiments were performed at CHOOZ [118] and KamLAND [119].

For detectors at distances less than 100 m from a reactor, the ratio of observed event rate to predicted rate shifted to 0.943 ± 0.023 with the new flux evaluation, leading to a deviation from unity at 98.6% C.L. which is called the reactor antineutrino anomaly (RAA). This reactor antineutrino anomaly is clearly illustrated in figure 4.1.4 and is still to be explained. The ratios of observed to predicted event rates, $R = N_{obs}/N_{pred}$, are summarised in Table 4.1.3. The anomaly triggers the search for sterile neutrinos close to experimental reactors. The comparison between the converted and measured spectra also exhibited a large distortion of the data with respect to the model between 5 and 7 MeV in antineutrino energy (see section 4.1.3). These two findings raised questions about the antineutrino predictions based on the conversion method. Several possible explanations of the deviation from

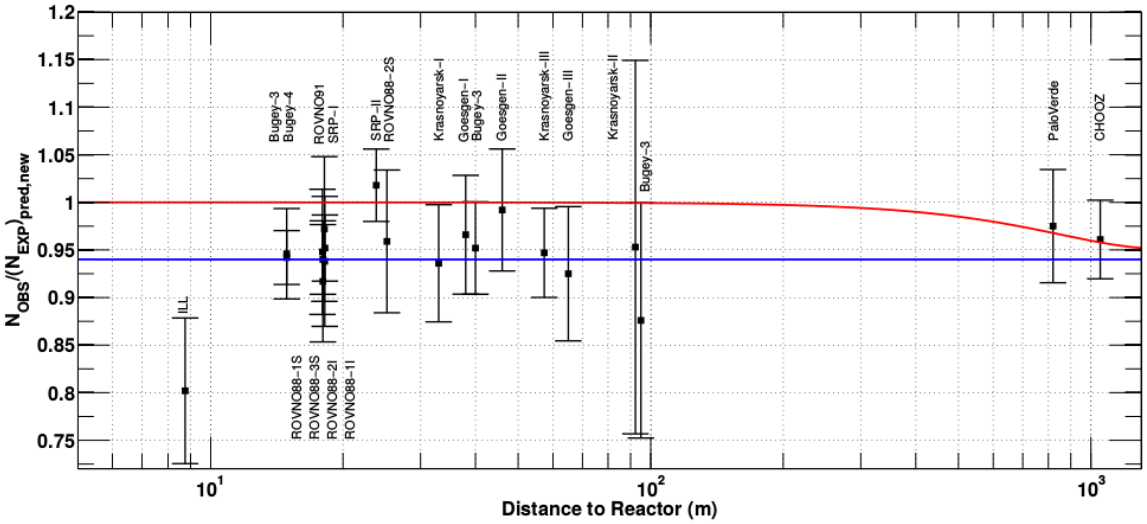

Figure 4.1.4: Illustration of the short baseline reactor antineutrino anomaly. The experimental results are compared to the prediction without oscillation, taking into account the new antineutrino spectra, the corrections of the neutron mean lifetime, and the off-equilibrium effects. Published experimental errors and antineutrino spectra errors are added in quadrature. The mean averaged ratio including possible correlations is 0.943 ± 0.023. The red line shows a possible 3 active neutrino mixing solution, with $\sin^2(2\theta_{13}) = 0.06$. The blue line illustrates a solution including a new neutrino mass state, such as $|\Delta m^2_{new,R}| \gg 1eV^2$ and $\sin^2(2\theta_{\text{new,R}}) = 0.12$.[104]

unity have been assessed [104]: an erroneous prediction of the antineutrino flux from the reactors, or a correlated artefact in the experiments, or a real physical effect if both previous cases are excluded. The anomaly cannot be associated with a single fissile isotope. The Krasnoyarsk and ILL experiments operated with nuclear fuel such that the difference between the real antineutrino spectrum and that of pure ^{235}U was less than 1.5%. They reported similar deficits to those observed at other reactors operating with a mixed fuel of ^{235}U, ^{239}Pu, ^{241}Pu and ^{238}U.

The anomaly could be explained by a common bias in all reactor neutrino experiments. The measurements used one of two techniques. They either used liquid scintillator counters, possibly doped with ^{6}Li, which is a technique that was discussed earlier (Bugey-3, Savannah river). Or they used integral detectors, where the total number of antineutrino interactions is measured by detecting only the neutrons from the IBD interaction in ^{3}He-filled counters. (Bugey-4, Rovno91, Rovno88 1I and 2I). Some experiments combined both techniques to measure both the positron and the neutron from the IBD interaction (ILL, Goesgen, Krasnoyarsk).

The elements discussed above argue against a trivial bias in the experiments, but a detailed analysis of the most sensitive of them would improve the quantification of the anomaly. Given the ranges of reactor neutrino energies and source-detector distances, the deficit could be explained by neutrino oscillations generated by a $\Delta m^2 \gtrsim 1eV^2$.

4.2 STERILE NEUTRINO SOLUTION

The short-baseline neutrino oscillation anomalies indicate that there is at least one additional squared-mass difference $\Delta m^2_{SBL} \sim 1$ eV^2, which is much larger than the solar and atmospheric squared-mass differences, that are respectively $\Delta m^2_{\text{sol}} \simeq 7.4 \times 10^{-5}$ eV^2 and $\Delta m^2_{\text{atm}} \simeq 2.5 \times 10^{-3}$ eV^2. This implies that the 3ν mixing framework must be extended with the addition of at least one light massive neutrino. The LEP measurements of the invisible width of the Z boson (see section 1.3) showed that there are only three active neutrinos with masses below half the Z^0 boson mass. Therefore, the additional neutrinos correspond in the flavor basis to sterile neutrinos - hypothetical neutral leptons that do not engage in the standard weak interactions but can mix with the ordinary active neutrinos. The sterile neutrinos appear fleetingly during the oscillation process.

Sterile neutrinos were already discussed in chapter 3 as an extension for the Standard Model in order to accommodate the observation that neutrinos ought to be massive to generate the neutrino oscillations. To accommodate the short-baseline mass splitting Δm^2_{SBL}, we consider the simplest framework with one additional neutrino mass state, corresponding to one sterile neutrino. Based on the different Δm^2 the possible orderings for the mass states are shown in figure 4.2.1.

The $2+2$ schemes on the left are strongly disfavored because they imply large active-sterile oscillations either of solar neutrinos or of atmospheric neutrinos, but the data exclude this possibility.
In the $1+3$ schemes to the right, the new ν_4 is lighter than the standard massive neutrinos that are at the eV scale. This is strongly disfavored by the cosmological upper bound below 1 eV on the standard neutrino masses, because the flavor neutrinos mainly mix with the standard massive neutrinos.
In the $3+1$ schemes in the center, the new ν_4 is at the eV scale and heavier than the three standard massive neutrinos. This is allowed by the existing experiments, because it can be a perturbation of standard 3ν mixing when $|U_{\alpha 4}|^2 \ll 1$ with $\alpha \in \{e, \mu, \tau\}$. This means that the non-standard massive neutrinos ν_4 must be mostly sterile.

The $3+1$ scheme can be considered as an effective framework for the study of short-baseline neutrino oscillations. This approach does not exclude the existence of other non-standard massive and mostly sterile neutrinos, but their mixing with the active neutrinos is assumed to be so small that

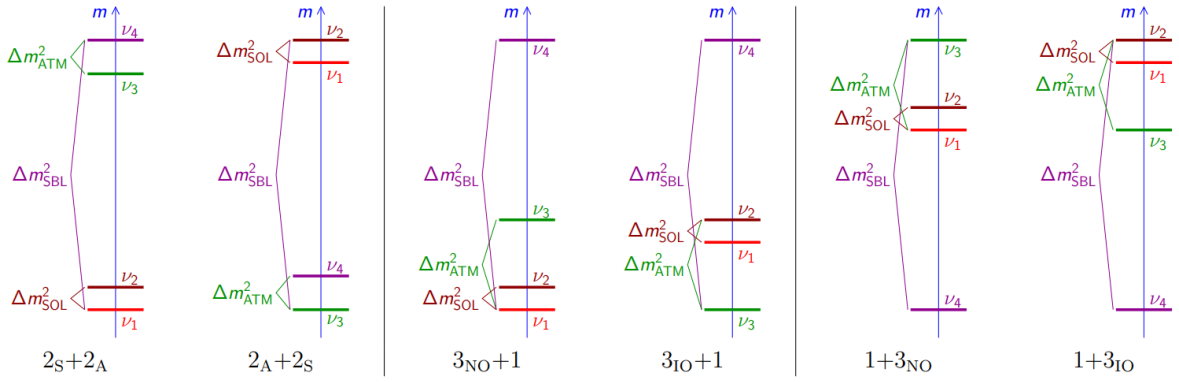

Figure 4.2.1: Schematic illustration of the 2+2, 3+1, and 1+3 neutrino mixing schemes.[103]

their effects are negligible in current neutrino oscillation experiments.

The relation between the active neutrino flavors and the sterile states, was given by equations 3.2 and 3.3. Recall that for the physical mixing only the first three rows of U have to be considered, as described by the first equation. As in section 2.3, it is common and useful to parameterize the mixing matrix in terms of mixing angles and phases. Considering only the physical mixing described by the first three rows, this becomes

$$U = \begin{pmatrix} c12c13c14 & s12c13c14 & c14s13e^{-i\delta_{13}} & s14e^{-i\delta_{14}} \\ \dots & \dots & c13c24s23 - s13s14s24e^{-i\delta_{14}-\delta_{13}} & c14s24 \\ \dots & \dots & c14c24s34e^{-i\delta_{34}} & \dots \end{pmatrix} \cdot \begin{pmatrix} 1 & 0 & 0 & 0 \\ 0 & e^{i\lambda_{21}} & 0 & 0 \\ 0 & 0 & e^{i\lambda_{31}} & 0 \\ 0 & 0 & 0 & e^{i\lambda_{41}} \end{pmatrix}$$

where the dots replace the elements with long expressions. The new mixing parameters are three mixing angles θ_{i4}, two Dirac CP-violating phases δ_{14} and δ_{34}, and a Majorana CP-violating phase λ_{41}. Oscillation experiments only involve ν_e and ν_μ and therefore depend on only two mixing angles, θ_{14} and θ_{24}, and one Dirac CP-violating phase, δ_{14}.

For the analysis of the short-baseline oscillation probabilities, the effects of the small Δm^2_{sol} and Δm^2_{atm} can be neglected, because they generate oscillations at larger distances. The effective short-baseline oscillation probabilities [88] are

$$P^{SBL}_{\overset{(-)}{\nu}_\alpha \to \overset{(-)}{\nu}_\beta} = \left| \delta_{\alpha\beta} - \sin^2(2\theta_{\alpha\beta}) \sin^2\left(\frac{\Delta m^2_{41} L}{4E}\right) \right|$$

where the amplitude only depends on the elements of the fourth column of the mixing matrix

$$\sin^2(2\theta_{\alpha\beta}) = 4\,|U_{\alpha 4}|^2 \left| \delta_{\alpha\beta} - \left|U_{\beta 4}\right|^2 \right|.$$

The electron and muon (anti)neutrino appearance and disappearance in short-baseline experiments have the following amplitudes:
$\overset{(-)}{\nu}_\mu \leftrightarrow \overset{(-)}{\nu}_e$ transitions have the amplitude

$$\sin^2 2\theta_{e\mu} = 4\,|U_{e4}|^2 \left|U_{\mu 4}\right|^2 = \sin^2 2\theta_{14} \sin^2 \theta_{24}$$

$\overset{(-)}{\nu}_e$ disappearance has the amplitude

$$\sin^2 2\theta_{ee} = 4\,|U_{e4}|^2 \left(1 - |U_{e4}|^2\right) = \sin^2 2\theta_{14}$$

$\overset{(-)}{\nu}_\mu$ disappearance has the amplitude

$$\sin^2 2\theta_{\mu\mu} = 4\left|U_{\mu 4}\right|^2 \left(1 - \left|U_{\mu 4}\right|^2\right) \simeq \sin^2 2\theta_{24}$$

Note that the effective short-baseline oscillation probabilities of neutrinos and antineutrinos are equal, because they depend on the absolute values of the elements of the mixing matrix. Therefore, CP violation cannot be measured in short-baseline experiments.

4.3 GLOBAL FIT OF STERILE NEUTRINO SEARCHES

The confirmation in 2011 of the reactor antineutrino anomaly, after the older LSND and Gallium anomalies, triggered the start of an intense experimental program. The analyses of a wide variety of short-baseline oscillation data are combined into global fits addressing the anomalies in terms of active-sterile neutrino oscillations.

The ν_e and $\overline{\nu}_e$ disappearance were investigated with reactor experiments. To eliminate the flux uncertainty, model independent searches have been performed by comparing the spectrum of $\overline{\nu}_e$ at different distances to the reactor. Most notable by NEOS/DayaBay and DANSS. The NEOS experiment [120] is a 0.8 ton Gd-based liquid scintillator detector, that took data in 2015-2016 at a distance of 24 m from the 2.8 GWth reactor unit 5 of the Hanbit Nuclear Power Complex in Korea. The powerful commercial station results in a high IBD rate of 1976 events per day, but because the reactor is not compact an averaged oscillation signal is measured. In order to make the measurement independent from the theoretical flux calculation, the measured $\overline{\nu}_e$ spectrum is normalised to the spectrum measurement of Daya Bay [79] at a baseline of about 550 m (Daya Bay was introduced in section 2.5.1). Because Daya Bay is on a different site, this procedure may lack robustness and lead to uncontrolled systematic uncertainties.
In the DANSS experiment [121] a highly segmented plastic scintillator detector with a volume of 1 m^3 is placed under an industrial 3.1 GWth reactor of the Kalinin Nuclear Power Plant in Russia. The detector is installed on a movable platform which allows to change the baselines between 10.7 m, 11.7 m, and 12.7. The high reactor power leads to 4910 IBD counts per day, but the energy resolution is low and the large core leads again to an averaging of the oscillation. To be independent from the reactor neutrino spectra predictions, the analysis is done by comparing the shape of the recorded energy spectra at different baselines.

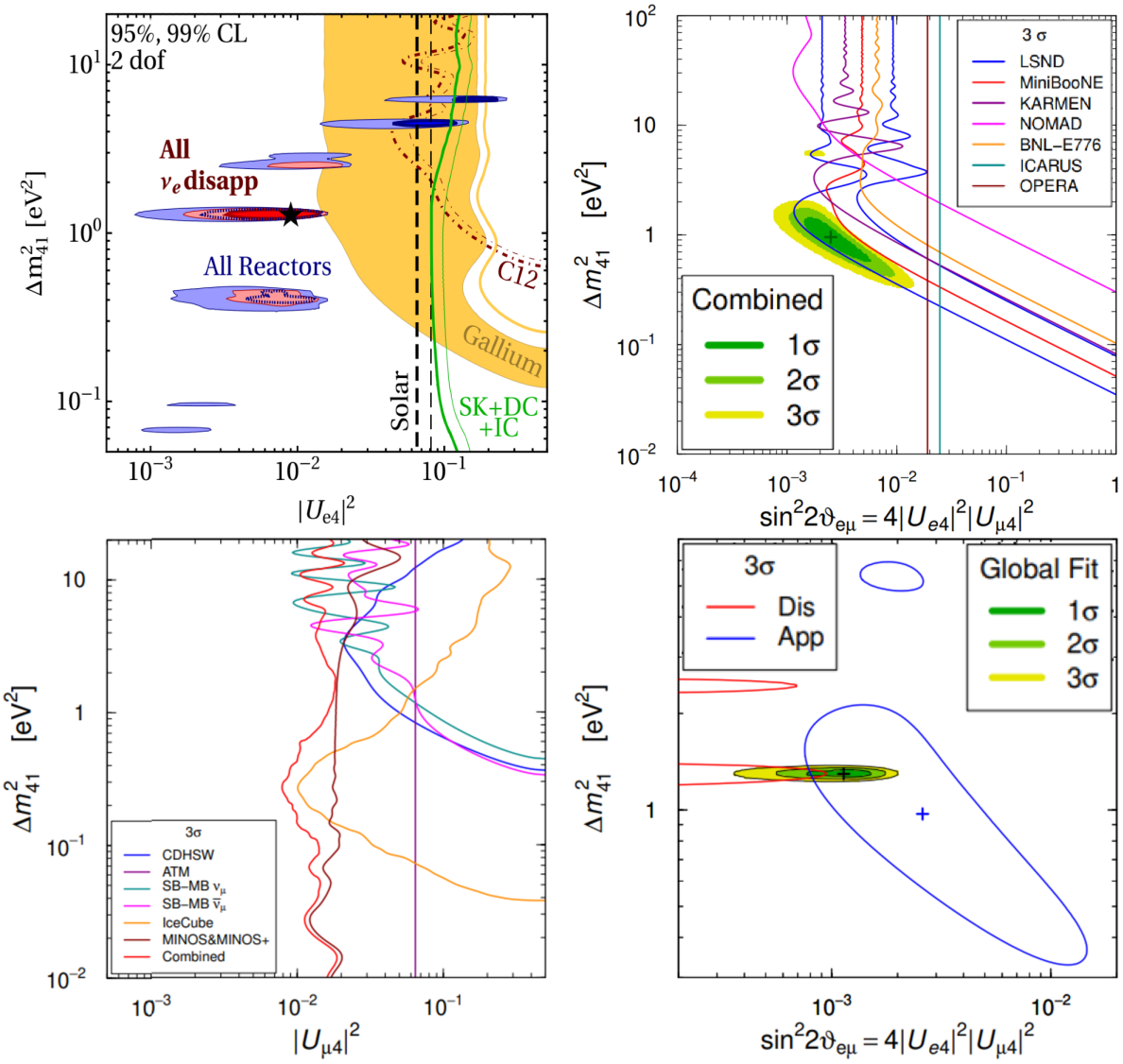

Figure 4.3.1: Top left: Results on SBL$\overset{(-)}{\nu_e}$ disappearance [122]. The blue shaded regions were obtained from a global fit of the reactor neutrino data including the NEOS/Daya Bay and DANSS spectral ratio data and the total event rates considering as free the dominant ^{235}U and ^{239}Pu reactor $\overline{\nu_e}$ fluxes and constraining the subdominant ^{238}U and ^{241}Pu fluxes around their theoretical predictions with a large 10% uncertainty. The red shaded regions have been obtained by adding the Gallium, solar, and $\nu_e^{12}C$ constraints, that are also shown separately. The figure shows also the atmospheric neutrino constraint obtained from the Super-Kamiokande (SK), DeepCore (DC) and IceCube (IC) data, that is comparable to the solar neutrino constraint. Top right: Results of SBL $\overset{(-)}{\nu}_\mu \to \overset{(-)}{\nu}_e$ appearance experiments without the low-energy MiniBooNE data [103]. All the lines exclude the region on their right at 3σ, except the LSND lins that enclose 3σ allowed regions. The shaded regions are allowed by the combined fit. Bottom: Results of SBL$\overset{(-)}{\nu_\mu}$ disappearance experiments (left) and global fit of appearance (App) and disappearance (Dis) data (right). All the lines in the left panel and the Dis lines in the right panel exclude the region on their right at 3σ. The App lines in the right panel enclose the 3σ allowed regions. The shaded regions are allowed by the global combined fit. [103]

The result of ν_e and $\overline{\nu}_e$ disappearance measurements, is shown in the top left panel of figure 4.3.1, from a global fit of the reactor neutrino data including the NEOS/Daya Bay and DANSS spectral ratio data and including total event rate measurements. For the latter, to avoid an incorrect flux prediction, the dominant fluxes are considered free and the subdominant ^{238}U and ^{241}Pu fluxes are constrained around their theoretical predictions with a large 10% uncertainty. The best fit point for the NEOS and DANSS data coincide at parameters around $\sin^2 2\theta_{ee} \sim 0.04 - 0.05$ and $\Delta m^2 41 \sim 1.3 - 1.4$ eV^2 [103]. This was an indication in favor of short-baseline active-sterile neutrino oscillations at the 3σ level that updates the older reactor antineutrino anomaly and can be considered as more robust, since it is not based on the theoretical flux calculations.
There is a tension between the allowed regions from model-independent reactor measurements and from the Gallium anomalies. This indicates that corrections to the theoretical reactor flux predictions are needed and that the efficiencies of the GALLEX and SAGE detectors may have been overestimated.

For $\overset{(-)}{\nu}_\mu \to \overset{(-)}{\nu}_e$ appearance, the experimental results are shown in the top right panel of figure 4.3.1, including measurements from LSND [92], MiniBooNE [96] (introduced in section 4.1.1) and KARMEN[93], OPERA [73] and others. Of all the experiments only LSND and MiniBooNE found indications in favor of SBL $\overset{(-)}{\nu}_\mu \to \overset{(-)}{\nu}_e$ transitions. However, most of the MiniBooNE low energy excess lies out of the L/E range of LSND and it is probably not due to oscillations. The controversial low-energy MiniBooNE data are omitted. The LSND results give a closed contour in the plane of the oscillation parameters. The other experiments provide exclusion curves that constitute upper limits on $\sin^2 2\theta_{e\mu}$ for each value of Δm^2.

ν_μ and $\overline{\nu}_\mu$ disappearance has not been observed so far, although it should show up if SBL active-sterile oscillations exist. The bottom left panel of figure 4.3.1 shows a summary of the exclusion curves found in the disappearance experiments SciBooNE-MiniBooNE, IceCube [123], MINOS and MINOS+[124], and the atmospheric neutrino bound [125]. The recent MINOS and MINOS+ bound is particularly severe for $\Delta m^2_{41} \sim 1$ eV^2 and determines the overall combined limit on $\left|U_{\mu 4}\right|^2$. This strong bound causes the strong appearance-disappearance tension, discussed below.

The global fit of appearance and disappearance data is shown in the bottom right panel of figure 4.3.1. The region within the blue contours is allowed at 3σ by the appearance data. The combined bound of $\overset{(-)}{\nu}_e$ and $\overset{(-)}{\nu}_\mu$ disappearance data exclude at 3σ all the region outside the two red semicontours. There is a strong tension between both results. The tension cannot be alleviated by considering more than one sterile neutrino, because the appearance and disappearance amplitudes are related. The appearance-disappearance parameter goodness-of-fit is as low as 0.015%, disfavoring the global 3+1 fit at 3.8σ. Therefore, the current status of the global fit of appearance and disappearance data indicates that the interpretation of the results of some experiment or group of experiments in terms of neutrino oscillations is not correct.

In summary, there are a number of experimental results that appear anomalous in the context of the standard 3 neutrino framework, and can be explained by a sterile neutrino with mass around 1 eV. At the same time, there are a number of results which are in conflict with this interpretation. The data collected to date present an incomplete, perhaps even contradictory picture, where 2-3σ agreement in favor of and in contradiction to the existence of sterile neutrinos is present. Taking into account the caveats like old and controversial data, it is clear that the results of the global fits cannot be considered as very accurate, but must be considered as indicative of the true solution, whose

accurate value can only be found with new experiments. A more ardent and complete test of the sterile neutrino hypothesis is needed, which will unambiguously confirm or refute the interpretation of past experimental results.

4.3.1 NEW STERILE SEARCHES

At the moment there is no definitive experimental result either in favor or against the eV-scale sterile neutrinos. The SoLid experiment and other dedicated experiments have been designed and built to make precision measurements of the energy spectrum at different distances in order to obtain accurate information on neutrino oscillations that are independent of the neutrino flux calculations. The experiments are similar in that they are located at very short baseline of a nuclear reactor and have a segmented detector design in order to get a position resolution on the oscillation pattern.

PROSPECT [126] is installed at the compact reactor core of the High Flux Isotope Reactor (HFIR) at Oak Ridge National Laboratory (USA). The reactor uses highly enriched ^{235}U and has a maximal power of 85 MW. The detector is a 2.0 m × 1.6 m × 1.2 m volume containing 4 ton of ^{6}Li doped liquid scintillator, as shown in the left panel of figure 4.3.2. Reflecting panels divide the volume into a two dimensional array of 11×14. Each rectangular segment is on both ends read out by a photo-multiplier tube. Events are reconstructed in 3D and Pulse Shape Discrimination (PSD) is applied. The energy resolution is 4.5% at 1 MeV. The detector is installed at the Earth's surface. They obtain an S/B of 1.36, collecting 771 IBD events per day. In order to be independent from $\overline{\nu}_e$ spectrum uncertainties, the IBD spectrum is measured at different baselines, at 6.7 m and 9.2 m, and normalised to the integrated measured spectrum over the baseline. The PROSPECT detector began data taking in 2018. They reported

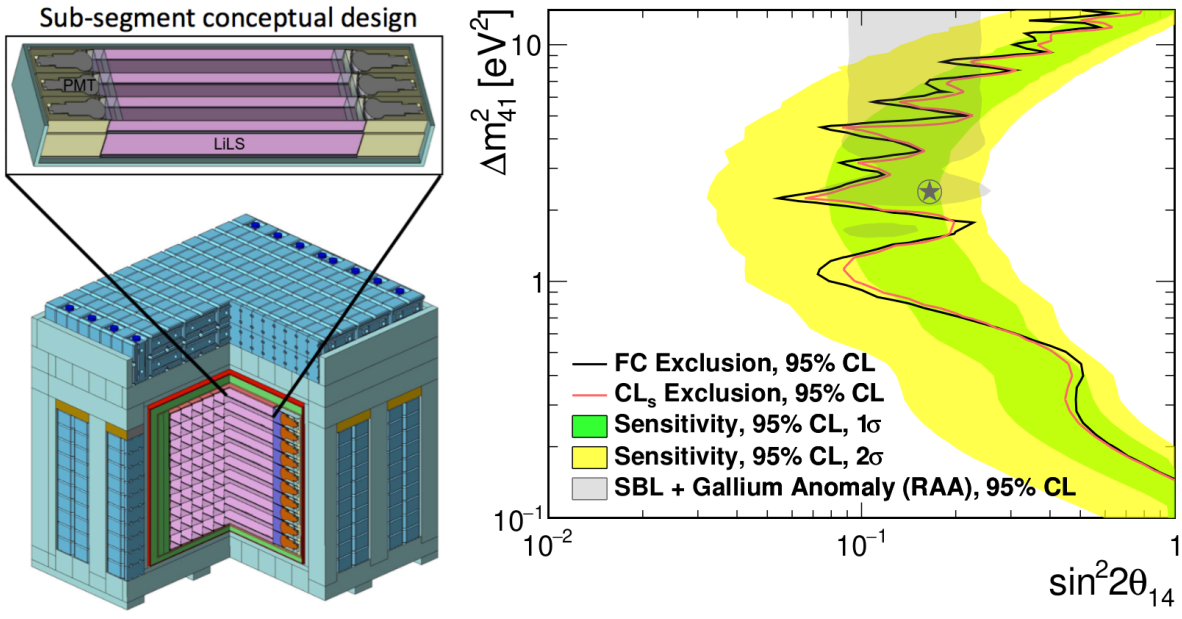

Figure 4.3.2: Left: cutaway diagram demonstrating primary PROSPECT detector design features. Right: Oscillation exclusion contours derived using the Gaussian CL and Feldman-Cousins (FC) methods. Also pictured are the 1σ and 2σ (green and yellow) exclusion ranges produced by PROSPECT toy MC datasets, as well as the RAA preferred parameters and best-fit point.

their latest results in July 2020 [127], using 96 days of reactor on data, as shown in the right panel of figure 4.3.2. They disfavor the Reactor Antineutrino Anomaly best-fit point at the 2.5σ confidence level. While a best fit to the data in the sterile neutrino parameter space is found at ($\sin^2 2\theta_{14}$, Δm^2_{14}) = (0.11, 1.78 eV^2), this preference is very mild with respect to the no-oscillation hypothesis. PROSPECT excludes a significant portion of the sterile neutrino parameters.

STEREO [128] is located at the 58 MW High Flux Reactor of the Institute Laue-Langevin (France). The compact reactor core is highly enriched in ^{235}U. The Gd doped liquid scintillator detector covers a baseline from 9.4 m to 11.1 m. The detector is shown in the left panel of figure 4.3.3. It is divided into a one dimensional array of six vertical and optically separated cells, readout by 48 photo-multiplier tubes from the top, surrounded by passive and active shielding. STEREO makes use of PSD technique on the delayed signal to suppress backgrounds induced by fast neutrons and achieve a S/B ratio of 0.9. To be independent of any flux prediction, STEREO uses a direct comparison between antineutrino spectra of all cells. STEREO released results in 2020 [129] based on data taking during 179 days of reactor on and 235 days of reactor off, which is shown in the right panel of figure 4.3.3. The best-fit point of the reactor antineutrino anomaly is rejected at more than 99.9% C.L. They excluded a significant portion of the sterile neutrino parameter space.

The SoLid collaboration is performing a competing experiment. We aim to publish our analysis results this year. Where STEREO has 1D segmentation and PROSPECT has 2D segmentation, SoLid is segmented in three directions. The detector consists of 12800 cubes. This makes the electronics design, data acquisition, and the calibration very challenging, but the extremely high segmentation allows 3D reconstruction and background-tagging. In addition SoLid is demonstrating a new and hybrid neutrino detector technology. The traditional experiments use volumes of liquid scintillator, possibly with dopants for neutron capture, which makes the traditional neutrino experiments prone to similar systematic effects. The SoLid detector uses a plastic scintillator, in combination with a screen that captures the IBD neutron and gives a distinct scintillation response.

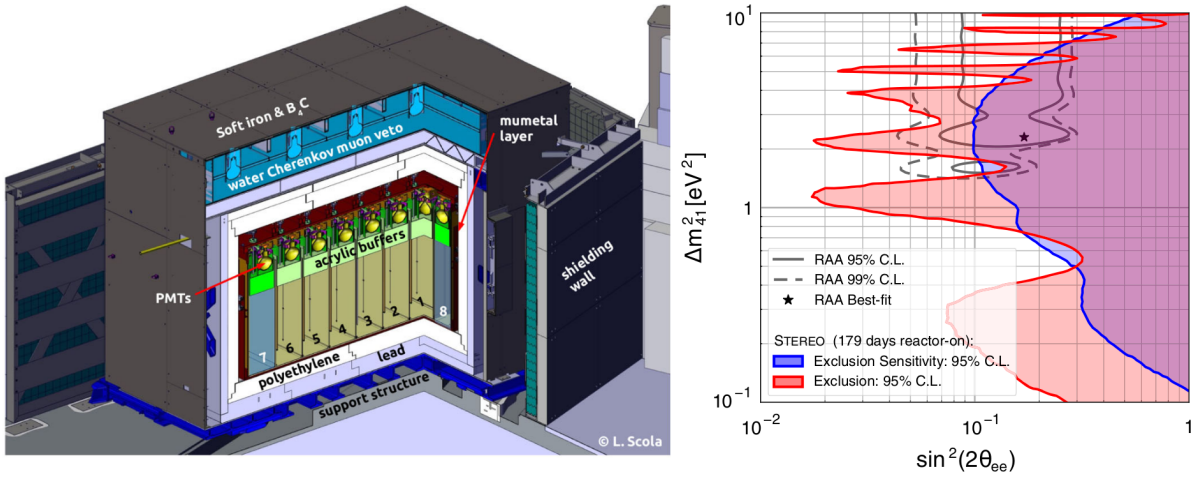

Figure 4.3.3: Left:Cutaway diagram of the STEREO detector setup. Right: Exclusion contour (red) and exclusion sensitivity contour (blue) at 95% C.L. Overlaid are the allowed regions of the RAA (grey) and its best-fit point (star). The contours and their underlying data are available.

4.4 IMPROVEMENTS ON REACTOR $\overline{\nu}_e$ SPECTRUM PREDICTIONS

The sterile neutrino hypothesis is not the only possible solution for the observed neutrino deficits. The reactor antineutrino anomaly could be due to an inaccurate prediction of the reactor neutrino spectrum.

For ^{235}U and ^{239,241}Pu, the only measured β-spectra are those from the research reactor at the Institut Laue Languevin (ILL) [105]. The ILL spectra have several shortcomings. They were acquired after a quite short irradiation time in a quasi-pure thermal neutron flux, between 12 hours and 1.8 days depending on the isotopes. The longest lived beta emitters haven't reached equilibrium yet. For antineutrino experiments, the irradiation time would be longer, like a whole reactor cycle duration of typically 1 year. During the cycle, other actinides are produced in the reactor core, because a fraction of the fission induced neutrons is captured by the dominant ^{238}U isotope, which leads to the production of new fissile isotopes: ^{239}Pu and to a lesser extent ^{241}Pu. In a pressurised water reactor, fission rates from both isotopes become comparable at the end of a cycle. The remaining fissions of ^{241}Pu and fast neutron induced fissions of ^{238}U share about 10% of the reactor power. As a result, the accurate prediction of the reactor $\overline{\nu}_e$ spectrum requires following the time evolution of these four isotopes and the knowledge of the associated β-spectra of their fission products, known as off-equilibrium corrections.

Moreover, in a standard PWR, the neutron energy spectrum exhibits more important epithermal and fast neutron energy components than in the ILL measurements. These higher energy components of the neutron flux add small contributions to the fissions of ^{235}U (as well as for the other fissioning isotopes) leading to different distributions of the fission products.
In addition, the converted spectrum exhibits oscillations due to the finite amount of virtual branches that were used. The total antineutrino spectrum from fission fragments appears continuous because thousands of branches contribute with a quasi-continuous endpoint distribution. Using only 30 virtual branches gives oscillations around each virtual endpoint energy, which can be smoothed out with sufficiently narrow slices of electron data.

4.4.1 SPECTRAL DISTORTION AT 5 MEV

The detailed analysis of reactor antineutrino energy spectra in recent years revealed an unexpected distortion. The Double Chooz experiment observed an excess in antineutrino events around a visible energy of roughly 5 MeV [130] compared to the Huber-Mueller model, often called the 5 MeV bump. The Daya Bay experiment confirmed the excess [131] and found a correlation between the magnitude of this excess and the evolution of the fuel composition during the burn up of ^{235}U and the breeding of ^{239}Pu [132]. Several data-to-prediction ratios are compared in figure 4.4.1. In comparison with the predictions from the Huber-Mueller model, good agreement was found with the flux arising from the fission of ^{239}Pu, while the fission of ^{235}U produced 7.8 % fewer antineutrinos than predicted, which could almost explain the experimental deficit by itself. This result would indicate that the reactor anomaly could not be explained by any neutrino oscillation since this should be independent of the fuel. These discrepancies point towards a potential problem in the theoretical predictions of the antineutrino spectrum for one or more fissile isotopes. It puts the integral β measurement by ILL and converted by Schreckenbach [107], Huber [109] and Mueller [108] into question. The 5 MeV

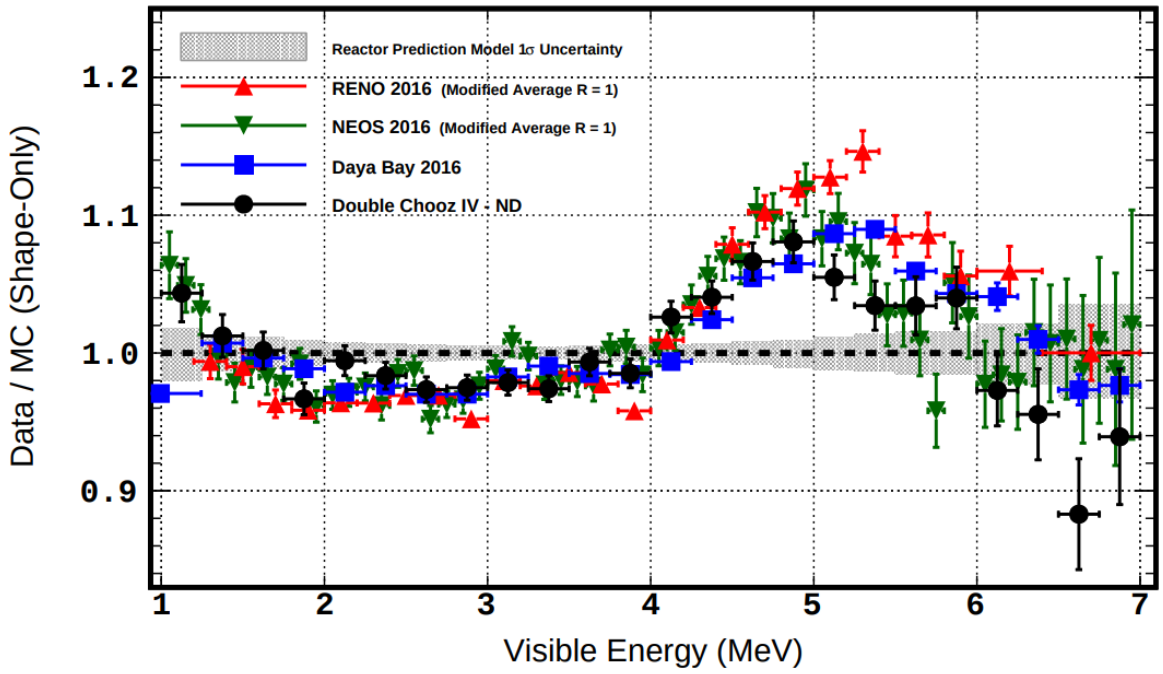

Figure 4.4.1: Shape-only reactor spectral distortion. The data to prediction spectral ratio for the DoubleChooz Near Detector [133](black), Daya-Bay [131] (blue), RENO [134] (red), NEOS [120] (green) are shown, exhibiting a common dominant pattern predominantly characterised by the 5 MeV excess. The reactor model prediction shape-only uncertainty is shown in grey, which is significantly smaller than the dominant rate-only uncertainties. The 5 MeV excess is compensated by a deficit region [1.5,4.0] MeV for all experiments due to the shape-only condition.[133]

bump implies the need for improved and alternative theoretical predictions, as alternative to the Huber-Mueller converted spectra.

4.4.2 SUMMATION METHOD TO PREDICT THE REACTOR $\overline{\nu}_e$ SPECTRUM

An alternative to the conversion method is the summation method [135]. In this method, the total antineutrino spectrum is built from the sum of all individual β-branches of all fission products predicted by an evolution code, weighted by the beta decay activities. This method relies completely on the available nuclear data of the fission yields combined with the beta decay data for the fission products.

For the typical fissile isotopes in a reactor, namely ^{235,238}U, ^{239,241}Pu, indicated by k, the β^- (or $\overline{\nu}$) spectrum per fission, $S_k(E)$, is calculated in the summation method as the sum of all β^- (or $\overline{\nu}$) spectra of all fission products, weighted by their activity A_{fp} ,

$$S_k(E,t) = \sum_{fp=1}^{N_{\rm fp}} A_{\rm fp}(t) \times S_{\rm fp}(E). \tag{4.1}$$

The spectrum $S_{fp}(E)$ of each fission product is itself a sum of N_b β-branches in which the parent nucleus can decay to the daughter nucleus (or in some cases an isomeric state), weighted by their respective branching ratios as

$$S_{\mathrm{fp}}(E) = \sum_{b=1}^{N_b} BR^b_{\mathrm{fp}}(t) \times S^b_{\mathrm{fp}}(Z_{\mathrm{fp}}, A_{\mathrm{fp}}, E^b_{0\mathrm{fp}}, E). \tag{4.2}$$

Z_{fp} and A_{fp} are the charge and atomic number of the parent nucleus. BR^b_{fp} and $E^b_{0\mathrm{fp}}$ are the branching ratio and the endpoint energy of the b^{th} branch of the fp^{th} fission product respectively. This information is extracted from beta decay data bases that contain for a tremendous amount of fission products the end-points, branching ratios, and spin/parities of β transitions. These equations are valid for both electron and antineutrino spectra. To obtain the corresponding expression for the antineutrino spectrum one can replace in the above formula the electron energy E by the antineutrino energy

$$E_{\bar{\nu}} = E^b_{0fp} - E$$

By definition this one-to-one relation is valid only at the single β-branch level. Thus it is a unique feature of the ab initio approach to predict electron and antineutrino spectra with the same precision.

Currently, the summation method is the only alternative to the conversion method based on the integral beta spectra measured in the 1980's at ILL [105]. Next to the spectra of the traditional fissile isotopes ^{235}U and ^{239}Pu, ^{241}Pu, the ab initio summation method can construct the spectrum associated with the fission of ^{238}U. The summation method allows to compute the corrections for the off equilibrium effects (due to the build-up of long lived fission products, and to neutron captures on fission products during the core cycle). The summation method can predict reactor antineutrino spectra over the full energy range from any fuel and under any irradiation conditions, which enables new generation reactor neutrino experiments to use a smaller energy binning and to complement their analysis at higher energies than 8 MeV.

The summation method heavily relies on the availability of beta spectra in nuclear databases, which are inevitably incomplete. Relying on measured total β spectra cannot be reduced beyond a certain level, and eventually virtual β branches (as in the conversion method) have to be used in addition to the a priori computed spectra.

The reconstructed spectra might suffer from an overestimation of the high energy part. This problem is due to the lack of data for exotic nuclei and from the "Pandemonium effect" [136]; Most of the nuclei involved have many β branches, most of which are determined form the γ radiations emitted subsequently to the β transition. A fraction of the beta branches connects the parent nucleus to very excited levels of the daughter nucleus. The strength of the associated low energy β-rays is either spread over multiple weak γ-rays or concentrated in one high energy gamma ray. In both cases, part or all the γ-cascade can be missed by the measurement apparatus. These features lead to an underestimation of high energy feeding and the resulting low energy beta spectra.

4.4.3 IMPROVED SUMMATION METHOD WITH TAGS AND PANDEMONIUM DATA

Pandemonium nuclei play a major role in the estimate of the antineutrino spectra using the summation method. The $^{102;104-107}$Tc, ^{91}Rb ^{86,92,94,105}Mo, and ^{87,88,101}Nb nuclei belong to the list of nuclei

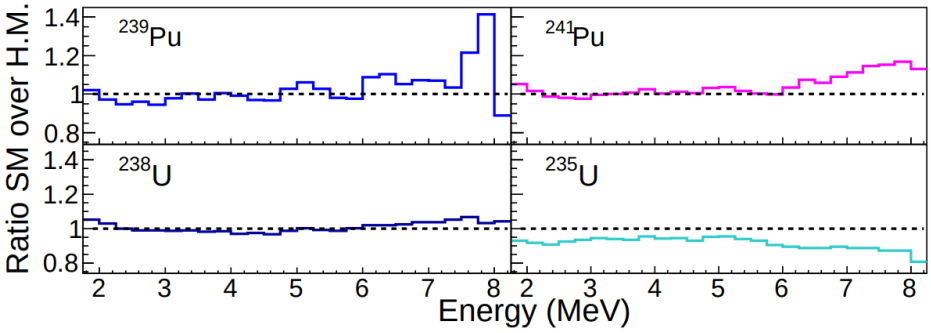

Figure 4.4.2: Ratios of the antineutrino energy spectra obtained with the summation method in 2018 [110] with the converted spectra for ^{239}Pu, ^{241}Pu, ^{235}U [109] and Mueller's prediction for ^{238}U [108].

suffering from the Pandemonium effect and contribute significantly to the ^{239}Pu decay heat. The beta feeding of these nuclei were measured in the last decade, with the Total Absorption Gamma ray Spectroscopy measurements (TAGS) [137]. The TAGS measurements are insensitive to the Pandemonium effect and solve a large part of the γ discrepancy.

Figure 4.4.2 shows the comparisons between the individual antineutrino spectra of the summation method as of 2018 by Estienne et al. [110] and those of the Huber-Mueller model for the four main contributions to the total number of fissions in a PWR. The summation spectra are taken at a time corresponding to the irradiation times of the ILL experiments for ^{235}U,^{239}Pu, and ^{241}Pu while the summation spectrum for ^{238}U is computed after 450 days of irradiation as was the case for Mueller's

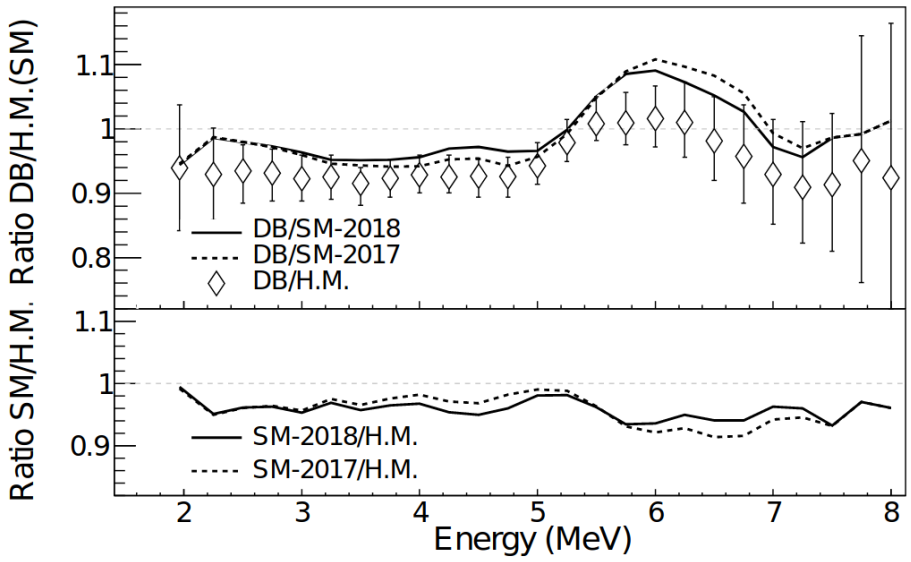

Figure 4.4.3: Top: Ratio of the Daya-Bay antineutrino energy spectrum with respect to the Huber-Mueller model (open diamonds), and with respect to the summation result of 2017 (dashed line) and 2018 (continuous line). Lower Panel: Ratio of the SM-2017 (dashed line) and SM-2018 (continuous line) antineutrino energy spectra to that of the Huber-Mueller model.[110]

spectrum. The normalisation of the summation spectra with respect to the Huber-Mueller ones indicate that the antineutrino deficit is mainly produced by the ^{235}U contribution to the antineutrino flux.

The impact of these few nuclei reaches 8% in the 2 to 4 MeV energy range for the Plutonium isotopes, and 3.5% for ^{238}U. The effect is thus large and in an energy region of utmost importance for oscillation analysis of reactor neutrino experiments. The inclusion of Pandemonium free TAGS data reduces the prediction of the neutrino flux, which implies an increasingly smaller discrepancy with reactor data, leaving less and less room for a reactor anomaly. The remaining discrepancy with the Daya Bay flux reduces to only 1.9 %, instead of 6 % for the Huber-Muller model.

However, even with the inclusion of the 2018 TAGS data, the 5 MeV bump is still there, as shown in figure 4.4.3. This spectral distortion cannot be explained by ingredients of the nuclear databases [138]. The spectral distortion has to be further surveyed with (very) short baseline neutrino experiments, by performing measurements over longer periods of time and at different reactors with different fuel compositions, especially at reactors with Highly Enriched Fuel reactors, such as in the SoLid experiment.

5

THE EXPERIMENTAL SITE AT THE BR2 REACTOR

The SoLid detector is operated near the Belgian reactor 2 (BR2) at the Belgian Nuclear Research Centre SCK-CEN in Mol [139] (figure 5.0.1). The BR2 research reactor operates on high enriched uranium fuel (HEU) in a very compact core, which makes it an intense source of $\overline{\nu}_e$, providing about $1.0 \cdot 10^{19}$ $\overline{\nu}_e$ per second at a nominal thermal power of 60 MW. The BR2 reactor is purposed for nuclear material and fuel R&D and production of medical isotopes (figure 5.0.1). The research reactor has vastly different design and operational characteristics than a typical, commercial reactor in a nuclear power plant. This makes the BR2 reactor highly suited for a short baseline oscillation search.

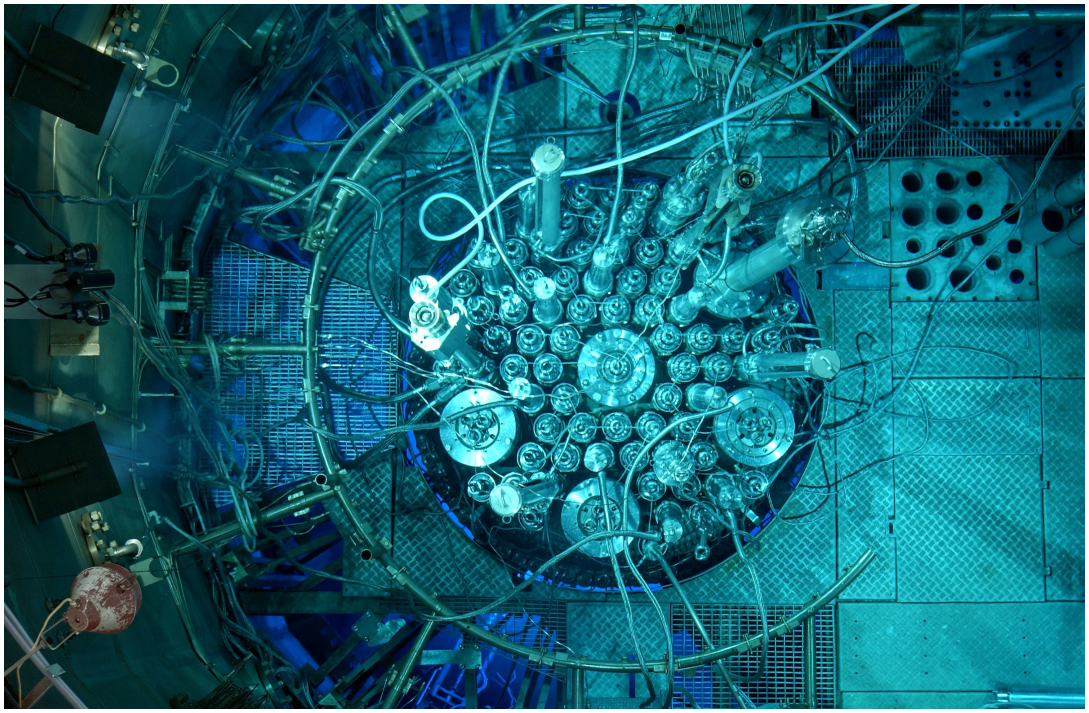

Figure 5.0.1: Top view of the fuel matrix of the BR2 tank-in-pool reactor core.[139]

BR2 has an uncommon HEU fuel of ~ 93.5% pure ^{235}U. Limiting the effective number of fissile isotopes to one facilitates reactor calculations and allows for a precise measurement of the ^{235}U spectrum. The HEU core is positioned in a beryllium matrix that reflects the neutrons. The beryllium matrix is an assembly of a large number of irregular hexagons which are skewed and form a twisted hyperbolic bundle around the central 200 mm H1 channel. The twisted design of the fuel rods, results in a small core diameter of approximately 0.5 m (figure 5.0.2, left). The small core ensures very little position smearing of the short baseline oscillations under investigation.

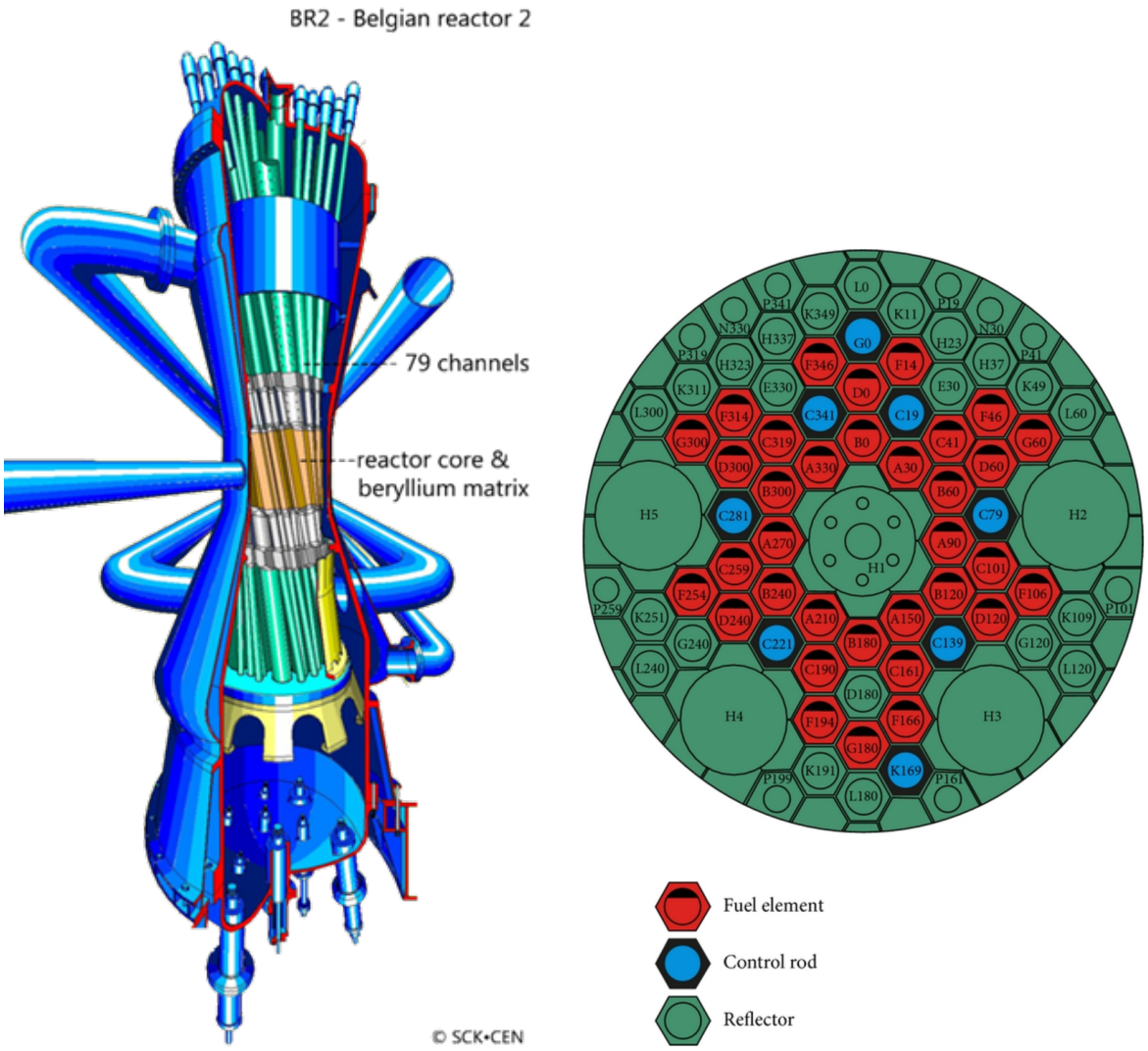

Figure 5.0.2: Left: Twisted core design of the BR2 reactor. Right: Horizontal cross section of BR2 reactor core with a typical fuel loading.[139]

The reactor has a tank in pool design. The water is used to cool the core and it also properly shields the core's radiation. The outer side of the concrete vessel is only 5 m away from the center of the reactor core, as can be seen on the floor plan (figure 5.0.3). Therefore, the SoLid experiment can be conducted at close proximity to the core. The space in the reactor hall is sufficient for a relatively compact, above-ground detector and modest passive shielding (figure 5.0.4). The SoLid detector is located at level 3 of the BR2 containment building in direct line-of-sight of the nominal reactor core center. The detector is positioned along an axis through the center of the core, with a baseline coverage from 6.4 m up to 9 m (see figure 12.1.2). Around 0,11 % of the anti electron neutrinos that emerge from the reactor core cross the detector and can interact in the detector volume [140].

The reactor is powered about half the year, in 6 cycles of about 1 month each (140 days). The reactor is licensed to operate at a power of up to 100 MW. In practice, the operating power varies between 45 and 80 MW.

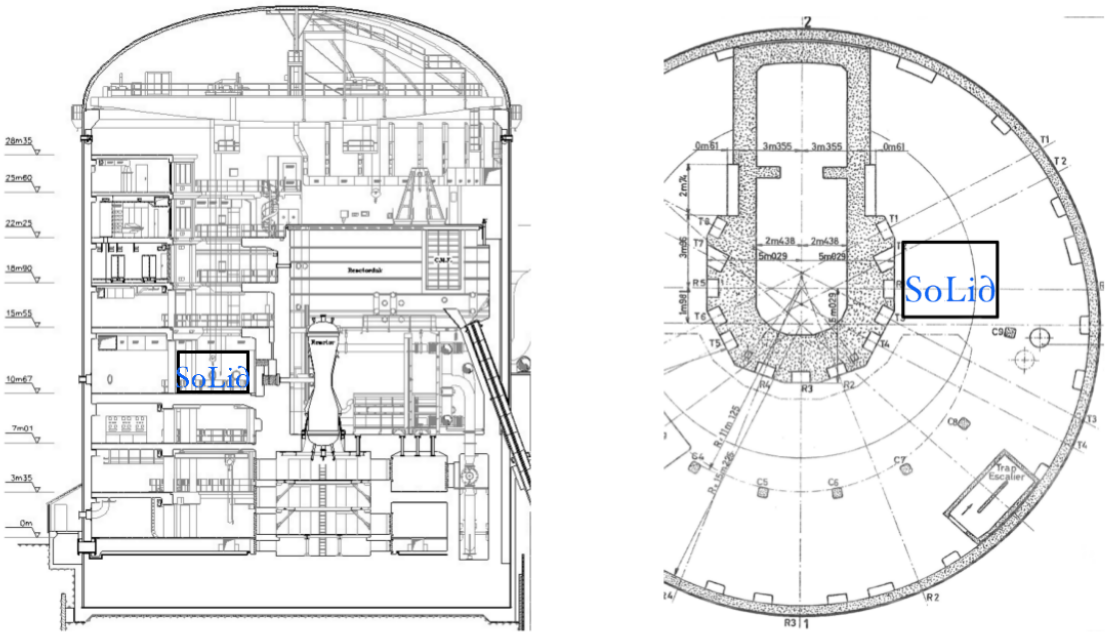

Figure 5.0.3: Schematics of the BR2 reactor building with the SoLid logo superimposed at the detector location in a box that corresponds with the shielding. Left: a vertical cut through of the reactor building. Right: the map of the third floor where the SoLid detector is located.[141]

Figure 5.0.4: Left: Hall of BR2 reactor building were the SoLid detector is located. Right: The detector and its passive shielding.

6

THE SOLID DETECTOR

The SoLid collaboration, short for **S**earch for **O**scillations with a **Li**thium-6 **d**etector, was established to search for the oscillation of electron antineutrinos to previously undetected sterile flavour states (see section 4.2 for an introduction). The SoLid experiment aims to measure the flux of reactor anti-neutrinos at a distance of less than 10 m from a reactor core. The SoLid detector is distinct from its competitors by its high segmentation. Where the STEREO detector [128] has a 1D segmentation, consisting of an array of vertical slabs, and the PROSPECT detector [126] has a 2D segmentation, consisting of a matrix of rectangular segments (see section 4.3.1 for the detector designs), the SoLid detector is segmented in 3D, being constructed of cubic cells. The high segmentation renders the SoLid detector a unique position resolution and topological discrimination power, essential in the search for sterile neutrinos. To this end, the highly segmented SoLid detector employs a novel and hybrid detector technology, based on PVT scintillators in combination with ^{6}LiF-ZnS(Ag) screens [142]. Traditionally, the majority of neutrino detectors consists of large volumes of liquid scintillator, which makes the neutrino sector prone to common systematic deviations. The SoLid detector intends to demonstrate this innovative detector technology.
The SoLid detector is suitable as a device monitoring non-proliferation as well [143]. The goal of the SoLid experiment is to provide a significant contribution to the ability of reactor monitoring via the new design. The classical approach based on liquid scintillator generates problems related to safety, compactness and sensitivity to backgrounds.

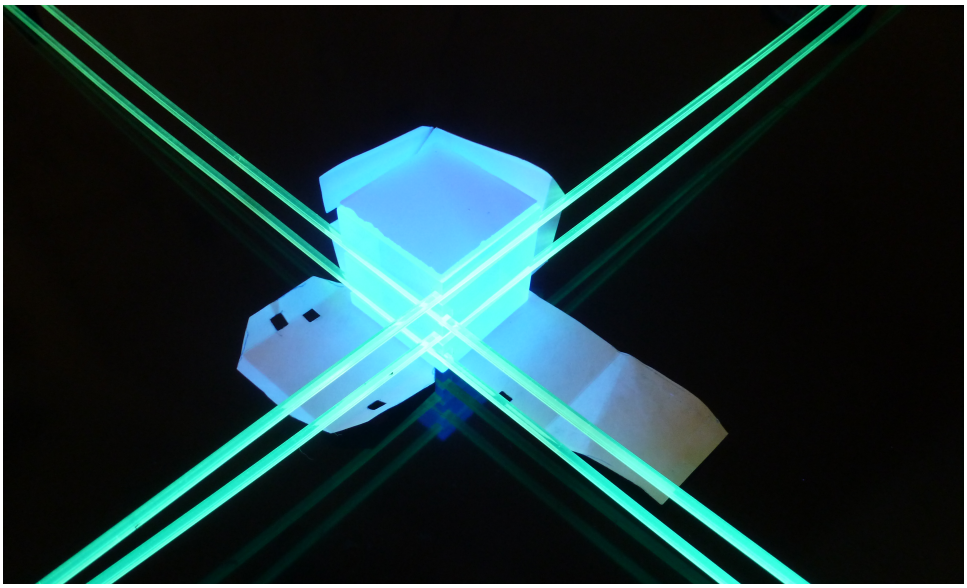

Figure 6.0.1: Picture of the two scintillators under UV light: the PVT cube and on top the ^{6}LiF:ZnS(Ag) sheet. WLS fibers run through the grooves and the reflective Tyvek wrapping is left open.

6.1 IBD DETECTION PRINCIPLE

The SoLid detector is optimised to detect reactor neutrino [144]. Reactor neutrinos interact with protons in the detector volume via inverse beta decay (IBD), resulting in a positron and a neutron that are correlated in time and space,

$$\overline{\nu}_e + p \longrightarrow e^+ + n \qquad (E_{\bar{\nu}_e} > 1.804\text{MeV}).$$

To optimally detect and discriminate both particles, we adopt a dual scintillator technology. $5 \times 5 \times 5$ cm^3 Cubes of ELJEN-200 Polyvinyl-toluene (PVT) [145] act as a scintillator for the positron prompt signal (see figure 6.1.1). The PVT properties are listed in table 6.1.1. The advantages of the PVT scintillators include fairly high light output, optical transparency, linear energy response and fast timing. This makes the material suited for fast timing measurements. The PVT also provides the proton-rich target for the $\overline{\nu}_e$. The IBD positron has energies below 10 MeV and its median range is less than 48 mm in PVT, which implies that the majority of the IBD positrons will be stopped in the same cell as they are produced in. The PVT produces a prompt and rapidly decaying scintillation signal due to the positron from the IBD reaction, from which both the location and the energy of the neutrino interaction can be determined.

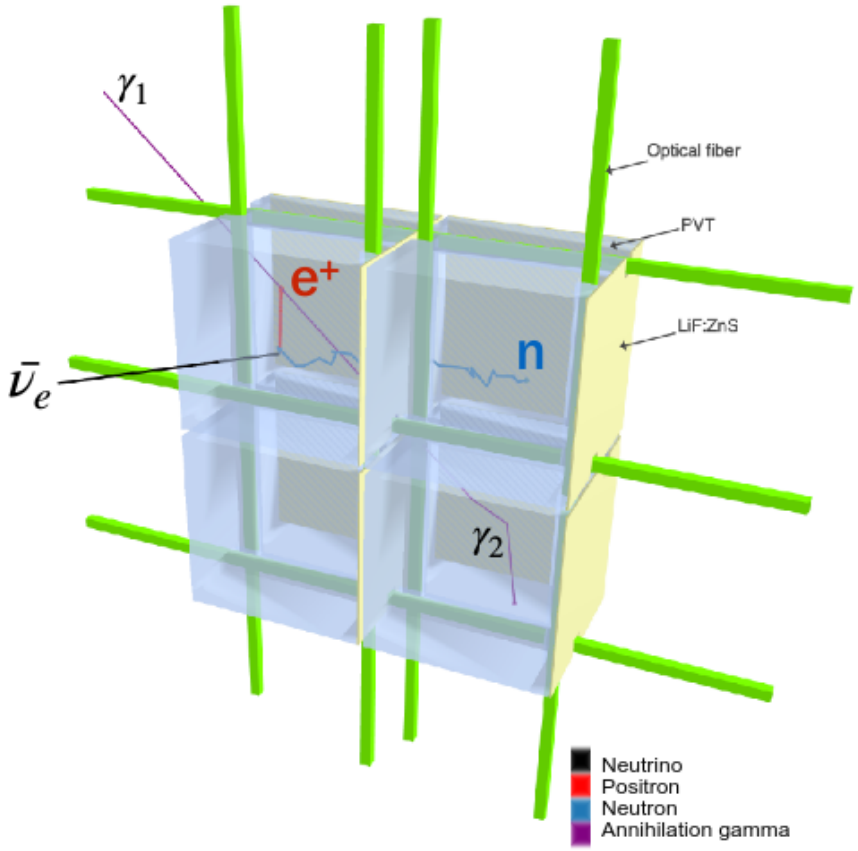

Figure 6.1.1: Principle of $\overline{\nu}_e$ detection in cells of combined scintillators. wavelength shifting fibers placed in perpendicular orientations collect the scintillation light.

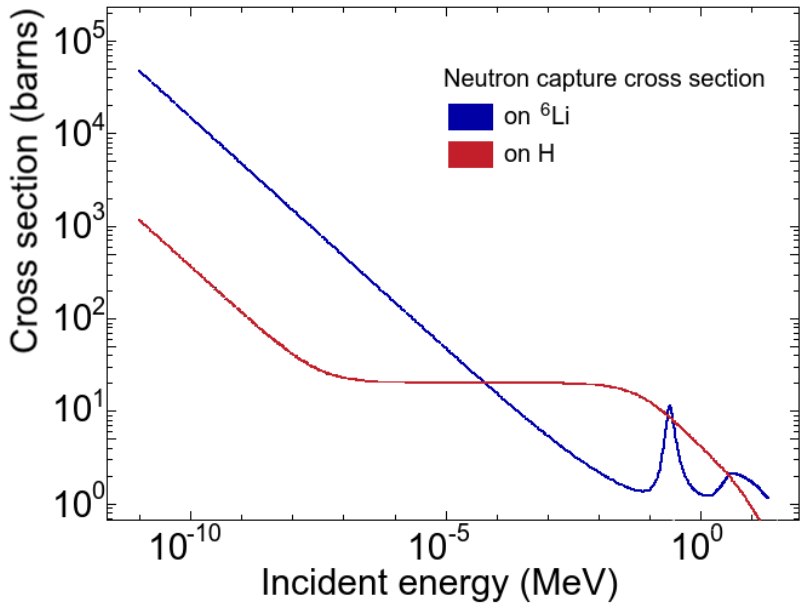

Figure 6.1.2: Neutron capture cross section on ^{6}Li and ^{1}H over a broad energy range. [146]

To detect the neutron that is produced in the IBD interaction, sheets of ^{6}LiF:ZnS(Ag) [147] are placed on two faces of each PVT cube. The PVT cubes acts as effective moderator for the neutrons. The neutrons reach thermal energies of ~0.025 eV after scattering in the PVT over a period of up to hundreds of microseconds and are subsequently captured in the ^{6}LiF:ZnS(Ag) layer via the interaction

$$n + {}^6Li \longrightarrow {}^3H + \alpha \qquad (4.78\text{MeV}).$$

The high neutron capture cross-section of ^{6}Li, being 939.9 barns for thermal neutrons, ensures that only 24 % of the IBD neutrons are captured on hydrogen, which has a capture cross-section for thermal neutrons of 30.4 barns [148] (see figure 6.1.2). The reaction produces an alpha and a tritium nucleus, sharing 4.78 MeV of kinetic energy. Both are highly ionizing and deposit all their energy within the sheet, scintillating in the ZnS(Ag) microcrystals. The scintillation light produced in the ^{6}LiF:ZnS(Ag) is optically coupled to the PVT cube via a thin layer of air between the two surfaces. The sheet is backed with a 225 μm thick MELINEX-339 reflective backing to improve the light collection. In the cube, the light is internally reflected at the polished PVT-air interface. The light collection is further enhanced by wrapping a reflective fabric of woven polymer (DuPont Tyvek wrapping of type 1082D [149]) around each unit cell. The tyvek also ensures optical insulation between the detector cells.

Crucially, the scintillation time scale of ZnS(Ag) is significantly longer in duration, at $\mathcal{O}(1)$ μs, than that of PVT, at $\mathcal{O}(1)$ ns. This is exploited by the collaboration for several purposes. With a sampling of 40 MHz, pulse shape discrimination (PSD) can identify during signal reconstruction whether a given scintillation signal was produced in the ZnS (characteristic of a neutron capture) or in the PVT ($e^+/\gamma/\mu$-like)with high efficiency and purity (see chapter 8). A neutrino event is then defined by the time coincident detection of a positron and a neutron. In addition, the neutron trigger is activated by the characteristic fast succession of several scintillation peaks by ZnS(Ag) (see chapter 7).

Light output (% Anthracene)	64
Scintillation efficiency (photons/MeV e^-)	10 000
Wavelength of maximum emission (nm)	425
Light attenuation length (cm)	380
Rise time (ns)	0.9
Decay time (ns)	2.1
Pulse width, FWHM (ns)	2.5
H atoms per cm^3 ($\times 10^{22}$)	5.17
C atoms per cm^3 ($\times 10^{22}$)	4.69
e^- atoms per cm^3 ($\times 10^{23}$)	3.33
Density (g/cm^3)	1.023

Table 6.1.1: Properties of the EJ-200 PVT scintillator provided by the manufacturer ELJEN Technology.[145]

6.1.1 ENERGY QUENCHING IN PVT

The response of organic scintillators to particle interactions depends on the incident particle type and its energy, as was first discussed by Birks [150]. The incident particle causes within the plastic scintillator electron recoils and nuclear recoils (including proton recoils, carbon recoils and secondary alpha particles from ^{12}C(n,α) reactions). The former is dominant when the scintillator is irradiated by γ rays and electrons, while the latter becomes prominent when irradiated by heavier particles like neutrons. The scintillation response depends on the energy depositing primary and secondary particles (electron, neutron, alpha, carbon, ...) and their energy.

The response arising from heavier or slower particles, i.e. particles which produce a higher ionization and excitation density within the scintillator, is significantly reduced, i.e. quenched, in comparison to the scintillation output observed from an electron of the same energy [151], as is visible on graph 6.1.3. The relation between the energy of a nucleus and the amount of light given off by the scintillation process is non linear. For electrons there is only slight nonlinearity. Luckily, the latter is important to the SoLid experiment as the energy of the incoming neutrino will be reconstructed from the positron response.

For energies below about 5 MeV, the organic scintillator's light production can be represented as proportional to $E^{3/2}$. At higher energies, the scintillation output becomes approximately linear. Birks developed a formalism where the scintillation light yield of highly ionizing particles depends on the nature and stopping power of the particle, as

$$\frac{dL}{dr} = S\frac{dE/dr}{1 + kB \cdot \frac{dE}{dr}},$$

where dL/dr (cm^{-1}) is the scintillation yield per unit path length, S is the absolute scintillation factor (MeV cm^{-1}), dE/dr is the particle's stopping power (MeV cm^{-1}), and kB is the quenching factor for the scintillator (MeV^{-1} cm). This relation is based on the assumption that the passage of the particle through the plastic produces on the one hand excitations which are proportional to the energy deposit, dE/dr, but on the other hand the particle produces a local concentration of damaged or ionized molecules along its path, proportional to $B \cdot dE/dr$, which act as quenching agents where the capture

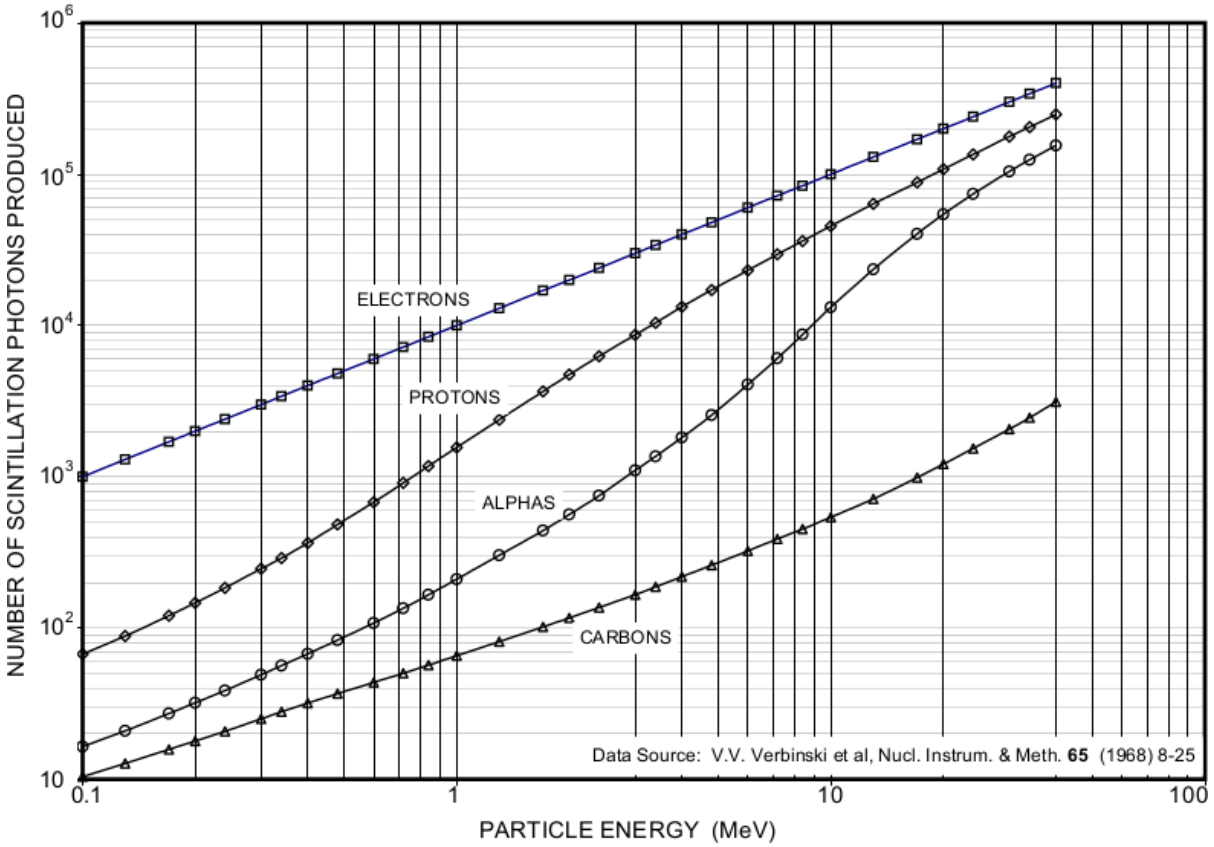

Figure 6.1.3: Response of the EJ-200 plastic scintillator, as measured by Verbinski et. al. One unit of energy is defined by the 1.28 MeV ^{22}Na gamma ray Compton edge.[145]

probability for the excitations is reduced with k. For an alpha particle, the dE/dr becomes very large so that saturation occurs along the track and Birks' formula becomes

$$\left.\frac{dL}{dr}\right|_{\alpha} = \frac{S}{kB}.$$

The absolute value of the quenching factor for specific materials is expected to depend only on the Birks factor kB, independently of the particle type. As a practical matter the product kB is treated as an adjustable parameter to fit experimental data for a specific scintillator. For the simulation of the readout system, which is described in chapter 13, the fine tuning of the Birks factor for the PVT scintillator resulted in a factor of 0.14 mm/MeV.

For the inorganic scintillator ^{6}LiF:ZnS(Ag) quenching effects can also occur from certain radiationless transitions between some excited states formed by electron capture and the ground state, in which case no visible photon results [151]. These represent loss mechanisms in the conversion of the particle energy to scintillation light. However, the light yield is more nearly proportional to deposited radiation energy than is typically observed in organic scintillators. Quenching processes that are present still lead to some nonlinearity, but to a much lesser extent than in organics.

6.2 DETECTOR DESIGN

To probe the Reactor Antineutrino Anomaly (RAA), the detector has to determine the neutrino oscillation which depends on the L/E ratio. The experiment must reach a compromise on the energy and spatial resolution in order to be sensitive to small effects in the oscillation pattern. Small cubes give a better position resolution, whereas larger cubes allow to contain and reconstruct better the energy that a particle deposits. Moreover, being on the surface, the experiment faces a challenging background and it is difficult to install substantial shielding. The SoLid detector was designed to best meet all of these experimental considerations [140]. It consists of a highly segmented 1.6 ton fiducial mass, split into 12800 detector cells. Each detection cell consist of a PVT cube and two ^{6}LiF:ZnS(Ag) screens that are wrapped in light insulating tyvek, as shown in figure 6.1.4. The cells are stacked in an arrangement of 50 planes of 16 by 16 cells. The cells are surrounded by a lining of four high density polyethylene (HDPE) bars that act as reflectors for neutrons that would otherwise escape the detector (see figure 6.1.4 left). Each detection plane is covered with two square Tyvek sheets to further ensure optical isolation from its neighbouring planes. The scintillation light is guided from the cells towards sensors by an orthogonal grid of wavelength shifting fibers (type BC-91 A from Saint-Gobain crystals [152]), with a square cross section of (3 × 3) mm^2 that are inserted through grooves on the X-Y edges

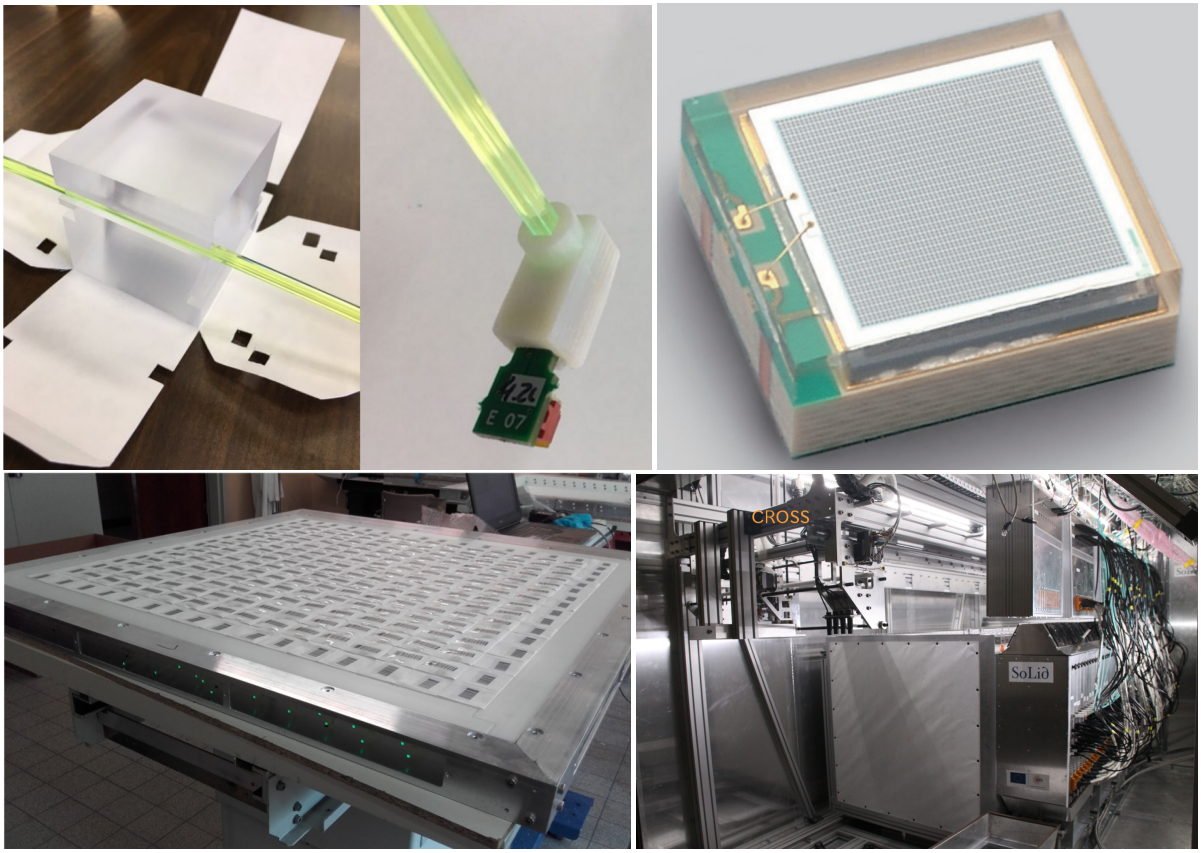

Figure 6.1.4: Top left: PVT cube on top of an open folded tyvek wrapping, with a fiber running through one of its grooves. Top center: MPPC attached to the end of the optical fibers with a 3D printed socket. Top right: The MPPC photo sensor. Bottom left: frame during construction. Bottom right: Module installed on the railsystem as integral part of the full SoLid detector.

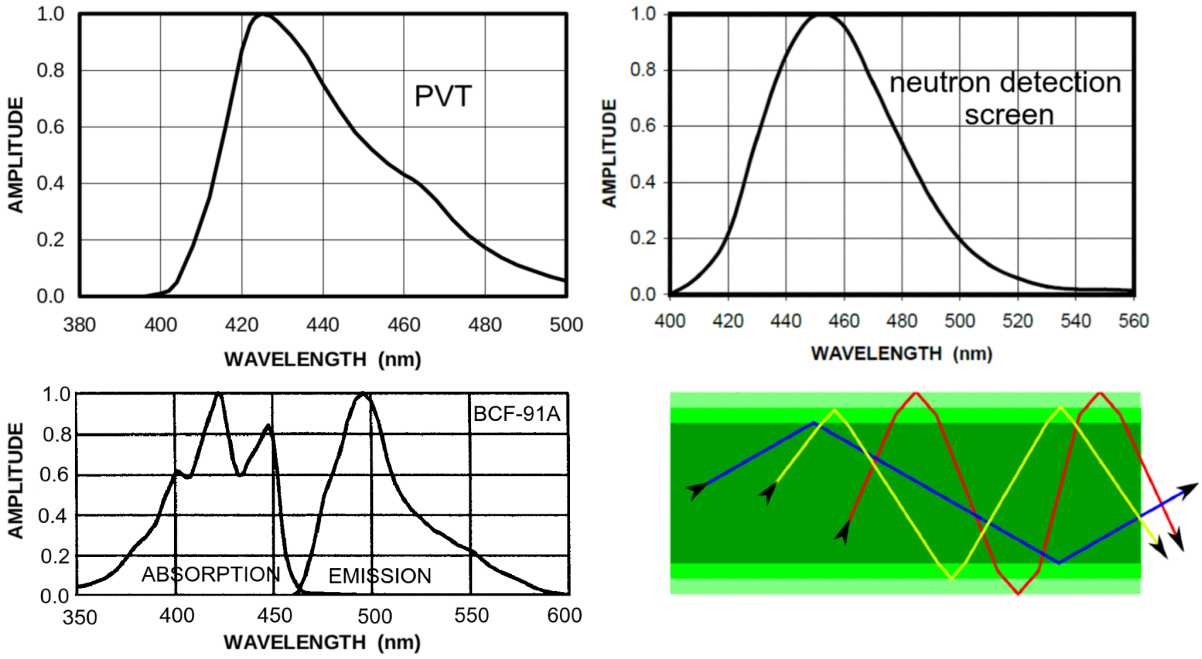

Figure 6.2.1: Top: Emission spectrum of the EJ-200 PVT scintillator [145] (left) and the Scintacor ZnS(Ag) scintillator [147] (right). Bottom Absorption- and emission spectrum of the WLS fiber [152] (left) and schematic sideview of a double cladded Wavelength Shifting Fiber (right). The lowering refractive indices enhance the trapping efficiency.

of the cubes. Placing the fibers onto two orthogonal faces of the cube enables the localisation of the scintillation signal via a hodoscope technique [153]. The fibers have a maximal absorption around the maximal emission of the SoLid scintillators, which are in the visible spectrum centered around 425 nm and 450 nm respectively, as shown in the top panel of figure 6.2.1. The fiber has a polysteryne based core that absorbs the blue scintillation light and re-emits it isotropically at a longer wavelength, i.e. lower energy, as green optical photons with an emission peak at 494 nm (see the bottom panel of the figure). The material has a short decay time of 12 ns. A portion of the re-emitted light is transmitted by total internal reflection along the WLS fiber towards the fiber end. The fiber is double cladded with polymethyl-methacrylate (PMMA) which have an increasingly lower refractive index (1.49 and 1.42) than the core (1.59) to enhance the trapping efficiency of light inside the WLS fiber. The trapping efficiency for the double cladded square fiber is around 7.3 % [152] and is independent of the scintillation event's location in the fiber.
Two fibers run along each row and column of cells, which results in 64 fibers per plane. This enhances the overall light yield, reduces the effect of attenuation loss as well as providing channel redundancy. One end of the fiber is coupled to a Mylar foil with a reflective aluminium coating, whilst the other is connected to a Hamamatsu silicon photomultiplier (SiPM) [154]. While travelling along the fibre, photons can be absorbed. Because of this light attenuation, the position of the sensor and mirror alternates between the parallel fibers to ensure a more uniform light response throughout the detector. The coupling between the fiber and the sensor affects the amount of photons that finally impinge on the sensor. Optical contact between the fiber and both the mirror and the MPPC is enhanced with a drop of optical gel.

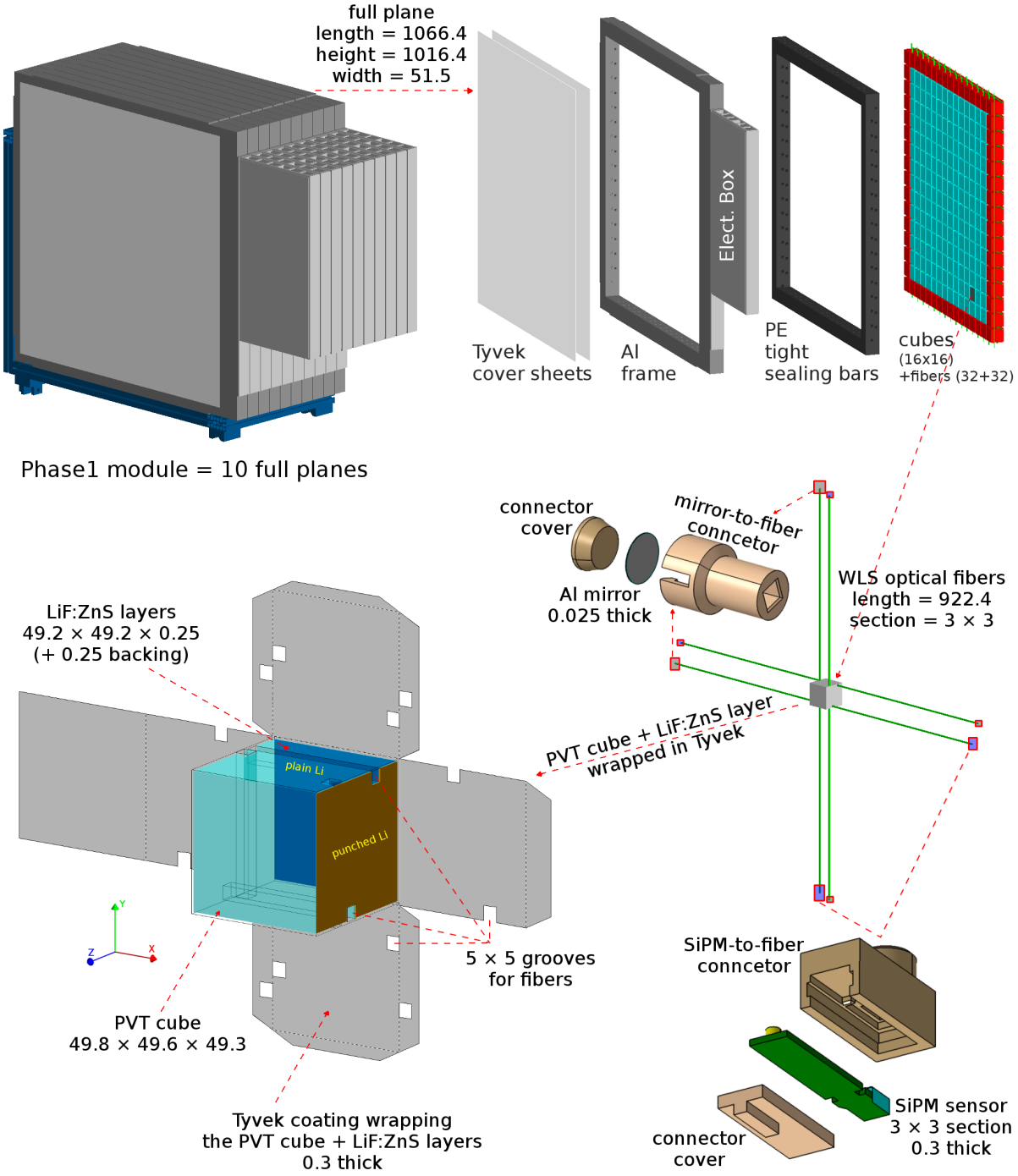

Figure 6.2.2: Technical diagram of a detector module (top left), an exploded representation of the SoLid frame (top right),the assembly of a detector cell (bottom left) and the configuration of the fiber readout system (bottom right). Indicated sizes are in mm.[140]

For the Phase I detector, SiPM of type S12572-050P were used that are capable of single photon detection. All data discussed and analysed in this thesis were recorded with the Phase I detector. In the summer of 2020, the sensors were upgraded to new Hamamatsu S14160-3050HS MPPCs that

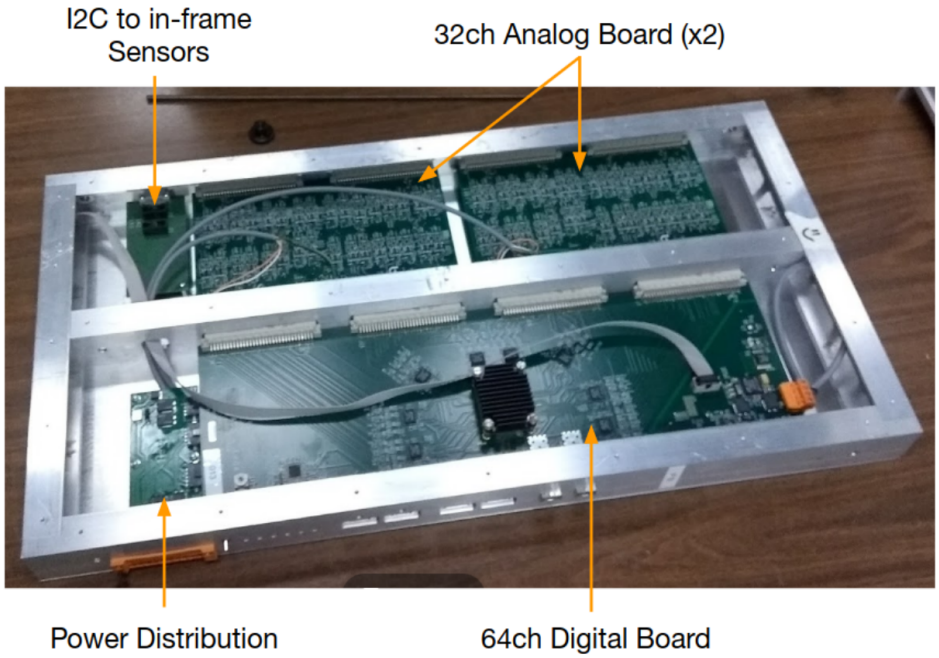

Figure 6.2.3: Picture of a fully assembled electronics enclosure for one detector plane containing two analog boards that are connected to a digital board. Environmental sensors are used to monitor temperature and humidity. The power supply provides the bias voltage to the plane sensors.[155]

achieve a higher photon detection efficiency for a lower operation voltage. They are expected to increase the energy resolution and the IBD detection efficiency.
The MPPC consists of an array of many Geiger mode avalanche photodiodes (APD), each one being a pixel (see Figure 6.1.4, top right). The sensors used in the SoLid experiment have 60 rows of 60 pixels with a pixel pitch of 50 μm, which leads to a total sensor size of (3×3) mm^2, which equals the fiber cross section. When a photon hits a pixel, a given charge is released, producing a fast current pulse with a specific amplitude, called gain. In the MPPC output signal, the pulses generated simultaneously by multiple pixels are superimposed onto each other. The main properties and characteristics of the sensors will be discussed in section 6.3. The MPPC bias voltage and signal are carried on twisted pair ribbon cables. Each of the 50 single detection planes has its own front-end electronics, mounted directly on its side within an aluminium enclosure (figure 6.2.2). The electronics are custom-made [155] and based on a combination of analog/digital front-end electronics and Field-Programmable Gate Array chips (FPGA).

The front-end electronics of a single detection plane, as shown in figure 6.2.3, consists of two 32-channel analog boards, a 64-channel digital board, together with a power distribution system. The analog boards' channels are connected to the 64 sensors of the plane. Each analog board contains an amplifier and biasing circuitry that equalises the amplitude response of each MPPC individually (see section 6.3). Due to the AC coupling between the sensor and the analog board amplifier, the mean signal over long time periods is forced to be zero. Because only signals that change, pass through the AC coupling, the DC offset and, depending on the filter, also low frequencies are blocked. As a consequence, the baseline of each channel depends on that channel's signal rate. The two analog

boards connect directly to a single 64-channel digital board for digitisation and triggering. Each digital board has eight 8-channel, 14-bit analog to digital converters (ADC), that process 40 Msample per second.

The planes are grouped in five modules of ten planes each (figure 6.5.1. The readout system operates on three levels: plane, module and full detector. Each digital board can be operated in standalone mode using an internally generated clock. The ten digital boards inside one module are synchronised by a module clock board, which can operate in both master and slave mode. An additional master clock-board allows to run the five detector modules synchronously. The trigger and readout logic is implemented on FPGA boards, as will be discussed in further detail in section 7.1. The digital boards of all detector planes can communicate with each other (e.g. their trigger decisions) via 2.5 Gbit links carried on copper cables.

The 50 detector planes correspond to a fiducial mass of 1.6 ton. The modules are installed on a rail system, that allows for an accurate positioning and alignment. Under normal detector operations all modules are closely grouped together with an average spacing of 0.5 mm between two modules. The detector is installed inside a thermally insulated shipping container, with dimensions $2.4 \times 2.6 \times 3.8$ m^3, which facilitates transport. When the detector is installed inside the container, the center of the reactor core coincides with the detector center in the horizontal direction ($\Delta x = 0$ mm) and it is a bit higher in the vertical direction ($\Delta y = 22.98$ mm).

It is possible to cool down and control the ambient air temperature in the container to a precision of 0.2 degrees Celsius. Six fans, mounted between the service box and the plane electronics enclosures, push air down towards a heat exchanger which is capable of removing the 200 W of heat generated by each module. Under normal data taking circumstances, the temperature of the SoLid detector is kept at a fixed value of 11 °C. This stabilises the MPPC responses at 1.4% level and reduces the thermal noise in the sensors by a factor of three compared to operation at room temperature. In order to keep the relative humidity of the air inside the detector at acceptable levels the container is permanently flushed with dry air that enters the container at a low flow rate of 5 m^3/hour.

6.3 SPECIFICATIONS OF THE SIPM SENSORS

The most important properties of the MPPCs are specified in figure 6.3.1. That is the photon detection efficiency in function of the overvoltage and of the wavelength, and the dependence of the gain and crosstalk probability on the overvoltage. These properties will be discussed in the following sections and the respective model and parameters will be implemented in the readout simulation, which will be described in chapter 13.

6.3.1 VOLTAGE SETTINGS

The 64 sensors of one plane are biased from a common 70 V supply [155]. The break down voltages of 62.8 V are an inherent property of he MPPC sensors. The breakdown voltage, V_{BD}, is the bias point at which the electric field strength generated in the depletion region is sufficiently large for free carriers to produce additional carriers by impact ionisation, resulting in a self-sustaining avalanche. The

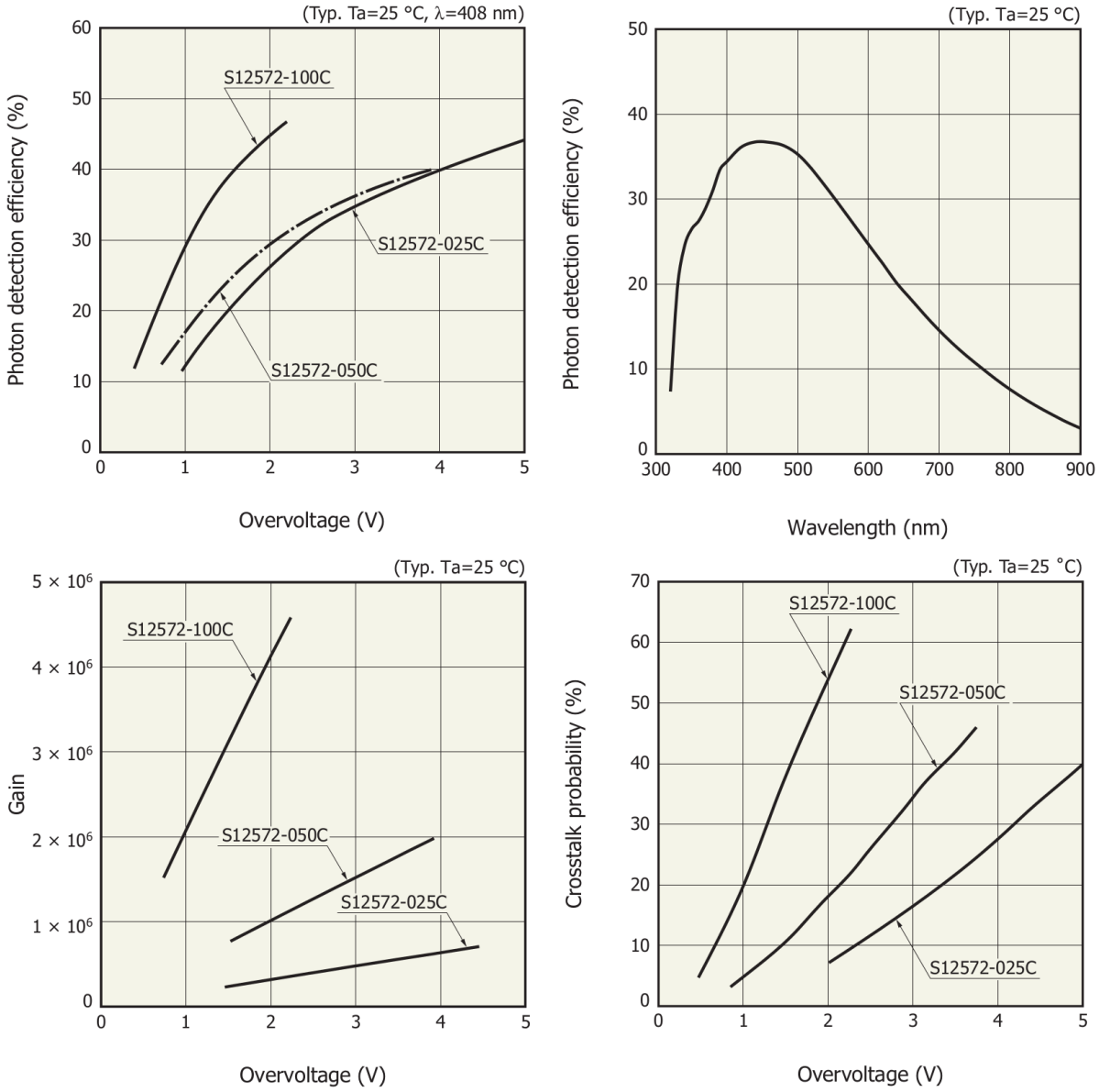

Figure 6.3.1: Characteristics of the Hamamatsu S12571-050P SiPM. Top left: photon detection efficiency in function of overvoltage, at 25 °C and for a wavelength of 408 nm. Top right: photon detection efficiency in function of wavelength, at 25 °C and at 2.6 V. Bottom: Pixel gain (left) and crosstalk probability (right) in function of overvoltage for several Hamamatsu SiPM models [154].

avalanche is terminated by using a large resistor in series with the diode. The current produced by the avalanche creates a voltage drop across the resistor (R_{quench}), which stops the avalanche when the voltage across the diode reaches V_{BD}. The charge produced in an avalanche is determined by the diode capacitance and the difference between the operation voltage, V_{op}, and the breakdown voltage, which is denoted as the overvoltage $V_{\text{ov}} = V_{\text{op}} - V_{BD}$.

The choice of the sensor overvoltage is a compromise between photon detection efficiency, pixel cross talk and thermal dark count rate. During the early days of the detector deployment, the operation voltage was set at 64.3 V, resulting in an overvoltage of 1.5 V. Since April 2018 the container was cooled to a temperature of 11°C, which reduced the dark count rate and allowed the operation voltage to be increased to 64.6 V, giving an average overvoltage of 1.8 V.

When an avalanche occurs in a pixel, the pixel's operation voltage, V_{pixel}, drops down to the breakdown voltage due to the quenching process and needs a certain time to reset [156]. The pixel voltage recovers to the nominal operation voltage with a time constant that is dictated by the RC circuit

$$V_{\text{pixel}} = V_{\text{pixel}} + (V_{\text{over}} - V_{\text{pixel}}) \cdot \left(1 - \exp^{-\frac{t}{\tau_{\text{rec}}}}\right). \tag{6.1}$$

The recovery time is determined as

$$\tau_{\text{rec}} = R_{quench} \cdot C_{pixel}. \tag{6.2}$$

With a pixel capacitance of 89.96 pF and a quench resistor of 270 Ω [154], the recovery time of the MPPC pixel is 24.29 ns. Considering photons that arrive close in time, the pixel recovery can significantly influence the SiPM response, because lower overvoltage implies a lower probability of triggering an avalanche.

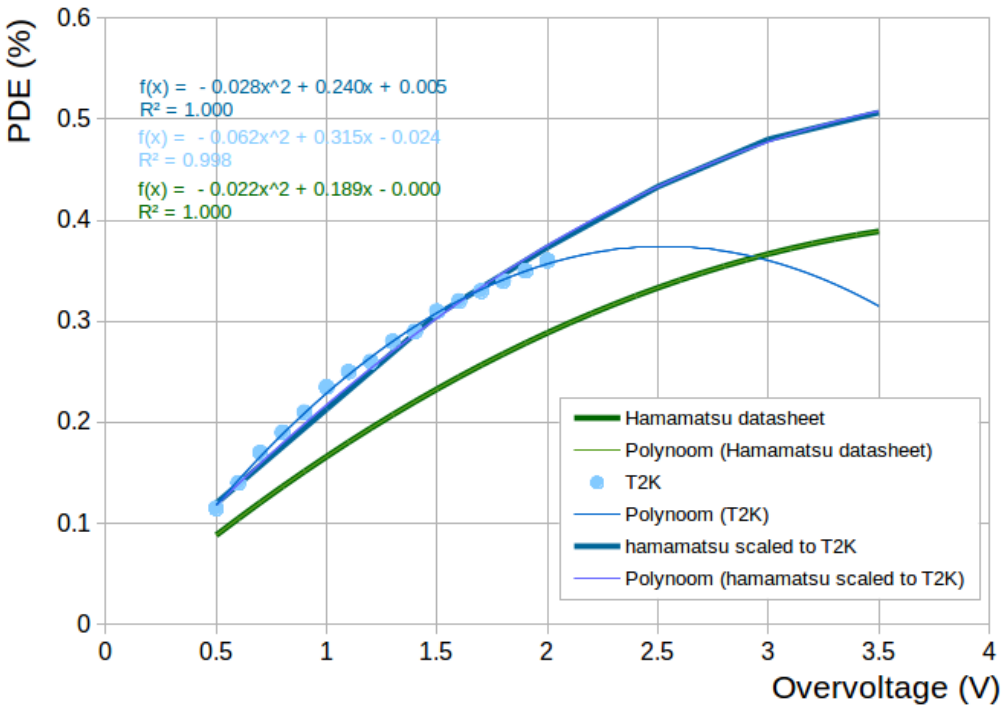

Figure 6.3.2: Left: In green the PDE stated by Hamamatsu is shown. the blue circles show the T2K measurements [156]. The Hamamatsu result is scaled to the T2K measurements, as shown by the dark blue line. The latter model is selected for implementation.

6.3.2 PHOTON DETECTION EFFICIENCY

The statistical probability that an incident photon will produce a Geiger pulse in one of the pixels is expressed as the photon detection efficiency (PDE). The PDE is given by the product,

$$PDE = QE(\lambda) \cdot \epsilon_{\text{pixel}} \cdot \epsilon_{\text{Geiger}}, \tag{6.3}$$

where the wavelength dependent quantum efficiency, $QE(\lambda)$, is the probability for an incident photon to generate an electron-hole pair in a region in which carriers can produce an avalanche. The geometric acceptance ϵ_{pixel} is the fraction of the total photodiode area occupied by the photosensitive area of the pixels. Hamamatsu reports an acceptance of 62% for sensors with 50 μm pixels. ϵ_{Geiger} is the probability for a carrier to initiate a Geiger discharge. The PDE depends on the overvoltage through ϵ_{Geiger} and on the photon's wavelength through QE. The top left panel of figure 6.3.1 shows the photon detection efficiency in function of the overvoltage, for a temperature of 25 °C and for a wavelength of 408 nm. The right panel shows the PDE in function of the wavelength for a fixed overvoltage of 2.6 V.

The SoLid experiment operates at a fixed temperature and a narrow wavelength range, but the variation of the overvoltage is significant, because of the voltage recovery after pixel avalanches and because the gain equalisation is done by adjusting the overvoltage, which is sensor dependent. The T2K collaboration made detailed measurements [156] with the Hamamatsu S12572-050P SiPM. SoLid uses the same sensors as T2K in a similar experimental setup. The findings of T2K are shown in figure 6.3.2 by blue dots, next to the Hamamatsu graph in green. In order to have a working PDE model for a broader energy range, the Hamamatsu result is scaled to the T2K data points, which has the following polynomial fit

$$P(PA) = -0.028 V_{\text{pixel}}^2 + 0.240 V_{\text{pixel}} + 0.005. \tag{6.4}$$

6.3.3 PIXEL AVALANCHE PULSE

When a pixel avalanche (PA) is induced in a sensor pixel, either by an incoming photon or a darkcount or crosstalk, the pixel produces a fast current pulse. The single PA pulse amplitude in ADC counts, is called the gain (expressed in ACD/PA). The gain depends on overvoltage (figure 6.3.1 bottom left). To keep the gain constant, the reverse voltage must be adjusted to match the ambient temperature or the element temperature must be kept constant. Since it turned out to be difficult to adjust the voltage appropriately, the sensor gain is stabilised by cooling the electronics with a chiller system.
The pulse has a specific shape because in Geiger mode the total number of electron-hole pairs produced in the pn junction of the photodiode is fixed by the external circuit [157]. Since the sensor pulses are very fast (a few ns) compared to the digital sampling (25 ns), the pulses are shaped to slow the signal over several samples, allowing a more accurate timestamp and amplitude to be measured offline. The signal from a channel of the SoLid detector is essentially made from a large number of small pixel avalanches (PA). It is key to understand and model it precisely.

The pulse shape is modeled with single PA that are selected in random data of the phase 1 detector. After a random trigger the noise is recorded without a zero suppression threshold (see chapter 7), such that the complete pulse shape of single PA can be determined. To collect single PA, peaks are selected that have an amplitude around the MMPC gain value, which is 32 ADC at the working overvoltage of 1.8 V (see top left panel of figure 6.3.3). A range of 30 samples around the peak is regarded,

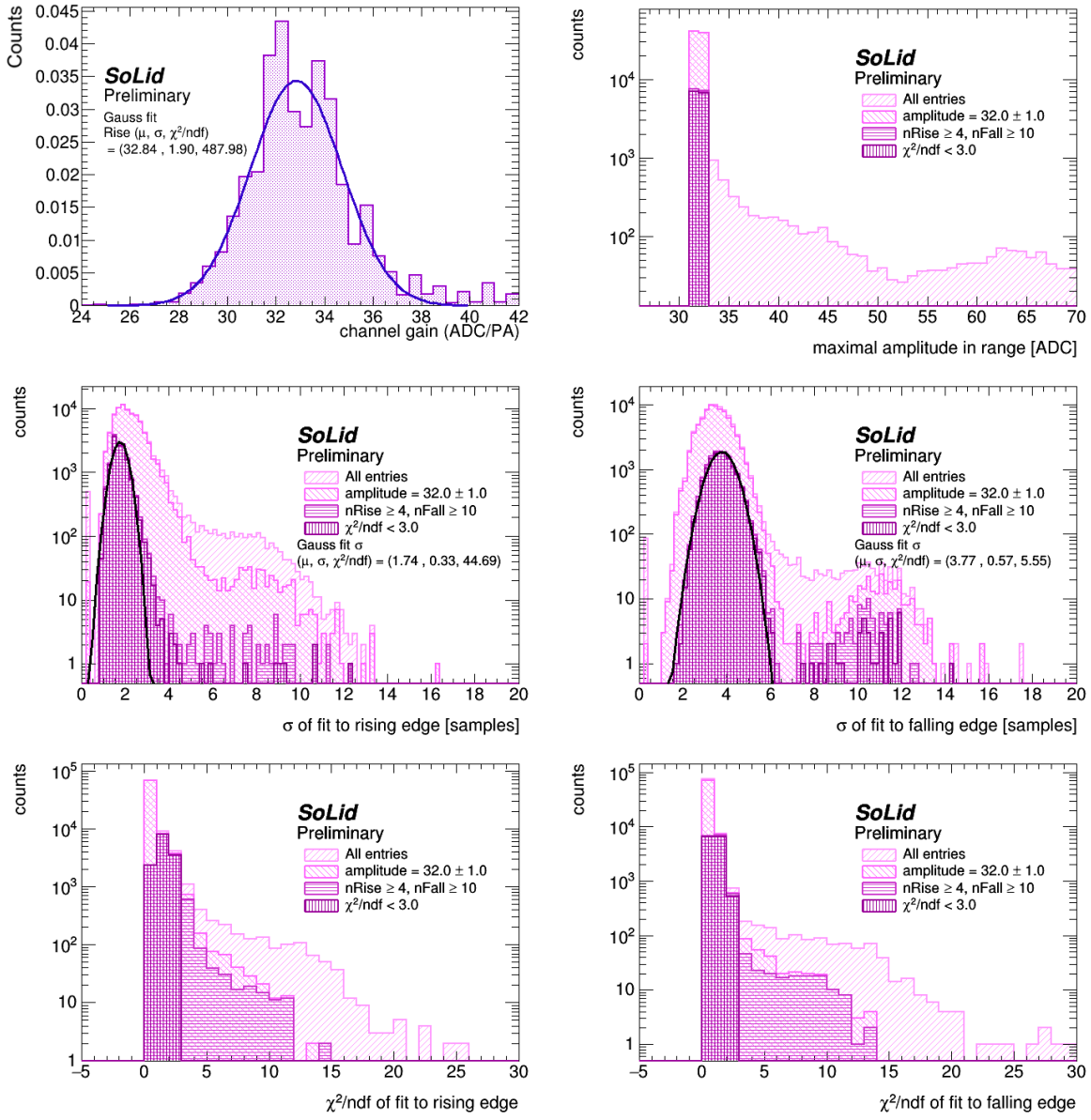

Figure 6.3.3: Parameters of interest when analysing the pulse shape of the pixel avalanche. Top left: gain values of the selected single pixel avalanches (PA) (left). The following distributions are obtained from selected PA. Top right: maximal amplitude in the selection range around the PA. Second row: standard deviation of the Gaussian fit applied to the rising edge of the PA. Third row: the χ^2/ndf of the Gaussian fit applied to the rising edge of the PA (left) and the falling edge (right).

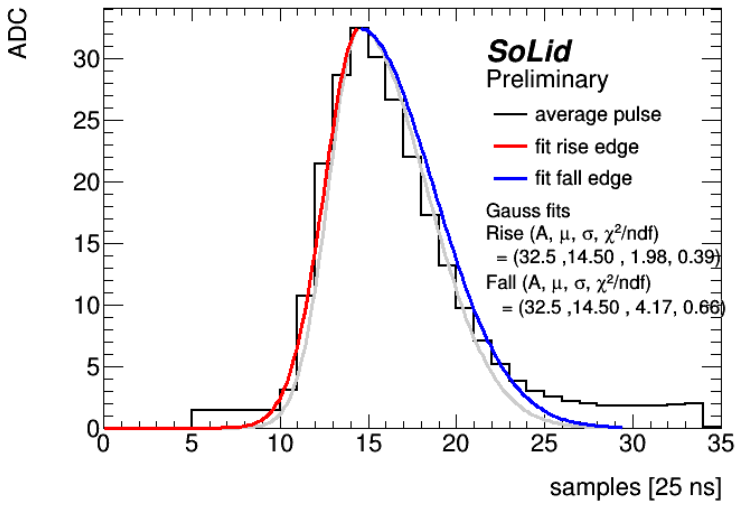

Figure 6.3.4: The average PA by taking the average of all selected PA, together with the Gaussian fit to the rising and falling edge.

provided that the maximal amplitude within the range is still close to the gain in order to avoid additional peaks with any amplitude that can have occurred in the range (see top right panel of figure 6.3.3). The pulse shape is modeled in time with two Gaussian shapes. The expressions for the rising edge and for the falling edge are respectively,

$$f_{\text{rise}}(t) = A_r \exp\left(-\frac{(t-t_p)^2}{2(\sigma_r)^2}\right) \tag{6.5}$$

$$f_{\text{fall}}(t) = A_f \exp\left(-\frac{(t-t_p)^2}{2(\sigma_f)^2}\right), \tag{6.6}$$

where t_p is the timestamp of the pixel avalanche which can be any time in nano seconds. The amplitude and mean of the Gaussian are fixed, being the value and position of the peak. This leaves the standard deviation as fitting parameter. The results are shown in the second row of figure 6.3.3. The corresponding χ^2/ndf value of the fits are shown in the next row, where ndf is the number of degrees of freedom. All the single PA that have a pulse fit with a χ^2/ndf below 3 are collected in an average pulse shape, which is shown in figure 6.3.4. The rising and falling edge of the average PA are fitted with two Gaussians as before, which is shown in red and blue. The standard deviations of the fits are respectively 1.98 samples and 4.17 samples. The pulse shape in gray is constructed from the average σ of all the fits to the separate PA, which are 1.74 samples and 3.77 samples for rising and falling edge respectively, as can be found in figure 6.3.3. These values are slightly smaller than those from the fit to the average PA, for which the tail is represented better.

6.3.4 THERMAL INDUCED NOISE

The sensors used in the SoLid experiment are capable of single photon detection. The main source of noise is therefore thermal noise, which is due to thermally generated electrons that create an avalanche in the high electric field region. Such a pixel avalanche is referred to as a dark count. An example of pulses that stem from sensor noise are shown in figure 6.3.5.

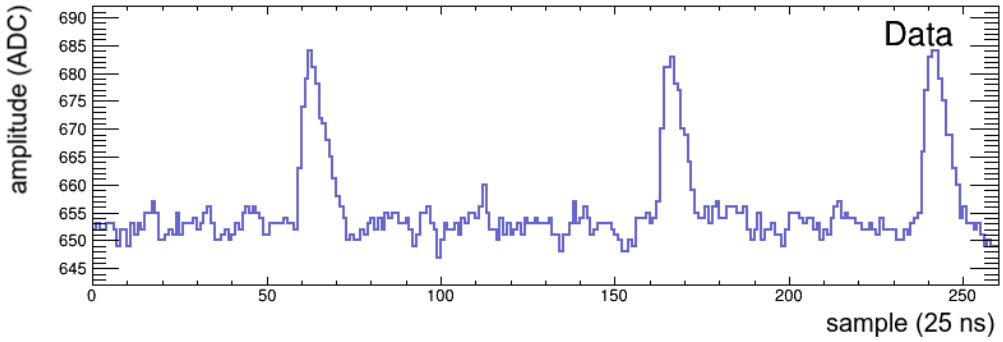

Figure 6.3.5: Example waveforms that contain dark counts from random, noise only data.

Any pixel avalanche can, in turn, initiate secondary avalanches through the mechanisms of afterpulsing and optical crosstalk. The latter are referred to as correlated noise and will be described in the following section. The variation in dark count rate (DCR) between individual MPPCs is expected to be large according to the Hamamatsu MPPC data sheet [154], quoting a variation of approximately a factor two. The channel dark count rate is determined from noise only data, that was taken with the random trigger. The noise contains single PA pulses from isolated dark counts, along with larger amplitude pulses, where additional crosstalk pulses or afterpulses were superimposed on the dark count pulse. The spectrum of the local maxima of all MPPCs is shown in figure 6.3.6, along with the spectrum of all sample amplitudes. Since each peak in the noise data stems originally from a dark

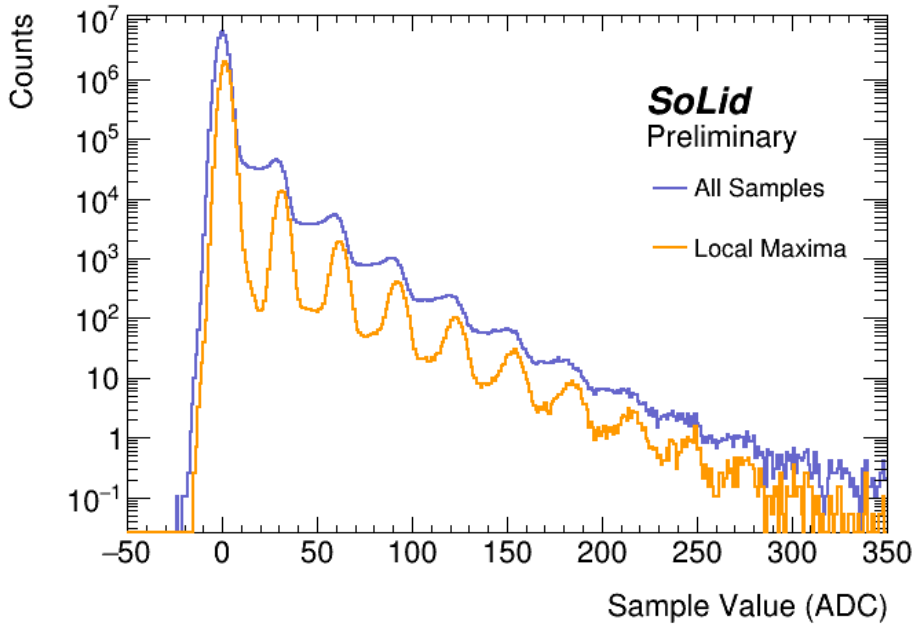

Figure 6.3.6: The number of darkcounts is estimated as the number of entries in the local maxima spectrum above 0.5 PA.

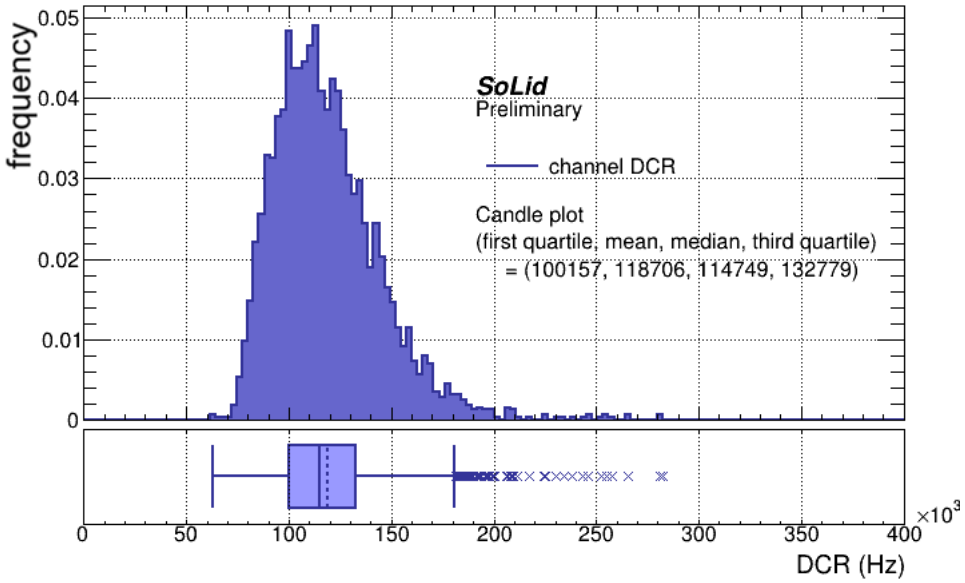

Figure 6.3.7: Top: Distribution of channel DCR. Bottom: candle plot of the channel DCR. The box spans from the first to the third quantile. The central line is the median value and the circle the mean value. The whiskers cover the full range of the set.

count, the number of dark counts is the sum of all the local maxima that have an amplitude, A, higher than half a pixel avalanche,

$$N_{\text{dc}} = \int_{0.5}^{\infty} A_{\text{localMax}}\, dA.$$

With the accumulated random noise, the dark count rate is determined from the number of dark counts and the acquisition time. The determined dark count rate per channel is shown in figure 6.3.7. The darkcount rate depends on the overvoltage that is applied to the sensor and on the ambient temperature. This relation is modeled as well, in order to be able to predict the DCR for different detector operation conditions. Measurements with a dedicated test bench [158] are shown in figure 6.3.8. The DCR increases with the overvoltage. The slope of the increase depends on the temperature. The value of the slope is determined in function of the temperature in the bottom part of figure 6.3.8. With the phase 1 detector, the channel dark count rate was monitored against changes in overvoltage, at a fixed temperature of 11 °C. The measurements and the slope value are added to the plots in figure 6.3.8. In comparison with the test bench, the DCR is lower for the phase 1 detector. The phase 1 results agree with testbench measurements below 2 °C.

The slope in function of temperature is fitted, following the procedure from the T2K collaboration to model the SiPMs that were used in the construction of the ND280 near detector [156], namely

$$DCR(V_{ov}, T[K])[kHz] = a \cdot (T - T_0)^{3/2} \cdot e^{-\frac{E}{2k(T-T_0)}} \cdot (V_{ov} - V_0). \tag{6.7}$$

The first three factors determine the slope in function of the temperature. a, V_0 and T_0 are treated as parameters in the model. The exponential part arises due to the fact that the thermal generation of electron hole pairs follows a Boltzmann distribution. The energy, E, corresponds to the silicon bandgap energy and k is the Boltzmann constant which relates energy at the individual particle level

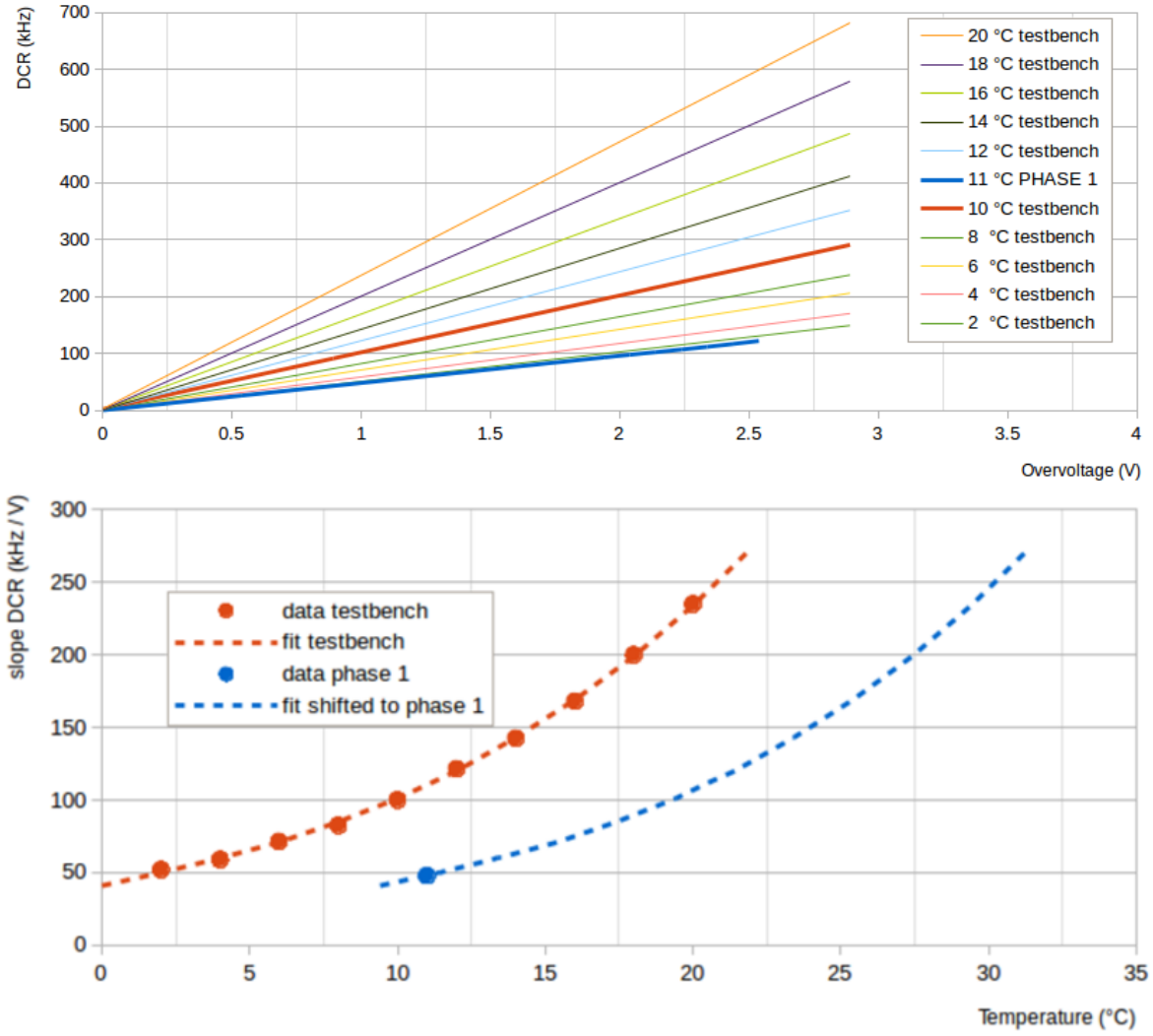

Figure 6.3.8: The top plot shows the channel dark count rate in function of over voltage, for a range of temperatures[158]. The dark count rate is taken as the number of local maxima above 0.5 PA. The slope of the DCR(OV) changes with temperature as shown in the bottom plot.

with temperature. Using E as a free parameter gives an indicator of the correctness of the model because the resulting value can be compared with the actual bandgap of silicon at room temperature

Poisson λ	30.08	
a	1977052412	kHz $K^{2/3}$ V^{-1}
E	1.12	eV
k	0.00008617	eV K^{-1}
V_0, testbench	0.109	V
V_0, phase1	-0.538	V
T_0, phase1	-9.41	K

Table 6.3.1: Parameters to calculate the dark count rate

(1.12 eV). V_0 is a temperature independent offset that corrects for the mismatch of the breakdown voltage calculated from the dark rate and from gain measurements. T_0 is a temperature shift that translates the temperature dependence of the DCR slope to the phase 1 dark count rate. The best fit values are listed in table 6.3.1. The temperature dependency of the DCR slope is expected to be the same for the phase 1 detector as for the testbench. Therefore, the fit result from the testbench is aligned with the phase 1 result by a temperature shift T_0, as shown in the bottom plot of figure 6.3.8.

6.3.5 PIXEL CROSS TALK

Optical crosstalk is the phenomenon where one pixel avalanche causes additional avalanches in neighbouring pixels. When undergoing an avalanche, charges near the junction emit photons as they are accelerated by the high electric field. These photons tend to be in the near infrared region and can travel substantial distances through the device. Typically one crosstalk photon is emitted for each 3×10^4 electrons crossing the junction. Such a photon can travel to neighbouring pixels and may initiate a subsequent Geiger avalanche there. The crosstalk can be minimised by minimizing the capacitance that the APD must discharge over.
The crosstalk probability is the probability that an avalanching pixel will initiate an avalanche in at least one secondary pixel. The cross talk probability is expected to depend only on the overvoltage (see figure 6.3.1 bottom right), and therefore, to be independent of the temperature and the channel. This is confirmed by measurements with a dedicated test bench for different sensors at different temperatures [158], that are displayed in figure 6.3.9.

The cross talk probability is determined from noise only data, that was taken with the random trigger. Each peak in the noise data originally stems from a dark count. If crosstalk pulses are superimposed on the original pulse, the peak amplitude is a multiple of the original. Since the dark count rate is low, the probability that two dark count events occur in the same 25 ns sample can be neglected. In

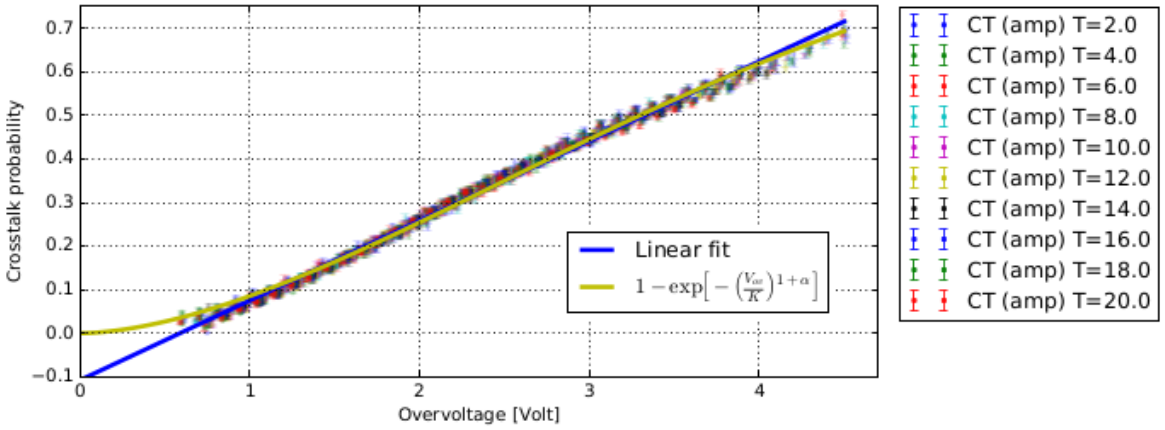

Figure 6.3.9: The crosstalk probability in function of the overvoltage for all measurements combined. After applying overvoltage corrections, no temperature dependence of the data is observed. Two two-parameter models are fitted to the data. In the region of interest for SoLid phase 1, from 1.5 V to 3.0 V, both fits are in agreement with each other.[158]

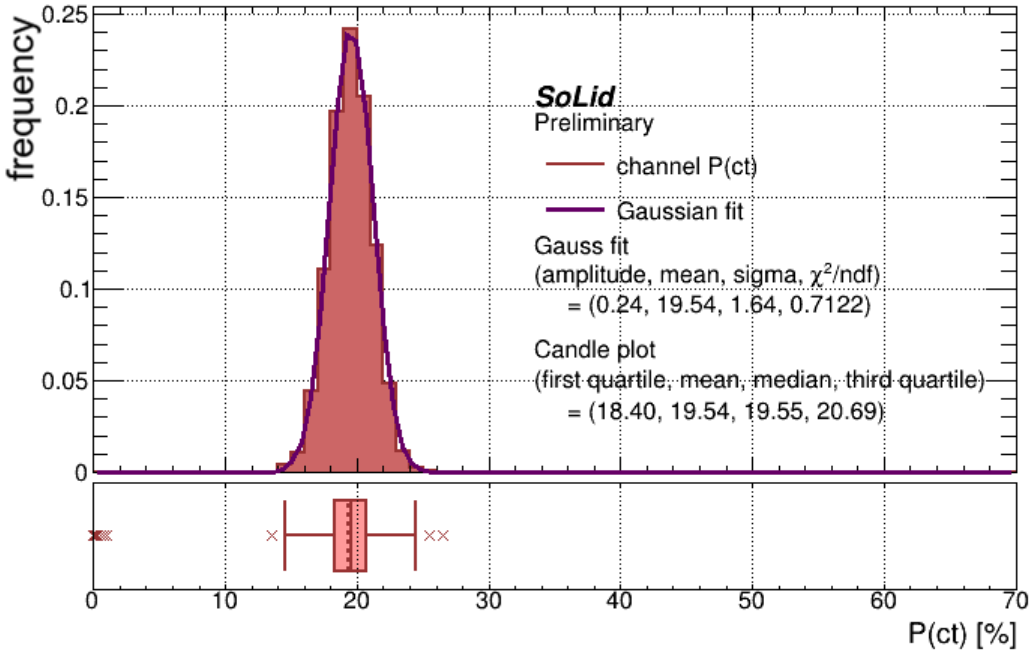

Figure 6.3.10: Top: Distribution of channel cross talk probability. Bottom: candle plot of the channel PCT. the box spans from the first to the third quantile. The central line is the median value and the circle the mean value. The whiskers cover the full range of the set.

these circumstances, the crosstalk probability can be defined as the number of dark count signals consisting of at least two single pixel avalanches, divided by the total dark count rate,

$$P_{CT} = \frac{\int_{>1.5A_{\text{localMax}}} dA}{\int_{>0.5A_{\text{localMax}}} dA} \tag{6.8}$$

The cross talk probability is calculated per channel with formula 6.8 from the spectrum of the local maxima, that was displayed in figure 6.3.6. The channel P(ct) is shown in figure 6.3.10. A Gaussian distribution is fitted to the histogram. At the bottom of the histogram, a candle plot indicates the positions of the quartiles.

With the phase 1 detector, the channel cross talk probability was monitored against changes in overvoltage, at an operation temperature of 11 °C [155]. The results are shown in figure 6.3.11. The values follow a linear relation given by

$$P_{CT}(V_{ov}) = 0.206 \cdot V_{ov} + 0.171. \tag{6.9}$$

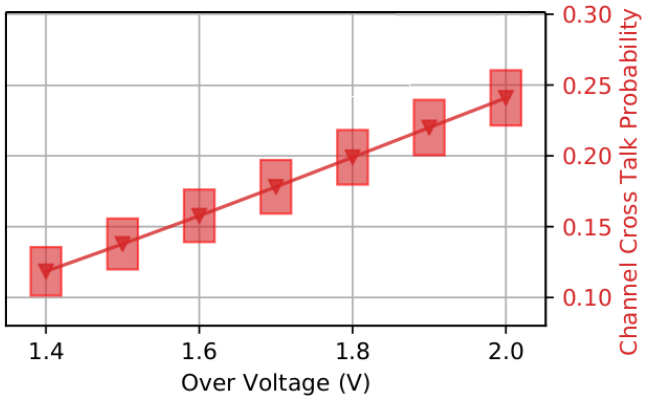

Figure 6.3.11: Cross talk probability in function of over voltage. The points show the channel mean, and the boxes show the standard deviation across all channels. The cross talk probability is taken as the ratio of the rates of the >2 PA to 1 PA signals for each channel. [155]

6.3.6 PIXEL AFTERPULSES

Whenever there was a pixel avalanche, the imperfections in the pixel can cause an additional avalanche at some later time in the same pixel. For the latest generation of MPPCs the after pulses can be safely neglected, as shown in figure 6.3.12. If desired to simulate afterpulses, this is possible in the readout simulation. Short afterpulses and long afterpulses are distinguished, where the occurrence of a short afterpulse eliminates the possibility of an additional long afterpulse.

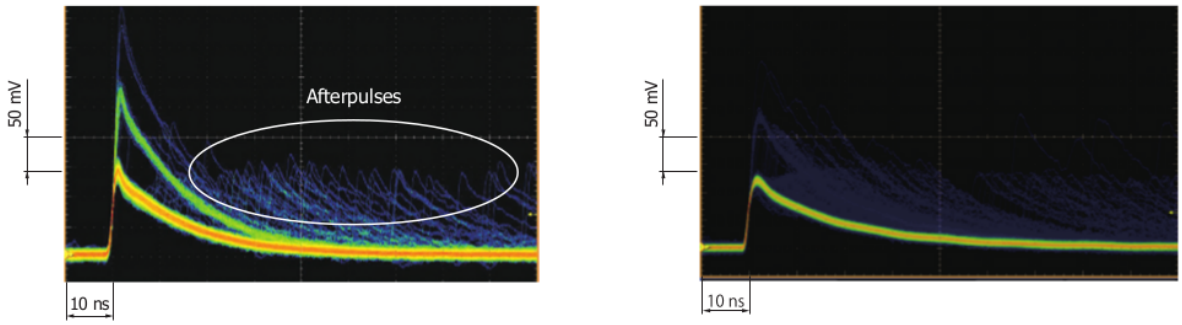

Figure 6.3.12: While an MPPC detects photons, delayed pixel avalanches may occur due to afterpulsing. In comparison to older models (left), the SiPM of Hamamatsu that SoLid uses (right) generate negligible rates of after pulses [154].

6.4 QUALITY ASSURANCE AND INSTALLATION

To validate the necessary performance of the SoLid detector and to identify defective components, a quality assurance process was developed during construction [159]. An automated calibration system called CALIPSO was constructed that performed an initial calibration of each of the planes before integration in the detector. The robot can place gamma and neutron sources in front of each

Reactor on period	days	P_{th} [MW_{th}]
12/06/18 - 10/07/18	28	60
21/08/18 - 11/09/18	21	58
02/10/18 - 23/10/18	21	56
13/11/18 - 11/12/18	28	58
06/02/19 - 05/03/19	27	45
26/03/19 - 30/04/19	35	53
02/07/19 - 06/08/19	35	48
17/09/20 - 22/10/19	35	54
05/11/19 - 03/12/19	28	58
09/01/20 - 07/02/20	29	60
03/03/20 - 31/03/20	28	58
17/04/20 - 18/05/20	31	56
10/06/20 - 07/07/20	27	56
Total	373	<55>

Table 6.4.1: Data collection periods during BR2 reactor operations and corresponding average thermal power. The recorded data is the Phase I data set.

detector cell, with sub-millimeter precision. With ^{22}Na, AmBe and ^{252}Cf sources, preliminary results for the light yield and neutron detection efficiency were validated for each cell. An average light yield of 83 PA/MeV/Cube was found without MPPC cross-talk subtraction, which was estimated to be around 17%, and a neutron detection efficiency of 60% (not optimised) were reached, with a good homogeneity over all detector planes. During the quality assurance process, some minor construction defects were identified and fixed.

After passing the quality assurance process, the first modules were mounted and commissioned at BR2 in November of 2017. Commissioning of the full detector was completed in February of 2018, after which it entered stable physics operations. Since then the experiment has been in continuous operation during all subsequent BR2 reactor cycles and refuelling periods. In between reactor cycles, in-situ detector calibrations were performed using the CROSS system. The periods during which the SoLid detector collected physics quality data during reactor on periods is summarised in table 6.4.1.

6.5 BACKGROUND SHIELDING AND MONITORING

There are many experimental challenges in establishing a measurement at very short baseline to a nuclear reactor core. The greatest difficulty comes from the background. This is the inevitable consequence of operating a detector a few meters from a nuclear reactor. The reactor emits a large number of gammas and neutrons. Moreover, the above-ground installation limits the protection against background induced by cosmic radiation. With 6 meter water equivalent (m.w.e.) overburden, the atmospheric backgrounds are challenging for the SoLid experiment. These backgrounds are described in section 11.3.

A passive shielding entirely surrounds the detector (figure 6.5.1). It consists of a 50 cm thick water wall of 28 ton surrounding its four sides. The top of the detector is shielded with a layer of 50 cm

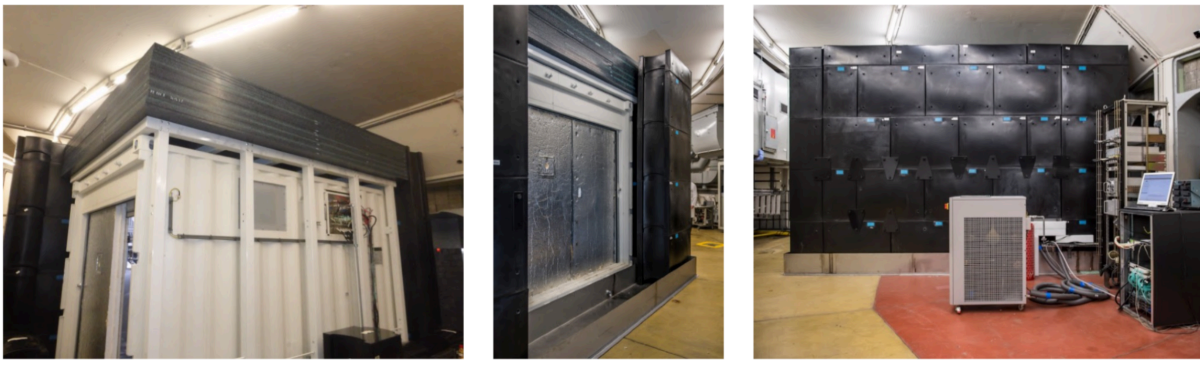

Figure 6.5.1: Outside view of the shipping container, enclosed with the black water containers of the waterwall, and with the HDPE shielding on top of it.

polyethylene in slabs of 2.5 cm thickness. In order to capture remaining thermalised neutrons, thin cadmium sheets with a thickness of 2 mm are sandwiched between the passive shielding and the container.

The concrete wall and the pool surounding the reactor vessel are penetrated by beam ports that can provide fluxes of neutrons from the reactor for experimental use. All beam ports to the experimental hall have been filled with boronated concrete and are shielded with 20 cm lead against reactor induced backgrounds. During the data collection periods, no interfering experiments were taking place in the environment of the SoLid detector. The reactor off periods allow for an accurate background determination.

During nominal data taking, the gamma background is monitored by a NaI scintillator located inside the container and the airborne radon concentration is monitored by a radon detector [160]. The environment of the BR2 containment building is continuously monitored during SoLid operation. Environmental parameters, such as temperature, humidity and pressure are constantly monitored, outside and inside the containment building. This specific readout is registered by the BR2 Integrated Data Acquisition System for Survey and Experiments (BIDASSE).

7

DATA ACQUISITION

Reading the 3200 channels of the SoLid detector with a high sampling rate results in an enormous data rate of 2 terabit per second (Tb/s)(see figure 7.0.1). It is handled by a combination of novel triggers, including a dedicated pulse shape discrimination trigger algorithm targeting neutron-like signals, and zero suppression. These techniques ensure a data reduction reduction by 4 orders of magnitude, down to 20 Mb/s, before the data is recorded on disk at the on-site DAQ server. During physics mode the mean recorded data rate corresponds to around 1.6 Tb/day.

For each plane, the trigger- and readout out logic is implemented on a Field Programmable Gate Array (FPGA). JTAG connectors are included for remote firmware programming. The readout software is written in the 'Golang' programming language [161], to take advantage of its intrinsic multithreading and memory management tools. The software can configure all readout electronics components for data taking, and performs continuous retrieval of data from all fifty detector planes in parallel.

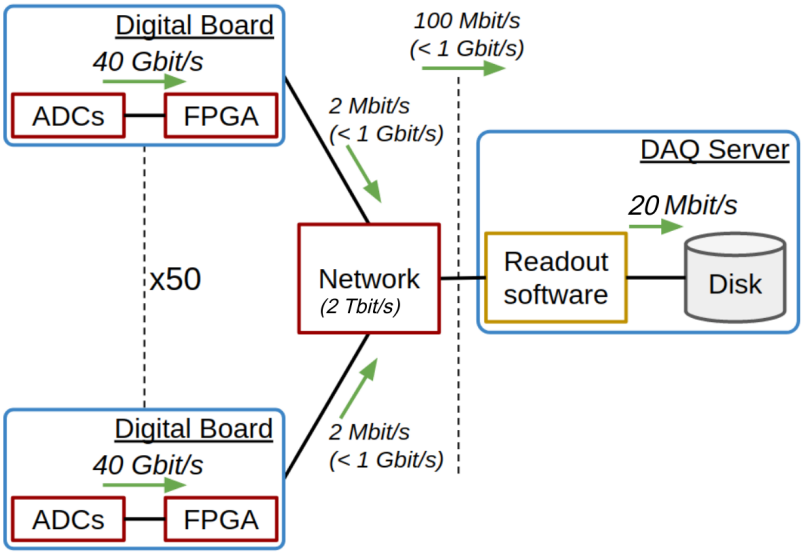

Figure 7.0.1: SoLid data flow from ADCs to disk. The rates stated are typical for physics data taking mode. The upper limits are also marked: the network sets the upper limit for each detector plane, whereas the recorded data-rate limit is due to the readout software.[155]

7.1 TRIGGER SYSTEM

The trigger system is designed to recognise and record the IBD interactions of reactor antineutrinos. Triggering on the IBD positron is not efficient because the rate of gamma rays that can mimic a

Sensor noise	100	GHz
Reactor gamma rays	100	kHz
Cosmic muons	100	Hz
Neutron	10	Hz
IBD	0.01	Hz

Table 7.1.1: Order of magnitude of the rates of different signals detectable by the whole SoLid detector.

positron signal is too high during reaction operation, as can be seen in the estimate of interaction rates in table 7.1.1. Therefore, the trigger strategy for neutrinos relies solely on triggering for the IBD neutron that causes a nuclear signal (NS) in the neutron detection screens. Since the NS signal consists of many peaks with a small amplitude (of the order of 5 to 40 PA), an amplitude-based NS signal search would be in direct competition with the gammas from the reactor, displaying an interaction rate that is 5 orders of magnitude larger than the IBD rate. The SoLid collaboration developed a dedicated neutron trigger scheme to effectively exploit the differences between both types of signals.

The NS trigger is the most complex part of the trigger system. It is based on the stochastic nature of the NS signal where sporadic pulses are emitted over several microseconds, as is shown in figure 7.1.1. The NS trigger of a channel counts the number of peaks that are over threshold in a rolling time window of 6.4 μs. The peak is defined as a sample being larger than its two neighbours. When sufficient peaks over threshold (PoT) are observed, the trigger fires.

In physics operation mode, the NS trigger searches for 17 peaks strictly above 0.5 PA in a window of 6.4 μs. These default parameters result in a neutron trigger efficiency of 75% and a neutron purity of 20% during nominal reactor on periods. The efficiency is defined by the ratio of triggered neutrons and the total number of captured neutrons. The latter is determined from the activity of the

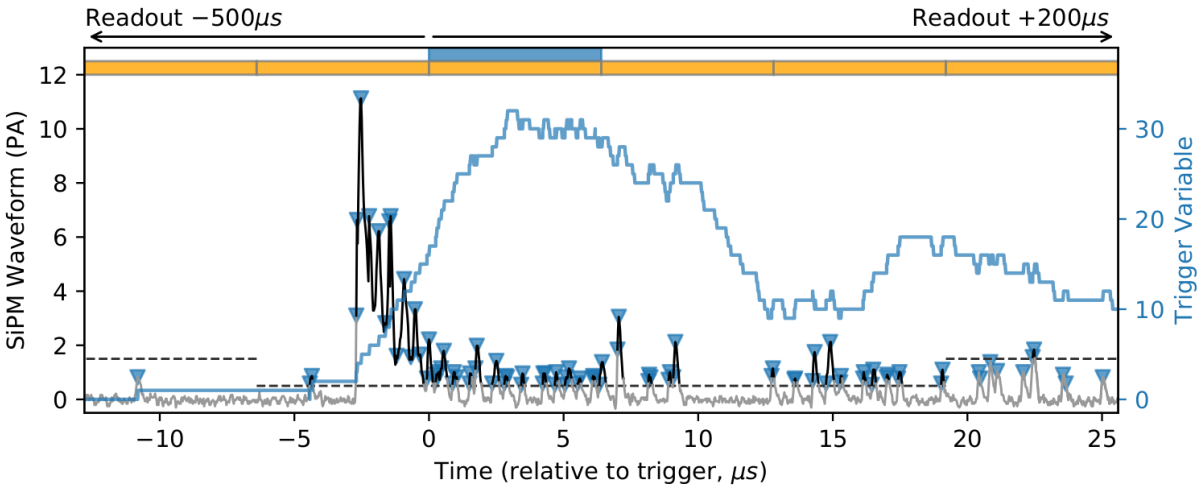

Figure 7.1.1: Example of a neutron waveform in black. The peaks over threshold (PoT) are indicated by blue arrows and the number of PoT in the rolling time window is shown by the blue line. The orange rectangles indicate the successive time blocks, with the triggered block highlighted in blue. The NS trigger prompts readout of a time region indicated at the top of the figure. The dashed lines show the zero suppression threshold, which is reduced in the blocks surrounding the trigger block.[155]

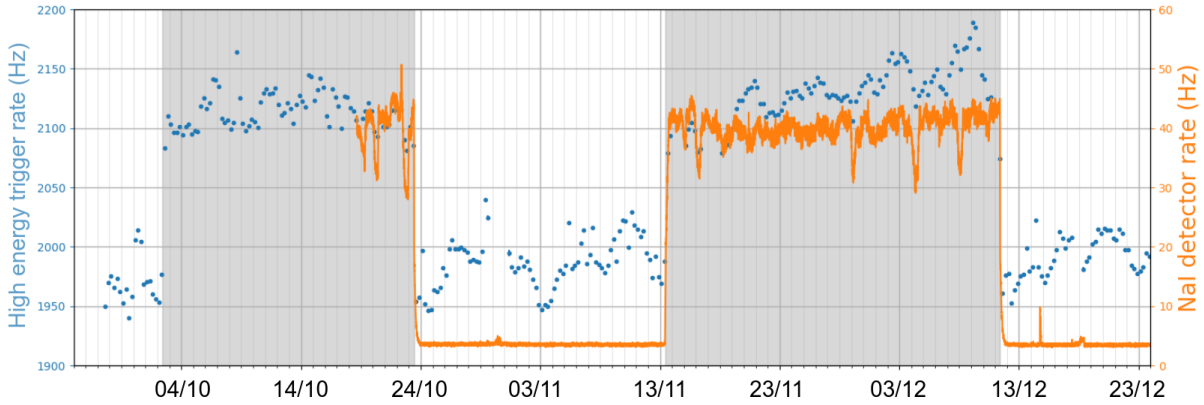

Figure 7.1.2: Long term trends of the high energy trigger rate (blue) and the NaI detector rate (orange). Reactor on periods are shown as grey bands.[140]

calibration source and from the capture efficiency obtained from simulation. The purity is defined as the number of triggers that pass an offline neutron identification and the total number of triggers. The 80% non-neutron triggers are mostly muon signals, which can be distinguished using an offline identification (see section 8). The neutron trigger inefficiency is due to a lack of scintillation photons that reach the sensor (which can be due to attenuation during photon transport through the ZnS sheet, cube and fiber) or because the peak density is too low. The NS trigger rate fluctuates around 40 Hz over the whole detector and does not change significantly with changing reactor conditions. This gives a data-rate of 15 MB/s which is the dominant component of the data rate.

In addition to the NS trigger, a high energy trigger and a periodic trigger are implemented to monitor the background and survey the detector stability. The high energy trigger targets high energy signals in the PVT scintillator, for example caused by muons. The high energy trigger is based on the status of channel amplitude threshold triggers. In default physics mode the threshold is set at 50 PA for each channel separately. The high energy trigger requires a time coincidence smaller than 75 ns between two orthogonal channel threshold triggers. Given that a detector cell feeds into four fibers, this corresponds to an energy threshold on the cube signal of of 200 PA, which is about 2 MeV. During nominal reactor on periods, the high energy trigger gives a rate of about 2.1 kHz and data-rate of 2 MB/s. This decreases by around 10% during reactor off periods. Figure 7.1.2 shows the change in high energy trigger rate between reactor on and off periods and how this is correlated to the γ rate measured by the NaI detector installed inside the container.

A periodic trigger has also been implemented that operates on the level of the whole detector. It is the most rudimentary trigger of SoLid and is used to continuously monitor the stability of the SiPMs and any external noise contributions. The periodic trigger is activated at a frequency of 1.2 Hz, thus enabling a measure of baseline position, sensor gain, and sensor dark count rate to monitor the proper functioning of the detector.

Every channel has its own threshold trigger and NS trigger that evaluate the incoming data stream on a sample-by-sample basis. After every 256 samples, which is denoted as a block, the channel triggers forward their status to their respective plane triggers. The plane trigger can prompt readout of the plane based on the status of its channel triggers and the status of the detector's periodic trigger. Which data in space and time will be read out is determined by the trigger type, namely the high

energy trigger (type 0), the NS trigger (type 1), or the random trigger (type 3). The trigger types are listed in ascending priority. The trigger type is stored as a trigger record, along with the plane ID, the ID of the channels that fired and the time stamp (situated at the last sample of the triggerblock).

7.2 READ OUT SYSTEM

By default, all detector channels in the triggered detector plane are read out for each trigger. This is useful to reconstruct complicated event topologies offline, which include low amplitude signals that are shared between multiple fibers. Additional data can be recorded in time and space, depending on the trigger type with highest priority that prompted for read out.

A network of time buffers is present for each channel, where incoming samples are temporarily stored. This allows data from before the rigger to be read out, along with the data that are incoming. A block diagram of the per-plane FPGA firmware implementation is shown in Figure 7.2.1. The incoming data samples are first placed in a FIFO latency buffer, which is non-zero suppressed (NZS) and can store up to 512 waveform samples. This buffer is used to delay samples prior to being zero suppressed. Once a sample iterated through the NZS buffer, it is zero suppressed (ZS) and enters the window buffer. The ZS discards all samples that have an amplitude below the ZS threshold, which is necessary for data reduction. A default ZS threshold of 1.5 PA is always applied. If the plane trigger fired, then the trigger sequencer can change the ZS threshold, depending on the trigger type. Given the length of the non-ZS buffer, this new zero suppression threshold operates on data that arrived 512 samples (i.e two blocks or 12.8 μs) before the trigger signal.
The plane sequencer sets the duration of data readout in units of blocks from both before the trigger (i.e stored in the ZS buffer), and after the trigger (i.e not yet entered the ZS buffer). The smallest amount of data that can be read out is a single block, corresponding to 256 waveform samples (6.4 μs). At the moment of triggering, the ZS latency buffer is already filled with up to 1536 waveform samples that arrived before the trigger. The duration stored in this buffer depends on its size and the ZS compression rate - a compression factor of 50, due to ZS at 0.5 PA, allows up to 2 ms to be stored. In practice, to avoid frequent buffer overflow, the buffer is limited to 500 μs, which is suitably large for the IBD buffer for each neutron trigger.

The read out space-region is set by propagating the plane trigger decision to a pre-set number of neighbouring detector planes on either side of the triggered plane. The number depends on the

Trigger type	Condition	Trigger rate (Hz)	Data rate (MB/s)
NS	$N_{\text{peak}>0.5PA}$> 17 in 6.4 μs window	80	15 (71%)
threshold	waveform sample > 50 PA		
High energy	Δt < 75 ns between orthogonal channel's threshold triggers	2100	2 (10%)
Periodic	periodically	1.2 Hz	3.9 (19%)

Table 7.1.2: Summary of trigger settings and associated data rates during reactor on physics data taking.

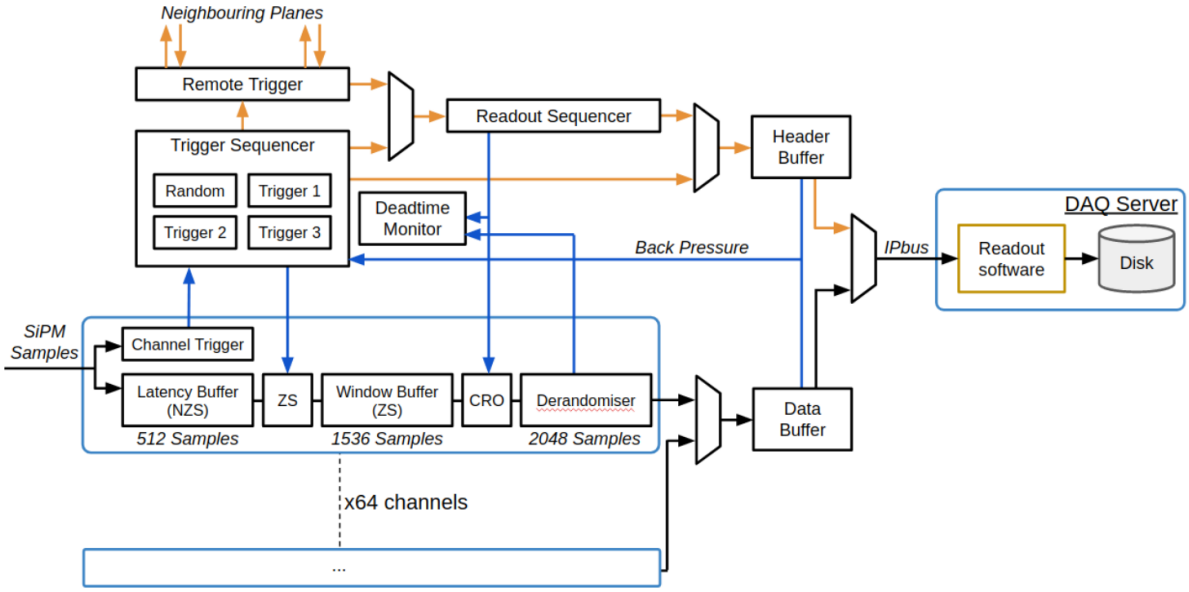

Figure 7.2.1: Block diagram of the plane level FPGA firmware implementation. Incoming SiPM samples update channel triggers and first iterate through the latency buffer before being zero suppressed and possibly enter the window buffer. The channel triggers communicate their status to the plane trigger. If the latter fires a certain trigger type, the readout sequencer determines which blocks will be read out, both from the buffers and from incoming samples. The plane trigger decision is passed on to neighbouring planes in order to read out a certain space region.[155]

trigger type. Each plane has a readout sequencer that determines which data are recorded for each trigger (either local or remote triggers):

- **The NS trigger** causes a spacetime region to be read out, that is optimized in order to reconstruct the IBD positron that precedes the IBD neutron signal. 99,66 % of the positrons is contained in this region [162]. The region contains the triggered plane, along with its three neighbouring planes on either side, during a time span of 700 μs. Knowing that the positron event took place before the neutron capture in the case of the IBD, the buffer is set to contain [-500: 200] μs. The selection efficiency of the annihilation gammas from the positron in this spacetime region is 81.4 %.

  For this trigger mode, the ZS threshold is reduced for blocks containing and directly following the trigger, which is useful to improve the light collection of NS type signals.

- **The high energy trigger** leads to the read out of the trigger block with the default threshold. No other planes or other blocks are read.

- **The random trigger** prompt the entire detector to be read out simultaneously during two successive blocks, which totals 512 samples. The signal is not zero suppressed. All data is read out, giving a data rate of 3.9 MB/s.

In cases of overlapping space-time regions due to triggers in close proximity, the readout time window is extended as required for each affected detector plane, and does not result in additional dead time. The readout settings are listed in table 7.2.1. When triggered, data from all channels are

Trigger type	default ZS thresh	ZS threshold after trigger	RO Space	RO Time (μs)	RO Time (blocks)
3 Forced	1.5 PA	0 PA	Whole detector	12.8	+2
1 Neutron	1.5 PA	0.5 PA	Triggered plane ± 3	-500, +200	-80, +30
0 High energy	1.5 PA	1.5 PA	Triggered plane	6.4	+1

Table 7.2.1: The settings specifying the space-time region that is read out following a certain trigger.

concatenated per block and stored in a data buffer that will be read out over IPbus [163] by the local DAQ disk server. When there is overflow in the derandomiser or the data buffer (e.g due to a high trigger rate), the plane triggers are halted and no more data is collected from this plane. The detector plane is said to be in plane dead time. Should the overflow occur during the concatenation of channel data, some channels may be excluded, incurring channel dead time. Once the overflow has been cleared, triggers resume and the dead time periods are encoded in the data steam. Plane and channel deadtime were observed during calibration to have a non-negligible effect on the reconstructed signals.

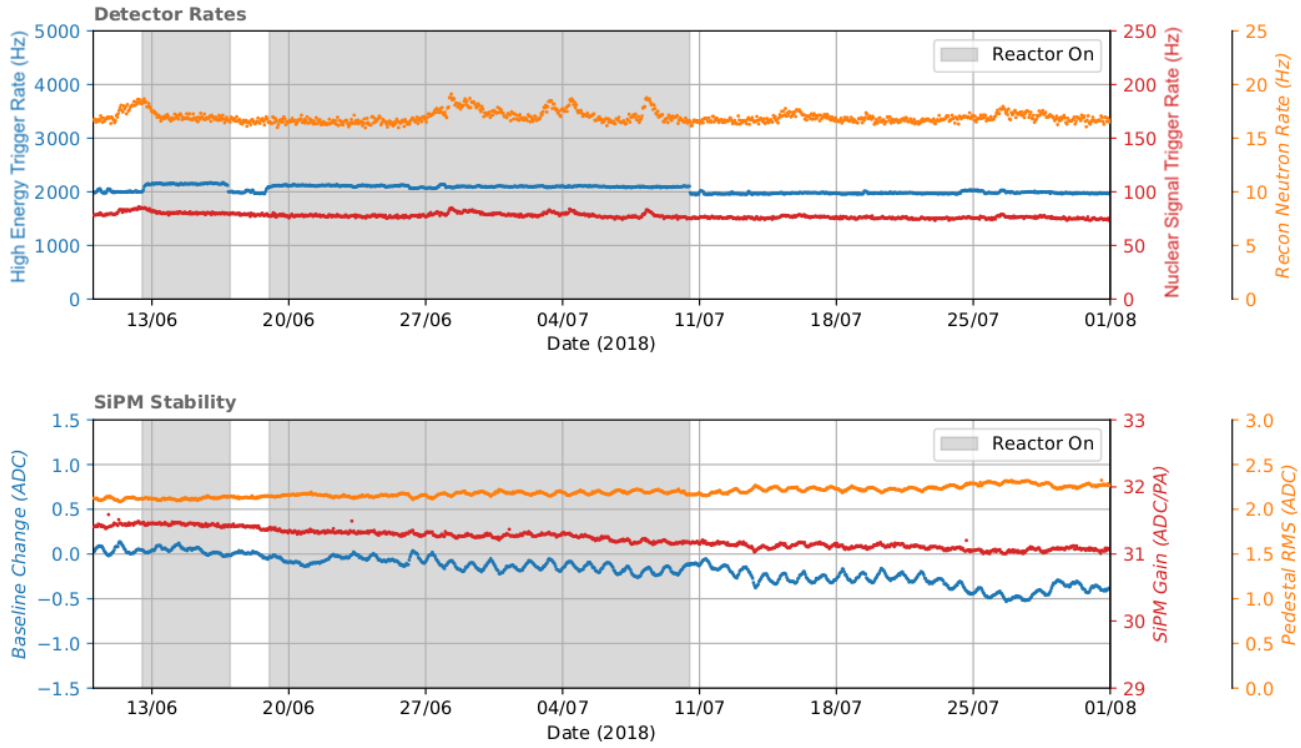

Figure 7.2.2: Weekly trends of various detector metrics. The threshold trigger rate is the only metric sensitive to the reactor on-off transition. [155]

7.3 DATA QUALITY MONITORING

The full SoLid Phase I detector has been in highly stable data taking mode, for both reactor on and off periods since April 2018 up to June 2020, apart from the calibration measurements and some short shutdowns for small interventions. In total, the Phase I detector recorded 373 days of physics quality data. A small part of this data will be rejected in the final analysis, e.g. in case unstable environmental or data taking conditions were noted. During the full operation time, run control operations are controlled via a dedicated python based web application. The application also provides an interface for the SoLid's Data Quality Monitor (SDQM). It runs on Python-based scripts and automatically processes online a small fraction of each run with SoLid's reconstruction and analysis software (Saffron2). The output distributions, such as SiPM gains and detector deadtime, can be inspected via the web application and are stored in an online database, along with physics variables, such as background rates, pressure, temperature and humidity, that are periodically measured with the NaI- and Rn-detectors and with several environmental sensors. This set of measurements serves as input to an automated alarm system. In case stable data taking is obstructed, alerts are prompted to contact persons. Long term trends of trigger rates and SiPM measurements are shown in figure 7.2.2. The transition between reactor on and off can be seen in the changes in the threshold trigger rate. While the reactor is on, the deviation of the neutron and threshold trigger rates are 2% and 1% respectively over a 1 hour period. The SiPM measurements show small changes over the long term, as well as day-night variations. These changes are correlated with temperature changes up to 0.5°C inside the detector container. The small increase in temperature increases the dark count rate of the SiPMs, causing the baseline values to change by up to 2% relative to the gain. The variations observed in these metrics are all < 2%, and are not correlated with changes in the trigger rates.

8

EVENT RECONSTRUCTION

The electromagnetic signals caused by particles that triggered the detector readout will be reconstructed by offline software into physics objects. The first step in the reconstruction chain is to combine associated waveforms into a cluster. Next, the physical process that caused the cluster is identified. The coincidences between specific types of clusters are made. In addition, the fine detector segmentation allows to precisely reconstruct the topology of the events.

For the offline reconstruction and analysis of the (simulated) data, the dedicated C++ software Saffron2 was developed in the collaboration [164]. The Saffron2 code reads in the data until a gap bigger than 350 blocks (2,240 ms) is encountered. The data in memory is called a cycle. This method aims to group physically correlated events in one cycle and is optimised to limit memory usage. While reconstructing the signals, the raw data and all intermediate reconstruction objects stay in memory, allowing simultaneous access to all information. Once the set of reconstruction algorithms has been applied for the cycle, the properties of the reconstructed signals are recorded on disc.

8.1 WAVEFORM CLUSTERING

The detector output consists of a continuous flow of waveforms sampled at 25 ns (see chapter 7). Since the signal is read out at a low zero suppression threshold, the data contains a large amount of thermal noise, which must be rejected effectively in order to analyse the large amount of data produced by the 3200 channels of the detector. The physical events that occur in specific detector cells only feed scintillation light into the channels that are connected to these cells, whereas the thermal noise arises on all channels. Channel waveforms are clustered based on their timing, in order to collect the waveforms that are associated to one event.

All waveforms within a plane that are close enough in time, less than 175 ns or 7 samples, are collected into a cluster object through an iterative procedure. The time window is optimised such that the secondary waveforms of an NS signal are collected as well, while no thermal noise waveforms are added to an ES cluster. Subsequently, clusters are merged when their start times lie within 7 samples (targeting clusters on different planes) or when clusters with common channels overlap in time or start close in time (less than 21 samples). The waveforms that are not part of a cluster are discarded.

Figure 8.1.1 shows two examples of clustered waveforms; one for an electromagnetic signal from the PVT scintillator and one coming from scintillation in a ^{6}Li:Zns(Ag) screen. The PVT signal results in a very short cluster, with a small number of included waveform blocks. For the ZnS scintillation the cluster window includes many more consecutive waveform blocks and is significantly longer in time. A study of this method has shown that 99% of the waveforms with a peak above 20 PA, that most

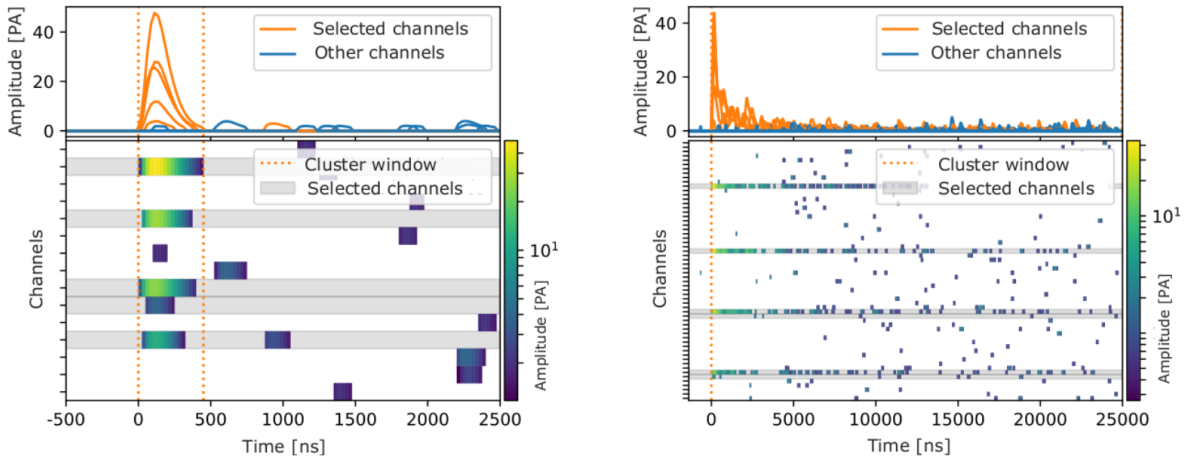

Figure 8.1.1: Left: Example of an ES signal, containing waveforms caused by PVT scintillation. Right: Example of an NS signal by scintillation in the ZnS(Ag) screen. In the lower panel, the highlighted channels contain the coincident signals that are clustered together. The top panel shows the corresponding waveforms.[165]

likely correspond to physical events, are part of a cluster. The remaining 1% is allocated to waveforms potentially containing signal, but for which the start time does not coincide with other channels. The majority of waveforms below 10 PA, mostly related to noise, were discarded.

For each cluster, the positions of the cubes where the interaction took place are reconstructed from the present channels. Combining the information from these channels, the amplitude and integral of the signal can be computed. In figure 8.1.2, the maximum amplitude that is measured in a cluster is shown in function of the cluster length l. Several structures appear. Events with a maximum amplitude around 500 PA are caused by the saturation of ADCs. The saturation corresponds to an energy of approximately 20 MeV, which only happens when a muon passes through the detector. The length of these clusters is almost completely contained in a window of 25 μs. Next, the contribution of maximum amplitudes between 0 and 200 PA, is a priori composed of ES events, for which the cluster length remains very short, namely under 3 μs. Finally, events that have a maximal amplitude below 100 PA and a cluster length greater than 25 μs are assigned to NS signals.

Note that it will be difficult to reconstruct events that occur very close in time as separate events, due to the use of zero suppression and the use of a window to append waveforms. During physics data taking this will not be a major concern, given the interaction rates to which the SoLid detector is subject. However, during calibration measurements the interaction rate is higher and the pile up of events has to be taken into account.

8.2 SIGNAL IDENTIFICATION

The primary distinction that can be made between the signals is the origin of their scintillation. The SoLid detector uses a hybrid technology, combining two different scintillators, namely PVT and ^{6}LiF:ZnS(Ag) (see chapter 6). The scintillators produce a different signal (see chapter 13), and will be

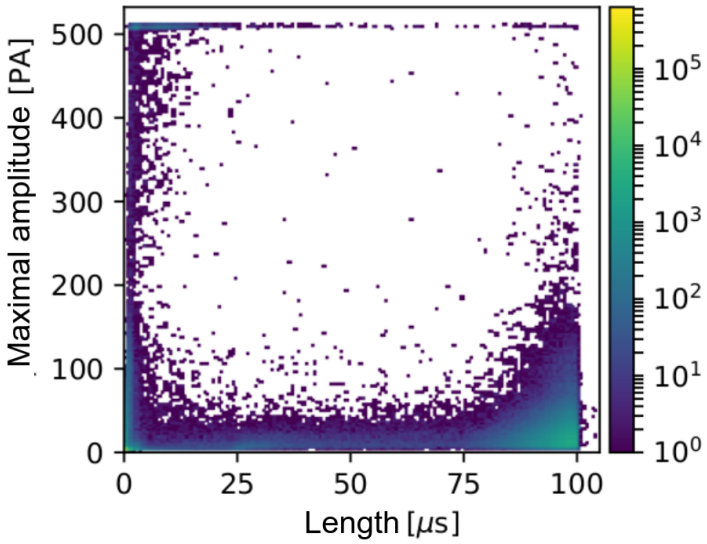

Figure 8.1.2: Maximum amplitude reached by any cluster channel versus the cluster length l in data. The lower right corner contains mainly NS, the lower left contains ES and the upper left corner is composed of muon signals.[165]

denoted respectively as electromagnetic signal (ES) and nuclear signal (NS). In addition, signals from muons get their own category because they can leave a clear track through the detector. It is more interesting to reconstruct the total track, rather than a collection of individual cubes. Below, these signals are listed with their main characteristics and the contribution of the main physical processes:

- **Electromagnetic signals (ES)** are generated by the interaction of one or more particles in PVT scintillator cubes, such as gamma rays, electrons, positrons and muons (see chapter 11 of a description of the backgrounds). Recoil protons, set in motion by the elastic collision of a fast neutron in the detector, also end up in this category, as well as the signals induced by thermal noise, even if their contribution is contained below 6-7 PA amplitude. The PVT scintillation time scale is very short, in the order of 100 ns. The shape of the ES signals is dominated by the response of amplifiers. The collection of all time coincident cubes make up one ES event.

- **Nuclear signals (NS)** originate in scintillation in the ^{6}Li:Zns(Ag) screens, induced by heavy particles. This mechanism targets the capture of an IBD neutron on ^{6}Li, resulting in the production of an alpha and a tritium nucleus that scintillate in the ZnS(Ag). However, the majority of signals composing this category are not neutron captures, but deposits from individual alpha nuclei, coming from radioactive decays in the chains of naturally occurring ^{238}U, ^{235}U and ^{232}Th. The ZnS(Ag) scintillation has a stochastic nature resulting in a rather long signal, in the order of 10 μs, composed of a series of peaks where the amplitude of the signal is proportionally small compared to its integral.

- **Muon signals** are caused by high energetic muons from cosmic origin. Three muon types are discriminated that are shown in figure 8.2.1:
  - Type 0: Clipping muons, that only cross one or two cubes at an edge of the detector. Due to the low multiplicity and the absence of a track, it will be difficult to separate these signals from a high energy ES.

Signal	origin	Rate	Amplitude
ES	Thermal noise	100 MBq	< 10PA
	reactor γ	100 kBq	10-100 PA
NS	Alpha	10 Bq	< 50 PA
	Neutron	1 Bq	< 40 PA
ES + NS	IBD	0.01 Bq	50-200 PA (ES)
muon	muon	100 Bq	> 150 PA

Table 8.2.1: Signal rates in orders of magnitude and amplitude ranges for the different signal types.

- Type 1: Muons that travel close to the vertical and cross many cubes, but only one detector plane. It will be impossible to resolve the ambiguity about the angle of entry into the detector.
- Type 2: Muons that traverse multiple detector planes and deposit energy in many cubes, giving signals on a large number of detector channels. The segmentation of the detector allows to reconstruct the track of these muons.

The Saffron2 code applies a set of identification algorithms to tag the waveform clusters with their type of underlying process. The algorithms mainly use the cluster lengths, amplitudes and integrals of the included waveforms to perform the identification. The count rate of the reconstructed signals is shown in table 8.2.1. Priority is given to the reconstruction of muon signals, followed by NS signal.

MUON SIGNAL

In the reconstruction phase, it is not feasible to discriminate the clipping muons that affect a (few) cube(s) at the detector edge from ES signals. Therefore, at this stage only the type 1 and 2 muons that make long, energetic tracks through the detector can be reconstructed as muon signal. The track can be fitted with a straight line.

When a cluster contains many high amplitude channels (at least 11 channels with 200 ADC amplitude signals) in both the horizontal and vertical direction, the muon reconstruction is initiated. After removing channels that have no neighbouring channel within the cluster, the positions of the horizontal and vertical fibers allow to interpolate the track left by the muon in the XZ plane and in the YZ plane, respectively. By combining the two projections, the track is reconstructed in three dimensions. The track is characterised by the azimuthal angle between the track and the Y axis (vertical to the detector) and the polar angle between the track and the X axis of the detector (horizontal along the front).

NUCLEAR SIGNAL

Nuclear signals (NS) originate in the scintillation inside the ^{6}LiFZnS(Ag) screens by neutron capture or by alpha particles. The algorithm aims to reconstruct NS from clusters that were not previously reconstructed as a muon signal. The scintillation from ZnS(Ag) is characterised by a long decay time $\mathcal{O}(\mu s)$ and is typically not very bright due to the additional coupling to the PVT cube. As primary

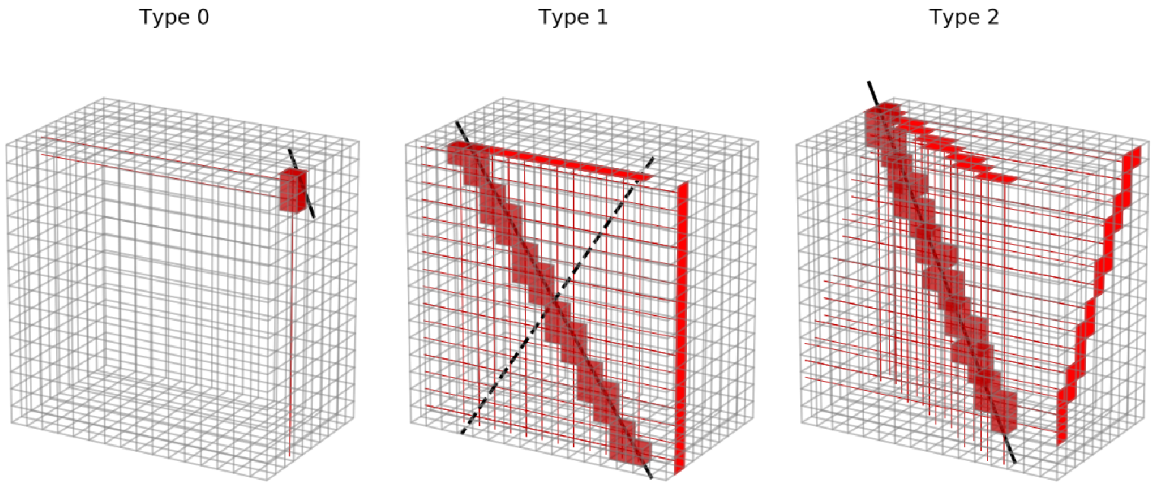

Figure 8.2.1: Examples of reconstructed muon signals in a module of the SoLid detector. The black line shows the reconstructed track, inducing energy deposits in the cubes shown in red. Affected channels are displayed in red on the exterior faces of the detection module. Left: trace of a type 0 muon traversing few cubes on an edge of the detector. Center: trace of type 1 muon crossing only one plane. Two possible tracks can be reconstructed and it is not possible to resolve this ambiguity. Right: trace of type 2 muon crossing several planes.

selection criterium the cluster has to be at least three blocks long and stay below an amplitude of 10000 ADC, i.e. 312 PA.

The NS are always expected in a single cube, since the scintillating particles only travel short distances, and the detection cells are light insulated. Candidate cubes are established inside the cluster, based on the number of peaks over threshold (PoT) in a time window of 25 μs. To make sure the candidate cube contains a NS rather than an ES, the discrimination power of the IonA value is exploited. IonA is the ratio of the integral Q_{long}, which is the mean integral in a time window of 25 μs, averaged over the channels participating in a cluster, over the amplitude $\overline{A}$, which is the average of the maximum amplitudes per channel

$$\begin{aligned} IonA &= \frac{Q_{long}}{\overline{A}} \\ &= \frac{\frac{1}{n_c}\Sigma_{c=1}^{n_{channel}}\Sigma_{i=0}^{t_{long}} ADC_c(i)}{\frac{1}{n_c}\Sigma_{c=1}^{n_c}\max(ADC_c)} \end{aligned}$$

Here, n_c, is the number of channels of the candidate NS having waveforms in the cluster time window, i represents the time since the start of the cluster, t_{long} indicates the long integration window and $\max(ADC_c)$ is the maximum sample in the cluster time window on the channel c. NS are mainly characterised by a long scintillation time and multiple waveform peaks, leading to a large integral for relatively low amplitudes, as shown in figure 8.2.2. ES events are found to have an IonA value of around 10, while the NS have a value around 50. Requiring IonA > 25 drastically reduces the ES contribution and reduces the number of clusters to be examined by a factor of 55, saving numerous digital processing operations.

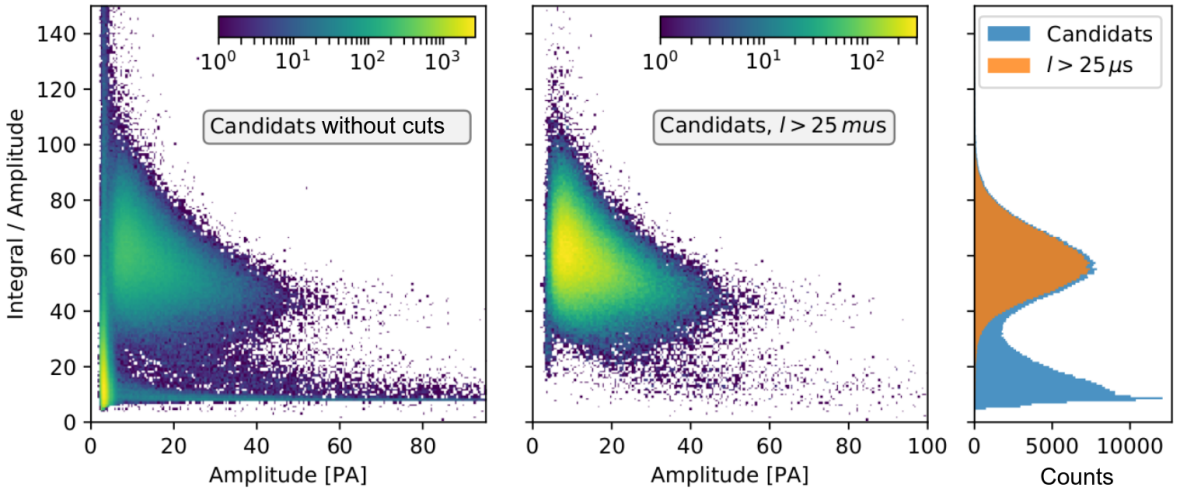

Figure 8.2.2: Integral versus amplitude of the clusters of NS candidates. Left: All candidates. Center: candidates after clipping along the length of the clusters l > 25 μs. Right: projection of two distributions.[165]

The cube with the highest mean PoT value is labeled as NS signal. The remaining channels are reprocessed iteratively by the algorithm, in case multiple NS occurred in coincidence, which should be a rare occurrence, except for neutron calibration runs.

VARIABLES CHARACTERISING THE NS SIGNAL

The NS cluster gets assigned the properties of the cube with the highest mean PoT value. The coordinates of the NS cube X_n, Y_n, Z_n, become the vertex position of the NS signal. The timing of the NS signal is determined offline, as the NS trigger occurs at the end of the signal when sufficient peaks where counted over threshold. The time is stored both in ns and in samples of 25 ns.

ELECTROMAGNETIC SIGNAL

Electromagnetic signals (ES) are considered to be the only remaining signals after the identification of muons and NS. However, in order to minimise contamination by other non-reconstructed signals, only clusters that have a length of less than 75 samples (1.8 μs) are considered, since ES are characterised by a very short pulse shape. Furthermore, all channels that don't pass the amplitude threshold of 144 ADC (~ 50 keV) are removed from the cluster.

Since ES signals consist of a single peak, it is possible to reconstruct the time of the signal with a precision better than the duration of a sample (25 ns). This is done by performing a weighted average of the signal, over the 7 samples centered around the maximum. Preliminary studies indicate that this method achieves a real time resolution of the order of 10 ns, even for low amplitude signals. In order to eliminate a large part of thermal noise, the samples that are more than 75 ns away from the sample with maximal amplitude are discarded. Figure 8.2.3 shows that for the cluster channels, the samples that are further than 3 samples from the maximal amplitude have in general an amplitude of less than 5 PA, compatible with the noise hypothesis.

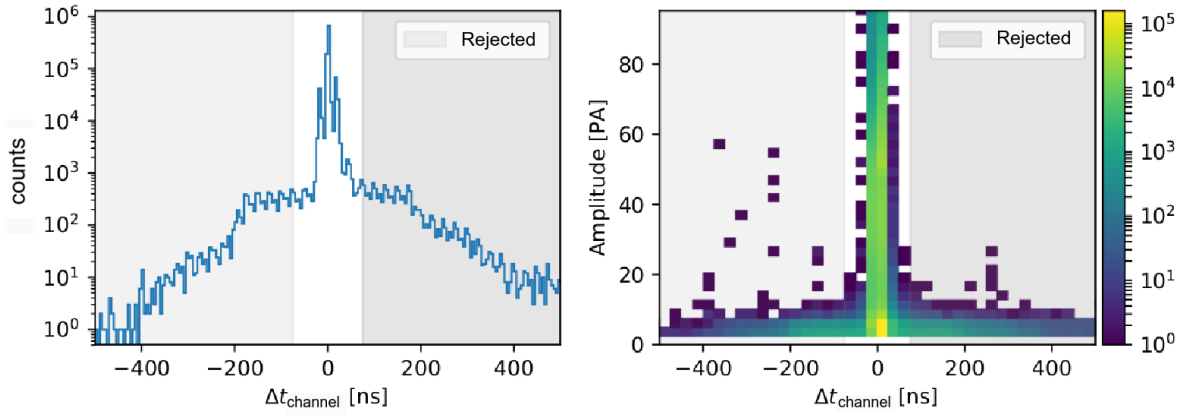

Figure 8.2.3: Left: Distribution of the time differences between the peaks and the maximum of the ES cluster (Δt channels). Right: Time distribution of a peak as a function of its amplitude. The shaded areas represent the peaks rejected during the reconstruction.[165]

Finally, the interaction cubes are reconstructed from the channels, in order to profit from the granularity of the detector. A single cube feeding photons into the four connected channels gives an unambiguous reconstruction. However, when channels receive photons from multiple cubes, it is more challenging to distribute the visible energy over the detection cells by crossing the information of horizontal and vertical channels. The bottom panel of figure 8.2.4) shows examples of an (un)ambiguous cube reconstruction. A Bayesian approach using a Maximum Likelihood-Expectation Maximisation (ML-EM) [166] is implemented with a physics-driven prior for the light distribution over the channels given by the Poisson statistics. The algorithm is provided at the first step with the cubes which are at the crossing of the most energetic fibers. The algorithm iteratively determines new parameters for the distribution of energy between fibers.

VARIABLES CHARACTERISING THE ES

The characteristics of the ES signal will be important to discriminate the IBD signal from the background. Moreover, the reactor neutrino's energy and position are directly related to the energy and position of the ES signal caused by the IBD positron.
The vertex position of the ES event corresponds to the position of the cube with the highest energy, X_p, Y_p, Z_p. The volume that is occupied by the ES cluster is determined as the smallest box required to contain all cubes that saw a signal. This is called prompt volume since the IBD positron causes a prompt ES signal, whereas the IBD neutron gives a delayed NS signal.

Two methods are implemented for the determination of the energy in a reconstructed ES object. The first method is defined as the sum of all energies from the recorded channels in the ES event. This reduces the energy losses in the reconstruction, but the larger number of involved channels makes it more complex. The second method is based on the cube level information. The energy of the reconstructed cube with the highest energy is added together with the energies in the crown of 8 cubes surrounding it inside its plane. This method is more robust because the reconstruction involves less channels, but could have a larger bias and a lower energy resolution. During cube reconstruction, the signals are converted from ADC to PA with the channel specific gain and the effect of the channel

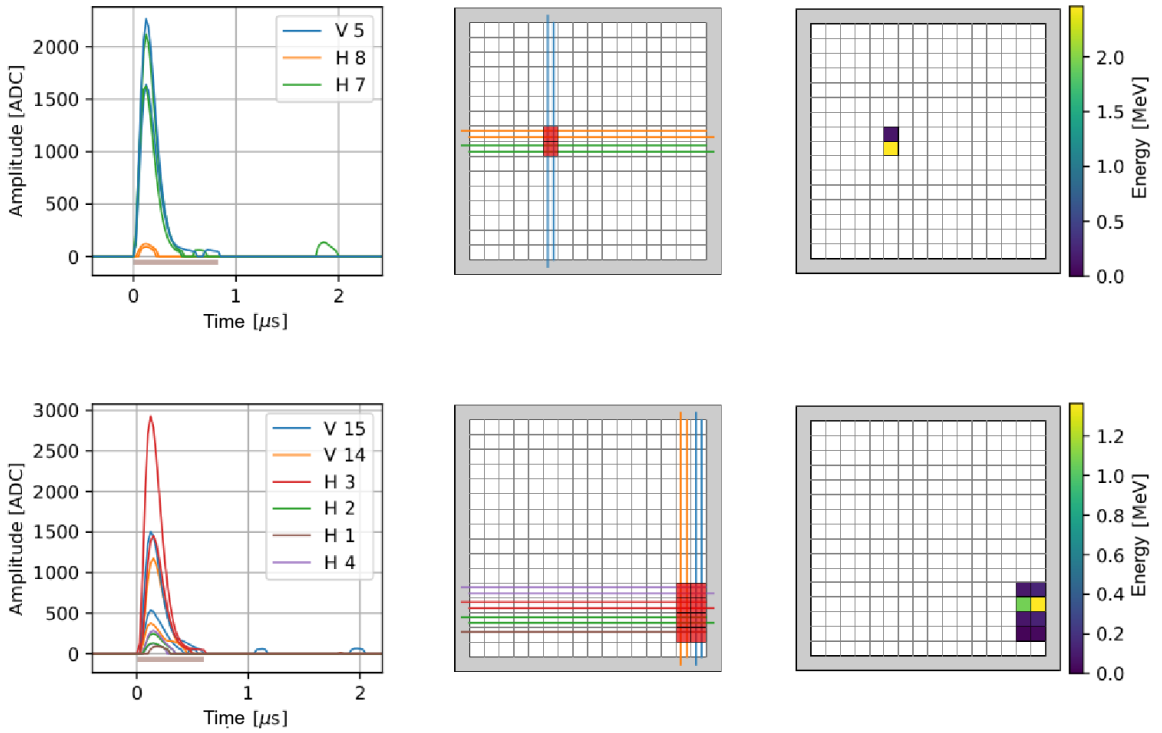

Figure 8.2.4: Two examples of ES signals for which the channels are shown in the affected planes. The cubes shown in red are candidates for energy deposits. Top: unambiguous ES cluster where 6 affected channels correspond to two cubes. Bottom: ambiguous ES cluster composed of 11 fibers, where the number of cubes is between 4 and 8.[165]

specific couplings is accounted for (as will be described in section 9.3). For both methods, the signals on respectively channels and cubes are converted from PA values to energy using the light yield per cube, corrected for attenuation and fiber-sensor coupling, which are determined from calibration data.

In addition to the choice of energy estimator, the amplitude threshold during the ES reconstruction has an influence on the reconstructed energy. A lower threshold increases the efficiency to select the positron annihilation gammas, which can add to the energy. But they could also be very helpful to discriminate the IBD signal from background events. The trade-off is that additional thermal noise will complicate the signal reconstruction.

8.3 Reconstruction of ES-NS coincidences

The SoLid detector is designed to detect anti-neutrinos through the Inverse Beta Decay (IBD) which result in a positron and a time correlated neutron (see section 6.1). Therefore, an IBD event in the SoLid detector is characterised by the coincidence of an ES signal issued from the positron interaction and a delayed NS signal from the neutron. The last step of the Saffron2 reconstruction chain is the association of ES and NS signals. This drastically reduces the amount of data to be analysed.

To qualify for a coincidence, the ES cluster must reach a minimum energy of 1 MeV and must be within 600 μs of the NS signal. This time difference makes sure that all the ES are used that are in the time buffer that is read for an NS triggering. For every ES that meets this condition, a coincidence object is created. Note that there can be multiple ES signals coincident with the same NS. For each coincidence pair, a number of characteristic variables are determined.

8.3.1 VARIABLES CHARACTERISING THE ES-NS COINCIDENCE

The first important metric to characterise the coincidence is the time difference. It is expressed as the difference between the times of NS and ES signals:

$$\Delta t = t_{NS} - t_{ES}$$

A positive Δt will represent an event where the NS signal arrives after the ES signal. Coincidences can have a Δt of between -600 μs and 600 μs. To characterise the topology of ES-NS coincidences, variables are considered that represent the spatial difference between the most energetic cube of the ES event and the reconstructed cube of the NS signal, namely ΔX, ΔY, and ΔZ. The differences are expressed in number of cubes and are determined analogous to the time difference. In addition, the distance between the ES and NS signals, R, is

$$R = \sqrt{\Delta x^2 + \Delta y^2 + \Delta z^2}.$$

During the IBD search, background contamination is coming from neutrons that were generated by muons or atmospheric neutrons. One of the methods to reduce the impact of this contamination is to reject events close to a muon. For each coincidence, the time difference between the NS and the last muon (of type1 or type 2) that crossed the detector is measured. Since multiple spallation neutrons can be produced, also the time distance from the NS to another NS, both forward and backward in time, is determined.

8.4 TOPOLOGICAL RECONSTRUCTION

The ES signal carries essential information for the IBD search, since both the positron and the annihilation gammas contribute to it. The presence of 511 keV annihilation gammas is a powerful discriminant as they don't occur for any of the background signals. The topological reconstruction [167] aims to discriminate the positron ionisation effects from the subsequent interactions from the annihilation gammas.

The reconstruction algorithm optimally exploits the granularity of the detector response. All the cubes of the ES event are assigned their most probable origin. The most energetic cube is defined as the annihilation cube, *AC*, in which most of the ionisation from the positron occurs. The cubes around the *AC* are gathered to isolate the remaining contribution from the positron. This gives a volume of 3 × 3 × 3 cubes with the *AC* cube in the center. The cubes outside of this envelope are assumed to detect the energies deposited by the two annihilation gammas. This is supported by the fact that the mean path of a 0.5 MeV photon is 10.6 cm which exceeds the envelope distance. In addition, the study at the GEANT4 level of the origin of the energy deposits shows that about 99%

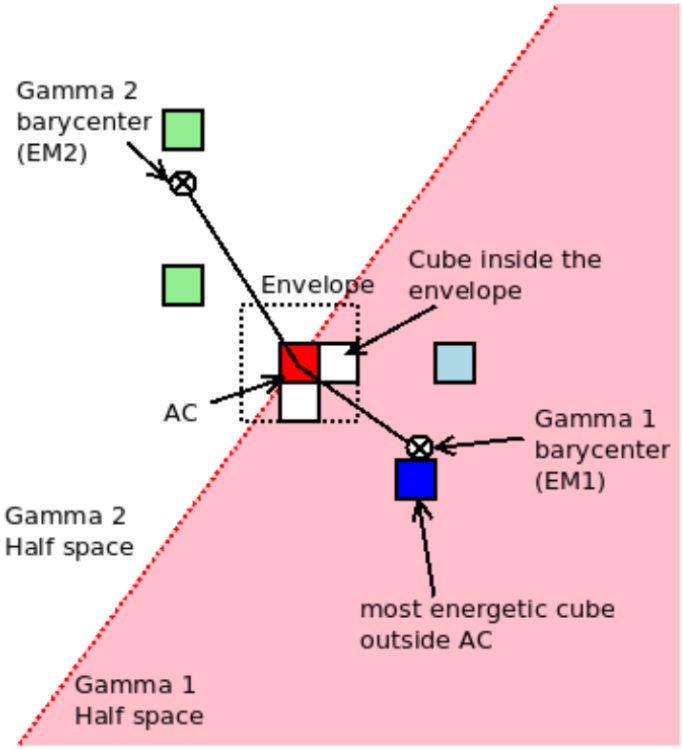

Figure 8.4.1: Schematic view of the topological reconstruction. The most energetic cube is reconstructed as annihilation cube (red) and the surrounding cubes are designated as envelope (white). The most energetic cube outside the envelope is associated with a first annihilation gamma. Energy deposits in cubes in the other detector hemisphere (green) are associated with the second annihilation gamma.[167]

of event cubes outside the envelope are receiving an energy deposit from one of the annihilation gammas.

All cubes outside the envelope are assigned to one of the annihilation gammas, separated by a half plane, as indicated in figure 8.4.1. The reconstruction is driven by the fact that the two annihilation gammas are back-to-back when the positron is annihilated at rest. The list of cubes associated to each reconstructed gamma are used to build the energy and the barycenter (weighted in energy) of the annihilation gammas $E_{\gamma 1}$ and $E_{\gamma 2}$. In case there is only one annihilation gamma reconstructed, the second gamma is searched for inside the envelope. Cubes at the envelope corners opposite the $E_{\gamma 1}$ are selected. The ES events are categorised by a number with two digits, based on the presence of specific cubes. The first digit indicates the number of cubes in the envelope, and the second the number of reconstructed annihilation gammas. The numbers of envelope cubes and gammas in general does not exceed two, therefore the most occurring topologies are 00, 01, 02, 10, 11, 12, 20, 21, and 22. The efficiency of the topological reconstruction procedure is computed based on the comparison between the GEANT4 truth and the expected corresponding signal that is obtained with the readout simulation [167]. The efficiency to reconstruct the AC cube is 98.0 ± 0.3 %. The efficiency to reconstruct cubes that receive an energy larger than 50 keV in the GEANT4 simulation is 51.4 ± 0.1 %. The fraction of reconstructed cubes that do not match with a GEANT4 cube over the total number of reconstructed cubes is 15.7 ± 0.1 %.

9

CALIBRATION OF THE SOLID DETECTOR

The SoLid experiment searches for an oscillation pattern induced by a light sterile neutrino state. The search requires a sensitivity to distortions in the energy spectrum of reactor antineutrinos of around 10%. A very good neutron detection efficiency, high light yield, good energy resolution, energy linearity and homogeneous detector response are critical for the success of the experiment. In order to guarantee the minimal requirements, the detector is periodically calibrated with an automated robot using a combination of gamma and neutron sources. The highly segmented detector results in an elaborate and complex calibration because multiple cubes are read out by the same channel.

9.1 CROSS CALIBRATION ROBOT

In order to monitor the detector response throughout the data taking periods, calibration measurements are performed in situ approximately once a month with an automated calibration robot called CROSS. As shown in the left panel of figure 9.1.1, CROSS is installed on a railsystem above the SoLid detector. Radioactive sources can be installed manually on the calibration arm from outside the container and shielding.

Between every two detector modules a gap can be opened, where CROSS can maneuver the calibration source in front of detector cells with sub-millimeter precision in the XY axes. Within the gap, 55% of the plane surface is accessible, as indicated by the blue area on the right panel of figure 9.1.1. Due to spatial constraints above the detector, CROSS cannot carry a longer arm, and therefore cannot

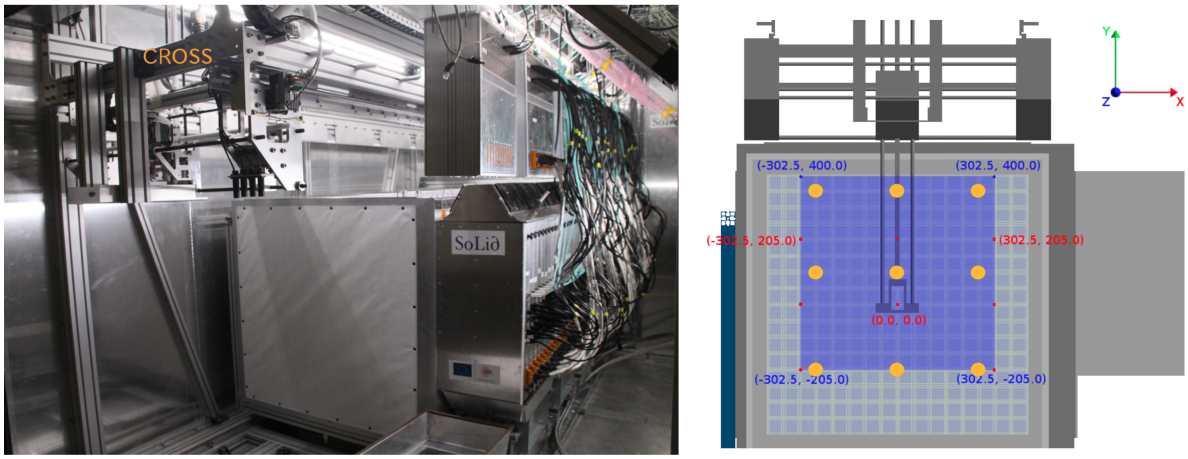

Figure 9.1.1: Left: CROSS calibration robot on a railsystem above the detector. Right: Diagram of CROSS, indicating the range of movement of the calibration arm (blue) and the calibration points (orange).

go lower. Within these constraints, 9 calibration points are chosen in the gap to obtain satisfactory coverage of the planes. Because of the limited amount of 54 calibration points, CROSS cannot reach all the cubes of the module. With the runs in one gap, the cubes in the five planes on either side of the gap are calibrated. To collect sufficient statistics for the calibration of a cube, data from all 9 calibration points in the nearest gap are combined, normalised to their exposure time. The measurements in the planes furthest away from the source suffer attenuation effects and a flux that decreases as $1/R^2$.

9.1.1 CALIBRATION SOURCES AND READOUT SETTINGS

GAMMA SOURCES

The primary gamma source for calibration of the energy response of the PVT scintillator is the ^{22}Na source. The ^{22}Na source undergoes β^+ decay to the first excited state of ^{22}Ne. The positron promptly annihilates leaving two back to back gamma rays of 511 keV each. The coincident signals from the annihilation gammas allow reconstruction of the associated small energy deposits. The ^{22}Ne de-excites with the emission of a 1.27 MeV γ. The presence of several gammas makes this source slightly more complex, but this will be used to our advantage.

For a good coverage of the PVT response over a wide energy range, the collaboration uses additional calibration gamma sources. Bizmuth (^{207}Bi) decays to ^{207}Pb via electron capture, accompanied by the emission of gammas of 1.063 MeV and 1.770 MeV. Cesium (^{137}Cs) undergoes beta decay to the short lived ^{137m}Ba which de-excites to ^{137}Ba via the emission of a gamma of 0.661 MeV. Cobalt (^{60}Co) undergoes beta decay to ^{60}Ni, with the emission of 1.173 MeV and 1.332 MeV gammas. Finally, the AmBe that is mainly used as neutron source (see below), produces carbon nuclei that are often in an excited state (with a branching ratio of about 60 %) that decay with the emission of a gamma of 4.4 MeV, which are very useful as higher energy calibration point for the ES calibration of the detector.

The calibration of the energy response of the detector is performed about every month with ^{22}Na and typically lasts 24 hours. For each of the 54 positions, two runs of 600 seconds each are performed. Only the threshold trigger is activated on the five planes on either side of the active calibration gap. A threshold of 7.5 PA ($\approx$ 300 keV) is used, with coincidence requirement on orthogonal channels of the same plane. Trigger and readout settings during CROSS calibration with the sodium source are listed in table 9.1.1.

NEUTRON SOURCES

The collaboration has two sources for neutron calibration. In order to determine the absolute neutron efficiencies, the activities of the neutron sources have to be known. The AmBe [168] source is composed of a mixture of Beryllium, ^{9}Be, and Americium, ^{241}Am. The decaying ^{241}Am functions as an activator by producing the α particle that reacts with the ^{9}Be, which ultimately yields a neutron by the following process,

$$\alpha + {}^{9}Be \longrightarrow n + {}^{12}C$$

The conversion factor α - n is not known accurately, and varies from source to source. The measured activity is 1794 $\pm$ 35 neutrons per second.

	Gamma calibration	Neutron calibration
Neutron trigger	off	on
peak threshold	/	> 0.6 PA
Number of peak threshold	/	> 17 peaks
High energy trigger	on	off
sample threshold	> 7.5 PA	/
Plane trigger	on	on
HE flag threshold	1	1
Read out		
default ZS threshold	1 PA	1 PA
ROblocks before trigger	0 blocks	4 blocks
ROblocks after trigger	1 block	15 blocks
Neighbour planes	0 planes	0 planess

Table 9.1.1: Trigger and readout settings during CROSS calibration campaigns

In order to have a second neutron emitter to estimate the systematics uncertainties related to the Monte-Carlo neutron transport as well as the NS reconstruction analysis, a fission source is used, namely ^{252}Cf. The branching ratio to spontaneous fission is 3.092 ± 0.008 %. Per spontaneous fission on average 3.764 ± 0.002 neutrons are produced. The activity of this source is more complicated than for AmBe, because ^{252}Cf has a relatively short lifespan and some of its descendants are also neutron emitters. The activity induced by the isotopes of ^{250}Cf and ^{248}Cm have to be taken into account as well, but the correction to be applied remains very low (less than a percent). The calibration carried out on January 17, 2017 indicates an activity of 3804 ± 34 neutrons per second.
The neutron metrology laboratory in the National Physics Laboratory [169] (UK) has estimated the relative uncertainties on the source activities to be 1.9% for AmBe and and 0.9% for ^{252}Cf.

The neutron calibration of the detector is performed about every month and typically takes two to three days, with an exposure time of 50 minutes per point for the AmBe source, respectively 60 minutes for the ^{252}Cf source. This results in a cumulative statistic greater than 1.0×10^8 (respectively 1.70×10^8) events. Only the neutron trigger is activated, requiring 17 peaks above half a PA. Trigger and readout settings during CROSS calibration with the neutron source is listed in table 9.1.1.
During calibration runs with a neutron source, the level of NS signals increases by more than an order of magnitude, going from 20 Hz in physical mode to about 1 kHz in neutron mode. To contain the data transfer rate at levels below 20 MB/s, the size of the readout window associated with the neutron trigger is reduced by a factor of 5.5 (recording 20 blocks instead of 110 blocks during physics mode). The neutron trigger is not propagated to neighbour planes, which allows to obtain an additional reduction with a factor 7.

MUONS

Tracks from muons that cross the SoLid detector at a relatively high rate, can be accurately reconstructed. The ionising behaviour of muons is well known and their energy deposition per path length is about 2 MeV cm^{-1}. By determination of the path length of a muon in the detector, the deposited

energy can be calculated and compared to the detected number of PAs. This information enables monitoring the detector response on a daily basis, and to study the detector response at high energy.

9.1.2 PLANE DEADTIME AND SIGNAL PILE-UP

The planes closest to the calibration source are affected by a dead time phenomenon. When the data rate to be transferred becomes too big for a plane, its acquisition is stopped for a given time. The plane channels only reappears at a new run. Stopping and restarting of the plane acquisition is notified by FPGA signals, which allows to determine the effective time of interrupted data collection. The impact of this dead time strongly depends on the count rate.

In regard of the neutron calibration, the data taken for the ^{252}Cf source is more affected by dead time as it emits several neutrons at the same time with energies lower than AmBe which are therefore captured closer to the source. These two effects greatly increase the probability of saturating the acquisition. The probability of dead time fluctuates between planes, reaching 11% for the ^{252}Cf and 1.6% for the AmBe source [165].

Another troublesome phenomenon is the occurrence of signal pile up. During the signal clustering procedure, it is difficult to separate events sharing the same channels and arriving very close in time. This effect is negligible for the rates observed in physics mode, but it becomes important in calibration runs, in particularly for the planes closest to the calibration gap, and in case the source emission has multiplicity. In case of neutron calibration, the pile up is quantified by reconstructing the temporal coincidences of real NS-NS signals within a plane and extrapolating the distribution to small time differences. For AmBe, the correction is less than 0.5% but can reach 3% for the closest planes in case of the ^{252}Cf source [165].

9.2 CALIBRATION OF THE ES SIGNAL FROM PVT SCINTILLATOR

The PVT scintillator is one of the scintillators composing the unit cell of the detector. PVT scintillation signals are reconstructed by the software as ES signal. The ES signal caused by the IBD positron, will be used to reconstruct the neutrino's energy, emphasising the necessity of adequate calibration. Especially, the PVT light yield per MeV of deposited energy, and the energy linearity over a wide energy range are of importance.

The visible light yield of a cube is measured as the sum of the amplitudes on the four connected channels, and is expressed in a number of pixel Avalanches

$$\begin{aligned} LY^{\text{vis}}_{\text{cube}}(x,y,z) = \sum_{\text{side}} E_{\text{dep}} \times LY^{\text{real}}_{\text{cube}}(x,y) \times \epsilon_{\text{cube}} \times \epsilon_{\text{plane}}(z) \\ \times \epsilon_{\text{acc}} \times \left(\epsilon^{\text{side}}_{\text{att}}(L_{\text{dir}}) + \epsilon^{\text{side}}_{\text{att}}(L_{\text{indir}}) \times \epsilon^{\text{side}}_{\text{mirror}}\right) \times \epsilon^{\text{side}}_{\text{coupling}} \end{aligned} \tag{9.1}$$

The summation runs over the channels on the four sides of the detector that are connected to the cube at (x, y, z). The visible channel amplitudes are the result of an intricate light collection scheme. E_{dep} is the true deposited energy inside the cube in MeV. $LY^{\text{real}}_{\text{cube}}$ is the intrinsic light yield of the PVT

scintillator. Each cube has an intrinsic efficiency, expressed as ϵ_{cube}. ϵ_{acc} is the geometrical acceptance of the fibers. $\epsilon_{\text{plane(z)}}$ provides an efficiency per plane due to its electronics. $\epsilon_{\text{att,dir}} + \epsilon_{\text{att,indir}}$ is the attenuation efficiency along the fibers, ϵ_{mirror} is the mirror reflectivity and $\epsilon_{\text{coupling}}$ is the coupling efficiency. These terms are a priori unknown and will be derived from measurement in section 9.3, in order to insert them in the readout simulation, which will be described in section 13.4.

From measurements, we have access to the channel amplitudes, A, that are determined as

$$A[PA] = \frac{A_{\text{rec}}[ADC] - \text{pedestal}}{\text{gain}[ADC/PA]}, \tag{9.2}$$

where A_{rec} is the detected amplitude and the gain and intercept are characteristic to the sensor. The visible light yield from the PVT scintillator is calibrated with the use of the 1.274 MeV gamma from the ^{22}Na source. The gamma interacts via Compton scattering. Given the granularity of the detector planes, only a fraction of the total gamma energy is deposited within each PVT cube. Consequently no narrow photopeak can be reconstructed within individual cubes. However, the shape of the energy deposition spectrum in the PVT scintillator, featuring the compton edge, translates in the spectrum of the visible energy of the scintillator having the same shape. The centroid of the Compton edge is defined as the visible cube light yield. The complex Compton edge spectrum is fitted by two methods [159] to extract the cube light yield.

One method is based on an analytical fit of the Compton edge, consisting of a Gaussian convolution of the cross section model (based on the Klein-Nishina formula) with an energy dependent resolution [151]. The convolution accounts for the stochastic energy resolution. For a given cube undergoing calibration, it is assumed that a 1.27 MeV gamma interacts within the cube only via Compton scattering and that the gamma only scatters once per cube. The fit result is shown in the top panel of figure 9.2.1.

The second method consists of comparing the recorded ^{22}Na γ-spectrum from calibration runs with the simulated true energy spectrum from a dedicated GEANT4 simulation, varying the energy scale and energy resolution. The energy distributions can be simulated for all cubes, for each position of the source. The comparison between data and simulation is performed using a Kolmogorov-Smirnov (KS) test, that computes as goodness-of-fit parameter the largest vertical distance between the measured and simulated cumulative distribution. This method allows determining both the energy resolution and the light collection of the detector.

When comparing both methods, their agreement deteriorates with plane depth. This is understood as the gamma attenuation effect impacts the analytical fit that operates under the assumption that the gammas reach cubes with the same energy. However, the gammas can interact before they reach the cube, which will be more prominent for planes further away from the source. In addition, there was tension between the results for the planes next to the source, which is induced by plane dead time and signal pile-up. This was resolved by focusing on cubes that caused the trigger. Once the corresponding efficiencies have been derived from simulation, the obtained results are consistent within 2% and meet the required energy scale precision.

For standard data taking in physics mode at BR2, an average light yield of 96.7 PA/MeV/cell with a root-mean-square (RMS) of 7.5 PA/MeV/cell was measured without MPPC cross-talk subtraction, which is estimated to be around 20%. The cross-talk corrected LY is 78 PA/MeV/cell. The stochastic energy resolution, $\sigma_{st}(E) = \sqrt{LY \cdot E}$, is of the order of 12%. The average of the visible LY per plane

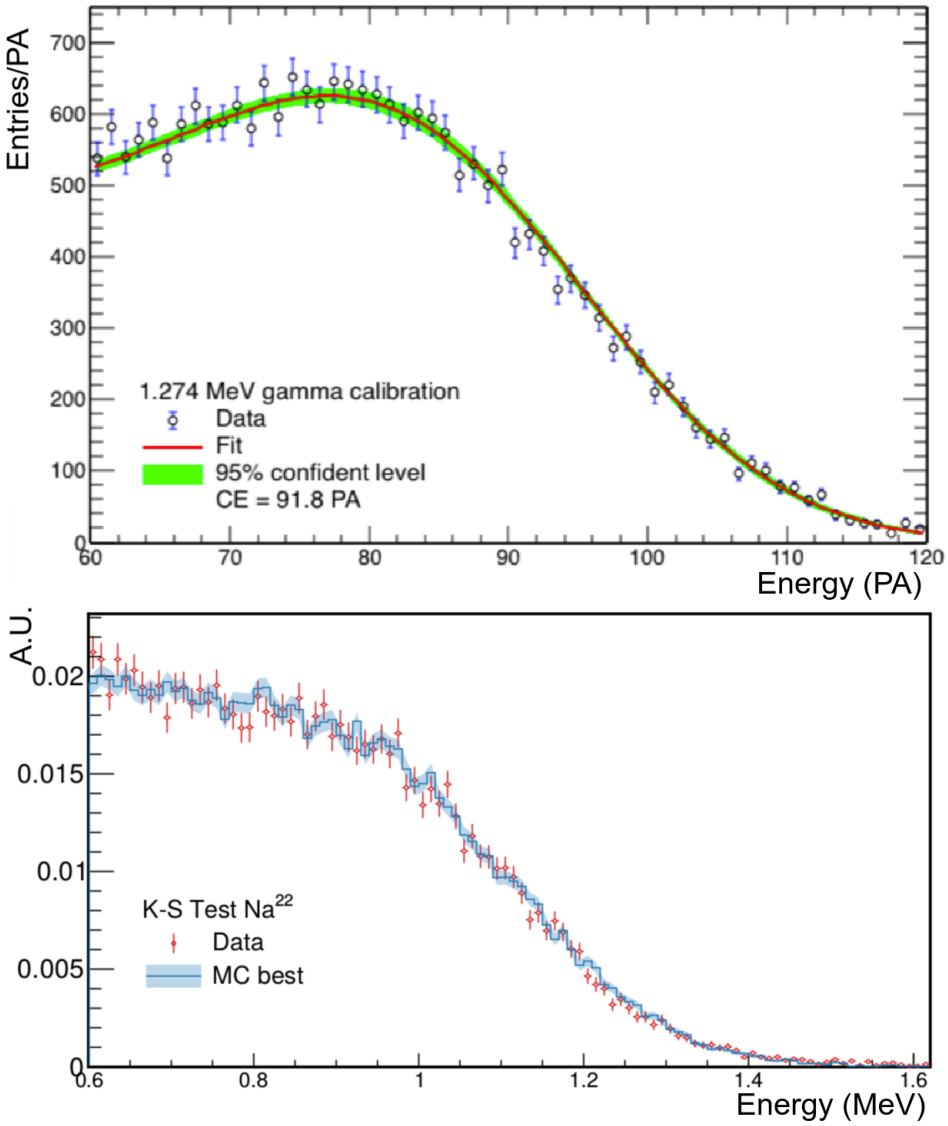

Figure 9.2.1: Compton edge profile for a calibration sample in a SoLid cube using a ^{22}Na gamma source. The spectrum is dominated at high energy by the deposits of the 1.27 MeV gamma. Top: The centroid of the Compton edge is obtained by fitting the data with a Gaussian convolution of the energy deposition function. Bottom: The centroid of the CE is determined by comparing Monte-Carlo and data using a Kolmogorov-Smirnov (KS) test.[140]

is found to be uniform over the detector, as shown in figure 9.2.2, and stable over time. The variation of the mean value of the LY and the RMS of its distribution are within 2% over a period of one year.

Therefore the visible LY of a cube at a certain position can be determined as the average over all detector planes. The result is shown in figure 9.2.3. In the pattern of the visible LY, the fiber specific attenuation, the channel specific coupling between fiber and sensor, and the cube specific LY are clearly visible. These attenuation effects will be determined, in section 9.3.1. The visible cube LY will be reproduced by simulation in chapter 14.

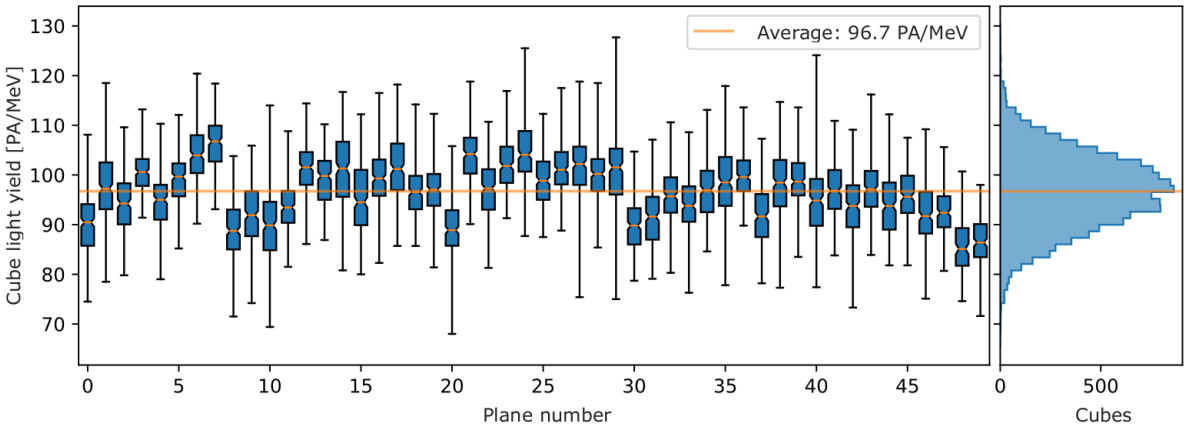

Figure 9.2.2: Candle plots for 50 planes showing light yield, measured with ^{22}Na gamma source during the calibration campaign in September 2018. Filled boxes represent cubes between the first and the third quartiles. Black lines represent outliers below and above those. The orange line shows the detector average light yield.[140]

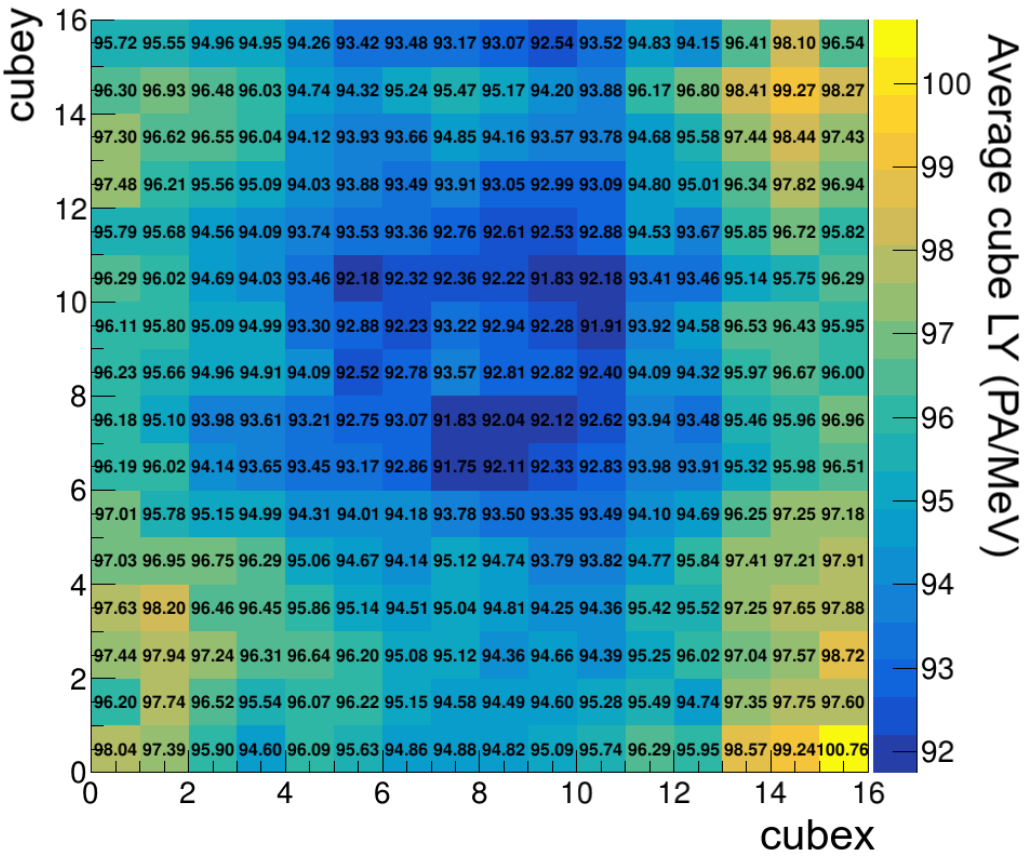

Figure 9.2.3: For the September 2018 calibration campaign, for each cube position, the average LY over all detector planes.[159]

ENERGY LINEARITY

The linearity of the energy response is investigated with higher energy, gamma calibration sources and with crossing muons, in addition to the ^{22}Na source. The theoretical Compton Edges are well known for the different gamma sources and are listed in table 9.2.1. The ratio of the light yields measured with the ^{22}Na and AmBe sources are consistent with what is expected for linear behavior as shown on the left panel of figure 9.2.4.

Gamma source	E_γ (MeV)	E_{CE} (MeV)
^{22}Na	0.511	0.341
^{137}Cs	0.661	0.477
^{207}Bi	1.063	0.858
^{60}Co	1.173	1.04
^{22}Na	1.274	1.054
AmBe	4.4	4.198

Table 9.2.1: Available gamma sources with their Compton edges and enabled triggers

The reconstructed energy is shown on the right panel of figure 9.2.4 in function of the true deposited energy for the three calibration sources and a cosmic muon sample. The calibration measurements confirm the linear response of the PVT scintillator over the energy range of importance for the SoLid experiment. The linear energy response greatly simplifies the energy reconstruction and reduces the related systematic errors.

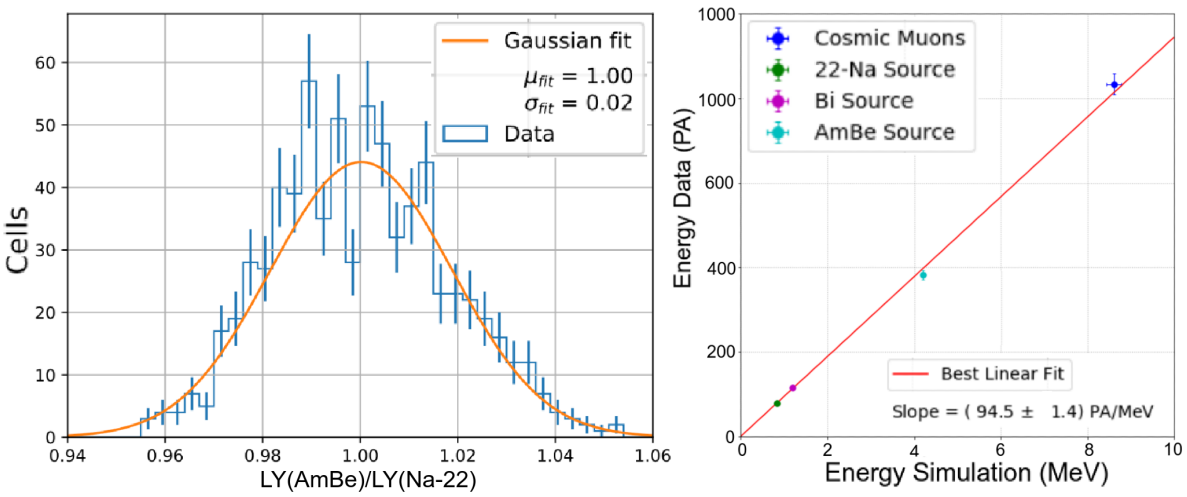

Figure 9.2.4: Left: Ratio of the Light Yield (PA/MeV/cell) obtained with a ^{22}Na source (1.72 MeV) and an AmBe source (4.4 MeV). Right: Demonstration of the linearity of the reconstructed energy of the PVT scintillator, as function of the fitted dE/dx for muons, or the Compton edge position for the gamma calibration sources.[140]

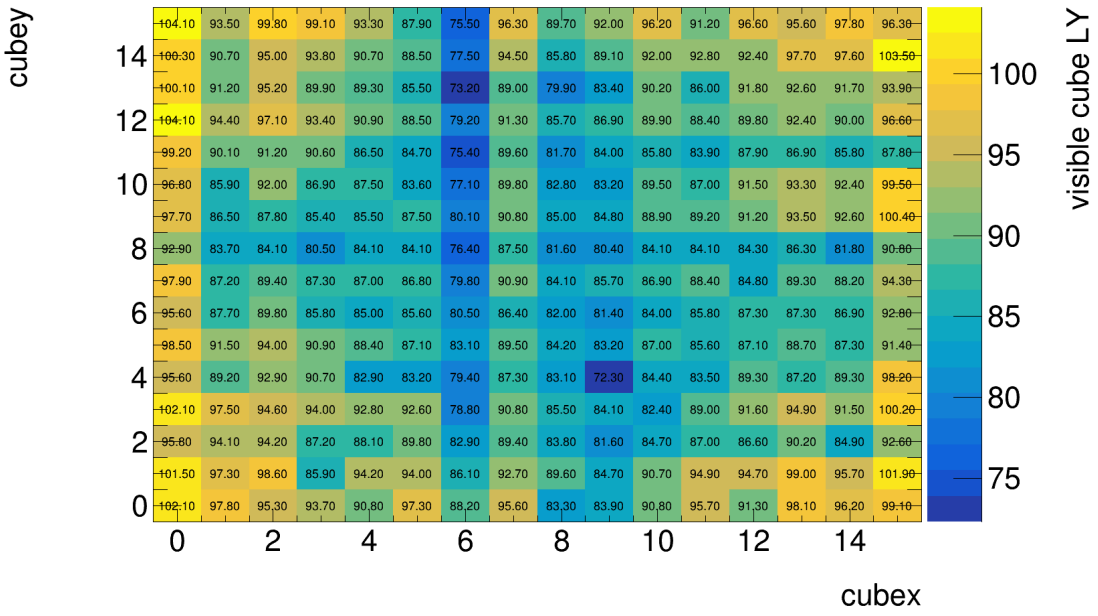

Figure 9.3.1: visible cube LY of plane 8, determined as the compton edge of the ^{22} Na 1.27 MeV gamma.

9.3 CALIBRATION OF THE PARAMETERS CONCERNING PHOTON TRANSPORT

The detector design was optimised towards high position and energy resolution, in order to make a precise measurement of the L/E dependency of the neutrino oscillation probability. This resulted in a highly segmented detector with a high number of readout channels. The detector has variations in the performance of its 12800 unit cells and 3200 readout channels that influence the analysis results. The parameters concerning photon generation and transport are entangled in the visible cube light yield, as described by equation 9.1. 22400 parameters will be derived in the present section to describe the detector response. An example of the calibrated visible LY for a specific plane is shown in figure 9.3.1. An overall attenuation pattern is visible, along with fluctuations that can be traced back to channel level or cube level.

From the calibration measurement, the fiber specific attenuation length, the channel specific coupling between fiber and sensor and the cube specific LY will be determined. The calibration parameters are determined and corrected one by one. The final distribution of corrected LY is expected to be uniform. In section 13.4 all calibration parameters will be implemented in the readout simulation, starting from the real LY from a cube and applying all attenuation effects in order to approach the data distribution as good as possible.

9.3.1 THE FIBER SPECIFIC ATTENUATION LENGTH

All of the 3200 WLS fibers of the SoLid detector have a specific attenuation length that accounts for the photon losses during fiber transport. The fiber attenuation length is determined by monitoring the

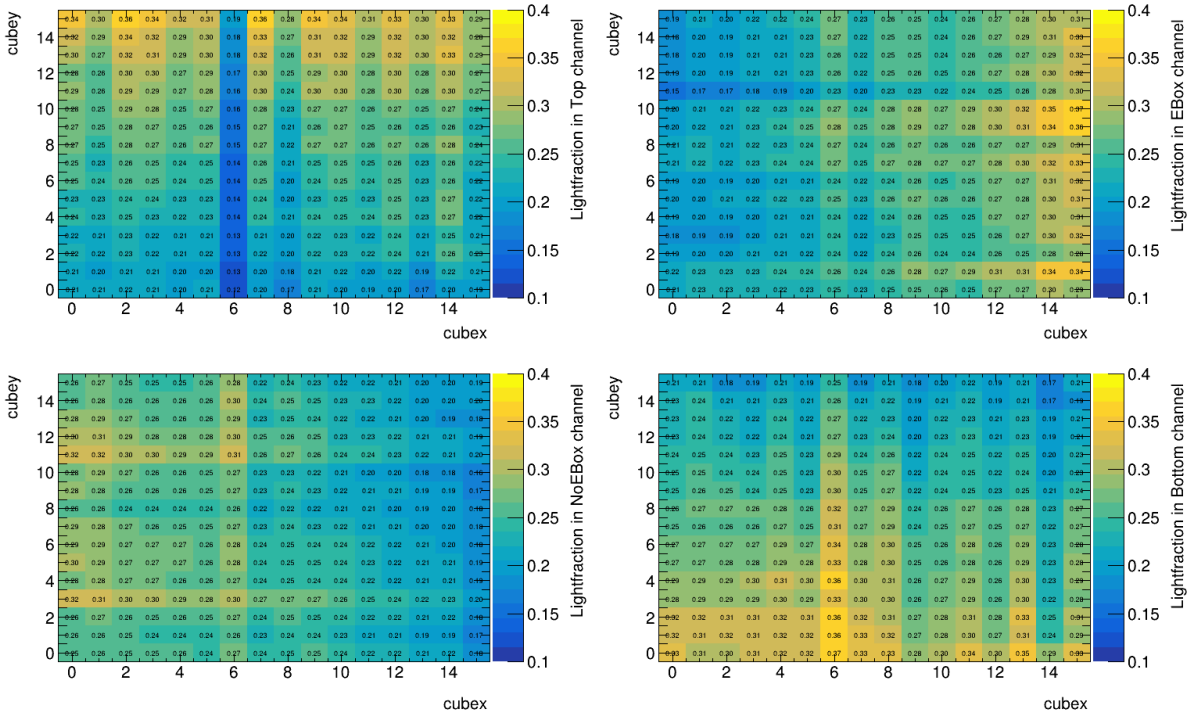

Figure 9.3.2: Distribution of light fraction that the sensors detect on the top, right, left and bottom for plane 8.

ratio of the signal amplitude on the fiber against the total signal amplitude of the cube on all attached fibers.

$$A_{\text{frac,fiber}} = \frac{A_{\text{fiber}}}{LY^{\text{vis}}_{\text{cube}}}. \tag{9.3}$$

where $LY^{\text{vis}}_{\text{cube}}$ is calculated as in equation 9.1. Only events consisting of a single cube with a visible cube LY that approaches the center of the Compton Edge within 1% are used for this study. Figure 9.3.2 shows for the four sides, the average light fraction that the sensors receive from the cubes. The top left distribution, shows the light fraction seen by the sensors at the top side of the detector, from the light emitted by the cubes that the fiber from the sensor runs through. The attenuation pattern is clearly visible, where a smaller light fraction is received from cubes that are further away from the considered side.

In order to obtain the attenuation length, L_{att}, the data points of each column (resp. row) are normalised against the edge value and fitted with an attenuation function,

$$\text{Att}_{\text{top or right}}(x) = c \cdot \left(\exp^{-\frac{(15-x)\cdot 5.80+2.54+5.27}{L_{\text{att}}}} + R \cdot \exp^{-\frac{(184.48)+((15-x)\cdot 5.80+2.54+5.27)}{L_{\text{att}}}} \right) \tag{9.4}$$

$$\text{Att}_{\text{left or bottom}}(x) = c \cdot \left(\exp^{-\frac{x\cdot 5.80+2.54+5.27}{L_{\text{att}}}} + R \cdot \exp^{-\frac{(184.48)+(x\cdot 5.80+2.54+5.27)}{L_{\text{att}}}} \right) \tag{9.5}$$

The reflection coefficient R of the mirror at the fiber end opposing the sensor, is fixed at a value of 0.80. The cube x y coordinates are converted into cm with the dimension of the detector cell being 5.80 cm. The distance from cube edge to sensor of 5.27 cm is added. And the distance of half a cube (2.54 cm) that the light travels on average in the affected cube through the fiber is added as well. The first term

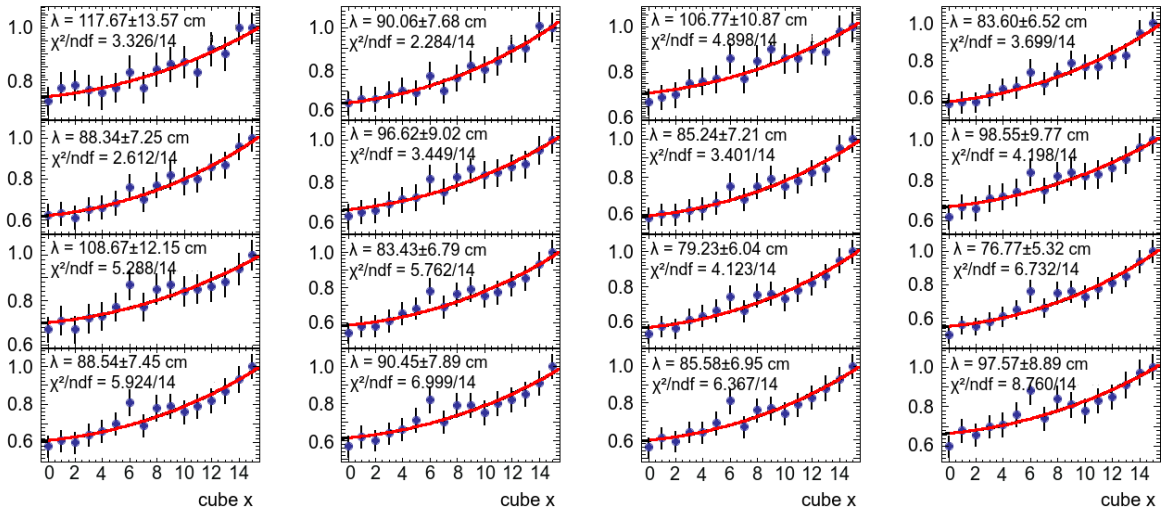

Figure 9.3.3: Result of the fit procedure for fibers attached to the sensors at the detector side where the electronics box is mounted.

corresponds to attenuation of photons that travel directly towards the sensor while the second term is for photons that travel first to the mirror. The result of the fit procedure for the 16 fibers with a sensor at the detector side where the electronics are situated is shown for one out of 50 planes in figure 9.3.3. The relevant plots for all planes are bundled in a document that is circulated in the collaboration [170]. The measured fiber attenuation lengths are collected in the distributions in figure 9.3.4.

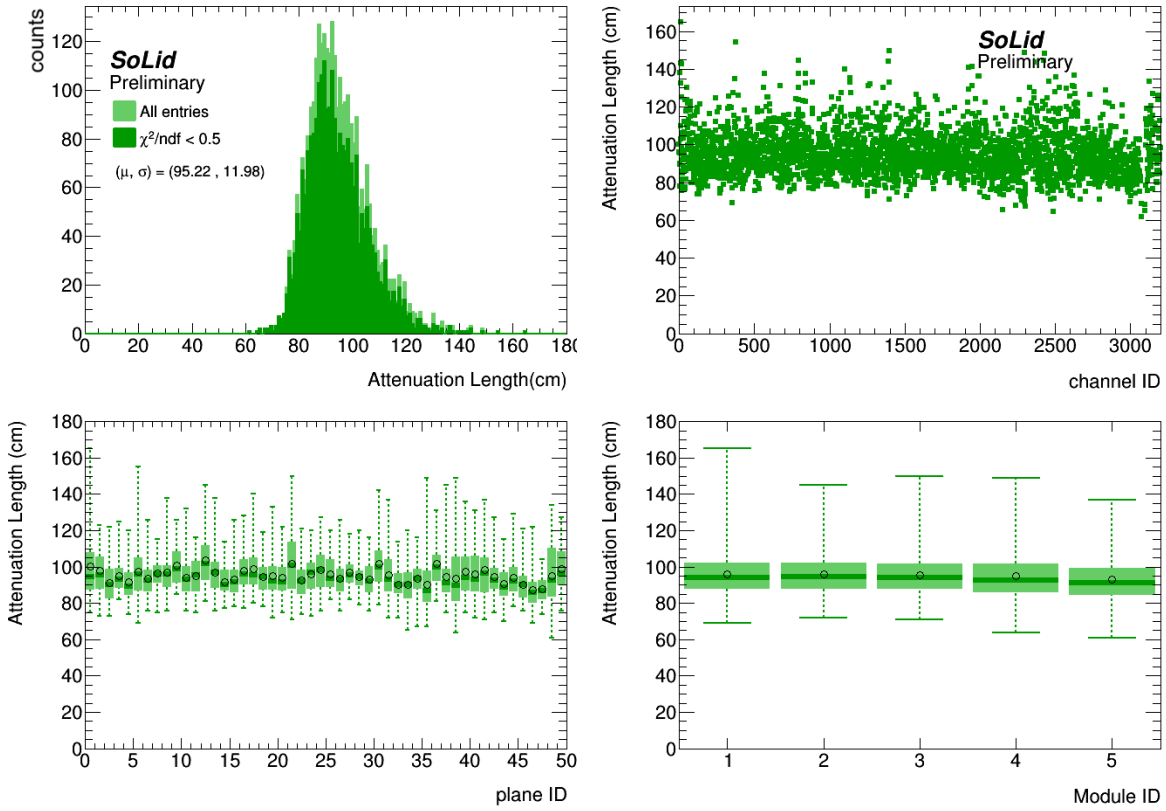

Figure 9.3.4: Fiber attenuation lengths that are determined ordered in a histogram, per channel, per plane and per module. The spread of the attenuation lengths per plane and per module is visualised by the candle plots. The circle corresponds to the median value, the box spans from the first to the third quartile and the whiskers span the range of the distribution, disregarding outliers.

9.3.2 THE CHANNEL SPECIFIC COUPLING BETWEEN FIBER AND SENSOR

The contact between the fiber and the sensor determines their optical coupling, which affects the light that the channel collects. The couplings are determined from the pattern of the visible cube LY, after the channel amplitudes are corrected for fiber attenuation,

$$A_{\text{corr}} = \frac{A}{\text{Att}(x)} \tag{9.6}$$

The corrected distribution is shown in figure 9.3.5 for plane 8. The attenuation pattern is no longer visible. The effect of the sensor coupling shows up clearly, through the fact that some rows and columns contain overall higher or lower values. The light amplitude that the channel receives, A_{corr}, is collected. In figure 9.3.6, the top left distribution, shows the light amplitude seen by the sensors at the top side of the detector, from the light emitted by the cubes. The difference in coupling is clearly visible, where some rows or columns are darker or brighter than others.

For the top and bottom sensors (resp. left and right sensors) the amplitudes are integrated over the column (resp. row) and normalised. The obtained distribution over the channels, reflects the couplings. The determined couplings are shown in figure 9.3.7.

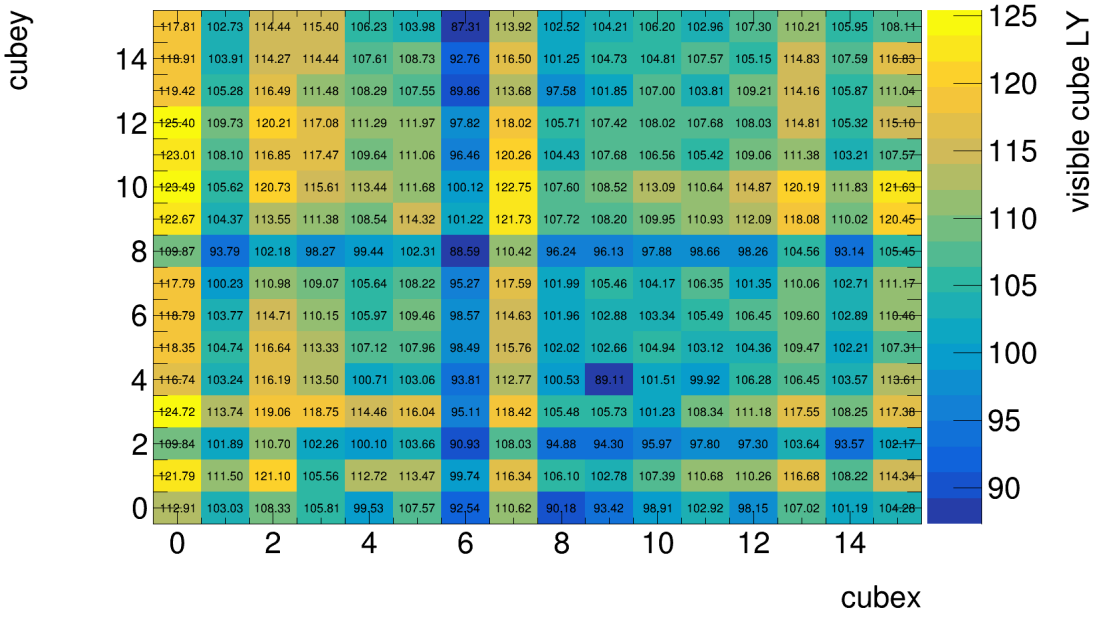

Figure 9.3.5: Attenuation corrected, visible cube LY from selected events for plane 8.

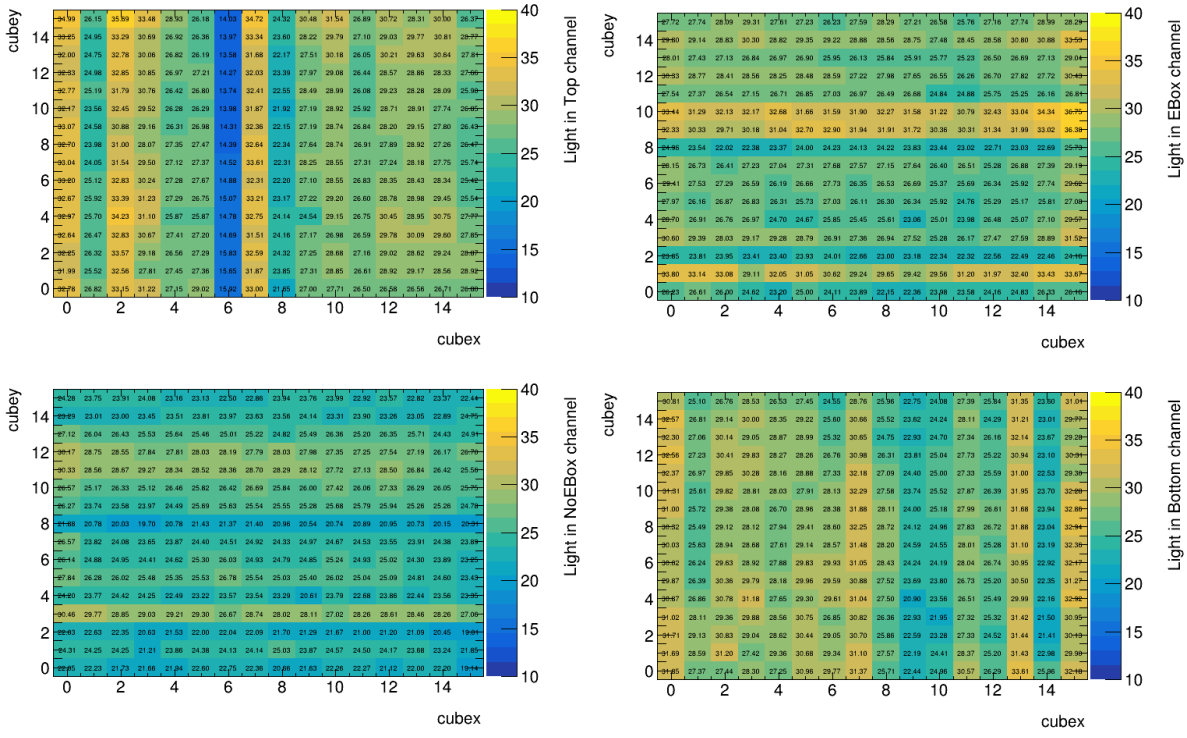

Figure 9.3.6: Distribution of light amplitude that the sensors on the top, right, left and bottom receive from the cubes in plane 8.

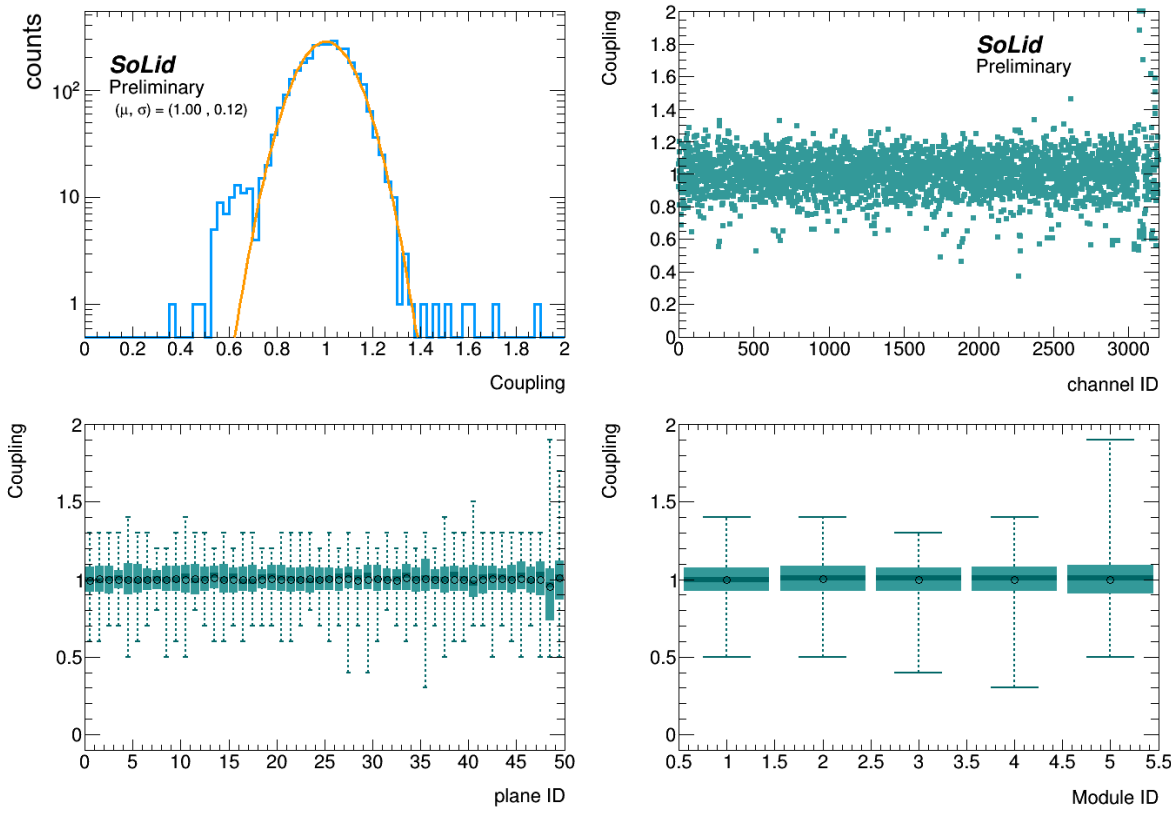

Figure 9.3.7: Couplings, from fiber to sensor, that are determined, ordered in a histogram, per channel, per plane and per module.

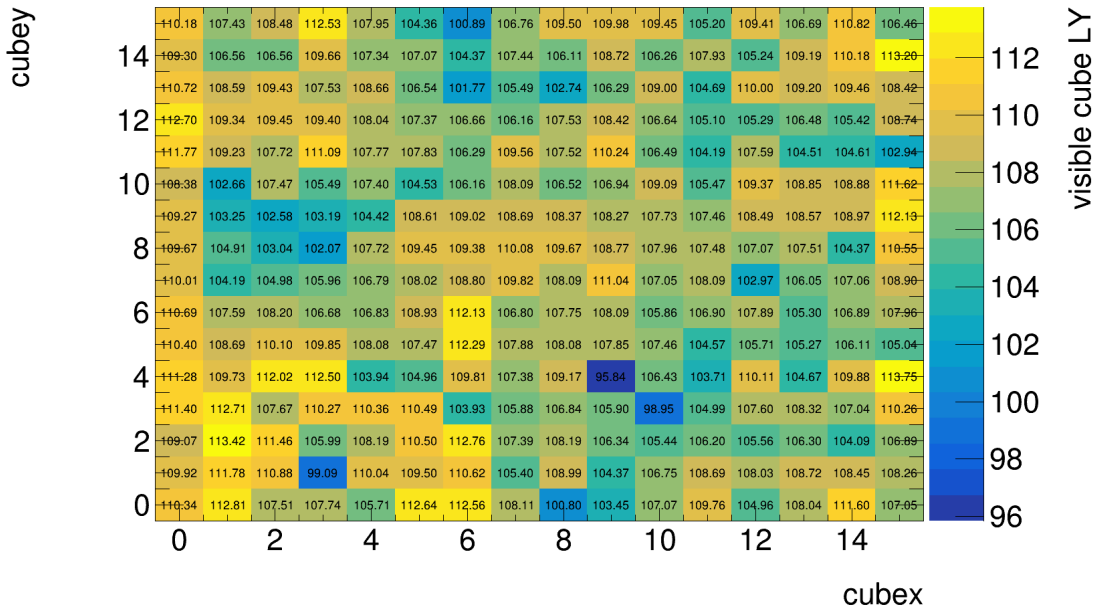

Figure 9.3.8: coupling and attenuation corrected, visible cube LY from selected events for plane 8.

9.3.3 CUBE SPECIFIC VARIATION IN LIGHT YIELD

The channel amplitudes are corrected for fiber attenuation, and coupling

$$A_{\text{Corr}} = \frac{A}{\text{Att}(x) \cdot \text{coupling}} \tag{9.7}$$

The corrected distribution is shown in figure 9.3.8. In comparison to the distribution that was only corrected against fiber attenuation effects (see figure 9.3.5), the effect of the different couplings of the channels is reduced. The pattern is more homogeneous. The variations that are left are due to fluctuation in the LY of the single cubes. The origin of this variation has a broad range, like variation in the tyvek performance, the cube polishing, the contact between cube and fibers and so on.

The average visible cube LY over all cubes is determined, and used to normalise each visible cube LY. Like this, a distribution around unity is obtained, reflecting the variation of the cube LY. The cube variations that are determined are shown in figure 9.3.9. After correction for fiber attenuation and coupling, we are left with only 3% spread in cube LY over the 12800 cubes!

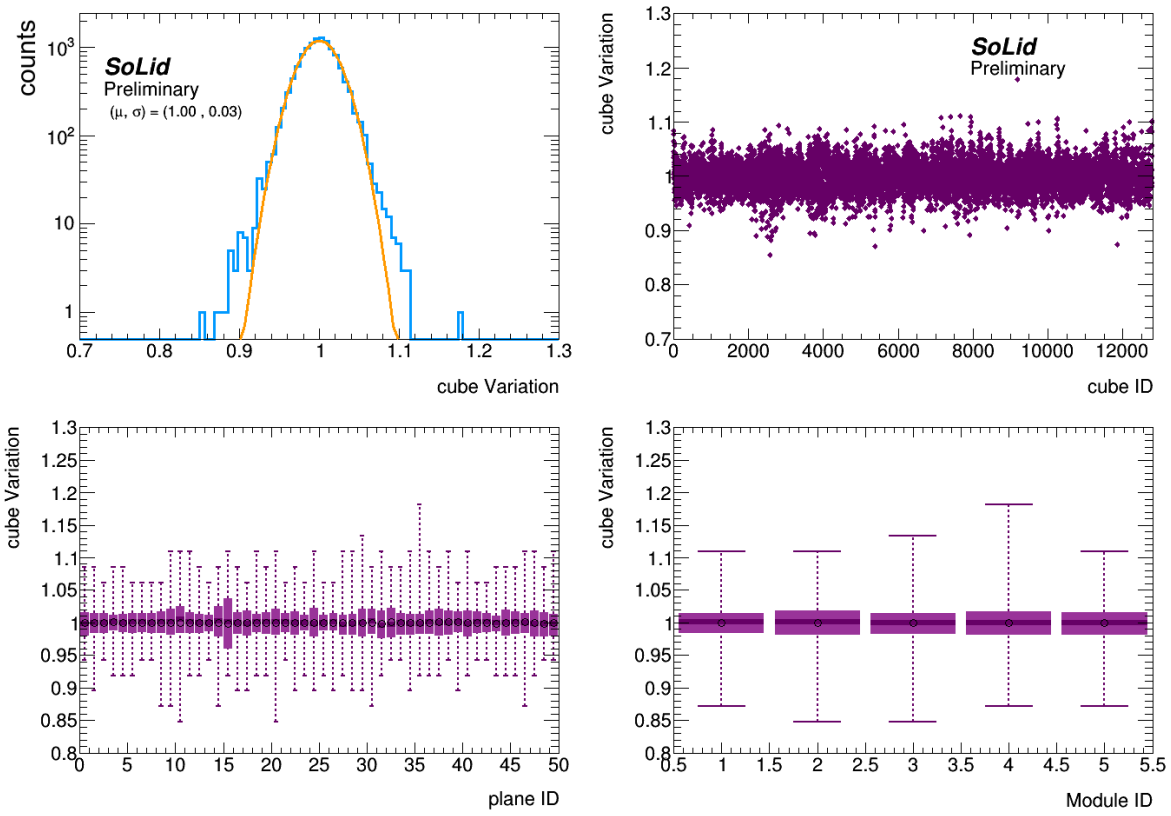

Figure 9.3.9: Variation in cube LY, ordered in a histogram, per channel, per plane and per module.

9.3.4 ATTENUATION CORRECTED VISIBLE LIGHT YIELD

Finally, the visible cube LYs are calculated from the channel amplitudes after correction for fiber attenuation, coupling, and cube-to-cube variation, $\mathrm{var}_{\mathrm{cube}}$, as

$$\sum A_{\mathrm{Corr}} = \left(\sum \frac{A}{\mathrm{Att}(x) \cdot \mathrm{coupling}} \right) \frac{1}{\mathrm{Var}_{\mathrm{cube}}}. \tag{9.8}$$

The resulting corrected visible cube LY is shown in figure 9.3.10. The result is homogeneous, with respect to the original distribution, where attenuation effects were visible.

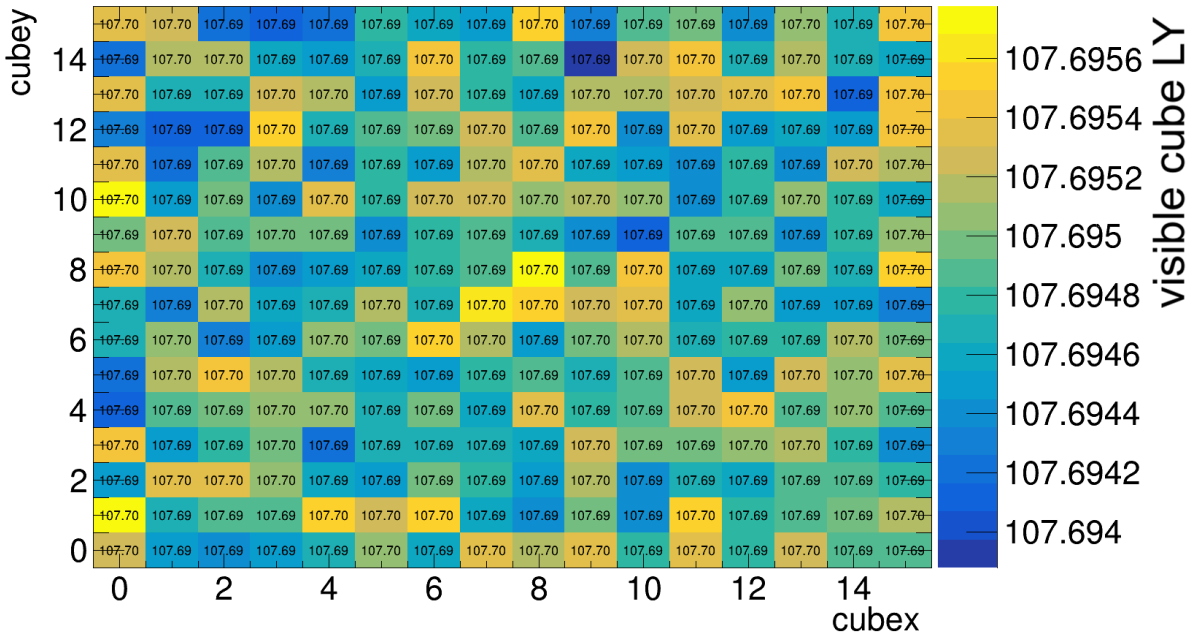

Figure 9.3.10: Variation, coupling and attenuation corrected, visible cube LY from selected events.

9.4 CALIBRATION OF THE NS SIGNAL IN ZNS

Next to the PVT scintillator, the ^{6}Li:Zns(Ag) scintillator is the main component of the unit cell of the SoLid detector. In terms of calibration, special interest goes out to the absolute and relative efficiency to detect neutrons.

9.4.1 NEUTRON DETECTION EFFICIENCY

The absolute neutron detection efficiency, ϵ_{det}, can be broken down to the product of the capture efficiency, ϵ_{capt}, (i.e. the probability that the neutron is captured on the ^{6}Li within a ^{6}Li:Zns(Ag) screen) and the reconstruction efficiency, ϵ_{reco},

$$\epsilon_{det} = \epsilon_{capt} \times \epsilon_{reco} \,.$$

In turn, the reconstruction efficiency can be factorized into the neutron trigger efficiency (the probability that the NS signal triggers the detector readout) and the identification efficiency (the probability of identifying the NS signal as a neutron during data analysis),

$$\epsilon_{reco} = \epsilon_{trig} \times \epsilon_{PID} \,.$$

The reconstruction efficiency depends only on the performance of the detector and its value is determined by comparing the measured data with Monte Carlo predictions.

ABSOLUTE CAPTURE EFFICIENCY

The capture efficiency is the probability for a given neutron starting at a given position with a given energy to be captured by ^{6}Li. The neutron capture efficiency is determined from Monte Carlo simulations of the neutron interactions in the detector, taking into account the neutron energy, the SoLid detector geometry, the hydrogen and ^{6}Li content and the capture cross section [171].

The neutron capture probability is greater for low energies and varies as 1/E. It is therefore important to model the transport of neutrons in an energy range covering several orders of magnitude, from meV to several tens of keV (the energy range of IBD neutrons), to several MeV (the energy range of neutrons from AmBe and ^{252}Cf sources). The vast majority of captures take place once the neutron reaches thermal energy (E_{th} = 1.5 k_BT ~ 0.025 eV), requiring more than ten elastic collisions on hydrogen. The thermalisation process induces a gap in time and position between the production of the neutron and its capture. It also leads to a competition between the capture on the ^{6}Li and radiative capture on hydrogen, but due to the ratio of their capture cross sections and despite the very different amounts of material, the probability of capture on lithium wins; for an IBD neutron produced in the detector with an average energy of around 50 keV, the probability of being captured on the ^{6}Li is 72%, while capture on ^{1}H is 24% probable and leaving the detector without interacting has a probability of 4%.

ABSOLUTE RECONSTRUCTION EFFICIENCY

The reconstruction efficiency is the probability to reconstruct and identify properly a neutron capture on ^{6}Li. Scintillation induced by this process is largely dominated by energy released in the ^{6}Li break-up

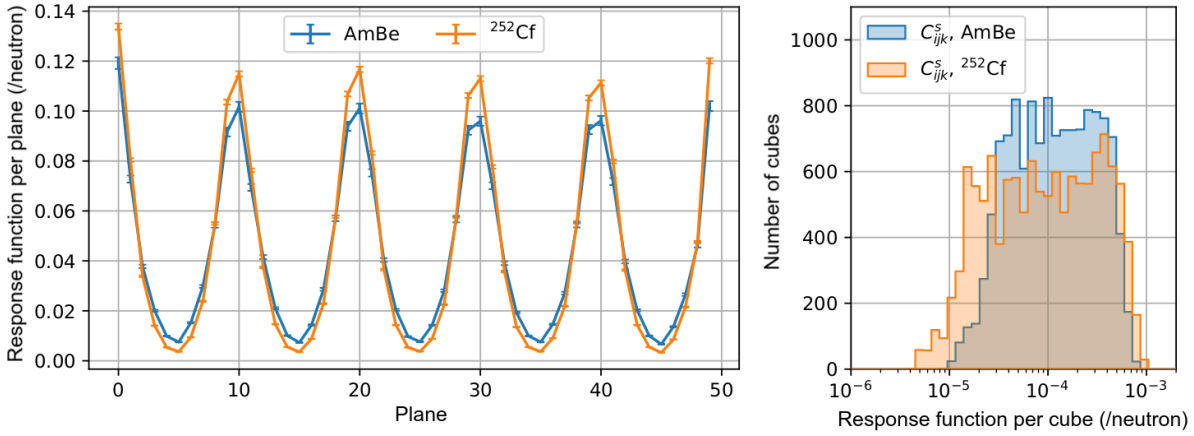

Figure 9.4.1: Left: Detector response function per plane obtained with an AmBe source and a ^{252}Cf source. Right: Distribution of the response function per cube [165]

and does not depend on the neutron history.

The absolute reconstruction efficiency is determined from actual neutron calibration runs with both the ^{252}Cf and AmBe sources, with well known source activities (respectively 1789 ± 35 neutron/s and 2463 ± 22 neutron/s). The number of reconstructed neutrons is compared to the predicted number of captured neutrons. When the total number of neutrons generated in gap g at calibration position p is expressed as $N_{tot}^{MC(g,p)}$, and when the number of those neutrons that interact in cube ijk is expressed as $N_{ijk}^{MC(g,p)}$, then the Monte-Carlo detector response function is expressed as the average of their ratio over all calibration points

$$C_{ijk}^{MC} = \frac{1}{9} \sum_{(g,p)} \frac{N_{ijk}^{MC(g,p)}}{N_{tot}^{MC(g,p)}}$$

The absolute reconstruction efficiency is determined per cube as the ratio of the detector response function, C_{ijk}^{s}, and the Monte-Carlo response function, C_{ijk}^{MC},

$$\epsilon_{\text{reco,ijk}}^{\text{abs}} = \frac{C_{ijk}^{s}}{C_{ijk}^{MC}}.$$

Figure 9.4.2 shows the distribution of the absolute reconstruction efficiency per cube. The Monte-Carlo response function is straightforward. But the detector response function, obtained from AmBe and ^{252}Cf sources and shown in the right panel of figure 9.4.1, is affected by conditions specific to the calibration data taking. The acquisition is subject to high count rates, which causes deadtime in the electronics and decreases signal reconstruction efficiency for events very close in time. The detector response function is obtained per plane by summing the response functions of the 256 cubes inside the plane, and is shown in the left panel of figure 9.4.1 for AmBe and ^{252}Cf. The response function is highest for planes close to the calibration gaps due to neutron multiplicity. The differences between the two response functions come from the difference in energy of the neutron flux emitted by the two sources. The neutrons from AmBe, which are more energetic, have a penetrating power greater than those of ^{252}Cf and therefore have a greater probability of reaching the center of the module.

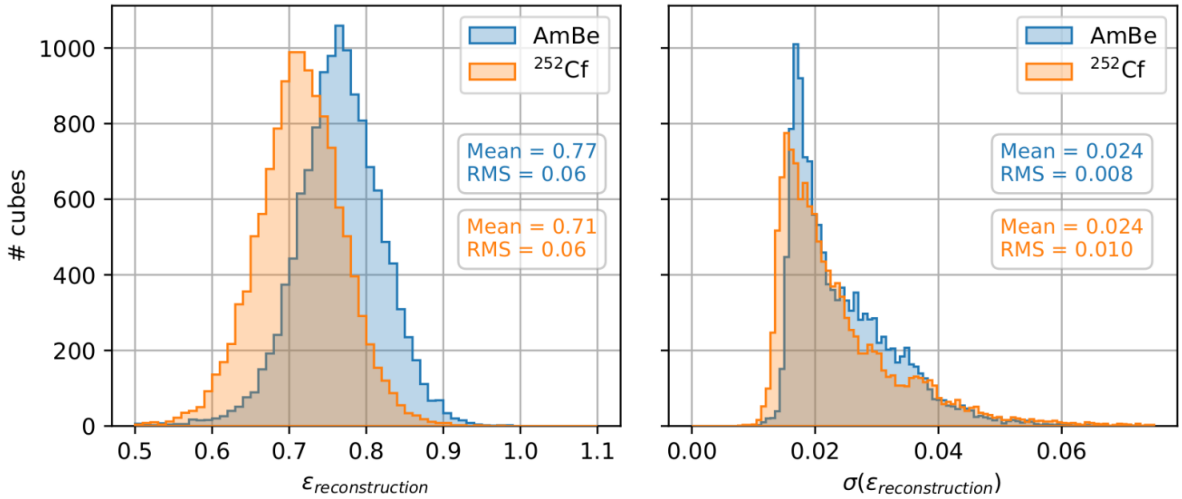

Figure 9.4.2: Left: Neutron reconstruction efficiency for the 12800 cells obtained with the AmBe (blue) and ^{252}Cf source (orange). Right: The total uncertainty on the neutron reconstruction efficiency for all detection cells obtained with the two sources (stat. + syst.). The right hand plot shows that the uncertainty is not the same for each cell, which is a consequence of statistics and accessibility during calibration with neutron sources.[165]

The absolute reconstruction efficiency per cube is shown in figure 9.4.2. Despite a very good relative agreement, a systematic shift of about 7% between the sources is observed. The uncertainties are not sufficient to explain the difference and so far it has remained unclear what causes this. For now the average of the two scans is used, being $\epsilon^{abs}_{reco} \approx 73.9 \pm 3.3$ %. The efficiency of neutron reconstruction is therefore greater than 60%, with a dispersion between cubes less at 10%, which is compatible with physical goals. The absolute systematic uncertainties, which are below 5% at the module level, are dominated by the uncertainty on the source activity and the Monte Carlo detector model.

Combining the neutron reconstruction efficiency with the average neutron capture efficiency of 72 %, the total IBD neutron detection efficiency becomes $\epsilon^{abs}_{det} \approx 52\%$, with a relative uncertainty between detector modules below 2%.

RELATIVE RECONSTRUCTION EFFICIENCY

The relative reconstruction efficiency is obtained as the ratio between the response function of the detector, C^s_{ijk}, and the average response function obtained over the 40 central planes of the detector (see figure 9.4.3). the relative neutron reconstruction efficiency per plane is homogeneous at 5% level across the detector, except for the planes in front and in the back of the detector, due to the higher probability for neutrons to escape.

The main source of systematic errors is coming from the simulation. The accuracy of the GEANT4 model is affected by the knowledge of the geometry and position of materials. In addition, uncertainties are induced by the neutron transport in the detector. The GEANT4 simulation used the nuclear database ENDF/B VI, where in the meantime ENDF/B VIII is published, with updated neutron cross sections for ^{6}Li and Hydrogen. A detailed recollection of the error budget can be found in the following reference [165]. Overall, the current results are sufficient to perform an oscillation study as provided

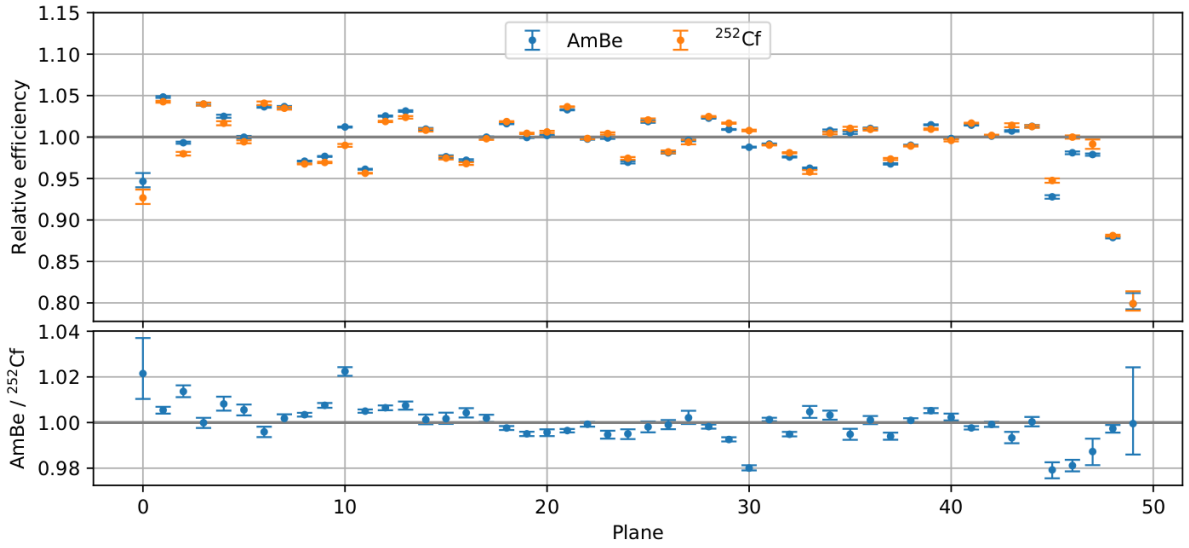

Figure 9.4.3: Top: Relative neutron reconstruction efficiency for the 50 planes obtained with the AmBe (blue) and ^{252}Cf source (orange). Bottom: Ratio of the relative neutron reconstruction efficiency obtained with the two different neutrons sources.[140]

for in the SoLid experiment. The SoLid neutron reconstruction efficiency could be estimated at the percent level per module.

9.5 ZnS(Ag) SCINTILLATION TIME CONSTANTS

The specific time characteristics of the ZnS(Ag) scintillation signal are used by the collaboration to activate the NS trigger and to perform pulse shape discrimination. The scintillation time scale can be modeled with three exponential decays, in order to emulate the scintillator response with the readout simulation that will be described in chapte r13.

The ZnS response after neutron capture, is determined from calibration measurements with the AmBe neutron source. The thermalised neutrons from the IBD process should behave identical to those from the neutron calibration source, since neutrons that were caused by different processes cannot be distinguished anymore once they are thermalised. The calibration data sample is selected from interactions in a $4 \times 4 \times 4$ volume around the source and is composed of $> 99.9\%$ neutrons. For each measurement, the neutron cube is selected and the mean waveform is constructed over the affected channels as shown in figure 9.5.1. As first approximation, the the average neutron waveform is fitted as shown in figure 9.5.2, where the third exponential is first fitted to the tail starting at sample 400. The second and first exponential are fitted consequently, while regarding an increasingly large time range, starting respectively at sample 30 and 0. The fractional contribution of each exponential is found as the ratio of its integral to the integral of the sum.

The final values for the time constants are determined by scanning ranges around the initial values that were obtained with the fits, in order to optimise the average waveform agreement between data and MC especially at the peak. For the simulation the ZnS(Ag) scintillation, 52 % of the generated

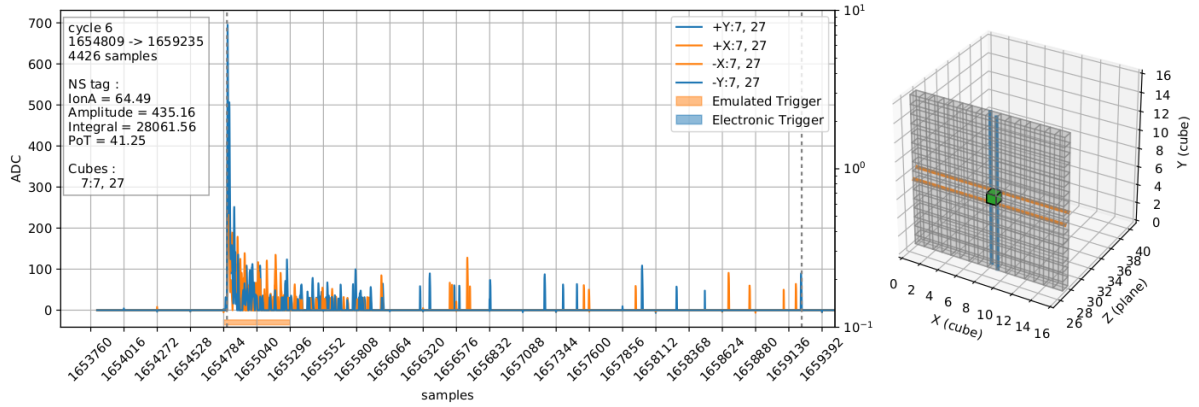

Figure 9.5.1: Neutron waveforms that are picked up by the four channels (left) running through the neutron cube (right). The waveforms are used to make the average neutron waveform.

photons follow a decay time constant of $\tau_3 = 653$ ns, 31 % of the photons follow $\tau_2 = 91.48$ ns, and the remaining 17 % follow the time constant $\tau_1 = 12.86$ ns.

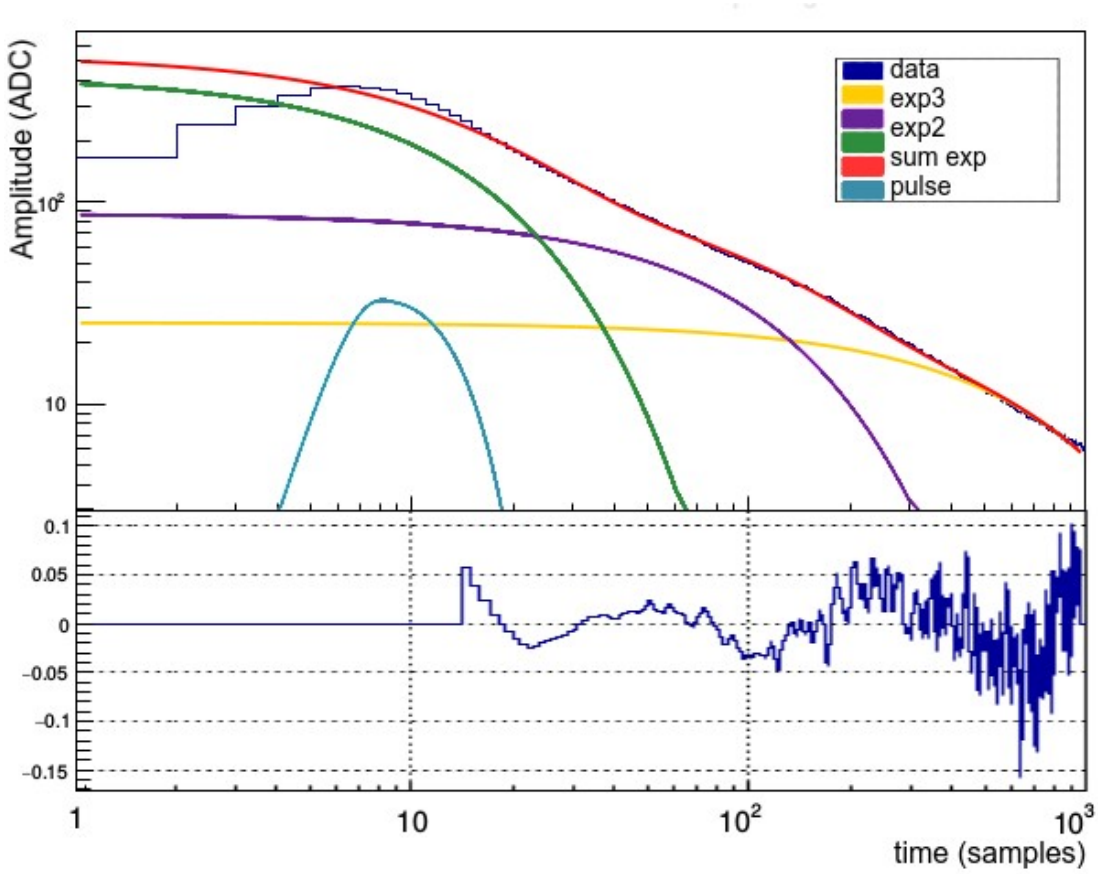

Figure 9.5.2: Result of the fit with three contributions from different exponential decay functions, for the average neutron waveform. The single pixel avalanche is indicated in light blue.

9.6 PERMANENT CALIBRATION WITH MUONS

By virtue of the detector's segmentation, tracks of high energy muon, that pass the detector at a high rate, can be accurately reconstructed. This enables monitoring the detector response on a daily basis and to study the detector response at high energy.

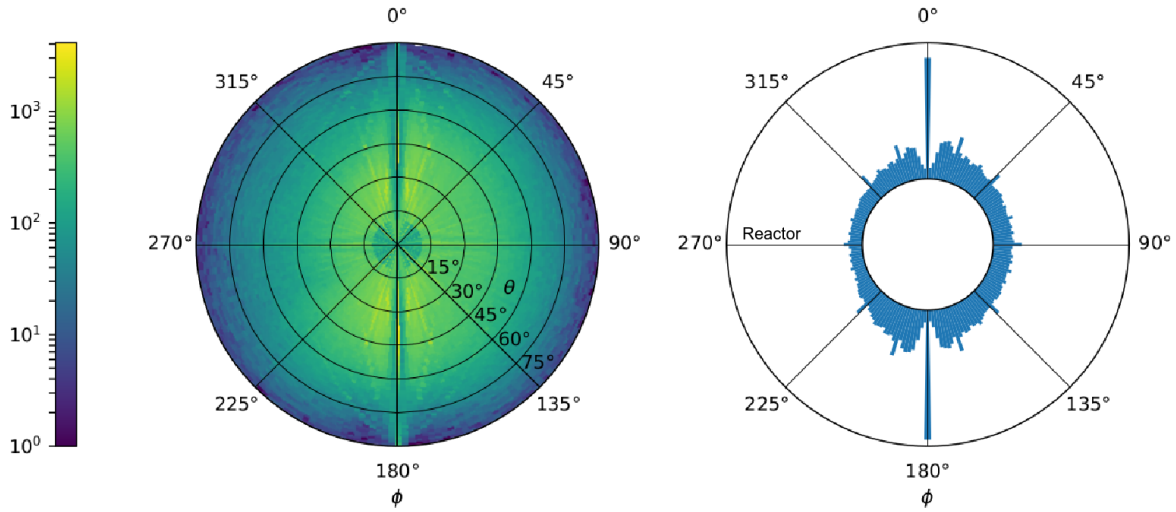

Figure 9.6.1: Left: Angular distribution of the reconstructed muons in the detector. ϕ is the polar angle, θ the azimuthal angle. Right: Relative flux in function of the polar angle.[165]

The directionality of the reconstructed 3D muon track is characterised by the azimuthal angle, θ, between the track and the Y axis (vertical to the detector) and the polar angle, ϕ between the track and the X axis of the detector (horizontal along the front). The angular distribution of the muon tracks is shown in figure 9.6.1. The flux decreases for higher θ where the muon enters more horizontally. The structures in the 0° and 180° directions are related by the orientation of the detector planes. The direction of the reactor (270°) is indicated on the figure. The reduced flux from this direction is due to the pool and the reactor core.

The muon rate can be determined from the time difference of incident muons, which is shown in figure 9.6.3. The distribution has an additional contribution from Michel electrons. Muons can decay inside the detector, creating a Michel electron and two neutrinos

$$\mu \longrightarrow e + \overline{\nu}_e + \nu_\mu$$

Due to the track like nature of a Michel electron, it will get reconstructed as a muon as well (an example is shown in figure 9.6.2). This results in the time difference between muons having two exponential contributions. At the millisecond scale due to the muon rate, and at the microsecond scale due the muon decay. The muon rate is 258.953 ± 0.194 Hz. The fitted muon decay time of 2.252 ± 0.022 μs is in sufficient agreement with the literature value of τ = 2.1969811 ± 0.000002 μs. The muon rate is strongly anti-correlated with the atmospheric pressure (-0.81), as shown in figure 9.6.4. With higher pressure, the muons have to traverse a higher density of atmosphere, which leads to a decreased muon flux at reactor level. The correlation is used to build a model to estimate the

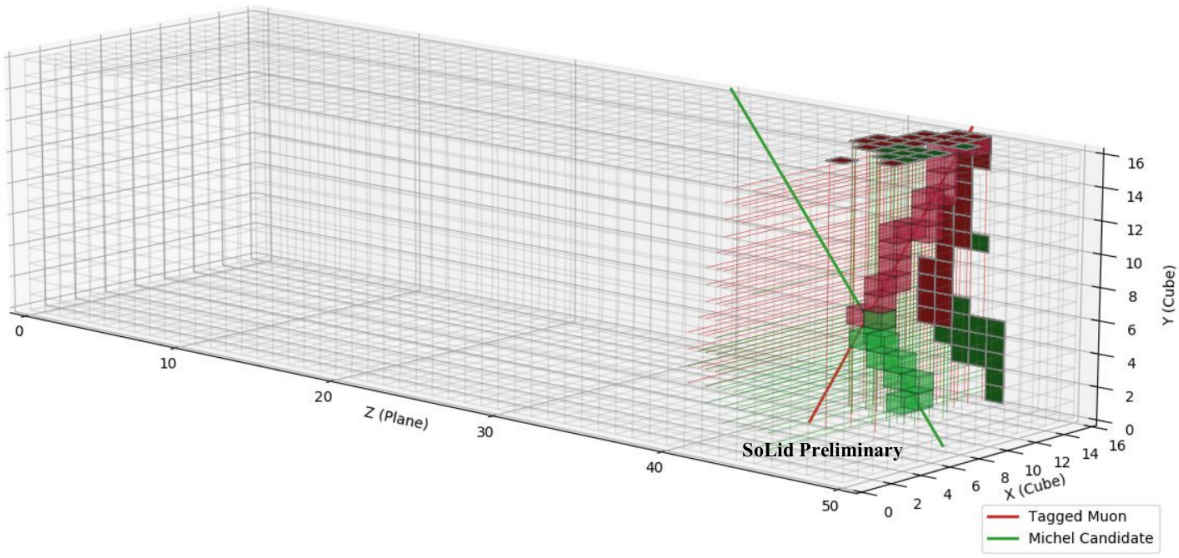

Figure 9.6.2: Example of a muon decay with the production of a Michel electron. [172]

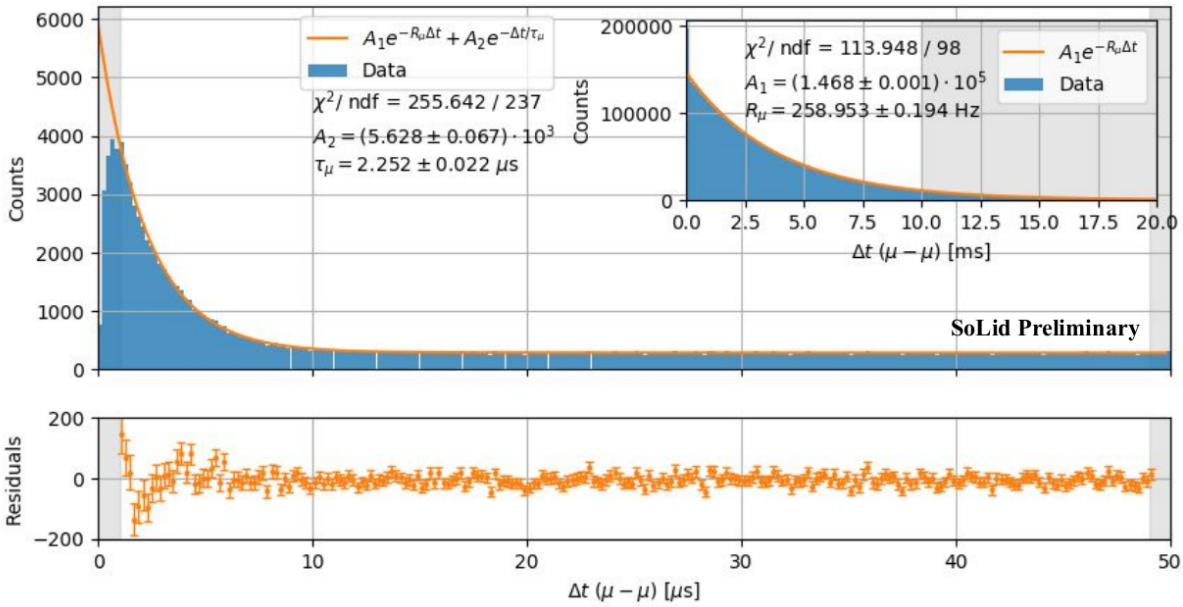

Figure 9.6.3: Time difference between reconstructed muon signals, showing a contribution from Michel electrons after muon decay. The muon rate and lifetime are determined from the exponential fit.[172]

atmospheric background during reactor on periods, based on measurements of the atmospheric pressure, as shown in the bottom panel of figure 9.6.6. The rate is stable over the reactor transition.

The muon stopping power gives an additional handle to monitor the PVT energy response, outside of the dedicated calibration periods. The energy deposit of muons is constant over the tracklength, resulting in a characteristic dE/dx. To isolate the response from a single detector cell and to avoid light leakage between neighbouring cells, horizontal muons are used for this study, that cross only

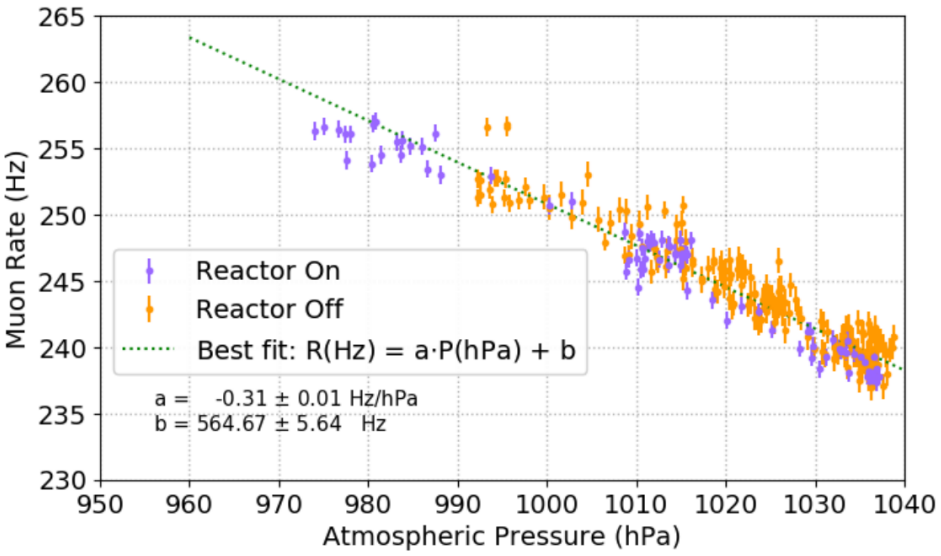

Figure 9.6.4: The rate of reconstructed muons in function of the atmospheric pressure, measured over 9 days of reactor on and 14 days of reactor off. The data shows a strong linear correlation.[172]

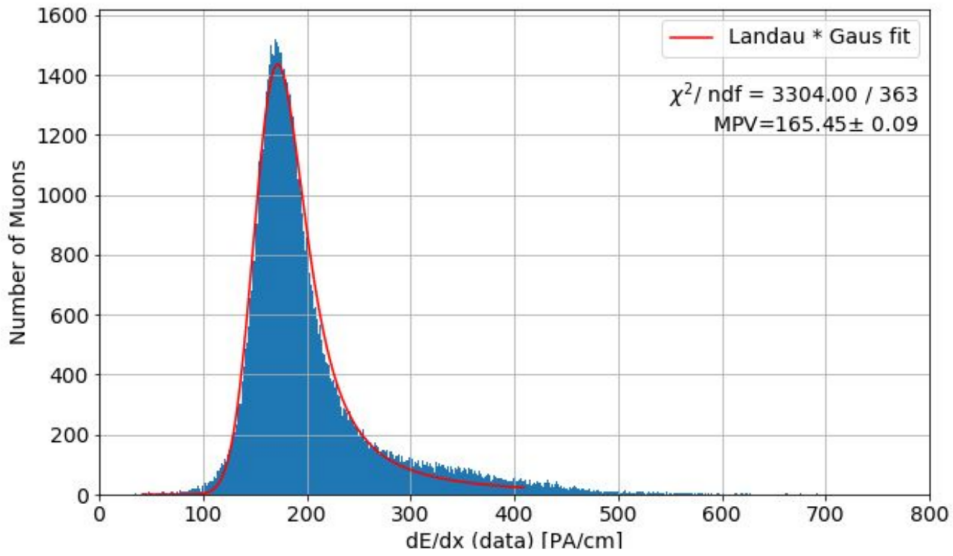

Figure 9.6.5: Stopping power of reconstructed horizontal muons showing the relation of deposited energy per path length of the reconstructed muon track.[140]

one cube in a plane. Every channel of the central cube is required to measure a time coincident signal. In order to determine the tracklength as accurate as possible, the allowed track angles are limited. As fiducial volume the inner part of the detector is used of $6 \times 6 \times 44$ cubes. The muon stopping power as measured with the SoLid detector is shown in figure 9.6.5. The evolution of the relative energy scale of the detector is monitored by the trending of the muon energy response. The top panel of figure 9.6.6 shows that the relative energy scale variations stay below 2%, despite larger variations in environmental conditions such as the humidity.

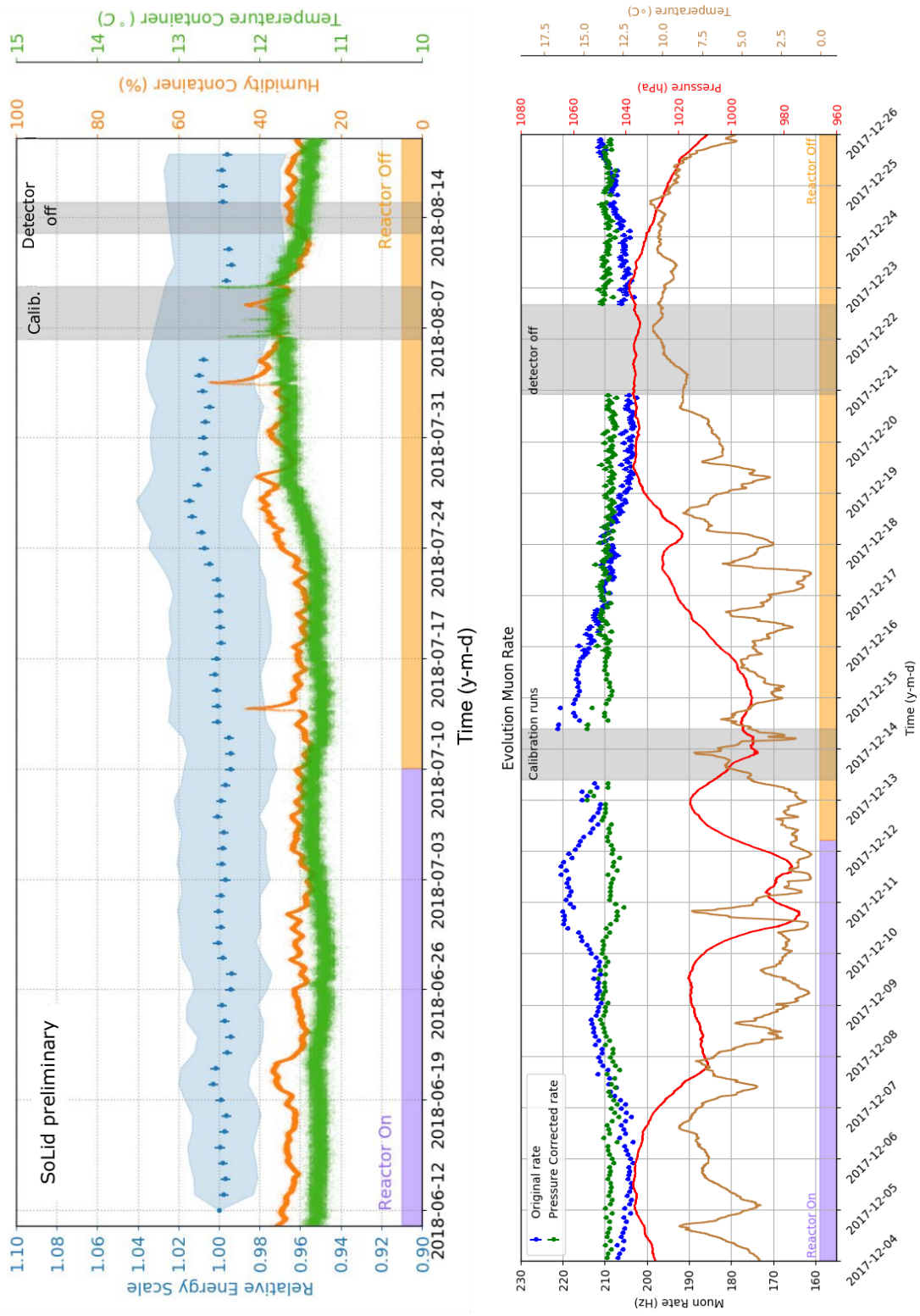

Figure 9.6.6: Top: Evolution of the relative energy scale determined from the muon data, corrected for gain and baseline variations, and averaged over all detector channels. The error bars represent the statistical uncertainty, the blue band shows the distribution over the channels. Bottom: Muon rate monitoring in December 2017, during reactor on and off periods. After correction for atmospheric pressure variations, the muon rate is stable over time.[173]

10

PRODUCTION AND DETECTION OF REACTOR NEUTRINOS

Large quantities of antineutrinos are produced in the BR2 reactor due to beta decays of the fission products. Given that the average energy released per fission is about 200 MeV, the BR2 reactor that operators with a power around 60 MW generates about 10^{18} fissions/s. A key ingredient in the success of the SoLid experiment is the accurate prediction of the specific BR2 antineutrino flux at any time during the reactor cycle. A detailed simulation is developed to calculate the BR2 antineutrino spectrum for each cycle, i.e. for a given fuel loading map and operation history.

10.1 BR2 ANTINEUTRINO SPECTRUM

The number of antineutrinos of a specific energy emitted over the time t_{run} by the whole reactor core, designated as $N_\nu^{\text{emit}}(E)$, is found as the time integral over the convolution of the fission rate and the reactor's total antineutrino spectrum,

$$N_\nu^{\text{emit}}(E,t) = \int_0^{t_{\text{run}}} \int_{\text{core}} \frac{P_{\text{th}}(t)}{\sum_k \alpha_k(x,t) < E_f >_k (t)} \sum_k \alpha_k(x,t) S_k(E,t)) dx^3 \, dt. \tag{10.1}$$

The fraction represents the fission rate. It accounts for the number of fissions that occur during the runtime. It is the ratio of the thermal power over the average energy released per fission of any of the fuel isotopes ($^{235,238}U$, ^{239,241}Pu). $< E_f >_k (t)$ is the mean energy released by a fission of the fissile isotope k, which is calculated from nuclear theory and can be retrieved from nuclear databases. $\alpha_k(x,t)$ stands for the percentage of fissions undergone by the isotope k, relative to all isotopes, at a certain position in the reactor core and at a specific time during the reactor cycle.

The second factor represents the average antineutrino spectrum of the total BR2 core. That is the average number of antineutrinos emitted per fission by *any* of the isotopes. It is constructed from the antineutrino spectra $S_k(E)$ of the k isotopes. $\alpha_k(t)$ stands for the time-dependent percentage of fissions undergone by the isotope k, relative to all isotopes.
The fission spectra $S_k(E,t)$ for the main isotopes are obtained by either of two methods, namely the conversion method and the summation method. In the conversion method, the spectra are taken from a reference of choice that converted measured β spectra based on the law of energy conversion. The available spectra were discussed in chapter 4 and shown in figure 4.1.2.
In the summation method, the antineutrino spectrum is build 'ab-initio' from the knowledge of all the beta branches of the fission products of the isotopes, thanks to the numerous information available nowadays in nuclear databases. For the SoLid simulation, the equilibrium regimes are simulated by the conversion method and the summation method provides the off-equilibrium corrections.

10.1.1 POWER HISTORY

The thermal power history during the reactor cycle, $P_{th}(t)$, is provided by the BR2 operators at SCK-CEN. Their first method to determine the power is based on the enthalpy balance in the reactor's water cooling circuits, which is determined with measurements of the water flow and temperature in the circuits. The second method to determine the reactor power is based on the measurement of the average core neutron flux through their activation of oxygen in the cooling water. The ^{16}O that is present in the cooling water is activated by fast neutrons through the reaction

$$^{16}O(n,p) \longrightarrow ^{16}N.$$

The nitrogen isotope ^{16}N β decays to ^{16}O, with a half life of 7 s. Monitoring the ^{16}N activity allows to determine the thermal power evolution of the reactor. The SoLid experiment does not use the result of the second method because of the uncertainties related to the flow of primary cooling water towards the ionisation chamber to measure the ^{16}O. The result from the first method is used, which has an estimated uncertainty around 5 to 8 % [174]. The error budget is driven by the uncertainty associated to the calibration of the devices measuring the cooling water temperature and flow, and by offsets introduced during the processing of these measurements.

For simulation purposes, time steps for the reactor power evolution were chosen to take into account the power variation but also the needs of the reactor calculation. In total 25 time steps have been chosen for a full reactor cycle of around 30 days, with finer discretisation during reactor off-on transitions.

10.1.2 FUEL INVENTORIES AND FISSION RATES

The fission rate in the reactor core, i.e. the first factor of 10.1, depends on the average energy released per fission of any of the fuel isotopes. This is determined by

$$< E_f > (t) = \int_{core} \sum_k \alpha_k(x,t) < E_f >_k dx^3,$$

where $< E_f >_k$ is the mean energy released by a fission of the fissile isotope k, which is calculated from nuclear theory and can be retrieved from nuclear databases. $\alpha_k(x,t)$ stands for the percentage of fissions undergone by the isotope k, relative to all isotopes, at a certain position in the reactor core and at a specific time during the reactor cycle. The expression is integrated over the whole reactor core.

The fission rates in the reactor core depend on the momentary fuel composition, which varies during reactor operation due to the burn up of ^{238}U and the breading of ^{239,241}Pu. However, the BR2 reactor with an enrichment of about 93.5% ^{235}U, has very little ^{238}U and as a consequence only a minuscule amount of the plutonium fissile isotopes are produced. The fission fraction of ^{235}U is over 99%.
Nevertheless, the evolution of the fuel composition is simulated in detail [176]. An SCK-CEN team developed a 3D simulation of the BR2 reactor within the MCNPX code [177] (Monte Carlo for N Particles), that allows to simulate the neutron transport through the reactor. The 3D geometry and burn-up model of the BR2 core is a complete description of BR2's hyperboloid reactor core composed of twisted and inclined reactor channels (see figure 10.1.1). The fuel elements, the beryllium matrix,

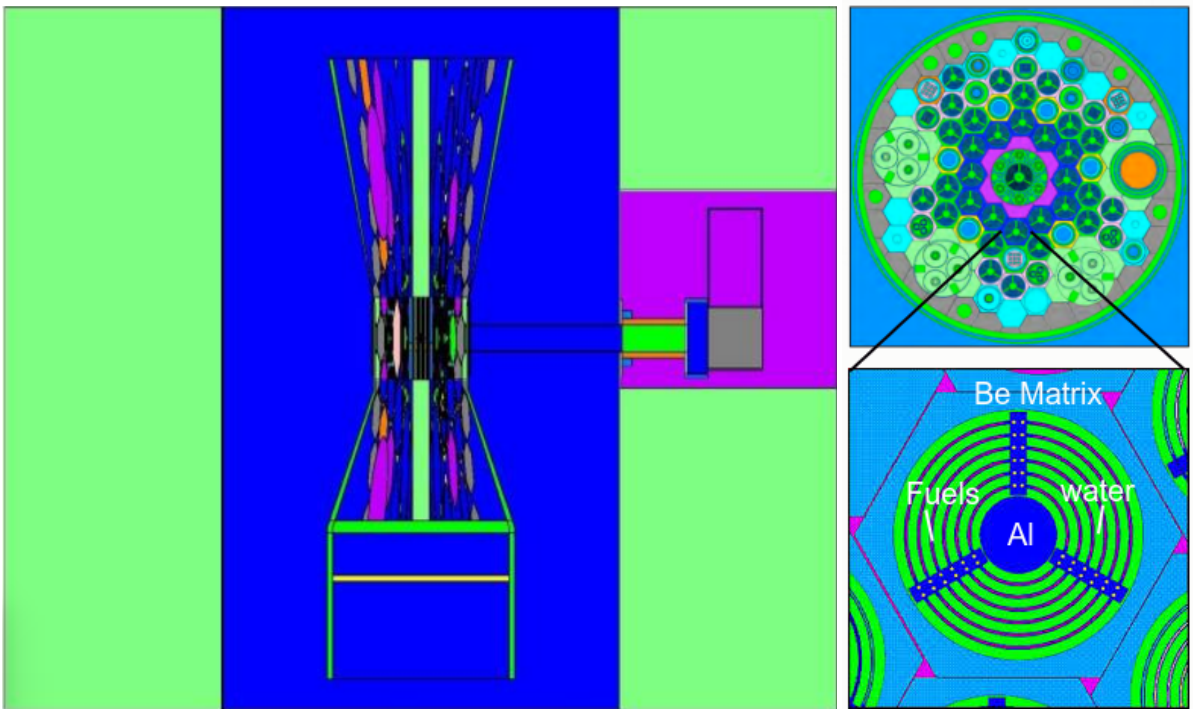

Figure 10.1.1: Left: MCNP model of the twisted hyperboloid fiber bundle of the BR2 reactor including the vessel and the bio shield. Right top: Cross section at mid-plane of the MCNPX BR2 reactor core model. Right bottom: Close up of a fuel cel.[175]

experimental devices and control rods loaded in the channels are modeled in detail.

For the evolution calculation of the isotope composition, The MCNPX simulation is coupled with the CINDER90 depletion code [178]. The latter predicts the isotope inventory over time based on the initial fuel composition and power history. This allows to evolve all the fission products over time, under exposure to varying neutron fluxes. At each timestep, the fuel inventories are extracted, being the spatial distribution of the fissile isotopes, the fission products and the fission rates. The evolution of the fission rates during cycle 3 in 2018 is shown in figure 10.1.2.

The combined statistical and systematic errors on the fission rates during burn up are calculated to be less than 3% for ^{235}U, ^{238}U and ^{239}Pu and about 10% for ^{241}Pu. The dominant systematic sources come from the geometrical approximation, the modeling of beryllium poisoning and the limited number of unique fuel materials in the simulation. The uncertainties for the different isotopes are summarised in table 10.1.1. The combined uncertainty on the ^{235}U fission rate is 8.5% and dominated by the uncertainty on the reactor power measurement.

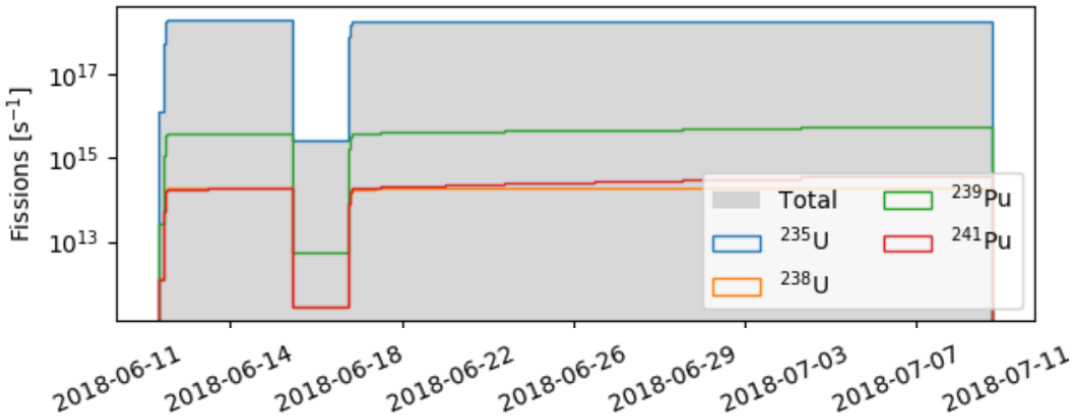

Figure 10.1.2: Evolution of the fission rates during cycle 3 of the BR2 reactor in 2018. ^{235}U contributes more than 99.9 % of the fissions. [179]

Isotope	Geometry details	Berylium poisoning modeling	Fission energy	Number of unique fuel materials	Monte Carlo statistical uncertainty	Combined uncertainty
235U	1.53 %	0.5 %	1 %	1.02	1 %	2.4 %
238U	1.03 %	0.5 %	1 %	1.02	1 %	2.1 %
239Pu	1.98 %	0.2 %	1 %	1.03	1 %	2.6 %
241Pu	1.66 %	0.4 %	1 %	10.0	1 %	10.2 %

Table 10.1.1: Conservative estimates on the relative uncertainties on the main input parameters for the calculation of the fission rates with the BR2 reactor model.[180]

10.1.3 ANTINEUTRINO SPECTRUM

Based on the simulation of the complete reactor model and fission distributions, the BR2 $\overline{\nu}_e$ spectrum can be determined with an antineutrino spectrum that was obtained with the conversion method or the summation method [175]. When using the conversion method, the simulated rate of the main fissile isotopes can be convoluted with the average converted antineutrino spectra, $S_k(E)$ from a reference of choice (which were introduced in section 4.1.3). The reactor's emission spectrum and flux can be determined as described in equation 10.1. This approach gives a quick access to a first antineutrino calculation.

In addition, a second approach was implemented by a team from SUBATECH, in which the summation method is readily applied to the fissions in the BR2 reactor (see section 4.4.2 for a description of the summation method). In order to use the ab-initio summation method, the MNCP/CINDER90 code is coupled to a more precise depletion code, namely MURE (MCNP Utility for Reactor Evolution)[181]. The MURE code is coupled to nuclear databases containing all beta decay branches of the fission products for a given fissile isotope. In addition to the simulation of the reactor core evolution, the MURE code can compute the associated antineutrino energy spectrum following the formula 4.1. A $\overline{\nu}_e$ flux that was determined specifically for the BR2 reactor with the summation method is shown in figure 10.1.3.

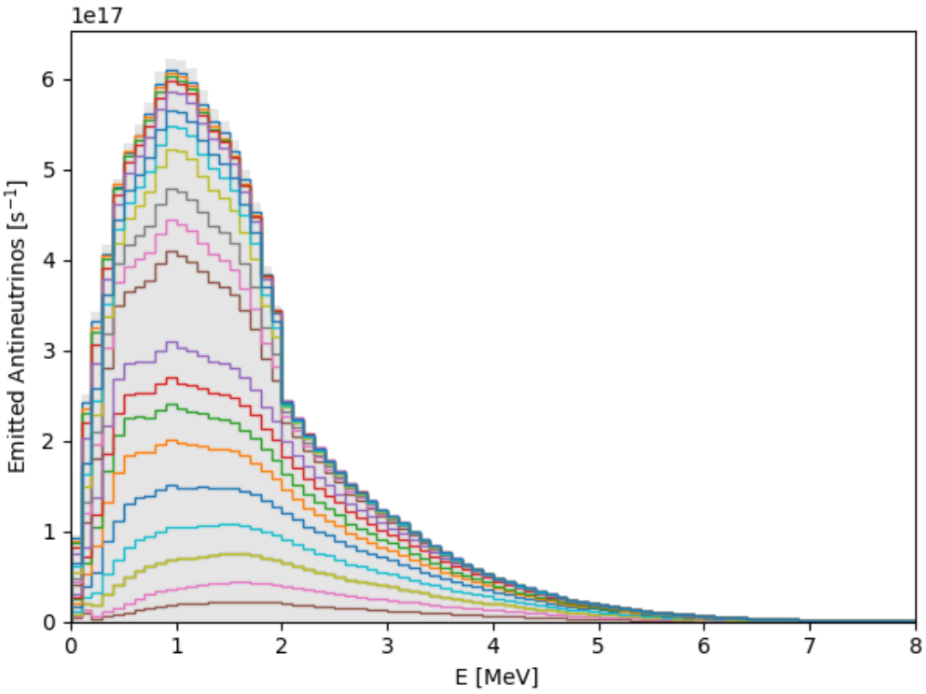

Figure 10.1.3: Emitted antineutrino spectrum calculated with MCNP fission rates and using the summation method in MURE. The different colors correspond to summations after cumulative time steps of 0.02 days during reactor start up of Cycle 01 in 2015.[175]

10.2 INTERACTION OF REACTOR NEUTRINOS IN DETECTOR

The most widely exploited process to detect $\overline{\nu}_e$ originating from nuclear reactors is the inverse beta decay (IBD) reaction, which is the highest cross-section interaction process at typical reactor energies (see figure 1.6.1 in section 1.6). An incident reactor anti neutrino can interact with a proton within the detector volume via the exchange of a weak boson (figure 10.2.1). The proton converts into a neutron and a positron is produced in the interaction.

$$\overline{\nu}_e + p \longrightarrow n + e^+ \qquad (E_{\overline{\nu}_e} > 1.804 MeV)$$

The IBD interaction poses a detection energy threshold for the antineutrino of 1.804 MeV, which is the mass difference between the initial and final states.

The IBD interaction spectrum in the detector is dictated by several factors

$$N_\nu^{\text{int}} = N_p \cdot \frac{1}{4\pi L^2} \int_0^{t_{\text{run}}} \int_{\text{core}} n_f(x,t) S(E) \sigma_{\text{IBD}}(E) dx^3 \, dt \tag{10.2}$$

with the number of fissions

$$n_f(x,t) = \frac{P_{th}}{\sum_k \alpha_k(x,t) < E_f >_k (t)}$$

and the BR2 antineutrino spectrum

$$S(E) = \sum_k \alpha_k(x,t) S_k(E,t))$$

that were both determined in section 10.1 from k fission isotopes. The geometrical acceptance of the detector to the neutrino flux is naively given by the factor $1/4\pi L^2$. The extension and temporal variation of the core geometry will be taken into account for the dedicated simulation in section 10.3. Only the neutrinos that emerge under a certain angle from the BR2 reactor, will have a trajectory that traverses the detector. Some of these neutrinos will interact within or close to the detector volume. The proton content of the detector is denoted as N_p. The reactor neutrinos can engage in an IBD interaction with the protons, so the number of available protons has a linear impact on the interaction rate. Whether the encounter of a reactor neutrino with a proton leads to an interaction, is expressed by the IBD interaction cross section $\sigma(E)$.
Each of these factors has to be modeled according to the precise configuration parameters of the SoLid experiment, in order to obtain an accurate prediction of antineutrino interaction rate in the detector.

The IBD cross section σ_{IBD} is an energy-dependent variable that reflects the probability that an incident antineutrino will interact per target atom. It is well defined [182, 183] and depends on the positron energy, E_{e^+}, and momentum, p_{e^+}, as

$$\sigma(\overline{\nu}_e p \rightarrow e^+ n) = \kappa E_{e^+} p_{e^+} \tag{10.3}$$

$$= \frac{G_F^2 |V_{ud}|^2 E_{e^+} p_{e^+}}{\pi}(1+\Delta R)(f^2+3g^2). \tag{10.4}$$

G_F is the Fermi coupling constant and V_{ud} is a mixing parameter of the CKM matrix [36, 37]. Radiative corrections are included by means of ΔR and f and g are respectively the vector and axial-vector coupling constants. The resulting κ value is $0.958 \pm 0.003\ 10^{-43}$ cm^2 MeV^{-2}. Therefore, for reactor neutrinos of 6 MeV the cross section is about $2 \cdot 10^{-3}$ femtobarn.

The proton content N_p is determined for all the basic components within the sensitive detector volume, based on their weights that were measured during detector construction and on their average proton densities, which are quoted by the manufacturers. In addition, the proton content can be determined from the GEANT4 simulation [2] that will be described in chapter 12, in which all the detector parts were defined together with their composition and density. The values are summarised in table 10.2.1. PVT makes up ~94 % of the proton number in the active region. By taking into account all proton-rich materials, the possible effect of antineutrino interactions with matter between their point of emission and the detector can be accounted for in the simulation.

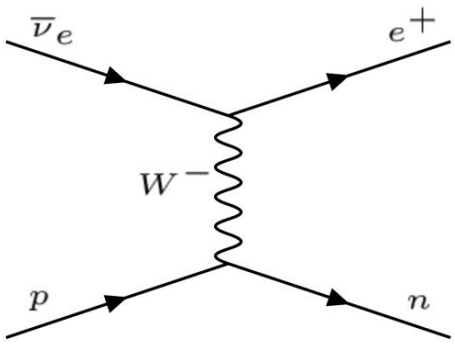

Figure 10.2.1: Feynman diagram of inverse beta decay process.

	Mass (kg)	H density ($\times 10^{22}$ cm^{-3})	H content	Relative H content (%)
PVT	1.5293×10^3	5213	7.7921×10^{28}	94.10
LiF:ZnS(Ag)	3.4190×10	2.34267	3.5939×10^{26}	0.43
Li backing	1.6206×10	3.4596	4.0633×10^{26}	0.49
Tyvek wrap+sheet	3.2381×10	3.2629	2.7826×10^{27}	3.36
WLS fiber core	2.1601×10	4.85696	9.9917×10^{26}	1.21
WLS fiber cladding	7.1660×10	5.72629	3.4351×10^{26}	0.42

Table 10.2.1: Masses and hydrogen content of the major detector components.[184]

The interaction neutrino spectrum is related to the product of the reactor $\overline{\nu}_e$ emission spectrum and the IBD cross section which both depend on the $\overline{\nu}_e$ energy. The former decreases with energy, while the latter increases. Therefore, the interaction spectrum rises from the threshold value at about 1.8 MeV, reaches a maximum around 4 MeV and vanishes after 8 MeV. At the high energy end, the spectrum is dominated by the very energetic transitions of rare exotic nuclei and cannot be accurately predicted. However, the antineutrino rates become negligible above 8 MeV, being < 0.5% of the total detected rate.

The exact shape of the interaction spectrum depends on the choice of spectra $S_k(E)$ for the different fissile isotopes in the reactor core in equation 10.2. Several literature references provide neutrino spectra for the four common fissile isotopes, ^{235,238}U, ^{239,241}Pu. The reference isotope spectra from

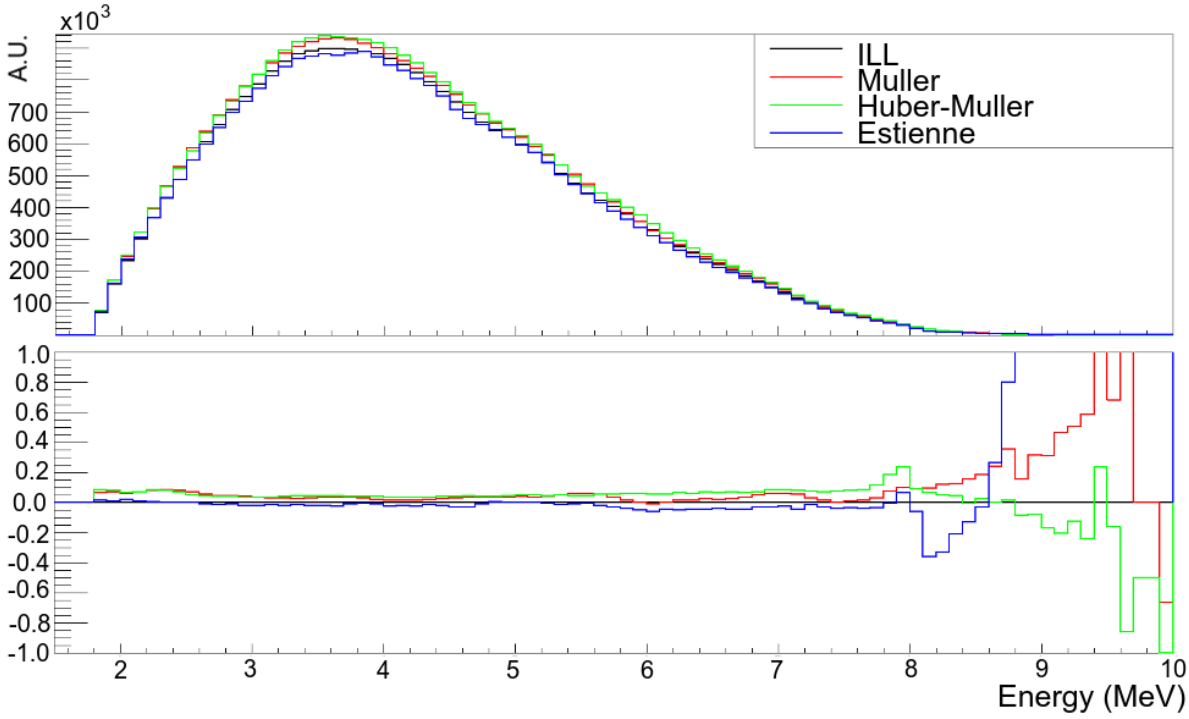

Figure 10.2.2: Interaction spectrum obtained by combining the IBD cross section with the neutrino emission spectra obtained from different sources.[179]

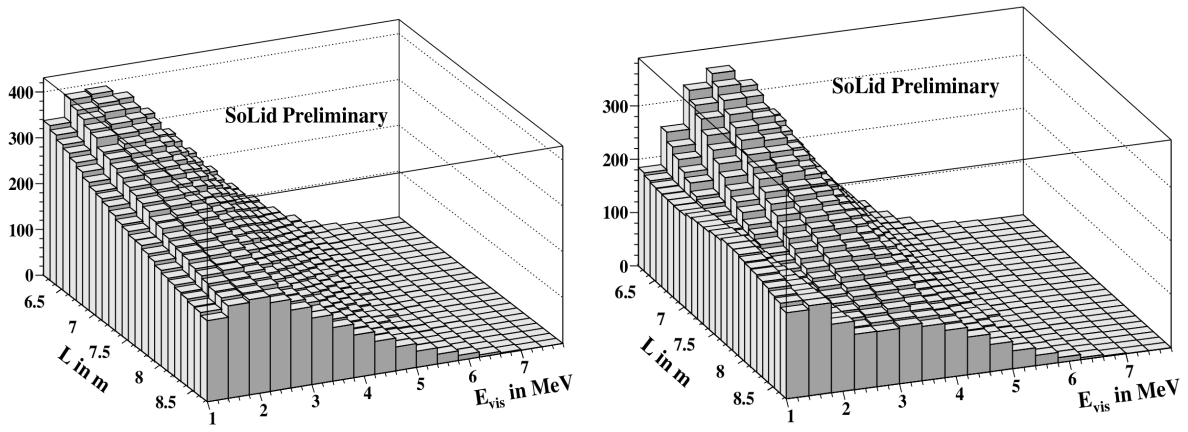

Figure 10.2.3: Number of IBD events as function of neutrino energy, E_ν, and traveled distance, L, without (left) and with (right) oscillations to a sterile neutrino state with $\Delta m^2_{14} = 1.78$ eV^2 and $\sin^2(2\theta_{ee})$ is chosen as 0.5 such that the oscillation effect is more prominent.[185]

Schreckenbach (denoted as ILL), Huber-Muller (improved conversion method) Estienne (summation method) and Muller (alternative parametrisation) were described in chapter 4 and visualised in 4.1.2. The respective interaction spectra for the BR2 reactor for one cycle are shown in figure 4.1.2), starting at the IBD energy threshold.

Neutrino oscillations into a sterile flavour state would alter the interaction spectrum with the probability

$$P_{\bar{\nu}_e \to \bar{\nu}_e} = 1 - \sin^2(2\theta_{14}) \sin^2\left(\frac{\Delta m^2_{41} L}{4E}\right).$$

The interaction spectrum in equation 10.2 can be multiplied with this probability to include the effect of sterile neutrino oscillation, for certain oscillation parameters Δm^2_{41} and $\sin^2(2\theta_{14})$. For a discussion about these parameters, see section 2.5 chapter 2. The oscillation manifests itself over distance L and energy E. In order to map the oscillation pattern over L/E, the SoLid experiment groups the recorded IBD events in a range of (L,E) bins. The recorded reactor-detector distances are grouped in L-bins with a size that corresponds to a certain number of detector planes. In general 5 bins are taken, which corresponds to the 5 detector modules. This increases statistics per bin and avoids module effects on the oscillation pattern. Figure 10.2.3 illustrates the expected IBD signal distribution for cases where oscillation to a sterile neutrino state and is absent and present.

10.3 IBD SIMULATION WITH SOLO

A dedicated framework to generate large numbers of IBD events was developed by the SoLid collaboration, called SoLO [179]. It combines the BR2 reactor flux model, the geometrical detector acceptance and the neutrino interaction process, in order to provide representative signal prediction for data Monte Carlo comparisons. The result of SoLO is a list of neutrinos, detailing its in-core generation point, energy and momentum, travelled distance, interaction point in the detector, and the interaction time. The output from the SoLO generator can be fed to GEANT4 [2], which is described in chapter 12.

For simulation purposes, only IBD events that occur in the detector are generated. Since the antineutrino flux from the reactor is assumed to be isotropic, only a fraction of the antineutrinos reaches the detector volume. Although the SoLid detector is relatively close to the reactor core, the total detector acceptance, defined as the fraction of $\overline{\nu}_e$ that crosses the detector, is only $\approx 0.11\%$. The geometrical efficiency is taken into account in the interaction spectrum in equation 10.1 by the weight $1/4\pi L_i(x)^2$. The generation of neutrino interaction vertices happens on a voxel-by-voxel basis, where the detector volume is split in voxels of $5 \times 5 \times 5 cm^3$. All surrounding, inactive material in the simulation is also divided in these voxels. For each individual voxel i, the number of IBD interactions is calculated by using its distance $L_i(x)$

$$N_\nu^{\text{int}} = N_p \cdot \frac{1}{4\pi L_i(x)^2} \int_0^{t_{\text{run}}} \int_{\text{core}} \int_{E_i}^{E_{i+1}} n_f(x,t) S(E) \frac{\sigma_{IBD}(E)}{L_i(x)^2} dE\, dx^3\, dt \tag{10.5}$$

where the integration runs over the reactor core volume. The integration therefore slightly differs between reactor cycles, depending on the reactor fuel loading map.

For each voxel, the SoLO code generates a number of IBD events per isotope k, where the signal normalisation is determined with equation 10.5. To reduce statistical fluctuations two orders of magnitude more events are generated. For each event, a position inside the reactor core is sampled, according to the fission distribution obtained from MCNP/CINDER90, and a neutrino energy value is drawn from the E_ν spectrum, as well as an interaction point inside the detector voxel is picked.

Note hat the choice of isotope reference spectrum has an influence on the E_ν distribution. For the big SoLO processing, it is assumed that the BR2 spectrum is in equilibrium and follows the reactor power. A smooth parametrisation of the spectrum is used, that is provided by Muller. The phenomenological parameterisation of the fission antineutrino spectra is an alternative to the conversion and summation method. It is useful for sensitivity studies requiring different binning or energy domains. The parametrisation of the spectrum for a given isotope is constructed with the exponential of a polynomial

$$S_{k,\text{fit}}(E_\nu) = \exp\left(\sum_{p=1}^{6} \alpha_{pk} E_\nu^{p-1}\right)$$

with the coefficients α_{pk} determined by a fit to the data. The parametrisation concentrates only on energies higher than the IBD threshold. The corresponding interaction spectrum is shown in figure 10.2.2.

For off-equilibrium effects, during ramp up of the reactor, the more detailed summation method is used. It follows the reactor power over time and uses nuclear info to determine the contribution of the fission isotopes and their fission products for each time step. The method offers a time dependent neutrino spectrum, but it is time consuming and requires the most computational resources. The profile of the neutrino interactions in the detector is shown in figure 10.3.1. The materials with a high proton density, such as the frames and HDPE shields, as well as the cell structure of the PVT cubes agree clearly visible. The quadractic decrease of IBD events with increasing distance to the reactor (in the z coordinate) is evident. The accurate simulation of the reactor geometry has a big influence on the position of the isotope fission and therefore on the travelled distance towards the detector. Shifting the whole reactor core 10 cm in each of the three orthogonal directions results in a relative difference of 3 % in the IBD interaction rate in the detector.

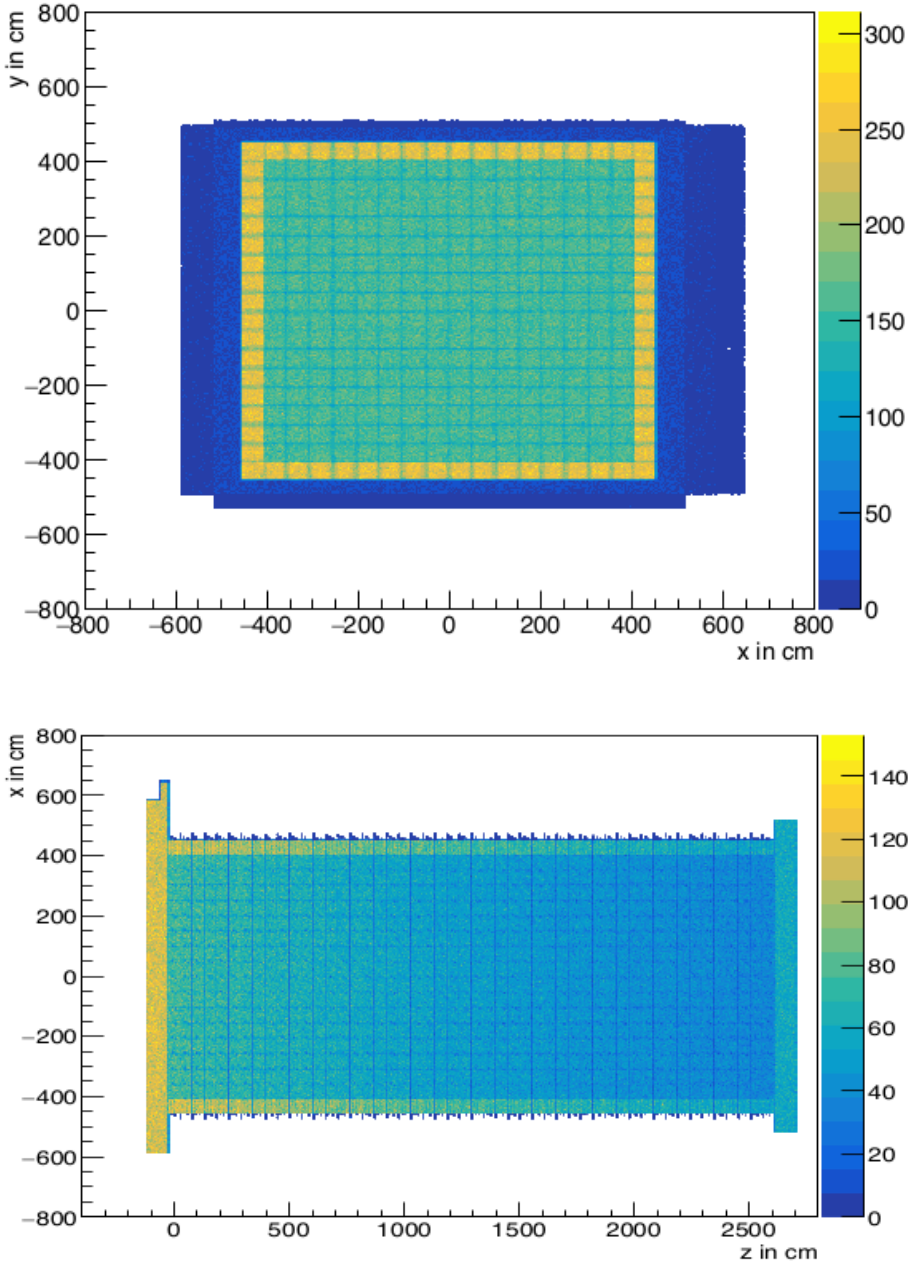

Figure 10.3.1: Heat maps showing the position distribution of the IBD events throughout the SoLid detector, seen from the back of the detector towards the reactor (top) and seen from the top (bottom). See figure 12.1.2 for the coordinate system.[179]

To simulate the detector response, the generated IBD events from SoLO are interfaced with the GEANT4 simulation [2] that models the detector (see chapter 12). The GEANT4 output will be subsequently processed with the Readout simulation that models the detector response and outputs waveform signals (chapter 13). Finally the simulated signals will be reconstructed and analysed with the software that handles the data processing (chapter 8).

11

BACKGROUND PROCESSES

The interaction of interest for the SoLid experiment is that of the reactor antineutrino. The anti electron neutrinos from the BR2 reactor core can interact via the inverse beta decay (IBD) within the detector volume. This interaction will result in a specific IBD detection signal, composed of a scintillation signal from the PVT scintillator and a delayed signal from the ^{6}Li:ZnS(Ag) scintillator.

The neutrino signals are hidden between background signals. The main backgrounds come from Bismuth-Polonium decay chains, muons and cosmic backgrounds (atmospheric neutrons and spallation neutrons caused by atmospheric muons)[186]. The background can be divided in two types, namely the accidental backgrounds, which originates from an accidental combination of a PVT and ^{6}Li:ZnS(Ag) signal and the correlated backgrounds, which are time correlated PVT and ^{6}Li:ZnS(Ag) signals. The latter arises mainly from cosmic muons, muon-induced spallation neutrons, atmospheric neutrons and radioactivity that is naturally present in the detector materials.

11.1 RADIOACTIVE CONTAMINATION

The SoLid experiment comes with a natural contamination of trace amounts of radioactive thorium and uranium. These elements originated in the formation of our solar system and due to their half lifes exceeding billions of years, they still occur in the earth's crust, with respectively 2.7 and 10.5 mg/kg[187]. The unavoidable contamination of the detector materials and the structures surrounding it follow the natural abundance of the isotopes. Natural uranium consists of 99.27% ^{238}U, 0.72% ^{235}U, and trace amounts of ^{233,234,236}U. Natural thorium is composed of 99.98% ^{232}Th, 0.02% ^{230}Th and trace amounts of ^{227,228,229,231}Th isotopes.

The three most abundant elements have long decay chains that lead to stable lead, as shown in figure 11.1.1. These elements and their descendants are one of the main background sources for any experiment looking for rare events. First of all, the SoLid detector contains intrinsic radioactivity from trace amounts of Bizmuth in the detector materials. Most troublesome is the ^{214}Bi isotope, present in the ^{6}Li:Zns(Ag) screens, which decays along the ^{238}U radioactive decay series. In addition, an exogenous source of radioactivity emerges from those elements, since they are ingrained in the concrete of the reactor building. All of their decay chains contain an isotope of radon. Being gaseous, radon can easily diffuse from materials close to the experiment and find its way to the detector. This will be discussed in section 11.1.2.

11.1.1 BIZMUTH CONTAMINATION OF THE NEUTRON DETECTION SCREENS

The LiF component of the neutron detection screens is the most worrisome component regarding radiopurity. The activity of bulk amounts of this material were measured in the underground low

$$
\begin{array}{l}
{}^{238}_{92}\mathrm{U} \xrightarrow[4{,}468\times10^{9}\ \mathrm{y}]{\alpha} {}^{234}_{90}\mathrm{Th} \xrightarrow[24{,}1\ \mathrm{d}]{\beta^-} {}^{234\mathrm{m}}_{91}\mathrm{Pa} \left\{ \begin{array}{l} \xrightarrow[1{,}17\ min]{0{,}16\%} {}^{234}_{91}Pa \xrightarrow[6{,}7\ h]{\beta^-} {}^{234}_{92}\mathrm{U} \\ \xrightarrow[1{,}17\ min]{99{,}84\%\beta^-} \end{array} \right. \\
{}^{222}_{86}\mathrm{Rn} \xrightarrow[3{,}8235\ \mathrm{d}]{\alpha} {}^{218}_{84}\mathrm{Po} \xrightarrow[3{,}05\ \mathrm{min}]{\alpha} {}^{214}_{82}\mathrm{Pb} \xrightarrow[26{,}8\ \mathrm{min}]{\beta^-} {}^{214}_{83}\mathrm{Bi} \xrightarrow[19{,}9\ \mathrm{min}]{\beta^-} {}^{214}_{84}\mathrm{Po} \xrightarrow[164{,}37\ \mu s]{\alpha} {}^{210}_{82}\mathrm{Pb} \xrightarrow[22{,}26\ \mathrm{y}]{\beta^-} {}^{210}_{83}\mathrm{Bi} \xrightarrow[5{,}013\ \mathrm{d}]{\beta^-} {}^{210}_{84}\mathrm{Po} \xrightarrow[138{,}38\ \mathrm{d}]{\alpha} {}^{206}_{82}\mathrm{Pb} \\
{}^{226}_{88}\mathrm{Ra} \xrightarrow[1600\ \mathrm{y}]{\alpha} {}^{222}_{86}\mathrm{Rn} \\
{}^{230}_{90}\mathrm{Th} \xrightarrow[7{,}7\times10^{4}\ \mathrm{y}]{\alpha} {}^{226}_{88}\mathrm{Ra} \\
{}^{235}_{92}\mathrm{U} \xrightarrow[7{,}038\times10^{8}\ \mathrm{y}]{\alpha} {}^{231}_{90}\mathrm{Th} \xrightarrow[25{,}52\ \mathrm{h}]{\beta^-} {}^{231}_{91}\mathrm{Pa} \xrightarrow[3{,}276\times10^{4}\ \mathrm{y}]{\alpha} {}^{227}_{89}\mathrm{Ac} \left\{ \begin{array}{l} \xrightarrow[21{,}773\ \mathrm{y}]{98{,}62\%\beta^-} {}^{227}_{90}Th \xrightarrow[18{,}718\ \mathrm{d}]{\alpha} \\ \xrightarrow[21{,}773\ \mathrm{y}]{1{,}38\%\alpha} {}^{223}_{87}Fr \xrightarrow[21{,}8\ min]{\beta^-} \end{array} \right. {}^{223}_{88}\mathrm{Ra} \xrightarrow[11{,}434\ \mathrm{d}]{\alpha} {}^{219}_{86}\mathrm{Rn} \\
{}^{219}_{86}\mathrm{Rn} \xrightarrow[3{,}96\ \mathrm{s}]{\alpha} {}^{215}_{84}\mathrm{Po} \xrightarrow[1{,}778\ \mathrm{ms}]{\alpha} {}^{211}_{82}\mathrm{Pb} \xrightarrow[36{,}1\ \mathrm{min}]{\beta^-} {}^{211}_{83}\mathrm{Bi} \left\{ \begin{array}{l} \xrightarrow[2{,}13\ min]{99{,}73\%\alpha} {}^{207}_{81}Tl \xrightarrow[4{,}77\ min]{\beta^-} \\ \xrightarrow[2{,}13\ min]{0{,}27\%\beta^-} {}^{211}_{84}Po \xrightarrow[0{,}516\ s]{\alpha} \end{array} \right. {}^{207}_{82}\mathrm{Pb}_{(\mathrm{stable})} \\
{}^{232}_{90}\mathrm{Th} \xrightarrow[1{,}41\times10^{10}\ \mathrm{y}]{\alpha} {}^{228}_{88}\mathrm{Ra} \xrightarrow[5{,}75\ \mathrm{y}]{\beta^-} {}^{228}_{89}\mathrm{Ac} \xrightarrow[6{,}13\ \mathrm{h}]{\beta^-} {}^{228}_{90}\mathrm{Th} \xrightarrow[1{,}91\ \mathrm{y}]{\alpha} {}^{224}_{88}\mathrm{Ra} \xrightarrow[3{,}62\ \mathrm{d}]{\alpha} {}^{220}_{86}\mathrm{Rn} \xrightarrow[55{,}6\ \mathrm{s}]{\alpha} {}^{216}_{84}\mathrm{Po} \xrightarrow[146\ \mathrm{ms}]{\alpha} {}^{212}_{82}\mathrm{Pb} \\
{}^{212}_{82}\mathrm{Pb} \xrightarrow[10{,}64\ \mathrm{h}]{\beta^-} {}^{212}_{83}\mathrm{Bi} \left\{ \begin{array}{l} \xrightarrow[60{,}55\ min]{64{,}07\%\beta^-} {}^{212}_{84}Po \xrightarrow[299\ ns]{\alpha} \\ \xrightarrow[60{,}55\ min]{35{,}93\%\alpha} {}^{208}_{81}Tl \xrightarrow[3{,}05\ min]{\beta^-} \end{array} \right. {}^{208}_{82}\mathrm{Pb}_{(\mathrm{stable})}
$$

Figure 11.1.1: Radioactive decay chains identified in the SoLid detector: The cascades used in this manuscript are indicated in blue.[165]

background radiation facilities of Modane and Boulby. The most accurate measurement, indicated an activity of 69 ± 35 mBq/kg of pure LiF. The second largest contamination is found in ZnS, for which the upper limit on the rate is at least 5 times smaller. The detector has a total of 8.9 kg LiF, which yields a rate of 614 ± 311 mBq, which is also consistent with the measured intrinsic background rate by a dedicated analysis (see section 15.2.2).

Whether a decay chain shows up as an IBD like event is determined by the half life of the intermediate isotope before alpha decay. If the half life is similar to the thermalisation and capture time of the IBD neutron, the resulting time coincidence is similar to that of an IBD interaction, albeit with a non-neutron induced NS signal. Only the alpha-decay from ^{214}Bi to ^{214}Po followed by a beta-decay to ^{210}Pb in the uranium series is a relevant IBD background with the halflife of ^{214}Po around 164.3 μs. In the chain ^{212}Bi $\rightarrow$ ^{212}Po $\rightarrow$ ^{208}Pb, the half life of the intermediate isotope is 299 ns which is shorter than the IBD timing. The ^{212}BiPo background can be easily rejected by a minimum Δt requirement of 5 μs to $9 \cdot 10^{-4}$ % of the original. All other decay chains have intermediate isotopes with too long half lives, namely between 1.8 ms and $245.5 \cdot 10^3$ yr. The longer decays do not contribute to the correlated background, they do however contribute to the accidental background.

The cascade of the ^{214}Bi-^{214}Po disintegration constitutes a background when selecting IBD events. The ^{214}Bi isotope decays to ^{214}Po via beta emission with an end-point energy of Q_β = 3.27 MeV. The resulting Polonium isotope decays towards ^{210}Pb by emitting an energetic alpha particle with a fixed energy of E_α = 7.8 MeV. The β particle escapes the ^{6}Li:Zns(Ag) screens and scintillates in the PVT scintillator, resulting in a prompt signal. The energetic alpha particle can cause a delayed signal in the ZnS(Ag) scintillator, mimicking neutron capture.

Two categories can be distinguished in the ^{214}Bi-^{214}Po decays: decays to the ground state (19.1%) and decays to excited states (80.9%). For beta decays to the ground state, all energy is distributed between the emitted electron and neutrino. There are however also 65 excited states of ^{214}Po to which ^{214}Bi can decay. These excited states are extremely short lived, the remaining energy is radiated away almost instantaneously, decaying to the ground state via one or more gammas. In decays to excited states, the electron and the neutrino combined take at most 2.66 MeV of the 3.27 MeV. The remaining energy is carried away by photons with energies up to 3.18 MeV. Figure 11.1.2 shows the beta energy spectrum of ^{214}Bi decays, along with the IBD positron energy spectrum that is obtained from GEANT4 simulations [2]. The spectra overlap which indicates that the correlated background due to BiPo will be hard to reject. An important difference comes from the IBD neutron. After neutron capture the alpha and tritium particles share 4.78 MeV of kinetic energy, whereas the BiPo alpha caries ~7.8 MeV. In addition, a powerful discriminant may come from the fact that the IBD positron causes annihilation gammas, while no annihilation occurs for BiPo. However, the gamma rays that accompany the β decay can pose a background to the annihilation gammas.

The topologies of BiPo decays where ^{214}Bi decays to the ground state are fairly straightforward and are illustrated in figure 11.1.3. The β signal is contained in a single cube since the range of a 3 MeV electron in PVT is only 0.7 cm[188]. Since the electron is emitted from the lithium screen, it will scintillate in one of the two cubes facing the screen. As the electron is emitted isotropically, in 50% of cases the ES signal will be detected in the same ccell as the α signal and in the cube at $X+1$ or $Z-1$ with respect to the α cube in 25% of cases each.

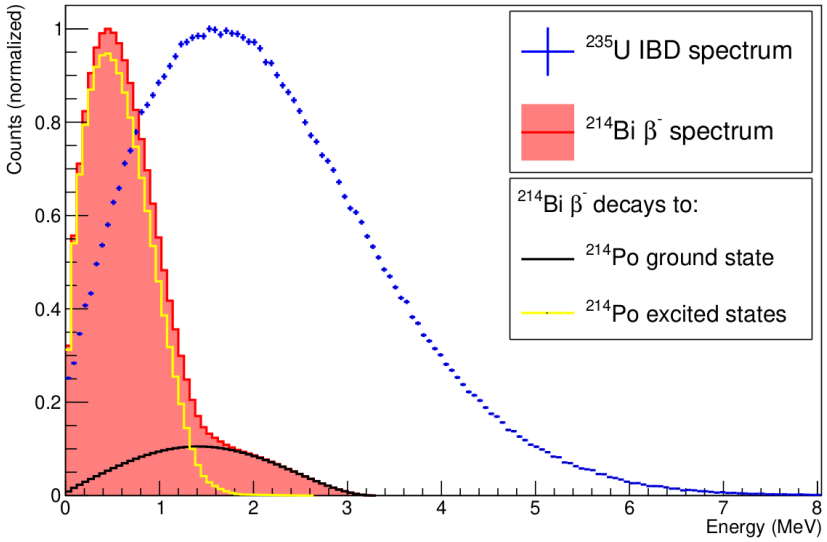

Figure 11.1.2: Comparison of the electron energy spectrum in ^{214}Bi beta decay (red, filled) to the positron energy spectrum from IBD interactions originating from ^{235}U (blue). Also shown are the contribution from decays to the ground state of ^{214}Po (black) and to excited states (yellow).[162]

For ^{214}Bi decays into excited states of ^{214}Po, these gammas are not contained to the three cubes in which the electron can deposit its energy. The lowest Q-value of beta decays into excited states is only 0.09 MeV. Those emitted electrons will simply not be detected. The ES signal of much of the excited state decays is thus dominated by the gammas emitted in the ^{214}Po de-excitation. Additionally, not all decays from excited states to the ground state are allowed, which therefore take place via intermediate states. This leads to on average 1.34 gammas being emitted in a single decay as good as simultaneous (the longest living excited state has a half life of 99 ps). Each gamma can undergo Compton scattering multiple times. Both these characteristics increase the number of cubes with an ES signal in the detector, increasing the ES signal multiplicity.

11.1.2 EXOGENOUS RADON CONTAMINATION

Apart from the contamination of the lithium screens itself, the same radioactive elements are ingrained in the concrete of the BR2 containment building, which gives an additional source of correlated background. Concrete is a mixture of water, cement and filler. Both water and filler have a relatively low concentration of uranium and thorium. However, cement has a ^{226}Ra activity between 37 and 64 Bq/kg [189]. For the structural parts such as the ceiling and floors ordinary concrete was used and for the reactor vessel heavy barite concrete was used, where the filler of sand and gravel is partially or completely replaced by ground barite ($BaSO_4$). The heavy concrete has a stronger attenuation against high energy gammas from the reactor pool, because of the higher density of the barite concrete in comparison with the ordinary concrete (3.5 g/cm^3 instead of 2.3 g/cm^3) and its higher atomic number.

Due to the chemical similarity of barium and radium, radium is readily adsorbed into $BaSO_4$ crystals, resulting in relatively high concentrations of radium (typically between 9.2 and 15 Bq/kg but this could go up to 1 kBq/kg)[190]. The large amount of concrete in the BR2 building, over 5000 ton, creates a

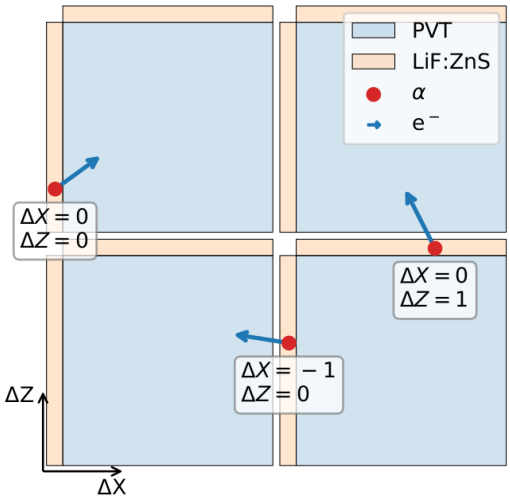

Figure 11.1.3: Diagram representing the different topologies expected for the ^{214}Bi-^{214}Po cascade without gammas. The β particle from the ^{214} Bi-decay annihilates in the PVT cube, while the energetic α particle from the ^{214}Po decay excites the ZnS scintillator. The detector is represented in the plane $\Delta Y = 0$.[165]

vast and virtually everlasting supply of radium. Luckily, most of the concrete is located far enough from the detector such that only gaseous isotopes can reach the detector to induce backgrounds. From all the elements in figure 11.1.1, only radon (Rn) is gaseous. It can collect in small cavities and seep out of microscopic cracks in the concrete, resulting in variations of the radon concentration in the air of the BR2 building and hence in the air surrounding the detector.

The airborne radon isotope can produce along its decay chain several α and β particles, most notably the Radon-Polonium cascade. The latter is characterised by the emission of two alphas close in time. Although the double alpha nature of the phenomenon is not a direct background noise in research of IBD events, the analysis of this coincidence provides important information to the nature of the background noise of the detector. A dedicated Rn-detector was installed inside the SoLid container, to constantly monitor the amount of ^{222}Rn [160].

11.2 REACTOR GAMMAS AND NEUTRONS

Given its location near a nuclear reactor, the SoLid detector site sees a lot of reactor induced backgrounds. The reactor induced gamma and neutron backgrounds scale with the reactor power and contribute to the accidental background, i.e. the background arising from the random coincidence of a gamma and an uncorrelated neutron. BR2 has a low reactor background compared to other research reactors and nuclear powerplants.

The gamma background was measured in situ[191] with two different Germanium detectors[192]. Figure 11.2.1 showcases the BR3 Ge-detector and the UGent Ge-detector. As Germanium detectors are energy sensitive, specific lines in the gamma ray spectrum can be distinguished and investigated. Figure 11.2.2 shows an example of the full recorded gamma spectrum during reactor operation, in

Figure 11.2.1: Germanium detectors, provided by SCK-CEN (left) and provided by Ghent University (Right)

which peak identification is performed. Peaks indicated with an asterisk are backgrounds related to reactor operation. The intense peaks come from the fission products ^{137}Cs and ^{60}Co, while ^{41}Ar is activated in the air by the capture of a reactor neutron on the natural ^{40}Ar in the air. Because it is an airborne element, the detected rate of ^{41}Ar depends a lot on environmental conditions such as the pressure in -and the ventilation of the reactor building. In addition isotopes from the decay chains of natural contamination are present, as shown in figure 11.1.1. ^{214}Bi is part of the ^{238}U series, whereas ^{212}Bi, ^{228}Ac ^{208}Tl and ^{212}Pb are part of the ^{232}Thorium series. ^{40}K is another source of radioactivity that is naturally present in the BR2 building materials.

Gamma ray spectra were recorded for different positions, orientations, shieldings, and reactor powers. For each measured spectrum, six reference lines were fitted, namely ^{214}Bi at 609 keV, ^{40}K at 1461 keV, ^{60}Co at 1173 keV, ^{60}Co at 1332 keV, ^{41}Ar at 1293 keV and the 511 keV annihilation line. The rate of the gamma spectrum was monitored during shut down of the reactor, starting from 54 MW. The spectrum was seen to increase with reactor power. The reactor on spectrum is dominated by the ^{41}Ar line at 1294 keV ($T_{1/2}$ = 1.83 h), while the line is not present for reactor off. The natural backgrounds stayed more or less constant, as did the lines from long-living fission products. Measurements at the R1 alcove in the reactor wall in front of the detector, showed that adding shielding in the alcove significantly reduced the annihilation line and the ^{60}Co lines with a factor 10. Measurements of the gamma spectrum from a Europium source behind a waterbrick demonstrated the benefit from additional shielding for the SoLid detector with a waterwall. The observed transmission for different lines in the ^{152}Eu gamma ray spectrum was on average 4.06 ± 0.98 %. Consequently, the SoLid

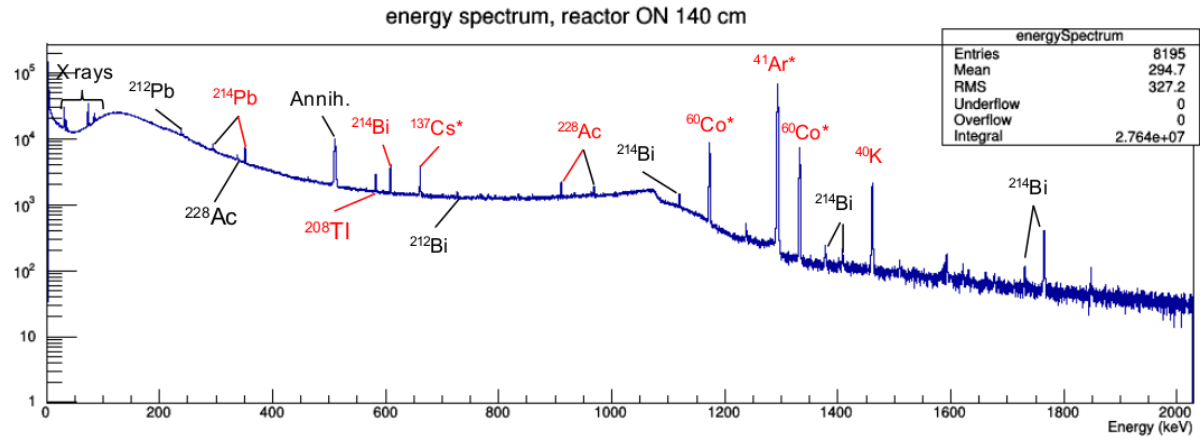

Figure 11.2.2: The gamma background spectrum measured with a Ge-detector at the position of the SoLid experiment in the BR2 reactor hall. Some of the characteristic gamma lines are labeled with the element they originate from.[191]

collaboration has built a water wall and HDPE ceiling to create a 50 cm thick layer of detector shielding.

The deposited gamma energies lie mainly below the trigger threshold of 2 MeV. Some gamma rays will give rise to an accidental coincidence background, when they occur in time proximity of a neutron like signal that is similar to the IBD time coincidence window. The time difference between accidental candidates is usually much larger than that of correlated events, and their Δt distribution can be considered uniform over the relevant range. The gamma and neutron signal do not originate from the same physical event and therefor create random topological configurations. The distribution of the spatial separation of both signals will be relative broad, compared to the IBD signal. Based on these characteristics, the accidental background can be estimated and subtracted from the signal. In addition, the low energy gammas could become a background for the annihilation gammas from the IBD positron.

11.3 COSMOGENICS

Cosmogenic signals in the detector arise from air showers induced by cosmic rays. When a cosmic ray, a high energy charged particle, impinges on the Earth's atmosphere, it will interact with oxygen -and nitrogen nuclei[193]. Energy transferred in the collision will heat the nucleus, requiring it to cool down via either neutron evaporation or breaking up. When the nucleus breaks up, an avalanche of particles is created, initiating a cosmic ray air shower. The cosmic ray is typically a proton (86%) or an alpha particle (11%) while the particles created in the cosmic ray air shower are pions (91%) and kaons (9%). The latter decay into gammas, muons and neutrinos and in case of kaons also into pions. Hard interactions of all air shower particles with atoms in the atmosphere can propagate the avalanche. Of the aforementioned particles, only muons, neutrinos and neutrons do not interact strongly with matter and can make it to ground level and even penetrate the earth up to a certain depth depending on their energy.

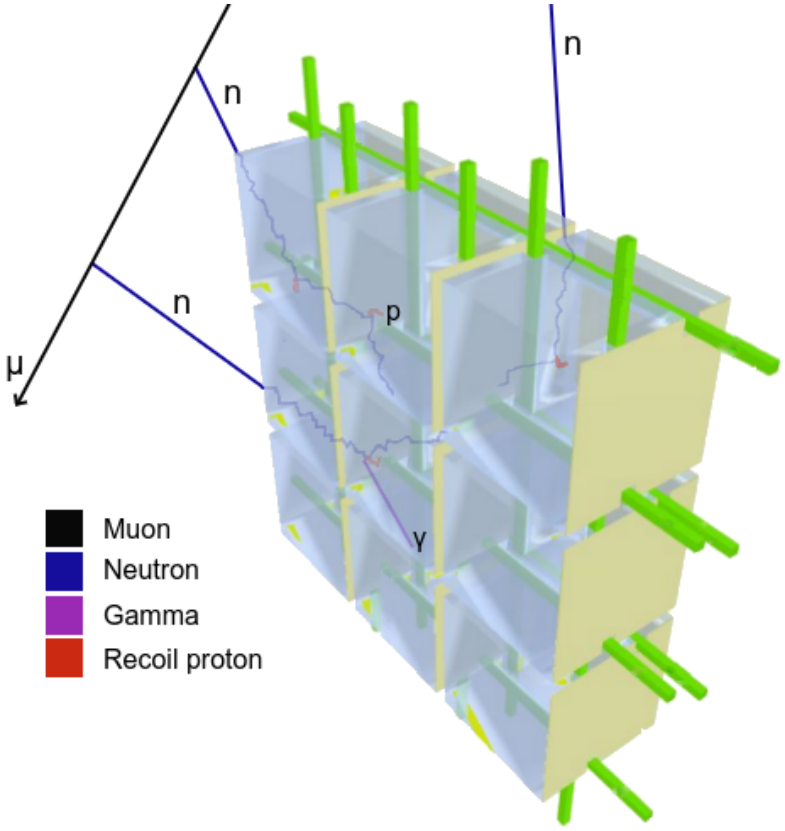

Figure 11.3.1: Sketch of muon induced spallation in material surrounding the detector and the resulting fast neutrons that may recoil on hydrogen nuclei and can be thermalised and captured afterwards in ^{6}Li of the neutron screens in the detector.

Because of the high rate of cosmic muons, most neutrino experiments take place below ground, in deep mines or under mountains, to minimise the related backgrounds. Unfortunately, SoLid is located at the BR2 reactor site at 10 m above ground level and with very little overburden, leaving a challenging background coming from both muon- and neutron secondary cosmic rays, as well as from the fast neutrons that are generated by the interactions of the former in the material surrounding the detector, as shown in figure 11.3.1. The expected detection rate of the atmospheric neutrino flux is so small that it can safely be ignored. The next section will discuss the effect of muons on the detector. The effect of the atmospheric neutrons will be discussed in the following section.

11.3.1 Cosmic muons

Sufficiently high energy muons can make it to ground level while still being minimally ionizing particles (MIP). When crossing the SoLid detector, the muons exhibit a narrow distributed stopping power. A MIP muon deposits in each PVT cube that it crosses a visible energy of 1.8 MeV/cm [144]. A muon can travel through a large number of consecutive cubes, leaving a high energy deposit in each cube that depends on the track length. These 'track muons' are highly recognisable, making them easy to reject, and even useful for continuous, online detector monitoring.

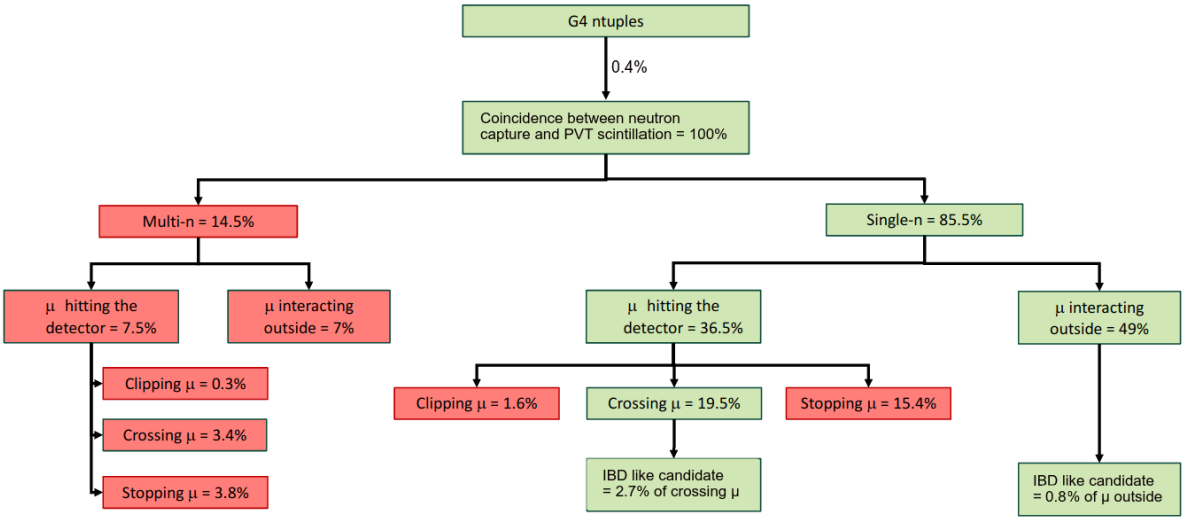

Figure 11.3.2: Classification of simulated muon events that cause a coincidence between a prompt PVT signal and a delayed neutron signal.[194]

Muons can also decay in the detector, resulting in the production of a Michel electron or positron with a characteristic delay corresponding to the muon life time. The muon track ends somewhere in the detector and is classified as a 'stopping muon'.
In some cases, muons can clip the detector edges, leaving an isolated energy deposit that can contribute to the accidental backgrounds in the detector. A track can not be reconstructed making the muon harder to discriminate. these clipping muons are referred to as 'cube muons'.

Cosmic ray muons can also induce spallation reactions in materials near or inside the SoLid detector that produce neutrons or radioisotopes. The rate of neutron production increases with muon energy and with material density. Roughly one third of the spallation neutrons are produced inside the detector, while the rest is created in surrounding structures. In the latter case, the high energy spallation neutrons can enter the detector and cause IBD like signals, posing a challenging background. They are hard to identify and reject, as the muon does not cross the detector. The topology of these events is identical to that of atmospheric neutrons and will be discussed in the next section.

With the cosmicGen generator and the GEANT4 software [2], that will be described in chapter 12, an equivalent of 32 real hours of muon events were produced. Muon events that had a coincidence between a neutron capture (NC) and an energy deposition in the PVT, were classified according to the types discussed above. The classification is shown in figure 11.3.2. Since only muon events that result in IBD like processes are of interest to the analysis, only events that result in a coincidence between a prompt PVT signal and a delayed ZnS(Ag) signal that come from spallation muons are classified. Only single neutron events have been selected since neutron multiplicity will be easily excluded from the IBD analysis. Stopping muons can be reconstructed and excluded as well. From the remaining events, the biggest contribution comes from crossing muons and muons interacting outside the detector. For these, IBD like events are selected, where the following requirements are imposed on the time difference, Δt, and the spatial distance, R, between the prompt, p, and delayed, d, signal, and on the prompt energy deposition, E_p,

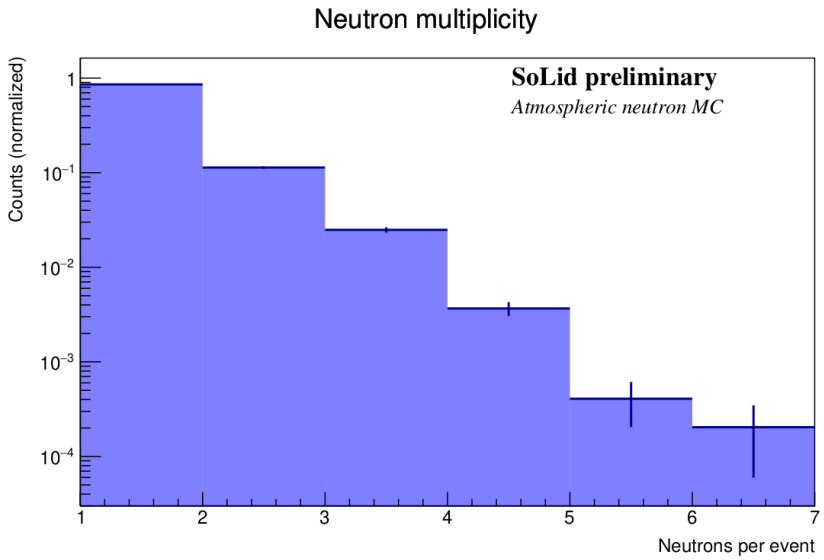

Figure 11.3.3: Captured neutron multiplicity for simulated atmospheric neutron events[162].

- Δt(d-p)$\in$ [0, 120] μs
- $0 \leq \Delta R(\text{d-p}) < 3$
- $E_p \in$ [100 keV, 10 MeV].

From the muons interacting outside the detector, relatively few are IBD-like. This is because external muons cause less PVT signals relative to neutron captures. Namely 15 PVT signals for each neutron capture, whereas for crossing muons 76 PVT signals are created for each neutron capture.

11.3.2 FAST NEUTRONS

The background component of fast neutrons consists of atmospheric neutrons and spallation neutrons caused by muons. The atmospheric neutrons have a complex energy spectrum ranging from sub-eV to multi-GeV. Due to its low overburden, the SoLid detector is subject to a high rate of fast neutrons. Only a fraction of muons and neutrons that enter the building reach the detector. The fast neutron rate is anti correlated with the atmospheric pressure, as the latter increases the density of the air column through which the muons and atmospheric neutrons have to propagate, which causes a higher attenuation. In addition, the passive water shield of 50 cm surrounding the experiment, and the Cd sheets placed on the outer walls of the container help to thermalise and capture some of the neutrons. Figure 11.3.1 shows that the fast neutrons (possible after muon spallation) can penetrate the shielding and enter the active detector volume where they create recoils on several hydrogen atoms.

These recoil protons cause a scintillation signal in the PVT. In order for recoil protons to be observed, their energy must be of the order of several MeV. As a result, the detectable proton recoil events are produced when the neutron has an energy greater than several MeV. For a proton recoil chain, a significant time deviation between their signals is not expected. The fast neutrons are moderated and

then detected as delayed signal. The typical time difference between the prompt and delayed signal for fast neutron recoils of ~ 70 μs makes this correlated background hard to discriminate from the IBD processes that have a time difference of ~ 60 μs. The slight difference between these Δt values found for fast neutrons and IBD neutrons is attributed to the generally higher energy of the atmospheric neutrons, which is assumed to increase their thermalisation time.

The time correlated background from fast neutron dominates the selected IBD event samples for PVT signals with energies above 5 MeV. However, the multiplicity of the fast neutrons signals, shown in figure 11.3.3, is higher than for IBD. For the simulation of one cosmic muon or one atmospheric neutron, if at least one neutron is captured in the detector, on average 1.7 neutrons are captured in total. In addition the fast neutron background has a high variety of topologies. Multiple proton recoils give rise to multiple PVT signals and gamma rays might be created in the collisions. The original muon may produce multiple spallation neutrons, giving rise to several neutron captures.

12

SIMULATION OF INTERACTIONS IN THE DETECTOR

Within the SoLid collaboration the particle physics group of the University of Antwerp has been largely responsible for the implementation and maintenance of the simulation software of the SoLid experiment. This simulation chain can be split up in three main parts: the generators of the events, the simulation of the geometry and the materials of the detector and the experimental site, and the simulation of the optical transport and the readout of the detector. The first two parts are described in the present chapter, while the latter is detailed in chapter 13.

The different interactions and decays in the detector are simulated with the simulation package for GEneration And Tracking of particles, GEANT4 [2]. The package contains C++ libraries that allow to track the energy loss and the creation of secondaries for particles and radiation, through complex materials and geometries. The simulation provides insight on the signature of the different processes in the detector. The geometrical structures can be conveniently simulated, including all involved materials with their properties. The GEANT4 toolkit contains the physical properties of the fundamental particles and interactions. The trajectory and interactions of particles can be simulated with Monte-Carlo methods in the BR2 reactor building and in the SoLid detector volume. The data of all particles and interactions, and the energy depositions inside the sensitive detector components can be stored.

12.1 SIMULATION OF THE EXPERIMENTAL SITE

The large structures of the BR2 building are only modeled by approximation in GEANT4 by the SoLid collaboration [141], based extensively on detailed blueprints of the reactor building and survey measurements performed prior to detector installation. The BR2 containment building, including the cylindrical inner and outer walls and dome cap are reproduced schematically. The concrete floors of level 3, where the detector is located, level 2 below the detector and levels 4 to 7 situated above the detector, as well as specific features such as staircases, elevator shafts, crane passways, and access holes are included in the model. These structures affect the transport of cosmic radiation, such as muons and neutrons, and are necessary to estimate the background rate in the detector. The container that houses the detector, the water wall, the shielding and the instrumentation inside the container are modelled without reproducing the fine details, but with accurate positioning. The visualization of the containment building and the container outline can be seen in figure 12.1.1.

Special care is taken to model in detail the reactor fuel tank, the water pool and its concrete walls with beam ports including concrete and steel plugs, the 20 cm thick lead shielding wall in between the SoLid detector and the radial beam port facing the reactor core, as shown in figure 12.1.2. The coordinate system (X,Y,Z) is a right handed system with the Z axis following the direction of the flux from the reactor, i.e. away from the core. The Y axis is oriented upward along the height of the detector.

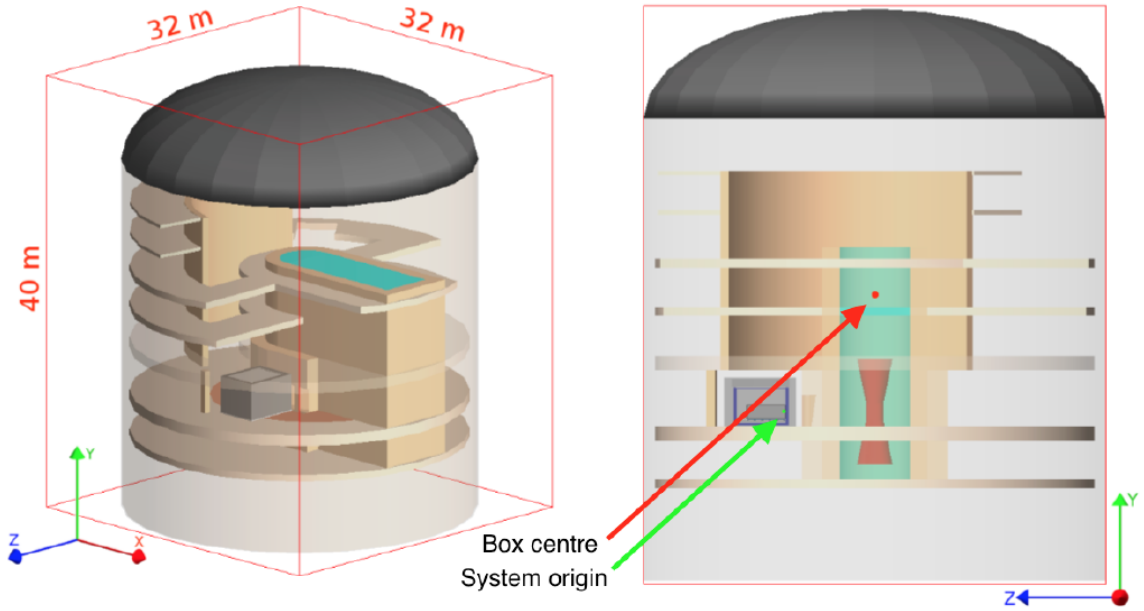

Figure 12.1.1: Overview of the entire BR2 geometry.[141]

The center (0,0,0) of the coordinate system for simulation purposes is located in the bottom corner of the PVT cubes array such that the cubes have positive coordinates. The BR2 structures considered here are simplified and with estimated dimensions.

The Phase I detector is simulated in great detail and with a high level of accuracy. The diferent components of the detection cells, the wavelength shifting fibers, the MPPCs and mirrors, the aluminium frames, tyvek sheets, and neutron reflectors are implemented. In addition, the CROSS calibration system, is modelled with precision, because of its proximity to the detector. The details of the different components, such as their composition, density and volume, can be found in the dedicated document [184].

12.2 SIMULATION OF PARTICLE INTERACTIONS

For different signal and background processes (that were described respectively in chapter 10 and 11), the relevant particles can be propagated through the geometry of the reactor building and the detector. Their possible interactions are dictated by the selected physical models in the GEANT4 simulation. Particular attention had to be paid for neutron transport. Of crucial importance to the SoLid experiment is the capture of thermalised IBD neutrons with an energy as low as 0.025 eV. However, for sub-eV energies, the elastic scattering of the neutron on hydrogen can no longer be simulated based on elastic cross sections in an ideal gas. The chemical bonds between atoms have to be taken into account, which modifies the cross sections and energy transfers. Since there is no available model or data for PVT, which contains almost all of the moderator, the collaboration relies

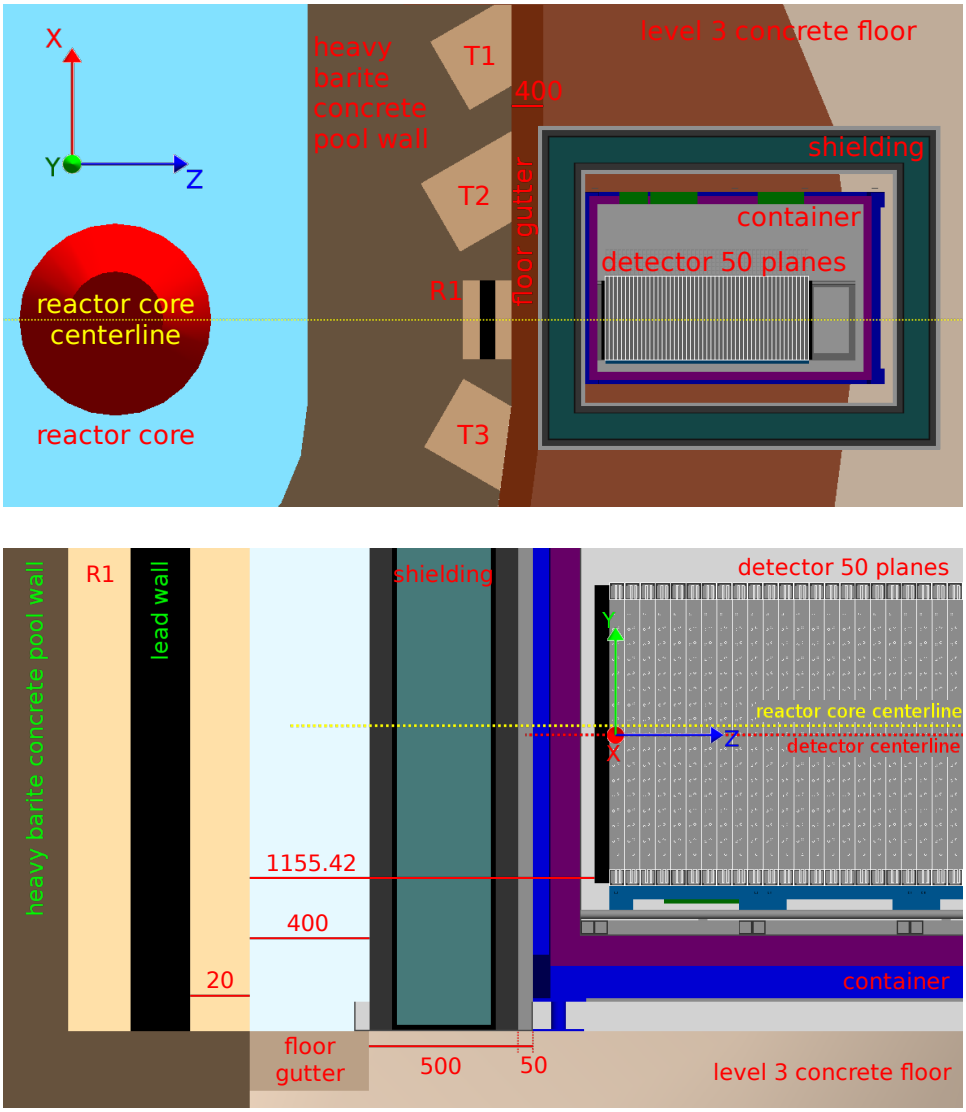

Figure 12.1.2: Top: Top view of SoLid detector in proximity of the BR2 reactor core with horizontal cut. Bottom: zoomed side view with vertical cut through X = 0.[184]

on reference cross-sections measured for polyethylene [195], whose chemical composition is very close to that of PVT. These features are imported in GEANT4 via dedicated neutron libraries.

12.3 EVENT GENERATORS

In addition to the particle generators provided by the GEANT4 software, the collaboration developed several event generators, specifically for the signal and backgrounds in the SoLid experiment.

The detector response to IBD interactions by BR2 reactor neutrinos can be simulated with GEANT4 using the input from the SoLO generator, which was described in chapter 10. The generator provides the GEANT4 simulation with a list of neutrino interactions inside the detector, specifying the neutrino's energy, momentum and interaction vertex. For each IBD event, a positron and a neutron are

generated with an energy and momentum derived from the one of the neutrino. The trajectory and energy depositions of the positron and its annihilation photons are simulated. The thermalisation and capture of the neutron and the energy deposition of the generated alpha and tritium particles are simulated as well.

To simulate events from the BiPo decay chain, random decay vertices are generated in the ^{6}LiF:ZnS screens throughout the detector, directly inside GEANT4. The subsequent decays with corresponding half lifes and energies are simulated. The GEANT4 simulation indicates that the capture efficiency for the BiPo alpha particle is around 99-100 %.

For calibration purposes (which will be described in chapter 9), several gamma and neutron sources are simulated. ^{252}Cf and AmBe neutron sources are modeled according to the energy spectra of the ISO standard from the International Organization for Standardization [168]. The decays of the gamma and positron sources, ^{22}Na,^{137}Cs, ^{207}Bi, are simulated as well.

Cosmogenic events are simulated with the dedicated CosmicGen code [173], with a realistic rate and spectrum. The muons are produced with the CRY generator[196], which is validated with the Guan [197] and Reyna [198] generators. The atmospheric neutrons are generated according to the Gordon parametrisation [199]. The neutron generation is scaled to the BR2 reactor site elevation and latitude, and cross-checked with the more general purpose CRY generator. In CosmicGen, the generation surface is located 30 m above the top of the detector. The extent of the surface is 300 m × 300 m, which is the smallest size that does not alter the angular distributions in the CRY generator significantly. To reduce the output file size, only secondary particles are stored that reach a predefined bounding box. Since interactions in the surroundings of the detector, especially in the wall of the reactor vessel, produce an important background, a bounding box was chosen that encompasses the whole BR2 building. Figure 12.1.1 shows how the box of 32 m × 40 m × 32 m is centered around position (-2, 8, -6.3).

The GEANT4 simulations provides the collaboration with the spatial and temporal distributions of the expected energy deposits for each of the possible interactions in the SoLid detector. This information will be passed to the readout simulation that is introduced in the following chapter.

13

THE READOUT SIMULATION

The readout simulation is a standalone readout software library which is specific to SoLid. The development and maintenance of this C++ code was my responsibility during my Phd and as such I developed and implemented most algorithms, based on dedicated lab bench measurements, reactor off data and manufacturer's specifications on detector components.

The readout simulation reproduces the detector response. The first part of the simulation concerns the scintillator response and is described in section 13.3. The light yield, the distinct time characteristics of the PVT and ZnS(Ag) scintillators, and the energy quenching in PVT are simulated. The photon losses due to scattering and absorption are factored in. The PVT scintillator's light yield will be further fine-tuned in section 13.4.1 to the measured light yield during calibration campaigns using gamma sources.
The simulation of the attenuation effects during optical transport in each channel separately is based on calibration measurements and is described in section 13.4. The simulation of photon generation and transport results in a time distribution of photons that arrive at any of the sensors.
The simulated signal, produced by the sensor and readout electronics, is described in section 13.1. The simulation reproduces the pixel voltage settings and voltage recovery model, the photon detection efficiency, and the different mechanisms of sensor noise, such as thermal noise and the probability of cross-talk. The characteristic pulse shape of a pixel avalanche is simulated and the sensor's pulses are converted into digital waveform signals. The signal is sampled with the same frequency and resolution as the ADCs of the SoLid detector.
In section 13.2 is described how the readout simulation emulates the trigger and readout logic that is used in the data acquisition systems. As a result, the readout simulation translates the simulated energy depositions, as produced by GEANT4, to data-like output waveforms.

I integrated the readout simulation in the Saffron2 framework such that the simulated waveforms can be stored in the same objects as data waveforms, and can be immediately analysed by Saffron2, avoiding the storage of intermediate data files and an additional output-input step. In addition, the readout simulation can use the tools that are available in Saffron2, such as the specification of the detector setup and the different reconstruction objects. Conversely, during reconstruction and analysis, the information provided by the readout simulation can be taken into account.

Because the tuning of the scintillator response and the optical transport relies on data versus Monte-Carlo comparisons of observed quantities, I will first describe the simulation of the sensor and the trigger- and readout system.

13.1 SIMULATION OF THE SENSOR

One of the main parts of the readout simulation is the simulation of the sensors. Each of the 3200 sensors of the SoLid detector are simulated as separate objects in the readout simulation. Each sensor receives a time distribution of incident photons from the algorithm that simulates the scintillation and photon transport (see sections 13.3 and 13.4). Each photon is randomly assigned to a pixel, such that the illumination of the pixel matrix is uniform, since the square cross section of the WLS fibers leads to a uniform flux of photons on the square MPPC sensors [200].

It can occur that there is a substantial empty time between generated photons. For example, the time between decays in the ^{214}Bi-^{214}Po decay chain can become $\sim 10^{17}$ ns, which is about a day. To avoid the intensive simulation of pure noise during this time, the simulation timespan is split into separate windows whenever the time between two photon arrivals is larger than 500 000 ns (about 75 blocks).

In section 6.3, models that describe the different operation mechanisms of the sensor were determined, along with the relevant parameters, based on measurements with dedicated testbenches [158], random noise-only data from the SoLid detector [155], and specification sheets from the manufacturer [154].

For the photon detection efficiency (PDE) and the recovery model of the pixel voltage, the analytic models given respectively by equation 6.4 and 6.1 are implemented as such in the readout simulation. For the simulated recovery model, the time t is the time since the last photon hit any pixel of the sensor. The PDE is evaluated in the readout simulation as the ratio of avalanches that are actually induced in the sensor, versus avalanche triggers that have the potential to induce an avalanche, such as incident photons or thermal noise. The PDE is 34.7 ± 1.5 %, which is in agreement with the implemented model that was shown in figure 6.3.2.

In the readout simulation, the dark count rates are generated for each channel separately, by selecting it from a Poisson distribution around the mean DCR that was obtained from data, namely 118.7 Hz. For each appointed channel, noise is generated based on its channel specific DCR. Each darkcount is assigned a time, which is uniformly random in the simulation window, and a sensor pixel which is also uniformly distributed. Whether the dark count actually leads to a pixel avalanche depends on the momentary overvoltage of the pixel. When the pixel is recovering, the probability is reduced as

$$P(PA) = \frac{DCR(t, V_{pix})}{DCR(t, V_{nom})}, \tag{13.1}$$

with the momentary pixel overvoltage V_{pixel}, compared to the nominal overvoltage V_{nom}.

The sensor simulation is based on a list of 'triggers' that can potentially induce a pixel avalanche. The avalanche triggers are processed in time order. The initial list of potential triggers consists of the incident photons and dark counts. For each potential trigger is determined whether it causes a pixel avalanche (PA) based on the PDE of 34%. If it does, the relevant information is stored to a list of avalanches. After an avalanche, the pixel is insensitive for incoming photons for a short time period because its overvoltage is reduced to zero. The pixel voltage restores to nominal overvoltage, following the exponential recovery model with a time constant of 24.28 ns. The crosstalk model determines

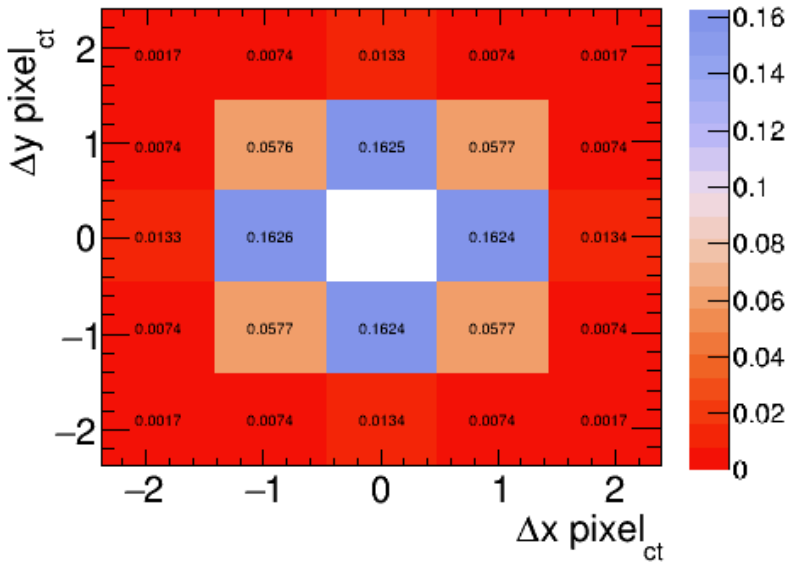

Figure 13.1.1: Pixel in which crosstalk occurs (relative to the initially firing pixel, and in the sensor).

whether additional noise is generated. The number of cross talk avalanches is determined from the crosstalk probability, $P(ct)$, of 19.5 %, that was obtained with data. The number of crosstalk events is Poisson distributed with a λ value [158] of

$$\lambda = -\log(1 - P(ct)) .$$

The crosstalk process happens instantaneously compared to the typical pixel recovery time (i.e. on a timescale of $\sim$ 1 ns or smaller). It is important to determine in which neighbouring pixel the cross talk occurs; when the pixel is recovering, subsequent cross talks face a lower PDE to induce an avalanche. The cross talk is assigned to a neighbouring pixel with a probability that is indicated in figure 13.1.1. For each cross talk, an additional trigger is inserted to the list of triggers in correct time order. This allows higher-order noise cascades to be dealt with in a natural way.

To obtain a digital waveform signal, for each PA, its pulse shape is modeled following equation 6.5, where the simulated timestamp of the PA, t_p, is used. The timestamp can have any value in ns. In order to obtain a signal with a sampling of 25 ns, the equation is evaluated for 10 samples before and 15 samples after the timestamp. The discrete pulse values are used to construct the waveforms. In case the samples of different PA coincide in time, their pulse values are added. If the samples follow one another, they are appended to each other and form one waveform. If the samples of different PA are further than 1 sample from each other, they become part of separate waveforms. In the end, the simulated signal consists of a vector of waveforms that are each specified by a timestamp and a vector of samples.

Finally, a constant baseline value and a small amount of white noise is added to the channels' waveform signals. These quantities are discussed and modeled from random noise data in appendix A. To simulate the noise, a Gaussian smearing is applied to the ADC sample amplitudes around the nominal baseline. The RMS of the noise corresponds to the values measured in data and equals 2 ADC.

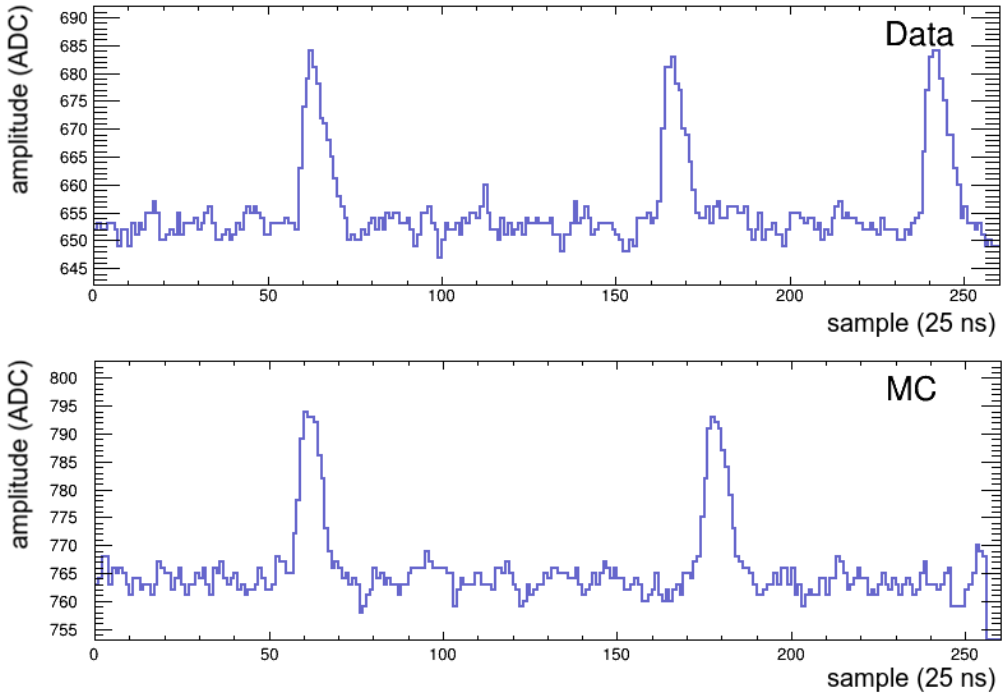

Figure 13.1.2: Example waveforms that contain dark counts from noise only data taken with the random trigger for data (top) and simulation (bottom).

13.1.1 Comparison between data and simulation

To validate the performance of the sensor simulation, noise waveforms are generated in dedicated noise windows on all detector channels. The noise is constructed from pixel avalanches caused by dark counts and cross talks and contains a baseline with white noise. An example of a simulated noise signal is shown in figure 13.1.2, alongside the noise present in real data. Since the simulated data is stored in the same format as real data, the analyses that were applied to data in section 6.3 in order to determine the pulse shape, the dark count rate and the cross talk probability can be applied to the simulation as well. The comparison of the results for data and simulation is shown here.

The amplitude spectrum of the noise samples is collected over all channels, for both data and simulation. Their absolute comparison is shown in figure 13.1.3. The data and Monte-Carlo spectra are scaled separately with respect to the total duration of the random noise, which is around 0,006 s for data and 0.64 s for simulation. The agreement of the absolute rate is very good. In the simulated spectrum, the amplitudes of multiple coinciding avalanches are more pronounced. The actual electronics may contain more noise or additional noise sources. The contributions of the amplitudes from multiple PA, indicate that the contribution from darkcounts and crosstalks is well simulated.

The comparison of the pulse shape of a single pixel avalanche (PA) in data and simulated waveforms is shown in figure 13.1.4. The central shape is reproduced well. Towards the edges, the pulse shapes are seen to deviate. For the simulation, when the average pulse shape is fitted with two Gaussians, the standard deviations of the fits are respectively 2.11 samples and 3.91 samples for the rising and falling edge. For the data pulses, we found 1.98 samples and 4.17 samples, which corresponds within 7 %.

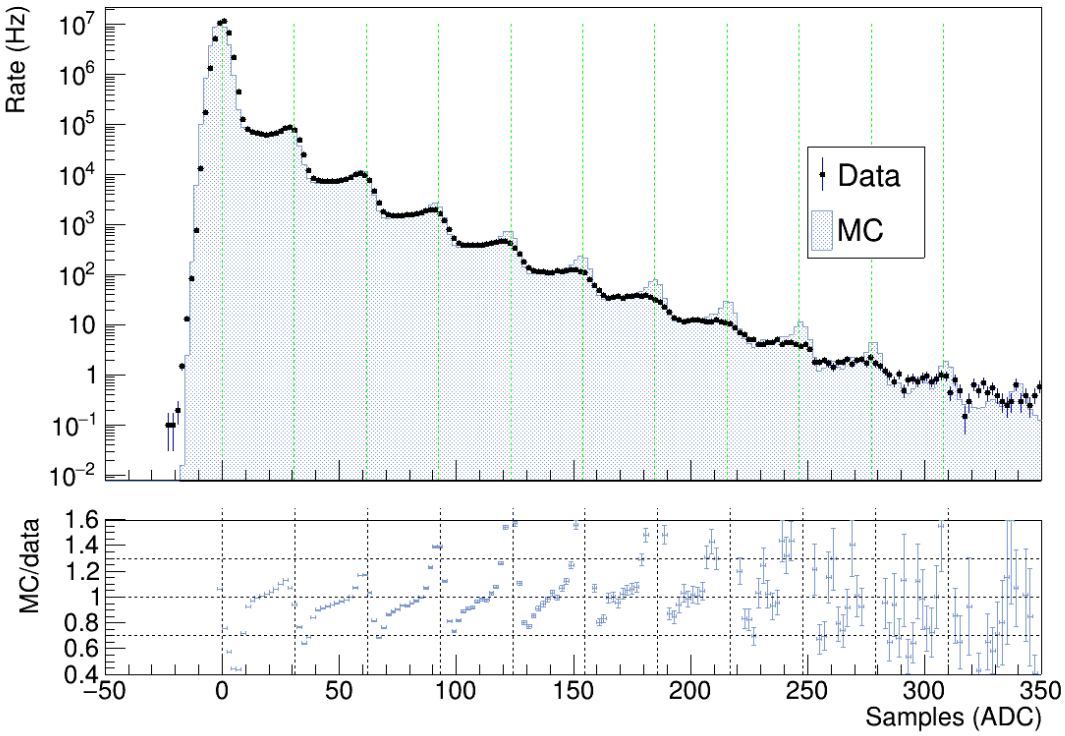

Figure 13.1.3: MC data comparisons for the amplitude spectra of the noise.

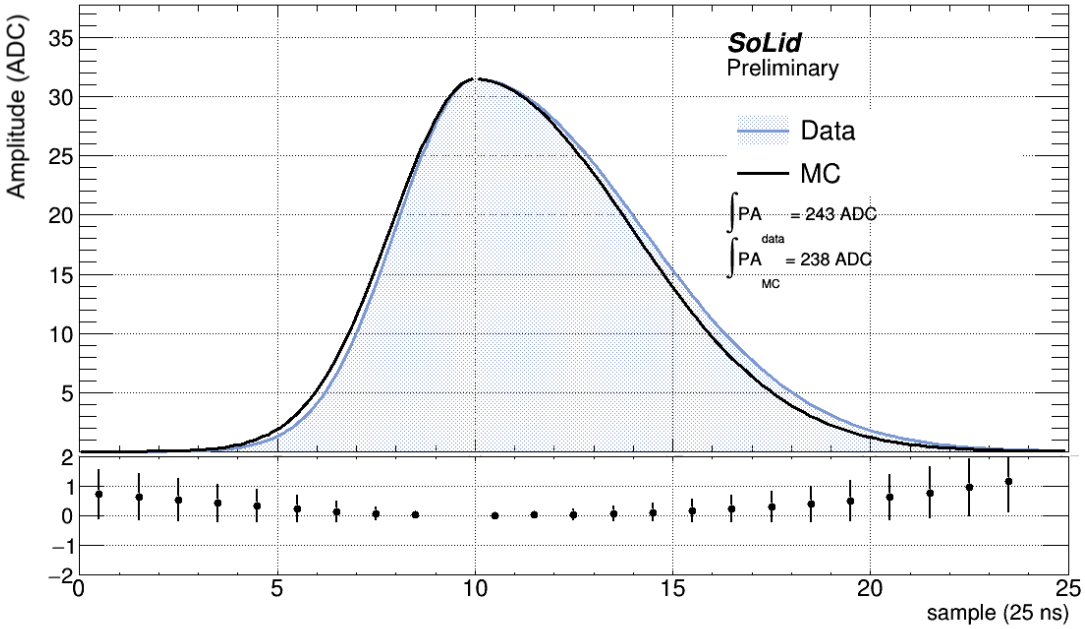

Figure 13.1.4: Comparison between the modeled pulse shape for data and simulation according to procedure 2, where a fit is performed on the average selected pulse.

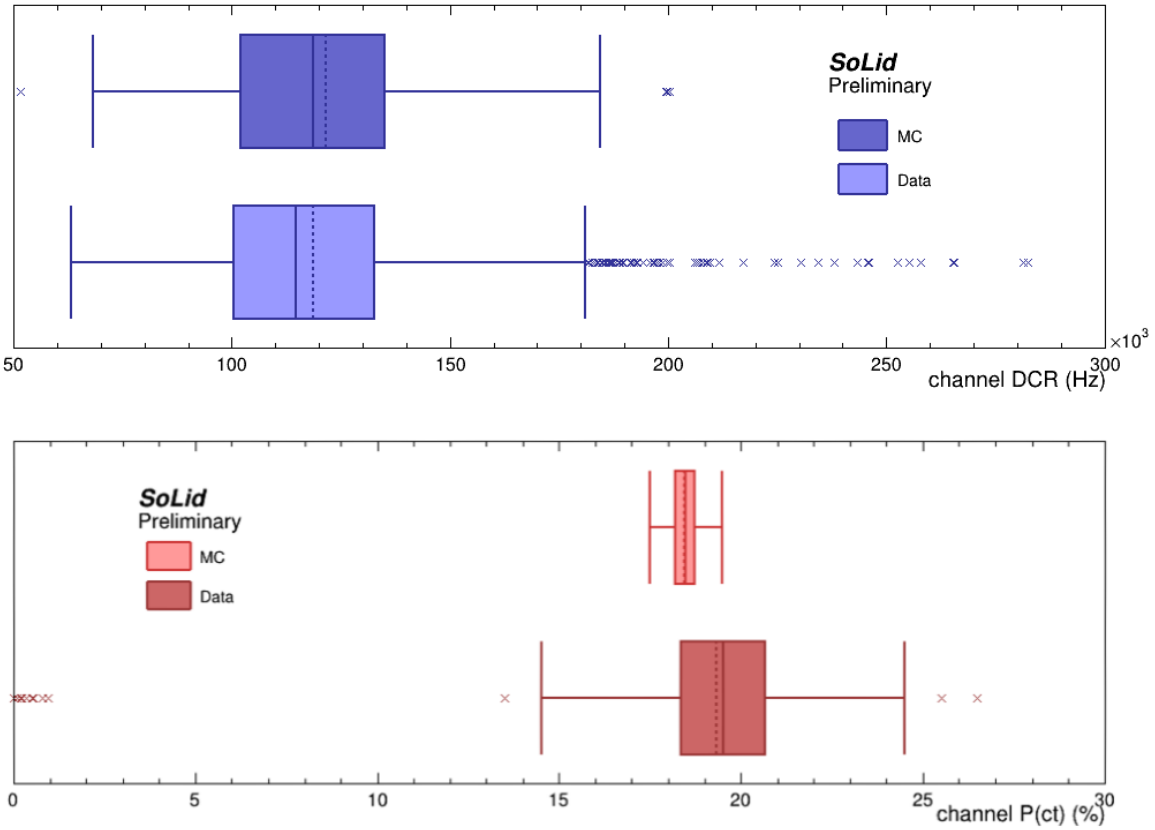

Figure 13.1.5: candle plots for data and simulation of the channel DCR (top) and of the crosstalk probability (bottom).

The integral of the pulse shape is another important metric as it is used for the integral on amplitude (IonA) value to discriminate NS signals. The integral is 243 ADC in data and 238 ADC in simulation, which agrees at the 2 % level.

The channel dark count rates obtained for data and simulation are compared in the top panel of figure 13.1.5 by the candle plots of their distributions. Good agreement in the average value and the spread of DCR is obtained. The data shows outliers towards higher rates. This is not surprising, as the variation between individual MPPCs is expected to be large. The average DCR is 118.7 Hz for data and 121.8 Hz for simulation, which agrees at the 3 % level.
The bottom panel of figure 13.1.5 shows the data versus Monte-Carlo comparison of the candle plots of the channels' cross talk probability. The range of the simulated cross talk probability is smaller because there was no randomisation applied to this value. The 0 values in data come from channels that are broken. The average values of the cross talk probability agree at the 5 % level, with values of 18.44 % for simulation and 19.54 % for data.

13.2 SIMULATION OF THE TRIGGER AND READOUT SYSTEM

The simulation of the trigger and readout system is discussed next, as it is needed in order to obtain simulation samples that can be compared to calibration data. The big difference between data and simulation is that in the real detector, the samples are collected continuously in time, while in the simulation, waveforms are simulated in concentrated regions around energy depositions. There can be a lot of empty time between waveforms.

The trigger simulation iterates over the simulation windows and over blocks of 256 samples contained within the window. For each channel, for the waveforms that lie (partly) within the boundaries of the current block, the waveform samples inside the block are processed by the channel triggers. The samples can set the flag of the channel trigger to true, based on the channel trigger logic that was described in chapter 7:

- The threshold channel trigger checks if the sample's amplitude is above 50 PA. If so, the flag is set to true. The sample time is stored in order to check its coincidences later on.
- The NS channel trigger checks if the sample is a peak and strictly larger than 0.5 PA. If so, the peak counter is increased and the peak's time and amplitude are added to corresponding vectors. To count the peaks within a time window of 6.4 μs that rolls over the samples, old peaks in the vector are removed if their time difference with the new peak is larger than the time window. If there are strictly more than 17 peaks in the vector, the flag of the NS trigger is set to true. When the simulation continues to the next simulation window, jumping over a time gap, then the neutron counter is reset, as is the stored previous samples.
- The random trigger counts the blocks and fires if the modulo with the periodicity is zero.

After the channel triggers have processed all the samples within the block, each plane trigger counts the boolean flags of all its channel triggers and resets them automatically to false. In order to check the coincidence requirement of the high energy trigger, the algorithm loops for each vertical threshold trigger over all horizontal threshold triggers, and checks if the time difference between any of their peaks is in a time coincidence, strictly closer than 75 ns. If so the high energy trigger is true.

In case the plane trigger fires, the trigger type is set according to the cause. The order in which the trigger types are checked determines their priority. Once all blocks are processed, the information from all the fired plane triggers determines which blocks from which planes have to be read out (denoted as RO blocks) and what zero suppression threshold should be applied, following the settings of table 7.1.2.

Finally, the actual read out is performed. First, all samples that do not lie within a RO block are discarded. This procedure changes the collection of waveforms as illustrated in figure 13.2.1. If the waveform started before a RO block, the waveform timestamp is updated. If a waveform spans over several RO blocks and there is a gap between the RO blocks (as is the case for the right waveform in figure 13.2.1), then the waveform is cut in separate waveforms that are read out. This procedure is repeated until there are only waveforms in RO block(s) left. Next, the zero suppression is applied.

When (several) sample(s) lie below the ZS threshold, the waveform is cut into separate small waveforms that contain only samples above ZS threshold. The algorithm checks sample per sample. If the

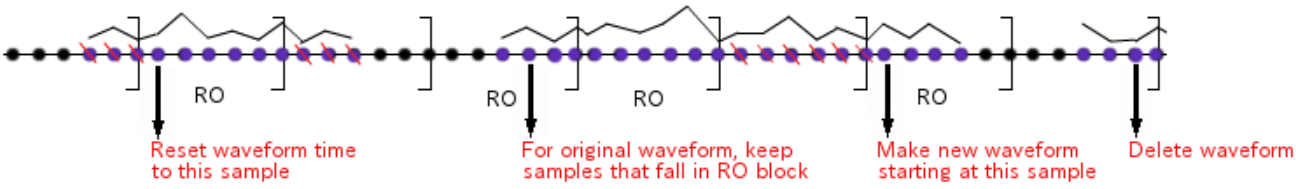

Figure 13.2.1: Schematic view of how waveforms are created that lie within ROblock(s).

sample lies above the ZS threshold then it is stored to a temporary vector. Whenever a sample is over ZS threshold but the former sample was not, the pending sample-vector is saved as one waveform and a new sample-vector is started. If at the end of the sample loop, the temporary vector is pending, then it is stored into the entry of the waveform that was initially processed, by resetting its sample-vector and timestamp. If there is no pending vector, the current waveform had no samples over ZS threshold and the initial waveform is deleted. The final set of zero suppressed, time ordered waveforms is the output of the readout simulation.

Since the readout simulation is integrated in SoLid's analysis software, which is described in chapter 8, the simulated waveforms can be stored in the same waveform objects that are used for the actual data. The simulated signal is, from a computational point of view, identical to the one that is read out from the real detector.

13.3 SIMULATION OF THE SCINTILLATOR RESPONSE

The readout simulation generates scintillation photons in the PVT cubes and the ^{6}LiF:ZnS(Ag) screens according to the energy they receive from an incident particle. The energy depositions that occur during an event are simulated with the GEANT4 software, which was introduced in chapter 12. The traversing particle deposits their energy in several small deposits, E_{dep} (MeV), over small tracks that are determined based on the mean free path in the material.

In the readout simulation only those photons are generated that will enter any fiber. Therefore, the value that has to be determined is essentially the combination of the real light yield and the fiber acceptance,

$$LY = LY^{\text{real}}_{\text{cube}}(x,y) \times \epsilon_{\text{acc}} \,.$$

The light yield will be tuned based on calibration data at the end of this chapter, once all intermediate parts of the readout simulation have been implemented and tuned. For PVT, the resulting LY will be 573 $\gamma\ MeV^{-1}$ and for the ZnS(Ag) scintillator, the LY is 668 $\gamma\ MeV^{-1}$.

13.3.1 ENERGY QUENCHING IN PVT

For the PVT scintillator, the readout simulation applies Birks' energy correction to each small E_{dep} with respect to the total energy deposit of the particle, E_{track}, over its total track length, L_{track} (mm),

inside one PVT cube. The total track is reconstructed by grouping together all energy deposits with the same particle ID and cube coordinates. The scintillation light yield is determined as

$$dL = N_{\gamma/\mathrm{MeV}} \cdot E_{\mathrm{quench}} = N_{\gamma/\mathrm{MeV}} \frac{E_{\mathrm{dep}}}{1 + kB \frac{E_{\mathrm{track}}}{L_{\mathrm{track}}}}. \tag{13.2}$$

where $N_{\gamma\mathrm{MeV}}$ is the PVT light yield of 10000 photons per MeV, in accordance with table 6.1.1. With a Birks constant kB of 0.14 mm/MeV the response of the EJ-200 PVT scintillator could be reproduced. For the ZnS(Ag) scintillator, energy quenching is neglected. The energy quenching has the greatest influence in PVT for protons, carbon nuclei and alpha particles, which are released for example by incident particles that cause nuclear recoils. For the SoLid experiment this is the case for atmospheric neutrons, cosmic muons, and spallation neutrons. Since the result was found to be the same for those cases, the light yield is visualised for atmospheric neutrons in figure 13.3.1. The literature values for the EJ-200 scintillator (see figure 6.1.3) are shown as well.

In the energy region of interest for the SoLid experiment, between 1 and 10 MeV, the simulation is in agreement with the values from the data sheet for electrons (grey versus black) and protons (brown versus red). These mechanisms cause the highest light yield. The alpha particles (dark blue

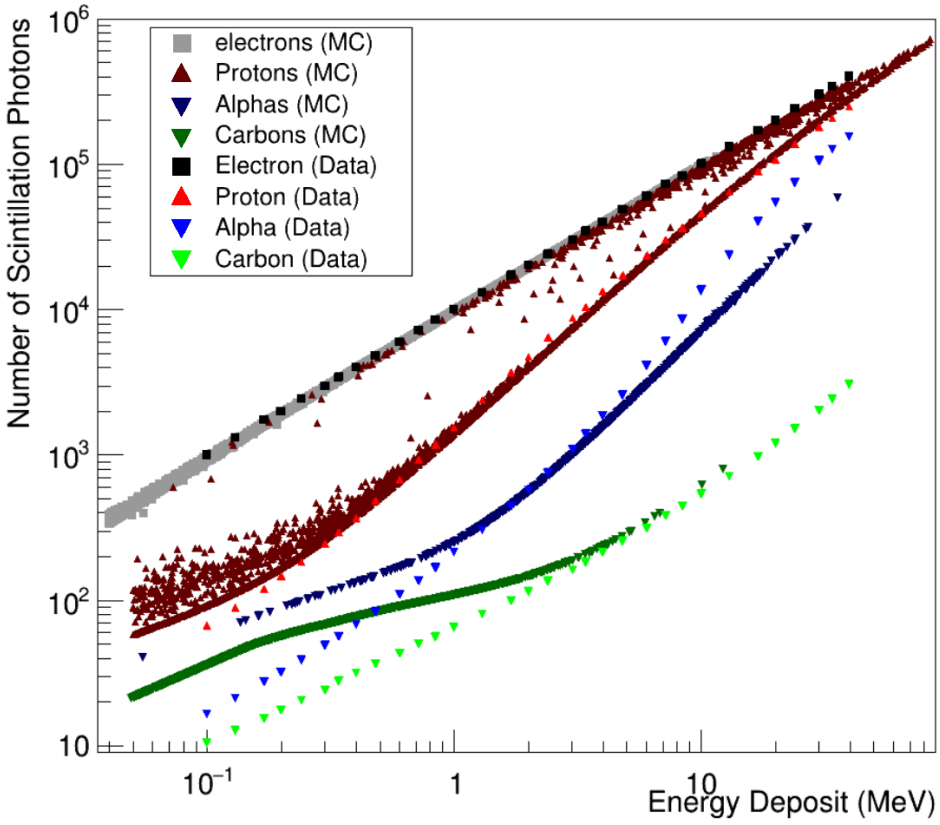

Figure 13.3.1: Simulated response of the PVT scintillator to energy depositions by the secondary particles generated after atmospheric neutron interactions, as modeled by the readout simulation (MC). The response as measured by Verbinski et al. is shown as well (Data). Squares indicate the response to electrons. Triangles show the response to particles that are caused by nuclear recoils. Courtesy of Yamiel Abreu.

versus light blue) show at high energy range deviations up to 40 % with the values from the data sheet. The carbon nuclei (dark green versus light green) show in the low energy range deviations of 30 %. However, the quenching effect is so big in these cases that the visible energy that they produce is small.

The agreement between data and simulation is not good for the alpha and carbon nuclei. The current description of the quenching effect on PVT used by the Solid experiment could be improved by a second order approximation. According to Reichhart et al. [201] the quenching factor is seen to have an energy dependence, increasing in gradient towards low energies. A clear deviation from Birk's formula is evident, indicating that the fraction of scintillation that is generated by low energy nuclear recoils appears to decrease even more rapidly. Craun et al. [202] argue that a better experimental fit can be obtained by including the second-order approximation for low-energies to the quenching factor, QF,

$$QF = 1 + kB\frac{dE}{dx} + C\left(\frac{dE}{dx}\right)^2.$$

In the readout simulation, the first order approximation, described by equation 13.2, is implemented. The Chandler experiment, which uses similar scintillator material, has studied the second order approach [203]. One of the greatest difficulties in working with the organic scintillators remains in the nonlinearity of the light output versus particle energy. This may be the cause of discrepancies in the energy response observed in cosmic simulations when comparing data and simulation, as shown in section 15.3. The second order approach could improve the background interpretation and discrimination. Luckily the most important signals of IBD and HNL are from electrons and positrons of 1-10 MeV for which the quenching model is in agreement with the data.

13.3.2 SCINTILLATION TIME SCALE

The scintillation photons are emitted according to a characteristic scintillation time scale, relative to the time after the actual energy deposition, t_{eDep}. The emission time is modeled as the sum of exponential decays with i different time constants,

$$t_{\gamma,i} = t_{\text{eDep}} + \text{Random}\left(\exp^{-\frac{t}{\tau_i}}\right). \tag{13.3}$$

For the PVT scintillator, the emission time is modeled with two exponential decays. For 80 % of the generated photons, the decay time constant is $\tau_1 = 2.1$ ns as taken from the ELJEN data sheet. For the other photons the constant is $\tau_2 = 10$ ns, which takes into account some randomisation and the average timescale the photons need to reach the fibers. This parameter will not have a substantial impact on the final signal as samples are measured only every 25 ns.

For the ZnS(Ag) scintillator, the scintillation time scale is modeled with three exponential decays, as determined in section 9.5. The time constants have a value of 12.86 ns, 91.48 ns, and 653 ns, with a fraction of respectively 17 %, 31 % and 52 %.

13.4 SIMULATION OF OPTICAL TRANSPORT

The scintillation photons can make their way to the light collecting fibers that run through the cubes, through scattering inside the PVT cube and diffusion on the Tyvek light insulator. This process is

factored in by the fiber acceptance ϵ_a cc. Each cube has an intrinsic efficiency, ϵ_{cube}, that has to account for the observed variations in the cube LY during calibration, as was determined in section 9.3.3. The cube-to-cube variation is implemented in the readout simulation. Some photons may leak through the fiber or the tyvek to neighbouring cubes that share a face with the original cube. This light leakage is discussed in appendix B.

In the readout simulation, half of the photons that enter a fiber go directly towards the sensor, while the other half travels towards the other end where they are possibly reflected by the mirror and still can make their way to the sensor. The final number of photons that arrive at the sensor, either direct or after reflection on the mirror, is modeled by

$$N_{\gamma,\,\text{direct}} = \frac{1}{2} C \cdot N_\gamma \cdot e^{-\frac{L_{\text{cube,sensor}}}{L_{\text{decay}}}} \tag{13.4}$$

$$N_{\gamma,\,\text{refl}} = \frac{1}{2} C \cdot N_\gamma \cdot e^{-\frac{L_{\text{cube,mirror}}}{L_{\text{decay}}}} \cdot P_{\text{refl}} \cdot e^{-\frac{L_{\text{mirror,sensor}}}{L_{\text{decay}}}}. \tag{13.5}$$

The fiber attenuation is modeled with the exponentials, where the distance between components a and b is expressed by $L_{a,b}$. The factor C accounts for the losses due to the coupling between fiber and sensor. In section 9.3 the attenuation lengths and couplings were determined from calibration data for each of the 3200 fibers separately. All these calibration parameters are implemented in the readout simulation in order to emulate the detector response with its complete set of inhomogeneities.

Since the photon collection is a random process, the number of photons that arrive at the sensor is fluctuated according to Poisson statistics. The arrival time of each photon at the sensor is determined by adding the travel time from scintillator to sensor to the emission time that was calculated in 13.3, resulting in the following,

$$t_{\gamma,\,\text{sensor}} = t_{\gamma,\,\text{emit}} + \frac{L}{v_{\text{light}}},$$

where v_{light} is the light velocity inside the fibers of 173 mm/ns [204]. Per channel, the incident photons are stored on a list with their relevant properties, which will be processed with the sensor algorithm that was described in section 13.1.

13.4.1 TUNING THE SCINTILLATION IN PVT

The readout simulation can finally be tuned at the deepest level, namely the photon generation inside the PVT scintillator. This is only possible once all higher level detector effects are simulated and tuned properly, since the real cube light yield will be compared with measurements, which have only access to the visible photon light yield, where all detector effects are entangled. The success of the photon generation tuning therefore depends on the accurateness of all previous effort.

The visible cube light yield was calibrated with the use of a ^{22}Na source section 9.2. To tune the readout simulation, ^{22}Na energy depositions that were produced by the GEANT4 simulation are processed with the full readout simulation and the output is compared with data. To this end, the simulated signal is analysed in exactly the same way as the calibration data (as described in section 9.3). That is, for many events, the visible cube LY is determined and collected into the sodium energy spectrum.

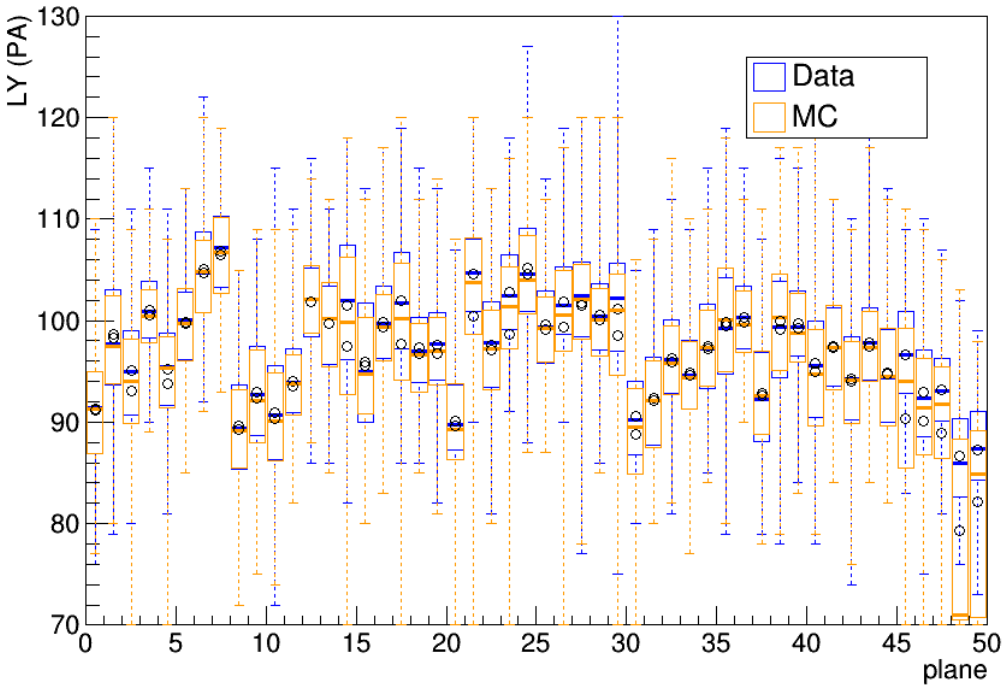

Figure 13.4.1: Differences between data and MC of the plane candleplots of the cube calibration LY. This LY is determined as the centroid of the Compton edge of the energy deposition of the 1.27 MeV gamma from a ^{22}Na source as described in chapter 9.

The centroid of the Compton edge of the spectrum is identified as the visible cube LY.

The value of the *real* LY is tuned, based on the comparison of the candle plot of the visible LY in data and simulation per plane on detector level. The result of the tuning is shown on figure 13.4.1. The value that has to be determined is essentially the combination of the real light yield and the channel acceptance (see section 13.3). The determined value is

$$LY^{\text{real}}_{\text{cube}}(x,y) \times \epsilon_{\text{acc}} = 573\ \gamma\ MeV^{-1}$$

In order to reproduce the variation of average light yield between the different planes, the additional factor, $\epsilon_{\text{plane}}(z)$, is determined and applied.

13.4.2 Comparison of attenuation parameters in data and simulation

To cross check the implementation of the large amount of calibration parameters, the simulated response to the sodium source is investigated in exactly the same way as was done for data. For the simulation chain, the ^{22}Na decay is simulated with GEANT4. The relative difference between the parameters that were obtained from data and from simulation for each separate channel is collected in the distributions in figure 13.4.3. Note that MC$_{input}$ is the parameter value that was determined from data.

For the fiber attenuation, the simulation has with an average value of 0.02 a slightly higher attenuation length. The effect is correlated with fiber position. For fibers with a sensor on top or on the side of the electronics box, a slightly higher simulated attenuation length is determined. This is probably due to the fact that these fibers make a better contact with the cube. For coupling and cube variation, the parameter values for data and MC coincide on average and have a spread of 2%, respectively 1%.

An example of a side by side comparison between data and Monte-Carlo of the visible cube light yield for one plane is shown in figures 13.4.5 and 13.4.6 . The agreement of the inhomogeneous effects is apparent, such as the gradient towards the edges, a variation between columns and rows due to variable fiber-sensor couplings and cube variations. The effects are implemented and well reproduced by the simulation. In addition, the relative difference between the visible cube light yield between data and Monte-Carlo is shown in figure 13.4.2. The absolute difference in light yield is very small. Results for each individual plane can be found in [170] and [205].

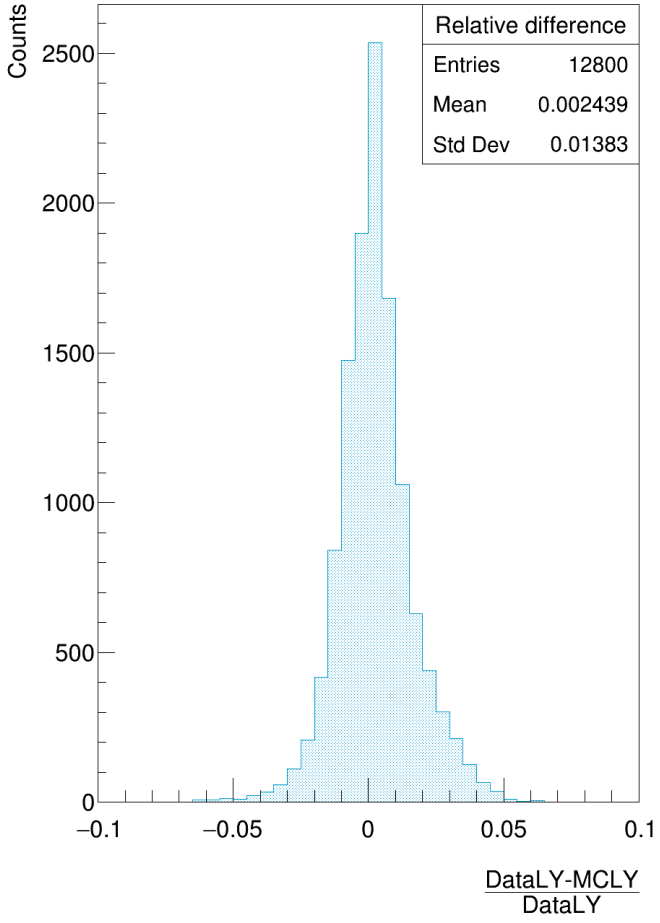

Figure 13.4.2: Relative difference between measured visible light yield in data and simulation.

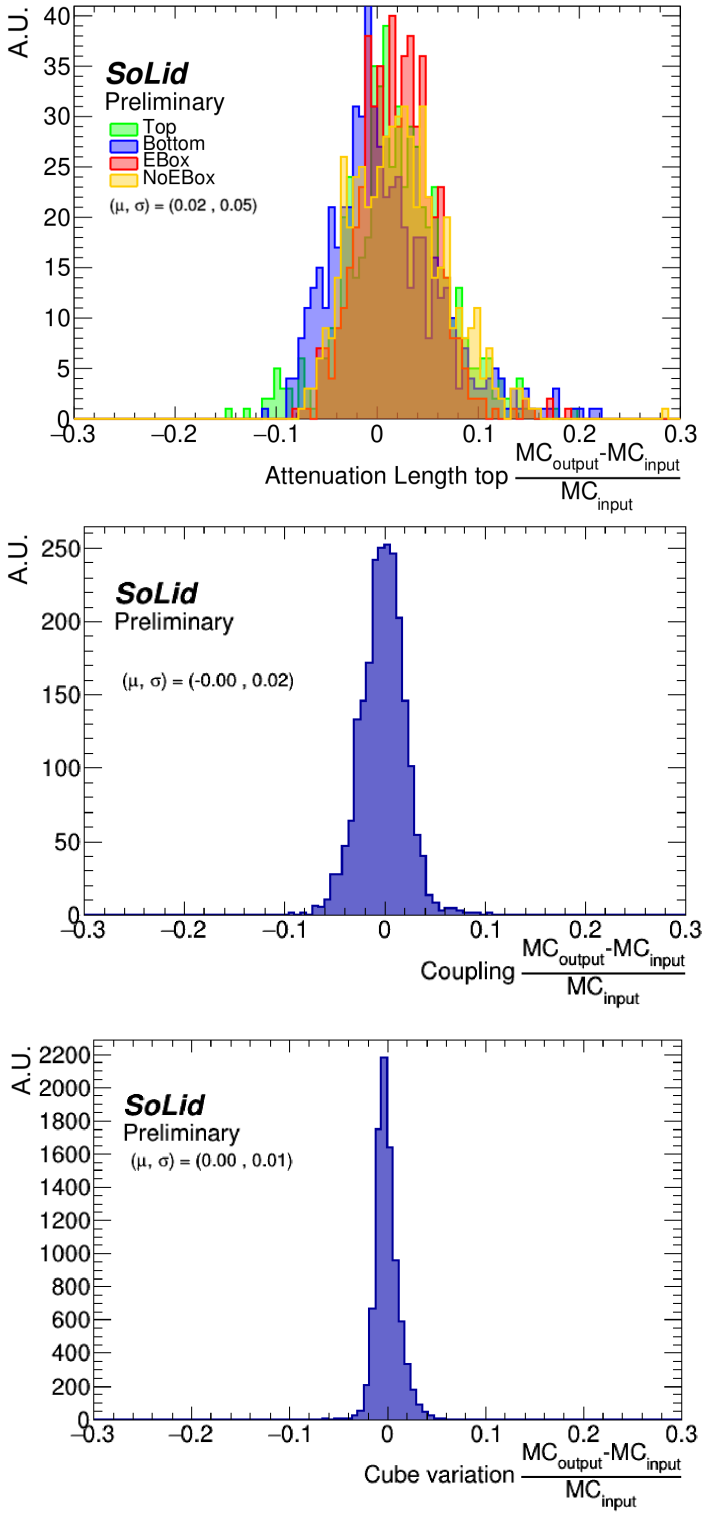

Figure 13.4.3: Difference in calibration parameters determined for data and simulation

13.4.3 COMPARISON BETWEEN WAVEFORMS IN DATA AND SIMULATION

Figure 13.4.4 shows an example of a waveform that was recorded in data and identified as an IBD-like event, compared to a waveform that was constructed by the readout simulation in response to an IBD event that was generated with the GEANT4 software. Waveforms that are the result of scintillation in PVT and in ZnS(Ag) have distinct features. The fast peak corresponds to PVT scintillation and the long waveform is produced by ZnS(Ag).

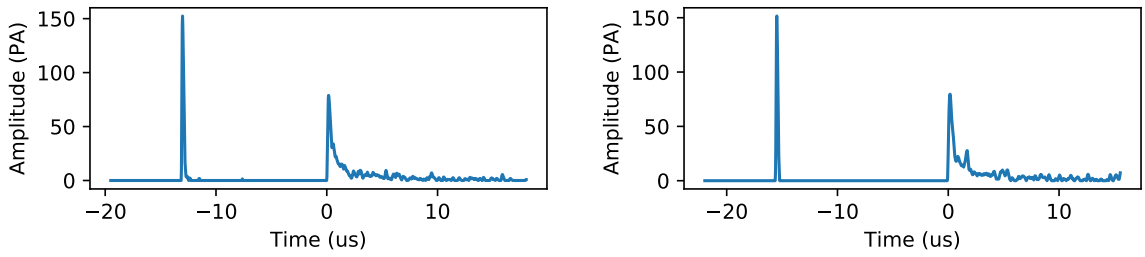

Figure 13.4.4: Left: example of the waveform from an IBD candidate reconstructed from data taking during reactor on period. Right: example waveform produced by the readout simulation as response to an IBD event generated with GEANT4.

For the simulation, the ZnS(Ag) scintillation is modeled based on neutron waveforms that passed the NS trigger and some selection criteria. Therefore the simulation produces ZnS(Ag) signals that have a neutron trigger efficiency of 100 %. The true trigger efficiency, as obtained from the neutron calibration campaigns (see section 9.4.1), has to be applied later in the analysis as an overall scale factor.

In addition, the response of the ZnS(Ag) scintillator depends in reality on the type of the incident particle. The subtle difference between signals induced by neutrons and by alpha particles (after ^{214}Bi-^{214}Po decay) is used by the so-called BiPonisher variable (see section 15.2.1). This difference can not be reproduced properly with the simulation. Instead, the true information that is available from GEANT4 is used to determine wether the signal was induced by neutrons or alpha particles. The corresponding BiPonisher value is sampled from a distribution that is measured in data, as shown in figure 15.2.2.

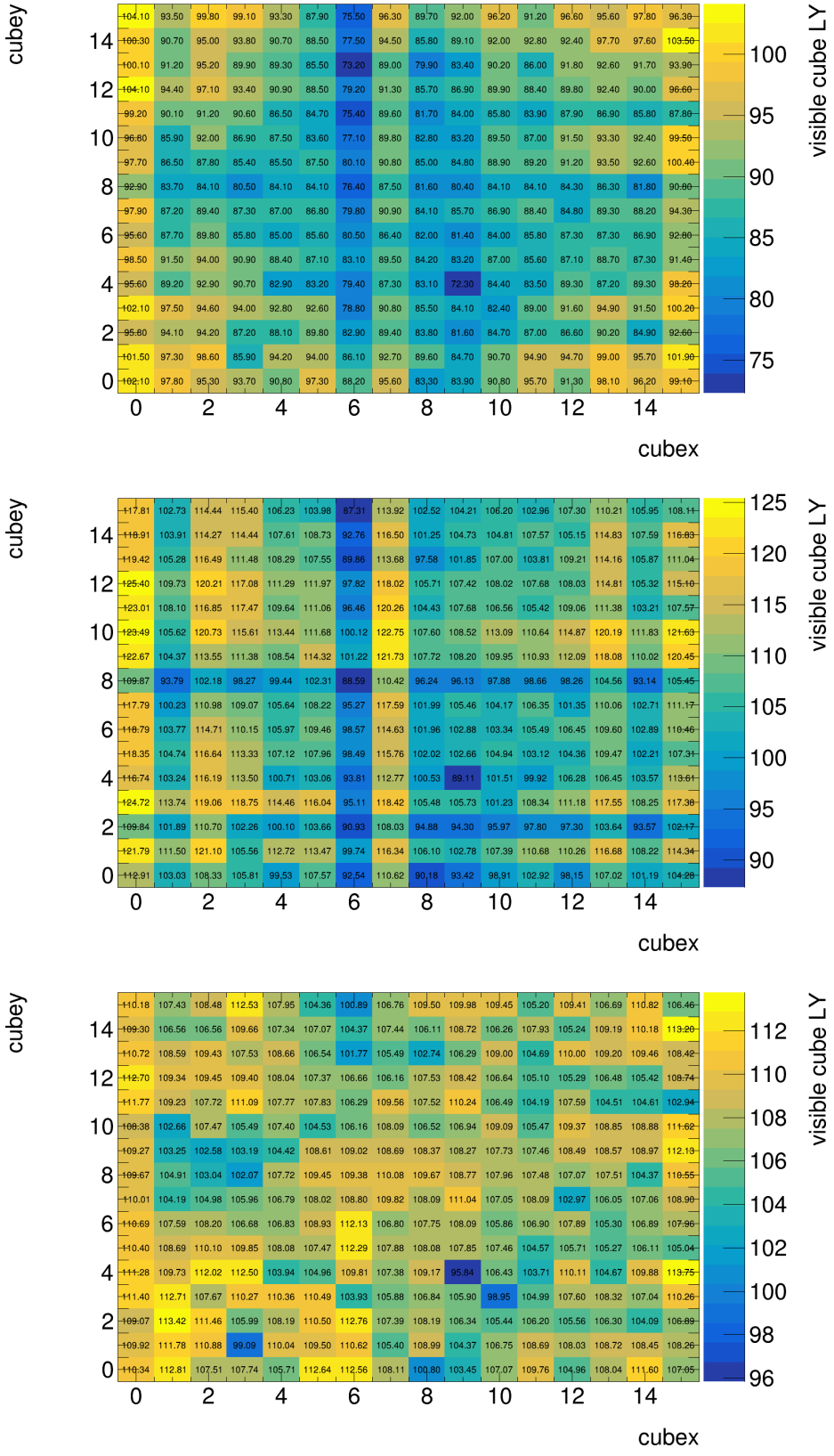

Figure 13.4.5: Comparison of LY pattern between data (here) and Monte-Carlo (next page), as originally determined (top), after correction for the fiber attenuation effect (center) and after correction for the coupling effect (bottom).

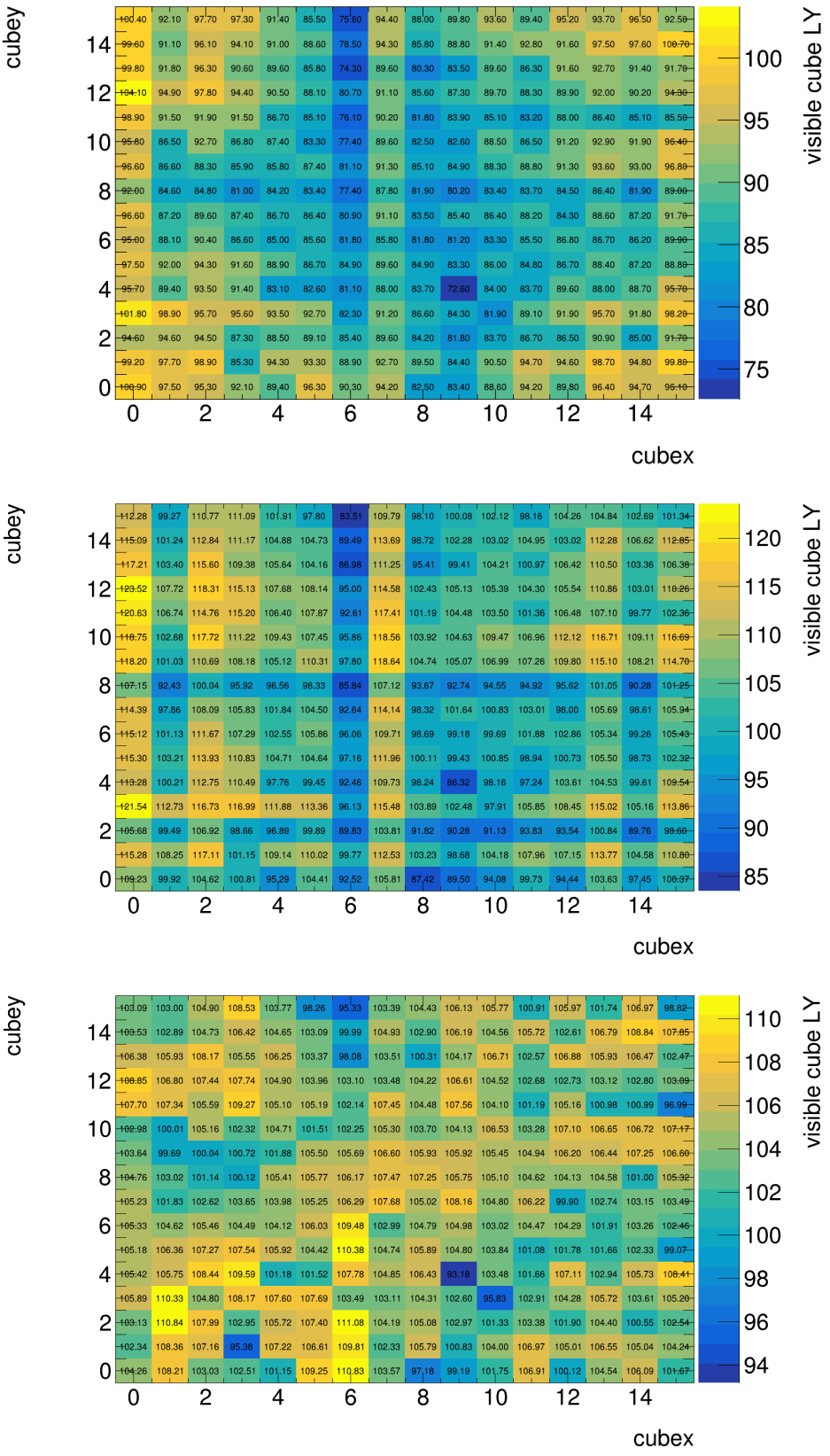

Figure 13.4.6: Comparison of LY pattern between data (previous page) and Monte-Carlo (here), as originally determined (top), after correction for the fiber attenuation effect (center) and after correction for the coupling effect (bottom).

14

VALIDATION OF THE TUNING OF THE READOUT SIMULATION

For the oscillation analysis, the fine-tuning of the readout simulation is indispensable. The optimisation of IBD selection cuts relies fully on simulated signal events and it is of utmost importance to validate the reliability of the simulation. In addition, the systematics and efficiencies will be derived using Monte-Carlo so we need to be confident in the ability of the simulation to reproduce the data.

14.1 DATA/MC COMPARISON OF THE PVT RESPONSE AND EFFICIENCY

To determine the calibration parameters in the previous sections, the centroid of the Compton Edge provided the single value of interest. The centroid represents the detector response to an energy deposit around 1 MeV. However, the goal of the calibration effort is to be able to reliably convert signals seen by the detector channels [PA] into the actual deposited energy [MeV] over a wide energy range.
This section focuses on the whole energy spectrum that is provided by the ^{22}Na source. The source emits one gamma ray of 1.274 MeV and two back to back annihilation gammas of 0.511 MeV. When the high energy gamma ray is seen in one module, then a single annihilation gamma can be found in the module opposite of the calibration gap. Like this, events of different and well defined energies can

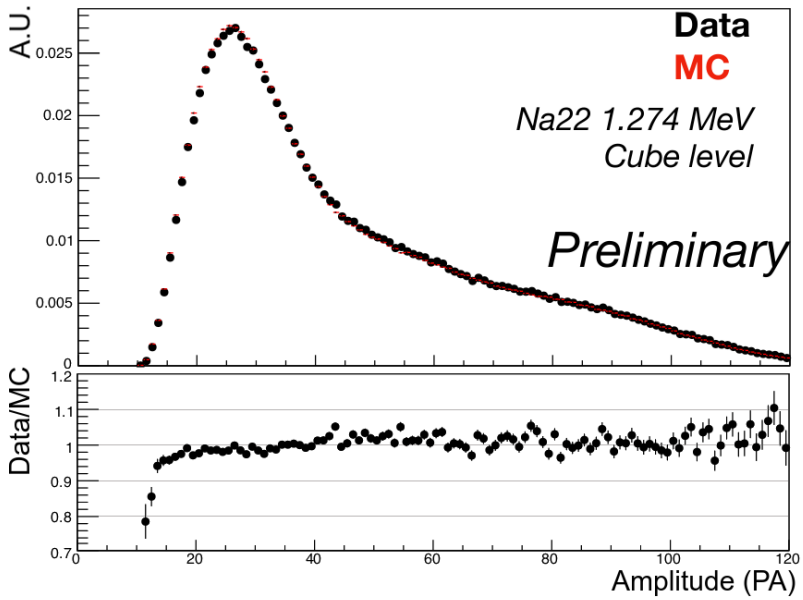

Figure 14.1.1: Absolute data Monte-Carlo comparison of the detector response to the ^{22}Na gamma ray with 1.27 MeV energy. Very good agreement is achieved over the energy range.[206]

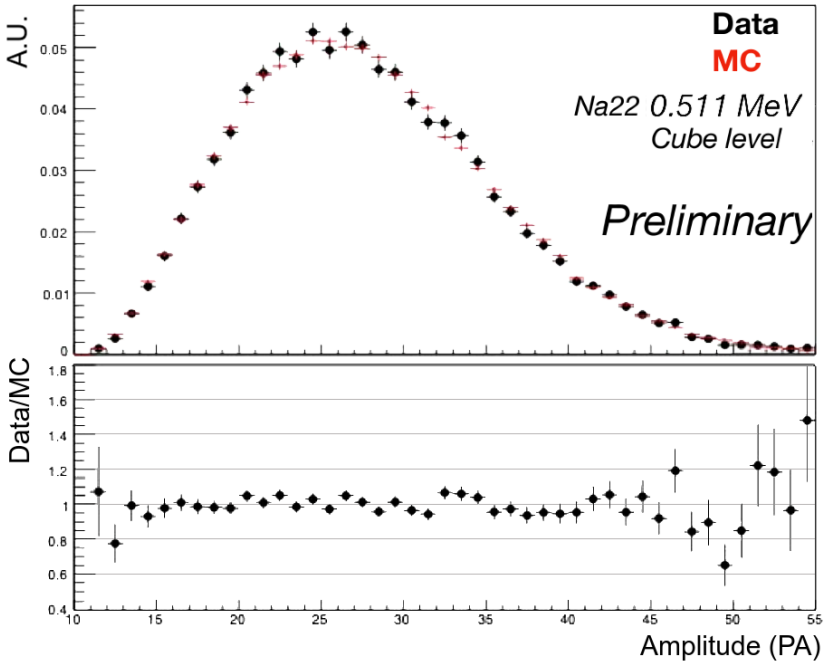

Figure 14.1.2: Data Monte-Carlo comparison regarding the detector response to the ^{22}Na gamma ray with 511 keV energy. The simulation is scale towards the data.[206]

be selected. The sodium calibration data were recorded with the random trigger to avoid trigger bias. Data and simulation are normalised to the exposure time, in order to make an absolute comparison.

The initial data/MC comparisons revealed that the data selection was suffering from plane dead time and channel dead time effects, which were discussed in section 9.1.2. If one of the annihilation gammas interacts in a plane in deadtime, the total reconstructed energy will be lower. This only affects the data, and shows up as an overestimation of high energy contributions in simulation. The initial discrepancy between data and MC was especially prominent in the closest plane to the source, amounting to a factor 2. Because the activity of the source is so high, the plane buffer was often saturated. For example, plane 29 was out 35% of the time. The issue of dead time has been avoided by focusing on the cubes that cause trigger. These data taking effects makes the data/MC comparison complicated, but a very good absolute agreement was achieved.

For the data/MC comparison, the 1.274 MeV gamma is tagged by selecting cubes where an energy above 60 PA is observed, which corresponds to 650 keV. This selection avoids the annihilation gammas that have a lower maximal energy. The absolute data Monte-Carlo comparison for all cubes with selected events is shown in figure 14.1.1. The global detector response is controlled within ± 10% and better than that in some regions.

A lower energy annihilation gamma is searched in the module opposite to where the 1.27 gamma was tagged. Only cubes are selected that are reconstructed isolated in a plane and for which all four channels see a signal above a 2.5 PA. Figure 14.1.2 shows the data Monte-Carlo agreement for the normalised energy spectrum of the annihilation gamma. When the data and MC spectra are scaled using the number of 1.274 MeV gamma tags, the shape is still well reproduced by the MC, but the data

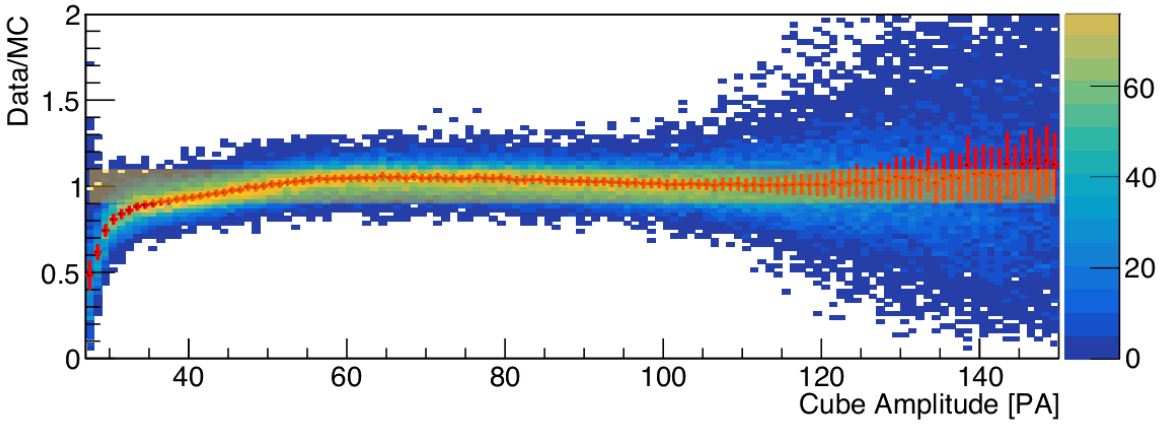

Figure 14.1.3: Ratio of detector response in data and MC to ^{22}Na gamma ray with 1.27 MeV energy. Each bin of the horizontal axis contains the data/MC ratios of all selected cubes around a calibration gap, for the specific amplitude of the bin. The red curve corresponds to the average of this distribution and the error bars represents 70% of the distribution. [207]

sees 20% less annihilation gamma than the simulation. The Monte-Carlo has a different efficiency to see the annihilation gamma. This is probably due to the difference in fiber efficiency at low energy between data and simulation.

The agreement between data and Monte-Carlo is also checked for the cubes separately. A global figure of the data/MC agreement is shown in figure 14.1.3. Here, cubes are selected that caused the trigger and therefore have at least two perpendicular channels. The threshold on the sum of the fiber channels is 5.5 PA. In the figure, each bin of the horizontal axis contains the data/MC ratios of all selected cubes around a calibration gap, for the specific amplitude of the bin. A single calibration position is used. The red curve corresponds to the average of this distribution and the error bars represents 70% of the distribution.

The discrepancy below 35 PA, which corresponds to 0.4 MeV, is due to fiber multiplicity. In data, cubes are more often reconstructed with at least one missing fiber. The simulation is more efficient than data to see low energy deposits. A systematic uncertainty will be derived to take this effect into account by randomly killing fibers in function of their amplitudes in the readout simulation.

14.2 TUNING AND DATA/MC COMPARISON OF THE ^{6}LI:ZNS(AG) CONTRIBUTION TO THE ES SIGNAL

The energy response of the detector to the prompt energy deposition is dominated by the PVT electromagnetic signal. The nuclear signal from the ^{6}LiF:ZnS(Ag) makes up the delayed signal, that is used for triggering and constructing coincidences. However, the ^{6}LiF:ZnS(Ag) gives a contribution to the prompt electromagnetic signal because the e^{-} from ^{214}BiPo decay that originates in the ^{6}LiF:ZnS(Ag) screen has to make its way through the screen to the PVT cube.

Since BiPo is one of our dominant backgrounds, the ES contribution from ZnS is determined based on 20 days of reactor off data (from 12/07/2018 to 31/07/2018), and the simulation is tuned accordingly. A BiPo enriched sample is obtained in the BiPo control region which is discussed in section 15.2.2 in chapter 15.

The optimal ZnS light yield was found to be the generation of 200 photons that will enter any fiber. The energy is reconstructed for the central cube of the ES cluster, for the crown of central cube and it 8 surrounding cubes in the plane, and for the total cluster, as shown in figures 14.2.1 and 14.2.2. An agreement within 5% is found for the dominant energy regions. Above 3 MeV and below 0.7 MeV the statistics are low. Note that this level of agreement was reached with a fiber threshold as low as 2.5 PA.

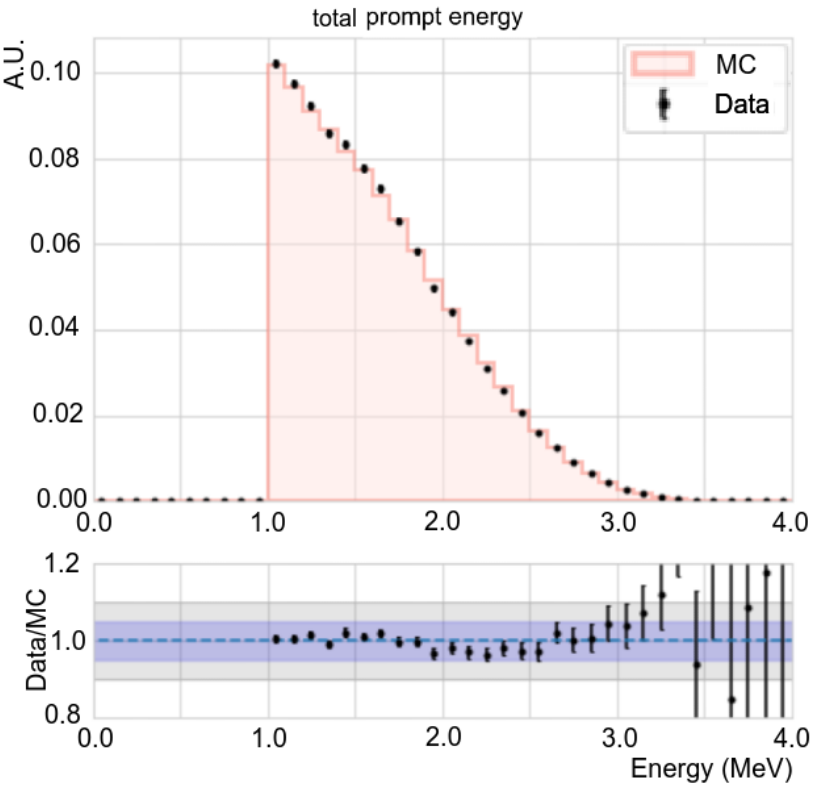

Figure 14.2.1: Data/MC comparison for the reconstructed energy of the central cube, for low energy BiPo prompt ES signals, that has contributions from PVT and ZnS scintillation. The simulation is in agreement with the data within 5% for the dominant energy regions.[207]

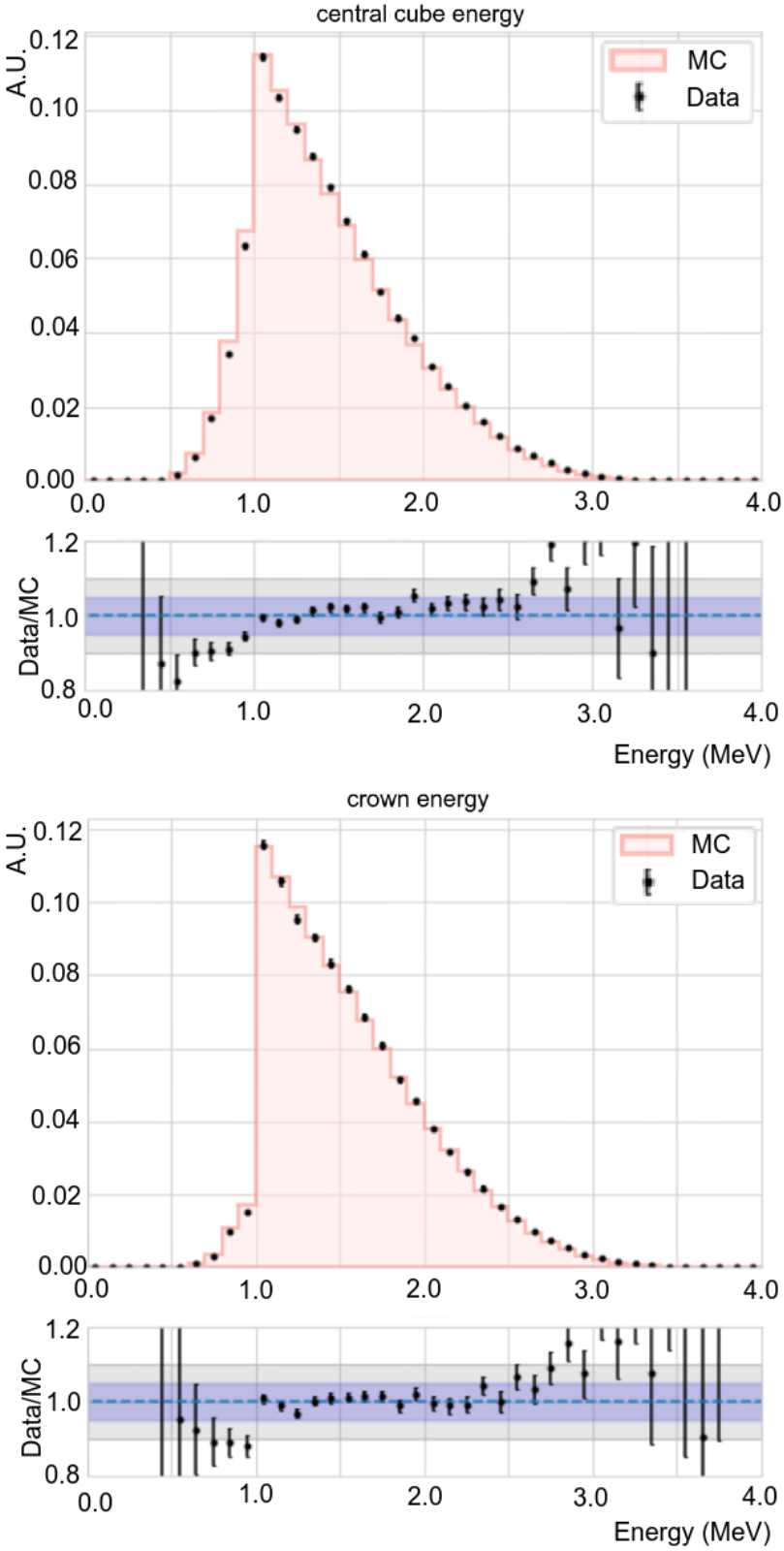

Figure 14.2.2: Data/MC comparison for the detector response to low energy BiPo prompt ES signals, that has contributions from PVT and ZnS scintillation. The top panel shows the reconstructed energy for the 9 crown cubes and the bottom panel shows the total ES cluster. The simulation is in agreement with the data within 5% for the dominant energy regions.[207]

15

ANALYSIS OF THE BACKGROUNDS AND VALIDATION OF THE SIMULATION

The SoLid detector is operated close to sea level, at very close proximity to a nuclear reactor. These conditions cause a high level of background that is challenging for any type of analysis design. The detector is subject to reactor induced backgrounds such as gamma rays and neutrons. In addition, the location, in combination with the low overburden (~ 6 m.w.e.), results in an overwhelming background of cosmic origin. The natural contaminations of detector components and reactor building top off the list. The different interactions that take place in the detector were discussed in chapter 11. The IBD signal is contained in the reactor on data, together with all unwanted background signals. Interactions that mimic the IBD signature have to be identified and rejected, i.e. interactions that result in a coincidence between some ES signal and some NS signal. The distinction is made between correlated coincidences and uncorrelated or accidental ones. The background signals are studied in the reactor off data. According to the current understanding there are three different types of correlated backgrounds in the reactor off dataset sample (which does not exclude the possibility that there are more). Namely, coincidences caused by ^{214}Bi-^{214}Po decays, by cosmics muons, and by atmospheric neutrons.

15.1 ACCIDENTAL BACKGROUND

Some ES signal and some NS signal can coincide by accident and mimic the IBD signature. The accidental background is mainly caused by uncorrelated gamma rays and environmental neutrons interacting in the detector. For the detected accidental coincidences, the ES and NS candidate do not originate from the same physical event. Therefore, the detected topologies contain random configurations. The resulting Δx, Δy and Δz distributions are expected to be broad. The accidental contribution to the signal selection can be largely reduced by topological cuts. In addition, the time difference between accidental ES and NS candidates is random, and their Δt distribution can be considered uniform over the relevant range.

Since the NS events are not necessarily delayed with respect to the ES event, the accidental background contribution to any signal can be estimated from coincidences with negative Δt; the on-time window that is used to select Δt, is shifted to an off-time window with negative Δt. The accidental background estimated in the off-time window can then be subtracted from the events in the on-time window. Different off-time windows are defined for different signal selections because of their different Δt characteristics. As discussed below, an accidental contribution will be estimated for the BiPo selection, for the fast neutron selection, and finally for the IBD selection.

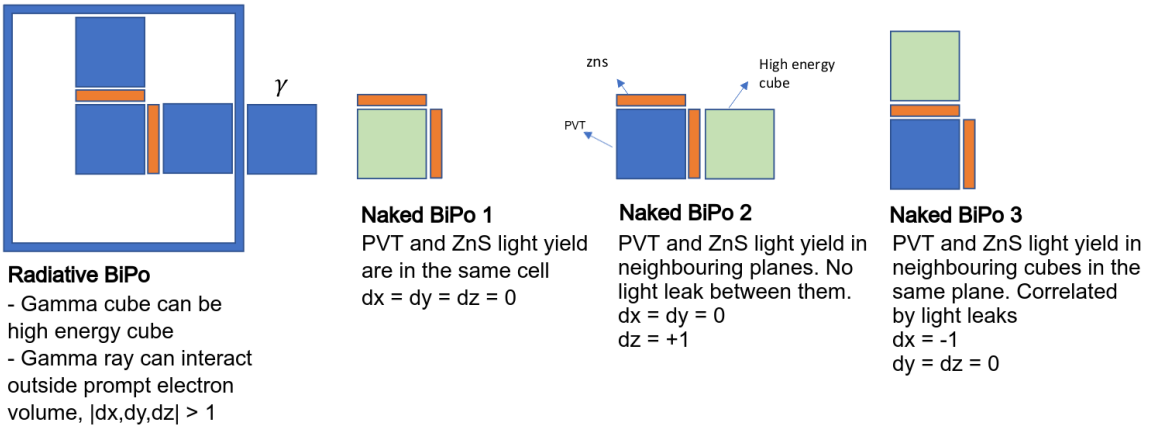

Figure 15.2.1: Different configurations of radiative and naked BiPo events, dependent on the relative position of the detector cell in which the ZnS and the PVT contribution to the ES signal was generated. The α and β particle are detected in the same cube if the electron stays in the same unit cell as the ^{6}LiF:ZnS screen is part of. If the electron is emitted to the other side and scintillates in the PVT of the adjacent unit cell, the ES and NS signals are detected in neighbouring cubes.

15.2 The correlated BiPo background

The ^{214}Bi-^{214}Po cascade in the Uranium chain consists of the^{214}Bi β^- decay, followed by the ^{214}Po alpha decay, which results in time correlated ES and NS signals that mimic the IBD signal. The BiPo events come in different configurations. There is naked BiPo, where the ES signal is coming exclusively from the emitted e^- that deposits part of its energy in the ZnS screen and in a PVT cube. The ES-NS coincidences of naked BiPo pose a direct background to the IBD signal.
In addition, there is radiative BiPo where a gamma ray is emitted directly after the β decay that can interact outside of the prompt volume as shown in figure 15.2.1. The radiative BiPo poses a background to the reconstruction of annihilation gammas from the IBD positron.

15.2.1 The BiPonisher parameter

The ^{214}Bi-^{214}Po signal can be discriminated by means of the BiPonisher parameter. This is a pulse shape discriminator that is based on a difference in the ^{6}LiF:ZnS(Ag) scintillation signal for the IBD and ^{214}Bi-^{214}Po processes. The BiPonisher allows to effectively reject ^{214}Bi-^{214}Po events from the IBD selection. For the current section however, it is used to select the ^{214}Bi-^{214}Po signals. The BiPonisher value is constructed based on the ratio of two integrals taken on the NS signal, one over a long time window of [0 - 87.5] μs and the other over a short window of [0 - 7.5] μs [165]. Compared to the NS signal from the IBD neutron, the NS signal from the ^{214}Po α decay has a higher amplitude and also a shorter decay time, due to the difference in average ionisation density. The scintillation difference is most visible in the first 25 μs of the signal, corresponding to the window where the zero suppression threshold is lowered to 0.5 PA for optimal signal collection. The values of the BiPonisher parameter peak for ^{214}Bi-^{214}Po signals slightly below 1.4 (see the left panel in figure 15.2.2). The selection requirement is therefore set on 1.45.

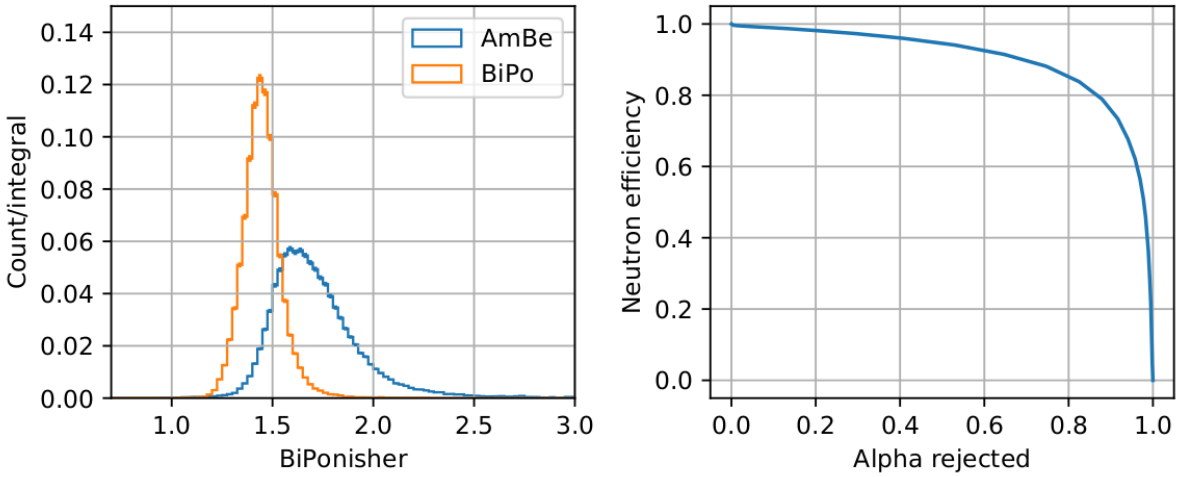

Figure 15.2.2: Distribution of BiPonisher values for neutron waveforms (AmBe) and alpha waveforms (BiPo) from data. For the simulated waveforms, BiPonisher values are sampled from these distributions.[165]

To qualify the separation of BiPonisher values for neutrons and α, the area under the receiver operating curve (ROC) is measured, that represents the loss of neutron efficiency as a function of the proportion of rejected alphas (figure 15.2.2 right panel). For the IBD analysis the BiPonisher cut reduces alpha contamination by 75% while sacrificing 15% of neutrons.

15.2.2 NAKED BIPO

The behaviour of the ^{214}Bi-^{214}Po background is studied in a dedicated control region. The obtained pure ^{214}Bi-^{214}Po sample also allows to validate the ^{214}Bi-^{214}Po Monte-Carlo from the readout simulation. The emitted e^- from the naked BiPo can reach one of the PVT cubes next to the ^{6}LiF:ZnS(Ag) sheets. Dependent on the relative location of the PVT cube, compared to the cell of the ^{6}LiF:ZnS(Ag) screen, three cases are discriminated and illustrated in figure 15.2.1. Considering the position of the ^{6}LiF:ZnS(Ag) sheets, events with ΔX = -1 and ΔZ = 1 will occur, while ΔY is always 0, because in that direction there is no sheet. An almost pure naked ^{214}Bi-^{214}Po sample is obtained from reactor off data using the following selection requirements

$$\Delta t \in [0,500]\ \mu s$$
$$\Delta X \in [-1,0]$$
$$\Delta Y = 0$$
$$\Delta Z \in [0,1]$$
$$R \leq 1$$
$$E_{\text{prompt}} \in [1,4]\ MeV$$
$$\text{BiPonisher} < 1.5$$

The Δt requirement between ES and NS signal is broad in order to contain the long ^{214}Po half life of 164.37 μs. The conservative energy cut envelopes the maximum ^{214}Bi β^- energy of 3.27 MeV. The

topological requirements take into account the expected configurations of the unit cells where the ES and NS signals are generated.

The set of selection cuts is applied to reactor off data and to BiPo simulations. The distributions of coincidence time and energy spectrum are shown in figure 15.2.3, where the simulation is normalised to the data rate. A very good agreement between the simulation and the data is observed. The Δt distribution was fitted with the exponential function

$$f(t) = a_1 e^{-t/\tau}$$

The constant term is left floating, to constrain the accidental background. The first bin shows a contamination of events arising from the interaction of fast neutrons in the detector and were disregarded for the fit. The obtained decay constant corresponds to a half life of $t_{1/2} = \tau \ln(2) = 163.7 \pm 2.3$ μs which is consistent with the ^{214}Po half life.

The BiPo purity in the control region is very high. The proportions of BiPo and neutron events in the control region are 99% and 1% respectively, which validates the BiPo selection [165].

The selection efficiency of ^{214}Bi-^{214}Po within the control region is evaluated with the simulation, and was found to be 32.9 %.Concerning the detection efficiency, ϵ_{det}=ϵ_{capt} $cdot$ ϵ_{reco}=$\epsilon_{capt} \cdot \epsilon_{\text{trig}} \cdot \epsilon_{pid}$, the capture efficiency of the alpha particle is considered as being 1 and the reconstruction efficiency is considered to be greater than that measured for the neutrons, since alphas deposit more energy than a break reaction on ^{6}Li.

The BiPo event rate within the control region is around 0.74 Hz across the detector, as shown on figure 15.2.4. Considering alpha detection efficiencies of 80% and 100%, the estimated BiPo decay rate in ^{6}LiF:ZnS(Ag) is between 2.25 Hz and 2.81 Hz. Time fluctuations of the BiPo rate around 10% are observed. However, the intrinsic contamination of the materials should not vary, given the extremely long lifetimes. The variation is due to a contribution of airborne ^{222}Rn that seeps into the detector. The Radon decays in the air to its descendants on the radioactive chain, and they collect on dust that enters the detector through the electronic cassettes and diffuses through the grooves in which the fibers are inserted. This results in a homogeneous background contribution that can vary over time.

The rate of the NS triggers is correlated to the BiPo rate with a correlation factor of 0.94, as shown in the left panel of figure 15.2.4. The BiPo selection is restrictive but therefore has a high purity. The correlation indicates that radioactive decays are the main contributor to the integrated NS rate.

The BiPo contamination is seen to vary between the different batches of ^{6}LiF:ZnS(Ag) that were produced and delivered by the manufacturer. Batches 0, 1 and 2 have average count rates per cube of respectively $0.4 \cdot 10^{-5}$ Hz, and $7.4 \cdot 10^{-5}$ Hz and $9.3 \cdot 10^{-5}$ Hz. Apparently, a source of contamination has been introduced into the manufacturing process. Unfortunately, the radiopurity measurements were carried out only for batch 0. And the ^{6}LiF:ZnS(Ag) screens from this best performing batch 0 are only used at the outer layer of the detector.

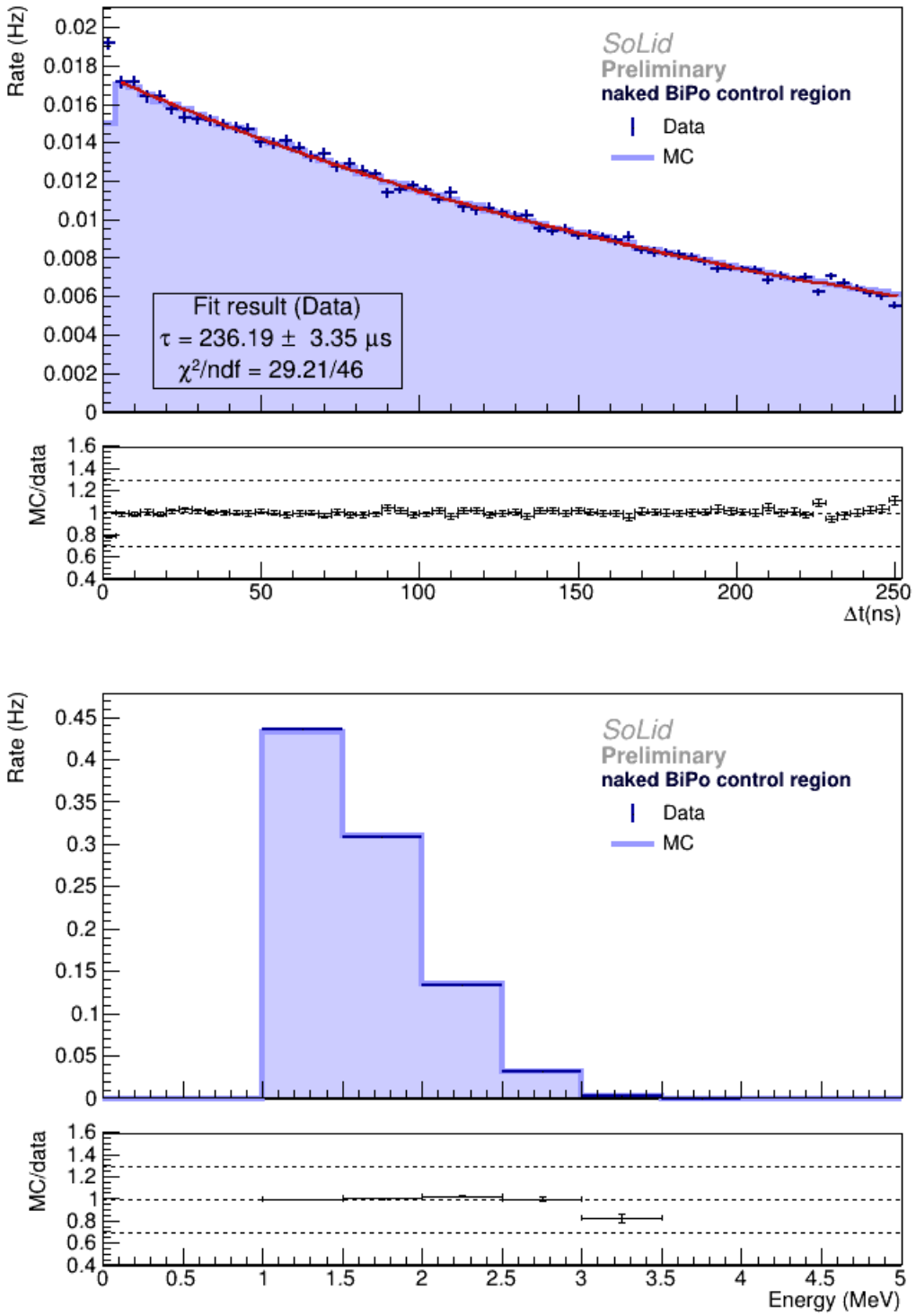

Figure 15.2.3: Data versus simulation comparisons in the control region of naked BiPo. Top: distribution of time differences, fitted with an exponential. Bottom: Energy spectrum of the prompt ES signal of naked BiPo.

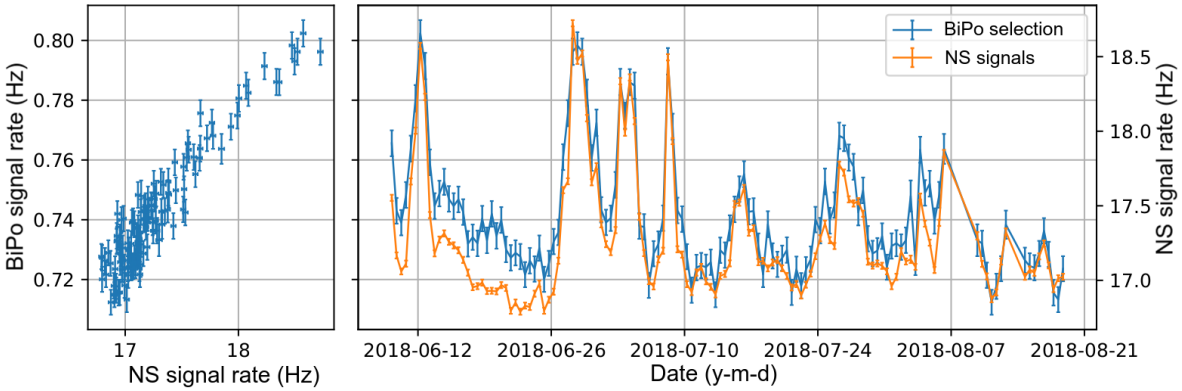

Figure 15.2.4: Left: Rate of BiPo signals in function of the rate of NS signals. The observables are correlated with a factor of 0.94. Right: Time evolution of the BiPo signal rate and the NS signal rate.[165]

15.2.3 Radiative BiPo

In more than 80% of the cases the decay of ^{214}Bi results in an excited state of ^{214}Po that de-excites with the emission of one or more gammas. These gammas give an interesting case study because resolving the annihilation gammas from the IBD positron would give a strong IBD discriminant. The control region for the radiative BiPo is obtained through the selection:

$$\Delta t \in [120 : 500] \mu s$$
$$R \leq 4$$
$$E_{\text{annihilation cube}} \in [1, 6] \text{ MeV}$$
$$E_{\gamma 1} \in [0.1, 0.6] \text{ MeV}$$
$$E_{\gamma 2} \in [0.1, 0.6] \text{ MeV}$$
$$\text{BiPonisher} < 1.5$$

For the same reason as for the naked BiPo case,, a large characteristic time difference is taken. The distance R is this time larger because the gamma rays can travel further. The energy deposition of the gammas is expected to be small. The energy range in the annihilation cube is larger than for the naked BiPo because gammas can interact in this volume. For the radiative BiPo, the data/MC comparison for the variables of interest are shown in figures 15.2.5 to 15.2.10. The simulation is scaled to the data rate. The overall agreement is satisfactory though some discrepancies at the level of 10% can be observed in the reconstructed gamma energies and the dotproduct of their lines of flight. These mismodellings must be accounted for by assessing a systematic uncertainty.

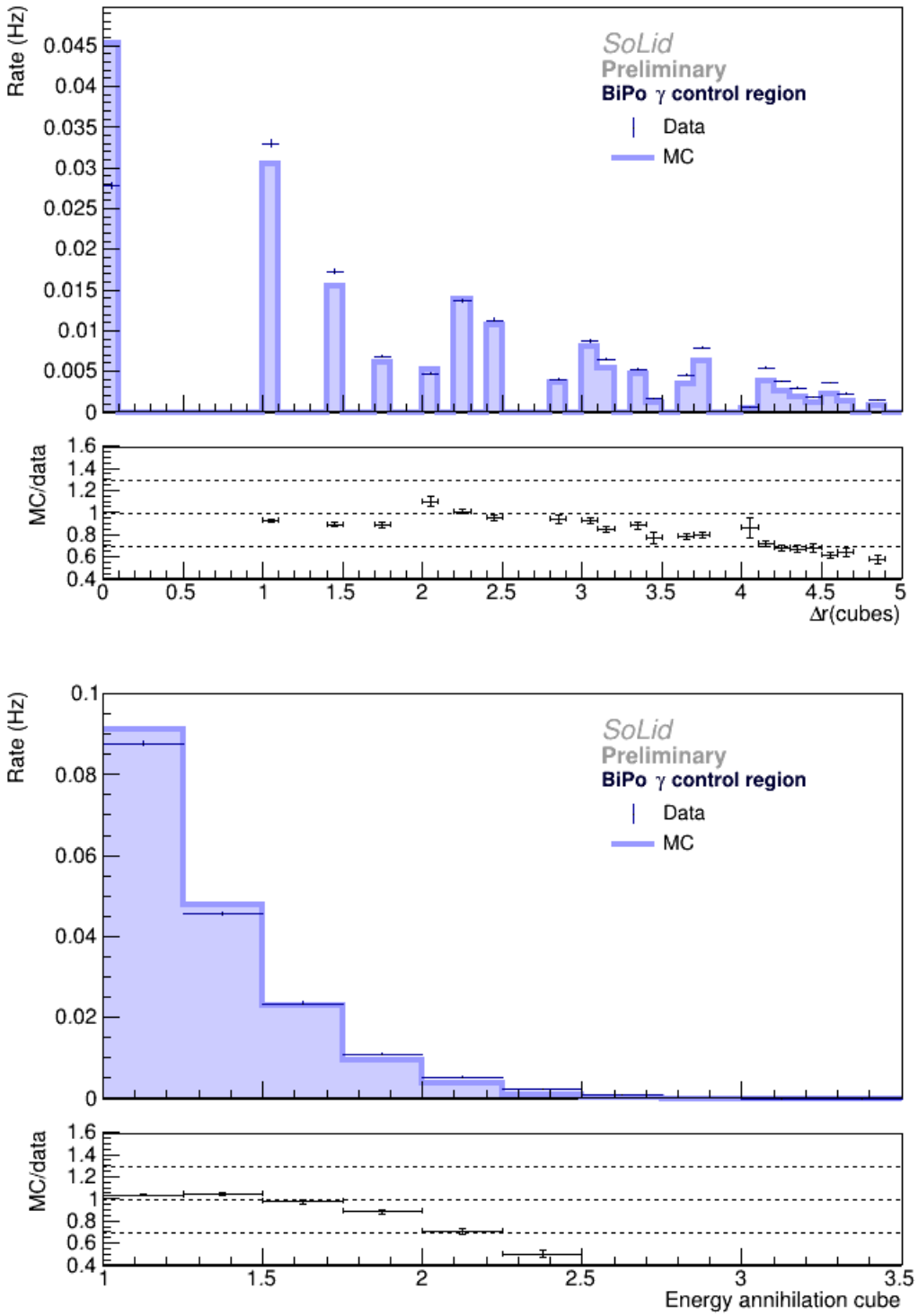

Figure 15.2.5: Data Monte-Carlo comparisons in the control region of radiative BiPo: The spatial distance between ES and NS signals (top) and the energy of the annihilation cube (bottom). The simulation is scaled to the data rate.

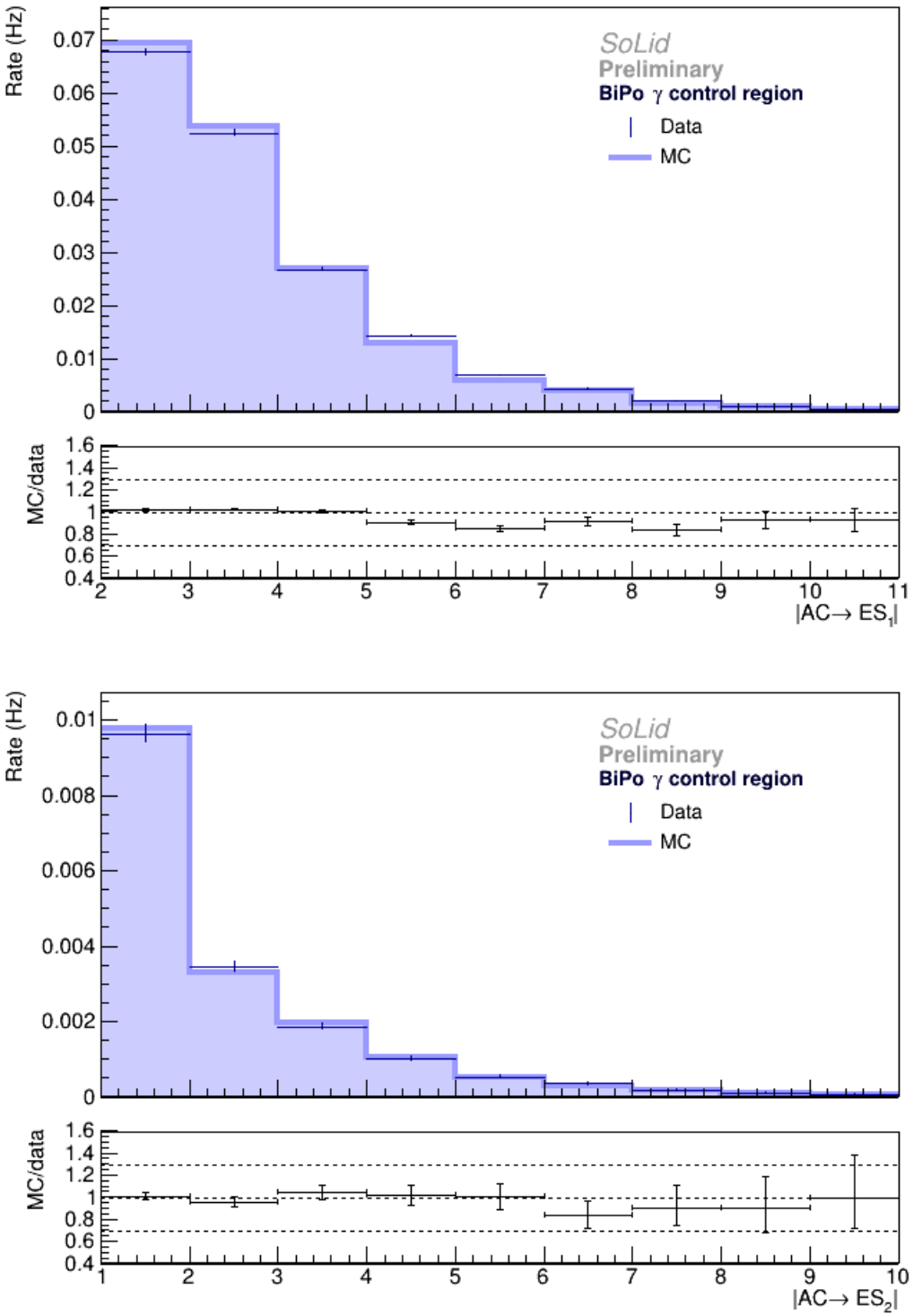

Figure 15.2.6: Data Monte-Carlo comparisons in the control region of radiative BiPo: The distance between the cube and the annihilation gamma's cubes. The simulation is scaled to the data rate.

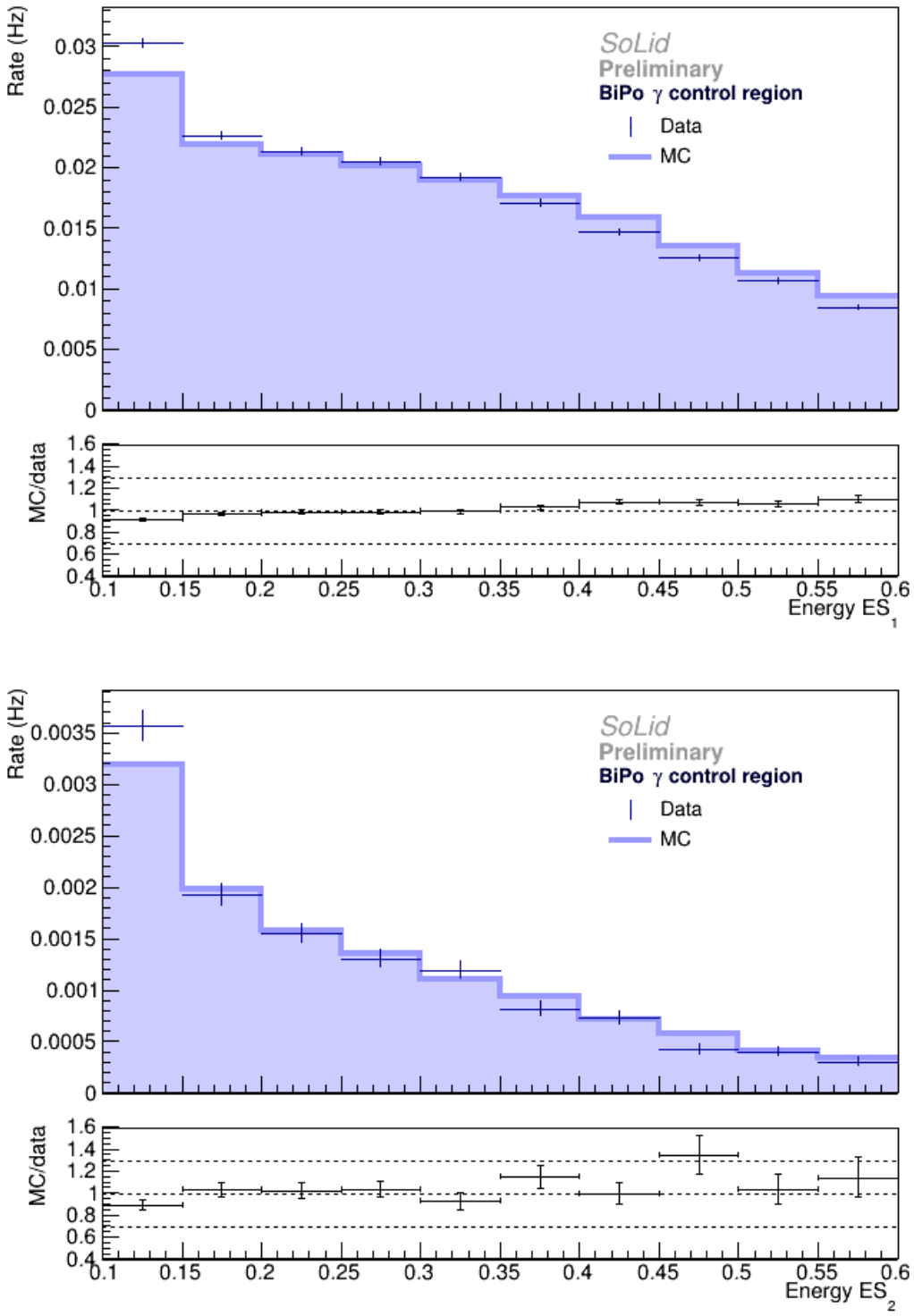

Figure 15.2.7: Data Monte-Carlo comparisons in the control region of radiative BiPo: The energies of both annihilation gammas. The simulation is scaled to the data rate.

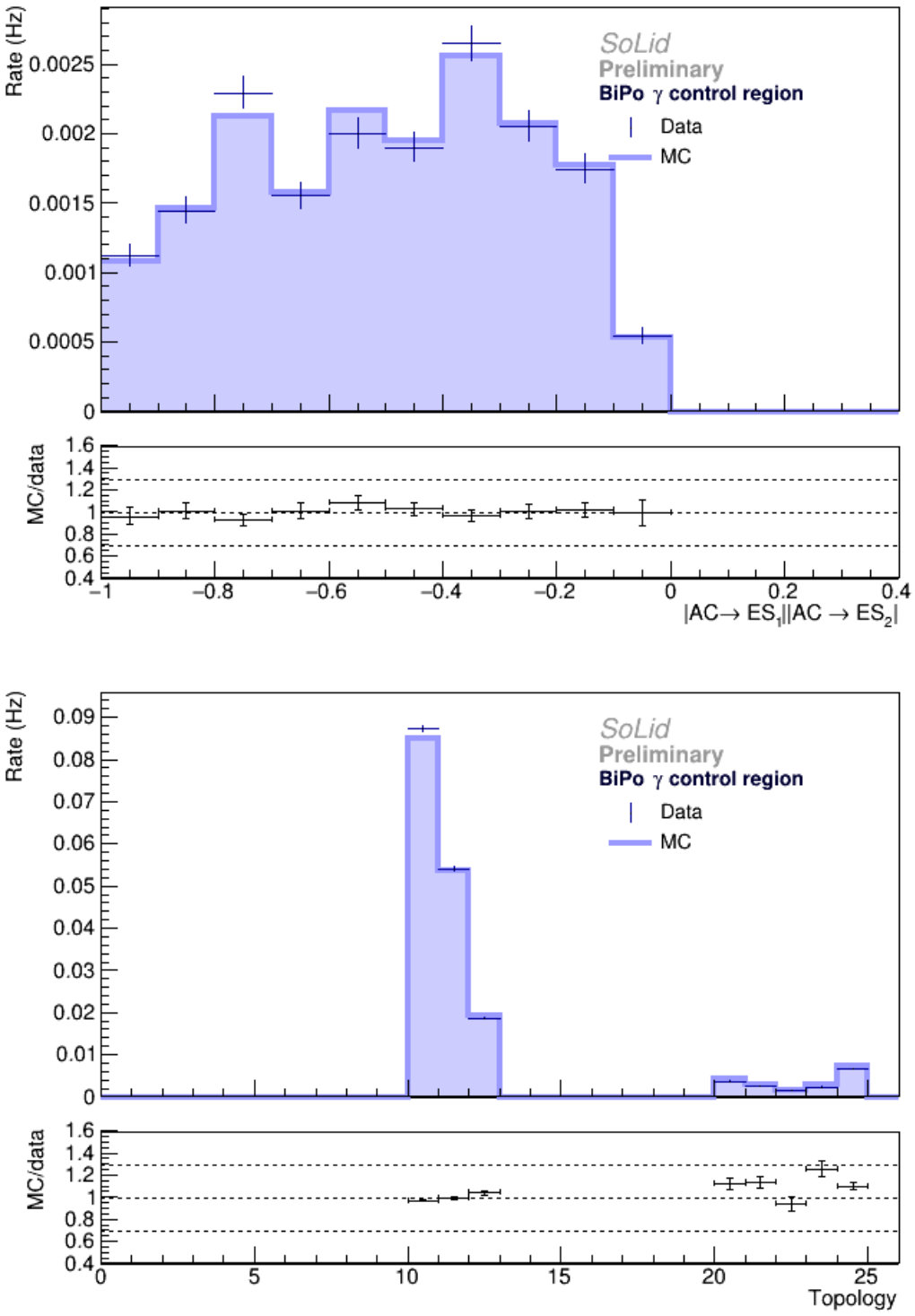

Figure 15.2.8: Data Monte-Carlo comparisons in the control region of radiative BiPo: The dot product between the vectors of the gammas with the annihilation cube (top) and the occurrence of the defined topologies (bottom). The simulation is scaled to the data rate.

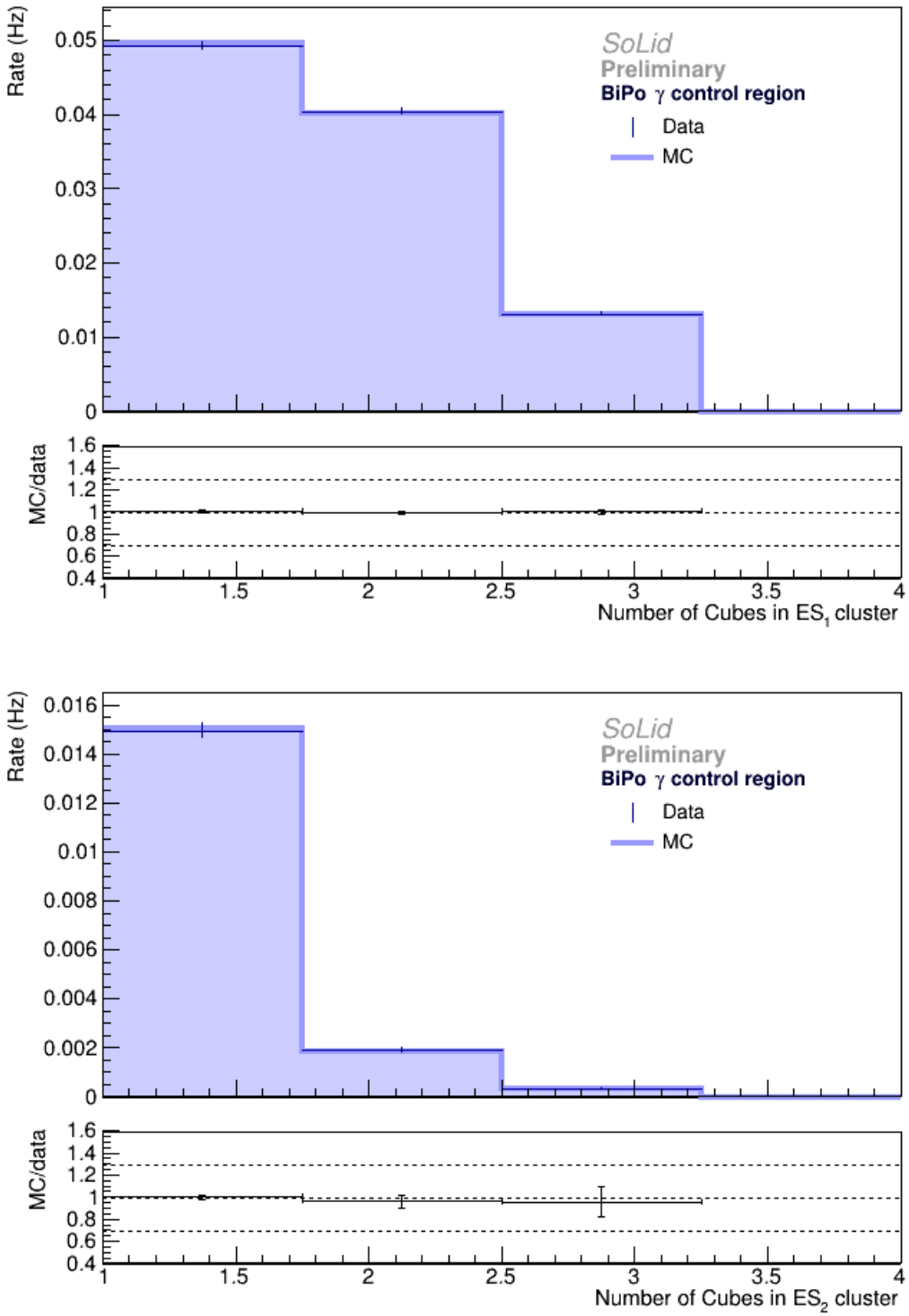

Figure 15.2.9: Data Monte-Carlo comparisons in the control region of radiative BiPo: The number of cubes in the ES clusters of the annihilation gammas. The simulation is scaled to the data rate.

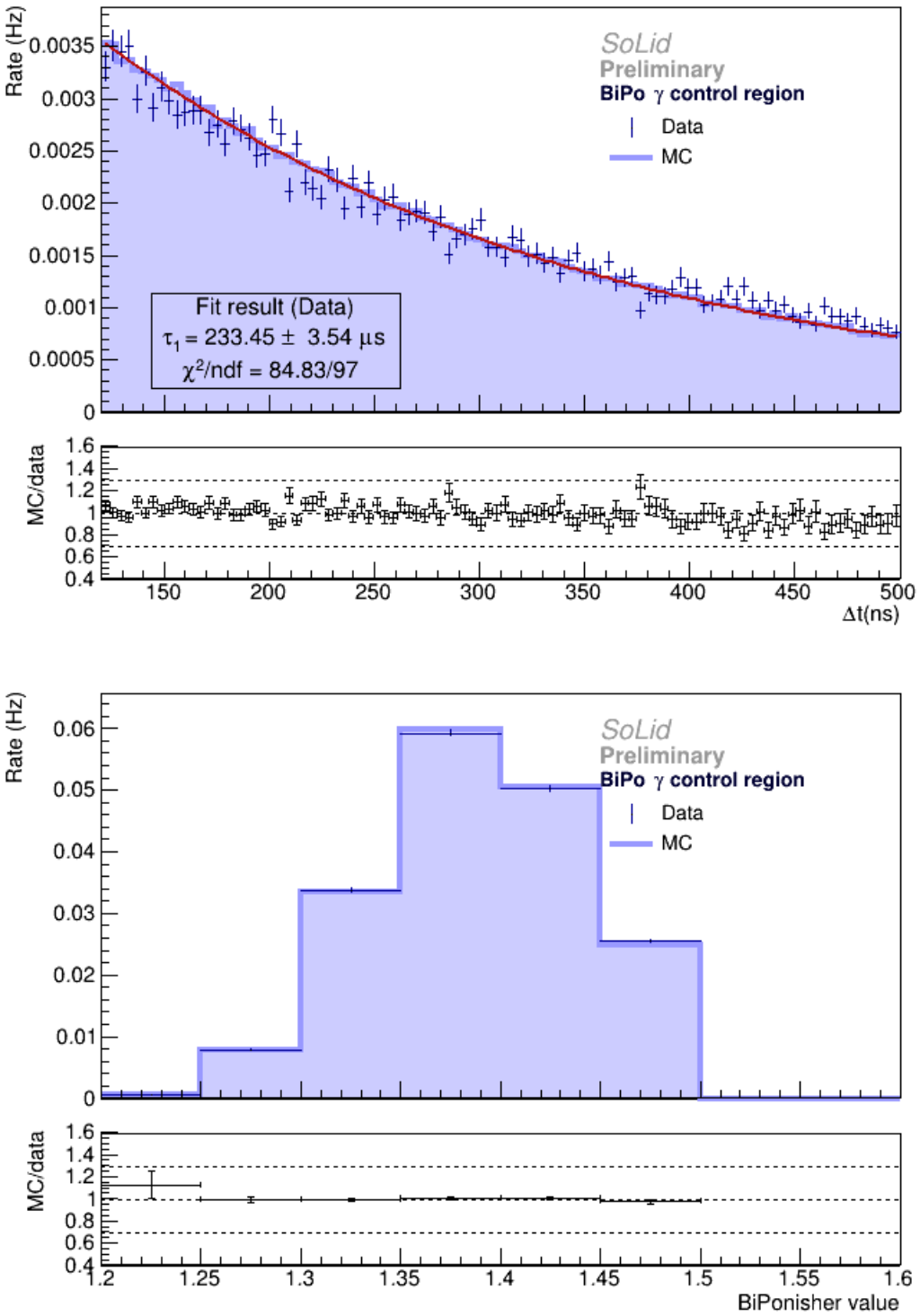

Figure 15.2.10: Data Monte-Carlo comparisons in the control region of radiative BiPo: The Δt_{NS-ES} (top) and the BiPonisher value (bottom). The simulation is scaled to the data rate.

15.3 THE CORRELATED COSMIC BACKGROUND

Cosmic particles cause one of the largest backgrounds for reactor neutrino experiments with low overburden. Fast neutrons, which either come from atmospheric showers or are caused by cosmic muons that spallate neutrons from nuclei in the material surrounding the detector, can enter the active detector material and recoil on hydrogen atoms. The recoil protons cause a prompt ES signal, while the neutrons are moderated and then detected as delayed NS signal. This coincidence poses a background to the IBD signal. It is not possible to discriminate in data between the fast neutrons from atmospheric origin and from muon spallation origin. Their contributions will be estimated based on simulation. As the cosmic background of fast neutrons is independent of the reactor operation, its rate and properties are determined from reactor off data and compared to dedicated simulations. The control region of fast neutrons is constructed with the following cuts:

$$\Delta t \in [0:200]\ \mu s$$
$$R \in [1,5]$$
$$E_{\text{prompt}} \in [4,20]\ \text{MeV}$$

The Δt requirement is adapted to the expected capture time of the neutrons. Although fast neutrons can travel further, the requirement on the distance R is limited to 5 cubes, to study the cosmic background in the IBD like region. The energy requirement ensures the rejection of almost all BiPo events. The Δt distribution of the selected events is shown in figure 15.3.1. A fit in the time window [0,500] μs is performed with two exponentials and a constant contribution for the accidental coincidences. The fit indicates time constants of $\tau_1 = 14.5 \pm 10$ μs and $\tau_2 = 72.9 \pm 4$ μs, which is in very good agreement with the expected capture time for these neutrons. The distribution of BiPonisher values indicates that the fast neutron control region has a neutron contribution of 99% and only 1% BiPo alpha's [165].

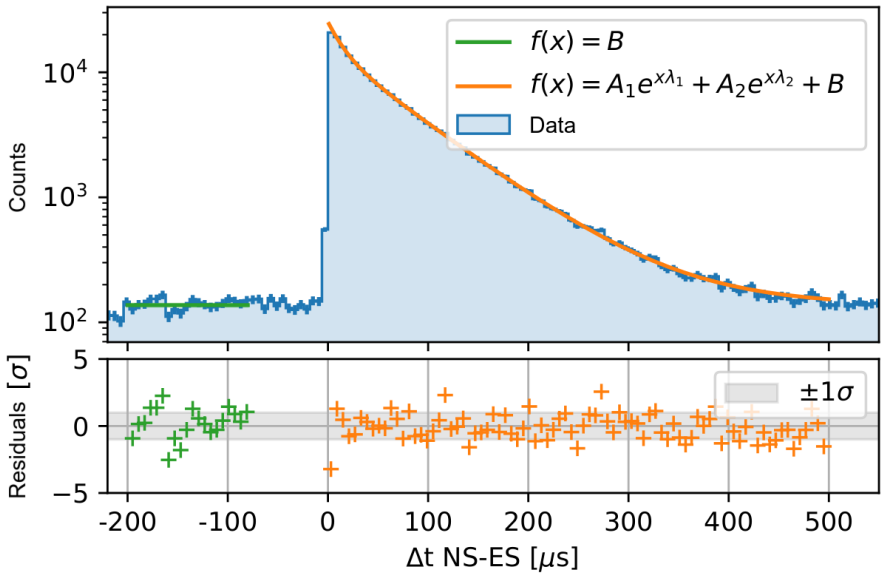

Figure 15.3.1: Distribution of Δt in the fast neutron control region. The accidental contribution is estimated from the time region [-200:-80] μs. The distribution in [0:500]μs is fitted with the sum of two exponentials.[165]

The readout simulation is used to study the contribution of fast atmospheric neutrons and muon induced spallation neutrons to the correlated cosmic background, by means of comparing their simulated rate to reactor off data in the fast neutron control region,

$$\mathrm{Roff}_{\mathrm{fast\,n}} \approx \mathrm{Roff}_{\mathrm{acc.\,corr.}} + \mathrm{MC}_{\mathrm{atm.n}} + \mathrm{MC}_{\mathrm{spall.n}}.$$

Here, $\mathrm{Roff}_{\mathrm{fast\,n}}$ is the fast neutron selection in the reactor off data, $\mathrm{MC}_{\mathrm{atm.n}}$ is the atmospheric neutron simulation sample and $\mathrm{MC}_{\mathrm{spall.n.}}$ is the spallation neutron simulation sample. The accidental contribution, $\mathrm{Roff}_{\mathrm{acc.\,corr.}}$, is not simulated but selected from reactor off data in an off-time window with the same range as the correlated one, but shifted by -600μs.

For an absolute comparison, the data- and simulation selections are all rescaled to one day. The produced simulations amount to an estimated real time of 109487 s for the muon MC (1.267 days) and 134123 s for the atmospheric neutron case. Note that the simulation samples are produced with a constant pressure. The data are not corrected for variations in atmospheric pressure but is selected from a period with on average a constant pressure, namely from cycle 3 of 2018 from July 20th until July 26th, amounting to a data taking period of 564518 s (6.533 days). The study of the cosmic backgrounds indicates that the reactor off data consists of 16 % of accidentals, 49 % spallation neutrons and 35 % of atmospheric neutrons.

For all variables, shown in figures 15.3.2 to 15.3.7, a good agreement between data and simulation is found. Only for the prompt energy, the simulation overestimates the visible energy, as compared to data. This is probably due to the occurrence of deadtime in the actual detector. High energetic fast neutrons can cause the plane buffer to become saturated which causes the data taking of the concerned plane to be halted. In addition, because of channel deadtime the events in real data record less energy because only the contribution of the remaining channels is reconstructed as prompt energy.

15.3.1 MUON VETO

Time vetoes can be applied to reduce the cosmic background, as muons are often the precursor of a fast neutron event. The muon veto excludes a coincidence if the time difference of its NS signal to the last detected muon is smaller than 200 μs. Another way to suppress the cosmic background is based on NS and ES signal multiplicities, which are usually higher for a fast neutron event than for an IBD interaction, since multiple neutrons can be produced in a spallation process and the energetic proton recoils are often recorded as several ES signals. The NS time veto avoids NS multiplicity by rejecting events in a time span around an NS signal.

Currently, the vetoes are not used in the IBD analysis as they induce too much detector dead time. For example, the muon veto would reject about 10% of events in the cosmics control region, while inducing a dead time after the passage of each muon, resulting in a generalised dead time of the order of 6%.

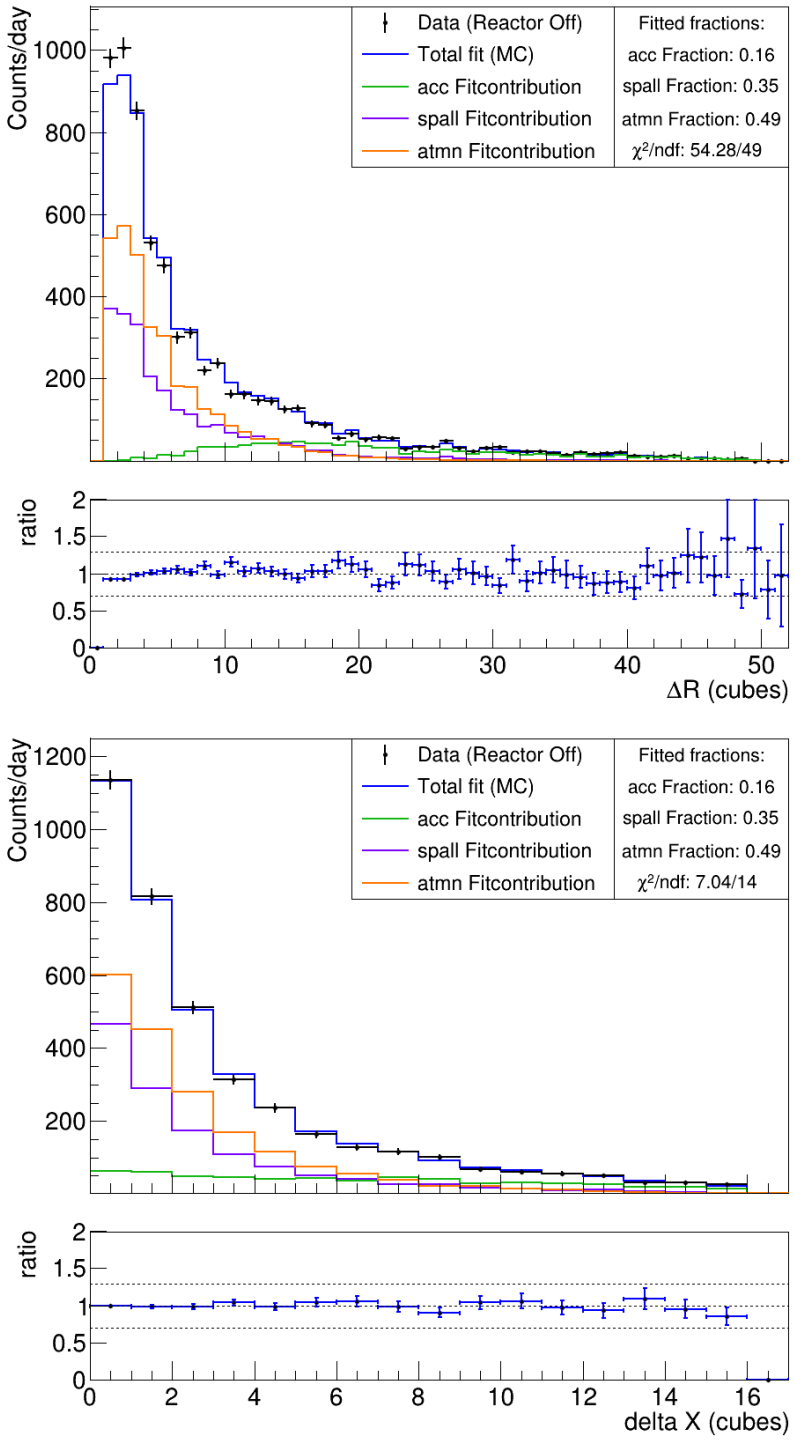

Figure 15.3.2: The reactor off data in the fast neutron control region with a weighted sum of simulated atmospheric neutrons, simulated spallation neutrons and accidentals from data, for the distance and the Δx between the prompt and delayed signal.

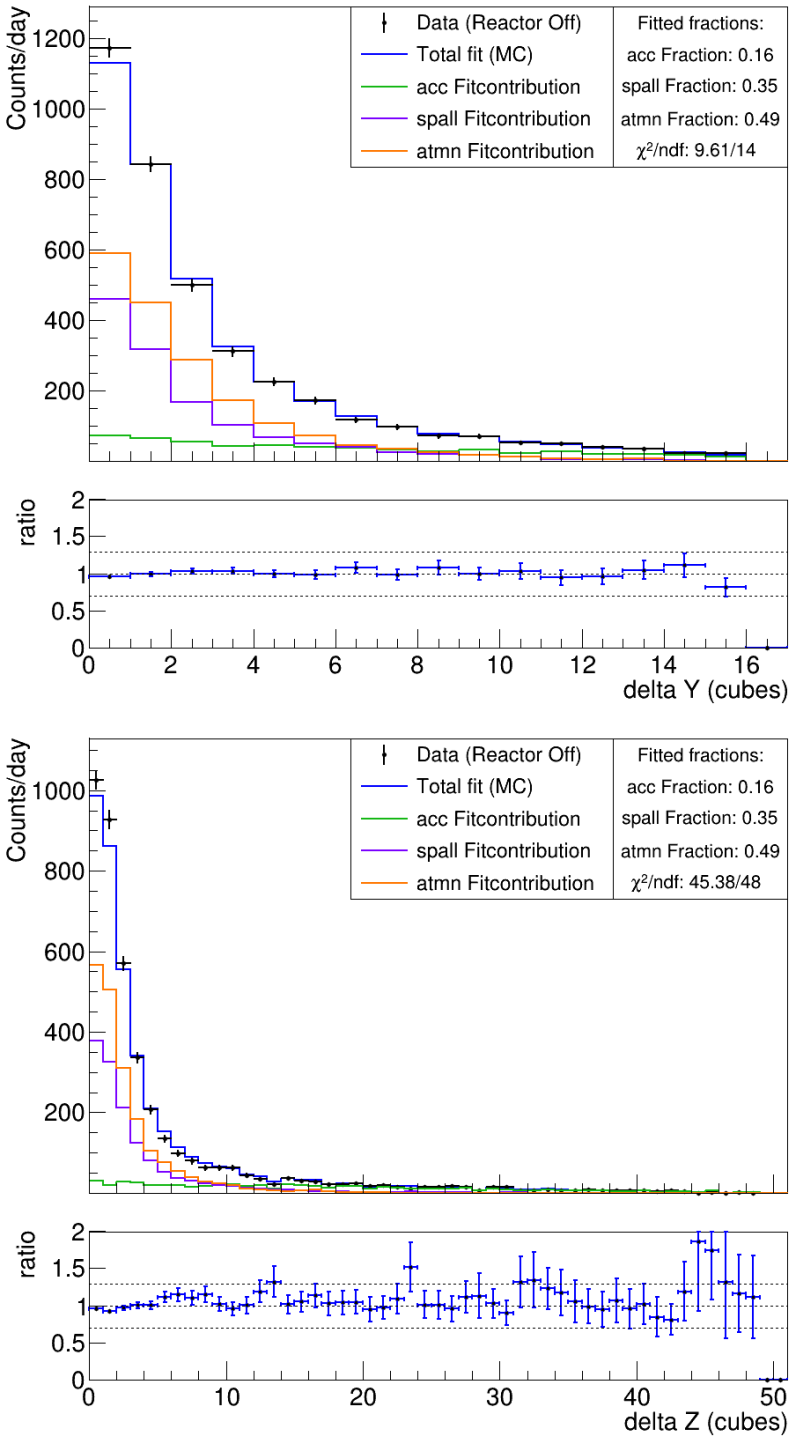

Figure 15.3.3: The reactor off data in the fast neutron control region with a weighted sum of simulated atmospheric neutrons, simulated spallation neutrons and accidentals from data, for the Δy and the Δz between the prompt and delayed signal.

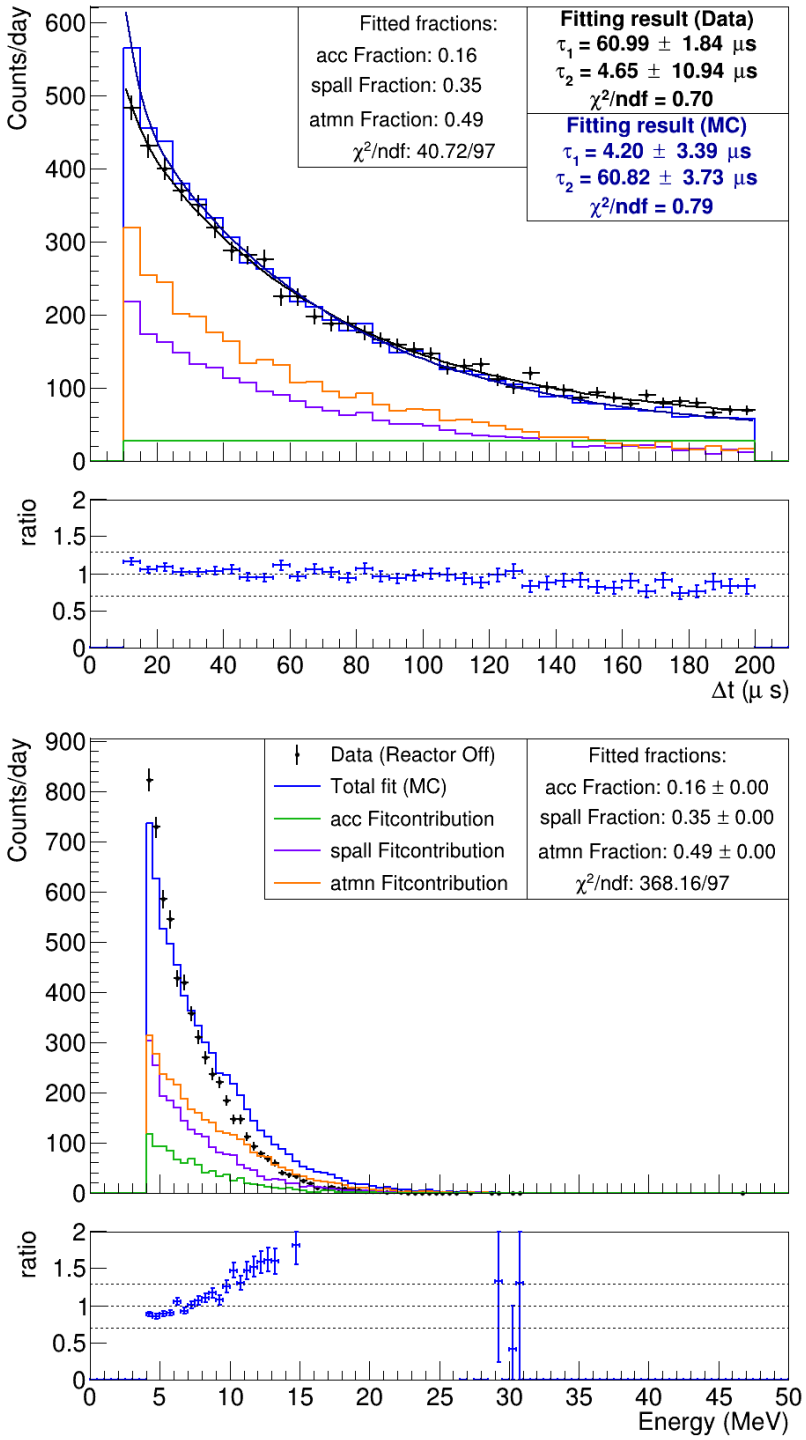

Figure 15.3.4: The reactor off data in the fast neutron control region with a weighted sum of simulated atmospheric neutrons, simulated spallation neutrons and accidentals from data, for the time difference between the prompt and delayed signal and for the energy of the prompt signal.

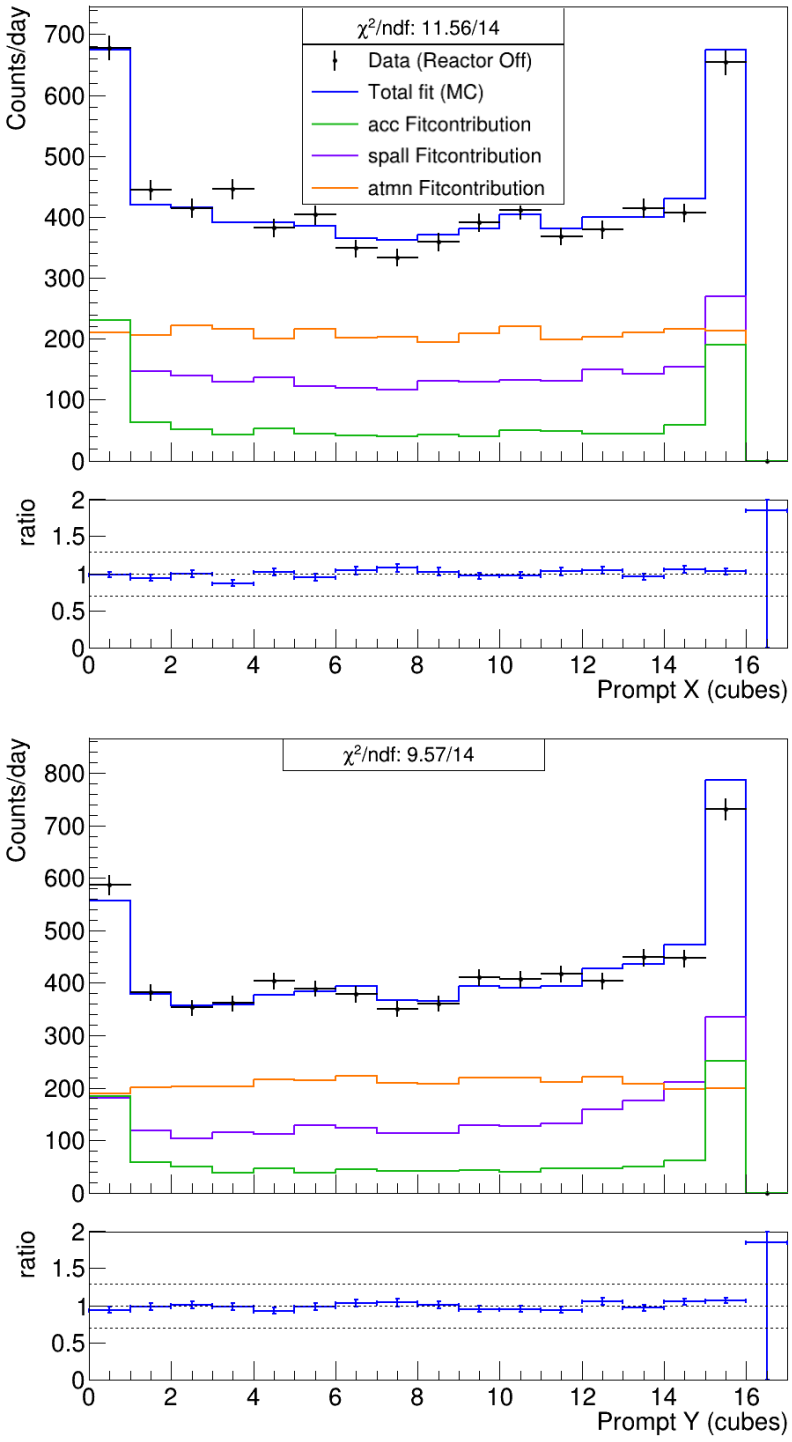

Figure 15.3.5: The reactor off data in the fast neutron control region with a weighted sum of simulated atmospheric neutrons, simulated spallation neutrons and accidentals from data, for the x and y position of the prompt signal.

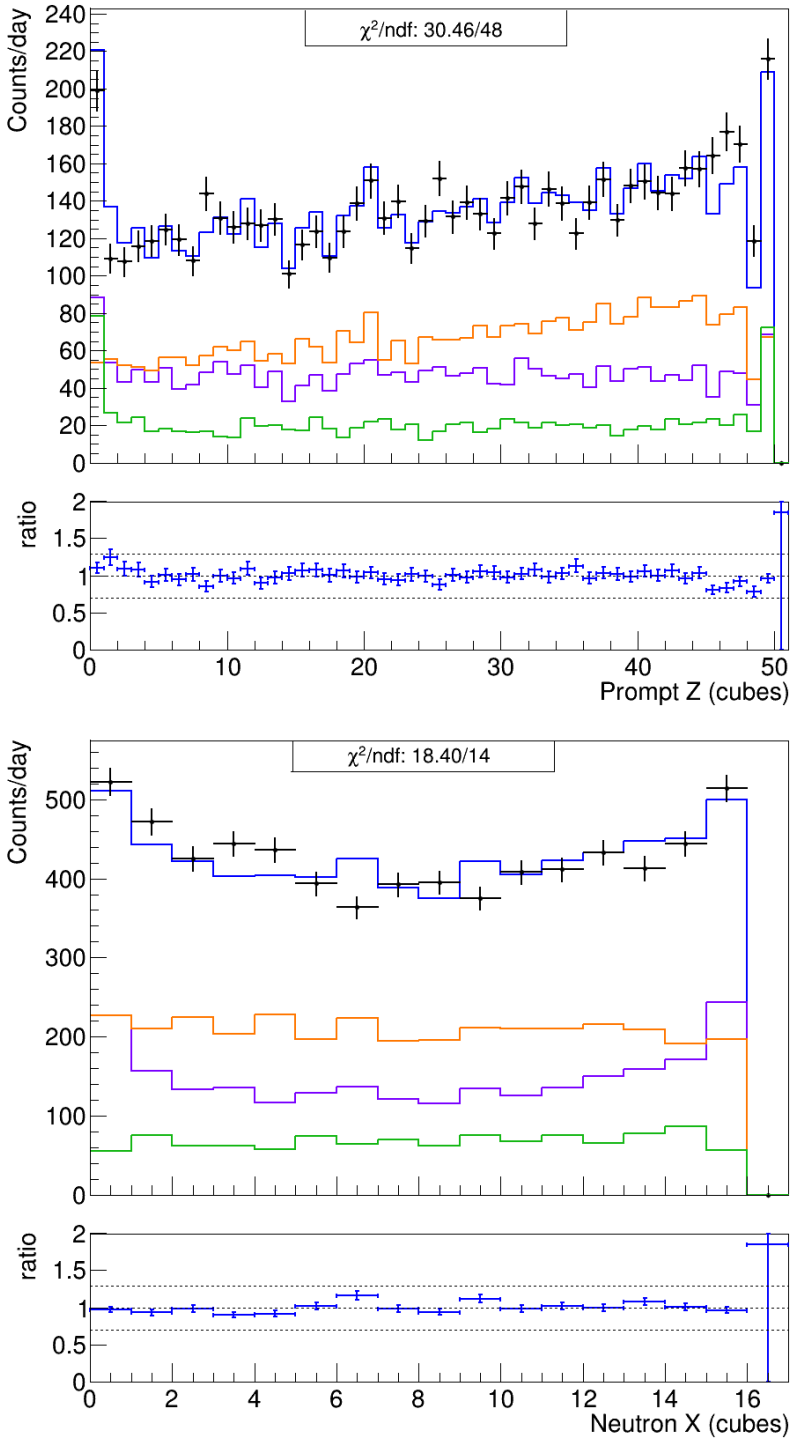

Figure 15.3.6: The reactor off data in the fast neutron control region with a weighted sum of simulated atmospheric neutrons, simulated spallation neutrons and accidentals from data, for the z position of the prompt signal and the x position of the delayed signal.

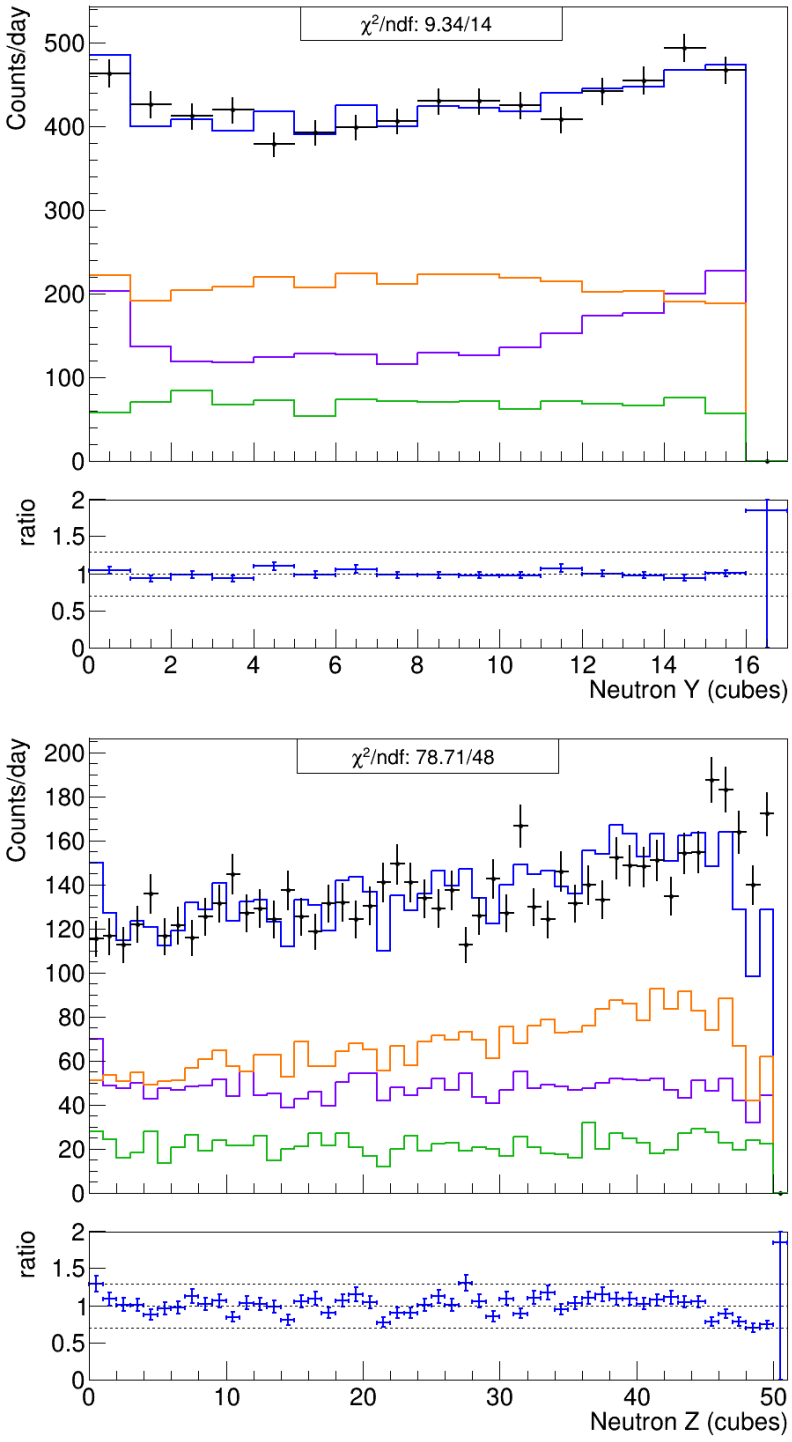

Figure 15.3.7: The reactor off data in the fast neutron control region with a weighted sum of simulated atmospheric neutrons, simulated spallation neutrons and accidentals from data, for the y and z position of the delayed signal.

16

IBD ANALYSIS

The SoLid experiment will investigate oscillation patterns in the L/E behaviour of electron anti neutrinos at very short baseline from a nuclear reactor. In order to do so, the reactor neutrinos have to be identified with the highest possible S/B ratio while simultaneously retaining a high IBD detection efficiency.

The following chapter is concerned with the neutrino IBD analysis of the physics data of the SoLid experiment. The analysis is constructed and tested with a limited open data set, taken from June 9th 2018 until August 18th 2018. This period includes 34 days of reactor off, as well as the third reactor on cycle of 2018 that lasted 22 days and for which the reactor was operated at a power of 60 MW. In the unblinding strategy, the other physics data will be opened and processed once the analysis is ready. At the time of writing, the data are still blinded.

Like for any very short baseline reactor neutrino experiment, the main challenge is to separate IBD signals from the background noise. The properties expected for IBD events will be determined based on the study of Monte-Carlo simulations. Several variables of interest will be determined, that show great discrimination power towards the prominent backgrounds. A set of selection criteria or cuts will be defined to reduce the contribution of background noise as much as possible. Since these selection criteria also have a significant impact on the IBD signal, they have to be optimised to obtain the highest possible IBD detection efficiency and signal-to-background ratio.

16.1 PREDICTION OF THE IBD SIGNATURE

The characteristic signature of IBD events in the highly segmented SoLid detector is investigated based on the full simulation of cycle 3 of the BR2 reactor in 2018. The spatial distribution of nuclear fissions, as modeled by the BR2 teams, is integrated in the SoLO software (see chapter 10), which propagates the neutrinos in the detector. At each IBD interaction point, the GEANT4 simulation generates corresponding neutrons and positrons and tracks them through the detector volume (see chapter 12). Each of their energy depositions is passed on to the readout simulation which simulates the response of the scintillators and how the signal transferred through the detector readout and trigger system (see chapter 13 and 7). The simulated signals are finally subject to the reconstruction chain of the Saffron2 software (see chapter 8). The simulated data will be in the same format as the actual data. The Saffron2 code delivers a file with a list of reconstructed ES-NS coincidences and their reconstructed variables. This is the starting point for the IBD analysis.

The expected distributions for the variables of interest for the IBD events are shown in figures 16.1.1 to 16.1.4, both at the level of the GEANT4 simulation (shown with black dots) and on the level of

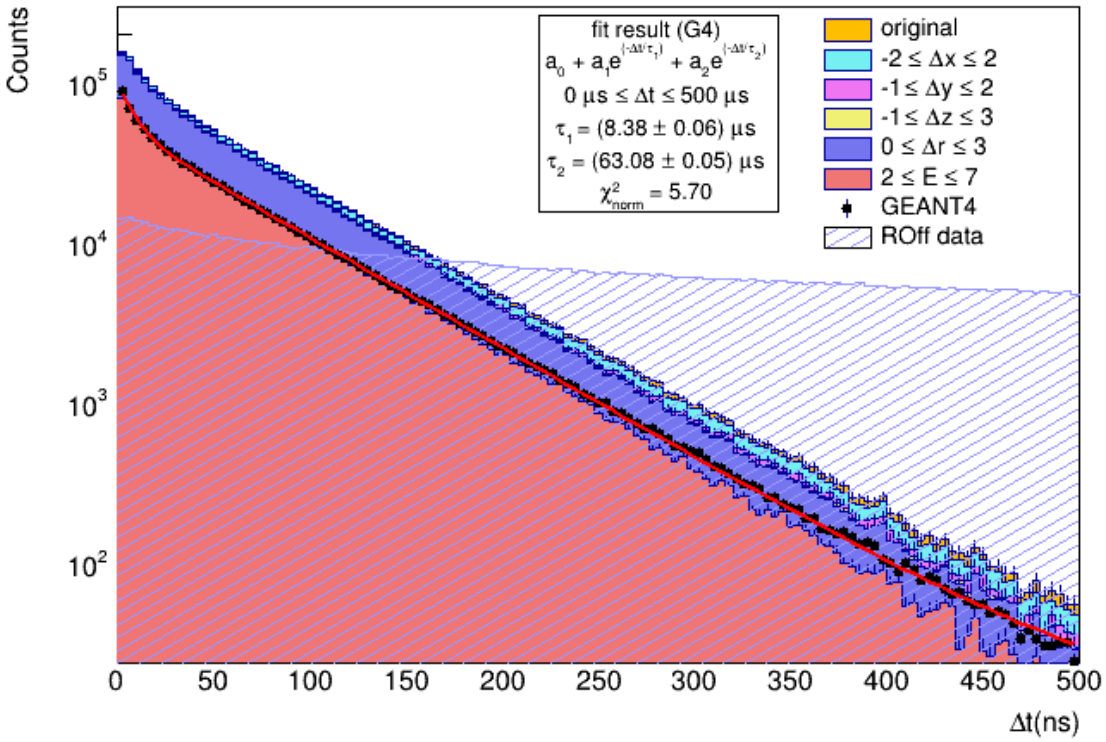

Figure 16.1.1: Distribution of time difference between the IBD positron and neutron (based on GEANT4 information, shown with black dots) and between the reconstructed ES signal and NS signal (based on readout simulation) with the consecutive cuts applied (represented by filled histograms). The time difference observed in reactor off data are overlayed with the shaded blue region.

reconstructed events that were processed by the readout simulation and Saffron2 (represented by filled histograms). The different colors correspond to consecutive selection cuts that will be applied to remove the background and that will be discussed in the following section. In addition, the shaded region indicates the distribution of full reactor off data, without any cuts applied. Both the GEANT4 and reactor off data are scaled to the red distribution in which all selection cuts were applied to reconstructed MC events. The reactor off data is considered to be an indication of the background for the IBD signal in the reactor on data.

The first important metric to characterise the IBD signal is the characteristic time difference, Δt between the prompt ES and delayed NS signal. The Expected distribution is shown in figure 16.1.1. The Δt values are positive as the neutron is delayed with respect to the positron. The GEANT4 distribution can be fitted with the sum of two exponentials. The contribution with the short capture time $\tau_1 = 8.38 \pm 0.06 \mu$s represents about 10% of events and is attributed to the capture of neutrons during their moderation process. About 90% of the events see a longer capture time $\tau_2 = 63.08 \pm 0.05 \mu$s where the thermalised neutron is captured. During calibration with the ^{252}Cf source, this exponential double structure was observed as well. The filled distributions of reconstructed MC events show that the application of the cuts leads to a steeper slope. This is because fiducial cuts remove coincidences with a big time difference. The reactor off data has a broad Δt distribution.

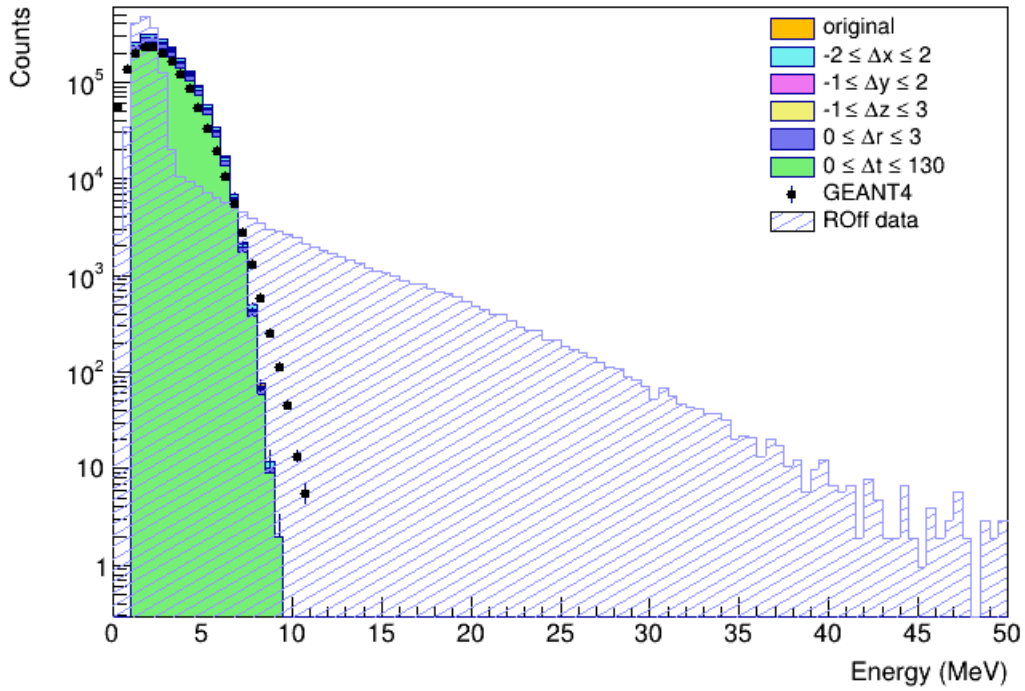

Figure 16.1.2: Distribution of the prompt energy of the IBD positron (based on GEANT4 information, shown with black dots) and of the reconstructed ES signal (based on readout simulation). The reconstructed ES prompt energies observed in reactor off data are overlayed with the shaded blue region. Both GEANT4 and reactor off distribution are scaled to the green distribution.

Another variable of interest is the reconstructed ES energy. The expected energy distribution, presented in figure 16.1.2, peaks around 2 MeV and becomes very small above 7.5 MeV. The reactor off data has a large contribution at low energy from the ^{214}Bi-^{214}Po decays inside the ^{6}LiF:ZnS(Ag) screens. The BiPo rate per cube is between three and four orders of magnitude higher than the expected IBD rate. BiPo is therefore the main background to the experiment in the energy region of interest before application of any selection requirements. At higher energies, the reactor off data contains background signals from cosmic origin.

The topology of the ES-NS coincidences is characterised by the spatial differences between the prompt ES and delayed NS signals, namely ΔX, ΔY, ΔZ and R. Figures 16.1.3 and 16.1.4 presents the distributions obtained from the simulations. The spatial difference rarely exceeds a distance of 2 cubes in any direction. Contrary to the distribution in ΔY, the two distributions ΔX and ΔZ are asymmetric. The negative ΔX is favored because of the position of the ^{6}Li:Zns(Ag) screens inside the unit cell. The positive ΔZ values are favored because of the directionality of the neutrino and the kinematics of the IBD interaction. The neutron keeps some momentum in the direction of the incoming antineutrino, during thermalisation. The distribution of R can take by definition, and because of the detector's granularity only certain positive values. The spatial distributions in the reactor off data have a broad spread. The high values are mainly due to accidental coincidences and cosmic backgrounds. The smaller distances have mainly contributions from BiPo decays.

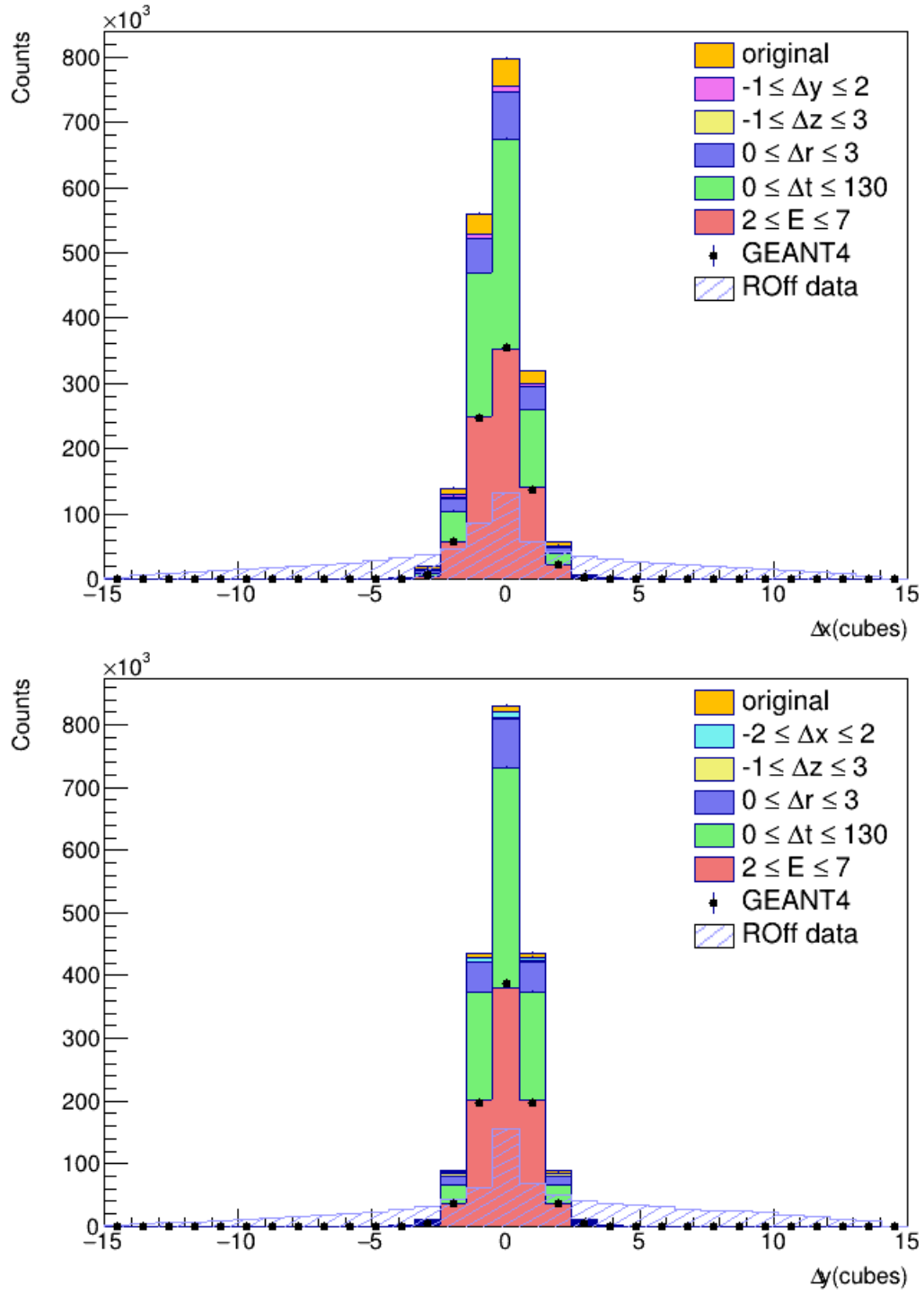

Figure 16.1.3: Distributions of spatial differences in x and y between the IBD positron and neutron (based on GEANT4 information, shown with black dots) and between the reconstructed ES signal and NS signal (based on readout simulation) with the consecutive cuts applied (represented by filled histograms). The spatial distributions observed in reactor off data are overlayed with the shaded blue region. Both GEANT4 and reactor off distribution are scaled to the red distribution.

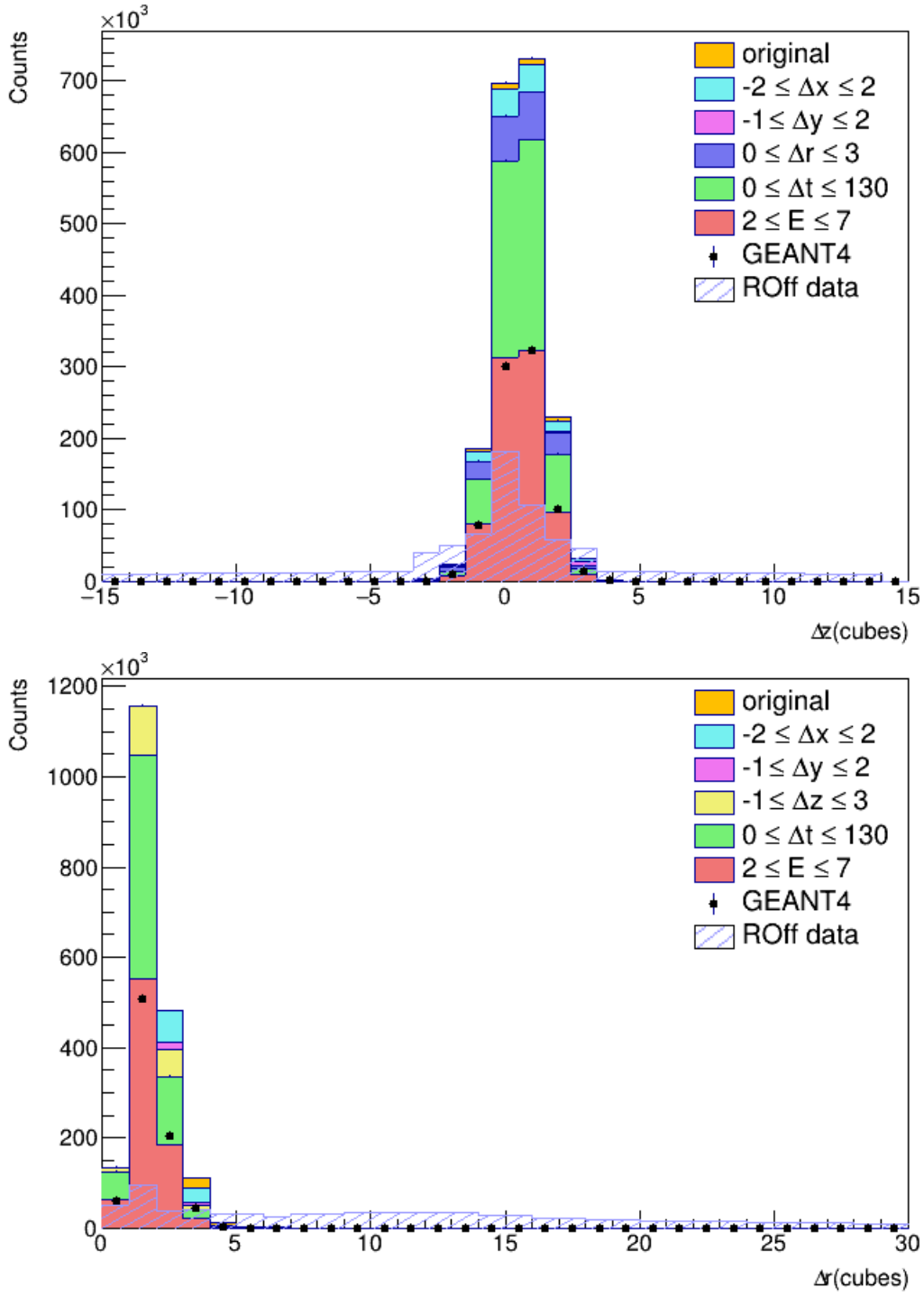

Figure 16.1.4: Distributions of spatial differences in z and in total between the IBD positron and neutron (based on GEANT4 information, shown with black dots) and between the reconstructed ES signal and NS signal (based on readout simulation) with the consecutive cuts applied (represented by filled histograms). The spatial distributions observed in reactor off data are overlayed with the shaded blue region. Both GEANT4 and reactor off distribution are scaled to the red distribution.

Recently, the collaboration put special interest into the annihilation gammas of the IBD positron, as they provide powerful discriminants over the backgrounds. The topological reconstruction of the positron annihilation cube (AC) and the annihilation gamma cubes is described in section8.4. Figures 16.1.5 to 16.1.9 show several variables of interest regarding annihilation gammas for the IBD simulation and for the raw reactor off data. The simulation was found to be trustworthy based on validation in the radiative BiPo control region (see section 15.2.3).

In regard to the reactor off data that contains the backgrounds, especially promising variables for signal discrimination are the spatial separation between the two gammas (expressed by the dot product of the vectors from the AC cube towards both gammas) and the energies of the reconstructed gammas. The latter is characteristic of the annihilation process. They are peaking for signal events at the Compton edge value of a 511 keV photon. Since the two photons are ranked by energy in the reconstruction, the discriminative power of the first gamma variable is stronger. In addition, a larger multiplicity of cubes in the envelope is characteristic of IBD candidates, resulting in topologies above 10 and 20. The numbers of cubes involved in the gamma clusters do not exhibit an obvious discriminative power, but add information through their correlations with other discriminative variables. The same holds for the separation distance between AC and the gammas and the distance between the two gammas.

Machine learning codes will be trained on the cases where no, one or two annihilation gammas are reconstructed, providing increasingly more information for IBD selection.

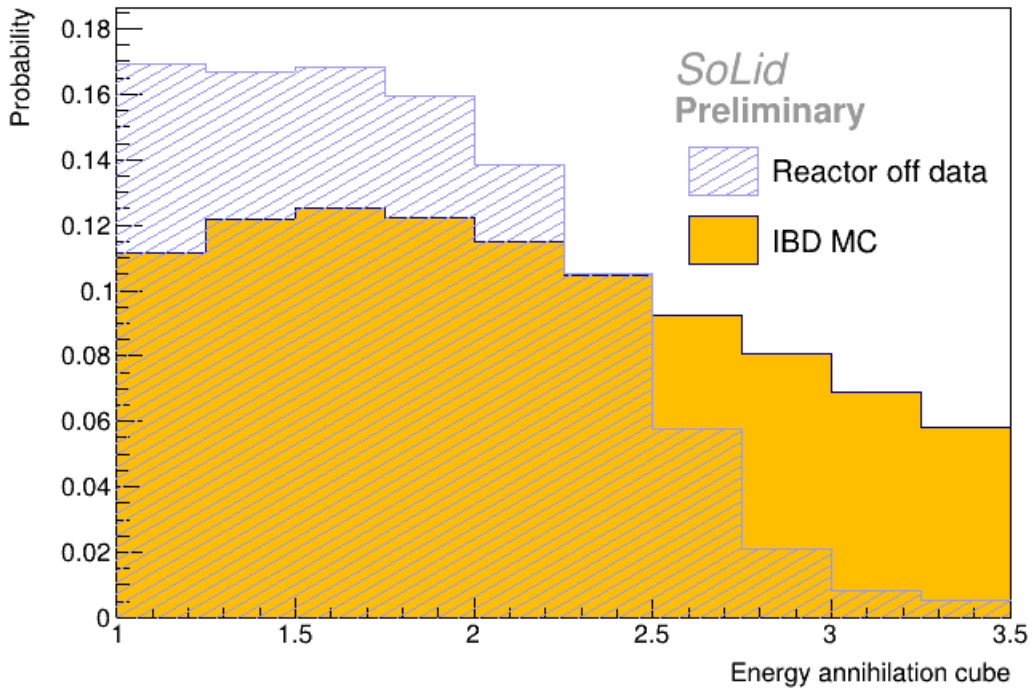

Figure 16.1.5: Prediction of the IBD signature in terms of the variables regarding annihilation gammas, based on simulation, versus the raw reactor off data: The energy of the annihilation cube.

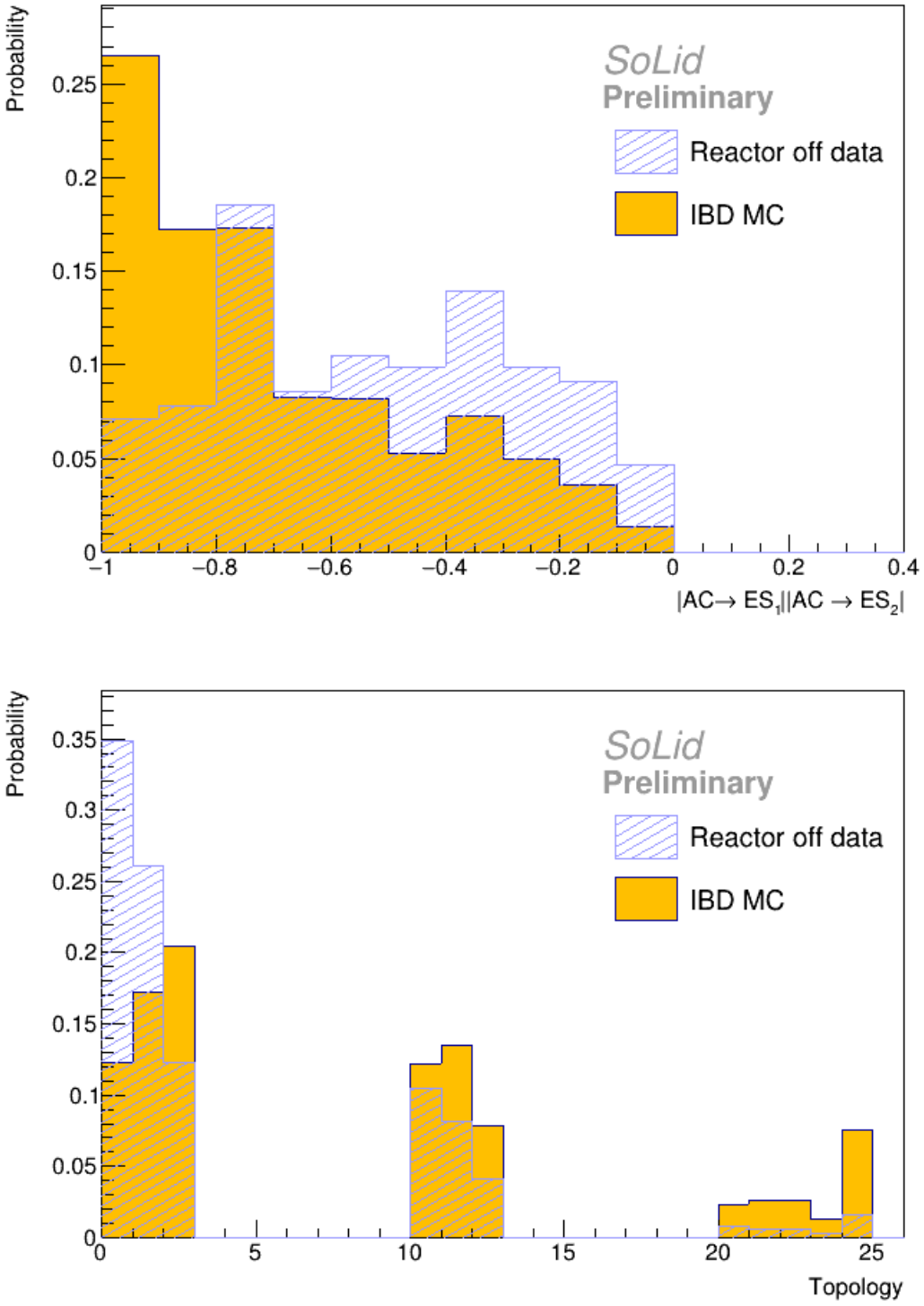

Figure 16.1.6: Prediction of the IBD signature in terms of the variables regarding annihilation gammas, based on simulation, versus the raw reactor off data: The dot product between the vectors of the annihilation cube with the gammas (top) and the occurrence of the defined topologies (bottom).

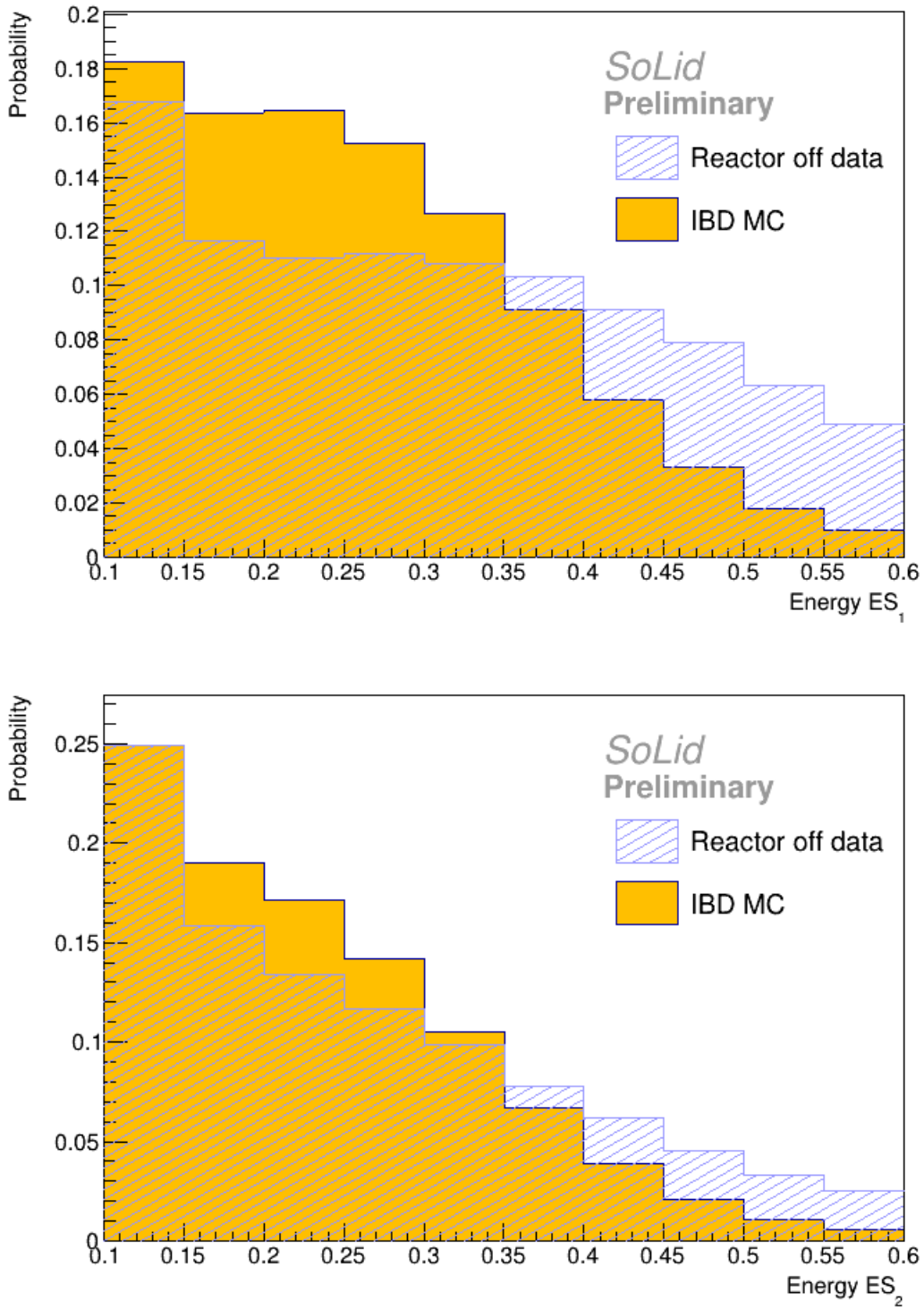

Figure 16.1.7: Prediction of the IBD signature in terms of the variables regarding annihilation gammas, based on simulation, versus the raw reactor off data: The energies of both the annihilation gammas.

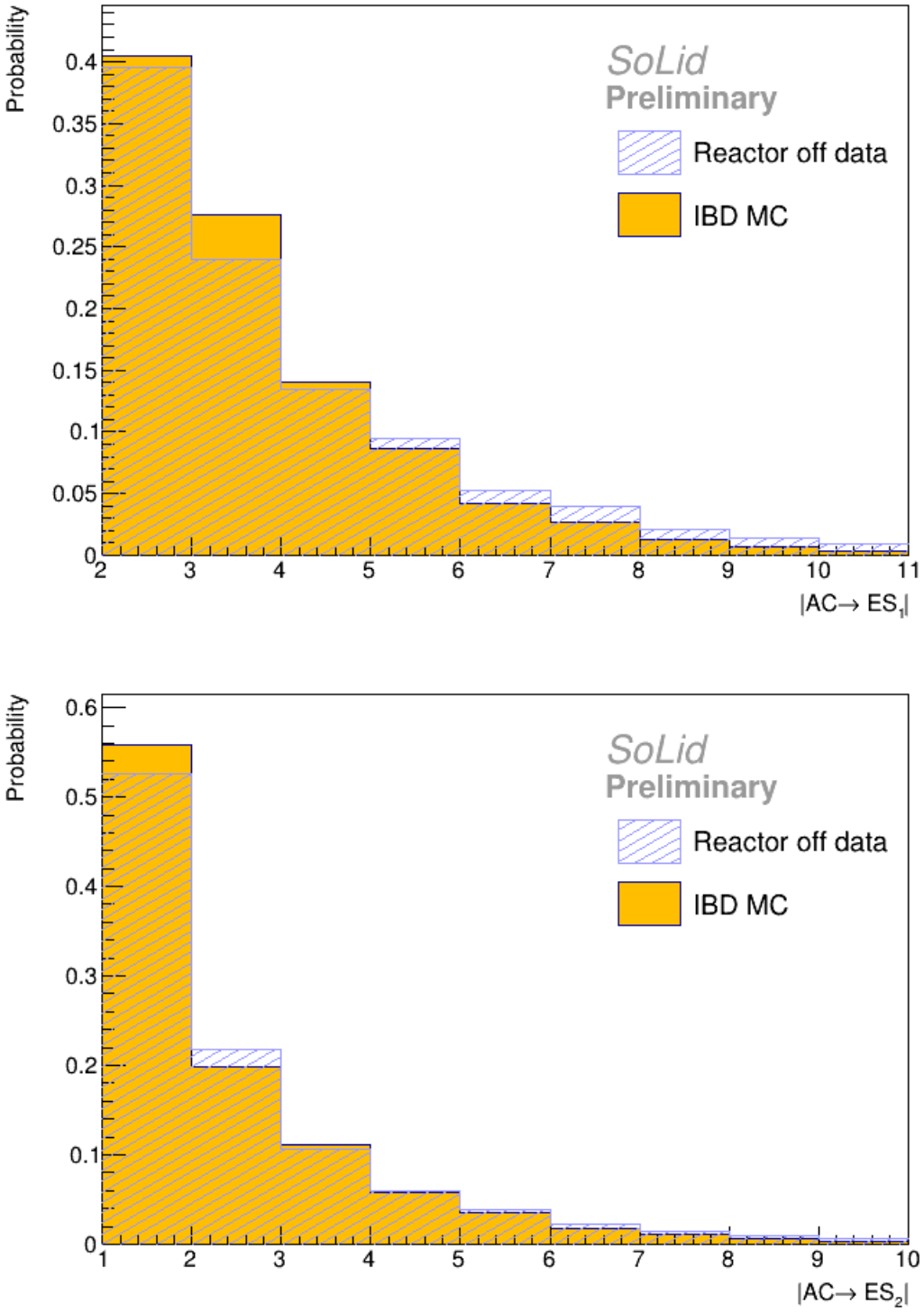

Figure 16.1.8: Prediction of the IBD signature in terms of the variables regarding annihilation gammas, based on simulation, versus the raw reactor off data: The distance between the cube and the annihilation gamma's cubes.

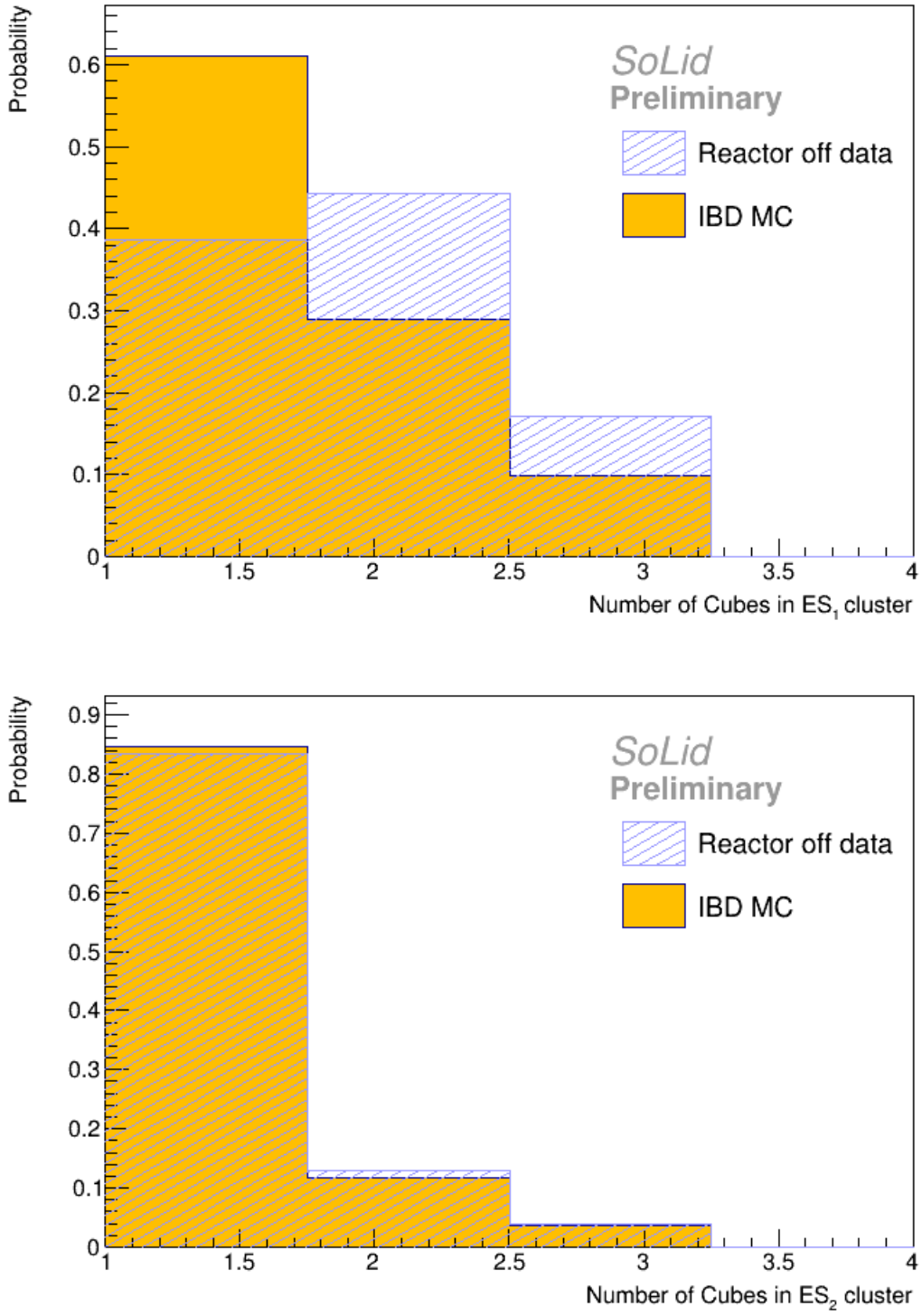

Figure 16.1.9: Prediction of the IBD signature in terms of the variables regarding annihilation gammas, based on simulation, versus the raw reactor off data: The number of cubes in the ES clusters of the annihilation gammas.

16.2 SELECTION PROCEDURES FOR THE IBD SIGNATURE

The initial, cut based IBD selection approach focused on the characteristics of the coincident positron and neutron signal. Currently, multiple approaches to resolve the positron's annihilation gammas are developed. The selection cuts are described in the following section, and the machine learning tools that try to exploit the annihilation signatures are described afterwards.

16.2.1 SELECTION CUTS FOR THE IBD SIGNATURE

To obtain an enriched sample of antineutrino induced IBD events from reactor on data, the event's parameter space is restricted with a sequence of selection criteria, namely

$$\begin{aligned} -2 \leq \Delta x \leq 2 \\ -1 \leq \Delta y \leq 2 \\ -1 \leq \Delta z \leq 3 \\ 0 \leq R \leq 3.4 \\ 0.5 \leq \Delta t \leq 130\ \mu s \\ 2.5 \leq E_{\text{reco}} \leq 7\ \text{MeV} \end{aligned}$$

Except for the last one, the cuts are defined based on the ES-NS coincidence that reduce the non-correlated backgrounds. Moreover, the temporal coincidence requirement rejects part of the BiPo while it keeps about 89% of the integral of the coincidences corresponding to the capture of a neutron. The cuts in Δx, Δy and Δz maximise the detection efficiency of the IBD positron. To avoid topologies where BiPo dominates, same cube ES and NS signals (ΔR = 0) are rejected. For the prompt ES signal, the lower limit reduces electronics noise and light leak effects, while the higher limit excludes high energetic particles such as (clipping) muons. The signal selection with these cuts, that are shown in figures 16.1.1 to 16.1.4 results in an estimated IBD selection efficiency of 43%.

When performing a complete cut based IBD analysis, the basic selection cuts are expanded. To avoid high energy fast neutrons with an extended topology, the ES volume is confined to

$$\Delta x \times \Delta y \times \Delta z \leq 297.$$

In addition, the following cuts can further reduce the BiPo background,

$$\begin{aligned} ES_2/ES_1 \leq 0.37 \\ \text{BiPonisher} > 1.495 \end{aligned}$$

where ES_1 is the energy of the highest energy ES cube and ES_2 of the second most energetic ES cube. For IBD signals, the second cube has a high probability to correspond with an annihilation gamma. It is therefore detected with a much lower energy. For a BiPo event, the second cube is very likely related to a gamma signal too, but since most populated excited states of ^{214}Po have energies of more than 1 MeV above the ground state, most emitted gammas will have larger energies than an annihilation gamma. The ES_2/ES_1 balance will be larger for the BiPo background than for the IBD signal. The BiPonisher cut is motivated by the discussion in section 15.2.1. An additional method for BiPo discrimination might be added in the future. The so-called BiPonator is based on image

recognition with a Convolution Neural Network. The first results promise an improvement of the α-neutron discrimination power with a factor 2.5, compared to the BiPonisher algorithm.

The signal selection with all these rectangular cuts results in an estimated IBD selection efficiency of ~10% and a remaining signal-to-background ratio of 0.06. As the high amount of remaining background events introduces a large statistical uncertainty that will reduce the experimental sensitivity, other, more advanced IBD selection methods were developed.

16.2.2 Machine Learning tools for the IBD selection

Two machine learning codes were developed for the IBD selection, based on multivariate analyses (MVA) techniques. They aim to exploit the additional information provided by the reconstructed annihilation gammas to classify the IBD events as signal, thereby increasing the signal to background ratio. Figure 16.2.1 shows that the signal and background have a correlation pattern between the discriminative variables. Therefore, the distinction between signal and background can be considered non-linear, raising the need for non-linear models. For a linear model it is expected that a linear combination of features (i.e. a linear cut in the higher dimensional variable space) can discriminate the signal from the background. Because only a tiny fraction of the data consists of signal, methods that are robust for class imbalance have to be used. Finally, the size of the dataset prohibits the use of methods that store the data, such as for example the K-Nearest Neighbors (KNN) classifiers, that make the assumption that similar events are in close proximity of each other in the parameter space.

The first MVA technique that is used is based on the uBoost package of the HEP ML Python library [208], which is dedicated to machine learning methods used in high energy physics. Since the complexity of the problem is modest, the learning method for the cut optimisation that was used, is based on Boosted Decision Trees (BDT)[209]. Because a decision tree is a linear classifier, it cannot grasp the non-linear behaviour of the data. BDT averages the output of many different 'weak' trees to introduce non-linearity. In every iteration over the data, a new tree is added to the BDT classifier that focuses on the mistakes that were made in the previous iteration, thus leading to convergence. The uniform method is used which retains a uniform selection efficiency in one or multiple physics variables, while optimising the signal and background discrimination. In the case of the IBD analysis, this is useful for the reconstructed z-position and energy variables, as a non-uniform selection in terms of L_{reco} and E_{reco} would greatly complicate the neutrino oscillation analysis that depends on the ratio L/E.

The second MVA technique uses the TMVA-package of the ROOT framework [210]. This Toolkit for MultiVariate Analysis (TMVA) provides a machine learning environment for the implementation of multivariate classification techniques. The classification method that is chosen for the IBD analysis is the Multi Layer Perceptron (MLP) and is an implementation of a neural network [211]. In general, a neural network (NN) can be considered to perform a mapping from a multidimensional space of input variables onto a one-dimensional space of output variables. The strength of a MLP is its ability to approximate any arbitrary relation. This makes it especially appropriate for complex non-linear data. This mapping is based on associations that the NN has developed from an example set of inputs and outputs, similar to the learning process in a human brain. By propagating produced errors back through the layers of the model, it adapts itself in every iteration (epoch) until convergence.

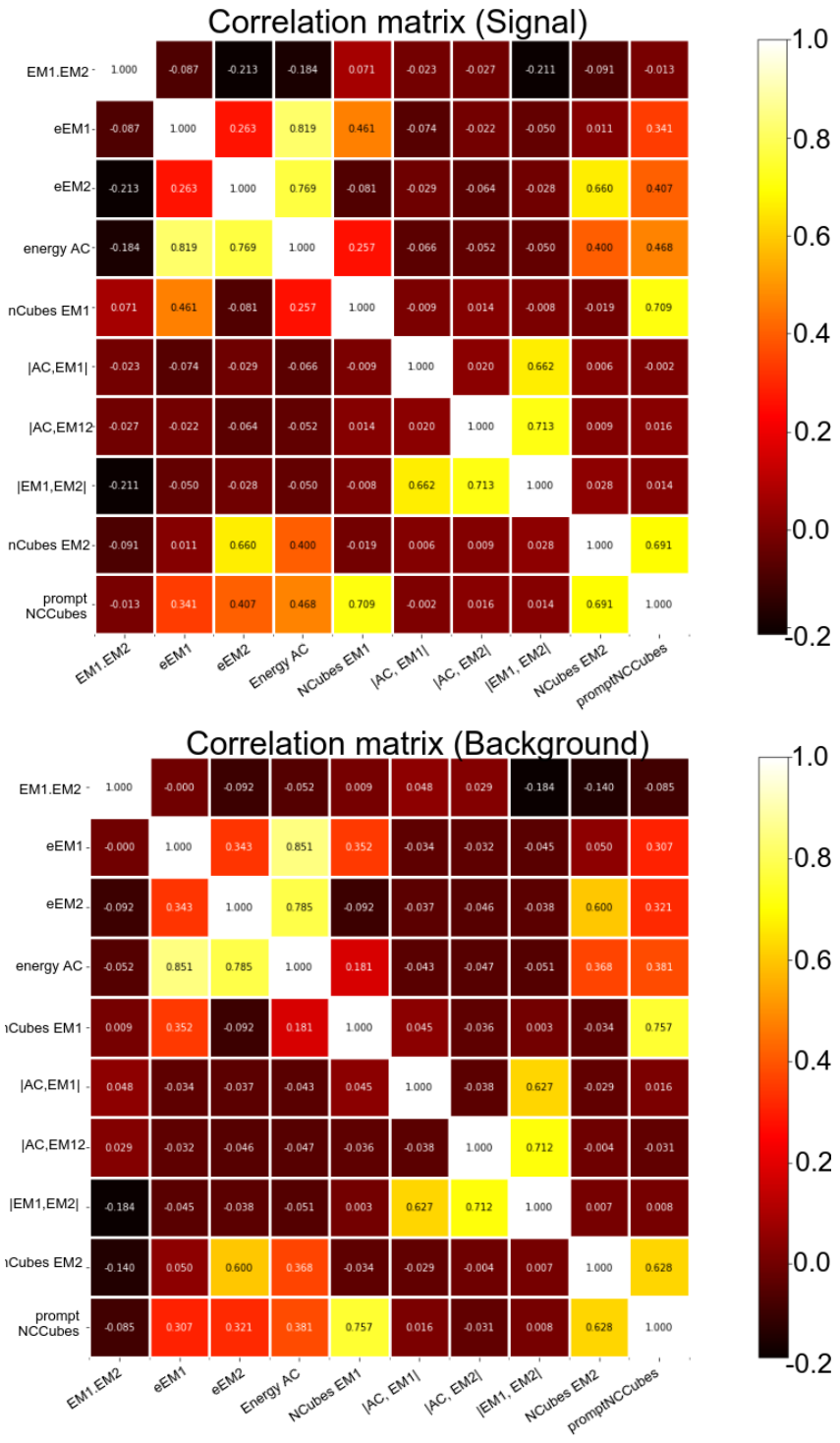

Figure 16.2.1: Correlation matrices for the discriminative variables for the simulated IBD (left) and reactor off data (right). For these matrices, events are selected with the topology 02, where no cubes are reconstructed in the envolope around the annihilation cube and two annihilation gammas are reconstructed.[167]

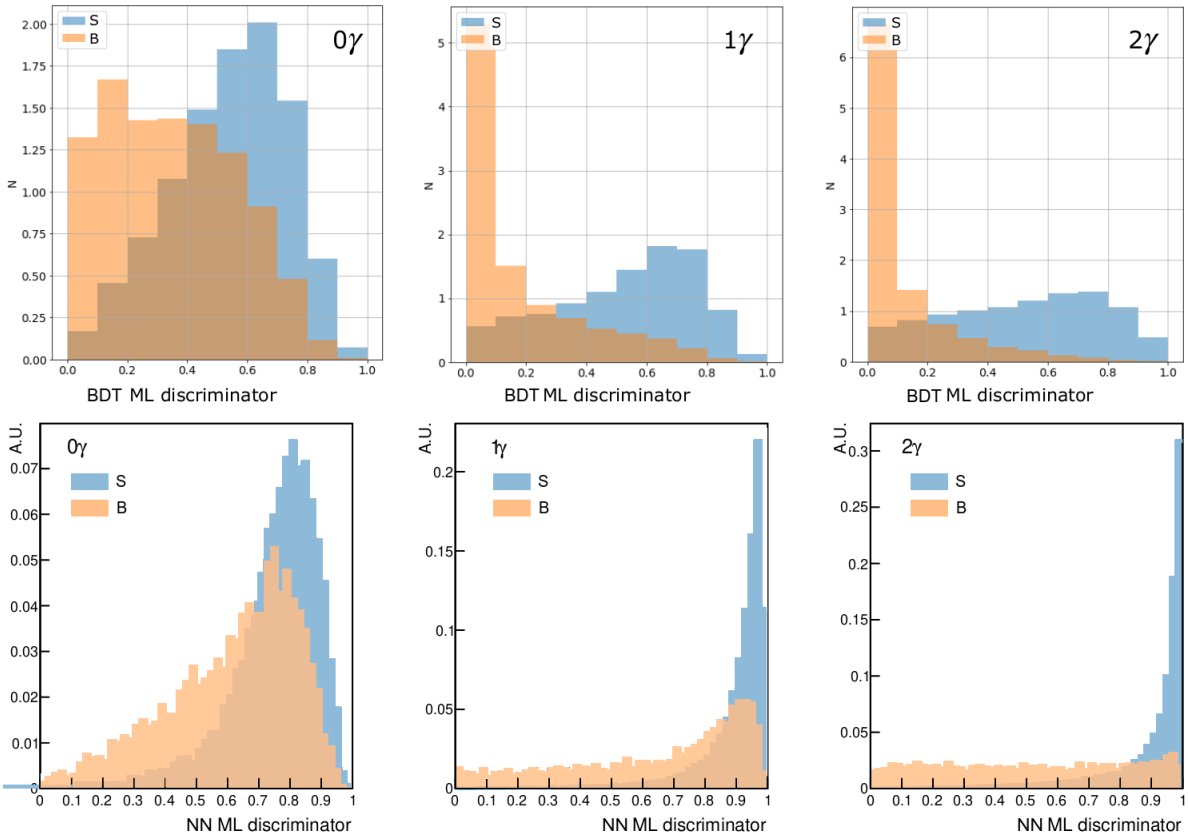

Figure 16.2.2: ML discriminators for the BDT method [212] (top) and the NN method [206] (bottom) for each of the three categories with different numbers of reconstructed gammas. The discriminators show a clear separation between the IBD signal (blue) and the background determined from reactor off data (orange).

The training of the multivariate classifier for signal events is performed with simulated IBD signals against reactor off data. Since the annihilation gammas deliver low-energy signals, a lower threshold on the channel amplitude was used during signal reconstruction. All channels with a signal amplitude above 80 ADC (2.5 PA) are regarded, instead of 144 ADC (4.5 PA). Since this poses a new challenge for the readout simulation, the energy response in the low energy range was tuned with a BiPo sample from reactor off data, as described in section 14.2.
A preselection cut is applied to the data that is less strict than for the standard IBD cut analysis:

$$
\begin{aligned}
-3 \leq \Delta x \leq 3 \\
-3 \leq \Delta y \leq 3 \\
-2 \leq \Delta z \leq 3 \\
0 \leq R \leq 4 \\
1 \leq \Delta t \leq 141\ \mu s \\
2 \leq E_{\text{reco}} \leq 7\ \text{MeV} \\
\text{BiPonisher} > 1.44
\end{aligned}
$$

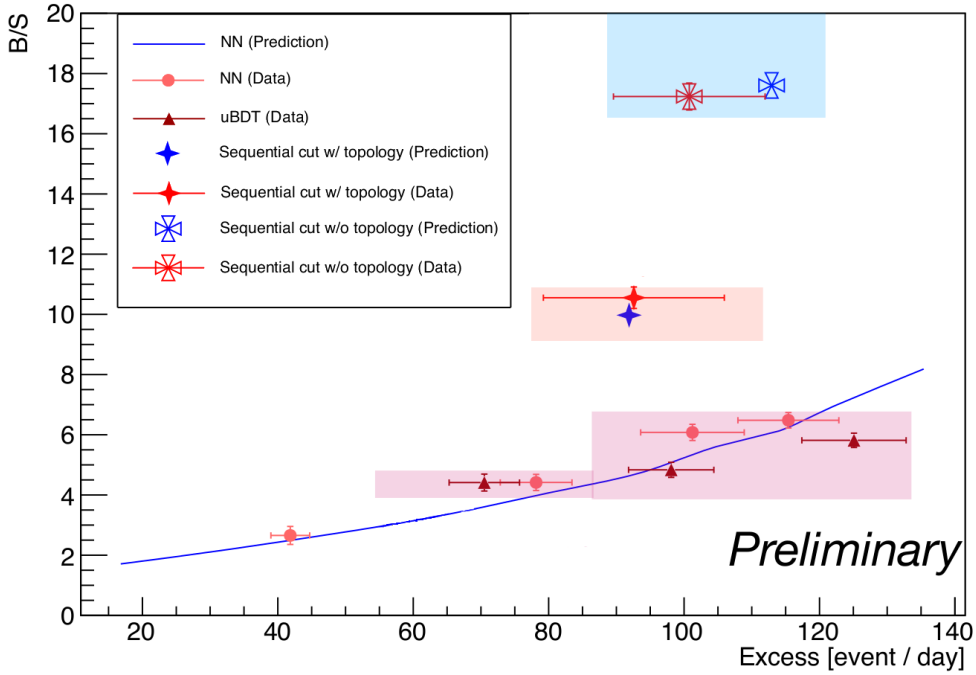

Figure 16.2.3: The background-to-signal ratio compared to the IBD selection efficiency for different IBD selection methods, namely using sequential cuts (with and without the use of the reconstructed topologies based on annihilation gammas), using the BDT ML method and using the NN ML method.[206]

The training is performed for three separate categories, namely for the cases where the number of reconstructed annihilation gammas is none, one and two (see section 8.4). For the cases with reconstructed annihilation gammas, additional input variables are used that are related to the reconstructed gammas and that were discussed in section 15.2.3. The output of the training consists of a new variable, that takes different sets of values for the signal and background events, in case the model was successful in discriminating them. The discriminators for the BDT method and the NN method are shown in figure 16.2.2. Based on the difference between the distributions, a discriminator cut is determined that optimises the Figure of Merit (FoM). For both analyses, it was opted to use the value $S/\sqrt{S+B}$ as FoM. Figure 16.2.3 demonstrates the background-to-signal ratio that was obtained in combination with a certain IBD selection efficiency for different selection methods.

16.3 BACKGROUND SUBTRACTION

The events collected by any of the IBD selection procedures described above, are still contaminated by the backgrounds that were discussed in section 11. The different, left over background components can be determined from different regions of the Δt distribution, as is shown on figure 16.3.1. The signal region, S_{signal}, has an accidental contamination. This contamination can be estimated from the negative part of the distribution that is populated exclusively by accidental events, after it has been scaled to the signal region. The signal region also has a contamination from ^{214}Bi-^{214}Po decays. This contamination can be estimated from the tail of the distribution that is populated by BiPo events, and extrapolated to the signal region. Note that the tail also has an accidental contamination, so this

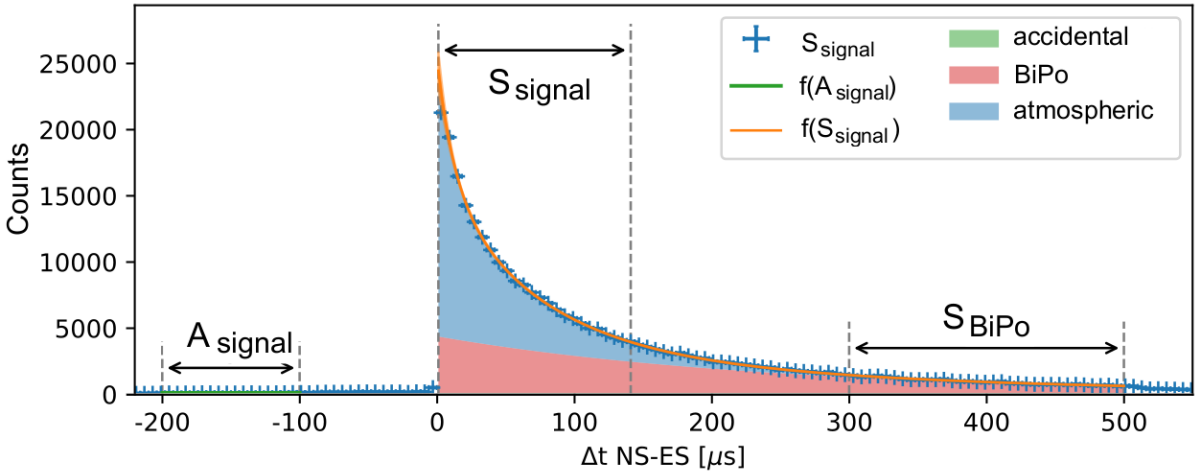

Figure 16.3.1: Distribution of time difference between the reconstructed ES signal and NS signal.[165]

has to be subtracted from the BiPo estimation before extrapolation. This reasoning already gives the following subtraction method for the accidental and BiPo backgrounds

$$S_{\text{signal-acc-BiPo}} = S_{\text{signal}} - a_1 \cdot A_{\text{signal}} - b \cdot (S_{\text{BiPo}} - a_2 \cdot A_{\text{signal}}). \tag{16.1}$$

Here, S_{signal} is the signal selection. A_{signal} is the accidental selection that is based on the IBD selection cuts, but with negative Δt values. The factor a_1 is a scaling factor that accounts for a possible difference in the width of the accidental window and the signal window. S_{BiPo} is the BiPo selection, that is also based on the IBD selection cuts but with a shifted Δt window to [300, 500] μs and with an inverted BiPonisher cut. The factor a_2 is analogous to a_1 but is used to scale the accidental selection towards the BiPo selection. Finally the factor b allows to extrapolate the BiPo contamination to the signal window, based on the knowledge of the exponential behaviour of the BiPo Δt distribution. b is the ratio of the integral over the BiPo time window and that over the IBD time window.

The remaining cosmic background can not be estimated from the Δt distribution or from another parameter, as this background's parameter values largely overlap with those of the IBD signal. A cosmic selection is made from the reactor off data. First, the IBD signal selection is applied to the reactor off data. The accidental and BiPo background components are subtracted from this selection by the above described method. The remaining events are the atmospheric selection,

$$S_{\text{cosmic}}(\text{ROff}) = S_{\text{signal-acc-BiPo}}(\text{Roff})$$

The atmospheric selection from reactor off data has to be extrapolated to the signal selection of the reactor on data. This is challenging as the cosmic background rate is correlated with the atmospheric pressure P_{atm}, which varies over time. The relation is determined by a linear fit of the cosmic background component in function of the pressure, as shown in figure 16.3.2, of the form

$$S_{\text{cosmic}}(P_{\text{atm}}) = f(P_{\text{atm}}) = a \cdot P_{\text{atm}} + b.$$

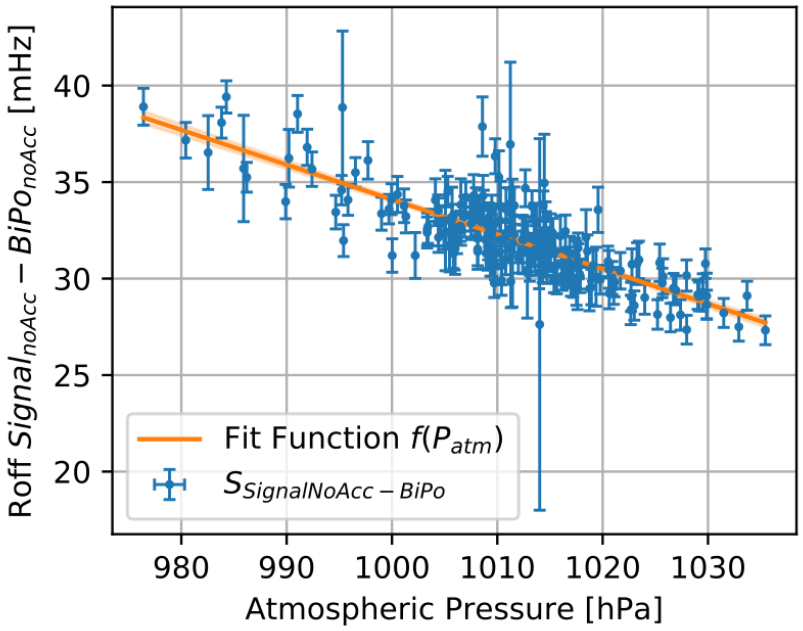

Figure 16.3.2: The cosmic background component in reactor off data as a function of the atmospheric pressure. The linear fit is used to determine the atmospheric correction factor.[172]

To extrapolate the cosmic selection, measured during a reactor off period at pressure P_j, to the reactor on signal selection, measured during a reactor on period at pressure P_i, the correction factor c is constructed, as the ratio

$$c = \frac{\frac{1}{N_{ROn}} \Sigma_{i=1}^{N_{ROn}} f(P_i)}{\frac{1}{N_{ROff}} \Sigma_{j=1}^{N_{RO}} f(P_j)}$$

The IBD selection is finally obtained by subtracting the cosmic background component from equation 16.1,

$$\text{Excess}_{\text{Ron}} \equiv S_{IBD}(\text{ROn}) = S_{\text{signal-acc-BiPo}}(\text{ROn}) - c \cdot S_{\text{cosmic}}(\text{ROff}).$$

This final selection contains the excess of coincidences in reactor on data, which are likely neutrino IBD events.

16.4 IBD SIGNAL EXCESS

The SoLid experiment applies a blinding strategy where the IBD selection strategies are developed, trained and tested with an open dataset, containing only 7% of the total amount of data recorded with the Phase I detector. The final analysis will be applied to the full dataset, which is currently still blinded. The open dataset contains the data taken between June 9 and August 18 of 2018 and covers the reactor on cycle 3 from the 12th of June to the 10th of July 2018. The reactor on and reactor of samples exist of:

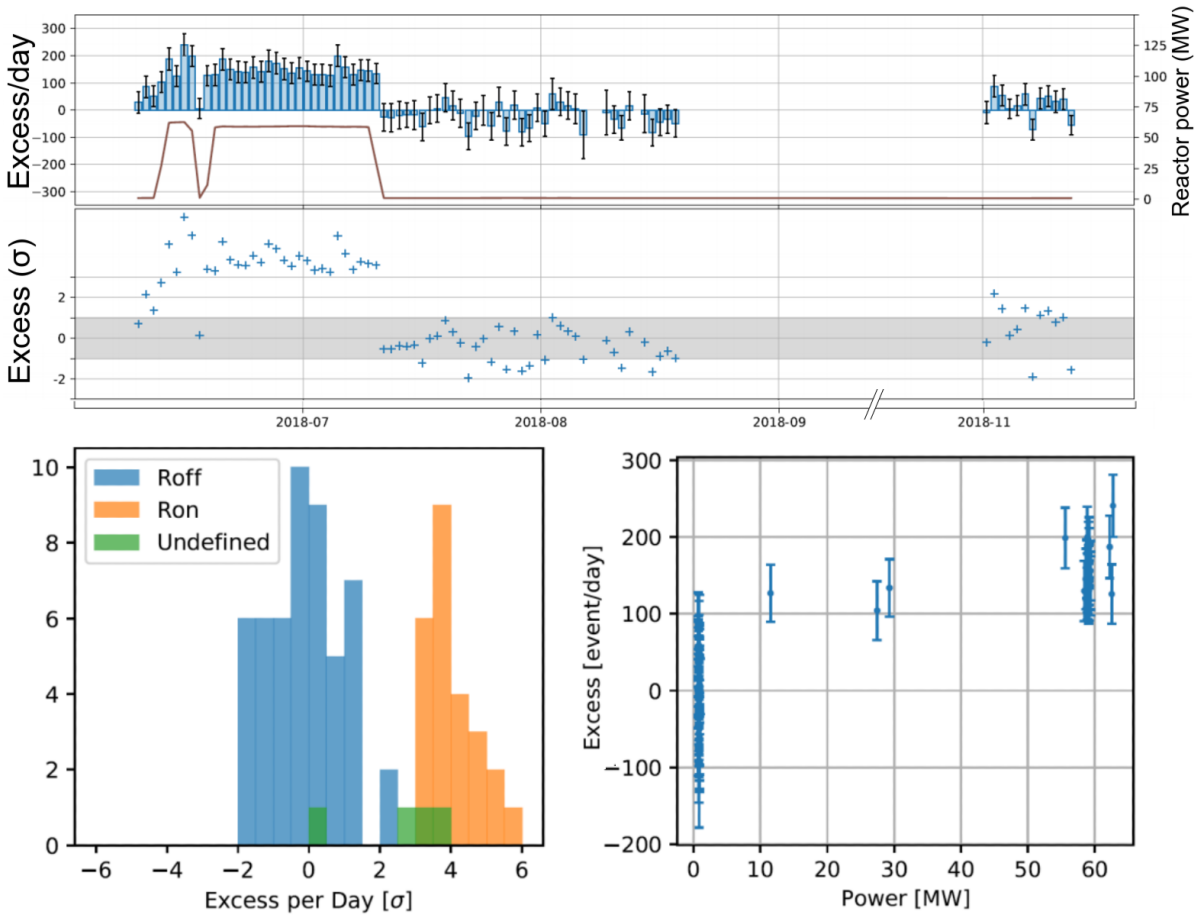

Figure 16.4.1: Top: the recorded excess of coincidences, likely due to IBD events, for each selected day in the open data set. The evolution of the reactor power is shown in brown. The excess per day in terms of the standard deviation σ is shown as well. Bottom: (left) time projection of the excess into the bins that show the excess per day. (right) Correlation between the excess and reactor power.[212]

- On: Every reactor day of cycle 3 of 2018, except for the periods of temporary reactor shutdown from June 13 to 15, 2018 and from June 20 to July 9, 2018. For transition periods where the reactor is turned on or shut down, the data are taken into account as reactor on when the average reactor power is above 40 MW. In total 25 days of reactor on data are available.
- Off: Only a few reactor off days between June 9 and August 18, 2018 are used. All days during reactor transition, or during which the detector was under maintenance, or those used for the uBDT training and or during the period from August 7 to August 8 are excluded. This results in a total of 18 days reactor off data.

To obtain the IBD excess that is shown in figure 16.4.1, the IBD selection was performed with the uBDT method, which was described in section 16.2.2. The remaining background was subtracted following the method described in section 16.3. The excess of coincidences is shown for each day of the reactor on and off periods in the open data set. As expected, the excess increases with the reactor power, as demonstrated by the bottom panel of figure 16.4.1. An average excess of 156 events/day is observed. This preliminary result was based on analysis tools that are still under validation and is only used as an example to illustrate the described concepts. The background components in the

signal selection were determined from the Δt distribution during the background subtraction method. For the most important reconstruction parameters in regard to the oscillation analysis, namely E and L (which is the z coordinate in 1 dimension), are shown in the left side of figure 16.4.2. The BiPo background has a big contribution at low energy but drops rapidly due to the Q_β = 3.27 MeV of ^{214}Bi. Some events above 4 MeV remain which are attributable to neutron contamination. The atmospheric background is distributed more evenly over the energy range. Finally, the shape of the IBD excess is compared to the IBD simulation in the right side of figure 16.4.2.The agreement with the simulation is good, within statistical uncertainties.

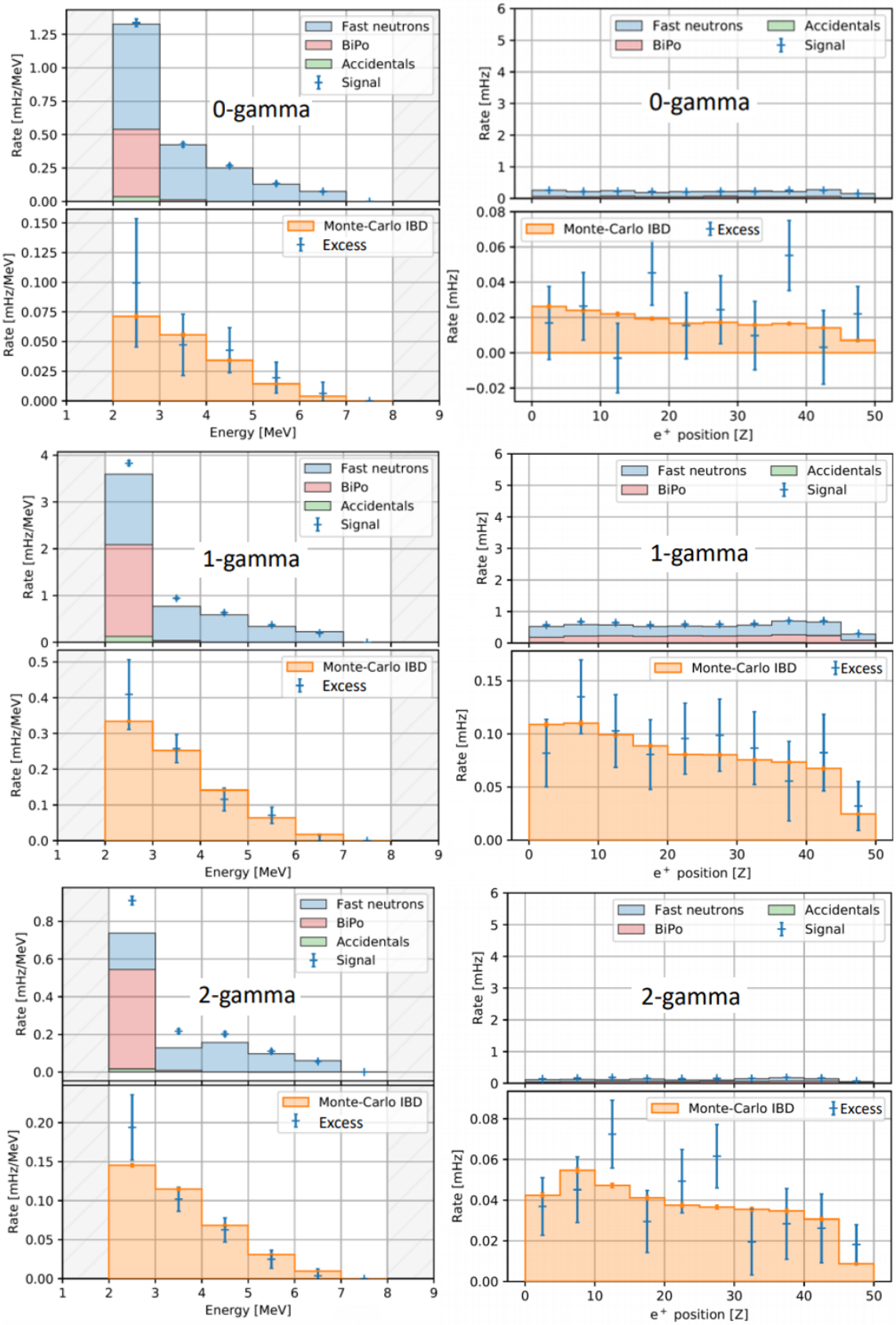

Figure 16.4.2: Left: Background components within the signal selection for the reconstructed energy and position. The difference between selection and backgrounds is the IBD like excess. Right: the reconstructed energy and length distributions for the IBD like excess in reactor on data and the IBD simulation.[212]

17

OSCILLATION ANALYSIS

The SoLid collaboration is taking precision data to assess the reactor antineutrino anomaly. The flux of reactor antineutrinos is studied in energy and travelled distance, in order to make a measurement of their oscillation pattern. A fraction of the $\overline{\nu}_e$ that emerge from the reactor core and cross the detector, will interact in the detector volume. The sterile hypothesis argues that neutrinos can oscillate into the sterile state and escape detection altogether, which causes a deficit in detection rate. The eV-scale mass splitting implies meter scale oscillation lengths. This effect can be investigated with the SoLid detector at very short baseline to the BR2 reactor core. By assessing the disappearance pattern of the reactor neutrinos, the existence and characteristics of the sterile neutrino can be pinpointed. The probability that an electron antineutrino of energy E is found as such after travelling a distance L, could be influenced by oscillation into the sterile state, as indicated by the formula

$$P_{\overline{\nu}_e \to \overline{\nu}_e} = 1 - \sin^2(2\theta_{14}) \sin^2\left(\frac{\Delta m^2_{41} L}{4E}\right).$$

The oscillation probability is dictated by the properties of the neutrino states, namely the mixing angle θ_{14} and the squared mass difference Δm^2_{14}. The experimental coverage of the $\overline{\nu}_e$ rate over a range of L/E requires a good position and energy resolution, which the SoLid detector obtains by deploying a highly voxelised detector that consists of 5^3 cm^3 detector cells.

17.1 HYPOTHESIS TESTING

The characteristics of the selected IBD events are interpreted in terms of the physical model of sterile neutrino oscillations. For the SoLid oscillation search, the null hypothesis, H_0 states that the data can be described by the well established framework of the mixing of three neutrino flavours. This is equivalent to $(\sin^2(2\theta_{14}),\ \Delta m^2_{41}) = (0,\ 0)$. The alternative hypothesis, H_1, supports the 3+1 neutrino model where oscillations can occur to an additional, sterile neutrino state that is driven by the non-zero oscillation parameters. The hypothesis testing is performed with the frequentist approach, where the probability of a certain experimental outcome is considered as the relative frequency of its occurrence when repeating the same experiment many times.

The agreement between the data and a given hypothesis is quantified by the goodness-of-fit parameter, χ^2. For the oscillation analysis the Pearson's χ^2 statistic [213] is used [185], given by

$$\chi^2 = \sum_{ij}^{N} \left(\frac{D_{ij} - P_{ij}}{\sigma_{ij}}\right)^2$$

The parameter is determined as a sum over discrete bins ij, where the i index refers to the reconstructed position, L_{reco}, and the j index refers to the reconstructed energy, E_{reco}. Currently 10 energy

bins and 5 position bins are used, essentially dividing the detector volume into its modules [214]. The data are represented by D_{ij} and the model prediction under a certain hypothesis is given by P_{ij}. The significance of a discrepancy between the data and the hypothesis is then quantified by the p-value, that is defined as the probability to find a value for the fit statistic in the region, where the compatibility with H_0 is equal or less than the level of compatibility observed with the actual data.

In order to account for correlated systematic uncertainties in the model, a covariance matrix is used, denoted as V [214]. The diagonal of the matrix contains the statistical and uncorrelated systematic uncertainties for the model prediction, while the correlated uncertainties populate the off-diagonal matrix elements. Each element $V_{\alpha\beta}$ of V represents the relation between bin $\alpha(i,j)$ and bin $\beta(k,l)$ in the (L_{reco}, E_{reco})-data. The covariance matrix is a sum of sub-matrices, for example separate error matrices for energy resolution, position-dependence and so on. Such an error matrix can be determined by varying the value of the parameter in the simulation within its error margins, and monitoring the IBD energy spectra. By determining the variation bin by bin you build up the covarience matrix. With the data and prediction rewritten to matrix format, the χ^2 definition becomes

$$\chi^2 = (D-P)^T V^{-1} (D-P) \tag{17.1}$$

$$= \sum_{\alpha}^{N} \sum_{\beta}^{N-1} (D_\alpha - P_\alpha)^T V^{-1}_{\alpha\beta} (D_\beta - P_\beta). \tag{17.2}$$

The exact observable that is compared between the data and the model prediction, governs to which aspect of the oscillation model the hypothesis test is most sensitive. For an oscillation analysis that has a minimal dependence on the uncertainties in both the shape and the normalisation of the reactor flux prediction, a relative fit can be defined. In that case, the observable is based on comparisons between the obtained spectra for different detector baselines. This approach is only possible for experiments that use segmented or multiple detectors.

For the first oscillation analysis result, the SoLid collaboration uses the relative fit, similar to the principle of the fits from PROSPECT [126] and STEREO [128]. The SoLid collaboration uses the detected spectrum in the detector cell closest to the reactor as the reference for the prediction in the others cells, as this cell has the highest statistics. For each energy bin j, the reference value from the first bin, $i = 0$, is denoted as R_{0j}. The relative prediction P^R_{ij} for the other detector cells (i > 0) is then calculated as

$$P^R_{ij} = \frac{P_{ij}}{P_{0j}} R_{0j}.$$

Note that the sum in equation 17.2 now runs over one position bin less.

Currently, most part of the data from SoLid detector are still blinded. In order to demonstrate the performance of the SoLid oscillation analysis, a fake data set was constructed that has roughly the same size as the total SoLid Phase I dataset, using the neutrino generator SoLo and a realistic covariance matrix. The fake data are generated based on the no-oscillation prediction, which is confirmed by the χ^2/ndf value of 43.8/40 = 1.095 that implies a good agreement of the null hypothesis (where ndf stands for number of degrees of freedom). The fake data will be referred to as data hereinafter.

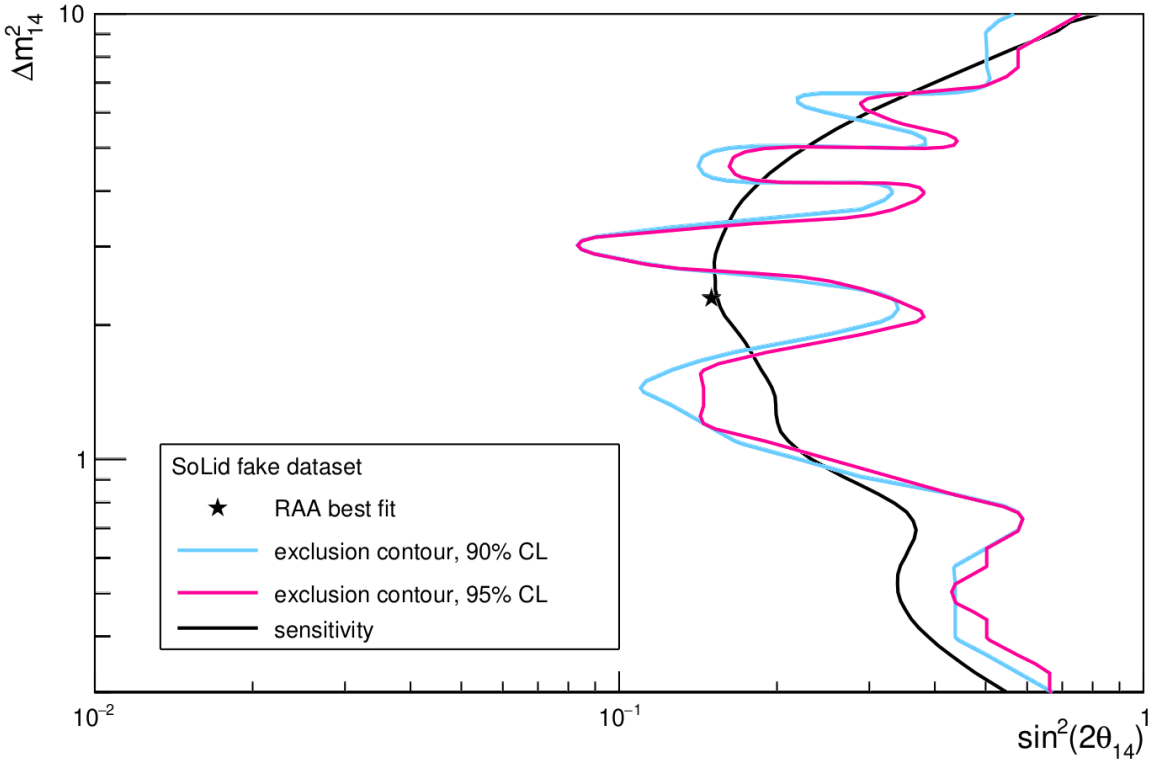

Figure 17.2.1: Exclusion contours determined from the fake dataset, based on a relative fit, for 90% confidence level (blue) and 95 % confidence level (pink). The parameter values to the right of the contour are excluded. The expected sensitivity contour for the fake dataset at 90% confidence level is based on the statistical uncertainties only is shown in black.[214]

17.2 TESTING THE ALTERNATIVE HYPOTHESIS

With the goodness-of-fit parameter χ^2, one can test the confidence level for a range of alternative hypotheses by comparing the data to models that include non-zero oscillation parameters $(\sin^2(2\theta_{14}),\ \Delta m^2_{41})$. First of all, the parameter values that minimise the χ^2 value can be determined in order to find the alternative model that provides the best fit. The so-called best fit point for the SoLid fake data was found at $(\sin^2(2\theta_{14}),\ \Delta m^2_{41}) = (0.14,\ 2.2eV^2)$ with a minimal χ^2/ndf of 39.25/38 = 1.033. This best fit point happens to lie in close proximity to the best fit point for the reactor antineutrino anomaly, and will therefore be denoted in the following also as RAA best fit.

The confidence level for other points of the parameter space can be determined by constructing an additional goodness-of-fit parameter, by comparing the χ^2 value for the parameter values in each point, p, to the χ^2 value of the best fit point, BF, namely

$$\Delta\chi^2 = \chi^2_p - \chi^2_{BF}.$$

From many fake experiments for the point p, a distribution of $\Delta\chi^2$ values is obtained. For a desired confidence level (CL), (e.g. 90%, 95%, 3σ, ...) the corresponding critical $\Delta\chi^2_{c,p}$ can be found from the distribution. When all points p are treated, this method results in a map of $\Delta\chi^2_{c,p}$ values corresponding

to the chosen CL, in function of $(\sin^2(2\theta_{14}),\ \Delta m^2_{41})$.

A confidence interval or exclusion contour can be drawn by comparing the observed $\Delta\chi^2$ value of the data to the predefined critical values, $\Delta\chi^2_{c,p}$. A particular point in the $(\sin^2(2\theta_{14}),\ \Delta m^2_{41})$ parameter space is said to lie within the inclusion interval, at the prescribed confidence level, if $\Delta\chi^2(\text{data}) < \Delta\chi^2_{c,p}$. As a result, a curve can be drawn that divides the parameter space in an allowed region to the left of the curve and an excluded region to the right. The exclusion contour for the fake dataset is shown in figure 17.2.1. for the 90% and 95% confidence levels.

Finally, the sensitivity contour of the experiment can be determined. The sensitivity of an experiment is defined as the average expected exclusion limit for many runs of the experiment. This limit can be derived by generating the exclusion contour based on the fit in which the data are replaced by the null hypothesis prediction. The sensitivity contour for the SoLid fake dataset, based on the relative oscillation fit, is shown in figure 17.2.1. The sensitivity decreases for larger values of Δm^2_{41}, because for these high values, the oscillation length is smaller than the detector bin size, which results in an average reduction of the detected flux. Similarly, low Δm^2_{41} values are only visible for larger values of L/E, and the largest distances covered by the detector modules are not large enough for the experiment to be sensitive there. The consistency of the exclusion result with the sensitivity is an important check. Results that are in agreement with the null hypothesis should on average not go beyond the expected sensitivity. Otherwise, they indicate a signal or an erratic interpretation of the data.

As mentioned, the SoLid collaboration is currently still working on the validation of the IBD analysis techniques and the full Phase I dataset is not available yet for further analysis.

18

THE HEAVY NEUTRAL LEPTON HYPOTHESIS

Heavy Neutral Leptons (HNL) are a possible extension to the Standard Model (SM). The HNL enter the SM as right handed, sterile neutrinos. The new sterile neutrino(s) could have any mass, as discussed in chapter 3. Motivated by several anomalies that pointed to neutrino oscillations with $\Delta m^2_{SBL} \sim 1$ eV^2, the SoLid experiment was designed to search for sterile neutrinos with a mass around the eV scale. In this chapter, we will investigate the sensitivity of the SoLid detector to sterile neutrinos with larger masses, that are usually called Heavy Neutral Leptons.

With the SoLid experiment, we aim to search for HNL, complementary to the eV scale oscillation analysis. This would extend the BSM program of SoLid while requiring no detector modifications. The new fermions in our study are assumed to have masses around 1-10 MeV. Due to the presence of mixing they are unstable, and their subsequent decay products can be observed.

In order to judge the potential of the SoLid experiment, the constraints will be reviewed that have been placed on the HNL parameters so far by an international search program. The quantities that are accessible in experiments are the physical HNL mass, m_N, and the mixing with the active neutrino flavors that are governed by the entries of the extended PMNS matrix (see chapter 3), namely $U^2_{\alpha N}$, where $\alpha \in \{e, \mu, \tau\}$. Since the SoLid detector probes $\overline{\nu}_e$ from the BR2 reactor (see chapter 6), the values of $U^2_{\mu N}$ and $U^2_{\tau N}$ are not accessible in our experiment. In the following sections, the constraints that have been put on U^2_{eN} in different mass ranges will be reviewed. We need to determine the largest values of U^2_{eN} that are consistent with all experimental and observational data and that can be be investigated in our experiment.

18.1 CURRENT BOUNDS ON THE HNL PARAMETER SPACE

Because of the small but nonzero mixing $U_{\alpha N}$ between the sterile neutrinos and the active ones, HNL participate in any weak process the active neutrinos do, but the strength is suppressed by the sterile-active mixing angles. Heavy neutral leptons are probed in direct searches, in which the HNL appear as real particles, as well as with indirect searches, where the HNL only appear as virtual particles through higher order quantum correction loops, and also through cosmological observations.

Direct searches either probe the kinematical effects on particles that are produced together with the HNL (for example kink searches in the electron spectrum of β decay, or peak searches in the electron spectrum of meson decays), or they probe the particles that are produced once the HNL decays itself (in reactor and accelerator neutrino experiments). We will review separately the bounds from direct searches below and above 100 MeV in sections 18.1.1 and 18.1.2. The bounds from indirect searches will be discussed in section 18.1.3 and the restrictions from cosmological observations will

be considered in section 18.1.4. The searches use in general a model independent phenomenological approach, assuming only a single HNL is kinematically accessible, while any other HNL, if present in the theory, are sufficiently heavy and do not affect the analysis. This leaves two free parameters to be constrained: the mass of the relevant HNL and its interaction with an active neutrino of flavour α.

18.1.1 Direct HNL searches in the mass range below 15 MeV

The limits on the coupling of HNL with ν_e in the low mass range that were obtained with direct searches are described in the following subsections. The bounds at the 10 eV - 100 keV mass range were obtained through kink searches in beta decays of different nuclei. The bounds between 1 and 15 MeV, which is the mass range of interest for the SoLid experiment, were obtained from searches for HNL decay products from reactor neutrinos and from solar neutrinos. This mass range also has a bound from peak searches, but that will be discussed in section 18.1.2.

Kink searches in beta decay spectra

Sufficiently light sterile neutrinos, with masses between 10 eV and 100 keV, may be produced in β^- decays of nuclei. Due to its mass, the HNL influences the kinematics of the emitted electron. The natural observable is the spectrum of outgoing electrons, which is proportional to the following kinematical factor,

$$|U_{eN}|^2 \sqrt{(E_0 - E_e)^2 - m_N^2} + (1 - |U_{eN}|^2)(E_0 - E_e).$$

with the electron energy E_e, the β spectrum endpoint E_0, and the HNL mass m_N. At $E_e < E_0 + m_N$, only the second term contributes, which comes from decays into active neutrinos, while at higher energies E_e, sterile neutrinos contribute as well. Thus at critical energy $E_e = E_0 + m_N$ one expects a kink in the electron spectrum. Based on its absence, upper limit are placed on sterile-electron neutrino mixing $|U_{eN}|^2$ for a given mass of sterile neutrino m_N [215], which are shown in figure 18.1.1.

Decay of HNL from solar ^{8}B decay

A heavy neutrino with a mass up to 15 MeV can be produced in the ^{8}B decays in one of the side branches of the pp fusion reaction chain in the Sun, $^8B \rightarrow ^8Be + e^+ + \nu$, and can then decay in flight. If heavy neutrinos with mass $\geqslant 2m_e$ are emitted in the solar ^{8}B decays, then the decays $\nu_N \rightarrow \nu + e^+ + e^-$ should occur.

The Borexino [216] experiment at the underground GranSasso National Laboratory (LNGS) has been used to obtain limits on $|U_{eN}|^2$ in the range of 1 MeV to 15 MeV, by searching the solar HNL decay inside the active detector volume. The decay mode is required to be as slow as $\sim$ 500 s, which is the time needed for the particle to reach the detector. The Borexino detector, consists of a transparent, nylon sphere of 4.25 m diameter, filled with 278 tons of liquid scintillator, mounted at the center of a concentric 5.50 m diameter sphere that supports 2212 photomultipliers (PMT). Ultra-pure water provides shielding against neutrons and external γ rays. The major part of the background at low energies is induced by the activity of ^{208}Tl, ^{14}C, ^{85}Kr, and ^{39}Ar, and at higher energies by muons. A muon veto and muon identification cuts remove most of the muon induced background, removing

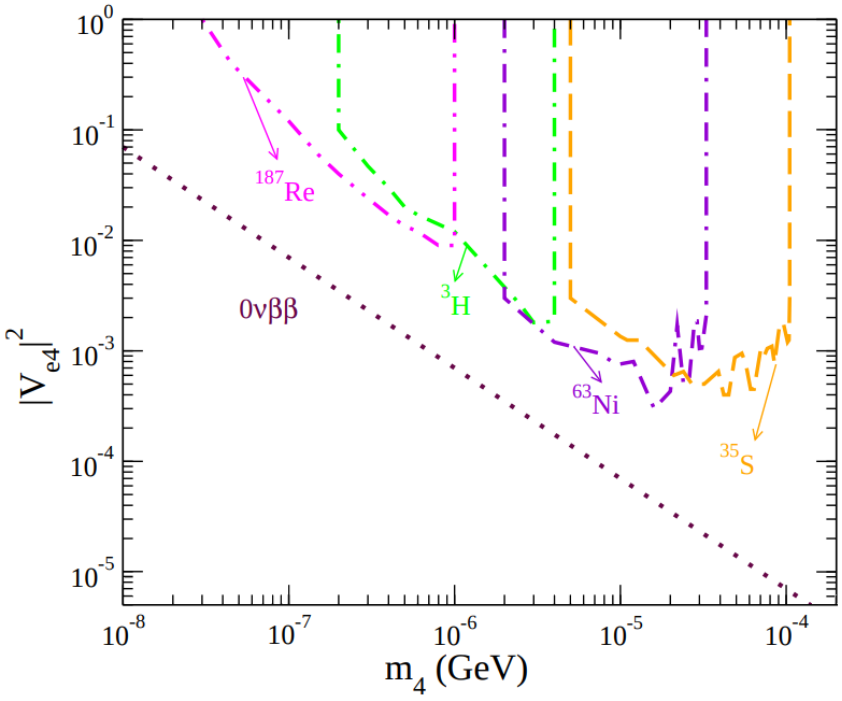

Figure 18.1.1: Limits on the coupling parameter of HNL with ν_e, in function of the HNL mass in the low mass range, 10 eV-100 keV. Bounds were obtained with kink searches in beta decays of different nuclei, namely ^{187}Re, ^{3}H, ^{63}Ni, ^{35}S, ^{20}F, at 95 % C.L. [215].

all events above 4.5 MeV. The energy of the e^+e^- pair is measured in order to perform a counting experiment, that set limits on the mixing parameter of a massive neutrino in the HNL mass range between 1 MeV and 15 MeV, as shown on figure 18.1.2.

HNL DECAY AT A NUCLEAR REACTOR

A nuclear reactor is a strong source of ν_e up to energies of ~ 12 MeV. It may also be a strong source of HNL in the corresponding mass range of sensitivity 1-12 MeV. An experimental search for the HNL decay $\nu_N \rightarrow \nu + e^+ + e^-$ can put limits on the coupling $|U_{eN}|^2$ of a massive neutrino in the range of 1 MeV to 10 MeV. This is the search we intend to perform with SoLid.

Such an experiment has last been performed in 1995 at the nuclear power reactor 5 of the Bugey plant in France [217]. It is a pressurised light water reactor with a maximal thermal power of 2800 MW, providing a maximal total flux of $3 \times 10^{20} \bar{\nu}_e$/sec in the energy range 1-12 MeV. The reactor neutrino spectrum was obtained via the Conversion method, based on the ILL spectrum (this procedure is detailed in section 4.1.3.

The detector consists of two position sensitive multiwire XY chambers (MWPC) with dimensions of 190 cm × 180 cm × 9 cm, which are both sensitive to the electrons and positrons originating from HNL decay. A He-filled bag of 5.4 m^3, adjacent to the MWPCs, acts as decay volume. An active veto shield is provided by six surrounding 200 cm × 200 cm × 9 cm MWPCs. Copper and aluminium sheets (1 mm)

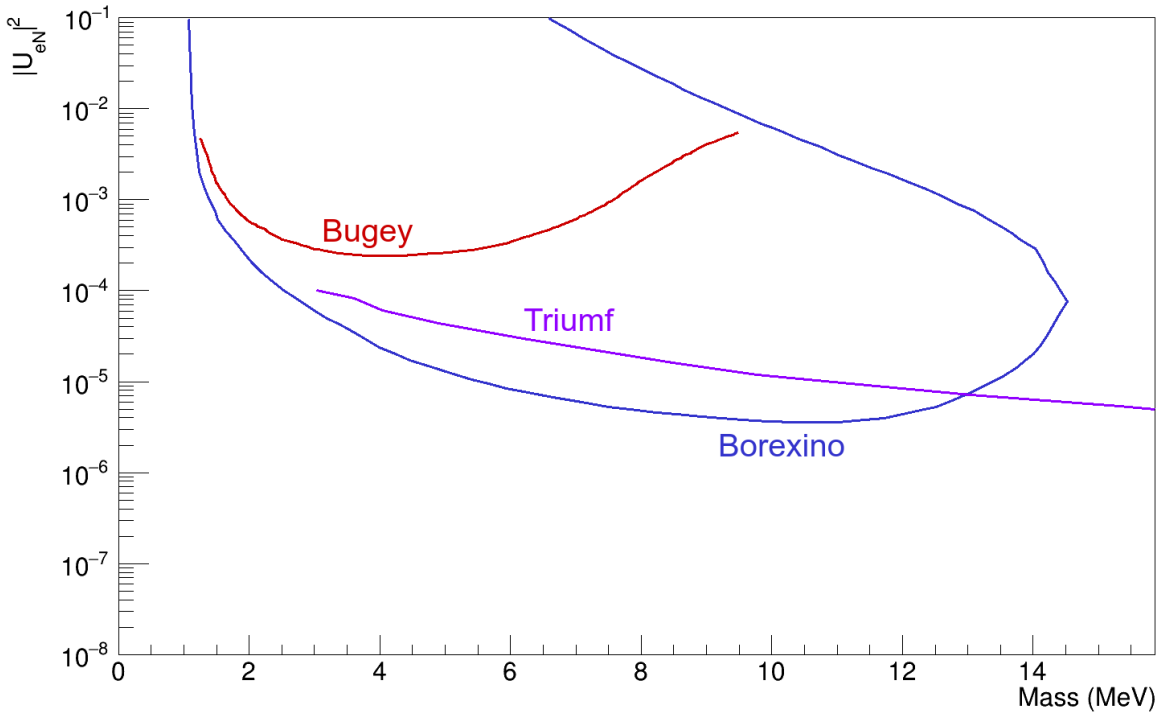

Figure 18.1.2: Limits on the coupling parameter of HNL with ν_e, in function of the HNL mass in the mass range, 1 - 15 MeV. Bounds were obtained from HNL decay searches from reactor neutrinos at Bugey [217] and from solar neutrino at Borexino [216]. The Triumf contour [218] was obtained with $\pi \rightarrow e\nu$ peak searches which are discussed in section 18.1.2.

are used as passive shielding. Electrons and positrons from the HNL decay would deposit typically $\approx$ 20 keV in each of the XY chambers, almost independently of the mass and energy of the HNL. A detection threshold of 6 keV was set for every channel of the anode and cathode planes and for the veto chambers. A fast trigger was generated when a signal was detected coincidently by all four wire planes within a time window of 4 μs and no veto signal occurred during this time. After application of all off-line cuts, an event rate of about 0.5 Hz was obtained. The cosmic muon background, the gamma background and the ^{222}Rn activity in the laboratory was monitored by dedicated detectors. This showed that 20 % of the trigger rate could not be accounted to these backgrounds. The difference was attributed to β active fission products attached to aerosols. The absence of a significant enhancement of the counting rate during reactor on periods, was translated into bounds on the coupling $|U_{eN}|^2$. The bounds are included on figure 18.1.2.

18.1.2 Direct HNL searches in mass range above 100 MeV

The HNL mass range above 100 MeV is not within the reach of the SoLid experiment. However, a lot of interest was given to the GeV scale seesaw model, motivated by the fact that these HNL can explain not only neutrino masses, but also the baryon asymmetry of the Universe [219] and Dark Matter [90], most notably in the Neutrino Minimal Standard Model (νMSM) [220]. HNLs wih GeV masses can be efficiently searched for with the existing experimental technologies. Due to the absence of a signal,

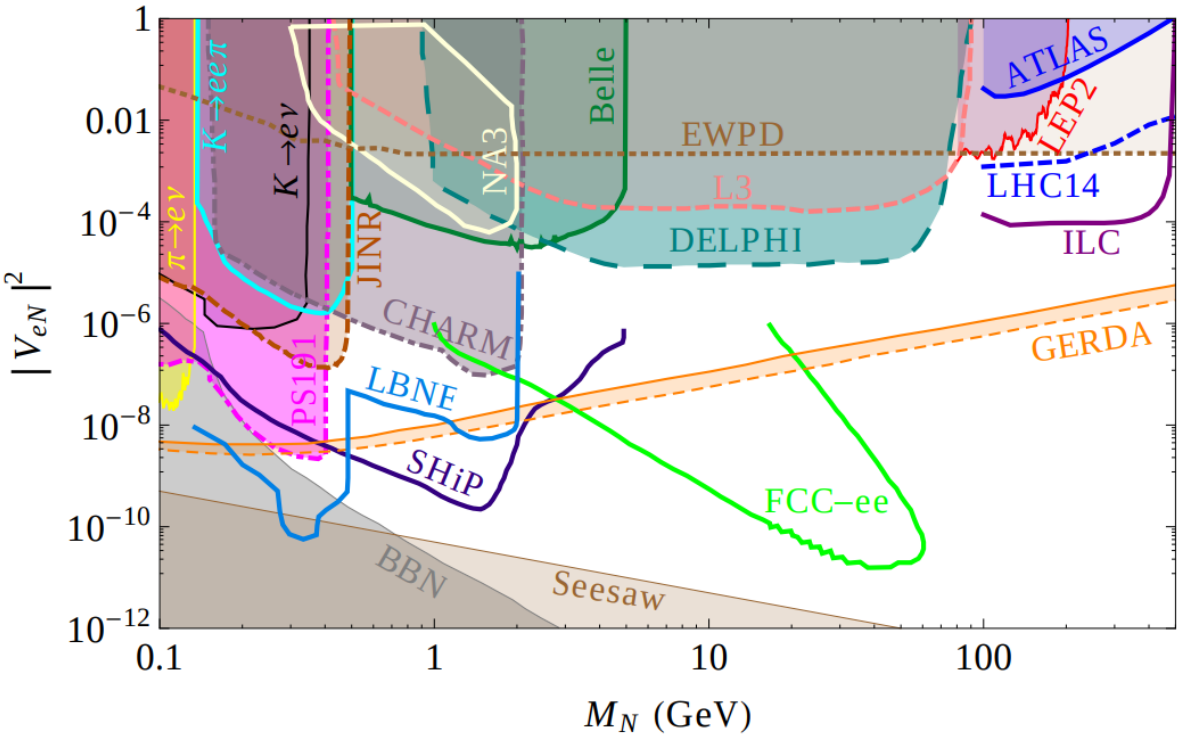

Figure 18.1.3: Limits on the mixing between the electron neutrino and a single HNL in the mass range 100 MeV - 500 GeV. The areas with yellow contour labeled $\pi \to e\nu$ and black contour labeled $K \to e\nu$ are excluded by peak searches. 90% C.L. limits are shown from the major beam dump experiments. The most significant improvement for HNL below the B meson mass could be made with the SHiP experiment [219], or with the DUNE (LBNE) experiment, shown by the projected limits. The orange exclusion line is from neutrinoless double beta decay experiment GERDA. (see [221] and references therein).

various search experiments have set upper bounds on the mixing parameter $|U_{\alpha N}|^2$ in function of the HNL mass. Figure 18.1.3 shows the bounds on electron mixing $|U_{eN}|^2$.

PEAK SEARCHES IN MESON DECAY

For $\mathcal{O}(100)$MeV HNL masses, stringent bounds are obtained by peak searches through the study of meson decay. An intensive beam of protons hitting a fixed target, can create, depending on its energy, pions, kaons, D mesons and B mesons. HNLs can be produced by decays of the heavier mesons like the ordinary neutrinos through the neutrino mixing. The energy of the daughter lepton is determined only by masses of particles in the two-body decay. Peak searches look in the energy spectrum of the outgoing charged lepton for a peak corresponding to the HNLs. The magnitude of the neutrino mass can manifest itself as a monochromatic line in the charged lepton energy spectrum.

These peak searches provide strong bounds on the sterile-active mixing, while ignoring the ultimate fate of the sterile neutrino, which may be extremely long lived. Meson decay peak searches have taken place for $\pi \to e + \nu_N$ (TRIUMF [218]) and $K \to e + \nu_N$ (NA62 [222]) and strongly bound active-sterile mixing angles at low masses. The peak searches will be extended to higher masses with heavier meson

decays, such as B mesons by BELLE [223]. Peak searches tend to perform worse at higher masses in comparison to bounds from experiments which derive their signal from the decay of the heavy neutral lepton, which is discussed in the following section.

HNL DECAY IN BEAM DUMP EXPERIMENTS

The tightest bounds on GeV scale HNL come from beam dump experiments [221]. Proton collisions with a target produce mesons and baryons which can decay into heavy neutral leptons. HNL themselves can decay into SM particles if kinematically allowed via weak interactions induced by mixing with active neutrinos. In beam dump experiments, the subsequent decay of the HNL into SM particles will be searched for inside a detector some distance from the source.

The heavier the HNL is, the more decay channels open up. The signal events are very clear. The HNL decays look as a production of SM particles out of nowhere and becomes a realistic process for fixed target and collider experiments. The HNL decay rate is that typical for all the weak decays multiplied by the squared mixing angle,

$$\Gamma_{N\to weak} \propto |U_{\alpha N}|^2 G_F^2 m_N^5.$$

If the HNL decay length is shorter than the detector size the number of signal events is suppressed as $|U_{\alpha N}|^2$. In the more realistic case where the decay length l_N exceeds the detector size L_d, so that sterile neutrinos decay mostly outside the detector, the number of events is more strongly suppressed, by $|U_{\alpha N}|^4$. Production is suppressed by $|U_{\alpha N}|^2$ and only small part of sterile neutrino $\sim \tau_N$ decays inside the detector which gives the additional $|U_{\alpha N}|^2$. With decreasing mixing the sterile neutrino lifetime grows. This significantly diminishes the sensitivity of the direct search experiments to the mixing angles. Due to the absence of a signal, various search experiments such as PS191 [224], NA3 [225], and CHARM [226], have set upper bounds on the mixing parameters $|U_{\alpha N}|^2$ in function of the HNL mass. Figure 18.1.3 shows the bounds for mixing with ν_e.

There are also experiments where both sterile neutrino production and decay happen inside a single detector volume. The propagation of the sterile neutrino in the detector media is unobservable. The particles accompanying the sterile neutrino production and the products of the sterile neutrino decays are observable. This signal can be searched for based on a displaced secondary vertex, and, since HNL in this mass range are Majorana fermion, the accompanying particles and decay products may form final states which are rare or forbidden within the SM physics given the type of initial particles, such as same sign leptons.

HNL DECAY ABOVE THE B MESON MASS RANGE

If heavy neutral leptons exist with masses higher than this of the B meson, they can be produced in the decay of the gauge bosons. Bounds have been derived based on Z decays in LEP data, and based on W decays in the LHC data. The searches from DELPHI [227] and L3 [228] for decays of HNL produced in Z decays remain to be the strongest to date in the mass range $m_B < m_N < m_W$ and are indicated on figure 18.1.3.

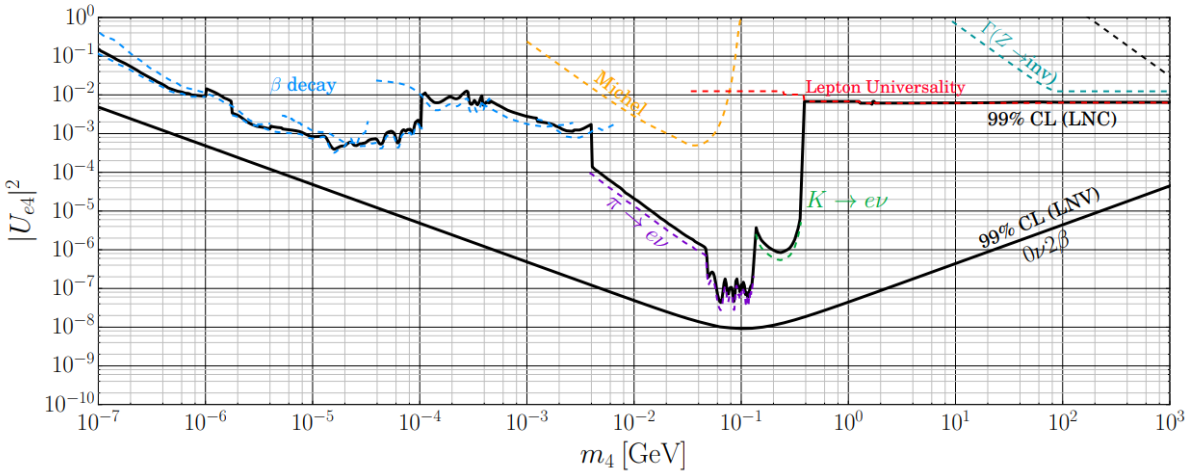

Figure 18.1.4: The global 99% CL upper limits on the value of $|U_{eN}|^2$ as a function of m_N.[229]

18.1.3 INDIRECT HNL SEARCHES

In addition to direct searches, in which the HNL appear as real particles, the HNL are also probed through indirect searches, where the HNL only contribute as virtual particles. The existence of HNL would affect essentially all low energy observations of weak processes [229]. This includes lepton flavour violating decays, neutrinoless double β decay, lepton universality tests, neutrino oscillation, and electroweak precision data. Some of these processes are discussed below.

Some bounds from indirect searches were already shown on figures 18.1.1-18.1.3 alongside the bounds from direct searches. In the previous sections, neutrino production and decay were governed uniquely by the weak interactions. However, it is not necessary that neutrinos are Majorana particles or that the decay of the heavy neutrino is mediated only by weak interactions. Constraints using HNL decay products are also model specific. Figure 18.1.4 shows a combined constraint from indirect searches and from direct searches where the conservative phenomenological assumption has been made that HNL decay invisibly. Note that these approaches do not provide a global fit to the properties of heavy and light neutrinos, but they demonstrate that no significant deviation from the SM predictions has been observed to impose bounds on $|U_{eN}|^2$.

The observation of **neutrinoless double beta decay** would be a clear sign that neutrinos are Majorana fermions. The limit on the $0\nu\beta\beta$ half life leads to an upper limit on $|U_{eN}|^2$ as a function of a generic heavy neutrino mass m_N. The $0\nu\beta\beta$ bounds are shown in figure 18.1.2 and 18.1.3 and seem very severe. However, the $0\nu\beta\beta$ limits may be significantly weakened in certain cases when a cancellation between different terms may happen, e.g. due to the presence of Majorana CP phases [229]. In general, the Majorana nature of neutrinos does not guarantee an observable $0\nu\beta\beta$ rate in all models.

Lepton universality in the SM says that charged-current interactions couple to the three lepton families, e, μ, τ with a universal constant: $g_e = g_\mu = g_\tau$. Such universality can be studied at the subpercent level by measuring the ratios of decay rates of charged leptons, mesons, and the W boson. If a heavy neutrino exists, then the measured values of $|g_\mu/g_e|$, $|g_\tau/g_\mu|$, and $|g_\tau/g_e|$ can deviate from unity, because the heavy neutrino might be too heavy to be produced in a given decay. Recently, a

clear indication of lepton universality violation has been found [21]. This discrepancy between data and SM prediction cound indicate that systematic uncertainties have been underestimated. Another possibility is the existence of HNL could introduce the tension with the SM prediction. This opens interesting research oppurtiny in terms of heavy neutral leptons.

Loop-induced lepton flavor violating decays of charged leptons are predicted to be extremely rare in the SM, far beyond experimental reach, due to the smallness of the light neutrino masses. If there is a heavy neutrino with mass $\gtrsim 1$ MeV, the rates of these processes can be enhanced, perhaps to the point of being observable. Examples of such decays include $\mu - e$ conversion and three-body charged-lepton decays such as $\mu^- \to e^- e^+ e^-$. These were some of the weak processes that may be affected through mixing with sterile neutrinos but there are more [229].

18.1.4 COSMOLOGICAL BOUNDS

Heavy sterile neutrinos have also been investigated for their effect on cosmological observables, such as the Hubble constant, the primordial abundance of light nuclei, the cosmic microwave background (CMB), supernova luminosities, Big Bang Nucleosynthesis, and Large Scale Structure formation.

For example, considerations about the big bang nucleosynthesis (BBN) put upper bounds on the HNL lifetime, due to their effect on the evolution of the early universe [230]. This in turn leads to lower bounds on $|U_{\alpha N}|$. The BBN describes the formation of all the light elements in the early universe. When changing the properties of the universe around the first second, one affects the predicted abundance of helium and deuterium which can be compared to present day astronomical observations. The existence of HNL could speed up the expansion of the universe due to the additional energy. This would imply that the weak reaction rates between neutrons and protons will become slow in comparison to the expansion rate. Thus the neutron to proton ratio $r_p = n_n / n_p$, will freeze out at a higher value. Since r_p is directly linked to the observable deuterium and helium abundances this renders BBN constraints complementary to direct experimental searches. If the HNL decay after BBN, they contribute to the effective number of relativistic degrees of freedom, which is constrained by observations of the CMB and light element abundances.

Figure 18.1.5 shows bounds on the mixings of a general extra sterile neutrino species with the SM active flavours as a function of the sterile neutrino mass, for sterile neutrino masses ranging from eV's up to the 1 GeV region. The cosmological bounds are very severe in the mass region of interest for the SoLid experiment. However, the cosmological bounds are not as robust as the ones from laboratory searches as they typically depend on the production mechanism of sterile neutrinos in the early universe and on the cosmological evolution. In a non-standard model of the early universe, these bounds may not apply.

A wide program of experimental work is desirable, with a varied methodology, to best identify new physics. Model dependent factors make it possible for discrepancies to occur between peak searches, beam dump experiments and cosmological constraints. It is necessary to perform experimental searches of heavy sterile neutrinos with increased sensitivity.

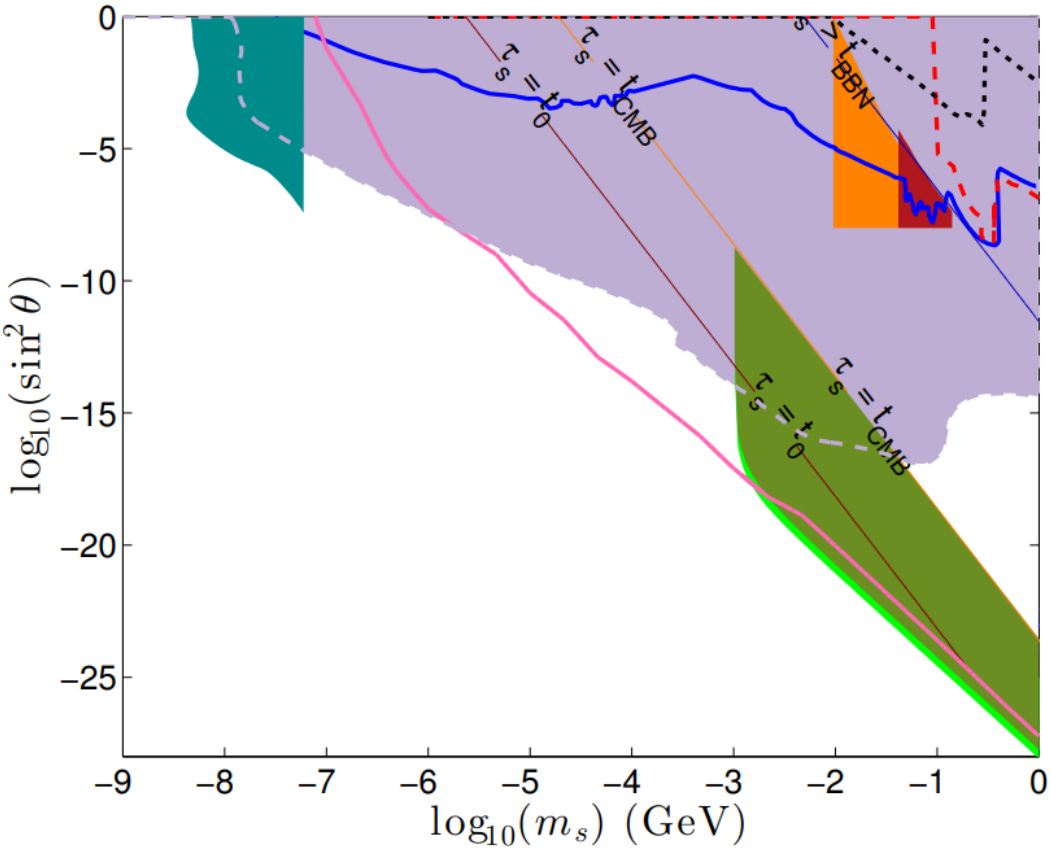

Figure 18.1.5: Combined cosmological bound from [230] (purple region). Regions excluded by constraints on helium production at BBN are shown, as measured from astrophysics (orange) and CMB (red). The green area is excluded from decays to electron-positron pairs, which alter the CMB temperature and polarisation power spectra. In the dark green area, mixing with only ν_μ and ν_τ is assumed. For mixing only with ν_e, the bright green area is excluded as well. The pink line denotes the upper limit based on X-ray constraints presented in. The cyan region in the top-left corner corresponds to CMB limits on massive extra neutrinos in the linear regime. For comparison; the upper limits from figure 18.1.4 on the mixing angle $\sin^2\theta_{eN}$ are shown (blue), and similar results from $\sin^2\theta_{\mu N}$ (dashed red) and $\sin^2\theta_{\tau N}$ (dotted black). (see [230]and references therein).

19

SOLID SENSITIVITY STUDY FOR HNL

19.1 HNL PRODUCTION

If Heavy Neutral Leptons exist and couple to electron neutrinos, these HNL must appear in nuclear beta decays, whenever a $\overline{\nu}_e$ oscillates into a HNL. The HNL flux from a nuclear reactor is proportional to the initial reactor neutrino flux, $\Phi(E_{\bar{\nu}_e})$, suppressed by the coupling parameter $|U_{eN}|^2$ and a phase space factor, leading to [217]

$$\Phi(E_N) = \theta(E_N - m_N)\,|U_{eN}|^2 \sqrt{1 - \left(\frac{m_N}{E_N}\right)^2}\,\Phi(E_{\bar{\nu}_e}).$$

E_N denotes the energy and m_N the rest mass of the massive ν_N. And $\theta(E_N - m_N)$ is the Heavyside step function that ensures the neutrino energy does not exceed its mass. For several HNL masses, the reactor ν_N spectrum is determined for the BR2 reactor and shown in figure 19.1.1. The electron neutrino flux for the BR2 reactor is used as input and is shown by the dashed line. A coupling factor

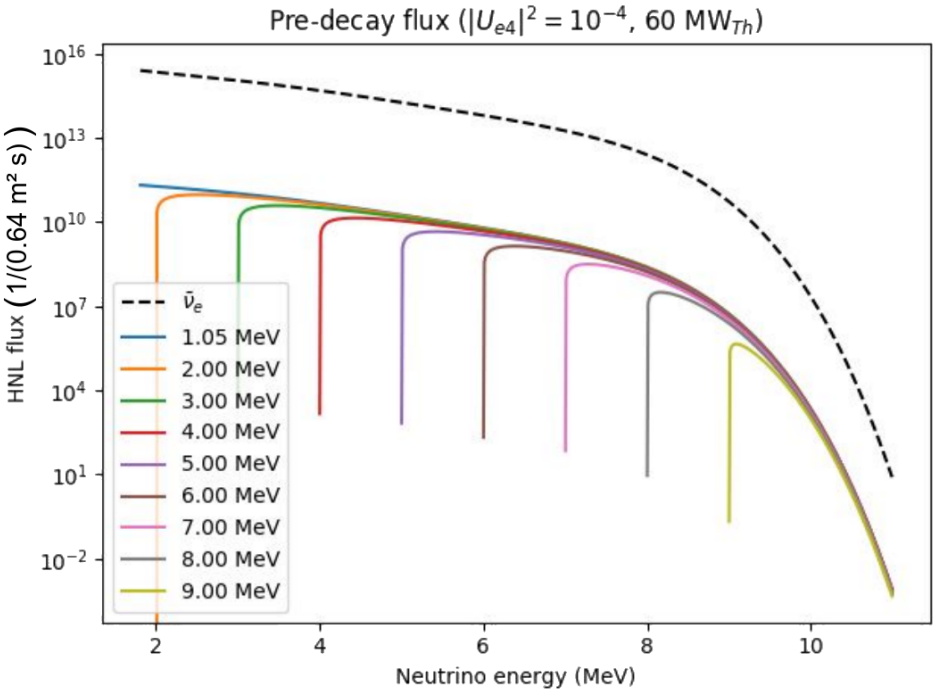

Figure 19.1.1: Expected HNL flux from the BR2 reactor that goes per second through a plane of the SoLid detector, in case of a coupling of $|U_{eN}|^2 = 10^{-4}$, for different proposed masses of the HNL, shown by the colors. The dotted line indicates the reactor $\overline{\nu_e}$ flux per plane per second.

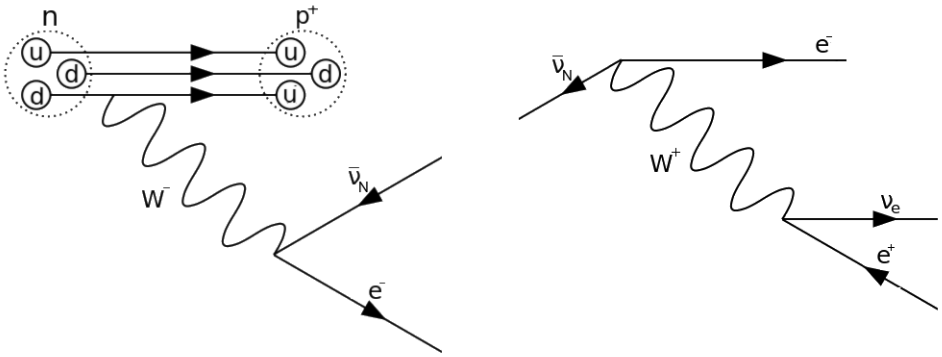

Figure 19.2.1: Feynman graph describing the appearance of HNL after nuclear beta decay and its subsequent decay in the e^+e^- mode.

of $|U_{eN}|^2 = 10^{-4}$ is taken as reference, which is slightly smaller than the best exclusion by the Bugey experiment of 0.8×10^{-3}. At lower energies, the cut off from the mass requirement is visible. For higher energies, the square root approaches 1 as its second term goes to 0. Therefore all spectra approximate the same behavior at higher energies.

19.2 HNL DECAY RATE

The heavy neutral leptons will generally be unstable, albeit possibly long-lived, allowing for decays-in-flight into SM particles. In the mass range of 1 MeV - 100 MeV, the heavy neutral lepton can decay via three different channels. In the *radiative mode* the HNL decays into a neutrino and a photon,

$$\nu_N \longrightarrow \nu_j + \gamma$$

if $m_N > m(\nu_j)$, with ν_j indicating a neutrino mass eigenstate. In the *invisible mode*, the HNL decays into three light neutrinos,

$$\nu_N \longrightarrow \nu_j + \nu_k + \overline{\nu}_k$$

with $\nu_{j,k}$ neutrino mass eigenstates. In the e^+e^- *mode* the HNL decays into a light neutrino and a positron-electron pair

$$\nu_N \longrightarrow \nu_j + e^+ + e^-$$

if $m_N > 2m_e$ = 1.022 MeV and j = 1, 2. This decay mode is shown in figure 19.2.1.

In the energy range of reactor neutrinos (below 9 MeV), the dominant decay into visible particles is into an electron-positron pair with a branching fraction of around 38% [231]. The decay rate for the e^+e^- mode is calculated in close analogy to the muon decay rate, taking into account the different phase-space factors due to the mass m_N of the heavy neutrino. In the center of mass system (c.m.s.) of the decaying neutrino one obtains

$$\Gamma_{c.m.s.} = \frac{G_F^2 m_N^5}{192\pi^3} |U_{eN}|^2 h(m_e^2/m_N^2) \tag{19.1}$$

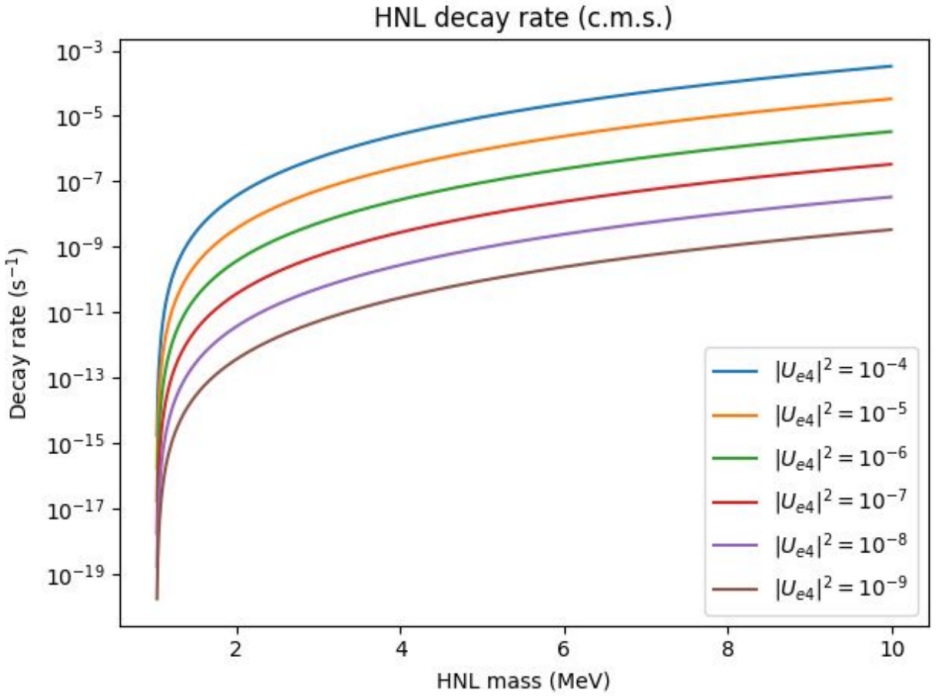

Figure 19.2.2: Decay rate of HNL in the accessible mass range, for different values of the coupling parameter. Courtesy of Simon Vercaemer.

with the Fermi constant G_F, and $h(m_e^2/m_N^2)$ the phase-space factor calculated following Gorbunov et alia [89]. For several HNL coupling factors, the decay rate is determined in function of the HNL mass and shown in figure 19.2.2.

19.3 HNL DECAY RATE IN THE SOLID DETECOR

The HNL lifetime in the center of mass system is inversely proportional to the decay rate from equation 19.1,

$$\tau_{c.m.s.} = \frac{1}{\Gamma_{c.m.s.}},$$

and therefore inversely proportional to the 5$^{\text{th}}$ power of the HNL mass and to the squared mixing parameter. The prediction of the HNL flux is combined with the prediction of the decay rate of equation 19.1. The decay rate in a SoLid-like experiment is determined for multiple values of $|U_{eN}|^2$ and as a function of the HNL mass, this is shown in figure 19.3.1. The e^+e^- decay rate was determined as outlined in the paper by Gorbunov and Shaposhnikov [89] and the reactor spectrum was obtained from the parametrisation by Mueller[108]. A SoLid like detector (80 cm by 80 cm by 250 cm) was assumed, starting at a distance of 6.2 m from the center of a small reactor core. As a reference, some lines with recognisable rates are added using horizontal lines.

We are most sensitive to HNL with masses between 4 to 7 MeV. For low energies the flux is the biggest, but the decay rate is the smallest. For high energies, the inverse is true. Therefore the biggest

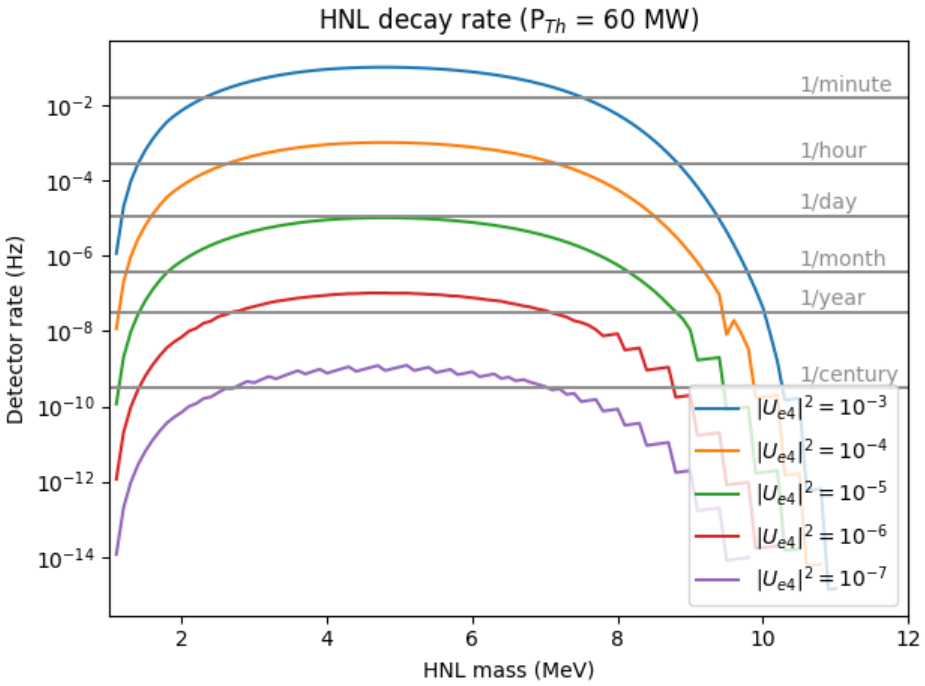

Figure 19.3.1: Rate of HNL decay inside a SoLid-like detector next to a BR2-like reactor. Courtesy of Simon Vercaemer.

decay rate comes from the intermediate energies. These decay rates can be converted into a threshold trigger rate using simple kinematics. In Figure 19.3.2 the results are presented in the HNL oscillation parameter space, where a threshold of 2 MeV is assumed. Possible energy depositions by the positron annihilation gammas are not counted towards this 2 MeV. Previous experiments have already placed exclusion limits on this parameter space, as discussed in section 18.1.1. These limits are superimposed on the trigger rate to indicate what signal rate needs to be extracted from the background in order to achieve a competitive result. In the mass range between 1 and 8 MeV, SoLid has a potentially stronger exclusion or even discovery potential, as compared to existing experimental limits.

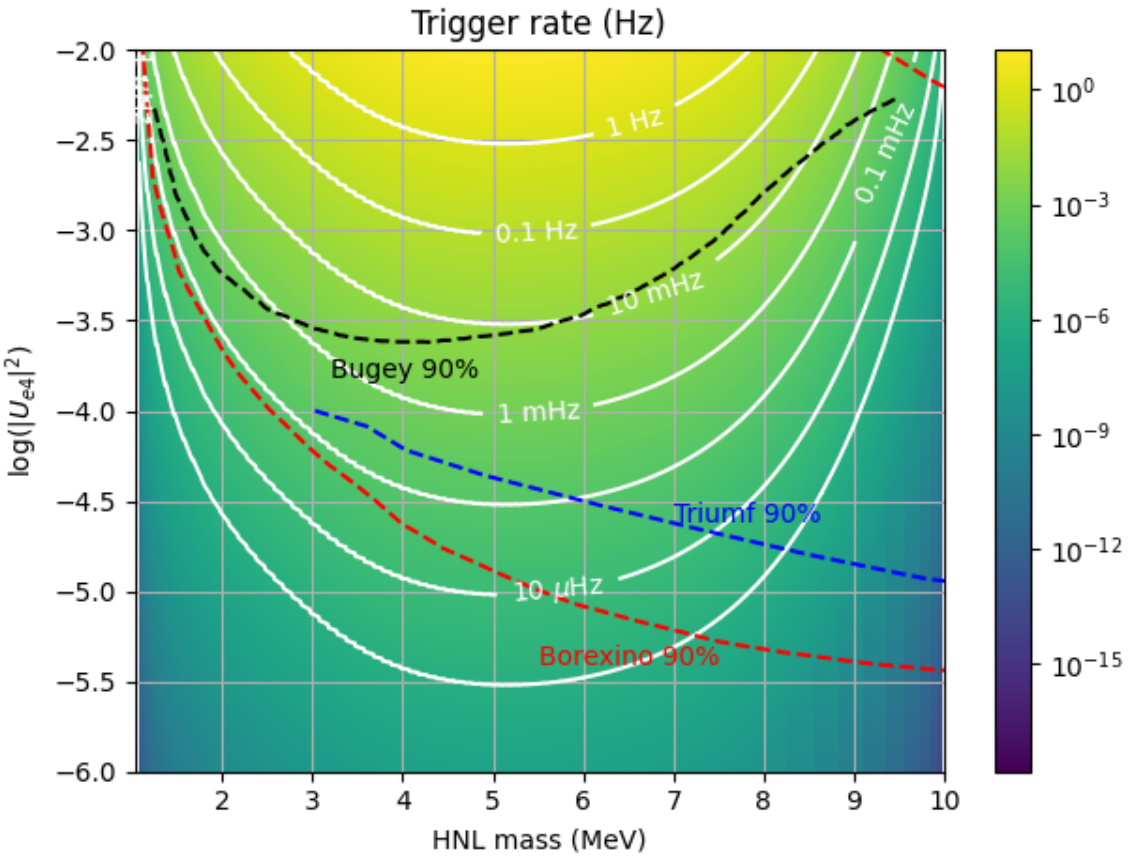

Figure 19.3.2: Expected trigger rate of the SoLid detector to HNL with accessible HNL masses and for different coupling parameters $|U_{eN}|^2$. The exclusion limits from the previous reactor experiment, Bugey [217], is superimposed, as well as from Borexino [216] and Triumf [218]. Courtesy of Simon Vercaemer.

19.4 HNL SIMULATION

HNL events are simulated with the use of the GEANT4 software that was described in chapter 12. The heavy neutral lepton is generated with the Pythia8 particle gun [232]. To this end, the existing muon decay mode in the Pythia8 package was adapted. The muon was replaced by a HNL and the outgoing ν_μ became a positron. The masses and charges are adapted accordingly. The Pythia8 generator is coupled to the SoLO generator, that was described in chapter 10. The neutrino momentum and energy prediction for the BR2 reactor is used as input, in order to obtain a realistic HNL flux. The drawback of this approach is that the IBD interaction cross section was already factored in to the SoLO generator, and had to be unfolded. Simulations are produced for HNL with masses between 2 and 9 MeV. The energy range is limited between 1.022 MeV and 9 MeV, respectively because of the $2m_e$ that has to be generated and the $\overline{\nu}_e$ spectrum.

In the GEANT4 simulation, the HNL decays into a positron, electron and a neutrino. The positron will annihilate, producing back-to-back 511 keV annihilation gammas. The kinematics of the outgoing positron and electron were studied for different masses and energies. Figure 19.4.1 shows several

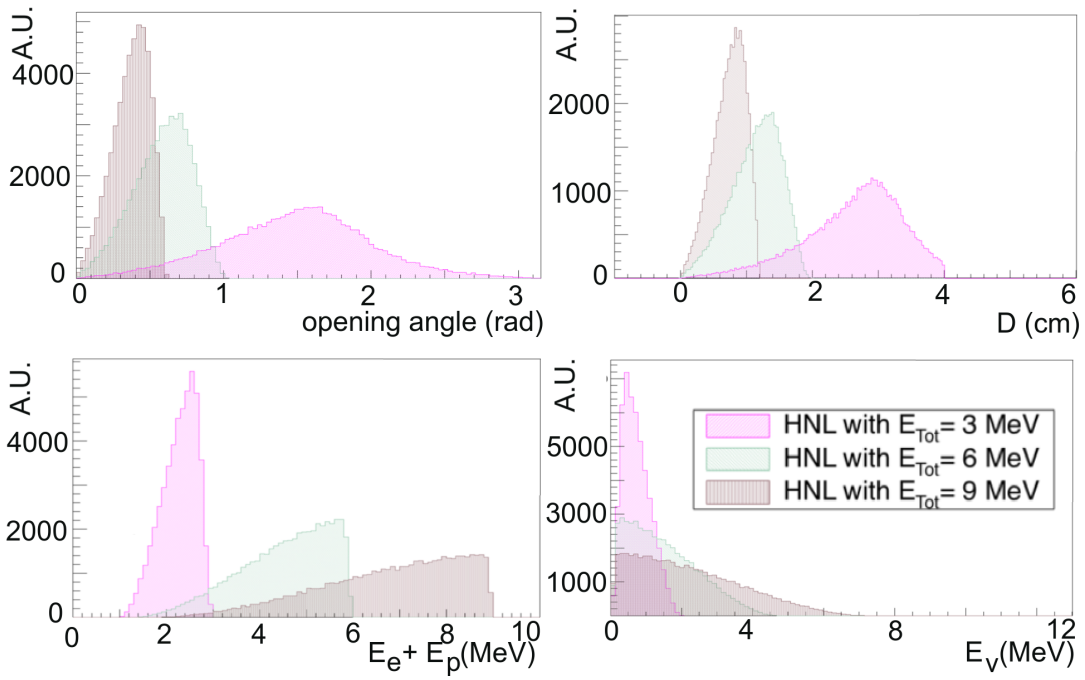

Figure 19.4.1: Prediction of the characteristics of the energy depositions of the HNL decay products inside the SoLid detector, based on GEANT4 simulations, for a HNL with 2.3 MeV mass, and several total energies. Top: The opening angle (left) and stopping distance (right) between the e^- and e^+. Bottom: the energy of the e^- and e^+ (left) and of the outgoing neutrino (right). Courtesy of Yamiel Abreu and Haifa Sfar.

distributions for a HNL with a mass of 2.3 MeV and a total energy of 3 MeV, 6 MeV, 9 MeV. In the top left panel, the opening angle between the electron and positron is shown. For higher energies, the HNL is more forward boosted and the angle between the particles is smaller. For smaller energies the opening angle approaches the limiting value of π. In those cases, the particles have a backward orientation with respect to the incoming HNL particle. The latter is confirmed by the longitudinal momentum which has negative values.
The top right panel shows the distance between the electron and positron after 2 cm of flight. The distance decreases with HNL energy because of the higher boost of the decay products. The bottom left panel shows the sum of the electron and positron energy, while the antineutrino energy is shown in the bottom right panel. The sum of both will be the total energy.

19.5 TRIGGER STUDY

The positron and electron, emerging from the HNL decay, both cause an electromagnetic scintillation signal (ES) in the detector. Their energy depositions happen most likely in the same cube or with very little spread. It is possible that additional cubes or clusters are created by the positron annihilation gammas. The HNL events that were produced with the GEANT4 simulation, are processed by the readout simulation (see chapter 13 and following) and the Saffron2 software (see chapter 8). With the simulation of the trigger system (see chapter 7), the trigger efficiency was determined for the various HNL masses, as indicated in figure 19.5.1. With a mass of 4 MeV, about half of the HNL that

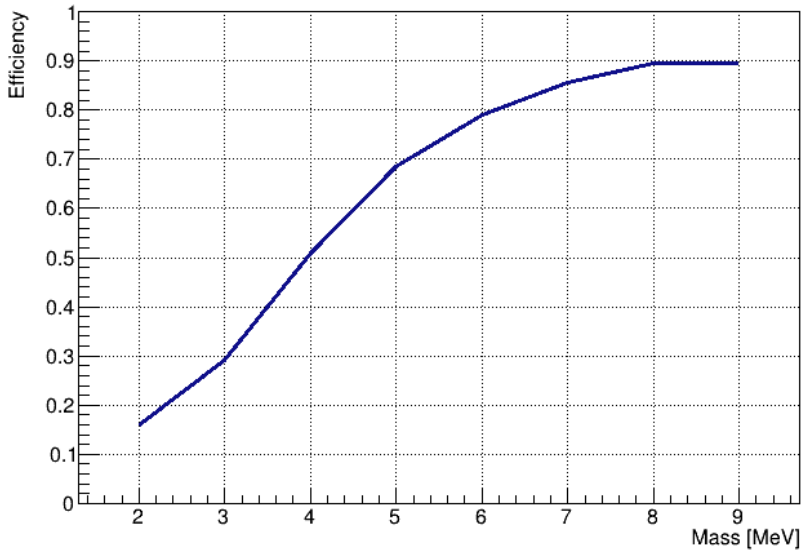

Figure 19.5.1: Efficiency of the SoLid high energy trigger that requires a coincidence with $\Delta t < 75$ ns between amplitude triggers of orthogonal channels with a threshold of > 50 PA. This corresponds to an energy deposit of about 2 MeV in the detector cell.

decay inside the detector will cause a trigger. For each triggered events, one or more ES clusters were reconstructed. During the HNL event, no neutron arises and no nuclear signal (NS) is expected. Therefore, the neutron trigger is not relevant for the HNL study.

19.6 HNL VARIABLES OF INTEREST

For the classic IBD analysis, the IBD signature consists of an ES and an NS signal, such that most variables of interest were based on the coincidence between both signals and the specifications of the ES cluster such as the prompt energy. The HNL signal consists of only ES clusters. If there are more than one cluster, those are coming from the annihilation gammas and are virtually coincident in time. The variables of interest (VOI) are based on the characteristics of the ES clusters. For the HNL with a mass of 6 MeV, the distributions of the VOI are shown in figure 19.6.5 - 19.6.4. The effect of the background reducing selection requirements that will be discussed in the following section is shown as well.

The top of figures 19.6.1 - 19.6.3 show the VOI regarding the position of the ES cluster in the x, y, and z coordinates. In the x direction (horizontal, left-right), the HNL events are highest at the detector center and decrease towards the edges, due to geometrical considerations concerning the relative positions of the reactor core and the detector. The asymmetry is not understood and can indicates an issue in the HNL generator in GEANT4. The z distribution (horizontal, front-back) shows a decrease in events towards the back of the detector that is facing away from the reactor.

The bottom of figures 19.6.1 - 19.6.3 contain the spread of the ES cluster in the x, y, and z direction. There is only little spread in the z direction because after the threshold trigger, only the triggering plane is read out (see chapter 7). The spread inside the plane, i.e. in the x and y direction, is symmetric and is due to the lightleaks and the annihilation gammas. The signals from the electron and positron

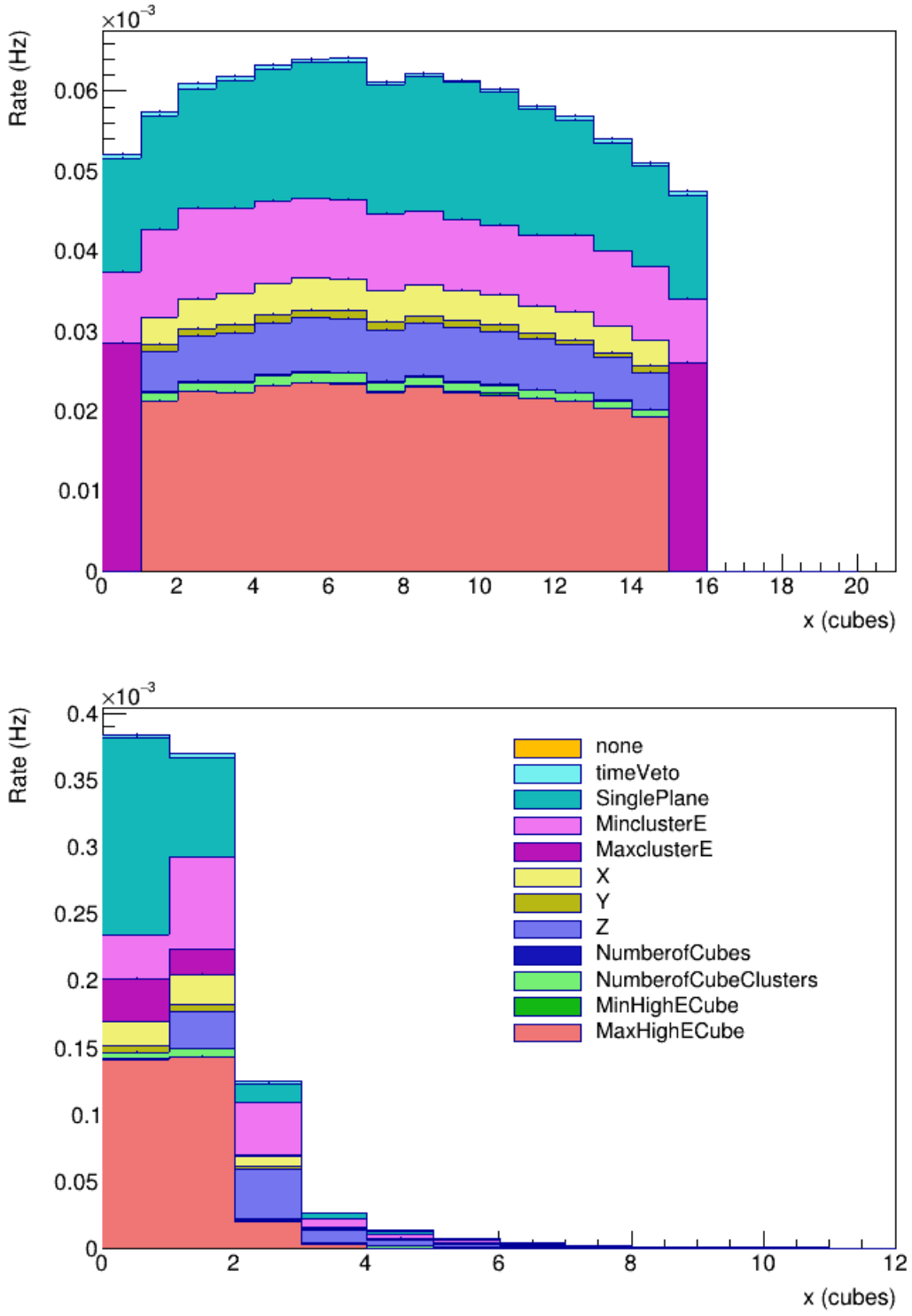

Figure 19.6.1: Distributions concerning the x position and spread of the HNL with a mass of 6 MeV and assuming $|U_{eN}|^2 = 10^{-4}$. The consecutive cuts that will be determined in section 19.8 are applied and represented by different colors).

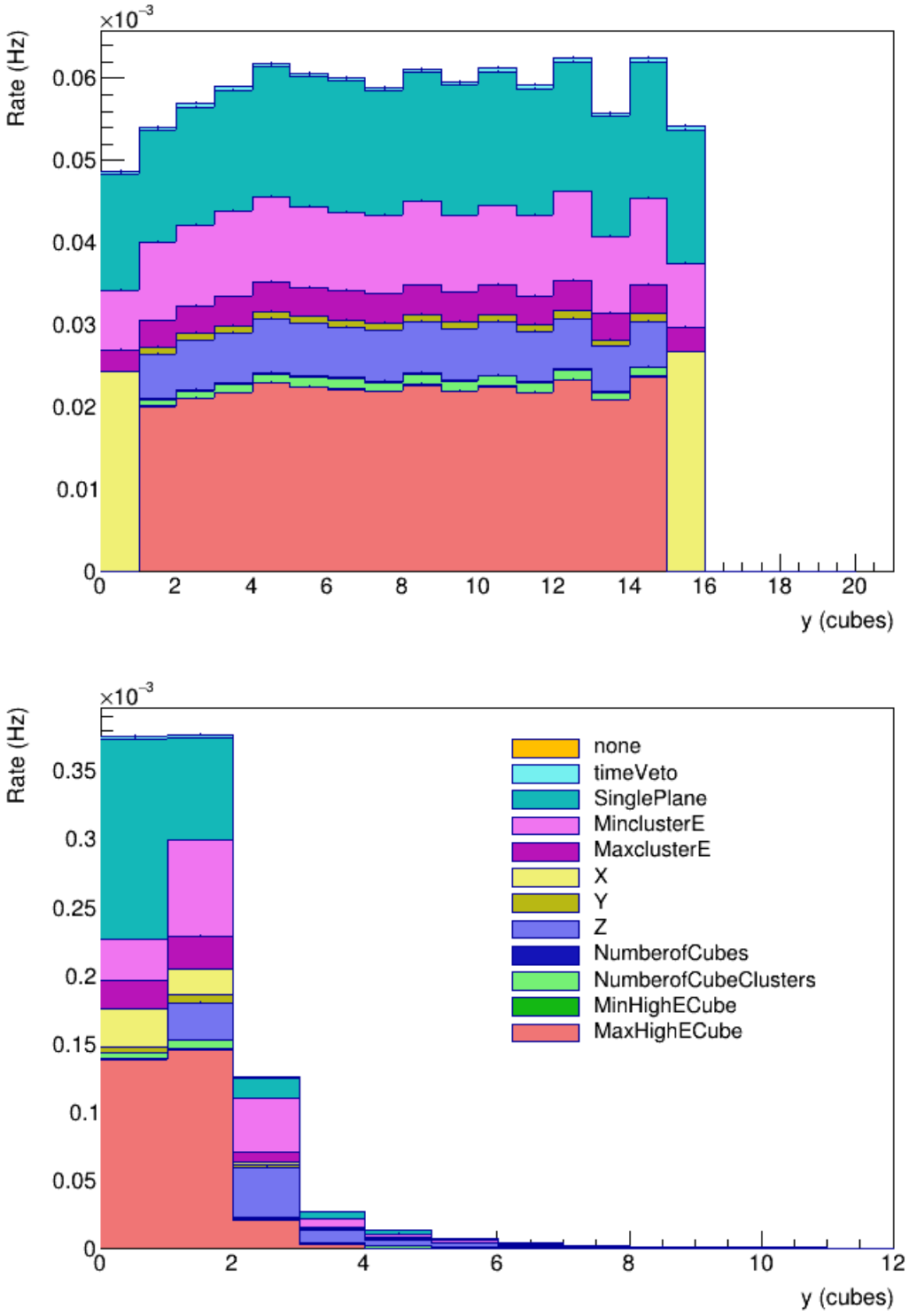

Figure 19.6.2: Distributions concerning the y position and spread of the HNL with a mass of 6 MeV and assuming $|U_{eN}|^2 = 10^{-4}$. The consecutive cuts that will be determined in section 19.8 are applied and represented by different colors).

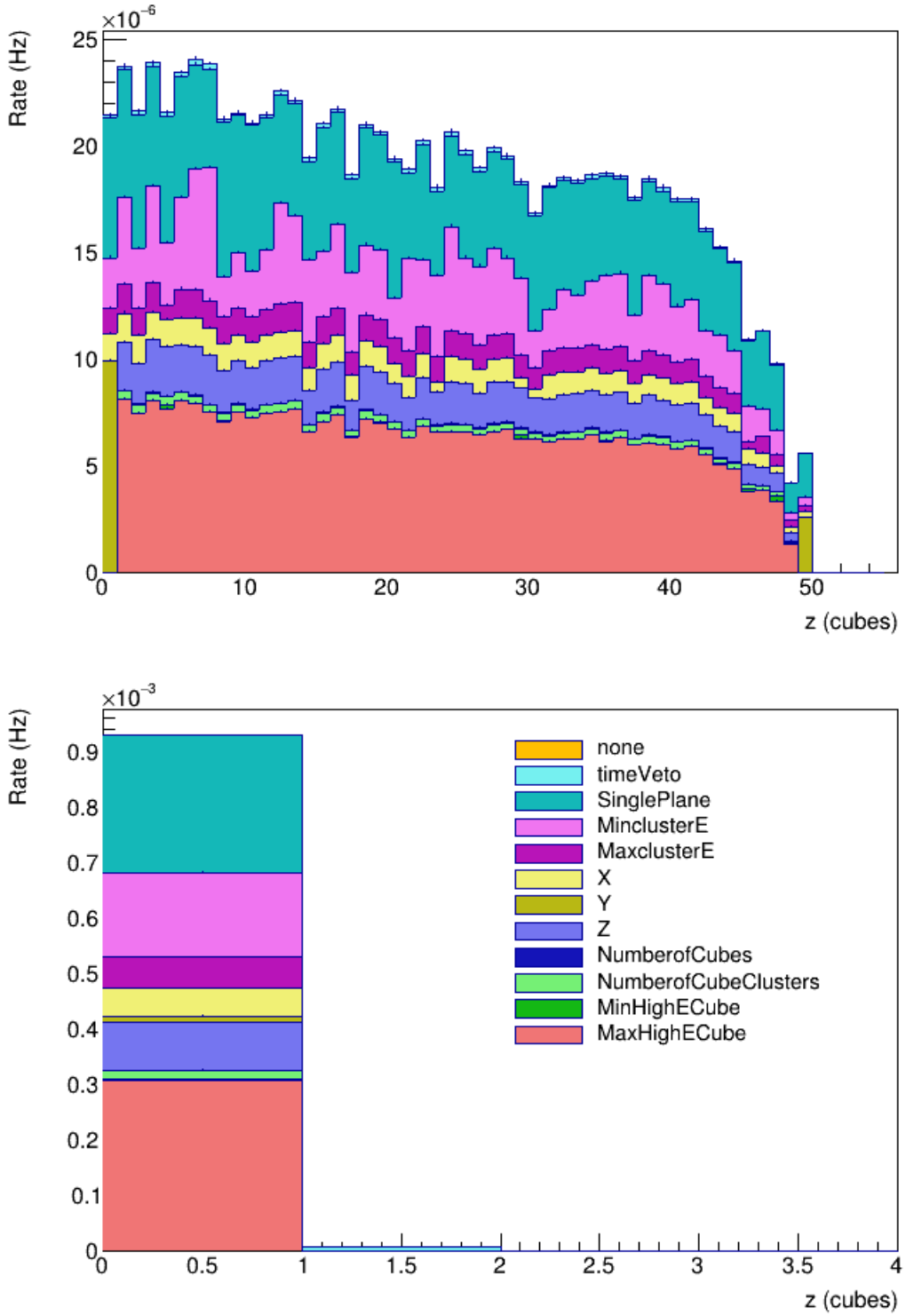

Figure 19.6.3: Distributions concerning the z position and spread of the HNL with a mass of 6 MeV and assuming $|U_{eN}|^2 = 10^{-4}$. The consecutive cuts that will be determined in section 19.8 are applied and represented by different colors).

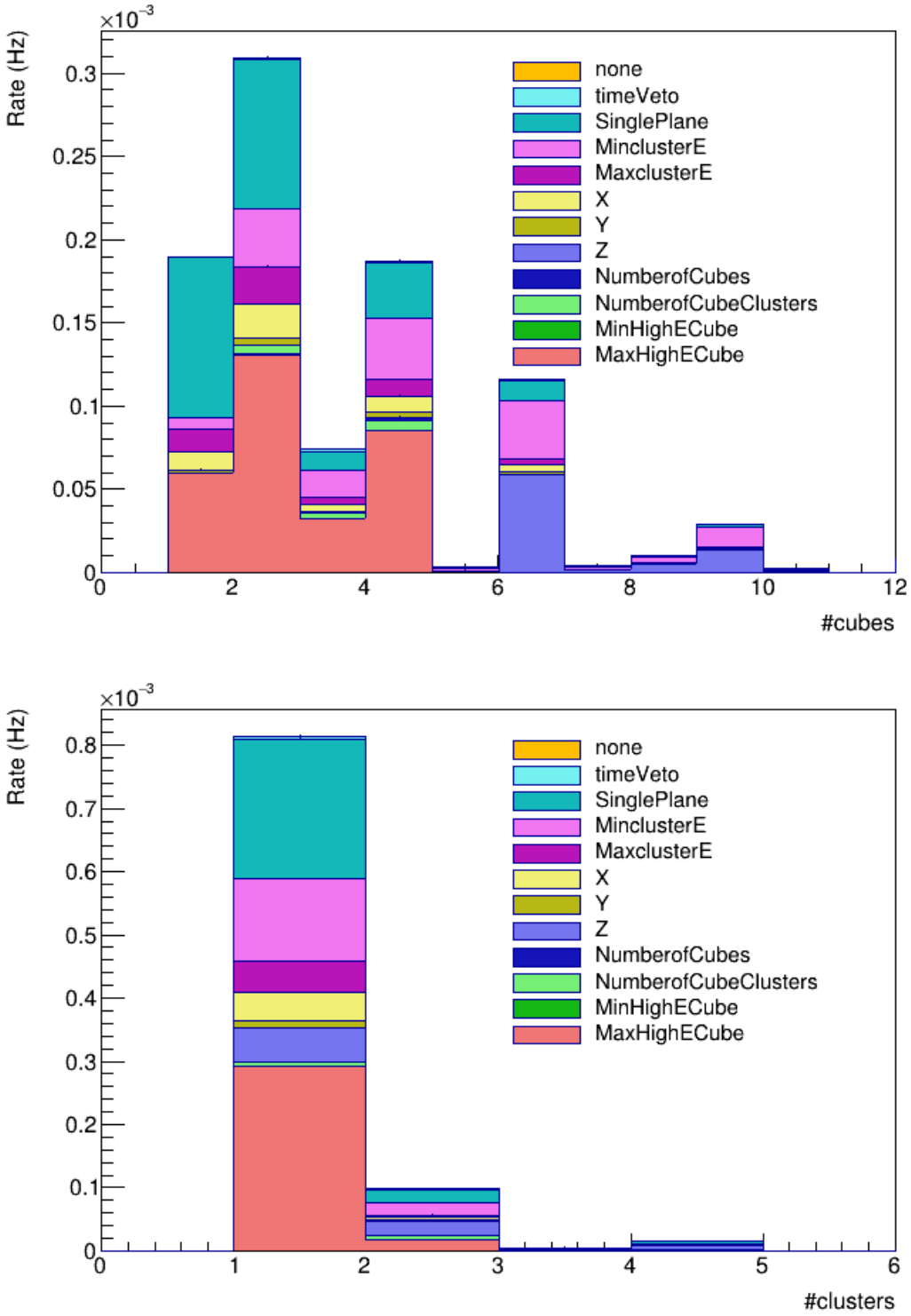

Figure 19.6.4: Distributions concerning the number of cubes and the number of clusters of the reconstructed HNL event with the consecutive cuts applied (represented by different colors).

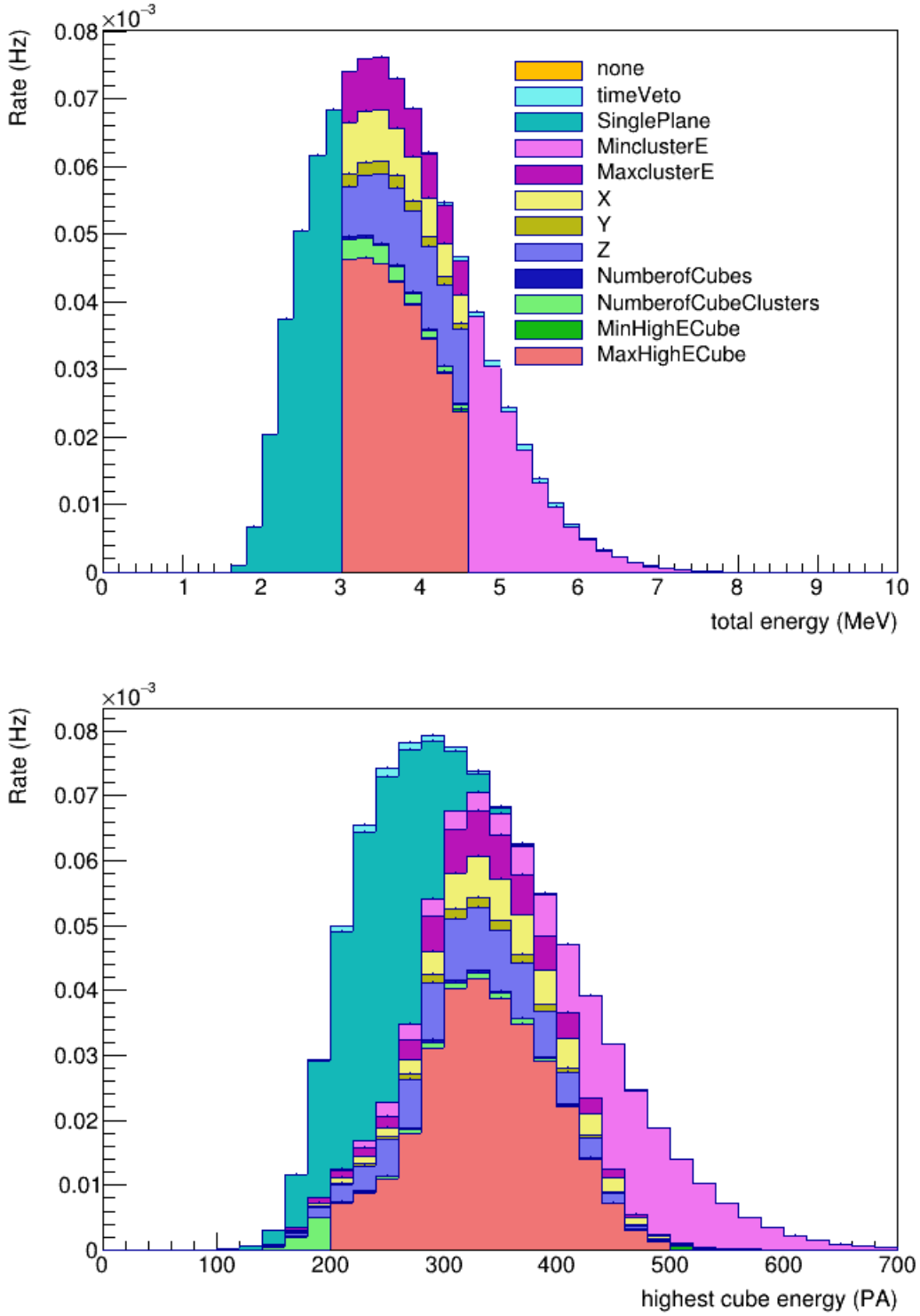

Figure 19.6.5: Distributions concerning the total energy and the energy of the cube with the highest energy of the reconstructed HNL event with the consecutive cuts applied (represented by different colors).

are well contained to the interaction cube because they travel on average half a centimeter per MeV [188], which makes an escape from the 5 cm cubes unlikely.

Figure 19.6.4 shows on top the number of cubes in the ES cluster. Note that the clustering is temporal. Most of the time, two cubes are contained in the cluster. The right panel shows the number of spatial ES clusters during the event. A spatial cluster is constructed from all cubes that are connected through the fact that they share a face with another cube in the cluster. In almost 90 % of the cases there is only one spatial cluster present in the event.

Figure 19.6.5 displays the energy of the ES cluster. The top panel shows the total reconstructed energy of the ES cluster in MeV, while the bottom panel show the energy of the cube with the highest energy in the cluster in PA.

19.7 MODEL FOR THE HNL BACKGROUND

For the HNL model that is studied in this analysis, the signal consists in general of a single ES cluster with a little spread, in the energy range between 1 and 9 MeV. With the coupling factor $|U^2_{eN}| = 10^{-4}$, and a HNL mass of 6 MeV, we expect a HNL rate of 0.94 mHz. The HNL analysis will face a huge background. In the context of the IBD analysis, several backgrounds were already studied extensively (see chapters 11 and 15).

The β^- decays of ^{214}Bi contaminants in the detector components result in an ES signal that mimics the HNL ES. This decay is followed by an α decay that converts the daughter nucleus, ^{214}Po, into stable lead ^{210}Pb. The BiPo background can be effectively reduced by discrimination based on the presence of the alpha induced NS signal close in time to the ES. The time veto that will be discussed in the following section already rejects 99.15 % of the BiPo signal that is detected with a rate of 0.65 Hz. BiPo does not pose a dominant background and will be ignored in the following. A similar reasoning applies to the IBD signal. The prompt e^+ signal can cause a background for the HNL, but because of the time coincidence with the neutron NS signal, a time veto can reject 77.6 % of IBD signals.

The events with a cosmogenic origin cause more prominent backgrounds for the HNL analysis. Fast atmospheric neutrons, created in the atmosphere by spallation processes, can reach the SoLid detector and cause ES signals by proton recoils. In addition, high energy cosmogenic muons can also reach the detector. If the muon leaves a track through the detector, it can be recognised and rejected. If the muon merely clips the edge of the detector, the signal might be reconstructed as an ES signal that mimics the HNL signal. The muon can also be stopped in the detector and decay, resulting once again in an HNL ES background. The muons can also spallate neutrons from the material that surrounds the detector, which can enter the detector and cause ES signals by protons recoil.

The HNL background is studied in the preselection region that has the following selection requirements: A time veto is applied to the time region around a neutron-like NS of 500 μs, and to the time region before an alpha-like NS of 1750 μs. The time region after a muon signal of 500 μs is also vetoed. In addition, the ES signal has to be contained to a single plane and the cluster energy is required to fall inside the region [2, 13.5] MeV.

When we compared the rate of the reactor off signal in the preselection region with the rate of the aforementioned backgrounds that were already studied for the IBD analysis, it became apparent that the majority of background components was missing in the simulation samples we already had. The reactor off data sample was taken during two days, spanning 155520 s. The rate of ES signals in the preselected reactor off sample is 126.91 Hz. For the cosmic simulations, the rate can be determined from the estimate of the real time by the generator. This gives 16.74 Hz of ES signals in the muon MC and 0.44 Hz of ES in the atmospheric neutron MC. For the IBD MC sample, the corresponding real time is estimated from the knowledge of the IBD interaction rate of 0.0138 Hz and the amount of simulated IBD events. An IBD ES rate at preselection level of 0.00136 Hz is found. Based on a similar reasoning about the BiPo signal that has an interaction rate of 2.5 Hz, at preselection level a BiPo ES rate of 0.006310 Hz is expected. The currently simulated background contributions add up to 17.19 Hz which is nowhere near the reactor off rate.
The contribution of the cosmogenic backgrounds was validated in a cosmic control region, that was obtained by adapting the HNL preselection cuts, where only the higher energy region above 4 MeV was regarded where only cosmogenics are expected. The cosmogenics MC samples were found to agree with the reactor off data in this region.

19.7.1 GAMMA RAY BACKGROUND

The behaviour of the missing background can be inferred from the reactor off signal that remains after subtracting the backgrounds that are already simulated (i.e. ^{214}Bi-^{214}Po, cosmic muons and atmospheric neutrons). Most notably is the asymmetry in the y coordinate (which can be seen in figure 19.7.3. The preselected reactor off rate drops exponentially from 17 Hz at the bottom of the detector to 6 Hz. For the top cubes, the rate jumps to around 9 Hz. None of the previous backgrounds can reproduce this signal, although ^{214}Bi-^{214}Po was found to behave similar to the missing background. A free fit of the available background signals to the reactor off data was found to approach the data well, with a ^{214}Bi-^{214}Po contribution of 80 %. Such a high ^{214}Bi-^{214}Po rate is not possible, but it indicates the missing background is in the low energy, around 2 or 3 MeV.

A candidate for the missing HNL background are gamma rays. Most gamma rays have an energy below the SoLid trigger threshold of 2 MeV, as can be seen on the measured spectrum in figure 11.2.2. Measurements with a Ge-detector with 90° collimation in front of the R1 beam port, where the SoLid detector is located, show a peak at 2614 keV, which is most likely coming from the β^- decay of Thallium, ^{208}Tl. The peak was still prominent when the measurement was done behind a waterbrick, indicating the rays can penetrate the detector's water wall. ^{208}Tl is present in the ^{232}Th series, which is one of the naturally abundant contaminations, as described in chapter 11 and visible on figure 11.1.1. The natural radioactive elements are ingrained in concrete and construction materials. The 2614 kev gamma ray from ^{208}Tl has a mean free path of 20 cm in lead and is therefore difficult to shield [233]. ^{208}Tl is a common background in experiments looking for rare events [234, 235, 236]. Based on the observation that the missing background has an increased rate at the bottom of the detector, the ^{208}Tl gamma rays most likely come from the concrete floor. This is the closest source to the detector and no passive shielding is present below the detector.

The ^{208}Tl gamma rays could also come from an intrinsic detector contamination. Next to ^{214}Bi, the ^{6}Li:Zns(Ag) screens also contain small traces of ^{212}Bi. In 36% of the cases ^{212}Bi α decays to ^{208}Tl, while

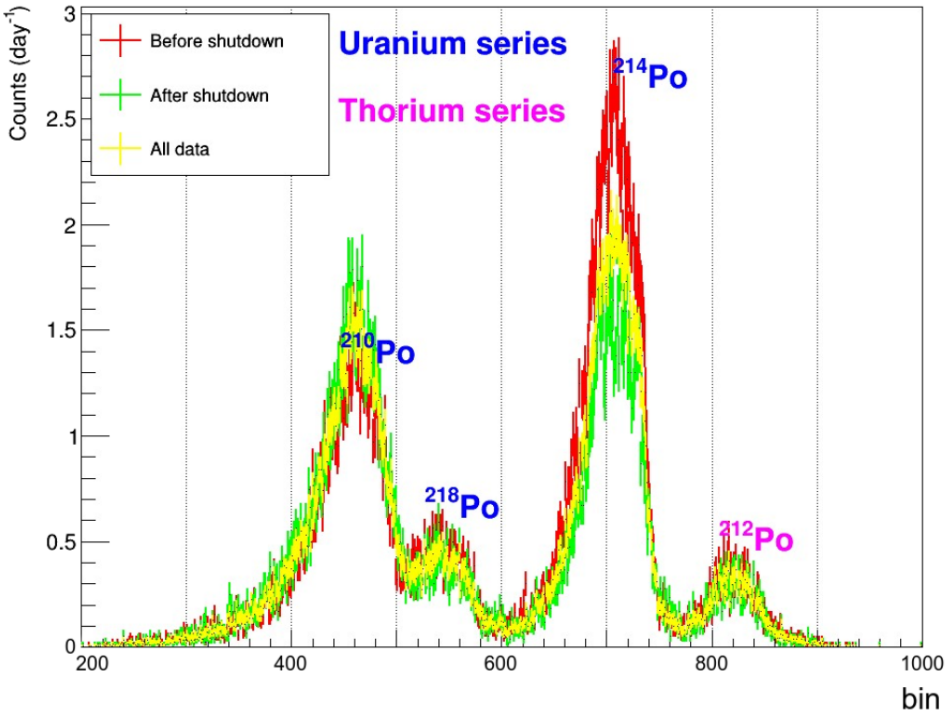

Figure 19.7.1: The energy spectrum of α particles as measured by the RaDoM detector that is installed inside the container, indicates that a small contribution of ^{212}Po is present in the airborne ^{214}Bi-^{214}Po.

in 64 % of the cases, it β^- decays to ^{212} Po, as indicated on figure 11.1.1. Based on the rate monitoring of ^{212}Po that is described below, the missing background is probably not coming from an intrinsic contamination. Inside the container, a RaDoM detector [160] is installed that measures the airborne BiPo part, by measuring the alpha energy. A small amount of ^{212}Po is measured as shown in figure 19.7.1.The ^{212}Po will cause NS triggers in the SoLid detector. The NS trigger rate is between 17 Hz and 19 Hz, dependent of the atmospheric pressure which attenuates cosmics and of the amount of Radon in the air. The NS rate is dominated by alphas, that are coming mainly from ^{214}Po. The halflife of ^{212}Po is much shorter with 299 ns, in comparison to 168 μs for ^{214}Po. By performing exponential fits to different regions of the time coincidences within the control region of BiPo, the contributions of ^{214}Po, neutron captures, and ^{212}Po can be separated, based on their respective time constants. The resulting rate of α decay of ^{212}Po and ^{214}Po is shown in figure 19.7.2. The ^{212}Po rate is negligibly small, with a rate around 8 mHz (notice it is scaled up by 10^3 in the figure).

A GEANT4 simulation of the ^{208}Tl background is produced by generating gamma rays of 2614 keV inside the third level concrete floor of the BR2 building, in an area that exceeds the waterwall by one meter. At the moment, we do not have a control region to validate the simulation of the gamma background. Neither do we have knowledge of the expected gamma rate in the detector. When assuming that the 86 % of missing background is completely due to ^{208}Tl gamma rays coming from the concrete floor, the simulated y distribution increased towards the bottom of the detector, as envisaged, but the increase became too steep. There must be another, maybe airborne, gamma source that results in a signal spread throughout the detector.

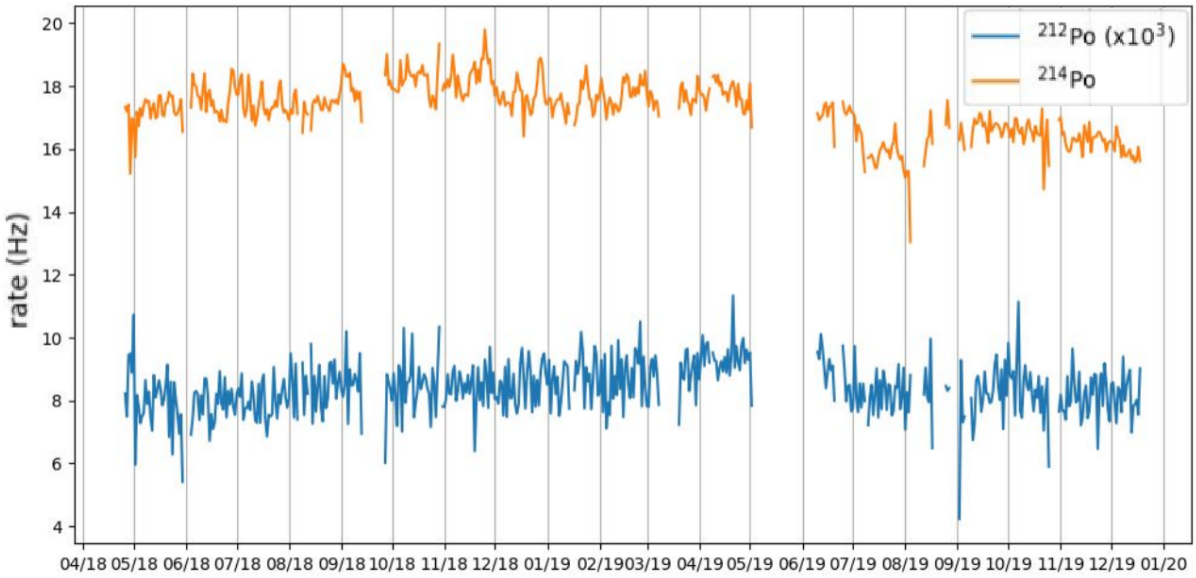

Figure 19.7.2: The rate monitoring of the ^{212}Po and ^{214}Po decays indicate that the rate of the former is negligible for the HNL analysis.

To investigate the different gamma sources with their spatial distribution and energy spectrum, dedicated measurements and studies have to be executed. Since the characteristics of the ^{214}Bi-^{214}Po signal showed to be a good representation of the missing background at preselection level and the signal is almost homegenous throughout the detector, I decided to use the BiPo simulation as model for an additional gamma background in the scope of this thesis. In addition, it will turn out that the rate of the background model under the consecutive selection requirements after preselection resembles the behavior of reactor off data, as will be shown in figure 19.8.9. The total simulated signal is reduced in the same way as the reactor off data are.

With a background model containing 40 % of ^{208}Tl and 46 % of ^{214}Bi-^{214}Po (representing gammas), the spatial distribution of ES events approached the reactor off data well. Only at the edges, the data was still underestimated. Since this will have a big influence on the fiducialisation cuts, the spatial distribution of the ^{214}Bi-^{214}Po simulation was forced to reproduce the missing background distribution and to retain sufficient statistics, the time veto was removed from the preselection of the ^{214}Bi-^{214}Po simulation. The final background model of the reactor off data in the HNL preselection region is shown in figures 19.7.3 - 19.7.7. Note that the agreement for the x and y distributions are by construction. While the agreement is not perfect in the other variables, it is acceptable and illustrates that we have understanding of the different components present in the background.

The background in the HNL preselection region can be modeled with 13.2 % muons, 0.3 % atmospheric neutrons, 40 % ^{208}Tl from the concrete floor and 46 % other gamma sources, that are modeled with the ^{214}Bi-^{214}Po simulation. The contribution of muons and atmospheric neutrons is based on the MC time information. This approach was validated in section 15.3. However, the energy distribution is not well reproduced. The contribution from muons is substantial, especially at the edges where clipping muons arise. The small contribution of ^{214}Bi-^{214}Po and IBD is also understood. The contribution of the gamma background is large, even bigger than initially expected.

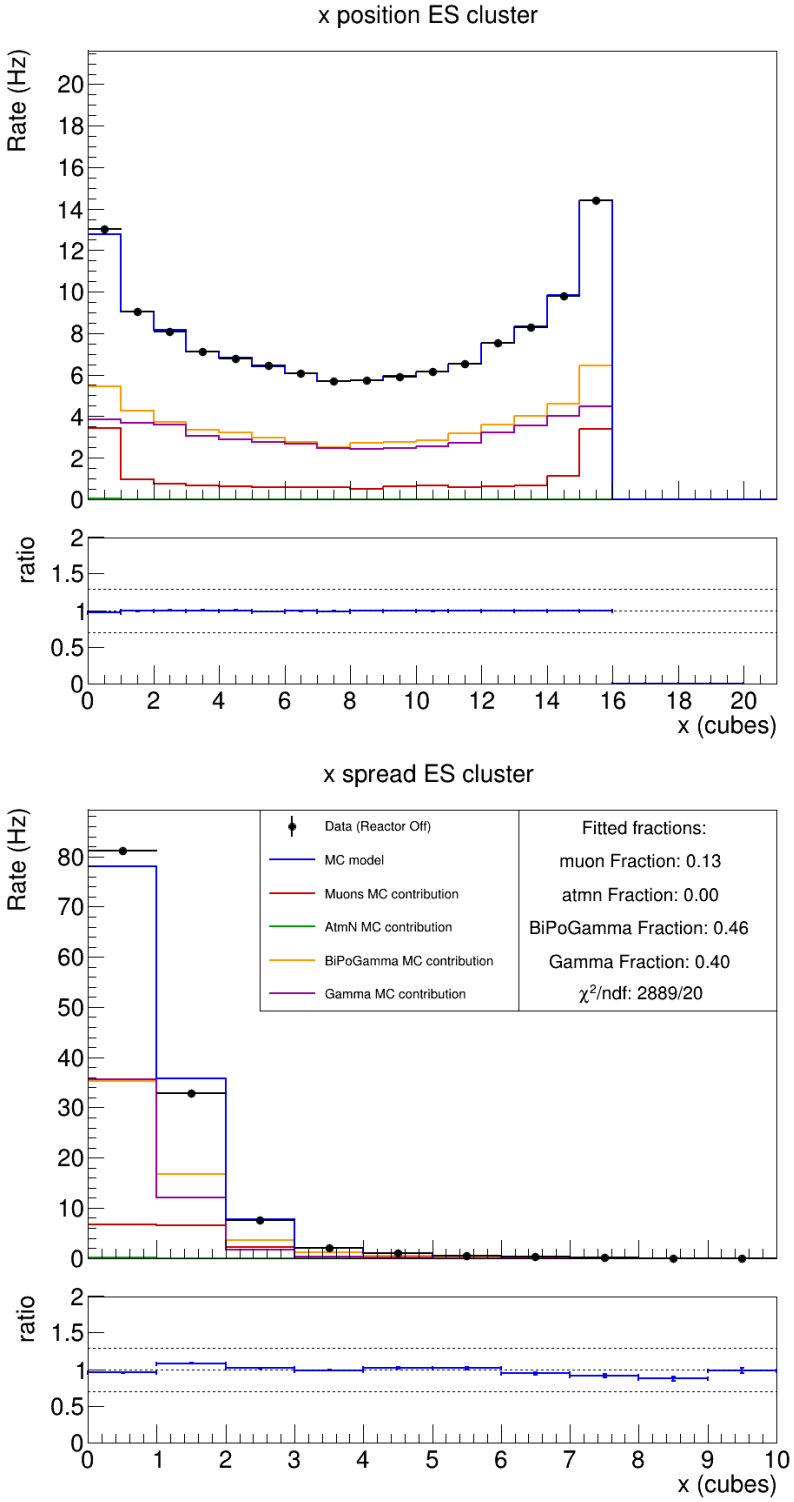

Figure 19.7.3: Spatial x distributions of the background model for the reactor off data in the HNL preselection region, containing simulations of muons, atmospheric neutrons, gamma rays from ^{208}Tl decay and additional gamma rays that are modeled with the ^{214}Bi-^{214}Po simulation.

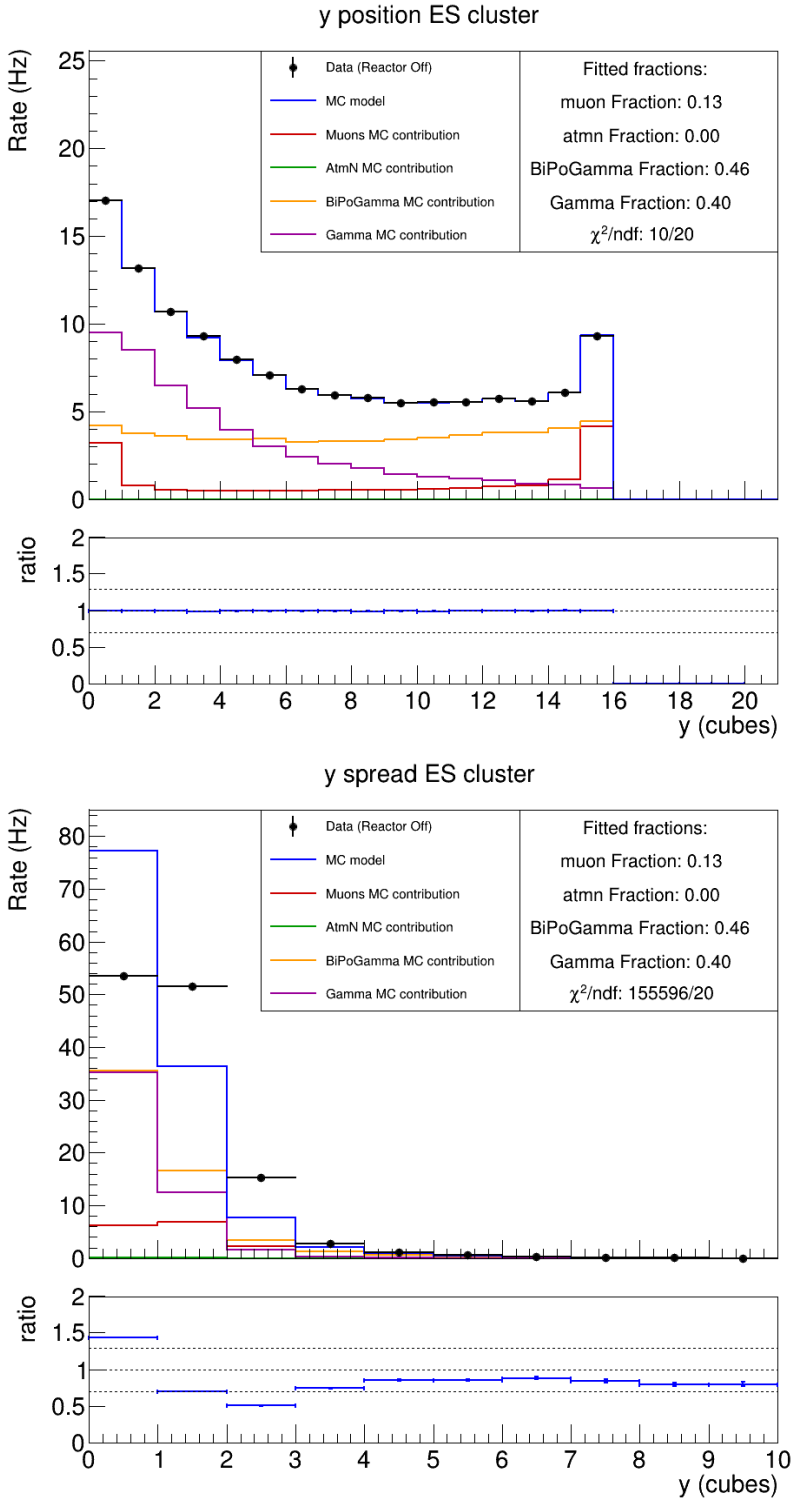

Figure 19.7.4: Spatial y distributions of the background model for the reactor off data in the HNL preselection region, containing simulations of muons, atmospheric neutrons, gamma rays from ^{208}Tl decay and additional gamma rays that are modeled with the ^{214}Bi-^{214}Po simulation.

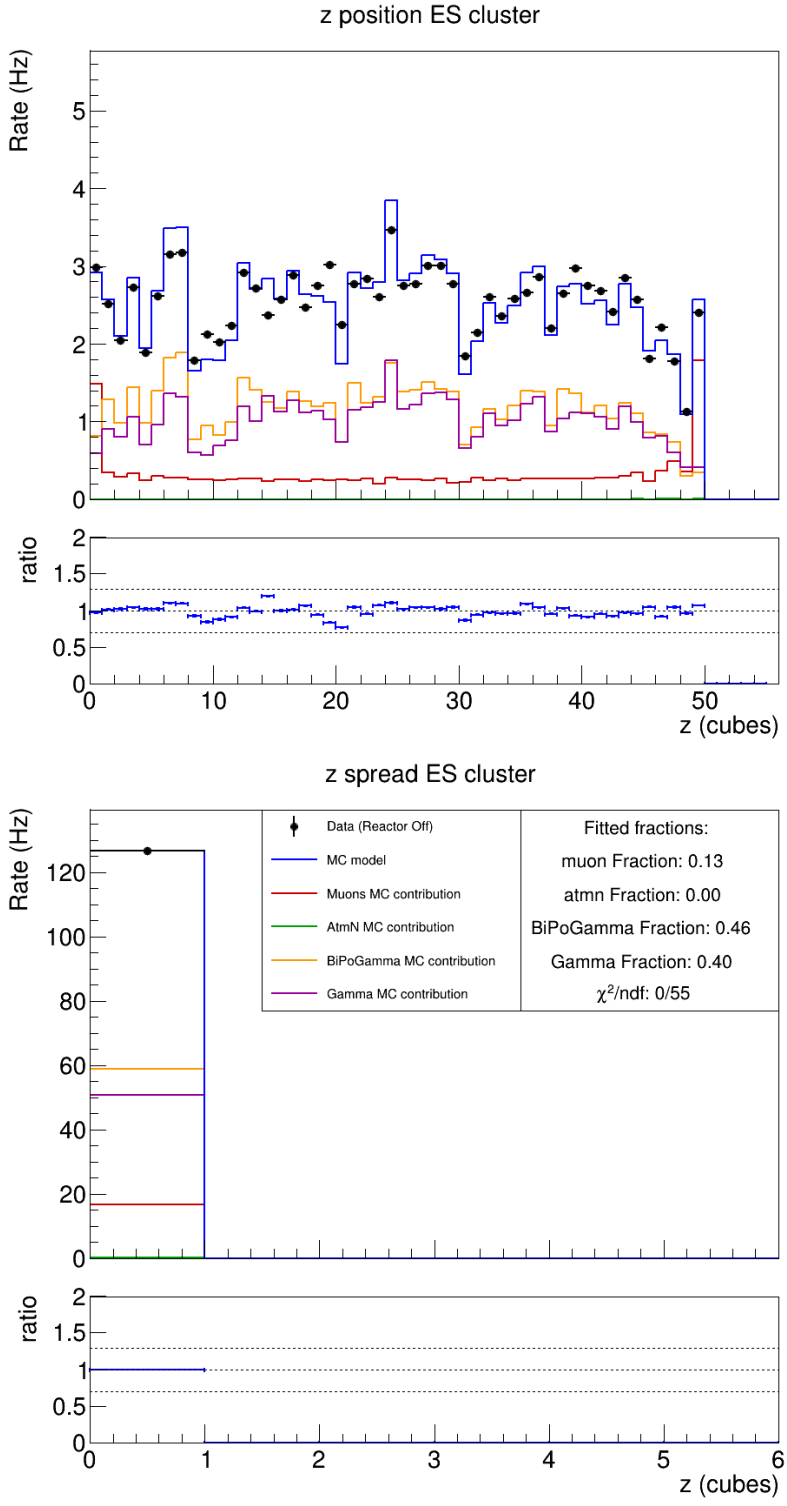

Figure 19.7.5: Spatial z distributions of the background model for the reactor off data in the HNL preselection region, containing simulations of muons, atmospheric neutrons, gamma rays from ^{208}Tl decay and additional gamma rays that are modeled with the ^{214}Bi-^{214}Po simulation.

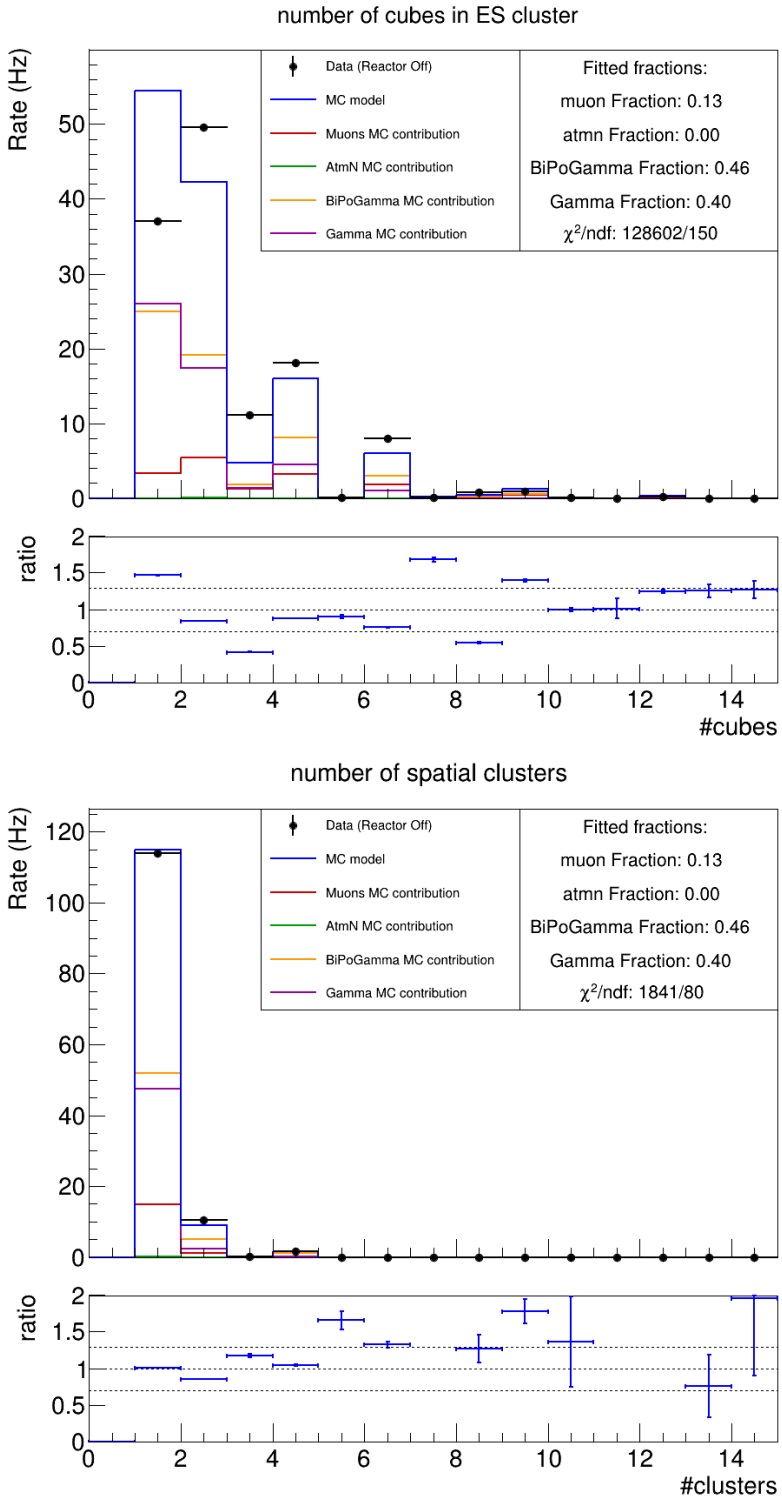

Figure 19.7.6: Size distributions for the background model for the reactor off data in the HNL preselection region, containing simulations of muons, atmospheric neutrons, gamma rays from ^{208}Tl decay and additional gamma rays that are modeled with the ^{214}Bi-^{214}Po simulation.

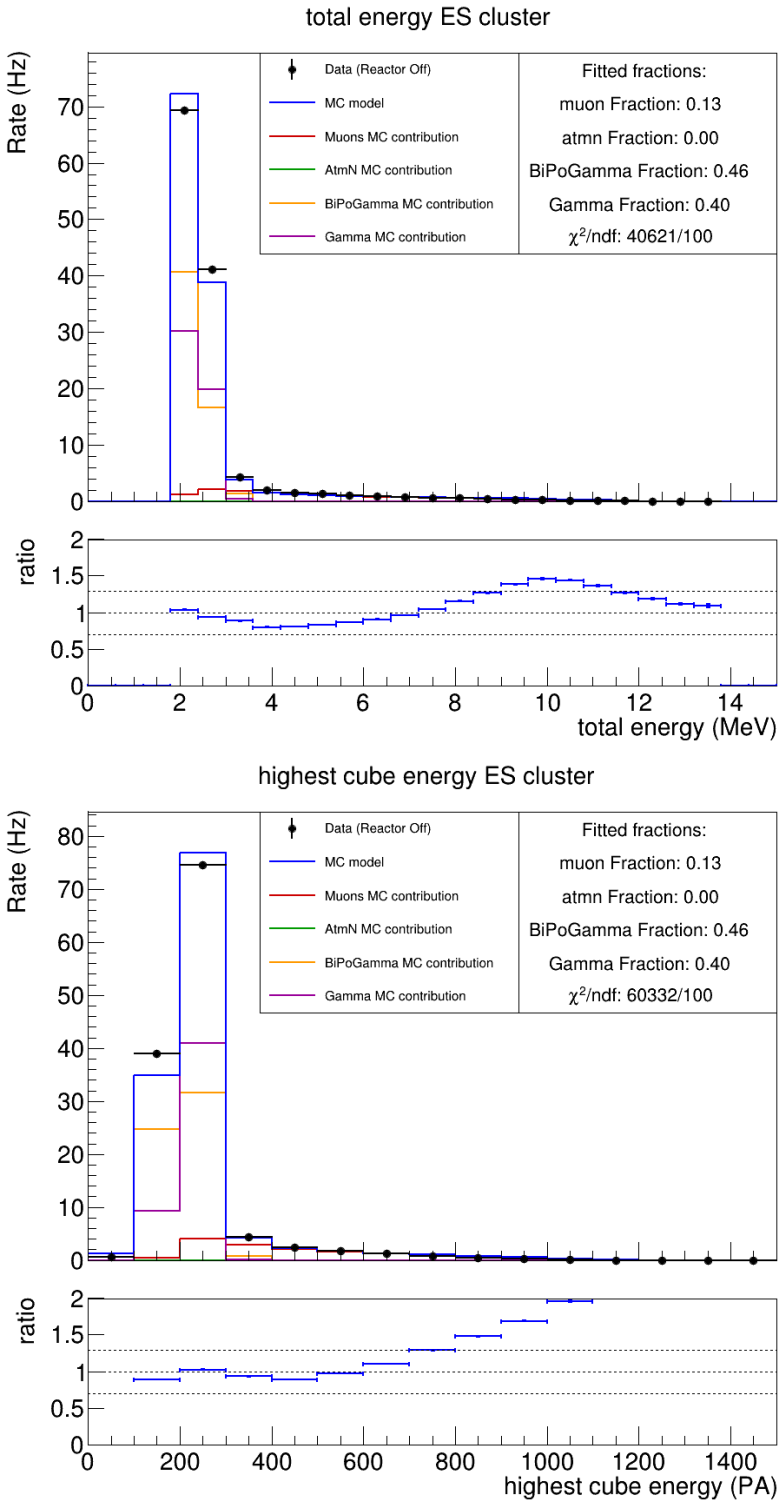

Figure 19.7.7: Energy distributions for the background model for the reactor off data in the HNL preselection region, containing simulations of muons, atmospheric neutrons, gamma rays from ^{208}Tl decay and additional gamma rays that are modeled with the ^{214}Bi-^{214}Po simulation.

19.8 HNL SELECTION CUTS

Based on the characteristics of the HNL variables of interest, a set of selection requirements is constructed, where the range of HNL masses between 2 and 9 MeV is monitored and where a coupling parameter $|U_{eN}|^2 = 10^{-4}$ is chosen, which is smaller than the strictest bound from Bugey [217], as was discussed in section 18.1.1. The cut values will be optimised with respect to the signal over background ratio and the signal efficiency and purity.

19.8.1 TIME VETO

The HNL signal consists of an ES cluster that is not in coincidence with any other signal. To stay clear from any ES signal that arises in coincidence with an NS signal (e.g. IBD and ^{214}Bi-^{214}Po events) or a muon signal, veto times are set around the latter. If the NS cluster has a BiPonisher value below 1.45, indicating the cluster was caused by an alpha, a pre-alpha veto of 400 μs is applied, targeting the ^{214}Po α decay with a half life of 167 μs in coincidence with an ES from a preceding ^{214}Bi β^- decay. If the BiPonisher value is above 1.45, the NS is most likely coming from a neutron capture. Because the neutron can be issued by an IBD event, in coincidence with an ES signal from the positron, the pre neutron veto has to encompass the neutron capture time of 68 μs. The neutron can also be spallated by an atmospheric neutron or muon, often accompanied by other spallation neutrons. Therefore, the neutron time veto is set to the time region before and after a neutron-like NS of 125 μs. Finally, when a muon decays inside the detector, Michel electrons can cause HNL like ES signals. In cosmic ray showers, the muons are often accompanied by neutrons. A post muon veto is applied of 125 μs.

The IBD and BiPo background are reduced to negligible rates, as discussed in the previous section. For the muon simulation, 93.6 % of ES signals pass the time veto, resulting in a remaining background rate of 22 Hz. And 73.5 % of ES signals in the atmospheric neutron simulation are kept, which is 0.51 Hz. All ES clusters in the gamma and HNL simulations pass the time veto as expected. In the reactor off data, 83.7 % of ES clusters are left after time veto.

19.8.2 SINGE PLANE REQUIREMENT

The HNL signal is contained to a single plane in the majority of cases, which is reflected in the z spread of one cube in figure 19.6.3. The gammas of the positron annihilation might interact a plane further. For the cosmogenic background, the ES cluster reaches up to 10 cubes. This is due to multiple neutron recoils and muons that missed reconstruction. The gamma signals are concentrated and contained to a single plane. To select the HNL signals, a single plane requirement is imposed. Application of this cut after the time veto leaves 0.46 Hz of atmospheric neutrons and 17.5 Hz of muons, within 240 Hz of reactor off data. Virtually all gamma signals pass this cut and again remain as dominant background.

19.8.3 LIMITS ON CLUSTER ENERGY

The energy of the HNL particle is limited by its mass and the reactor antineutrino spectrum. The energy falls in the range between 2 and 10 MeV and is well concentrated in a few cubes. The energy of the ^{214}Bi-^{214}Po prompt ES signal is lower and falls below 3 MeV. The ES clusters from cosmogenic

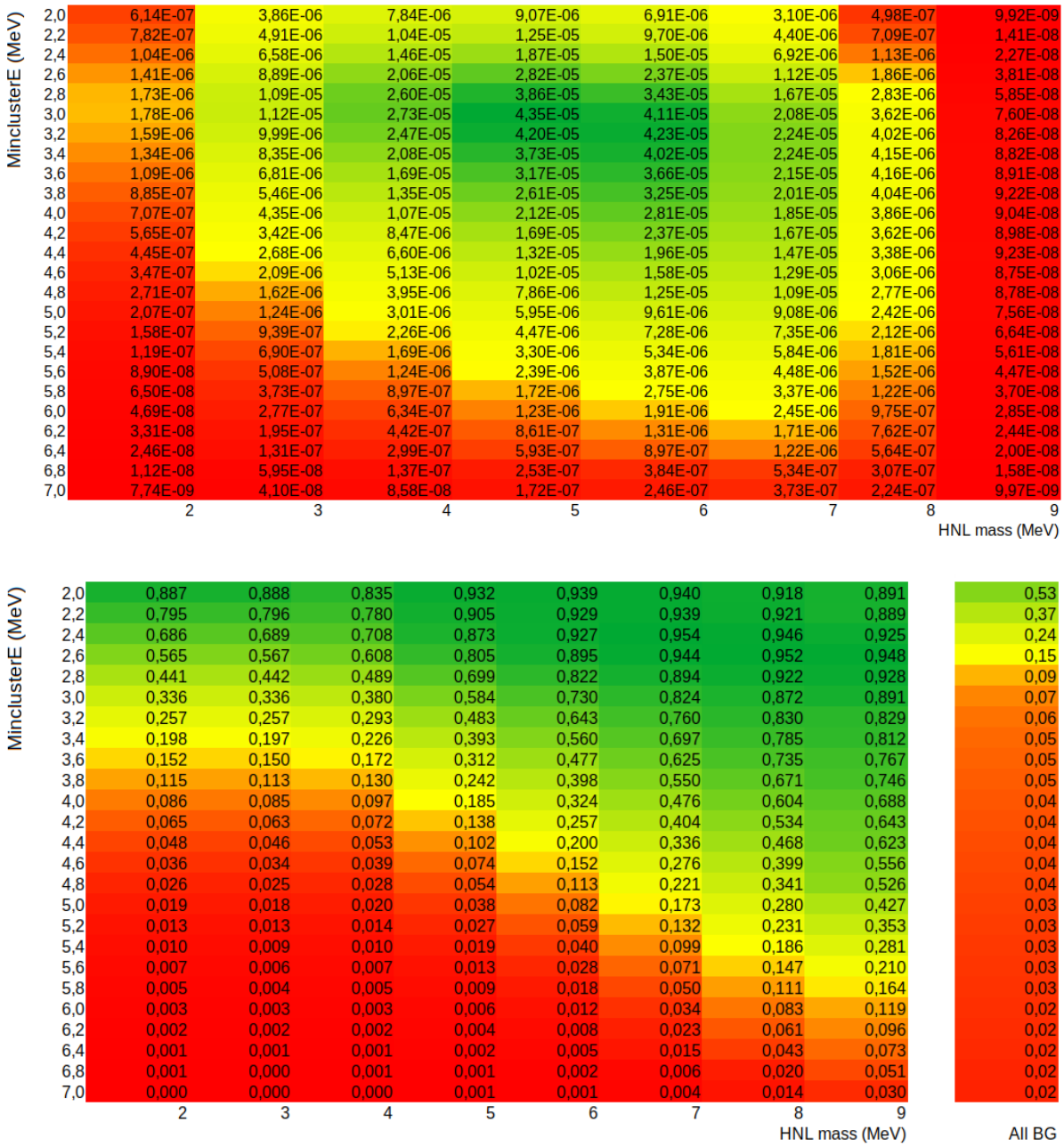

Figure 19.8.1: Scan of optimisation parameters when applying different energy thresholds, after application of the previous requirements. The scan is done for HNL with different masses. The optimisation parameters are S/B (top) and the signal efficiency (bottom left). The selection efficiency of the background signal is shown as well.

origin reach much higher energies, up to 50 MeV. Their reconstruction energy is limited by the 14 bit register of the ADC converter, which corresponds to about 5 MeV per fiber. The gamma rays are expected in the low energy range up to around 3 MeV. The cut value on the minimum of the energy of the complete ES cluster is optimised after application of the time veto and single plane requirement. A range of cut values is tested and optimised towards the signal over background ratio, the efficiency, the purity (which is the ratio of the signal rate and the signal plus background rate), and the product of

efficiency and purity. The obtained values for a range of selection criteria are shown in figures 19.8.1 - 19.8.3. The cuts will be optimised for HNL with a mass of 6 MeV, for which the highest interaction rate is expected with the model chosen for this analysis. The optimal S/B of $4.23 \cdot 10^{-5}$ is found for a cut value of 3.2 MeV. The signal efficiency is found to decrease for higher cut values as expected, with a slower decrease for more massive HNL. As final cut value, the optimum of the product of efficiency and purity is chosen at 3 MeV. In comparison to 3.2 MeV, 8 % more signal is retained, while keeping only 1 % more background under this cut.

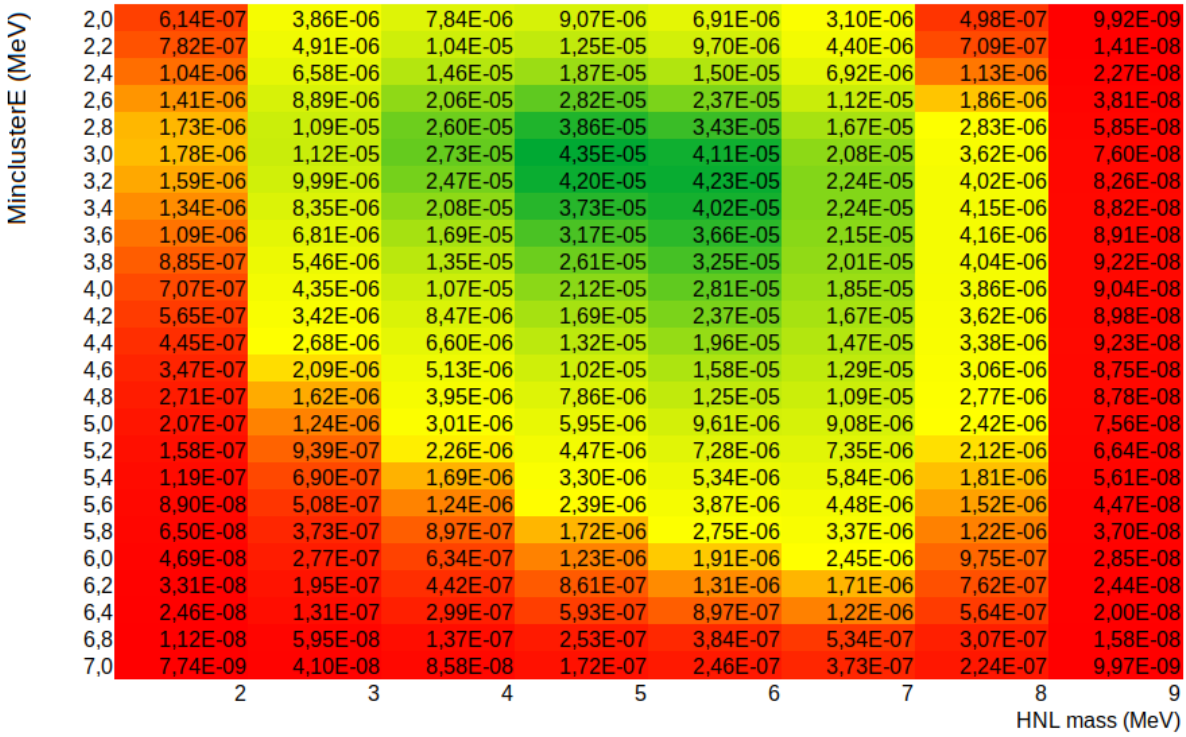

Figure 19.8.2: Scan of the purity when applying different energy thresholds. The scan is done for HNL with different masses.

The optimal cut value on the maximum of the cluster energy is found through an analogous procedure, where all previously determined cuts are applied. The maximal energy cut value is varied from 3.2 MeV to 11 MeV with increments of 0.2 MeV. The cut value of 4.6 MeV is selected that gives the best S/B and purity. The cluster energy is limited to the energy range of [3, 4.6] MeV as shown in the top panel of figure 19.8.4. At low energies, most gamma rays are excluded, while the neutron recoils in cosmogenic backgrounds are removed at higher energies. The HNL signal of mass 6 MeV occurs at this stage with a rate of 0.53 mHz, while 7.61 Hz reactor off data is remaining. The MC background is composed of 4.32 Hz muons, 0.14 atmospheric neutrons, 0.59 Hz ^{208}Tl gammas and 1.43 Hz other gammas, which adds up to a total MC background of 6.49 Hz. Note that the simulated background underestimates the reactor off rate. For all selection requirements, the same cut values were obtained with a background model from reactor off data and from simulation.

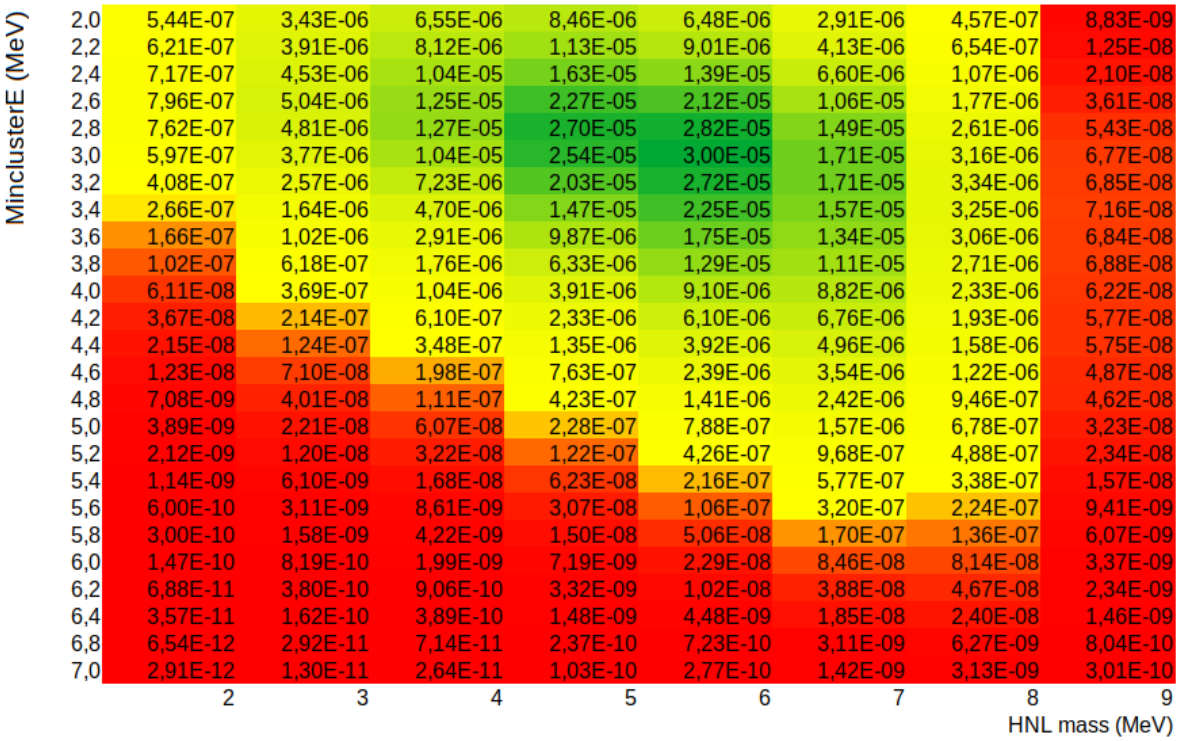

Figure 19.8.3: Scan of the product of efficiency and purity when applying different energy thresholds. The scan is done for HNL with different masses.

19.8.4 FIDUCIALISATION CUTS

The spatial distribution of the HNL signal is rather uniform over the detector, with a decline for planes further from the reactor core, and towards the detector edges. The bottom quarter of the detector sees up to 15 % less HNL because of the elevated position of the reactor core relative to the central axis of the detector. The bottom panel of figure 19.8.4 and figure 19.8.5 shows the spatial distributions of the background signal after all previous cuts have been applied. All background components are seen to increase towards the detector edges, contrary to the behaviour of HNL. A large background remains on each detector side from clipping muons and stopping muons. Since no muon track was reconstructed for these muons, they are identified as ES clusters. The ^{208}Tl gamma background increases at the bottom. The MC does not reproduce the full reactor data, because of the strict cuts on the cluster energy - a variable that is not perfectly reproduced by MC, probably due to not modelling channel dead time. Additional gamma background from radioactive descendants in the air are also probable. A study of the optimisation metrics was performed, for cutting 0 to 4 layers away. When more edge layers are cut away, the S/B and purity improve, while the efficiency decreases. This is expected based on the convex HNL distribution, versus the concave background distributions. The product of efficiency and purity is optimal when cutting away one edge layer. Since we do not understand the background at the edges well, this cut is desirable, although it is quite expensive, as 27.7% of the detector is edge. After fiducialisation, 3.83 Hz of reactor off data remains, which is a background reduction of 50%. The simulations indicate the background has an origin of 0.095 Hz atmospheric neutron, 1.81 Hz muons, 0.43 Hz ^{208}Tl gammas and 0.90 Hz other gammas. The signal of HNL with a 6 MeV mass becomes 0.41 mHz.

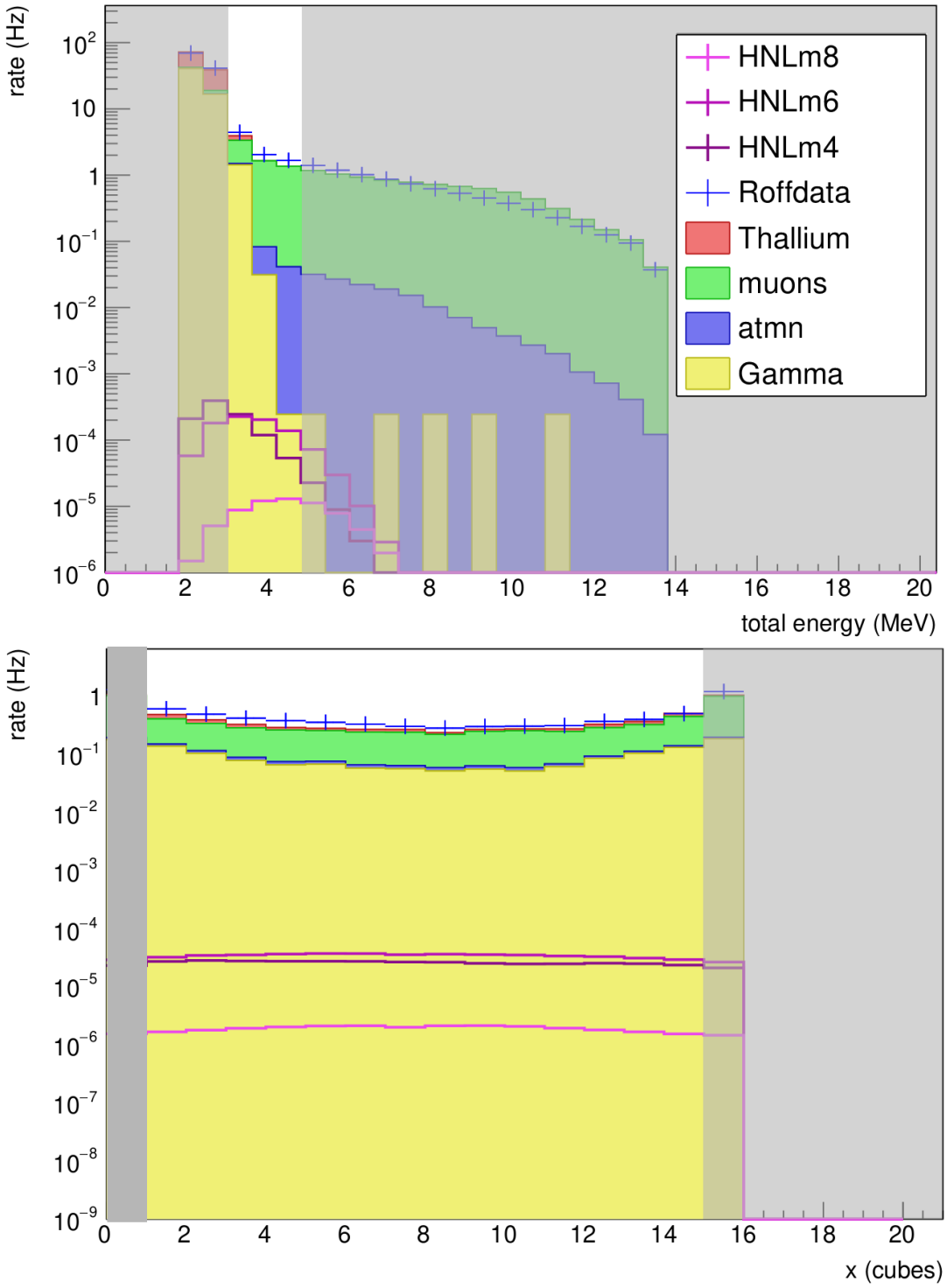

Figure 19.8.4: Top: effect of the low and high energy cuts on the total cluster energy of reactor off data and MC contributions in the HNL preselection region. Bottom: Effect of the fiducialisation cuts on the x distribution of reactor off data and MC contributions after application of all previous cuts.

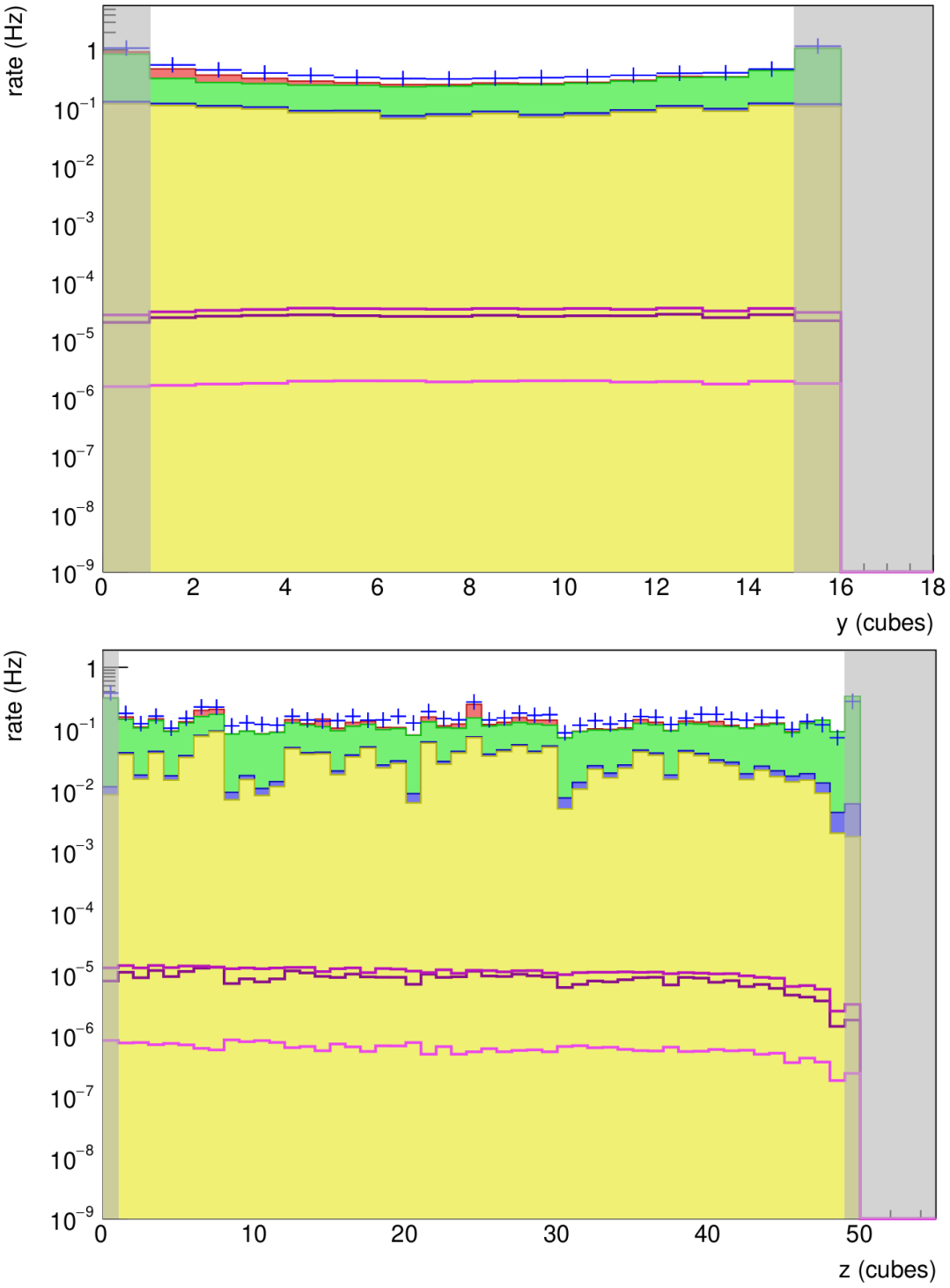

Figure 19.8.5: Effect of the fiducialisation cuts on the y and z distributions of reactor off data and MC contributions after application of all previous cuts.

19.8.5 CUT ON NUMBER OF ES CLUSTER CUBES

After the energy and the position of the ES cluster, its spatial spread is the subject of the next selection requirement. The number of cubes in the HNL ES cluster peaks at 2 cubes and has a substantial

contribution up to 4 cubes, as visible in figure 19.8.6. The spread of the cluster in the x and y directions is most of the time limited to one or two cubes, but can reach up to 6 cubes. The most challenging background that remains has a muonic origin, which has up to about 25 cubes in the ES cluster. These events are probably due to missed muons during reconstruction and due to multiple recoils.

Testing the cut on the number of cubes in the range from 1 to 8 cubes, an optimal cut value of ≤ 5 cubes is found, for both reactor off data and for the simulated background, with S/B of respectively $1.04{\cdot}10^{-4}$ and $1.17{\cdot}10^{-4}$. The cuts are visualised on figure 19.8.6 and remove 18 % of remaining reactor off data.

19.8.6 Cut on number of spatial clusters

The ES clusters that were considered so far are a collection of cubes that are close in time. For the present cut, the cubes are instead grouped in different spatial clusters. In about 90 % of the cases, the HNL signal consists of one spatial cluster. The second cluster is caused by one of the annihilation gammas. The probability to reconstruct both gammas in separate clusters is low. The muons and atmospheric neutrons consist often of more than one spatial cluster because of multiple recoils. The gamma background mainly consists of single cluster events. The optimal cut value on the number of spatial clusters is determined to be ≤ 3, as indicated on the bottom panel of figure 19.8.6. Relative to the previous cuts, the S/B ratio hardly improves.

19.8.7 Limits on energy of highest energy cube

The last selection requirement is applied to the energy of the cube in the ES cluster with the highest reconstructed energy, because the energy in the HNL ES cluster is expected to be concentrated, as visible on figure 19.8.7. Both reactor off data and simulated background show the best S/B and purity at a cut value of 300 PA. The product of efficiency and purity is optimal for a cut value of 200 PA and this value is chosen as cut. On the high energy end, the best S/B and purity are found for 400 PA, while the purity times efficiency is best for 500 PA. Again, the latter value is selected.

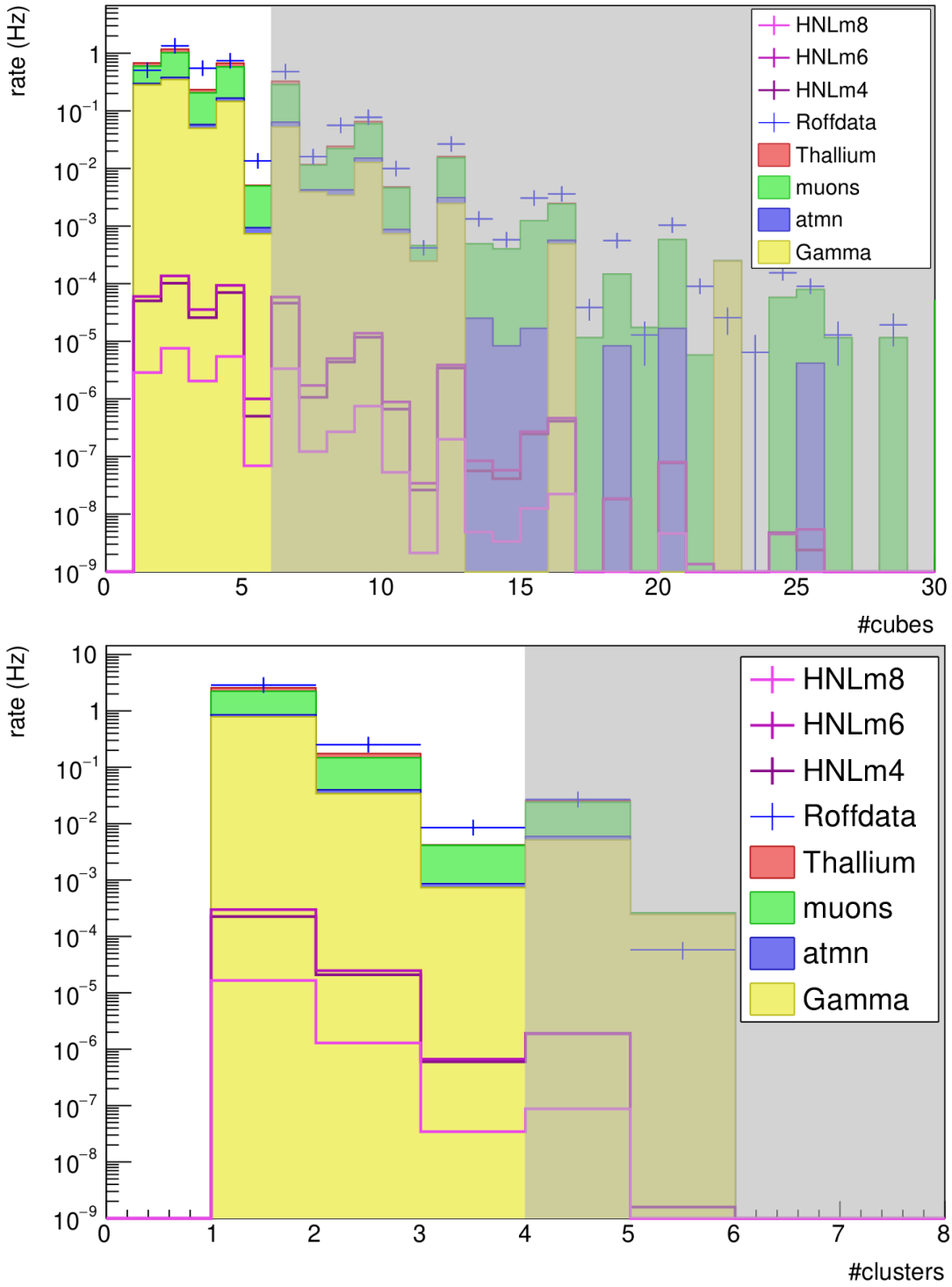

Figure 19.8.6: Effect of the cut on the number of ES cluster cubes (top) and on the number of spatial clusters on the remaining reactor off data and MC contributions.

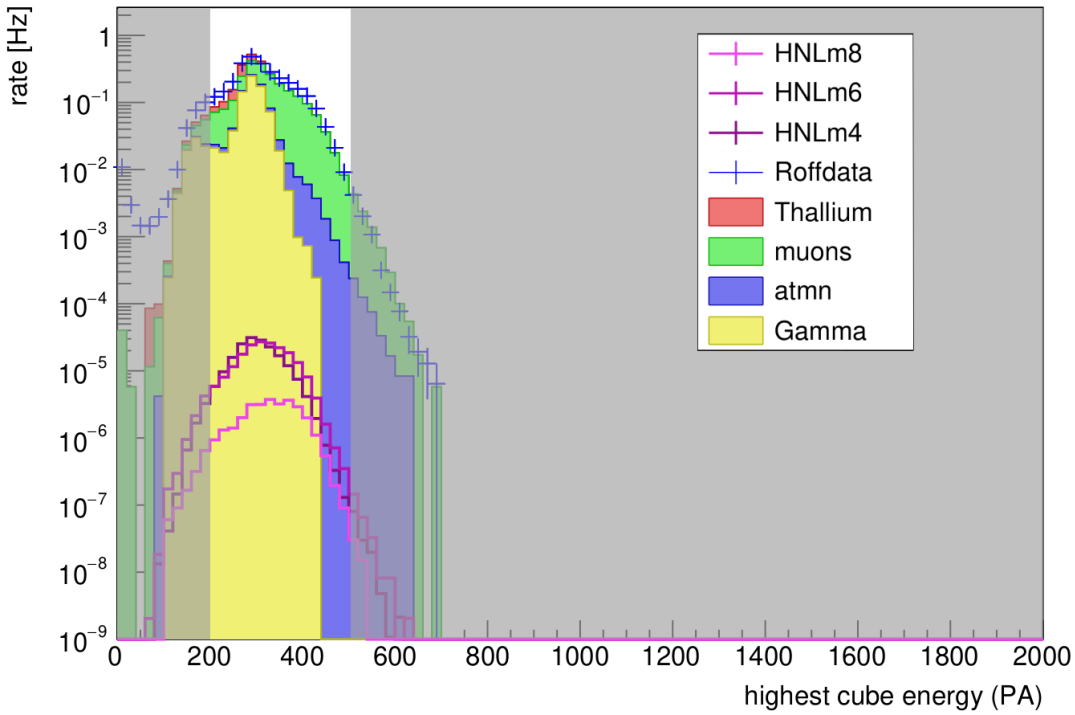

Figure 19.8.7: Effect of the cut on the energy of the cube with the highest energy in the remaining reactor off data and MC contributions.

19.8.8 Results of the optimisation procedure

By application of the optimised cuts, the reactor off signal is reduced from 292.10 Hz to 2.87 Hz, while retaining 0.31 mHz of the 0.94 mHz of HNL with a mass of 6 MeV, with $|U_{eN}|^2 = 10^{-4}$. This means an improvement of the S/B from 3.21 $\cdot 10^{-6}$ to 1.08 $\cdot 10^{-4}$. This corresponds to 1 HNL signal for every 9260 background events. The evolution of the optimisation metrics under the consecutive cuts is shown in figure 19.8.8. The signal efficiency of the cuts is 32.9 %, while only 0.98 % of ES clusters in reactor off data is kept.

The simulation indicates that from the remaining background, 54.96 % is caused by muons, 13.55% is induced by ^{208}Tl gammas from the floor, 28.58 % is coming from other gamma sources and the remaining 2.89 % is due to atmospheric neutrons. The HNL does not have very distinctive features. Therefore any small ES signal with sufficient energy poses a persistant background that is difficult to discriminate. The evolution of the rate of background contributions under the consecutive cuts starting from preselection level, is shown in figure 19.8.9.

The cut analysis is limited by the detector performance. Because of light leaks between adjacent cubes, the position resolution does not equal the detector cell size of 5 cm. Also, energy depositions in cubes that are close to each other are diffuse and cannot be discriminated properly. If we are able to resolve the annihilation gammas from the HNL positron, this could provide a distinctive signature with powerful discrimination. The Phase II of the SoLid detector is focusing on this feature.

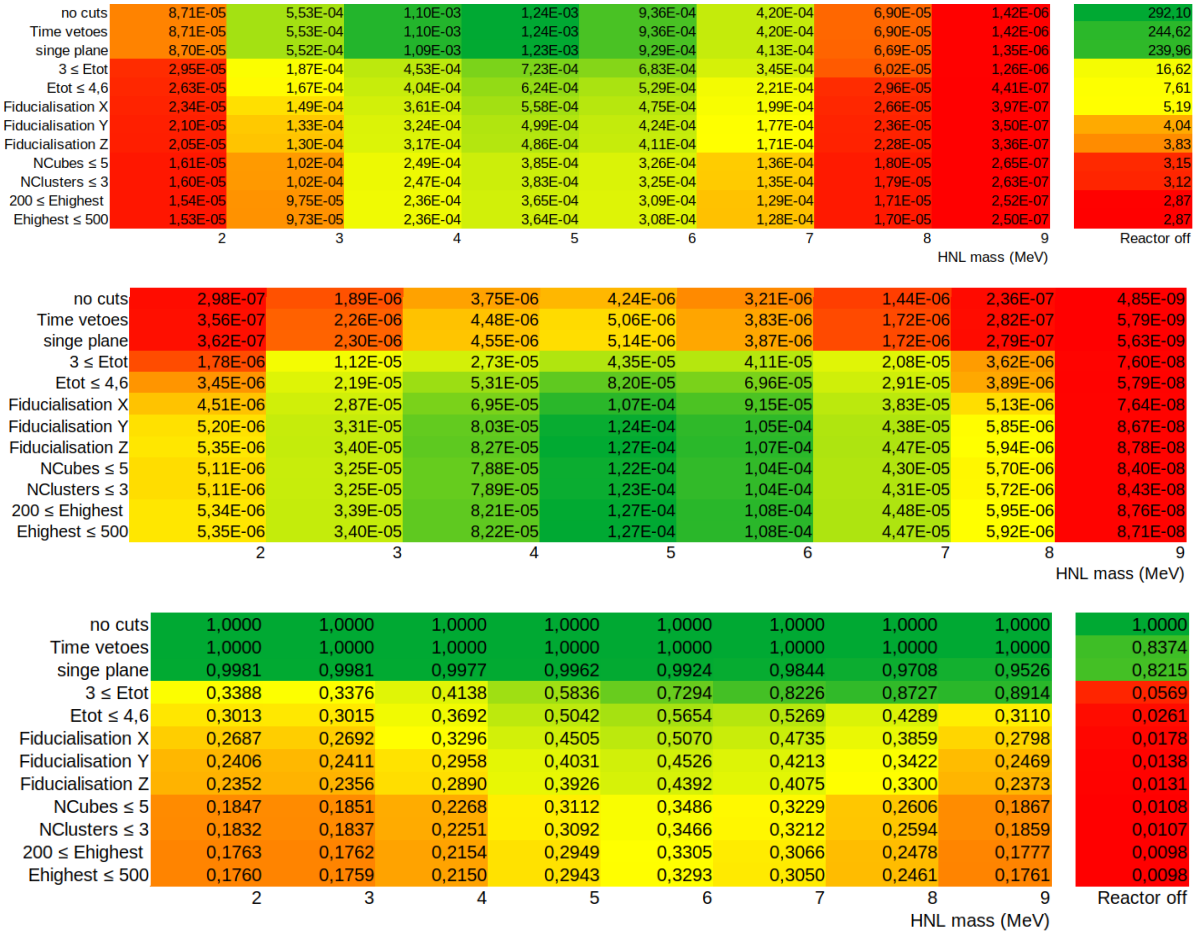

Figure 19.8.8: Evolution of the rates (top), the signal to background ratio (center) and of the signal and background selection efficiency (bottom) under application of the consecutive cuts.

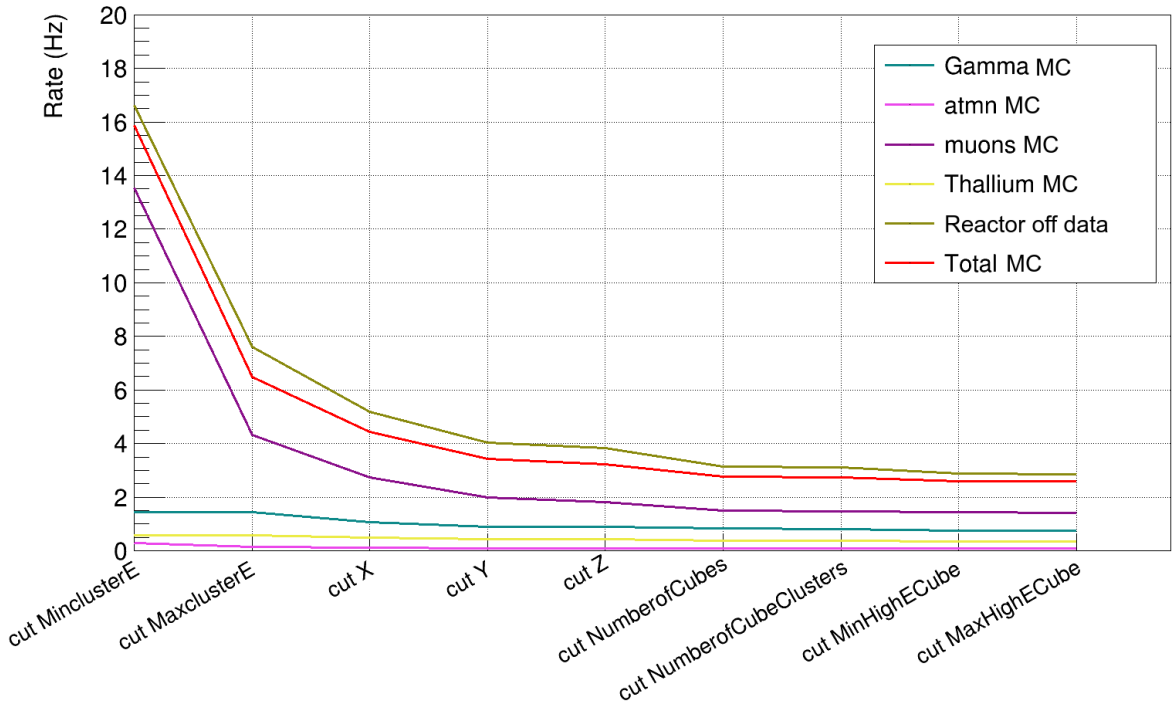

Figure 19.8.9: Evolution of the rate of the reactor off data and of the different simulated background components under the consecutive application of the HNL selection requirements.

19.9 Reactor on signal

The heavy neutral leptons could arise because of mixing with the reactor neutrinos, and are therefore only present in the reactor on data. The reactor off data were studied in the previous sections in order to understand and control the different background components. Upon inspection of the reactor on data in the HNL selection region, it becomes evident that the reactor off data as such is not sufficient as a background model for the reactor on data. More background or even additional background components are present in the reactor on data. The rate more than doubled, going from 2.87 Hz reactor off data to 6.01 Hz reactor on data, which is 2.09 times more. For several variables, the ratio plot of the reactor on and off data is shown in figures 19.9.2 - 19.9.4, along with their difference in yellow.

The reactor on signal behaves very similar to the background already present in the reactor off data, which is reflected in the ratio being 0.5 for most part. Most notably, the y distribution is different. The new background is dominant at the top of the detector, and decreases towards the bottom, indicating the background enters the detector from the top. The background also increases towards the detector front that is closest to the reactor. The background energy is substantial, and decreases in the HNL selection range from 3 MeV to 4.6 MeV. We suspect an additional gamma ray background is generated by the reactor operation. This hypothesis is supported by measurements of the gamma ray spectrum for different reactor powers that are shown in figure 19.9.1, namely for 55 MW in February 2017, and for 38 MW in May 2017. Peaks around 5 and 6 MeV can be seen. The highest peak is probably the 6129 keV gamma ray emitted during ^{16}N decay to oxygen. This reaction is used to monitor the reactor power from the activation of oxygen in the water of the pool by fast neutrons from the core (> 10 MeV),

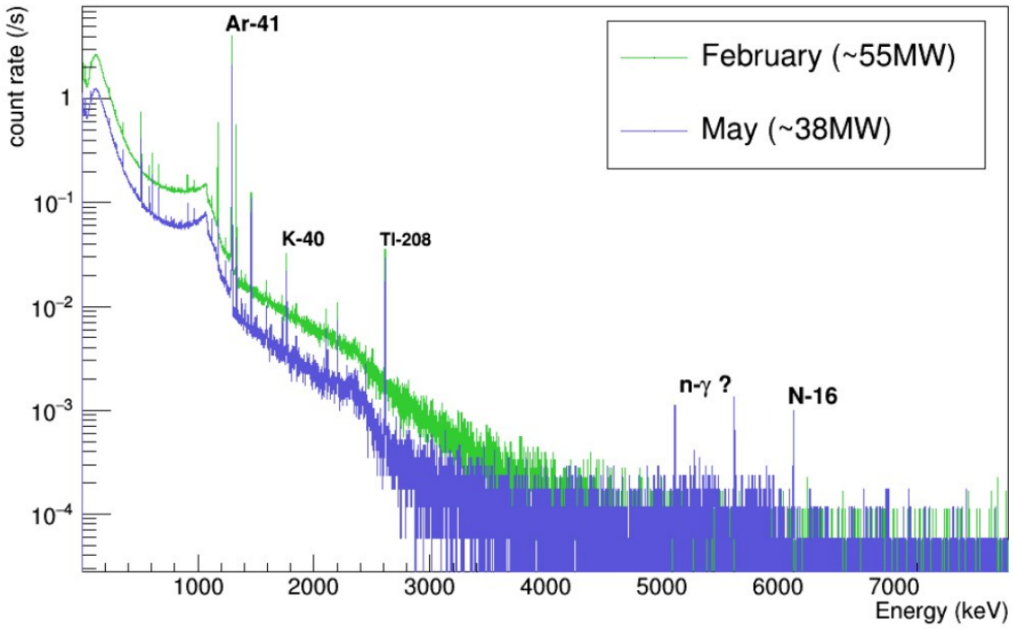

Figure 19.9.1: Measured gamma ray spectrum at the BR2 reactor in February and May 2017.

as was discussed in section 10.1.1. ^{16}N has a short half life of 7.1 s. In order to explain the reactor on signal, the continuous spectrum between 2.5 MeV and 5 MeV is interesting. It is seen to increase with reactor power and the integral can add up to a significant contribution. In order to perform the HNL analysis, the gamma ray background and its dependence on the reactor operation conditions has to be studied and quantified in more detail.

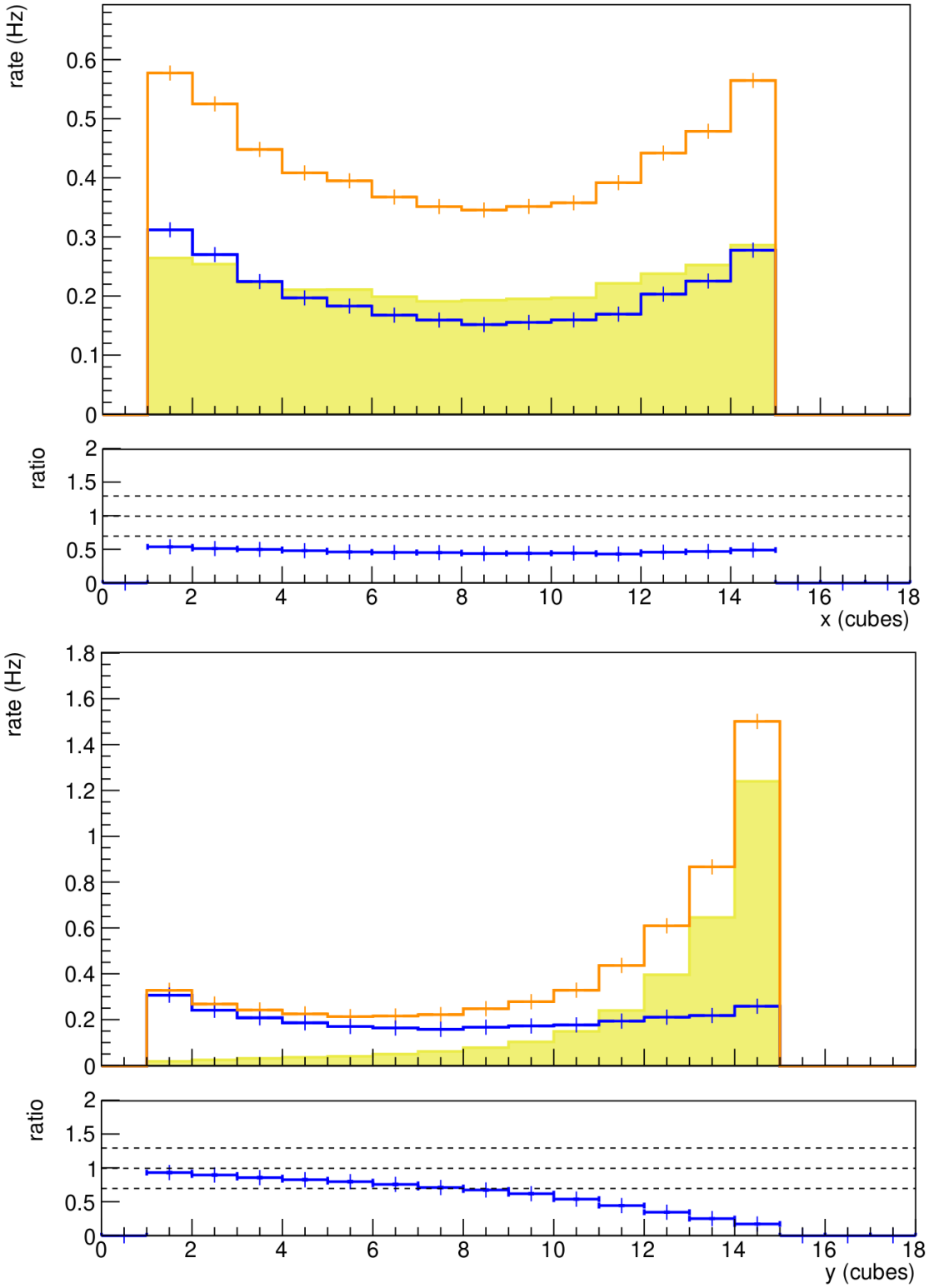

Figure 19.9.2: Ratio plot of the x and y distributions for reactor on and reactor off data in the HNL selection region.

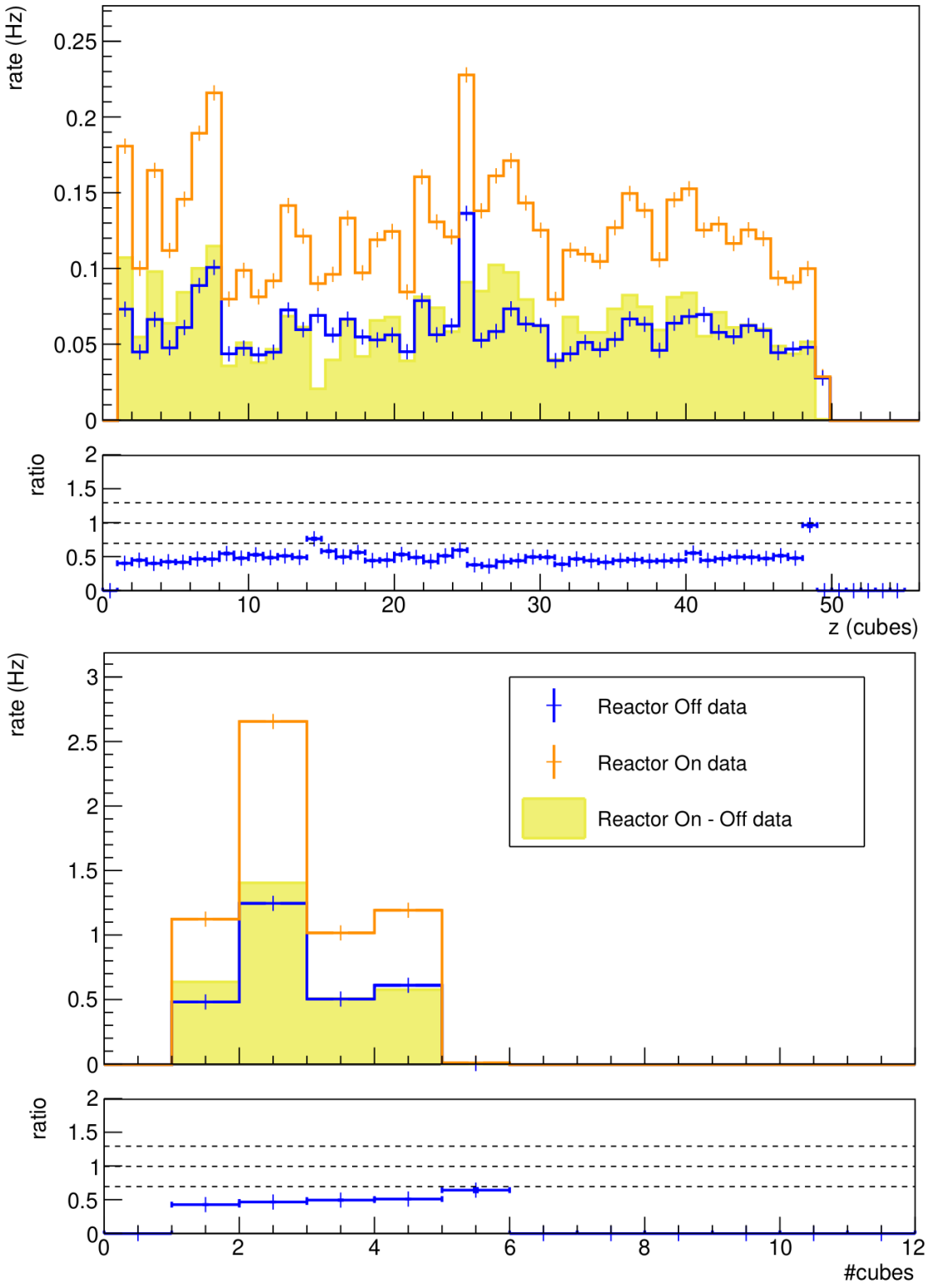

Figure 19.9.3: Ratio plot of the z- and number of cubes distribution for reactor on and reactor off data in the HNL selection region.

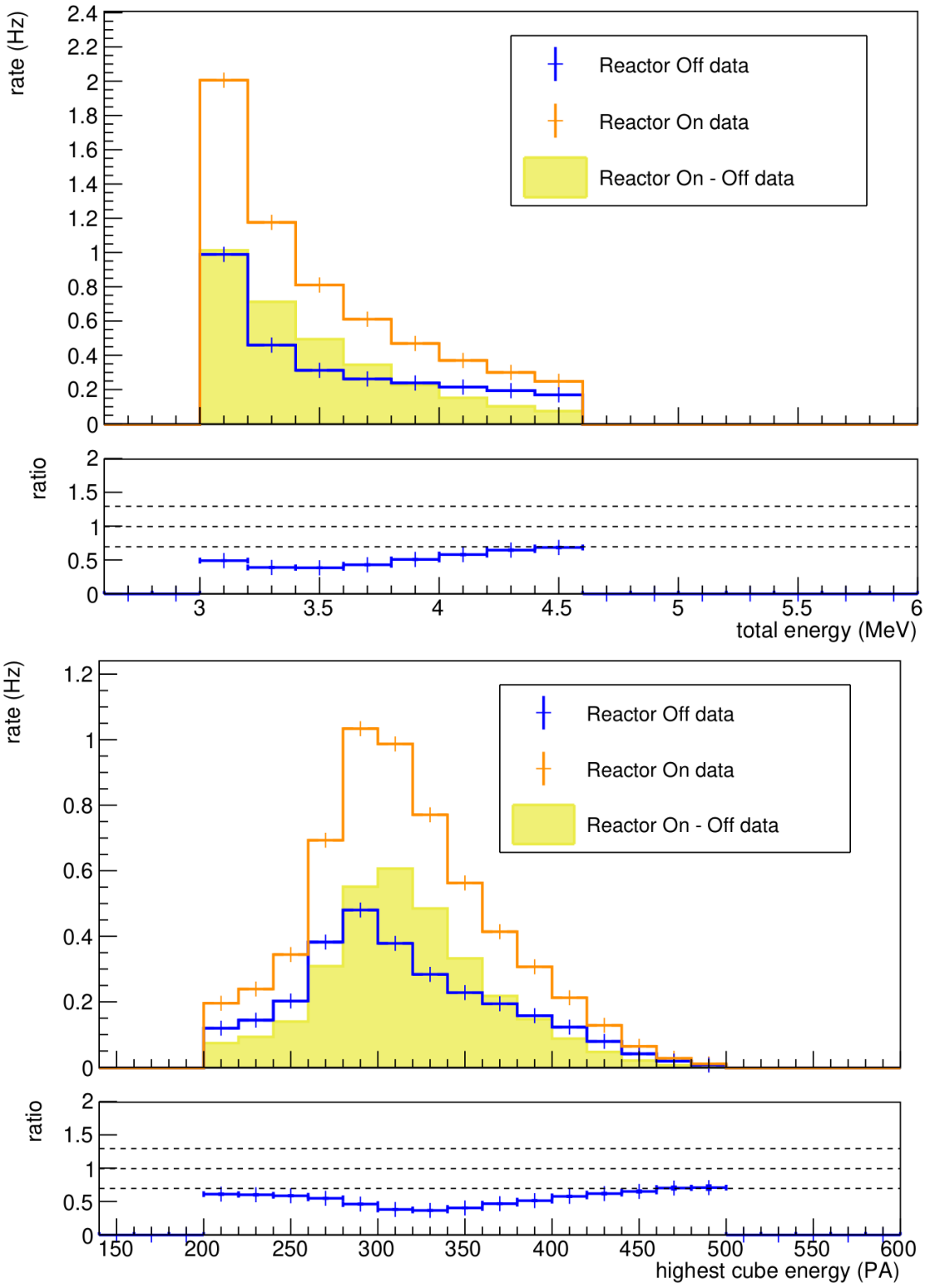

Figure 19.9.4: Ratio plot of the energy distributions for reactor on and reactor off data in the HNL selection region.

20

HYPOTHESIS TESTING

Based on the prediction of the background rate and the signal rate, likelihood regions can be constructed, that indicate whether an observation of n HNL-like events is likely due to background only, b, or if it is more likely to originate from background and signal being present, $b+s$. Since the reactor off data is not a good background model for the reactor on data, we take as background model the reactor on data from which the HNL signal rate is subtracted.

Given that the true outcome of an experiment is a statistical fluctuation of the expected background, b, the probability to measure n events is described by a Poisson distribution

$$L(n|b) = \frac{b^n e^{-b}}{n!}.$$

Conversely, if the outcome is the result of both background and signal, the probability to measure n events becomes

$$L(n|s+b) = \frac{(s+b)^n e^{-(s+b)}}{n!}.$$

The expected rate of HNL events, with a mass of 6 MeV and for a coupling parameter $|U_{eN}|^2 = 10^{-4}$, and the expected rate of events during reactor on periods in the HNL selection region were determined in the previous section. Given that in 2019, the BR2 reactor was operated during 148 days (start up and shut down not taken into consideration), the expected number of HNL signal events is 3938 and the expected number of reactor on events is $76.87 \cdot 10^6$. The background only hypothesis is found by subtracting the signal events from the reactor on events, and is shown in the left panel of figure 20.0.1, along with the background plus signal hypothesis, which is the number of reactor on events. The probability distribution for the two hypotheses is obtained by generating a high number of pseudo-experiments via a Monte Carlo random number generator.

A more convenient test statistic is a function of the expected number, which is able to rank an observation as signal or background-like. For this counting experiment, a suitable test statistic is Q, which is derived from the likelihood ratio Q',

$$Q = -2\ln(Q') \tag{20.1}$$

$$= 2s - 2n\ln\left(1+\frac{s}{b}\right), \tag{20.2}$$

with

$$Q' = \frac{L(n|s+b)}{L(n|b)}.$$

The advantage of the test Q is that it is positive for background only like outcomes, and negative otherwise. If it approaches 0, no clear separation can be made between the two hypothesis. The right panel of figure 20.0.1 shows the distribution of the test statistic Q, as obtained with equation 20.2 from the distribution of n.

20.1 CONFIDENCE LEVELS

Once an observation n_{obs}, with corresponding Q_{obs} has been made, the discovery or exclusion of the HNL signal can be stated with a certain confidence level. In figure 20.1.1 a measurement of $n_{obs} = 7.69 \cdot 10^7$ is taken as example, which corresponds to $Q_{obs} = -0.60$.
The false exclusion rate CL_{s+b} is determined as

$$CL_{s+b} = \int_{Q_{obs}}^{\infty} f_{s+b}(Q)dQ,$$

which is indicated on figure 20.1.1 by the blue area. The s+b hypothesis is rightfully excluded at the α confidence level if $CL_{s+b} \leq 1-\alpha$. And a real signal is falsely excluded with a probability α. The background only hypothesis is rejected, in favor of the b+s hypothesis, at the β confidence level if $1-CL_b \leq 1-\beta$, with

$$CL_b = \int_{Q_{obs}}^{\infty} f_b(Q)dQ.$$

the probability for the background to statistically fluctuate up to n_{obs} is smaller than $1-\beta$. The significance $(1-CL_b)$ is indicated as the red area in figure 20.1.1.

In high energy physics experiments, the convention is followed that a signal is excluded if $CL_{s+b} \leq 5$ %. This corresponds to an exclusion at the 95 % confidence level. We speak about discovery when β is equal to the fraction of the area of a Gaussian distribution obtained by integrating over 5 standard deviations,

$$\beta = \text{erf}^{-1}(2 - CL_b - 1),$$

with erf the error function

$$\text{erf}(x) = \frac{1}{\sqrt{\pi}} \int_{-x}^{x} e^{-x^2} dx.$$

The discovery is referred to as a 5σ excess in the number of observed events.

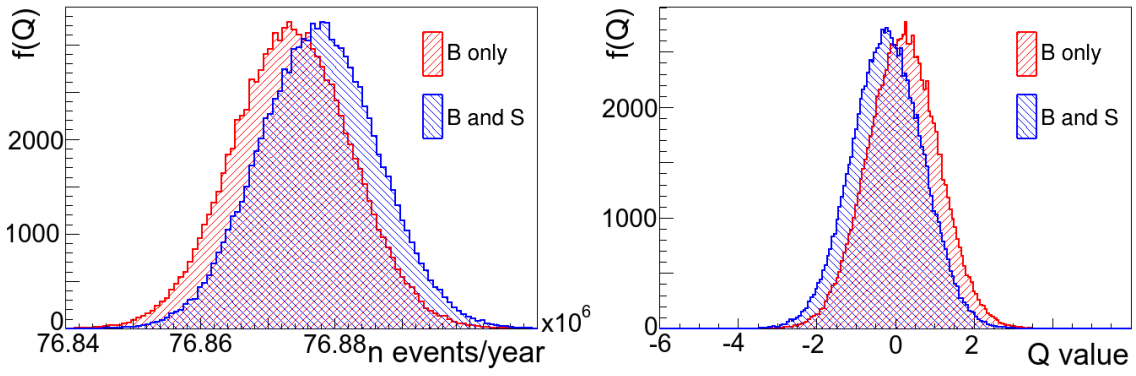

Figure 20.0.1: Distributions of the expected number of events in the HNL selection region (left) and of the test statistics Q (right) for the background only hypothesis (red) and the background plus signal hypothesis (blue) obtained with a high number of pseudo-experiments.

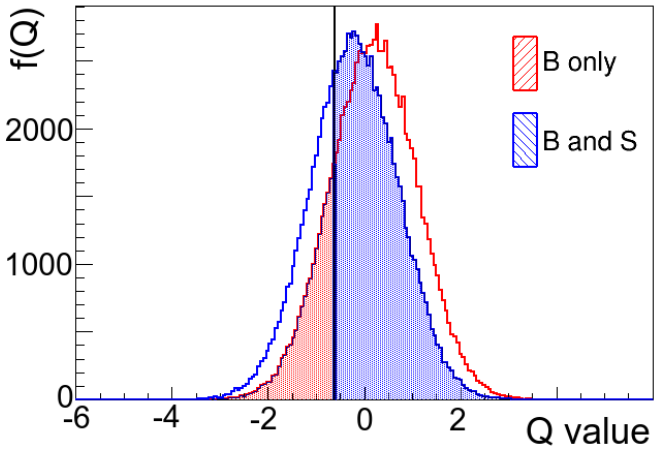

Figure 20.1.1: Test statistics for the background only and the background plus signal hypothesis. The observation Q_{obs} is represented by the black line. The shaded blue are is CL_{s+b}. The shaded red area is the significance $(1 - CL_b)$.

20.2 SoLid sensitivity

Preliminary HNL selection requirements were determined in section 19.8. The selection is applied to simulated HNL events with different HNL masses and for different values of the coupling parameter $|U_{eN}|^2$. The HNL selection rates are collected in figure 20.2.1. For coupling parameters $|U_{eN}|^2 \sim 10^{-4}$, a signal rate in the order of 0.1 mHz is obtained.

The 90 % exclusion limits on the parameter space from Bugey [217], Borexino [216] and Triumf [218] that were discussed in section 18.1.1 are added to the figure. For the SoLid experiment, 90 % CL for 148 days of data taking during reactor on periods (which is obtained in 1 year), is shown on figure 20.2.1 for different estimates of the background rate. In case the background rate equals the one that is currently obtained from reactor on data in the preliminary HNL selection region, namely 6.01 Hz, then the SoLid line 1 on the figure can be reached. In case the background rate can be reduced by one order of magnitude, SoLid line 2 can be reached. For the following lines, the background always decreases with an additional order of magnitude, until for line 5 the background rate is 0.0006 Hz.

With the preliminary selection requirements that were determined in the present thesis, the sensitivity of the Bugey experiment can be achieved. The advantage for this HNL study is the fact that the relevant data is already recorded with the SoLid detector and readily available. Once the HNL analysis is mature, we can apply it to the reactor on data set. We expect that once the background components for the HNL analysis are properly understood and simulated, especially the gamma ray background during reactor on periods, we will be able to improve the signal to background ratio. In this case, we can probe the parameter space for a smaller coupling parameter than the Bugey experiment. In comparison to the Borexino experiment, we might be able to improve the limit at the low mass range, below 4 MeV, but we will probably not be able to reach the sensitivity of the Borexino experiment at higher masses. In terms of laboratory experiments, we have the potential to put more stringent exclusion limits on the HNL parameter space in the low mass range.

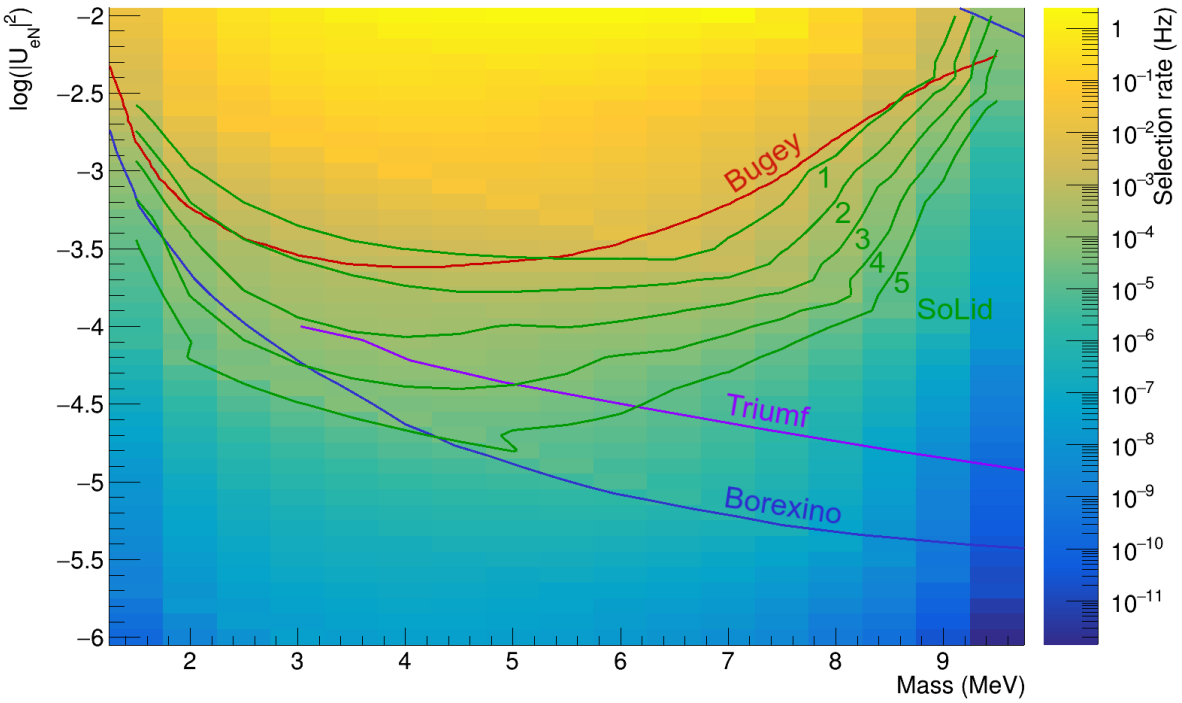

Figure 20.2.1: The rate of the HNL signal in the HNL selection region for different HNL masses and $|U_{eN}|^2$. 90 % exclusion limits of the Bugey [217], Triumf [218] and Borexino [216] experiments are superimposed. The 90 % CL of the SoLid experiment are shown for different estimates of the background rate, namely for 6.01 Hz, which is the reactor on rate in the HNL selection region (SoLid line 1), and for background rates that are various orders of magnitude smaller than this rate, namely 0.6 Hz (line 2), 0.06 Hz (line 3), 0.006 Hz (line 4) and 0.0006 Hz (line 5).

CONCLUSION AND OUTLOOK

Neutrinos are easy to produce but notoriously hard to detect. The particles are so elusive that physicists have not been able to determine their characteristics and behaviour exhaustively. Whenever we have drawn up a theory, neutrinos are seen to not abide by the rules we made up for them. New physics is needed. At the same time, this indefiniteness leaves room to assign the neutrino sector with properties that could explain the open questions in physics today. Massive neutrinos might be the reason why we live in a matter dominated universe. And the dark matter that seems to contribute to the mass content of the universe may have something to do with sterile neutrinos.

Since neutrino oscillations were established around 1990, that were driven by a mass difference between the neutrino eigenstates, it became apparent that neutrino mass terms had to be added to the Lagrangian of the Standard Model. In order to generate a mass term, neutrinos with a right handed chirality have to be added to the Standard Model. Only left handed neutrinos are observed through the weak interactions, which was therefore formulated as a chiral gauge theory. The right handed neutrinos, if they exist, do not interact via the forces of nature that are known to us. The right handed neutrinos would therefore be sterile neutrinos.

A priori, any number of different sterile neutrino eigenstates could exist in our Universe, with masses that could range from smaller than eV to TeV and beyond. A variety of anomalies in oscillation experiments prompted a world wide search program for sterile neutrinos in the eV mass region. The SoLid experiment was designed to specifically assess the reactor antineutrino anomaly at very short baseline from a nuclear reactor. We use a hybrid scintillation technology based on Poly-Vinyl Toluene scintillators in combination with ^{6}LiF:ZnS(Ag) screens, to detect and discriminate respectively the positron and neutron from the neutrino's IBD interaction. The oscillation probability of reactor $\bar{\nu}_e$ into a sterile state is dictated by the properties of the neutrino and apparent over distance and energy. The high segmentation of the detection volume, together with a high position and energy resolution, allows to investigate the disappearance probability of reactor $\bar{\nu}_e$.

In addition, we have evaluated the sensitivity of the SoLid detector to another mass range of the sterile neutrinos, called HNL. While cosmological observations argue that no additional neutrino states exist with masses below about 100 MeV, the desire to resolve the open questions in physics has motivated especially the search for HNL in the GeV mass range. However, no signal has been found and the bounds from various experiments are closing in the available parameter space. With the SoLid experiment, we envisage to probe the existence of HNL with masses between 1-10 MeV, by searching their decay signal at a nuclear reactor. This was last done in 1995 at the French Bugey reactor, even before the ν_τ was discovered. The Borexino experiment set bounds on this mass range based on measurements of solar neutrinos. The HNL decay search will be a complementary physics analysis, in addition to the search for eV-scale oscillations, that extends the BSM program of SoLid without detector modifications.

The deployment of the SoLid detector requires fundamental insight in the production, interaction and detection of the reactor neutrinos and of the various background sources. In addition, the operation of the detector has to be validated. To this end, a full simulation framework was developed. Based on the reactor fuel composition and distribution, the antineutrino flux and spectrum for each reactor cycle is simulated wit the SoLO software. With the GEANT4 toolkit, particles are generated for the signal and background sources and tracked through the experimental site. The particles' energy depositions in sensitive detector components are fed into the readout simulation, that emulates the full detector response. This thesis was dedicated to the simulation of the readout system.

In the readout simulation, the scintillation photons are generated based on the energy depositions inside one of the many detector cells. The photons can make their way to the sensors, where they can induce a pixel avalanche. The sensor algorithm adds noise contributions in the form of dark counts and pixel cross talk, taking into account the momentary pixel voltage that is modeled with a voltage recovery model. The electronics algorithm adds the avalanches together to waveforms, with a sampling of 25 ns. The final algorithm imitates the decision making of the trigger system and selects the waveform samples that will be stored, taking into account the variable zero suppression threshold. The simulated signal has the same format as the data which allows to analyse it with the same software. The various models in the simulation are implemented and tuned based on data from test benches, calibration campaigns, reactor off periods and manufacturers.

The readout simulation is validated by the data Monte-Carlo comparisons for the calibration measurements, as shown in figure 14.1.1, 14.1.2 and 14.1.3 for the PVT scintillator, and in figure 14.2.1 and 14.2.2 for the ZnS scintillator. An agreement around 5 % was obtained. When analysing the backgrounds in chapter 15, they are well reproduced by simulation in the figures following 15.2.5 and 15.3.2. Some discrepancy remains in the reconstructed energy of the fast neutron signal (figure 15.3.4, which probably stems from dead time in detector channels and planes that was not reproduced in simulation. Channel deadtime is already being implemented by shutting down increasingly more channels during the simulation.

The simulated neutrino events (figure 16.1.1 and following) predict the signature of the IBD interactions in the SoLid detector, which enabled the collaboration to construct neutrino selection cuts and train the Machine Learning models in order to discriminate the IBD signal from the huge amount of background events. The main sources of background are coming from radioactive contamination and from fast neutrons with cosmic origin. With the use of machine learning in addition to rectangular cuts, a signal excess of 90 ± 22.8 IBD events per day can be reached, with a rather low signal-to-background ratio of about 0.21 [237]. For each data set, the signal excess can be compared to the excess that is predicted by the simulation of the corresponding reactor period, where mixing with sterile neutrinos can be applied with various mixing parameters. This analysis allows to assess if the sterile neutrino hypothesis provides an appropriate model for the recorded data. Currently, only a small fraction of the SoLid Phase I data set is open to validate the oscillation analysis. The SoLid collaboration expects to open the remaining data this year to perform a complete oscillation analysis.

You may have noticed that competing very short baseline oscillation experiments at nuclear reactors have already published analysis results, most notably the PROSPECT and STEREO experiments. I wish to stress that the SoLid collaboration is using a novel detector design. Something the neutrino

community is in great need of. The detection technology of most neutrino detectors relies on liquid scintillators which are well understood. This narrow approach will pose at some point inevitably a limit on the development of neutrino physics. This is also the case for the competing experiments. The SoLid detector uses plastic PVT scintillators in combination with ^{6}LiF:ZnS(Ag) for neutron detection. The R&D and the commissioning of this detector required an extensive effort, as should have been expected. In addition, the detector is highly segmented. Where STEREO and PROSPECT consist of respectively 8 and 154 detector cells that are read by 48 and 308 PMT, SoLid is made from a staggering 12800 detector cells that are read by 3200 sensors. This results in a complex calibration of entangled and correlated effects. The SoLid collaboration has overcome many hurdles.

The biggest challenge at the moment remains the background that mimics the ES-NS coincidences from IBD. The drawback to obtain better background discrimination is in my opinion the light leakage between the individual detector cells, which degrades the cube resolution of 5 cm. Energy depositions in cubes that are close to each other become diffuse and cannot be discriminated properly. A solution could be provided by the annihilation gammas from the IBD positron that give a unique signature for the neutrino interaction. In order to resolve the annihilation gammas, the SoLid collaboration has upgraded the photosensors in the summer of 2020. The new Hamamatsu S14160-3050HS MPPCs in the Phase II detector achieve a higher photon detection efficiency for a lower operation voltage. They are expected to increase the energy resolution and the IBD detection efficiency, resulting in an improved sensitivity of the SoLid experiment to sterile neutrino oscillations. The study and analysis of the Phase II data will be done by the next generation of researchers.

For the analysis of the HNL decay signal, a preliminary selection requirement was constructed. For a coupling parameter $|U_{eN}|^2 \sim 10^{-4}$, which is slightly weaker than the current strongest limits indicate, an HNL signal of $\mathcal{O}$(mHz) is predicted by the simulation. Based on the expected sensitivity with 90% confidence in the HNL parameter space, the limit of the Bugey experiment could be reached and exceeded for an HNL mass below 4 MeV. In terms of laboratory experiments, we have the potential to impose stricter exclusion limits on the HNL parameter space in the low mass range.

Whatever I will do next, I will be sure to keep an eye on neutrino physics as the coming decade promises to be an exciting one. Next generation experiments will be able to determine the value of the CP-violating phase. The DUNE and Hyper-Kamiokande experiments with complementary experimental programs are currently in the design and proto-typing phase with the expectation of turning on around 2025. The mass ordering will be measured with those experiments and with the complementary experimental programs of JUNO and KM3NeT/ORCA, that use reactor and atmospheric neutrinos respectively. The mass hierarchy is expected to be known within the next decade. The absolute neutrino mass and the chiral nature of neutrinos are researched intensively as well. Stay tuned!

Appendices

A

THE SIGNAL BASELINE AND WHITE NOISE

In the absence of any pixel avalanche, the output signal from the electronics is a constant current with some white noise. This baseline value and its fluctuations are discussed and modeled here, in order to implement these second order effects in the readout simulation. The fluctuations on the baseline arise from leakage currents and noise in the readout electronics. It is therefore, in good approximation, independent of the overvoltage and is defined as the signal fluctuations in the absence of a pixel avalanche. The constant value of the baseline has a large variations between channels. The values are determined during calibration periods and stored in a database that can be accessed by the Saffron2 software, that was described in chapter 8. During analysis, the baseline is subtracted from the signal. It was observed that large changes (> 0.5 V) to the bias voltage, which change the SiPM dark count rate, can cause significant changes in the baseline, requiring the baselines to be recalibrated for input to the trigger. However, other changes to signal rate, including intense sources, or the reactor on-off transition do not require a recalibration.

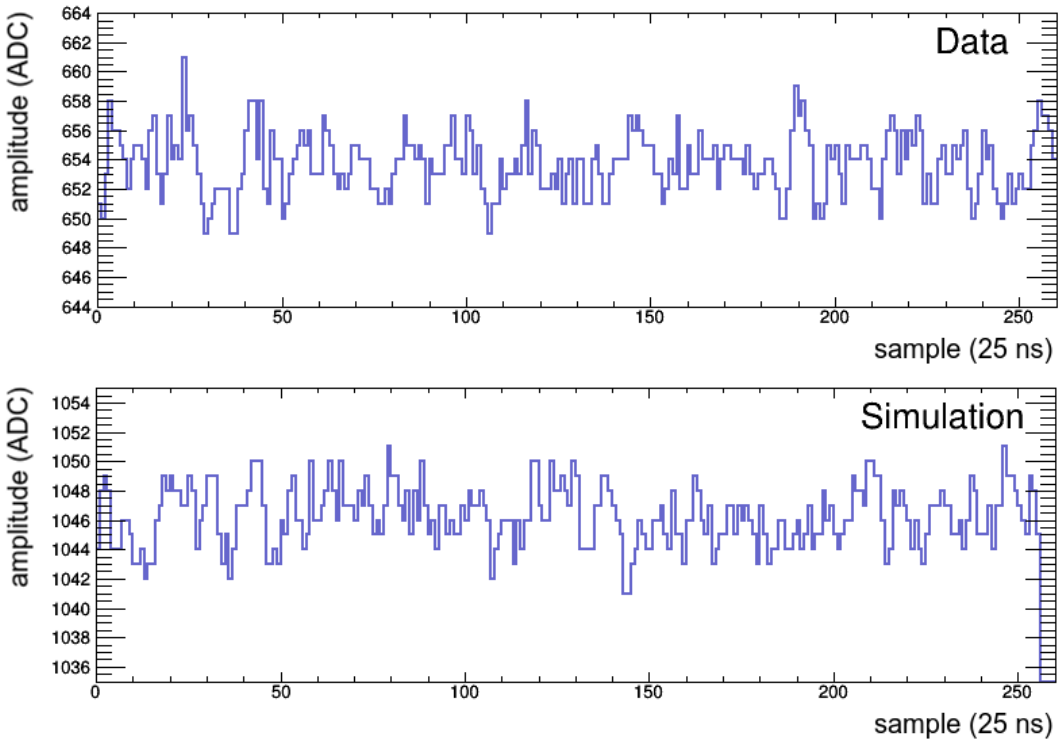

Figure A.0.1: Example of fluctuations in the baseline for data (top) and simulation (bottom).

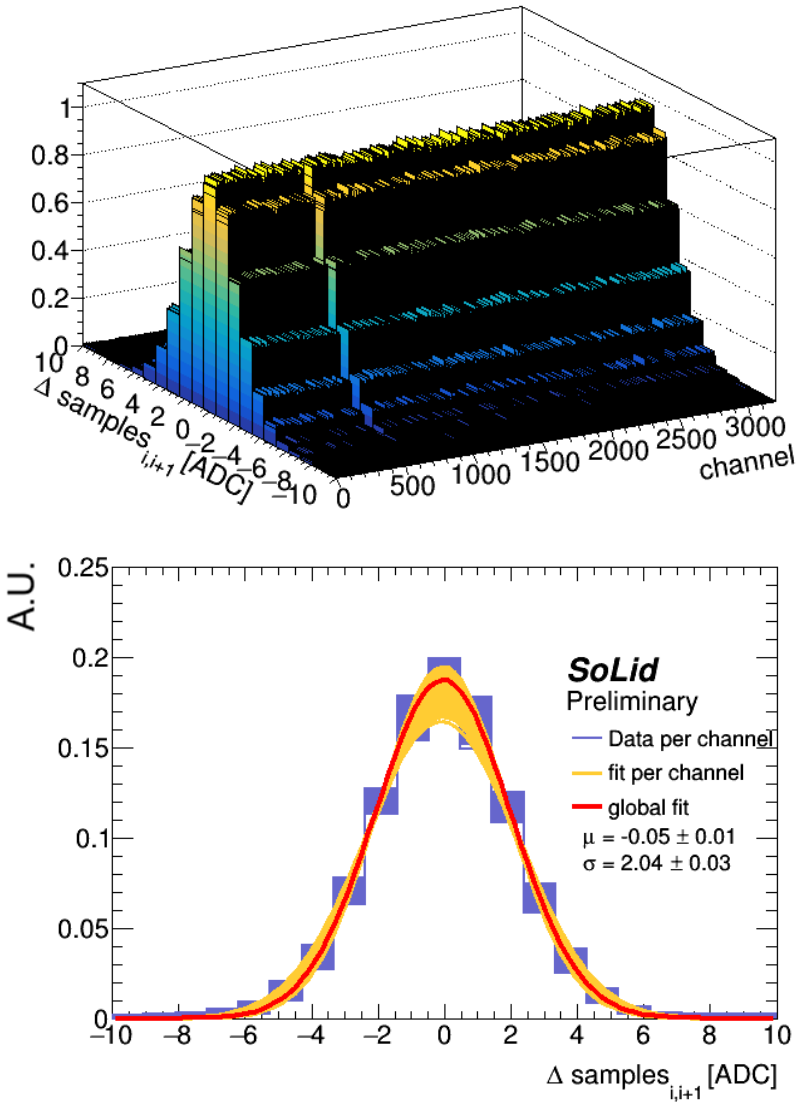

Figure A.0.2: Top: The difference between consecutive data samples in ADC per channel. Bottom: Collection of distributions and corresponding fits of the data sample differences, as well as the global data fit.

The fluctuations on the constant baseline are measured in pure noise data where the zero suppression threshold has not been applied. Figure A.0.1 shows an example of such a noise waveform. The fluctuations exhibit a correlation between successive samples. The difference between consecutive samples is determined for the 3200 channels and shown in the right panel of figure A.0.2. The standard deviation of the Gaussian fits has a small variation over the channels and is on average 2.05 ± 0.03.

In the readoutsimulation, a baseline value is added to each channel separately for the entire signal. Since the baseline will be subtracted during analysis, the exact value is not important. The baseline values are sampled from a normal distribution with a mean value of 800 ADC and a spread of 100 ADC, and the values are communicated to Saffron2. The fluctuation on a sample, Δ_i, is calculated by adding to the fluctuation of the previous sample, Δ_{i-1} a value that is sampled from a Gaussian distribution with $(\mu, \sigma) = (0.2)$. A tendency to return to the baseline is added, to make sure that the

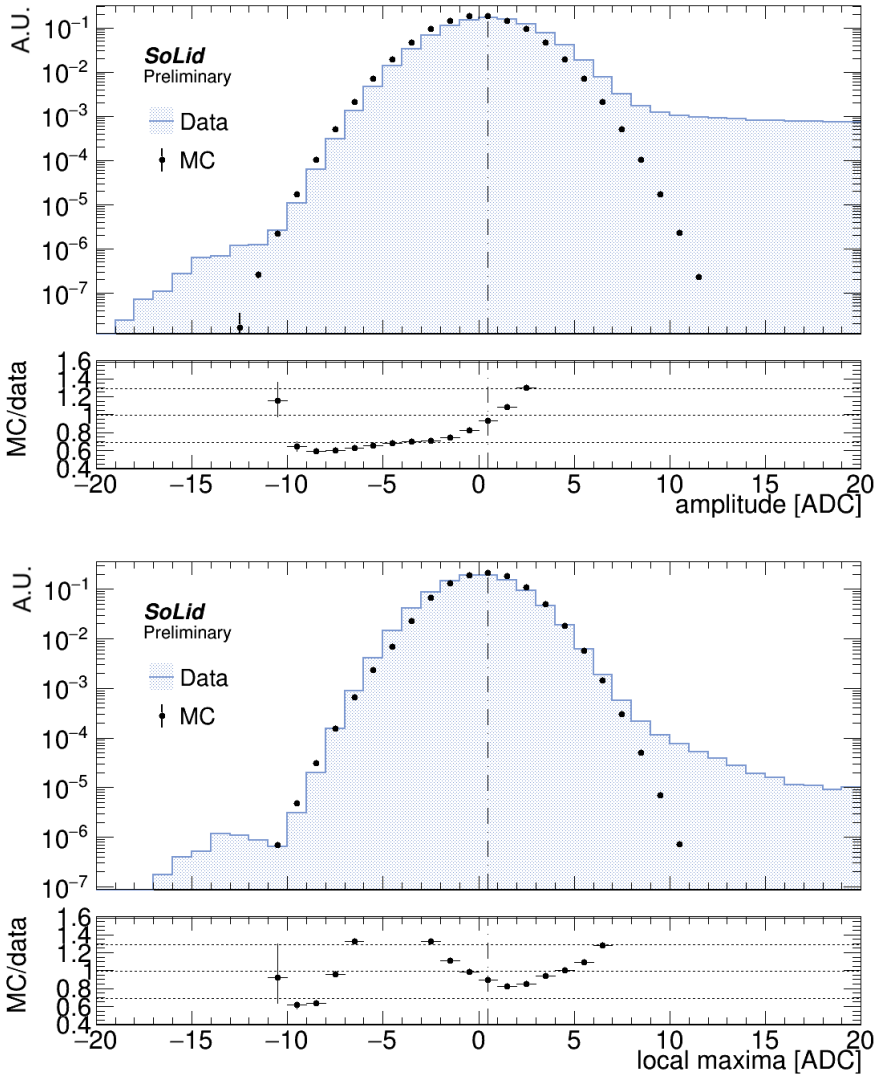

Figure A.0.3: MC data comparisons for the amplitude spectra of the noise (top) and the local maximal in the noise (bottom).

value does not increasingly deviate from the mean baseline value. Note that choosing for each sample a random value would not yield the envisaged result. The samples would not be correlated and be evenly spread around the nominal baseline value, resulting in a jitterish baseline. A comparison of the behavior of the fluctuating baseline in data and MC, is given in figure A.0.1. The spectrum of the noise samples is collected over all channels in the left panel of figure A.0.3. Analogously, the spectrum of the local maxima in the noise is collected in the right panel.

B

LIGHT LEAKAGE

The scintillation photons are guided to sensors outside the detector volume by fibers that run through grooves in the cubes. However, some photons may leak through the fiber, the groove or the tyvek to neighbouring cubes that share a face with the original cube. The leaked photons can enter one of the fibers that run through the neighbour cube and cause a significant signal on the channel [238]. The light leakage has to be accounted for in order to get the right reconstructed energy of an energy deposit and a correct measure of the spread of the signal induced by a particle.

Nuclear signals (NS) from the ^{214}Bi-^{214}Po decay chain are used to study the light leakage. Only NS signals can be considered as single cube interactions and the ^{214}Bi-^{214}Po events occur isolated in space and time. The cube where the interaction occurred is regarded as the central cube. The average waveform is constructed for the channels that go through the affected cube and its neighbouring cubes, and this for the affected plane and the planes next to it. The average total light yield, which is determined as the integral of the waveform, is shown in figure B.0.1 for the channels of interest.

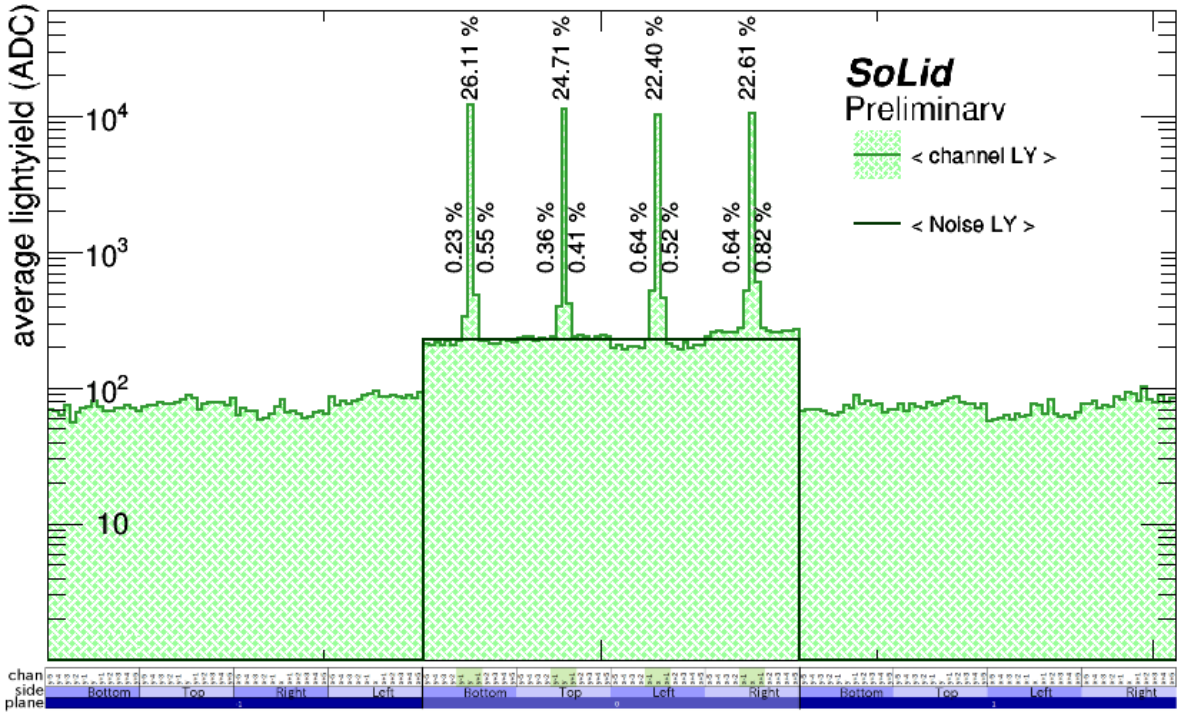

Figure B.0.1: Data: average value of the total light yield that the channels of interest receive.

The distributions to the left and the right of the histogram correspond to the neighbouring planes. The planes are well isolated so there is only a noise contribution. The noise contribution in the central plane is elevated because the zero suppression is lowered in the plane that triggered for readout. The average LY that is caused by the noise in the central plane is indicated on the figure. The excess LY on the central channels comes form the NS signal. Some of the light that was generated in the central cube clearly leaked to the neighbouring cubes and reached the neighbouring channels. The contributions of the twelve central channels to the NS signal are indicated on the figure.

About 4.17% of the LY ended up on the channels that only run through neighbouring cubes. And 95.83% of the LY was measured on the four central channels running through the central cube. Notice that such a fiber also has a contribution from two neighbouring cubes that share a face with the central cube and lie along the fiber. A larger LY is found on the vertical Y channels, especially on the channels that are at the bottom side of the detector. This asymmetry is due to the influence of gravity on the connection between the sensor and the fiber.

In the readout simulation, the scintillation photons, that are generated in the central cube after the energy deposition, are distributed over the central cube and its four neighbouring cubes. Several cubes will feed the same fiber. If x is the fraction of photons that leak away from the central cube, and if the four fibers of a cube each receive 25% of the photons in the cube, then the fraction of photon that end up on a fiber through the central cube is,

$$N_{\gamma,\text{central channel}} = \left(\frac{1}{4}(100-x) + 2\frac{1}{4}\cdot\frac{x}{4}\right)\cdot N_{\gamma,\text{central cube}}. \tag{B.1}$$

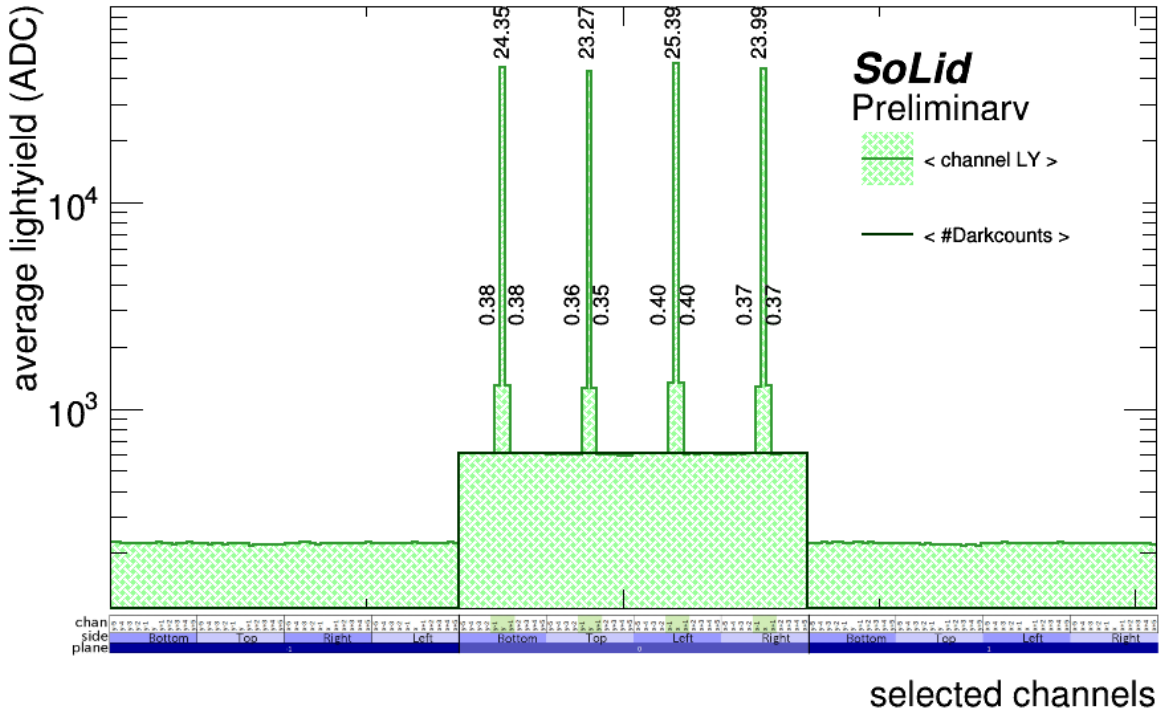

Figure B.0.2: MC: average value of the total light yield that the channels of interest receive.

where the first term is the contribution from the central cube and the other one from the two neighbouring cubes along that fiber. The fraction of photons that end up on a fiber that runs through a neighbouring cube is,

$$N_{\gamma,\text{neighbour channel}} = \frac{1}{4} \cdot \frac{x}{4} \cdot N_{\gamma,\text{central cube}}, \tag{B.2}$$

since a quarter of the leaking photons goes to the neighbour cube and from these, a quarter enters the fiber. Having four fibers through the central cube that receive fraction B.1 and 8 fibers that receive fraction B.2, the total amount adds up to 100%.
The central fibers have to receive the average photon amount of the central fibers in data, which is 23.96%, and the other fibers have to receive on average 0.52%. To obtain the desired number of photons on each fiber, the fraction of x has to be 8.32%. The average integrated waveform on the channels of interest for simulation is shown in figure B.0.2. With respect to data, the noise contribution is more evenly spread for simulation. The asymmetric effects are not implemented in the simulation.

To compare the light leaks between data and simulation, the light yield fractions on the twelve central channels are shown in figure B.0.3. To isolate the light leak effect, the dark count contribution was estimated and subtracted.

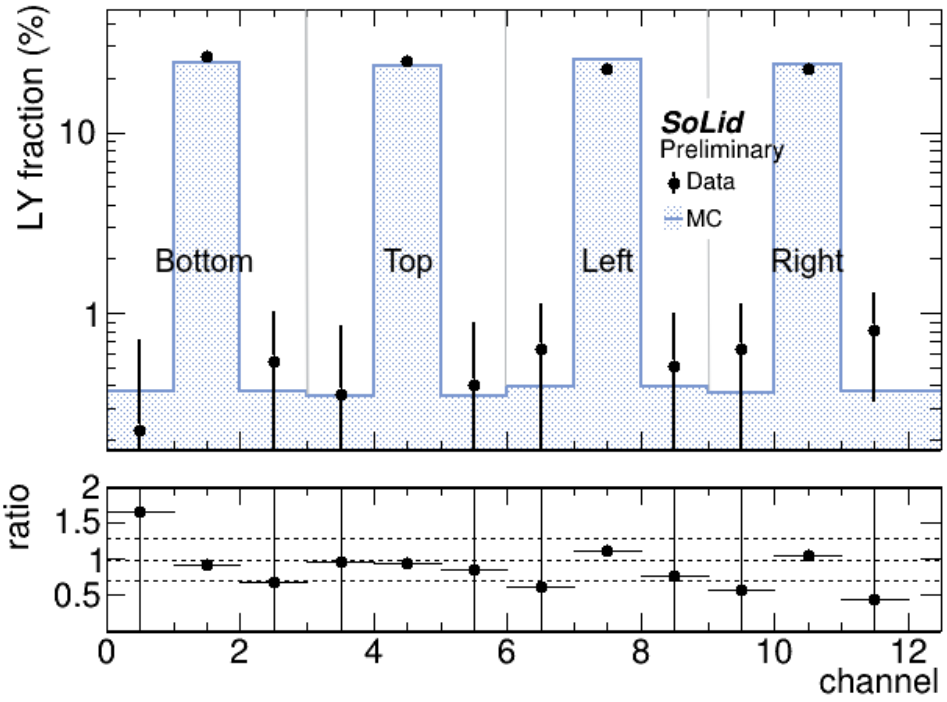

Figure B.0.3: Comparison between data and Monte-Carlo regarding the fraction of light on the central and neighbouring fibers for the four sides of the detector.

LIST OF ABBREVIATIONS

ADC	analog to digital converter
APD	avalanche photo diode
BBN	Big bang nucleosynthesis
BDT	boosted decision tree
BIDASSE	BR2 Integrated Data Acquisition System for Survey and Experiments
BR2	Belgian Research Reactor 2
BSM	Beyond the Standard Model Physics
CaliPSo	calibration plane for SoLid
CC	charged current interaction
CL	Confidence level
CMB	Cosmic microwave background
CMS	center of mass system
CPT	Charge, Parity, and Time Reversal Symmetry
CT	cross talk
CROSS	calibration on site SoLid
DAQ	Data acquisition
DIS	Deep inelastic scattering
DCR	dark count rate
ES	electromagnetic signal
EW theory	Electroweak theory
FoM	figure of merit
FPGA	field programmable gate array
FPNT	false positive neutron trigger
GLIB	gigabit link interface board
HDPE	high density polyethylene
HEU	Highly enriched uranium
HFIR	High Flux Isotope Reactor
HNL	Heavy Neutral Lepton
IBD	inverse beta decay
ILL	Institut Laue-Langevin
IonA	Integral-on-amplitude
KNN	K-Nearest Neighbors
KS test	Kolmogorov-Smirnov test
LArTPC	Liquid Argon Time Projection Chamer
LH	left handed
LY	Light yield
MC	Monte Carlo
MCNP	Monte Carlo N-Particle
MIP	minimally ionizing particle
ML	Machine Learning
MLP	Multi Layer Perceptron
ML-EM	Maximum Likelihood Expectation-Maximisation

MPPC	Multi-pixel photon counter
MSW effect	Mikheyev-Smirnov-Wolfenstein effect
MURE	MCNP Utility for Reactor Evolution
MVA	Multivariate analysis
m.w.e.	meter water equivalent
MWPC	multiwire proportional chambers
NC	neutral current interaction
n.d.f.	number of degrees of freedom
NEMENIX	neutrino measurement non income experiment
NN	Neural network
NS	Nuclear signal
OV	Over voltage
PA	pixel avalanche
PCB	printed circuit board
PDE	Photon detection efficiency
PId	particle identification
PMNS	Pontecorvo Maki Nakagawas Sakata (matrix)
PMT	photomultiplier tube
PoT	peaks over threshold
PSD	pulse shape discrimination
PVT	polyvinyl toluene
QCD	Quantum chromodynamics
QE scattering	quasi elastic scattering
QED	Quantum electrodynamics
RAA	reactor antineutrino anomaly
RH	right handed
RMS	root-mean-square
ROC curve	receiver operating characteristic curve
ROff	reactor off
ROn	reactor on
Saffron2	SoLid analysis framework, version 2
SDQM	SoLid Data Quality Monitor
SiPM	silicon photomultiplier
SM	Standard Model of particle physics
SM1	SoLid module 1
SNU	Solar neutrino unit
SoLid	Search for Oscillations with a 6 Li detector
SSM	Standard Solar Model
TAGS	Total Absorption Gammaray Spectroscopy
TMVA	Toolkit for MultiVariate Analysis
VOI	variable of interest
WLS fiber	wavelength shifting fiber
ZS	zero suppression
νMSM	Neutrino Minimal Standard Model

LIST OF FIGURES

LIST OF TABLES

AUTHOR'S CONTRIBUTIONS

This thesis provides an overview of the work I performed during my Phd. In 2017 and 2018, the SoLid detector was built, installed, commissioned and operated by the collaboration. I contributed to these tasks, by physically assembling the detector cubes and planes in the particle physics laboratory in Ghent and assisting in the installation of the detector next to the BR2 reactor. During data taking periods, I performed remote data quality shifts. As main responsibility I implemented, tuned and maintained the readout simulation.

The SoLid collaboration published several papers to which I contributed directly and indirectly, namely

- SoLid: A short baseline reactor neutrino experiment (December 2020), JINST 16 P02025
- Commissioning and Operation of the Readout System for the SoLid Neutrino Detector (August 2019), JINST 14 P11003
- Development of a Quality Assurance Process for the SoLid Experiment (December 2018), JINST 14 P02014
- Optimisation of the scintillation light collection and uniformity for the SoLid experiment (September 2018), JINST 13 P09005
- Performance of a full scale prototype detector at the BR2 reactor for the SoLid experiment (April 2018), JINST 13 P05005

On behalf of the SoLid collaboration, I made the following contributions to conferences

- Poster and video: Energy response characterisation of the SoLid detector, online Neutrino 2020 conference, organised by Fermilab, Chicago, USA (July 2020)
- Scientific secretary for the neutrino physics session, for the The European Physical Society Conference on High Energy Physics (EPS-HEP), Ghent, Belgium (July 2019)
- Talk: SoLid reactor neutrino detector, WONP conference about Nuclear Physics, Havana, Cuba (April 2019)
- Talk: SoLid reactor neutrino detector, Applied Antineutrino Physics (AAP) conference, California, USA (October 2018). Proceedings can be found here
- Talk: Performance of the SoLid reactor neutrino detector, Particle Physics at Neutron Sources (PPNS) conference, Institut Laue Languevin, Grenoble, France (May 2018). Proceedings can be found here

I got the opportunity to give a lecture at the preconference school of the Nuclear Physics Conference at INSTEC, university of Havana, Cuba, about Neutrino Physics (March 2019).

I was selected to participate as *Early-Career Researcher* to the debate on *the European Strategy for Particle Physics* of the *European Committee of Future Accelerators* (ECFA), CERN, Geneva, Switzerland (November 2019). The debate resulted in the following report: Report on the ECFA Early-Career Researchers Debate on the 2020 European Strategy Update for Particle Physics (February 2019).

I participated in the Neutron Town Meeting, CERN, Geneva, Switzerland (October 2018). The debate resulted in the following paper: Future Opportunities in Accelerator-based Neutrino Physics (December 2018).

In addition, I gave the following outreach talks

- Neutrinos and Beyond the Standard Model Physics, WINAK lezing (May 2021)
- Hoe worden atomen gevormd? Universiteit van Vlaanderen (March 2021), expected online in August
- De productie van illegale kernwapens opsporen, Wetenschap uitgedokterd (November 2020)
- Duizend neutrinos en atoombommen - hoe fundamenteel onderzoek leidt tot gevaarlijk spel, Spectrumlezing, University of Antwerp, (October 2020)
- Winner Press>Speak, Steriel neutrino, waar ben je nu?, Antwerp, Belgium (February 2020)
- Excursion to the BR2 reactor with the student association, SCK-CEN, Mol, Belgium (December 2019)
- Hoe elementaire deeltjes de wereld vormen, Moeilijke Dingen Makkelijk Uitgelegd, Kunstencentrum Vooruit, Ghent, Belgium (November 2019)
- Het spel van de elementaire deeltjes, for Pint of Science, Antwerp, Belgium (May 2019)
- Guest lecture: Elementaire deeltjes en het Standaard Model, Stedelijk Lyceum Hardenvoort, Antwerpen, Belgium (January 2019)
- Jacht op het Neutrino, for Pint of Science, Antwerp, Belgium (May 2018)

BIBLIOGRAPHY

[1] P. Minkowski, *$\mu \to e\gamma$ at a rate of one out of 10^9 muon decays?*, *Physics Letters B* **67** (1977) 421–428.

[2] GEANT4 collaboration, S. Agostinelli et al., *GEANT4: A Simulation toolkit*, *Nucl. Instrum. Meth.* **A506** (2003) 250.

[3] J. Chadwick, *The intensity distribution in the magnetic spectrum of beta particles from radium*, *Verh. Phys. Gesell.* **16** (1914) 383–391.

[4] W. Pauli, *Letter to Lise Meitner*, CERN *Pauli letter collection* (1930) .

[5] E. Fermi, *Tentativo di una teoria dei raggi β*, *La Ricerca Scientifica* **2** (1933) .

[6] S. L. Glashow, *The renormalizability of vector meson interactions*, *Nuclear Physics* **10** (1959) 107–117.

[7] S. Weinberg, *A model of leptons*, *Phys. Rev. Lett.* **19** (1967) 1264–1266.

[8] A. Salam and J. Ward, *Electromagnetic and weak interactions*, *Physics Letters* **13** (1964) 168–171.

[9] A. Pais, *Inward bound: of matter and forces in the physical world*. Clarendon Press, 2002.

[10] F. Reines and C. Cowan, *The Reines-Cowan experiments: Detecting the Poltergeist*, *Los Alamos Science,25* (1997) 4–27.

[11] H. Bethe and R. Peierls, *The neutrino in nature*, *Nature* **133** (1934) 532.

[12] R. Rhodes, *The making of the atomic bomb*. Simon and Schuster, 2012.

[13] U.S. Department of Energy, *The first reactor*. National Technical Information Service, 1982.

[14] C. L. Cowan, F. Reines et al., *Detection of the free neutrino: A Confirmation*, *Science* **124** (1956) 103–104.

[15] W. Pauli, *Telegram from Wolfgang Pauli*, CERN *Pauli letter collection* .

[16] Particle Data Group, *Review of Particle Physics*, *Progress of Theoretical and Experimental Physics* **2020** (2020) .

[17] J. Woithe et al., *Let's have a coffee with the standard model of particle physics!*, *Physics Education* **52** (2017) 034001.

[18] ATLAS collaboration, *Observation of a new particle in the search for the standard model higgs boson with the* ATLAS *detector at the* LHC, *Physics Letters B* **716** (2012) 1–29.

[19] CMS collaboration, *Observation of a new boson at a mass of 125 GeV with the* CMS *experiment at the* LHC, *Physics Letters B* **716** (2012) 30–61.

[20] S. Weinberg, *Dreams of a final theory.* Vintage Books, 1994.

[21] LHCb collaboration, *Test of lepton universality in beauty-quark decays*, 2103.11769.

[22] S. Borsanyi, *Leading hadronic contribution to the muon magnetic moment from lattice QCD*, *Nature* **593** (2021) 51–55.

[23] G. Danby et al., *Observation of high-energy neutrino reactions and the existence of two kinds of neutrinos*, *Phys. Rev. Lett.* **9** (1962) 36–44.

[24] K. Kodama et al., *Observation of tau neutrino interactions*, *Physics Letters B* **504** (2001) 218–224.

[25] S. Schael et al., *(*ALEPH, DELPHI, L*3,* OPAL *and* SLD *collaborations and the* LEP *electroweak working group,* SLD *electroweak group and* SLD *heavy flavour group collaborations), precision electroweak measurements on the Z resonance*, *Physics Reports* **427** (2006) 257–454.

[26] U. Katz and C. Spiering, *High-energy neutrino astrophysics: Status and perspectives*, *Progress in Particle and Nuclear Physics* **67** (2012) 651–704.

[27] S. Odenwald, *How long does it take light to get out from the inside of the sun?*, *Ask the Space Scientist, by* NASA (2012) .

[28] PTOLEMY collaboration, *Neutrino physics with the* PTOLEMY *project: active neutrino properties and the light sterile case*, *Journal of Cosmology and Astroparticle Physics* **2019** (2019) 047–047.

[29] G. Bellini et al., *Observation of geo-neutrinos*, *Physics Letters B* **687** (2010) 299–304.

[30] ICECUBE collaboration, *Neutrino emission from the direction of the blazar TXS 0506+056 prior to the IceCube-170922A alert*, *Science* **361** (2018) 147–151.

[31] KM3NET collaboration, *Sensitivity of the KM3NeT/ARCA neutrino telescope to point-like neutrino sources*, *Astroparticle Physics* **111** (2019) 100–110.

[32] Baikal-GVD collaboration, *High-energy neutrino Astronomy-Baikal-GVD neutrino telescope in lake baikal*, *Symmetry* **13** (2021) .

[33] A. Pietro et al., SNEWS*, the supernova early warning system*, *New Journal of Physics* **6** (2004) 114–114.

[34] A. Pich, *The standard model of electroweak interactions*, 1201.0537.

[35] M. Goldhaber, L. Grodzins and A. W. Sunyar, *Helicity of neutrinos*, *Phys. Rev.* **109** (Feb, 1958) 1015–1017.

[36] N. Cabibbo, *Unitary symmetry and leptonic decays*, *Phys. Rev. Lett.* **10** (1963) 531–533.

[37] M. Kobayashi and T. Maskawa, *CP-violation in the renormalizable theory of weak interaction*, *Progress of Theoretical Physics* **49** (1973) 652–657.

[38] C. S. Wu, E. Ambler, R. W. Hayward, D. D. Hoppes and R. P. Hudson, *Experimental test of parity conservation in beta decay*, *Phys. Rev.* **105** (1957) 1413–1415.

[39] J. A. Formaggio and G. P. Zeller, *From eV to EeV: Neutrino cross sections across energy scales*, *Reviews of Modern Physics* **84** (2012) 1307–1341.

[40] COHERENT collaboration, K. Scholberg, *Observation of Coherent Elastic Neutrino-Nucleus Scattering by* COHERENT, *PoS* **NuFact2017** (2018) 020.

[41] O. Smirnov, *Experimental Aspects of Geoneutrino Detection: Status and Perspectives*, *Prog. Part. Nucl. Phys.* **109** (2019) 103712.

[42] A. Aguilar-Arevalo et al., *The MiniBooNE detector*, *Nuclear Instruments and Methods in Physics Research Section A: Accelerators, Spectrometers, Detectors and Associated Equipment* **599** (2009) 28–46.

[43] MINOS collaboration, *Combined analysis of ν_μ disappearance and $\nu_\mu \to \nu_e$ appearance in* MINOS *using accelerator and atmospheric neutrinos*, *Phys. Rev. Lett.* **112** (2014) .

[44] MINERVA collaboration, *Design, calibration, and performance of the* MINERvA *detector*, *Nuclear Instruments and Methods in Physics Research Section A: Accelerators, Spectrometers, Detectors and Associated Equipment* **743** (2014) 130–159.

[45] J. N. Bahcall, *Solar models and solar neutrinos*, *Physica Scripta* **T121** (2005) 46–50.

[46] J. N. Bahcall, A. M. Serenelli and S. Basu, *New solar opacities, abundances, helioseismology, and neutrino fluxes*, *The Astrophysical Journal* **621** (2005) L85–L88.

[47] B. Aharmim et al., *Electron energy spectra, fluxes, and day-night asymmetries of ^{8}B solar neutrinos from measurements with NaCl dissolved in the heavy-water detector at the Sudbury Neutrino Observatory*, *Physical Review C* **72** (2005) .

[48] M. Altmann et al., *Complete results for five years of* GNO *solar neutrino observations*, *Physics Letters B* **616** (2005) 174–190.

[49] J. Raymond Davis et al., *Measurement of the solar electron neutrino flux with the homestake chlorine detector*, *The Astrophysical Journal* **496** (1998) 505–526.

[50] SAGE collaboration, *Results from* SAGE *(the Russian-American gallium solar neutrino experiment)*, *Physics Letters B* **328** (1994) 234–248.

[51] GALLEX collaboration, W. Hampel et al., *Final results of the Cr-51 neutrino source experiments in* GALLEX, *Phys. Lett. B* **420** (1998) 114–126.

[52] SUPER-KAMIOKANDE collaboration, *Evidence for oscillation of atmospheric neutrinos*, *Phys. Rev. Lett.* **81** (1998) 1562–1567.

[53] A. Bernstein et al., *Report on the depth requirements for a massive detector at homestake*, `0907.4183`.

[54] SUPER-KAMIOKANDE, K2K collaboration, T. Nakaya, *Atmospheric and long baseline neutrino*, *eConf, C020620* (2002) .

[55] B. Pontecorvo, *Inverse beta processes and nonconservation of lepton charge*, *Zh. Eksp. Teor. Fiz.* **34** (1957) 247.

[56] P. Di Bari et al., *Representing seesaw neutrino models and their motion in lepton flavour space*, *Journal of High Energy Physics* **2019** (2019) .

[57] C. Giganti, S. Lavignac and M. Zito, *Neutrino oscillations: The rise of the* PMNS *paradigm*, *Progress in Particle and Nuclear Physics* **98** (2018) 1–54.

[58] S. Bilenky, *Neutrinos: Majorana or dirac?*, *Universe* **6** (2020) 134.

[59] KTeV collaboration, A. Alavi-Harati et al., *Observation of direct CP violation in $k_{S,L} \to \pi\pi$ decays*, *Phys. Rev. Lett.* **83** (1999) 22–27.

[60] BABAR collaboration, B. Aubert et al., *Measurement of CP violating asymmetries in B^0 decays to CP eigenstates*, *Phys. Rev. Lett.* **86** (2001) 2515–2522.

[61] LHCb collaboration, R. Aaij et al., *Observation of CP violation in charm decays*, *Phys. Rev. Lett.* **122** (2019) 211803.

[62] T2K collaboration, *Constraint on the matter-antimatter symmetry-violating phase in neutrino oscillations*, *Nature* **580** (2020) 339–344.

[63] P. B. Denton et al., *CP-violating neutrino nonstandard interactions in long-baseline-accelerator data*, *Physical Review Letters* **126** (2021) .

[64] NOvA collaboration, *First measurement of neutrino oscillation parameters using neutrinos and antineutrinos by NOvA*, *Physical Review Letters* **123** (2019) .

[65] Q. R. Ahmad et al., *Measurement of the rate of $\nu_e + d \to p + p + e^-$ interactions produced by ^8B solar neutrinos at the Sudbury Neutrino Observatory*, *Physical Review Letters* **87** (2001) .

[66] SNO collaboration, B. Aharmim et al., *Measurement of the ν_e and total ^8b solar neutrino fluxes with the sudbury neutrino observatory phase-*III *data set*, *Phys. Rev. C* **87** (Jan, 2013) 015502.

[67] SNO collaboration, B. Aharmim et al., *Combined analysis of all three phases of solar neutrino data from the sudbury neutrino observatory*, *Phys. Rev. C* **88** (Aug, 2013) 025501.

[68] A. M. Serenelli, S. Basu, J. W. Ferguson and M. Asplund, *New solar composition: the problem with solar models revisited*, *The Astrophysical Journal* **705** (oct, 2009) L123–L127.

[69] A. Y. Smirnov, *The MSW effect and matter effects in neutrino oscillations*, *Physica Scripta* **T121** (2005) 57–64.

[70] S. Abe et al., *Precision measurement of neutrino oscillation parameters with KamLAND*, *Physical Review Letters* **100** (2008) .

[71] S. Boyd, *Neutrino Lecture writeups*, *University of Warwick* (2020) .

[72] S. Vagnozzi, *Weigh them all! Cosmological searches for the neutrino mass scale and mass ordering*. Springer International Publishing, 2019, 10.1007/978-3-030-53502-5.

[73] OPERA collaboration, *Observation of a first ν_τ candidate event in the* OPERA *experiment in the CNGS beam*, *Physics Letters B* **691** (2010) 138–145.

[74] I. Esteban et al., *The fate of hints: updated global analysis of three-flavor neutrino oscillations*, *Journal of High Energy Physics* **2020** (2020) .

[75] NOVA collaboration, *First measurement of neutrino oscillation parameters using neutrinos and antineutrinos by NOvA*, *Physical Review Letters* **123** (2019) .

[76] MINOS collaboration, *Measurement of neutrino and antineutrino oscillations using beam and atmospheric data in* MINOS, *Physical Review Letters* **110** (2013) .

[77] M. Jiang et al., *Atmospheric neutrino oscillation analysis with improved event reconstruction in Super-Kamiokande* IV, *Progress of Theoretical and Experimental Physics* **2019** (2019) .

[78] DEEPCORE collaboration, *Determining neutrino oscillation parameters from atmospheric muon neutrino disappearance with three years of IceCube DeepCore data*, *Physical Review D* **91** (2015) .

[79] DAYABAY collaboration, *Improved measurement of the reactor antineutrino flux and spectrum at Daya Bay*, *Chinese Physics C* **41** (2017) 013002.

[80] DOUBLECHOOZ collaboration, *Double Chooz θ_{13} measurement via total neutron capture detection*, *Nature Physics* **16** (2020) 558–564.

[81] RENO collaboration, *Measurement of reactor antineutrino oscillation amplitude and frequency at* RENO, *Physical Review Letters* **121** (2018) .

[82] KAMLAND collaboration, *Reactor on-off antineutrino measurement with KamLAND*, *Phys. Rev. D* **88** (2013) 033001.

[83] KATRIN collaboration, M. Aker et al., *Analysis methods for the first* KATRIN *neutrino-mass measurement*, *Phys. Rev. D* **104** (Jul, 2021) 012005.

[84] A. B. Balantekin and B. Kayser, *On the properties of neutrinos*, *Annual Review of Nuclear and Particle Science* **68** (2018) 313–338.

[85] T. Hambye et al., *Supersymmetric triplet higgs model of neutrino masses and leptogenesis*, *Nuclear Physics B* **602** (2001) 23–38.

[86] R. Foot et al., *See-saw neutrino masses induced by a triplet of leptons*, *Zeitschrift für Physik C Particles and Fields* **40** (1989) 441–444.

[87] GERDA collaboration, *Final results of* GERDA *on the search for neutrinoless double-β decay*, *Phys. Rev. Lett.* **125** (Dec, 2020) 252502.

[88] K. N. Abazajian et al., *Light sterile neutrinos: A white paper*, 1204.5379.

[89] D. Gorbunov and M. Shaposhnikov, *How to find neutral leptons of the νMSM?*, *Journal of High Energy Physics* **2007** (2007) 015–015.

[90] C. Picciotto and M. Pospelov, *Unstable relics as a source of galactic positrons*, *Physics Letters B* **605** (2005) 15–25.

[91] LSND collaboration, I. Stancu, *Further evidence for neutrino oscillations from* LSND*: The $\nu_\mu \to \nu_e$ decay-in-flight channel*, *Prog. Part. Nucl. Phys.* **40** (1998) 167–168.

[92] A. Aguilar et al., *Evidence for neutrino oscillations from the observation of electron anti-neutrinos in a muon anti-neutrino beam*, *Physical Review D* **64** (2001) .

[93] KARMEN collaboration, B. Armbruster et al., *Upper limits for neutrino oscillations $\overline{\nu}_\mu \to \overline{\nu}_e$ from muon decay at rest*, *Phys. Rev. D* **65** (Jun, 2002) 112001.

[94] MINIBOONE collaboration, A. A. Aguilar-Arevalo et al., *Search for electron neutrino appearance at the $\Delta m^2 \sim 1$ eV^2 scale*, *Phys. Rev. Lett.* **98** (2007) 231801.

[95] MINIBOONE collaboration, A. A. Aguilar-Arevalo et al., *Unexplained excess of electronlike events from a 1-GeV neutrino beam*, *Phys. Rev. Lett.* **102** (2009) 101802.

[96] MINIBOONE collaboration, A. A. Aguilar-Arevalo et al., *Event excess in the miniboone search for $\overline{\nu}_\mu \to \overline{\nu}_e$ oscillations*, *Physical Review Letters* **105** (2010) .

[97] A. Aguilar-Arevalo et al., *Significant excess of electronlike events in the MiniBooNE short-baseline neutrino experiment*, *Physical Review Letters* **121** (2018) .

[98] W. Van De Ponteseele, *Search for Electron Neutrino Anomalies with the MicroBooNE Detector*. PhD thesis, Oxford University, 2020.

[99] GALLEX collaboration, *Reanalysis of the* GALLEX *solar neutrino flux and source experiments*, *Physics Letters B* **685** (2010) 47–54.

[100] SAGE collaboration, *Measurement of the response of a Ga solar neutrino experiment to neutrinos from an Ar-37 source*, *Phys. Rev. C* **73** (2006) 045805.

[101] C. Giunti and M. Laveder, *Statistical significance of the gallium anomaly*, *Physical Review C* **83** (2011) .

[102] C. Giunti et al., *The gallium anomaly revisited*, *Physics Letters B* **795** (2019) 542–547.

[103] C. Giunti and T. Lasserre, *eV-scale sterile neutrinos*, *Annual Review of Nuclear and Particle Science* **69** (2019) 163–190.

[104] G. Mention et al., *Reactor antineutrino anomaly*, *Physical Review D* **83** (2011) .

[105] F. Von Feilitzsch, A. A. Hahn and K. Schreckenbach, *Experimental beta spectra from Pu-239 and U-235 thermal neutron fission products and their correlated anti-neutrinos spectra*, *Phys. Lett. B* **118** (1982) 162–166.

[106] N. Haag et al., *Experimental determination of the antineutrino spectrum of the fission products of U-238*, *Physical Review Letters* **112** (2014) .

[107] K. Schreckenbach, G. Colvin, W. Gelletly and F. Von Feilitzsch, *Determination of the anti-neutrino spectrum from U-235 thermal neutron fission products up to 9.5 MeV*, *Phys. Lett. B* **160** (1985) 325–330.

[108] T. A. Mueller et al., *Improved predictions of reactor antineutrino spectra*, *Phys. Rev. C* **83** (2011) 054615.

[109] P. Huber, *Determination of antineutrino spectra from nuclear reactors, Phys. Rev. C* **84** (2011) 024617.

[110] M. Estienne et al., *Updated Summation Model: An Improved Agreement with the Daya Bay Antineutrino Fluxes, Phys. Rev. Lett.* **123** (2019) 022502.

[111] H. Kwon et al., *Search for neutrino oscillations at a fission reactor, Phys. Rev. D* **24** (1981) 1097–1111.

[112] G. Zacek et al., *Neutrino-oscillation experiments at the gösgen nuclear power reactor, Phys. Rev. D* **34** (1986) 2621–2636.

[113] A. A. Kuvshinnikov et al., *Measuring the* $\overline{\nu}_e + p \rightarrow n + e^+$ *cross-section and beta decay axial constant in a new experiment at Rovno NPP reactor. (In Russian), Yad. Fiz.* **52** (1990) 472–479.

[114] G. S. Vidyakin et al., *Detection of Anti-neutrinos in the Flux From Two Reactors, Sov. Phys. JETP* **66** (1987) 243–247.

[115] Y. Declais et al., *Study of reactor anti-neutrino interaction with proton at Bugey nuclear power plant, Phys. Lett. B* **338** (1994) 383–389.

[116] B. Achkar et al., *Search for neutrino oscillations at 15, 40 and 95 meters from a nuclear power reactor at Bugey, Nuclear Physics B* **434** (1995) 503–532.

[117] Z. D. a. Greenwood, *Results of a two-position reactor neutrino-oscillation experiment, Phys. Rev. D* **53** (1996) 6054–6064.

[118] M. Apollonio et al., *Search for neutrino oscillations on a long base-line at the* CHOOZ *nuclear power station, The European Physical Journal C* **27** (2003) 331–374.

[119] A. Gando et al., *Constraints on* θ_{13} *from a three-flavor oscillation analysis of reactor antineutrinos at KamLAND, Physical Review D* **83** (2011) .

[120] Y. Ko et al., *Sterile neutrino search at the* NEOS *experiment, Physical Review Letters* **118** (2017) .

[121] I. Alekseev et al., *Search for sterile neutrinos at the* DANSS *experiment, Physics Letters B* **787** (2018) 56–63.

[122] M. Dentler, J. Kopp et al., *Updated global analysis of neutrino oscillations in the presence of eV-scale sterile neutrinos, Journal of High Energy Physics* **2018** (2018) .

[123] ICECUBE collaboration, M. G. Aartsen et al., *Searches for sterile neutrinos with the IceCube detector, Phys. Rev. Lett.* **117** (2016) 071801.

[124] P. Adamson et al., *Search for sterile neutrinos in* MINOS *and* MINOS+ *using a two-detector fit, Physical Review Letters* **122** (2019) .

[125] M. Maltoni and T. Schwetz, *Sterile neutrino oscillations after first MiniBooNE results, Phys. Rev. D* **76** (2007) 093005.

[126] J. Ashenfelter et al., *The* PROSPECT *reactor antineutrino experiment, Nuclear Instruments and Methods in Physics Research Section A: Accelerators, Spectrometers, Detectors and Associated Equipment* **922** (2019) 287–309.

[127] M. Andriamirado et al., *Improved short-baseline neutrino oscillation search and energy spectrum measurement with the* PROSPECT *experiment at* HFIR, *Physical Review D* **103** (2021) .

[128] N. Allemandou et al., *The* STEREO *experiment*, *Journal of Instrumentation* **13** (2018) P07009–P07009.

[129] H. Almazán et al., *Improved sterile neutrino constraints from the* STEREO *experiment with 179 days of reactor-on data*, *Physical Review D* **102** (2020) .

[130] Y. Abe et al., *Improved measurements of the neutrino mixing angle θ_{13} with the Double Chooz detector*, *Journal of High Energy Physics* **2014** (2014) .

[131] DAYA BAY collaboration, F. P. An et al., *Measurement of the Reactor Antineutrino Flux and Spectrum at Daya Bay*, *Phys. Rev. Lett.* **116** (2016) 061801.

[132] DAYA BAY collaboration, F. P. An et al., *Evolution of the reactor antineutrino flux and spectrum at Daya Bay*, *Phys. Rev. Lett.* **118** (2017) 251801.

[133] *Double Chooz θ_{13} measurement via total neutron capture detection*, *Nature Physics* **16** (2020) 558–564.

[134] RENO collaboration, J. H. Choi et al., *Observation of Energy and Baseline Dependent Reactor Antineutrino Disappearance in the* RENO *Experiment*, *Phys. Rev. Lett.* **116** (2016) .

[135] P. Vogel et al., *Reactor Anti-neutrino Spectra and Their Application to Anti-neutrino Induced Reactions. 2.*, *Phys. Rev. C* **24** (1981) 1543–1553.

[136] J. Hardy et al., *The essential decay of pandemonium: A demonstration of errors in complex beta-decay schemes*, *Physics Letters B* **71** (1977) 307–310.

[137] B. Rubio and W. Gelletly, *Total absorption spectroscopy*, *Romanian Reports in Physics* **59** (2017) 635–654.

[138] M. Fallot, *Very short baseline reactor neutrinos - motivation and overview*, *Neutrino 2020 Conference* (2020) .

[139] SCK-CEN BR2 Website.

[140] Y. Abreu et al., *SoLid: a short baseline reactor neutrino experiment*, *Journal of Instrumentation* **16** (2021) P02025–P02025.

[141] I. Pinera-Hernandez, *BR2 building geometry and model for SoLid* GEANT*4 simulations*, tech. rep., Universiteit Antwerpen, SDB-doc-716-v2, 2017.

[142] SOLID collaboration, Y. Abreu et al., *A novel segmented-scintillator antineutrino detector*, *JINST* **12** (2017) P04024.

[143] M. Verstraeten, *SoLid neutrino detector for reactor monitoring*, in *Applied Antineutrino Physics 2018 Proceedings*, 2019.

[144] SOLID collaboration, Y. Abreu et al., *Performance of a full scale prototype detector at the BR2 reactor for the SoLid experiment*, *JINST* **13** (2018) P05005.

[145] ELJEN technology, *General purpose plastic scintillator EJ-200*, .

[146] D. Brown et al., *Endf/b-viii.0: The 8th major release of the nuclear reaction data library with cielo-project cross sections, new standards and thermal scattering data*, *Nuclear Data Sheets* **148** (2018) 1–142.

[147] Scintacor, *Neutron Screens: Lithium-6 based screens for detection and imaging of thermal neutrons*, .

[148] K. Jansson, A. Al-Adili et al., *Measurement of the* $^6li(n,\alpha)$ *neutron standard cross-section at the* GELINA *facility*, *EPJ Web of Conferences* **122** (2016) 08006.

[149] Dupont, *Dupont Tyvek ®1082D*, .

[150] J. B. Birks, *Scintillations from Organic Crystals: Specific Fluorescence and Relative Response to Different Radiations*, *Proc. Phys. Soc. A* **64** (1951) 874–877.

[151] G. F. Knoll, *Radiation detection and measurement*. John Wiley, 2000.

[152] Saint-Gobain Crystals, *Scintillation products: scintillating optical fibers*, .

[153] K. Kuroda et al., *A scintillating-fibre hodoscope using a position-sensitive photomultiplier*, *Nuclear Instruments and Methods in Physics Research Section A: Accelerators, Spectrometers, Detectors and Associated Equipment* **300** (1991) 259–267.

[154] Hamamatsu photonics, *Technical Information* MPPC *and* MPPC *modules*, .

[155] Y. Abreu et al., *Commissioning and operation of the readout system for the SoLid neutrino detector*, *Journal of Instrumentation* **14** (nov, 2019) P11003–P11003.

[156] A. Vacheret et al., *Characterization and simulation of the response of multi-pixel photon counters to low light levels*, *Nuclear Instruments and Methods in Physics Research Section A: Accelerators, Spectrometers, Detectors and Associated Equipment* **656** (2011) 69–83.

[157] G. Barbarino et al., *Silicon photo multipliers detectors operating in geiger regime*, *ITECH Open Access Publisher* (2011) .

[158] W. Van De Ponteseele, *Characterisation and modelling of correlated noise in silicon photomultipliers for the SoLid experiment*, Master's thesis, Ghent University, 2016.

[159] SOLID collaboration, Y. Abreu et al., *Development of a Quality Assurance Process for the SoLid Experiment*, *JINST* **14** (2019) P02014.

[160] M. Caresana et al., *Real-time measurements of radon activity with the timepix-based* RADONLITE *and* RADONPIX *detectors*, *JINST* **9** (2014) P11023–P11023.

[161] Google, *Golang programming language*, .

[162] S. Vercaemer, *Commissioning of the SoLid experiment for the observation of electron antineutrinos at the BR2 reactor*. PhD thesis, Universiteit Antwerpen, 2018.

[163] L. Ghabrous et al., *IPbus: a flexible Ethernet-based control system for xTCA hardware*, *JINST* **10** (2015) C02019.

[164] S. Vercaemer, *Saffron2 documentation, internal*, tech. rep., Universiteit Antwerpen, 2020.

[165] V. Pestel, *Détection de neutrinos auprès du réacteur BR2 : analyse des premières données de l'expérience SoLid.* PhD thesis, Normandie Université, 2019.

[166] H. Chanal, *The CCube reconstruction algorithm, internal*, tech. rep., 2018.

[167] H. Chanal et al., *Topological reconstruction of IBD candidates, internal*, tech. rep., Université Clermont, SDB-doc-1594-v2, 2020.

[168] ISO, *Reference neutron radiations-part 1 : Characteristics and methods of production, Nuclear Instruments and Methods in Physics Research Section A: Accelerators, Spectrometers, Detectors and Associated Equipment* (2001) .

[169] National Physical Laboratory.

[170] M. Verstraeten, *Plane calibration results for each plane, SDB-doc-1459-v1*, tech. rep., 2019.

[171] B. Guillon and I. Pinera, MCNP/GEANT*4 benchmark for neutron transport in SM1, SoLid collaboration meeting, SDB-doc-245-v1* (2016) .

[172] G. Vandierendonck, *Cosmic and atmospheric background stability with (stopping) muons in the SoLid experiment, ICHEP Conference* (2020) .

[173] C. Moortgat, *The SoLid antineutrino detector: construction and commissioning with cosmic ray muons.* PhD thesis, Ghent University, 2018.

[174] J. Van Muiden, *Determination of the accuracy and precision of BR2, Universiteit Antwerpen, SDB-doc-256-v1*, tech. rep., 2016.

[175] S. Kalcheva et al., *Reactor Core Simulations for Determination of the Antineutrino Spectrum for the SoLid Experiment at BR2 Reactor, Proceedings Monte Carlo* (2017) Jeju, South Korea.

[176] L. Giot et al., *BR2 reactor coupled* MCNPX *and mure simulations for the SoLid experiment (antineutrino detection)*, in *European Research Reactor Conference (RRFM)*, p. 667, 2015.

[177] D. Pelowitz, *MCNPX users manual version 2.7.0, Los Alamos National Laboratory* (2011) .

[178] F. a. Gallmeier, *The cinder90 transmutation code package for use in accelerator applications in combination with* MCNPX, *ICANS XIX proceedings* (2010) .

[179] G. Lehaut, *Reator core simulation to IBD in SoLid with SoLO package, Université de Caen, SDB-doc-256-v1*, tech. rep., 2020.

[180] M. Fallot et al., *BR2 reactor simulation and antineutrino spectrum status , SoLid collaboration meeting, SDB-doc-1364-v1* (2019) .

[181] O. Meplan et al., *MURE, MCNP utility for reactor evolution: couples Monte-Carlo transport with fuel burnup calculations, NEA 1845* (2009) .

[182] J. A. Formaggio and G. P. Zeller, *From eV to EeV: Neutrino cross sections across energy scales, Rev. Mod. Phys.* **84** (2012) 1307–1341.

[183] P. Vogel and J. F. Beacom, *Angular distribution of neutron inverse beta decay, $\overline{\nu}_e + \overline{p} \rightarrow e^+ + n$*, *Phys. Rev. D* **60** (1999) 053003.

[184] I. Pinera-Hernandez and Y. Abreu, *Phase1 geometry model for the* GEANT*4 simulations, internal*, tech. rep., Universiteit Antwerpen, 2020.

[185] L. Kalousis and S. Vercaemer, *SoLid sensitivity contours*, tech. rep., Vrije Universiteit Brussel, Universiteit Antwerpen, SDB-doc-784-v1, 2017.

[186] SOLID collaboration, I. Pinera-Hernandez, *Identification of background components with the SoLid anti-neutrino detector*, in *2016 IEEE Nuclear Science Symposium and Medical Imaging Conference (NSS/MIC), France*, pp. 1–5, 2016. DOI.

[187] A. Demetriades et al., *Geochemical atlases of europe produced by the eurogeosruveys geochemistry expert group*, *Bulletin of the Geological Society of Greece* **43** (2017) 2350.

[188] M. Berger et al., *Stopping-power and range tables for electrons, protons, and helium ions,* NIST *standard reference database 124*, .

[189] R. Trevisi et al., *Natural radioactivity in building materials in the european union: a database and an estimate of radiological significance*, *Journal of Environmental Radioactivity* **105** (2012) 11–20.

[190] *The Environmental Behaviour of Radium: Revised Edition.* No. 476 in Technical Reports Series. International atomic energy agency, Vienna, 2014.

[191] L. Ghys and M. Ianthe, *Internal note on the measurement of the gamma ray background at* BR*2*, .

[192] M. Field, *Verification of the* ISOCS *characterization of the canberra LabSOCS system*, *Canberra* (2014) .

[193] D. Perkins, *Particle Astrophysics, Second Edition.* Oxford Master Series in Physics. OUP Oxford, 2008.

[194] I. Bolognino, *Characterization of the background from spallation muons and muon veto studies*, tech. rep., University of Nantes, SDB-doc-1418-v1, 2019.

[195] J. Granada et al., *Thermal neutron cross section and transport properties of polyethylene*, *Nuclear Instruments and Methods in Physics Research Section A: Accelerators, Spectrometers, Detectors and Associated Equipment* **261** (1987) 573–578.

[196] C. Hagmann et al., *Cosmic-ray shower generator (*CRY*) for monte carlo transport codes*, in *2007* IEEE *Nuclear Science Symposium Conference Record*, vol. 2, 2007. DOI.

[197] M. Guan et al., *A parametrization of the cosmic-ray muon flux at sea-level*, `1509.06176`.

[198] D. Reyna, *A simple parameterization of the cosmic-ray muon momentum spectra at the surface as a function of zenith angle*, `hep-ph/0604145`.

[199] M. Gordon et al., *Measurement of the flux and energy spectrum of cosmic-ray induced neutrons on the ground*, *IEEE Transactions on Nuclear Science* **51** (2004) .

[200] S. Nieswand, *Measurement of the exit characteristics of light from optical multimode plastic fibres* . PhD thesis, Rheinisch-Westfälischen Technischen Hochschule Aachen, 2014.

[201] L. Reichhart et al., *Quenching factor for low energy nuclear recoils in a plastic scintillator*, *Physical Review C* **85** (2011) .

[202] R. Craun and D. Smith, *Analysis of response data for several organic scintillators*, *Nuclear Instruments and Methods* **80** (1970) 239–244.

[203] C. Awe et al., *Measurement of proton quenching in a plastic scintillator detector*, *Journal of Instrumentation* **16** (2021) P02035–P02035.

[204] A. Artikov et al., *Photoelectron yields of scintillation counters with embedded wavelength-shifting fibers read out with silicon photomultipliers*, *Nuclear Instruments and Methods in Physics Research Section A: Accelerators, Spectrometers, Detectors and Associated Equipment* **890** (2018) 84–95.

[205] M. Verstraeten, *Monte-carlo tuning results for each plane, internal*, tech. rep., Universiteit Antwerpen, SDB-doc-1491-v2, 2019.

[206] D. Henaff, *Status of the SoLid experiment*, *ICHEP Conference* (2020) .

[207] M. Verstraeten, *Energy response characterisation of the SoLid detector*, *Neutrino 2020 Conference* (2020) .

[208] A. Rogozhnikov, *Machine Learning for High Energy Physics*, .

[209] J. Stevens and M. Williams, *UBoost: A boosting method for producing uniform selection efficiencies from multivariate classifiers*, *Journal of Instrumentation* **8** (2013) .

[210] A. Hocker et al., TMVA - *Toolkit for Multivariate Data Analysis*, `physics/0703039`.

[211] M. Jachowski, *Multivariate Analysis,* TMVA*, and Artificial Neural Networks*, .

[212] S. Hayashida, *Ibd analysis with machine learning (uBDT)*, tech. rep., SoLid Collaboration Meeting, SDB-doc-1607-v1, 2020.

[213] C. Patrignani et al., *Particle data group: Statistics*, *Chin. Phys. C.* **40** (2016) .

[214] I. Michiels, *Development of the oscillation analysis framework for the SoLid experiment.* PhD thesis, Ghent University, 2020.

[215] A. Atre et al., *The search for heavy Majorana neutrinos*, *Journal of High Energy Physics* **2009** (2009) 030–030.

[216] BOREXINO collaboration, G. Bellini et al., *New limits on heavy sterile neutrino mixing in* ^{8}B *decay obtained with the Borexino detector*, *Phys. Rev. D* **88** (2013) 072010.

[217] C. Hagner et al., *Experimental search for the neutrino decay* $\nu_3 \to \nu_j + e^+ + e^-$ *and limits on neutrino mixing*, *Phys. Rev. D* **52** (1995) 1343–1352.

[218] D. I. Britton et al., *Improved search for massive neutrinos in* $\pi^+ \to e^+ \nu$ *decay*, *Phys. Rev. D* **46** (Aug, 1992) R885–R887.

[219] S. Gninenko et al., *Search for GeV-scale sterile neutrinos responsible for active neutrino oscillations and baryon asymmetry of the universe*, *Advances in High Energy Physics* **2012** (01, 2013) .

[220] T. Asaka, S. Blanchet and M. Shaposhnikov, *The νMSM, dark matter and neutrino masses*, *Physics Letters B* **631** (2005) 151–156.

[221] F. F. Deppisch et al., *Neutrinos and collider physics*, *New Journal of Physics* **17** (2015) 075019.

[222] E. Cortina Gil et al., *Search for heavy neutral lepton production in K^+ decays*, *Physics Letters B* **778** (2018) 137–145.

[223] BELLE collaboration, D. Liventsev et al., *Search for heavy neutrinos at Belle*, *Phys. Rev. D* **87** (2013) 071102.

[224] G. Bernardi et al., *Further limits on heavy neutrino couplings*, *Phys. Lett. B* **203** (1988) 332–334.

[225] NA3 collaboration, J. Badier et al., *Direct Photon Production From Pions and Protons at 200 GeV*, *Z. Phys. C* **31** (1986) 341.

[226] CHARM collaboration, C. Santoni et al., *Searches for decays of heavy neutrinos in the* CHARM *experiment*, in *6th Moriond Workshop: Massive Neutrinos in Particle Physics and Astrophysics*, 1986.

[227] DELPHI collaboration, P. Abreu et al., *Search for neutral heavy leptons produced in Z decays*, *Z. Phys. C* **74** (1997) 57–71.

[228] O. Adriani et al., *Search for isosinglet neutral heavy leptons in Z^0 decays*, *Physics Letters B* **295** (1992) 371–382.

[229] A. de Gouvêa and A. Kobach, *Global constraints on a heavy neutrino*, *Phys. Rev. D* **93** (2016) 033005.

[230] A. C. Vincent et al., *Revisiting cosmological bounds on sterile neutrinos*, *Journal of Cosmology and Astroparticle Physics* **2015** (2015) 006–006.

[231] S. Pascoli et al., *MeV-scale sterile neutrino decays at the Fermilab short-baseline neutrino program*, *Journal of High Energy Physics* **2017** (2017) .

[232] T. Sjöstrand et al., PYTHIA *6.4 physics and manual*, *Journal of High Energy Physics* **2006** (May, 2006) 026–026.

[233] R. Oberer et al., *The use of Tl-208 gamma rays for safeguards, nondestructive-assay measurements*, *University of North Texas Libraries* (2009) .

[234] H. Qiao et al., *Signal-background discrimination with convolutional neural networks in the PandaX-III experiment using MC simulation*, *Science China Physics, Mechanics and Astronomy* **61** (2018) .

[235] R. Arnold et al., *Possible background reductions in double beta decay experiments*, *Nuclear Instruments and Methods in Physics Research Section A: Accelerators, Spectrometers, Detectors and Associated Equipment* **503** (2003) 649–657.

[236] I. Lam, *Internal backgrounds in the water phase of* SNO+, in *XXVIII International Conference on Neutrino Physics and Astrophysics*, p. 397, 2018. DOI.

[237] S. Hayashido, *Recent results of the solid experiment, https://indico.desy.de/event/28202/contributions/105958/EPS-HEP 2021 Conference* (2021) .

[238] M. Verstraeten, *Optical transport in the SoLid detector*, Master's thesis, Universiteit Antwerpen, 2016.